Proceedings

International Conference on Nuclear Science and Technology

Nuclear Society Of Iran | Atomic Energy Organization of Iran | Nuclear Sciences and Technologies Research Institute

Papers on:

Particle Accelerators : Based Large Scale Facilities and Nuclear Physics

*In this booklet, you will find the selected papers presented at the **First International Conference on Nuclear Science and Technology**, held from May 6-8, 2024, in Isfahan, Iran.*
We hope you find it informative and enjoyable!

ICNST 2024

Contact and Accessibility

icnst2024.com
registration@icnst2024.com


بسم الله الرحمن الرحیم

The Conference President's Message
ICNST 2024

Attendees, guests, and colleagues

I would like to warmly welcome you to the first International Conference on Nuclear Science and Technology (ICNST 2024). It has been a real honor and privilege to serve as the president of this conference. The conference this year has brought together an incredible diversity of authors and speakers from universities, government, and industry to share ideas and new perspectives on a wide range of radiation applications, nuclear reactors, particle accelerators, radiation measurements, fusion and plasma, stable and radioactive isotopes, radiation safety and security, nuclear agriculture, fuel cycle, lasers, education and training and nuclear governance.

Climate change, a new topic which has been added to this year's agenda as an important worldwide issue. a matter that has been brought up as a critical concern at the majority of IAEA conferences and nuclear scientific assemblies in recent years.

Panel discussions and exhibitions are being introduced as side activities in an attempt to keep this scientific meeting from becoming one-dimensional and increase its effectiveness.

More than 520 complete papers have been approved for this conference; when combined with the additional panels, get-togethers, and side activities, it is anticipated that over 1000 people will attend in person in the historical and touristic city of Isfahan. We look forward to welcoming participants to share their practical ideas and to enjoy an academical and cultural three days in Isfahan.

I'll close by wishing you everyone an incredible, instructive, and transformative experience during ICNST2024 and I hope that this conference can pave the route for academic materials to be used in industry and everyday life.

Prof. Javad Karimi-Sabet
President of ICNST2024
Javad Karimi-Sabet

welcome statment of scientific secretary ICNST 2024

"In the name of God, the Merciful,

Prior to giving the stage to address this distinguished forum, let me take this opportunity to express our deep gratitude, on behalf of all attendees, for His Excellency Mr. Islami's scientific, educational, and motivational remarks, as well as for his excellent organization of this conference.

I would also like to express our appreciation to His Excellency Dr. Mortazavi, Governor-General of Isfahan Province, for his constructive and useful support in enabling this meeting to take place.

This is a great pleasure and honor to extend a warm greeting to each and every one of you for the International Conference on Nuclear Science and Technology, scheduled from May 6th to May 8th, 2024, in the historic city of Isfahan, Iran.

With the aim of advancing our knowledge of nuclear science and technology, this conference is a major global convergence of experts, researchers, and practitioners. It is a platform for the sharing of creative concepts, the presentation of state-of-the-art research, and the formation of cooperative alliances.

As the scientific secretary of this prestigious event, I am particularly excited about the diverse array of participants expected to grace us with their presence. From the esteemed scientists and engineers of Russian universities and research centers to representatives from Islamic countries, friendly nations, and beyond, this conference promises to be a melting pot of perspectives, experiences, and expertise.

The extensive coverage of this conference is another aspect of its uniqueness. We have nearly 900 participants representing 22 countries around the world. Of the 900 participants, 620 are authors covering 13 major topics. There are 421 papers for oral and poster presentations, with additional documents for publication in ISC journals. There will be 3 plenary sessions, 16 panel discussions, 20 parallel oral presentation sessions, and 3 poster sessions.

Prof. Hosein Afarideh
Scientific Secretariat of ICNST2024

Organizers

Nuclear Society Of Iran (NSI)

Atomic Energy Organization of Iran (AEOI)

Nuclear Science and Technology Research Institute (NSTRI)

Scientific Partnership

International Atomic Energy Agency (IAEA)

Isfahan University

Sharif University

Kurchatov Institute

Amirkabir University of Technology (Tehran Polytechnique)

Shahid Beheshti University

Isfahan University of Technology

Shiraz University

Islamic Azad University

K. N. Toosi University of Technology

Ferdowsi University of Mashhad

Kerman Graduate University of Technology

Sahand University of Technology

University of Tabriz

Islamic World Scieence Citation Center

Journal of Nuclear Science and Technology (JonSat)

Radiation Physics and Engineering journal

Nuclear Watch

Cooperative Organization

Isfahan Governorate

Isfahan Municipality

Abbasi Hotel

Iran Atomic Energy Production & Development Co.

Iran's Nuclear Raw Materials & Fuel Production Co.

Radiation Application Development Co.

Ofogh Consulting Engineers Co.

Nuclear Power Plant Safety Development & Promotion Co.

Nuclear Power Plant Engineering & Construction Co.

Engineering & Design of Industrial Simulator Co.

Energy Industry Development Engineering Co

Atomic Power Plant Pepair & support

Nuclear Reactors Fuel Co.

Iran Radioactive Waste Management Co.

Mesbah Energy Co.

Iran Gharb Industrial, Mining and Energy Co.

Pars Isotope Co.

Center for Laser Science & Technology of Iran

Centrifuge Production of Iran Co.

Plasma Technology Development Co.

Rasa Technology and Innovation Center

Behyaar Sanaat Sepahan Co.

Nuclear Data Base of Iran (NDB)

Parto think tank (strategic studies of nuclear industry development)

International Conference Alerts

Local Scientific Board

RAW	NAME	ROLE	AFFILIATION
1	**Prof. Hossein Afarideh**	**Chairman of Local Scientific Board**	**Amirkabir University of Technology (Tehran Polytechnique)(AUT)**
2	**Prof. Mohammad Ghanadi Maragheh**	**Member of The Local Scientific Board**	**Nuclear Science and Technology Research Institute of Iran (NSTRI)**
3	**Prof. Mohammad Lamei Rashti**	**Member of The Local Scientific Board**	**Nuclear Science and Technology Research Institute of Iran (NSTRI)**
4	**Prof. Mohammad Bagher Ghofrani**	**Member of The Local Scientific Board**	**Sharif University of Technology (SUT)**
5	**Prof. Hosein Faghihian**	**Member of The Local Scientific Board**	**University of Isfahan (UI)**
6	**Prof. Javad Rahighi**	**Member of The Local Scientific Board**	**Institute for Research in Fundamental Sciences (IPM)**
7	**Prof. Seyed Amirhossein Feghhi**	**Member of The Local Scientific Board**	**Shahid Beheshti University (SBU)**

Scientific Committee

RAW	NAME	ROLE	AFFILIATION
1	**Prof. Ali Akbar Salehi**	**Member of The Scientific Committe**	**Sharif University of Technology (SUT)**
2	**Prof. Seyyed Javad Ahmadi**	**Member of The Scientific Committe**	**Nuclear Science and Technology Research Institute of Iran (NSTRI)**
3	**Prof. Farhoud Ziaee**	**Member of The Scientific Committe**	**Nuclear Science and Technology Research Institute of Iran (NSTRI)**
4	**Prof. Saeed Hamidi**	**Member of The Scientific Committe**	**University of Arak**
5	**Prof. Seyedzafarollah Kalantari**	**Member of The Scientific Committe**	**Isfahan University of Technology (IUT)**
6	**Prof. Naser Bagheri Moghaddam**	**Member of The Scientific Committe**	**National Research Institute for Science Policy (NRISP)**
7	**Prof. Naser Vosoghi**	**Member of The Scientific Committe**	**Sharif University of Technology (SUT)**
8	**Prof. Seied Rabi Mahdavi**	**Member of The Scientific Committe**	**Iran University of Medical Sciences**
9	**Prof. Meisam Torab Mostaedi**	**Member of The Scientific Committe**	**Nuclear Science and Technology Research Institute of Iran (NSTRI)**
10	**Prof. Fereydoun Abbasi Davani**	**Member of The Scientific Committe**	**Shahid Beheshti University (SBU)**
11	**Prof. Seyed Farhad Masoudi**	**Member of The Scientific Committe**	**K.N.Toosi University of Technology**
12	**Prof. Rasool Ruknizadeh**	**Member of The Scientific Committe**	**University of Isfahan (UI)**
13	**Prof. Gholamreza Raeesali**	**Member of The Scientific Committe**	**Nuclear Science and Technology Research Institute of Iran (NSTRI)**
14	**Prof. Asghar Sedighzadeh**	**Member of The Scientific Committe**	

15	**Prof. Hossein Kazeminejad**	**Member of The Scientific Committe**	**Nuclear Science and Technology Research Institute of Iran (NSTRI)**
16	**Prof. Seyyed Jaber Safdari**	**Member of The Scientific Committe**	**Nuclear Science and Technology Research Institute of Iran (NSTRI)**
17	**Prof. Omid Reza Kakuee**	**Member of The Scientific Committe**	**Nuclear Science and Technology Research Institute of Iran (NSTRI)**
18	**Prof. Alireza Keshtkar**	**Member of The Scientific Committe**	**Nuclear Science and Technology Research Institute of Iran (NSTRI)**
19	**Prof. Fereshte Haj esmail Beigi**	**Member of The Scientific Committe**	**Nuclear Science and Technology Research Institute of Iran (NSTRI)**
20	**Prof. Masoud Mahjour-shafiei**	**Member of The Scientific Committe**	**Nuclear Science and Technology Research Institute of Iran (NSTRI)**
21	**Prof. Mahmoud Payami Shabestar**	**Member of The Scientific Committe**	**Nuclear Science and Technology Research Institute of Iran (NSTRI)**
22	**Prof. Ali Bahrami Samani**	**Member of The Scientific Committe**	**Nuclear Science and Technology Research Institute of Iran (NSTRI)**
23	**Dr. Farhanaz Motamedi**	**Member of The Scientific Committe**	**Nuclear Science and Technology Research Institute of Iran (NSTRI)**
24	**Dr. Faezeh Rahmani**	**Member of The Scientific Committe**	**K.N.Toosi University of Technology**
25	**Dr. Ebrahim Moghiseh**	**Member of The Scientific Committe**	**Nuclear Science and Technology Research Institute of Iran (NSTRI)**
26	**Dr. Iraj Jabari**	**Member of The Scientific Committe**	**University of Isfahan (UI)**
27	**Dr. Nima Ghal-Eh**	**Member of The Scientific Committe**	**Ferdowsi University of Mashhad**
28	**Dr. Mitra Athari Alaf**	**Member of The Scientific Committe**	**Islamic Azad University Science and Research Branch**
29	**Dr. Gholamreza Etaati**	**Member of The Scientific Committe**	
30	**Dr. Amir Movafeghi**	**Member of The Scientific Committe**	**Nuclear Science and Technology Research Institute of Iran (NSTRI)**

Executive Committee

RAW	NAME	ROLE
1	Dr. Farshad Ghasemi	Chairman of the Executive Committee
2	Dr. Ehsan Molazadeh	Member of The Executive Committee
3	Dr. Seyyed Ghasem Biniaz	Member of The Executive Committee
4	Mr. Aliakbar Aminidoust	Member of The Executive Committee
5	Ms. Fatemeh Zamani	Member of The Executive Committee
6	Ms. Mahya Pazoki	Member of The Executive Committee
7	Mr. Hosein Maleki	Member of The Executive Committee
8	Mr. Maziar Dalili	Member of The Executive Committee
9	Mr. Shojaei	Member of The Executive Committee
10	Ms. Fatemeh Rezaei	Member of The Executive Committee
11	Mr. Reza Rafiei	Member of The Executive Committee
12	Ms. Seyyedeh Elham Ebrahimi	Member of The Executive Committee

Particle Accelerators：Based Large Scale Facilities and Nuclear Physics

Particle Accelerators : Based Large Scale Facilities and Nuclear Physics

ICNST 2024
International Conference on Nuclear Science and Technology
6- 8 MAY 2024 | Isfahan, Iran

Analysis of the Microscopic Details and Components of the Nuclear Fission for Protactinium Nuclei (Paper ID : 1041)

Sepiani M. [1*], Nasri Nasrabadi M[1,2]

[1] *Faculty of Physics, University of Isfahan, Isfahan, Iran*
[2] *Joint Institute for Nuclear Research (JINR), Dubna, Moscow Region, 141980, Russia*

Abstract

The nuclear fission of protactinium nuclei is a complex process influenced by an intricate interplay of nuclear components and microscopic details. This study presents a comprehensive analysis of the fission mechanism for $^{231\text{-}232}$Pa, emphasizing the role of parameters of fission barriers, static and dynamic deformations, the model predictions of nuclear level densities (NLD) at the fission saddle points and its change compared to the ground state, fission models and fission dynamics. Through a combination of theoretical modeling and advanced simulation techniques using nuclear reaction and evaporation codes, the neutron induced fission cross sections of ^{231}Pa is calculated and illustrate the profound impact of NLD on the static and dynamic deformations landscape. Our findings are corroborated with experimental data, which serve as benchmarks for the veracity of the proposed models. It is shown that the NLDs at saddle points have a significant effect on reaction results and fission path determination. It is shown that the effect of nuclear dynamic deformations should be included in the nuclear level density on the fission barriers so that the modeling can reproduce the experimental data. This study can be essential for understanding the behavior of nuclear reactors and the development of nuclear energy.

Keywords: Nuclear fission, Nuclear level density, Saddle points, Fission barriers, 231-Protactinium

Introduction

The multifaceted nature of neutron-induced competitive nuclear fission encapsulates a treasured yet intricate dynamical phenomenon, which holds a considerable significance in both fundamental physics and applied nuclear technology. It provides an exceptional window into the interplays between microscopic particle interactions and macroscopic statistical processes, which govern the stability and the eventual division of an atomic nucleus. This research delves into the core components critical to explicating neutron-induced competitive nuclear fission, with a concentrated focus on ^{231}Pa - an isotope whose fission characteristics lead to significant implications for both advanced reactor technology and nuclear waste transmutation. The intricacy of nuclear fission unfolds from the multifaceted interplay between neutrons and the target nucleus, where the formation of a compound nucleus and its subsequent passage over the

fission barrier entail a sophisticated sequence of quantum and thermodynamic events. The study of ^{231}Pa fission presents an exceptional opportunity to deepen our understanding of nuclear processes due to its unique position away from the beta-stability line, thereby challenging existing theoretical models. This research endeavors to dissect the intricacies of ^{231}Pa fission through the advanced nuclear reaction codes and theoretical modeling, primarily focusing on the nuclear level density (NLD) at the ground state and at the saddle point—the position where the nucleus contorts into a potential energy state favorable for fission. Our analysis quantitatively distinguishes the disparity in NLD between these two crucial stages, shedding light on its implications for the fission process. A pivotal focus is placed on the effects that dynamic (shapes and vibrations that occur during the fission process) and static deformations (inherent shapes at equilibrium) have on the NLD, thereby expanding our understanding of the microscopic origins of nuclear properties. Furthermore, this study rigorously evaluates the interaction between the NLD and the barrier parameters in shaping the fission cross-section calculations, challenging existing predictive capabilities. The NLD represents a cornerstone for characterizing the fission landscape; thus, our investigation delineates the stark contrast in NLD between the ground state and the saddle point. Key hypotheses suggest that dynamic and static deformations play a pivotal role in the modulation of NLD—affecting the perceived energy barriers that govern the likelihood of fission. In tandem with these deformations, this study scrutinizes the concomitant effects on fission cross-section calculations, which are heavily influenced by both NLD and the characteristic parameters of barrier heights and curvatures. Many theoretical models have been developed that investigate NLD and its related parameters under different conditions [1-19]. Several well-known and widely used models are used in reaction codes including the phenomenological models (the constant temperature model (CTM)[1] , the back-shifted Fermi gas model (BFG)[2] and the Generalized superfluid model (GSM)[20]) and the microscopic models[21-26]. We explore NLD models to ascertain the degree to which various theoretical approaches can replicate experimental observations. The fission barrier parameters (height and curvature) are amongst the most intricate aspects influencing fission probabilities. These barrier parameters directly correlate with the likelihood of the nucleus to undergo fission upon neutron absorption, thus playing an indispensable role in the estimation of fission probabilities. This comprehensive investigation elucidates the sophistication imbued within the fission of ^{231}Pa, highlighting the pivotal effects of NLD variation from ground state to saddle point, accompanied by the critical influence of barrier parameters. This research not only represents a significant stride in understanding neutron-induced fission mechanisms but also exemplifies the symbiotic relationship between advanced theoretical frameworks and practical applications in nuclear science. It is shown that the use of

different NLD models has a significant effect on the calculation of the competitive fission cross-section, and the NLD at the saddle points can have a very different behavior compared to the ground state. The behavior of NLD at saddle points depends on the dynamic deformation of nucleus and how to account for collective and shell effects.

Key Components of Competitive Fission

When a neutron collides with a target nucleus, it may be absorbed, leading to the creation of a compound nucleus (in an excited state). The compound nucleus undergoes de-excitation through various competitive channels. These channels include Gamma or Particle Emissions and Fission. In fact, at low excitation energies, the fission process occurs relatively slowly and competes with the evaporation processes from the compound nucleus that are studied by the Hauser-Feshbach formalism [27]. In this formalism, the decay probability through channel β is obtained from the ratio of transmission coefficient of channel β to the sum of transmission coefficient of all channels ($P_\beta = T_\beta / \sum T_\gamma$). The fission channel is very different compared to other channels because this channel is not directly related to the remaining nuclei of the compound nucleus that has undergone fission. The phase space of the final products has no effect on the reaction at the moment when the decision to split is made. Therefore, for a given compound nucleus energy level $J^{\pi_{CN}}_{CN}$, there is only one fission transmission coefficient. In some models that describe the fission of heavy nuclei (transition state model), the NLD of the fissile nucleus on the fission barriers (density of transition states) and the height and shape of the fission barrier play a decisive role in determining the probability of this channel. Fission transmission coefficient is usually calculated using the Hill-Wheeler model and based on the transition state model proposed by Bohr [28, 29]. The Hill-Wheeler expression determines the probability of quantum tunneling through a barrier with height B_f and width $\hbar\omega_f$ for a compound nucleus with excitation energy E^*_{CN}:

$$T_f^{HW}(E^*_{CN}) = \frac{1}{1+\exp\left[-2\pi\dfrac{(E^*_{CN}-B_f)}{\hbar\omega_f}\right]} \qquad (1)$$

In the transition state model shown in Fig.1, the fission process occurs through intermediate states of the compound nucleus, and the probability of fission is determined by the density of these intermediate levels.

The ground state excitation energy of the nucleus expressed as a function of deformation shows a bump which is the ground state barrier. On the top of this barrier, there may be several levels of the compound nucleus, and a fission barrier is assigned to each of these levels, which are called transition states. In the first-order approximation, the barrier of transition states is equal to the barrier of the ground state, which is shifted by the energy of the transition states relative to the peak of the barrier of the ground state. The transmission coefficient for a transition state with excitation energy ε_i above the peak of the fission barrier *i* become [30]:

$$T_f^{HW}(E_{CN}^*, \varepsilon_i) = \frac{1}{1+\exp\left[-2\pi \frac{(E_{CN}^* - B_f - \varepsilon_i)}{\hbar\omega_f}\right]} \quad (2)$$

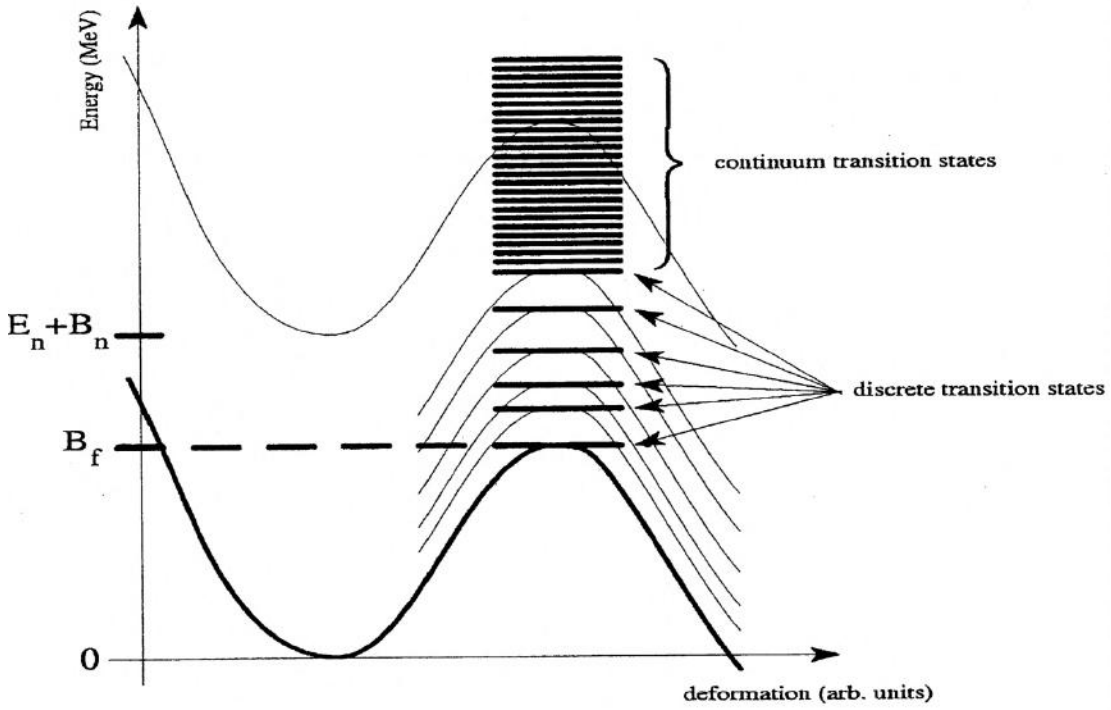

Fig. 1. Potential energy as a function of deformation (single-humped barrier)[30, 31].

For a compound nucleus with spin and parity $J_{CN}^{\pi_{CN}}$, all fission barriers associated with transition states with spin and parity $J_{CN}^{\pi_{CN}}$ will participate in the fission process. Therefore, the total fission transmission coefficient is equal to the sum of the individual fission coefficients for each barrier that may be tunneled through:

$$T_f^{J_{CN}^{\pi_{CN}}}(E_{CN}^*) = \sum_i T_f^{HW}(E_{CN}^*).\delta(i, J_{CN}^{\pi_{CN}}) + \int_{E_{Th}}^{E_{CN}^*} \rho_f(\varepsilon, J_{CN}, \pi_{CN}).T_f^{HW}(E_{CN}^*, \varepsilon).d\varepsilon \qquad (3)$$

Where $\rho_f(\varepsilon, J_{CN}, \pi_{CN})$ is the fission NLD (density of transition states) in the deformation of the fission saddle point. In this expression, if the spin and parity of the transition state are the same as the compound nucleus, then $\delta(i, J_{CN}^{\pi_{CN}}) = 1$ and otherwise $\delta(i, J_{CN}^{\pi_{CN}}) = 0$.

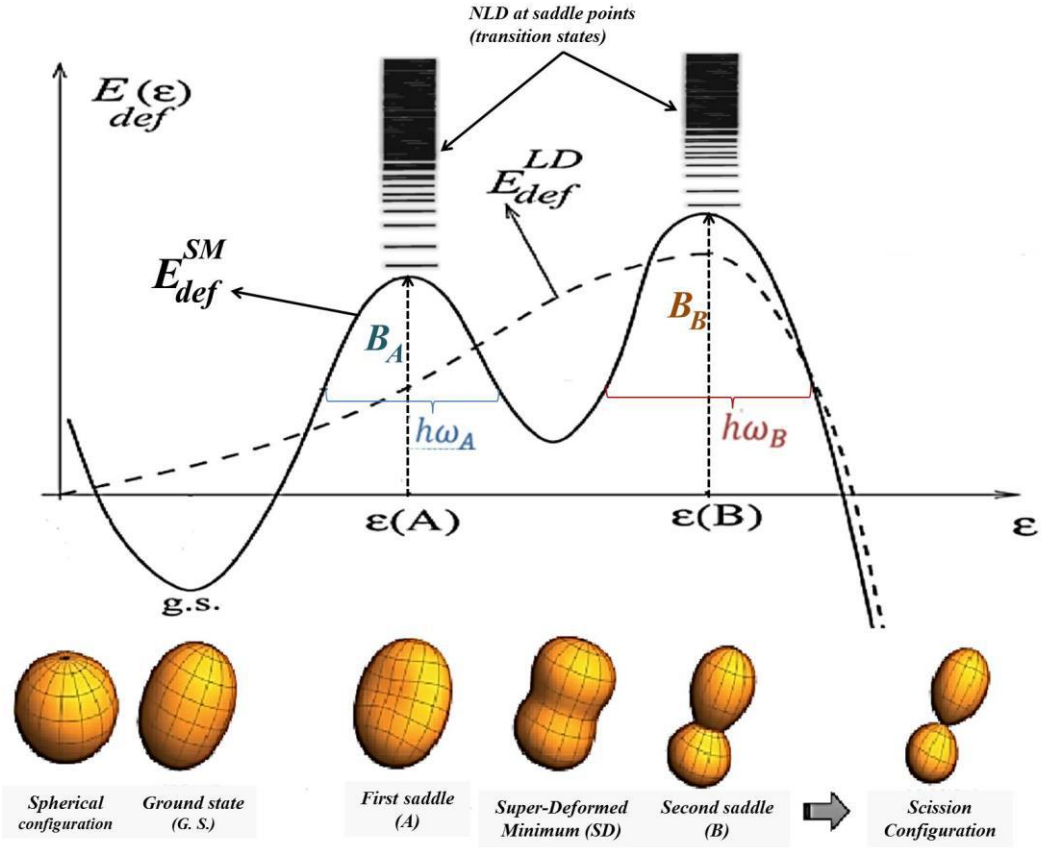

Fig. 2. Potential energy as a function of deformation (double-humped barriers) and fission dynamic [30, 31].

As shown in Fig.2, in many cases (especially in the mass region of actinides), multi-humped fission barriers (two or three peaks) are observed, which must be crossed in addition to the first barrier for fission to occur. The change in the shape of the fission barriers compared to the prediction of the liquid drop model (LD) and the creation of these multi-humped barriers is due to the application of shell effects (SM). Usually, a simple approximation can be sufficient to solve the multi-humped barriers problem. In the case of double-humped barriers, first, for each of the fission barrier A and B, the fission transmission coefficients are calculated. Then it is assumed that it is possible to separate the tunneling process through these two barriers

(such as the formation and decay of the compound nucleus) and express it as two separate stages (independence hypothesis). First, we calculate the probability of crossing the first barrier T_A, and then we multiply it by the probability of splitting. Once the first barrier is crossed, there are two possibilities: either crossing the barrier A and turning back with probability T_A, or splitting through the barrier B with probability T_B.

Therefore, as in the case of the probability of decay into an exit channel ($P_\beta = T_\beta / \sum T_\gamma$), it is obvious that the probability of splitting after passing the first barrier will be:

$$P_{fission} = \frac{T_B}{T_A + T_B} \tag{4}$$

As a result, the effective fission transmission coefficient for the double-humped barriers is:

$$T_{eff}^{J_{CN}^{\pi CN}} = \frac{T_A^{J_{CN}^{\pi CN}} . T_B^{J_{CN}^{\pi CN}}}{T_A^{J_{CN}^{\pi CN}} + T_B^{J_{CN}^{\pi CN}}} \tag{5}$$

In the case of the three-humped barriers, using the independence hypothesis leads to the following effective transmission coefficient:

$$T_{eff}^{J_{CN}^{\pi CN}} = \frac{T_{AB}^{J_{CN}^{\pi CN}} . T_C^{J_{CN}^{\pi CN}}}{T_{AB}^{J_{CN}^{\pi CN}} + T_C^{J_{CN}^{\pi CN}}} \tag{6}$$

where, $T_{AB}^{J_{CN}^{\pi CN}}$ is the previous transmission coefficient of the double barrier.

Fission level density

The NLD of the fissile nucleus in the deformation of the fission saddle point (on the fission barrier) and the parameters of the barrier are related. In the NLD of the deformed nuclei, the effects of deformation, shell and paring correlation are very effective. Since the phenomenological NLD models (based on Fermi gas model) do not take into account the important effects of deformation, the collective effects caused by deformation are included in NLD in both explicit and effective (implicit) ways. In the explicit method, the collective effects are multiplied as increasing factors in the intrinsic NLD:

$$\rho_{def}(E_x, J, \pi) = K_{Rot}(E_x, J)\rho_{\text{int}}(E_x, J, \pi) \quad (7)$$

Where collective rotational factor is $K_{Rot} = \sigma^2_{cut-off\perp} = 0.01389A^{5/3}(1+\beta_2/3)\sqrt{E_{ex}/a}$ for ground state deformation and axially symmetric nuclei. K_{Rot} for barriers depends on the type of symmetry or asymmetry of barriers. For axially asymmetric in barriers:

$$K_{Rot} = \left[\sqrt{\frac{\pi}{2}}\sigma^2_{cut-off\perp}(1+2\beta_2/3)\sigma^2_{cut-off\parallel} - 1\right] f(E_{ex}) + 1 \quad (8)$$

Where $\sigma^2_{cut-off\parallel} = 0.01389A^{5/3}\sqrt{aE_{ex}}/\tilde{a}$ and $f(E_{ex}) = 1/\left(1+exp\left(E_{ex} - E^{bar}_{col}/d^{bar}_{col}\right)\right)$ are parallel spin cut off parameter and a combination of Fermi functions (Where $E^{bar}_{col} = 45MeV, d^{bar}_{col} = 5MeV$), respectively.

In the effective (implicit) treatment, the effective NLD parameter (NLDP) is calculated for each saddle point. All phenomenological models of NLD at energies higher than a few MeV (after matching energy E_M) use the well-known Fermi gas relation[3]:

$$\rho_{FG}(U) = \frac{\sqrt{\pi}}{12}\frac{e^{2\sqrt{aU}}}{a^{1/4}U^{5/4}} \quad (9)$$

Where *a* is energy-dependent NLDP (to account for shell effects) [32-34]:

$$a(E_{ex}) = \tilde{a}\left(1+\delta W\frac{1-exp(-\gamma E_{ex})}{E_{ex}}\right) \quad (10)$$

Where δW is the shell correction energy and damping function of shell effects is $1-\exp(-\gamma E_{ex})/E_{ex}$ and the damping parameter (γ) determines the rate of approach of $a(E_x)$ to $\tilde{a} = \alpha A + \beta A^{2/3}$ (α&β&γ are global parameters [35]). The effective asymptotic NLDP for fission barrier is expressed as [30, 36]:

$$\tilde{a}^{eff} = \frac{A}{13}f(E_{ex}) + \tilde{a}(1-f(E_{ex})) \quad , \quad f(E_{ex}) = 1/\left[1+exp-\left(\left(E_{ex} - E^{bar}_{col}\right)/d^{bar}_{col}\right)\right] \quad (11)$$

Where $E^{bar}_{col} = 30MeV, d^{bar}_{col} = 5MeV$.

Results and discussion

First, by using TALYS nuclear reaction code [30] and all phenomenological and microscopic models of NLD without collective effect, the cross section of ^{231}pa fission reaction induced by neutron is calculated and compared with experimental data. The results of these calculations are shown in Fig.3.

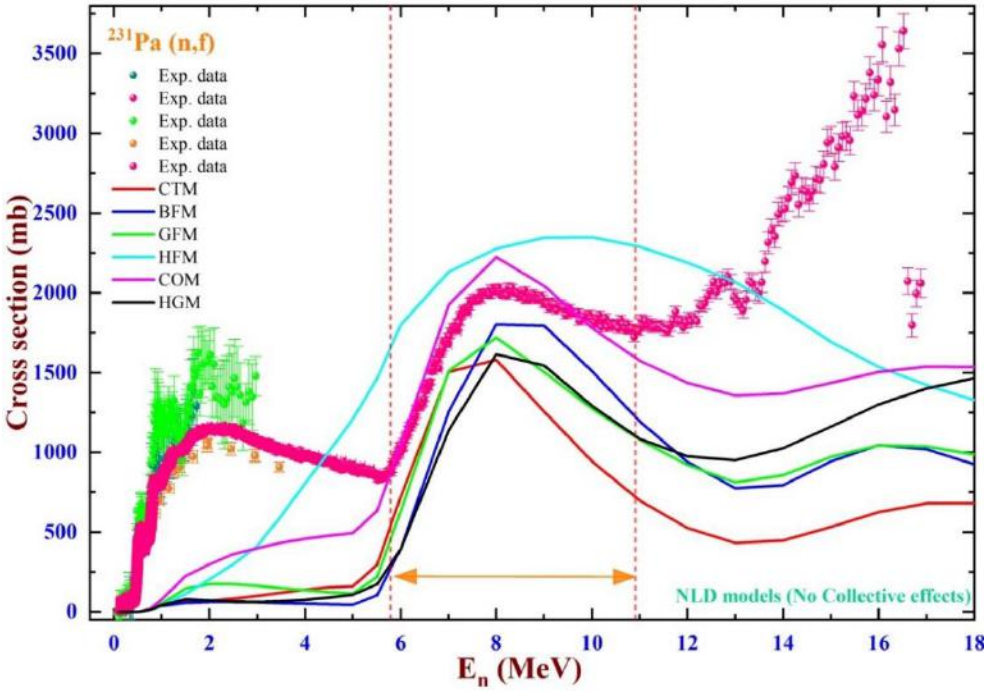

Fig. 3. Fission cross section calculations using various NLD model without collective effects.

It is clear that the use of different NLD models has a significant impact on the calculation results. In addition, these models, without considering the collective effect, practically cannot reproduce the experimental data except in the region of 6 to 11 MeV. Therefore, it is necessary to make corrections to include the effects of deformation and cumulative excitations in the NLD and its effective parameters as well as the parameters of fission barriers. As the results of these modifications are shown in Fig.4, these microscopic details in the fission process can have a significant impact and reproduce the fission cross-section with a much better quality.

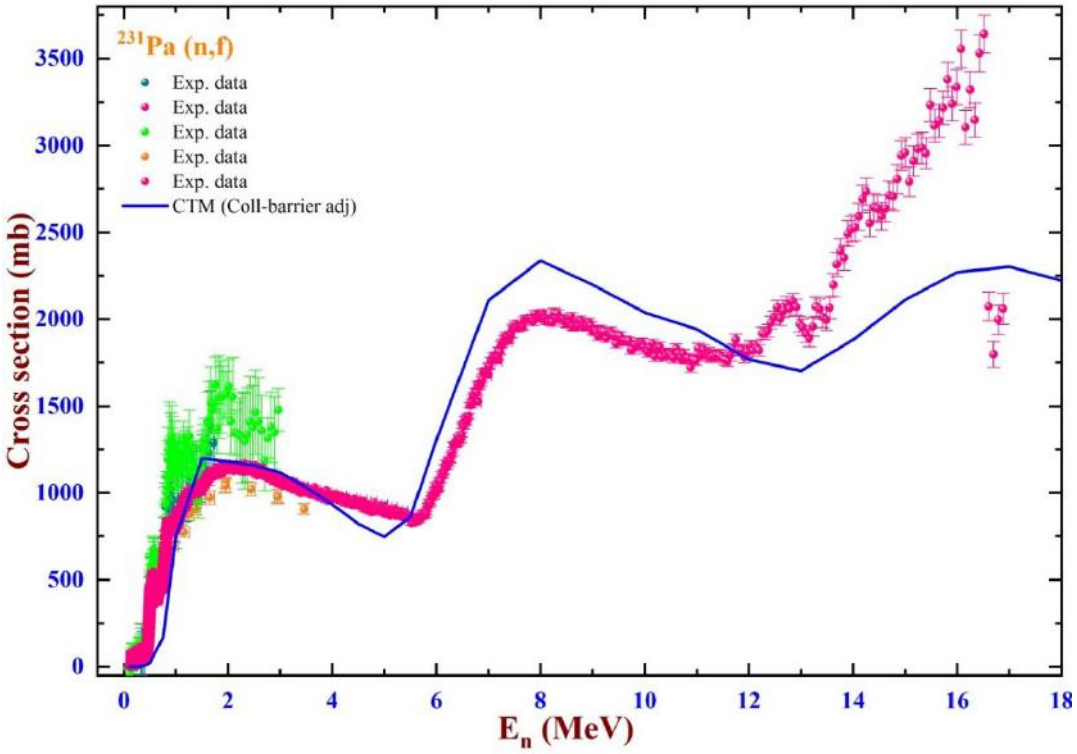

Fig. 4. Fission cross section calculations using adjusted CTM NLD model with collective effects and adjusted barrier parameters.

Table 1. The parameters of microscopic details of ^{231}pa(n,f) reaction for each barriers.

Nuclei	Barrier	a^{eff}	T	E_0	E_M	δW	B_f	hω	Barrier axiality
^{232}Pa	inner	28.18818	0.32817	-0.87829	2.07533	1.98466	5.0	0.60	axially symmetric
	outer	30.95610	0.53817	-3.76143	3.76052	3.78528	6.2	0.40	tri-axial
^{231}Pa	inner	28.16833	0.38172	-1.11469	4.91575	2.07699	5.5	1.0	axially symmetric
	outer	28.16833	0.40368	-0.85178	4.55453	2.07699	5.5	0.5	tri-axial

The parameters of microscopic details of ^{231}pa(n,f) reaction, which include NLD parameters (for example, for the CTM model: E_M matching energy ,T and E_0 parameters, effective asymptotic NLDP, spin cutoff parameters, Ignatyuk relation parameters at saddle points) and fission barrier parameters (curvature and height), are provided to calculate the fission cross section. These parameters are shown in Table1. As can be seen in Table 1 and Figure 4, many parameters of the CTM model of nuclear level density in the ground

state and on the inner and outer fission barriers have different values. This difference is due to the dynamic deformation of the nucleus compared to the deformation of its ground state during the fission process. In this investigation, the role of collective effects (rotational and vibrational) caused by this deformation on NLD is very significant and as it is known, by considering these effects in the calculations and also adjusting other NLD parameters, the results of the calculations and simulations can be brought closer to the experimental values to a great extent. Determining and investigating how each component changes during the dynamic fission reaction is still one of the challenging issues of nuclear physics and technology and is being developed along with the improvement of laboratory methods.

Conclusions

In this study, we have investigated the microscopic details and components of nuclear fission for protactinium nuclei. We have calculated the neutron-induced fission cross section for the 231Pa nucleus by determining the nuclear level density parameters at the saddle points on the fission barriers and the shape and parameters of the fission barriers (height and curvature). We have also obtained the optimized values for the microscopic details of competitive fission. The effect of dynamic deformation by shape-dependent rotational enhancements has also been considered in the NLD. It has been shown that different nuclear level density models have a significant impact on the results of the competitive fission reaction. It has also been shown that the different parameters of the NLD on the fission barriers are quite different from the ground state and their accurate determination is very important and decisive for the accurate determination of nuclear fission. This provides us with very important information about the dynamics and behavior of the nucleus during fission process. Our results show that the inclusion of dynamic deformation effects in the NLD leads to a significant increase in the calculated fission cross section. Our results also show that the different nuclear level density models have a significant impact on the results of the competitive fission reaction. This is due to the fact that the different models predict different values for the level density at the saddle points, which in turn affects the calculated fission cross section. The results of this study are important for understanding the dynamics of nuclear fission. The accurate determination of the fission barriers and the nuclear level density parameters is essential for the accurate prediction of the fission cross section. This information can be used to develop better nuclear models and to design more efficient nuclear reactors.

References

[1] A. Gilbert and A. Cameron, "A composite nuclear-level density formula with shell corrections," *Canadian Journal of Physics,* vol. 43, no. 8, pp. 1446-1496, 1965.

[2] W. Dilg, W. Schantl, H. Vonach, and M. Uhl, "Level density parameters for the back-shifted fermi gas model in the mass range 40< A< 250," *Nuclear Physics A,* vol. 217, no. 2, pp. 269-298, 1973.

[3] H. Bethe, "An attempt to calculate the number of energy levels of a heavy nucleus," *Physical Review,* vol. 50, no. 4, p. 332, 1936.

[4] M. N. Nasrabadi and M. Sepiani, "Generalization of phenomenological models of nuclear level density to high energies," *Physica Scripta,* vol. 90, no. 12, 2015, doi: https://doi.org/10.1088/0031-8949/90/12/125302.

[5] M. Aggarwal, "Dependence of spin induced structural transitions on level density and neutron emission spectra," *Nuclear Physics A,* vol. 983, pp. 166-174, 2019/03/01/ 2019, doi: https://doi.org/10.1016/j.nuclphysa.2018.12.010.

[6] B. K. Agrawal and A. Ansari, "Level density and level density parameter in medium heavy nuclei including thermal and quantal fluctuation effects," *Physics Letters B,* vol. 421, no. 1, pp. 13-17, 1998/03/05/ 1998, doi: https://doi.org/10.1016/S0370-2693(97)01604-3.

[7] V. Canuto, L. Fassio, and O. Rojo, "Statistical mechanics of a superfluid nuclear matter: (II). Nuclear level density," *Nuclear Physics A,* vol. 97, no. 1, pp. 223-231, 1967/04/17/ 1967, doi: https://doi.org/10.1016/0375-9474(67)90783-X.

[8] V. Canuto and L. S. Garcia-Colin, "Odd-even effect in the nuclear level density and superfluid model of nuclei," *Nuclear Physics,* vol. 61, no. 2, pp. 177-193, 1965/01/01/ 1965, doi: https://doi.org/10.1016/0029-5582(65)90890-4.

[9] V. W. Ingeberg *et al.*, "Nuclear Level Density and γ-ray Strength Function of $^{63}\mathrm{Ni}$," p. arXiv:2207.01571. [Online]. Available: https://ui.adsabs.harvard.edu/abs/2022arXiv220701571I

[10] M. N. Nasrabadi, "Extracting nuclear level density of 166Er using microscopic theory of interacting fermions," *Nuclear Physics A*, vol. 834, no. 1, pp. 103c-106c, 2010/03/01/ 2010, doi: https://doi.org/10.1016/j.nuclphysa.2010.01.031.

[11] M. Nasri Nasrabadi, "Isospin dependence of nuclear level density of 28Al considering symmetry energy and pairing corrections," in *Journal of Physics Conference Series*, May 01, 2011 2011, vol. 295, p. 012124, doi: 10.1088/1742-6596/295/1/012124. [Online]. Available: https://ui.adsabs.harvard.edu/abs/2011JPhCS.295a2124N

[12] M. R. Pahlavani and M. M. dinan, "Retraction: Nuclear level density and thermal properties of 270110, 278112, and 290116 superheavy isotopes in low excitation energies," *Canadian Journal of Physics*, vol. 97, pp. 464-464, April 01, 2019 2019, doi: 10.1139/cjp-2019-0156.

[13] S. Monga and H. Kaur, "Semiclassical level density parameter with collective enhancements in nuclei," *International Journal of Modern Physics E*, vol. 30, p. 2150020, January 01, 2021 2021, doi: 10.1142/s0218301321500208.

[14] M. N. Nasrabadi and M. Sepiani, "Study of components and statistical reaction mechanism in simulation of nuclear process for optimized production of 64Cu and 67Ga medical radioisotopes using TALYS, EMPIRE and LISE++ nuclear reaction and evaporation codes," in *4th International Congress in Advances in Applied Physics and Materials Science (APMAS 2014)*, March 01, 2015 2015, vol. 1653, p. 020076, doi: 10.1063/1.4914267.

[15] A. Aydin, H. Pekdogan, A. Kaplan, İ. Sarpün, E. Tel, and B. Demir, "Comparison of level density models for the 60, 61, 62, 64 Ni (p, n) reactions of structural fusion material nickel from threshold to 30 MeV," *Journal of Fusion Energy*, vol. 34, pp. 1105-1108, 2015.

[16] N. Kamal, S. Nizam, and A. A. Aziz, "The effects of nuclear level density model and alpha optical model potential to the excitation functions of novel therapeutic radionuclides," *Applied Radiation and Isotopes*, vol. 203, p. 111085, 2024.

[17] G. Indira and G. Anbalagan, "An investigation of the effects of optical model potentials and level density models on the calculation of excitation function for the production of medical isotopes 68 G e and 82 S r through alpha and proton induced nuclear reactions," *Indian Journal of Physics*, pp. 1-9, 2023.

[18] C. Schmitt, P. Nadtochy, and K. Mazurek, "Fission as a relevant probe of the nuclear level density away from β-stability," *Physics Letters B,* vol. 840, p. 137873, 2023.

[19] M. Nasri Nasrabadi and M. Sepiani, "Study of nuclear level densities for exotic nuclei," *Iranian Journal of Physics Research,* vol. 12, no. 1, pp. 67-75, 2019.

[20] A. Ignatyuk, J. Weil, S. Raman, and S. Kahane, "Density of discrete levels in Sn 116," *Physical Review C,* vol. 47, no. 4, p. 1504, 1993.

[21] M. Sepiani and M. Nasrabadi, "Determination of nuclear level density based on a fully microscopic statistical partition function method for 58Ni," *Journal of Physics G: Nuclear and Particle Physics,* vol. 50, no. 5, p. 055103, 2023.

[22] S. Goriely, F. Tondeur, and J. Pearson, "A Hartree–Fock nuclear mass table," *Atomic Data and Nuclear Data Tables,* vol. 77, no. 2, pp. 311-381, 2001.

[23] S. Goriely, S. Hilaire, and A. J. Koning, "Improved microscopic nuclear level densities within the Hartree-Fock-Bogoliubov plus combinatorial method," *Physical Review C,* vol. 78, no. 6, p. 064307, 2008.

[24] S. Goriely, "Global microscopic models for nuclear astrophysics applications," *Nuclear Physics A,* vol. 752, pp. 560-569, 2005/04/18/ 2005, doi: https://doi.org/10.1016/j.nuclphysa.2005.02.059.

[25] M. N. Nasrabadi and M. Sepiani, "Study of Collective Rotational Enhancement Factors for Nuclear Level Densities Using the Microscopic Theory of Interacting Fermions," *Acta Physica Polonica B,* vol. 45, p. 1865, January 01, 2014 2014, doi: 10.5506/APhysPolB.45.1865.

[26] Y. Alhassid, G. F. Bertsch, C. N. Gilbreth, H. Nakada, and C. Özen, "Level densities of heavy nuclei in the shell model Monte Carlo approach," in *European Physical Journal Web of Conferences*, June 01, 2016 2016, vol. 122, p. 02001, doi: 10.1051/epjconf/201612202001.

[27] W. Hauser and H. Feshbach, "The Inelastic Scattering of Neutrons," *Physical Review,* vol. 87, 1952.

[28] D. L. Hill and J. A. Wheeler, "Nuclear constitution and the interpretation of fission phenomena," *Physical Review,* vol. 89, no. 5, p. 1102, 1953.

[29] Å. Bohr, "Conf. on Peaceful Uses of Atomic Energy," ed: Geneva, 1955.

[30] A. Koning, S. Hilaire, and S. Goriely, "TALYS: modeling of nuclear reactions," *The European Physical Journal A*, vol. 59, no. 6, p. 131, 2023.

[31] *TALYS-1.96/2.0 Simulation of nuclear reactions, User Manual*. (2021).

[32] M. Sepiani and M. Nasrabadi, "Evidence on the high energy behavior of nuclear level density parameter," *Physica Scripta*, vol. 99, no. 1, p. 015302, 2024.

[33] A. V. Ignatyuk, G. N. Smirenkin, and A. S. Tishin, "Phenomenological description of energy dependence of the level density parameter," *Yadernaya Fizika*, vol. 21, no. 3, pp. 485-490, 1975. [Online]. Available: http://inis.iaea.org/search/search.aspx?orig_q=RN:06208426.

[34] N. R. Dwivedi, S. Monga, H. Kaur, and S. R. Jain, "Ignatyuk damping factor: A semiclassical formula," *International Journal of Modern Physics E*, vol. 28, p. 1950061, January 01, 2019 2019, doi: 10.1142/s0218301319500617.

[35] R. Capote *et al.*, "RIPL - Reference Input Parameter Library for Calculation of Nuclear Reactions and Nuclear Data Evaluations," *Nuclear Data Sheets*, vol. 110, pp. 3107-3214, December 01, 2009 2009, doi: 10.1016/j.nds.2009.10.004.

[36] P. Romain, B. Morillon, and A. Koning, "Neutron actinides evaluations with the TALYS code," *NEMEA-3 Neutron Measurements, Evaluations and Applications*, vol. 25, p. 113, 2006.

ICNST 2024
International Conference on Nuclear Science and Technology
6- 8 MAY 2024 | Isfahan, Iran

Review of Simulation and Evaluation Methods for Beam Dynamics in Particle Accelerators (Paper ID : 1046)

A. Khodamoradi[1], M. Mohamadian[1*]

[1]Physics and Energy Engineering Department, Amirkabir University of Technology, Tehran, Iran

Abstract

Particle accelerators are complex systems that require precise control of beam dynamics to achieve optimal performance. Several simulation and evaluation methods have been developed to study and improve the beam dynamics in particle accelerators. This review provides an overview of different methods for simulating beam dynamics, highlighting their basic features, capabilities, and specific applications with special attention given to the codes that are in more common use at the existing particle accelerator facilities. Additionally, it will cover the modeling of multiparticle dynamics and its underlying physics.

This review will encompass traditional techniques such as particle tracking, and numerical modeling, as well as advanced simulation tools. It will critically analyze the advantages and limitations of each approach. Furthermore, it will emphasize the significance of benchmarking and validation in the simulations, underscoring the necessity for accurate and dependable results.

By providing an in-depth analysis of these methods, the review aims to serve as a practical reference for individuals involved in particle accelerator operation, design, or research, aiding in informed decision-making and further advancement in the field.

Keywords: Beam Dynamics, Particle Accelerators, Simulation methods

Introduction

One of the most commonly used methods for simulating beam dynamics is the particle-in-cell (PIC) method. This method involves tracking the motion of individual particles in the accelerator using numerical simulations. PIC simulations can provide detailed information about the behavior of the beam, including its trajectory, emittance, and energy spread. This information is crucial for optimizing the design and operation of particle accelerators [1].

Another critical method for simulating beam dynamics is using beam dynamics codes, such as MAD-X and Elegant. These codes use a combination of analytical and numerical techniques to model the behavior of the beam in the accelerator. They can provide valuable insights into the complex interactions between the beam and the accelerator components, such as magnets and RF cavities.

In addition to simulation methods, there are many techniques for evaluating the beam dynamics in particle accelerators. One common approach is to use beam diagnostics, such as beam position monitors (BPM) and beam profile monitors, to measure the properties of the beam. These measurements provide valuable feedback on the accelerator's performance and help identify any issues that need to be addressed.

Furthermore, advanced techniques such as machine learning and artificial intelligence are increasingly used to analyze and optimize beam dynamics in particle accelerators. The techniques can help to identify patterns and correlations in large datasets, leading to improved understanding and control of beam dynamics [2].

Material and Methods

As previously stated, several approaches have been adopted to analyze beam dynamics, which are further discussed in four main categories.

1. Particle in Cell (PIC) Method

The particle-in-cell (PIC) method is a computational technique used to simulate the behavior of charged particles in electromagnetic fields. This method is commonly used to study the dynamics of particle beams, such as those found in particle accelerators and plasma physics experiments.

When simulating beam dynamics with the PIC method, the system is divided into a grid of cells, and the particles are represented as discrete entities. The electric and magnetic fields are calculated at each cell, and the particles are then moved in response to these fields. This allows for the simulation of the collective behavior of the particles as they interact with each other and with the fields.

The PIC method is particularly well-suited for studying the dynamics of beams because it can accurately capture the complex interactions that occur between the particles and the electromagnetic fields. This includes space charge effects, beam instabilities, and particle-wave interactions (Fig. 1).

By using the PIC method, we can gain insights into the behavior of particle beams and optimize the design and operation of particle accelerators and other beam-based systems. This can lead to improvements in performance, efficiency, and safety in a wide range of applications, from fundamental research to industrial and medical technologies [3].

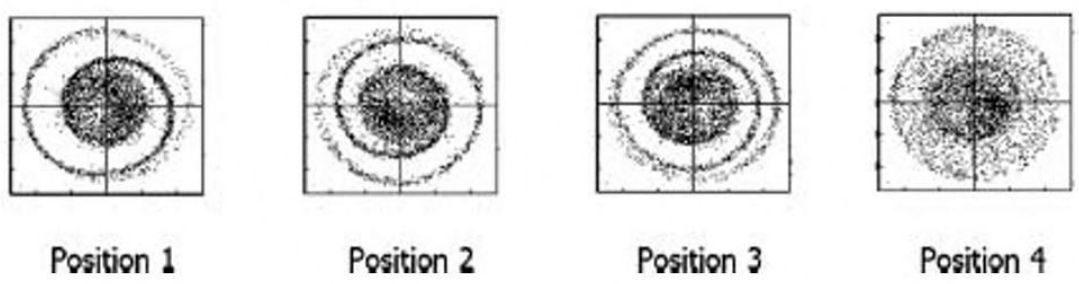

Fig. 1. The result of frequency drift analysis during the detection event: Ion density distribution at different positions on the time scale with the PIC method. [1]

As mentioned earlier, the particle-in-cell (PIC) method is widely used to simulate beam dynamics in different types of particle accelerators. Some accelerators that utilize PIC simulations for beam dynamics analysis include; 1. Linear accelerators (Linacs): These accelerators use radiofrequency (RF) cavities to accelerate particles in a straight line. PIC simulations are used to study the behavior of particle beams as they are accelerated and focused within the Linac structure. SSC-Linac [4], spallation neutron source Linac [5], and plasma accelerators [6] are some of the Linacs that use PIC for beam dynamic analysis. Fig.2 illustrates the particle distributions at the exit of the RFQ of SSC-Linac modeling with the PIC method [4].

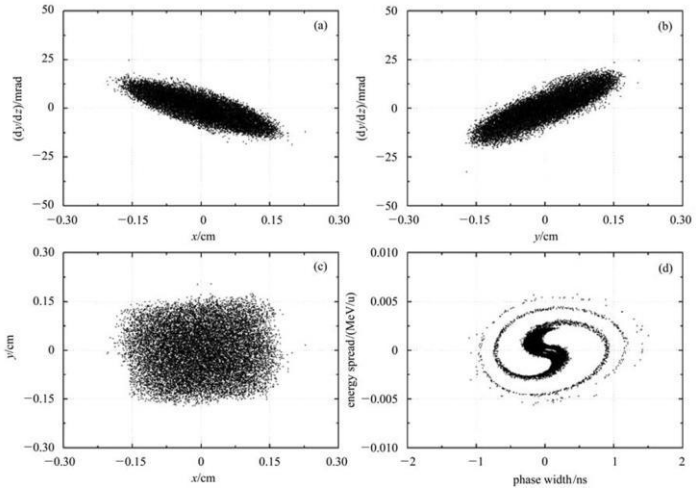

Fig. 2. The particle distributions at the exit of the RFQ at SSC-Linac. [4]

2. Circular accelerators (synchrotrons and cyclotrons): Synchrotrons and cyclotrons are circular accelerators that use magnetic fields to bend and focus particle beams. PIC simulations are employed to analyze the dynamics of the particle beams as they circulate and are accelerated within these machines [7]. For instance, DAEδALUS Superconducting Ring Cyclotron (DSRC) [8] and electron cyclotron [9] have utilized PIC for beam dynamic analysis. Fig.3 illustrates the initial distribution for injection through the spiral inflector at DSRC. Additionally, PIC has been used for beam dynamic analysis in synchrotrons such as CSNS/RCS [10] and RaDiO [11]. Fig. 4 describes the particle distribution with different potentials at the end of the injection process (500th turn) at CSNS/RCS [10], while Fig. 5 demonstrates the Synchrotron radiation captured by RaDiO [11].

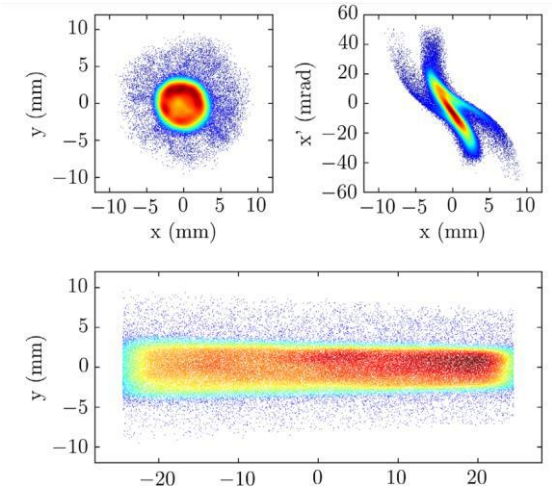

Fig. 3. Initial distribution for injection through the spiral inflector. The length of the bunch corresponds to one full RF period at 49.2MHz and an injection energy of 62.7 keV, centered at the synchronous phase. [8]

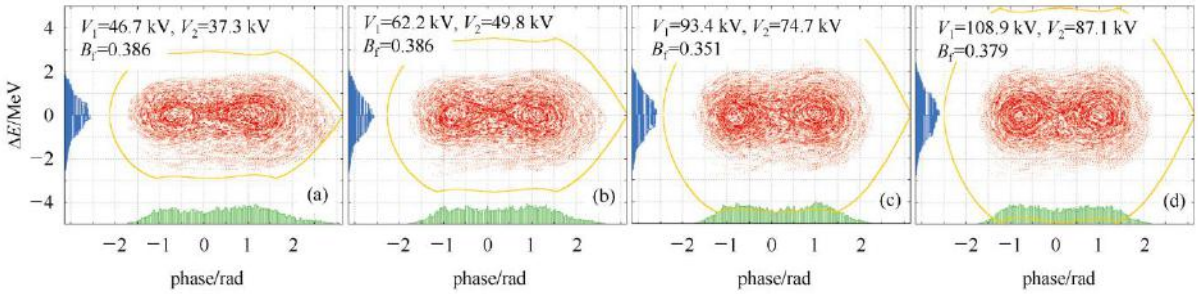

Fig. 4. Particle distributions with different V_1 and V_2 at the end of the injection process at CSNS/RCS. [10]

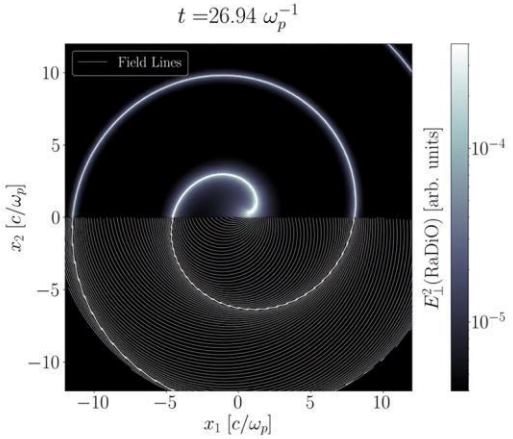

Fig. 5. Synchrotron radiation. Depiction of the E.M fields radiated by a charged particle undergoing circular motion in the x1x2 plane as captured by RaDiO. [11]

3. Particle colliders: Large particle colliders, such as the Large Hadron Collider (LHC) at CERN, use PIC simulations to study the behavior of high-energy particle beams as they are brought into collision. This helps in understanding the interactions and collisions between the particles [12].

4. Plasma-based accelerators: PIC simulations are also crucial for studying the dynamics of particle beams in plasma-based accelerators, which use plasma waves to accelerate particles to high energies. These accelerators are an active research area for future particle accelerators [13,14]. Fig. 6 illustrates the QuickPIC simulation of an LWFA experiment with a plasma channel that demonstrates laser guiding [14].

Therefore, the PIC method is a versatile tool for simulating beam dynamics in a wide range of particle accelerators, providing valuable insights into the behavior of particle beams and aiding in the design and optimization of accelerator systems [15].

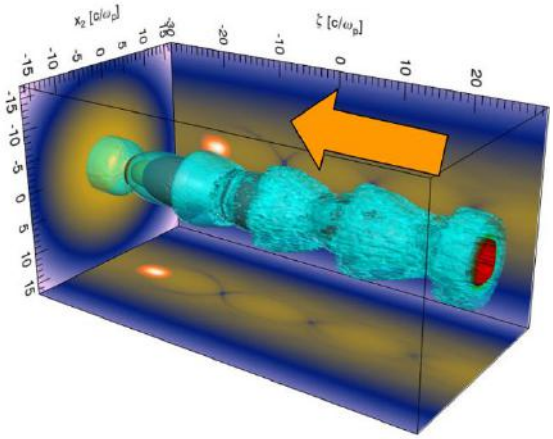

Fig. 6. QuickPIC simulation of an LWFA experiment with a plasma channel that demonstrates laser guiding. [14]

2. Beam Dynamics Codes

To analyze particle beam behavior in particle accelerators and other beam-based systems, computational methods called beam dynamics codes are implemented. These codes utilize sophisticated algorithms and numerical methods to simulate the motion and interactions of charged particles within the electromagnetic fields present in the accelerator [16]. Beam dynamics codes analyze beam dynamics by the following steps:

1. Tracking particle trajectories: Beam dynamics codes calculate the trajectories of individual particles as they move through the accelerator. This involves solving the equations of motion for each particle in response to the electromagnetic fields, space charge effects, and other forces acting on the particles. In particular, the electromagnetic fields in a beam line must satisfy Maxwell's equations, and the motion of a charged particle through those fields is determined by Hamilton's equations, with an appropriate (relativistic) Hamiltonian [17].

2. Emittance and beam optics: Beam dynamics codes analyze the emittance of the beam, which describes the spread of particle positions and velocities within the beam. They also simulate the focusing and steering of the beam using magnetic and electric fields, known as beam optics, to ensure that the beam remains well-collimated and stable [18,19] (Fig. 7).

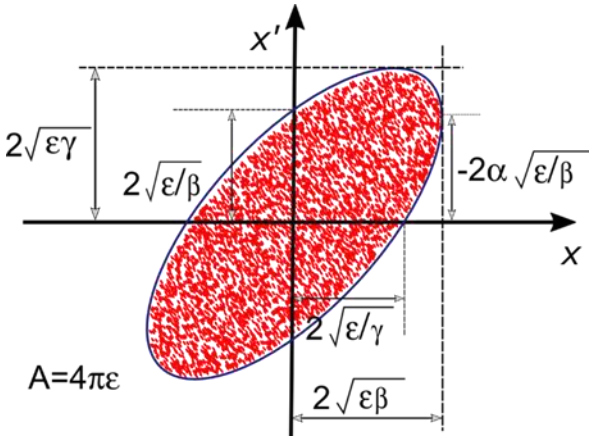

Fig. 7. The Twiss parameters are related to the ellipse proportions and orientation. [20]

3. Collective effects and instabilities: These codes study collective effects such as space charge, beam-beam interactions, and Wakefield, which can lead to instabilities and degradation of beam quality. They simulate the evolution of these effects over time and assess their impact on the beam [21].

4. Energy spread and beam cooling: Beam dynamics codes analyze the energy spread of the beam and the methods for reducing it, such as beam cooling techniques. They simulate the cooling processes and assess their effectiveness in improving the beam quality [22].

5. Beam diagnostics: These codes also simulate the response of beam diagnostics devices, such as beam position monitors and beam profile monitors, to understand how the beam properties can be measured and optimized.

Hence, beam dynamics codes play a crucial role in the design, optimization, and operation of particle accelerators by providing comprehensive insights into the behavior of particle beams and enabling researchers to improve the performance and efficiency of these complex systems.

Some widely used beam dynamics codes in the field of accelerator physics are MAD-X, Elegant, TraceWin, ASTRA, PTC-ORBIT, BEAMLINE, TDBSC, IMPACT, SYNCH, OPAL, CYCLONE, and SNOP. These codes are used for modeling and simulating the behavior of particle beams in accelerators, including synchrotrons, storage rings, linear accelerators, and free-electron lasers. Table 1 indicates a more complete list of the software and codes [23].

Table 1. Beam Dynamics Codes

Code	Reference(s) or Contact	Description
ASTRA	tesla.desy.de/—"meykopff	3D parallel, general charged particle beams incl. space charge
AT	sourceforge.net/projects/atcollab/	Accelerator Toolbox
BETACOOL	betacool.jinr.ru	Long-term beam dynamics: ECOOL, IBS, internal target
Bmad, Tao	www.Ins.cornell.edu/—dcs/bmad/	General purpose toolbox library + driver program
COSY INFINITY	www.cosyinfinity.org, [24,25]	Arbitrary-order beam optics code. Putting in use such as graphics libraries and parallel computation. The code is broadly applicable including cyclotrons, synchrotrons, FFAGs, electrostatic accelerators, linacs, RFQ accelerators, spectrometers, and transport lines allowing injection-to-extraction simulations.
CSRTrack	www.desy.de/xfel-beam/csrtrack	3D parallel PIC; includes CSR; mainly for e- dynamics
Elegant/SDDS suite	aps.anl.gov/eleganthtml	parallel; track, optimize; errors; wakes; CSR
ESME	www-ap.fnal.gov/ESME	Longitudinal tracking in rings
HOMDYN	Massimo.Ferrario@LNF.INFN.IT	Envelope equations, analytic space charge, and wake fields
IMPACT code suite	amac.lbl.gov	3D parallel multi-charge PIC for linacs and rings
LAACG code suite	laacg.lanl.gov	Includes PARMILA, PARMELA, PARMTEQ TRACE2D/3D
LiTrack	www.slac.stanford.edu/"emma/	Longitudinal Linac dynamics; wakes; GUI-based; error studies
LOCO	safranek@slac.stanford.edu	Analysis of optics of storage rings; runs under MATLAB
LUCRETIA	www.slac.stanford.edu/accel/i1c/codes	MATLAB-based toolbox for simulation of single-pass e^- systems
MaryLie	www.physics.umd.edu/dsat	Lie algebraic code for maps, orbits, moments, fitting, analysis
MaryLie/IMPACT	amac.lbl.gov	3D parallel PIC; MaryLie optics + IMPACT space charge
MAD-X	mad.web.cern.ch/mad	General-purpose beam optics
MERLIN	www.desy.de/—merlin	C++ class library for charged particle accelerator simulation
OPAL	amas.web.psi.ch, [26,27]	(Object-Oriented Parallel Accelerator Library) 3D parallel PIC; cyclotrons, FFAGs, linacs; particle-matter int.
ORBIT and ADVANCED ORBIT CODE	jzh@ornl.gov, [25]	Collective beam dynamics in rings and transport lines
PATH	Alessandra.Lombardi@cern.ch	3D PIC; linacs and transfer lines; matching and error studies
SAD	acc-physics.kek.jp/SAD/sad.html	Design, simulation, online modeling & control
SIMBAD	agsrhichome.bnl.gov/People/luccio	3D parallel PIC; mainly for hadron synchrotrons, storage rings
SIXTRACK	frs.home.cern.ch/frs/	Single particle optics; long-term tracking in LHC
STRUCT	www-ap.fnal.gov/users/drozhdin	Long term tracking w/ emphasis on collimators
Synergia	https://compacc.fnal.gov/projects	3d parallel PIC: space charge, nonlinear tracking, and wakes
TESLA	lyyang@bnl.gov	Parallel; tracking; analysis; optimization

Code	Reference(s) or Contact	Description
TRACK	www.phy.anl.gov/atlas/TRACK, [28]	3D parallel PIC, mainly for ion or electron Linacs
LIBTRACY	libtracy.sourceforge.net/	Library for beam dynamics simulation
TREDI	www.tredi.enea.it	3D parallel PIC; point-to-point Lienard-Wiechert
UAL	code.google.com/p/ual/	Unified Accelerator Libraries
WARP	DPGrote@lbl.gov	3D parallel ES and EM PIC with accelerator models
ZGOUBI	sourceforge.net/projects/zgoubi/	Magnetic optics; spin; sync radiation; in-flight decay
CYCLOPS code	[29]	TRIUMF has a special version of CYCLOPS that accommodates situations where the equilibrium orbit is slightly displaced from the nominal cyclotron median plane as a result of, for example, magnet imperfections.
CYCLONE	[25,30]	And Z3CYCLONE
SNOP	[25,31]	3D electric and magnetic field maps, used for analyzing particle beam dynamics in cyclotrons
PHASCOL	[25,32]	Analyzing beam dynamics in cyclotrons taking into account space charge effects
CASINO	[33,34]	Calculation of spiral inflector orbits
NAJO	[35]	Multiparticle, Three-dimensional, For analyzing cyclotron beam dynamics
NORTICA	[25,36]	The general purpose of this package is to assist in setting and tuning the cyclotrons taking into account the main field and extraction channel imperfections.
GPT	[25,37]	The General Particle Tracer, Completely 3D, Multiparticle, with Complete freedom in the initial particle distribution, and flexibility to position and orient all beamline components
MATLAB CODES	[25]	Such as CYTRACK and the code utilized in the SCENT project
DYNAMION	[38]	A Multiparticle beam dynamic code for high-current linear accelerators
CST Studio Suite®	www.cst.com	CST Particle Studio environment, Multiparticle Code, Solvers incl. Particle Tracking, Electrostatic PIC, Standard PIC, and Wakefield Solver. Utilizes Coupled Simulations and Parallelization.
COMSOL Multiphysics®	www.comsol.com	Multiparticle code, Utilizes Particle Tracing Module, Plasma Module, FEM and PIC Methods, Coupling Simulations and Parallelization. Suitable for many applications.

These codes and software play a major role in terms of the design, optimization, and operation of accelerator facilities around the world. Some of them are considered briefly.

MAD-X

MAD-X is a software tool used for the design, analysis, and optimization of particle accelerators. It is a widely used and highly versatile code that is particularly well-known in the field of accelerator physics. MAD-X stands for "Methodical Accelerator Design" and "eXecution" [39].

The MAD-X code is primarily used for simulating and modeling the behavior of particle beams in circular and linear accelerators. It provides a comprehensive set of tools for tracking particle trajectories, analyzing beam optics, and studying the dynamics of particle beams within the accelerator lattice. Key features of MAD-X include:

1. Beam optics design: MAD-X allows for the design and optimization of beam optics, including the focusing and steering of particle beams using magnetic and electric fields. It provides tools for simulating and analyzing the behavior of particle beams as they pass through accelerator elements, such as quadrupoles, dipoles, and accelerating cavities [39–43].

2. Lattice design and optimization: MAD-X enables the creation and optimization of the accelerator lattice, which defines the arrangement of accelerator components and their respective parameters. It allows for the modeling of complex accelerator structures, including integrating various beamline elements and optimizing the lattice for specific beam dynamics requirements [44–46]. Fig. 8 demonstrates the lattice function for a simple FODO structure [47].

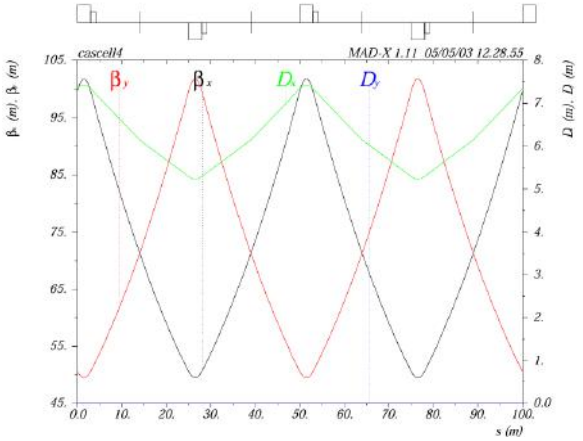

Fig. 8. Lattice function for a simple FODO structure. [47]

3. Particle tracking and simulation: MAD-X allows for the simulation of beam dynamics, including the study of emittance, dispersion, and beam stability [48–50] (Fig. 9).

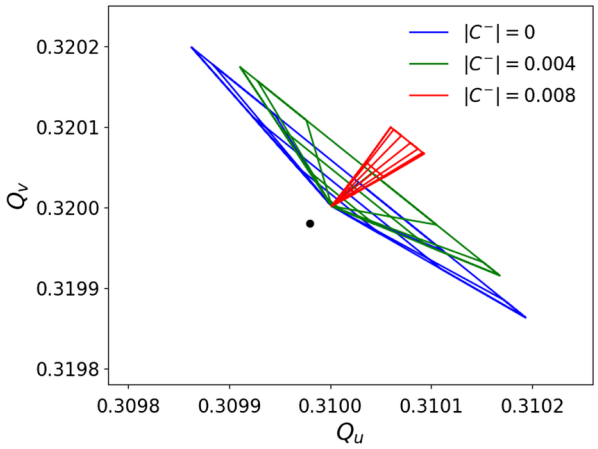

Fig. 9. MAD-X tracking results showing the tune footprint for different values of |*C*-| and constant tunes with $J_{oct} = 500\ A$. [50]

4. Advanced simulations: MAD-X offers capabilities for simulating collective effects, beam-beam interactions, and the impact of space charge on the particle beam. It also supports the simulation of beam cooling processes and the study of beam diagnostics [51–53] (Fig. 10).

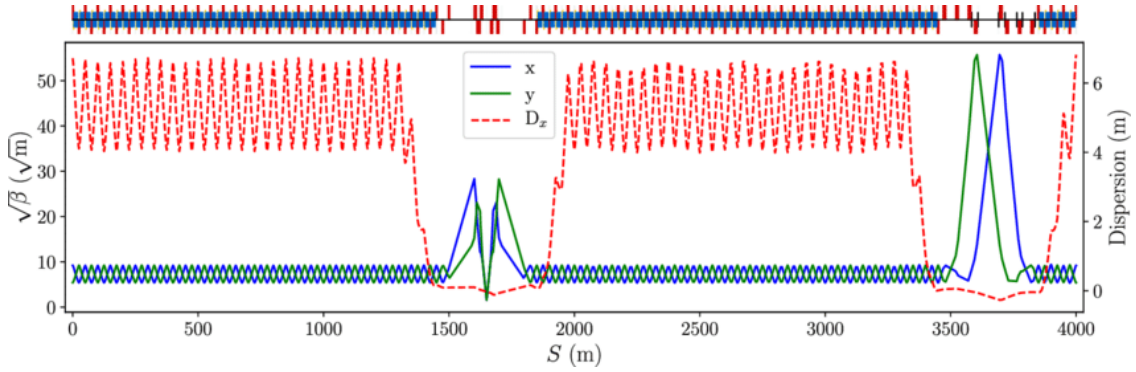

Fig. 10. MAD-X linear lattice functions of the example model. [53]

Elegant

Elegant is a widely used software package for simulating and analyzing the behavior of charged particle beams in accelerators. It is particularly well-known in the field of accelerator physics and has been widely adopted for the design, optimization, and operation of particle accelerators [54].

Most of the key features of Elegant are similar to the ones found in other software programs like MAD-X including; - Beam dynamics simulation: Elegant provides comprehensive tools for simulating the dynamics of charged particle beams, including tracking individual particle trajectories, analyzing beam optics, and studying the effects of collective phenomena such as space charge, beam-beam interactions, and Wakefield (Fig. 11). -Accelerator lattice design - Particle tracking and optimization - High-level scripting language:

Elegant provides a high-level scripting language for defining accelerator lattices, beamline elements, and simulation parameters. This allows users to easily define and customize their simulations, as well as automate complex tasks. - Integration with other software: Elegant is designed to integrate with other software packages commonly used in accelerator physics, such as particle tracking codes, data analysis tools, and visualization software [54–56] (Fig. 12).

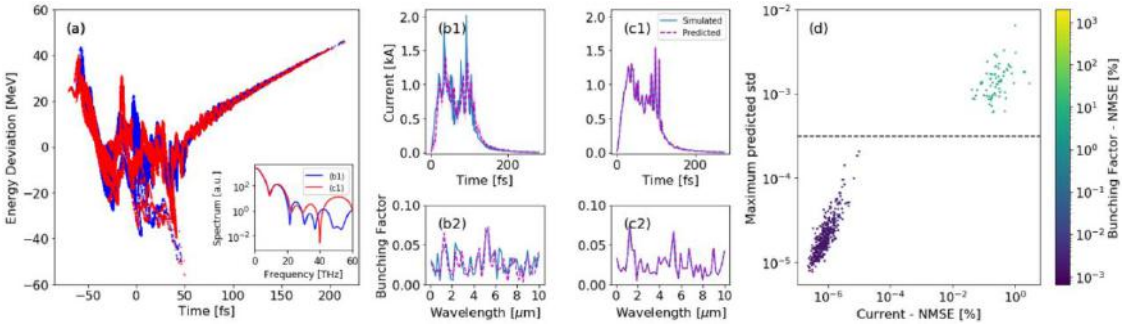

Fig. 11. LCLS-II super-conducting soft X-ray microbunching simulations in ELEGANT. [57]

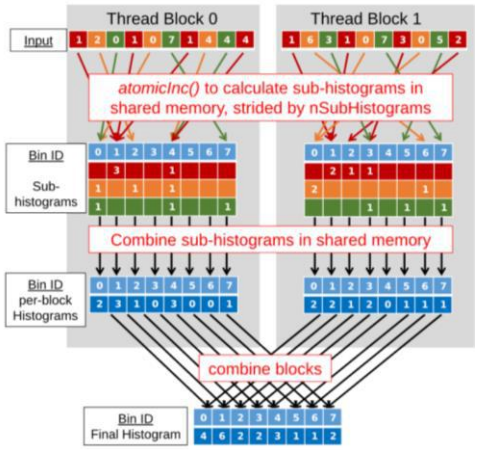

Fig. 12. A pictorial representation of the GPU Elegant histogram algorithm. [56]

OPAL

The main feature of the Opal software for beam dynamic simulation is its ability to accurately model and simulate the behavior of charged particle beams in accelerators and other beam transport systems. The software utilizes advanced physics algorithms and numerical methods to accurately model the behavior of charged particles as they travel through complex beamline systems. This includes simulating the effects of space charge, beam-beam interactions, beam instabilities, and other phenomena that can affect the performance of the beam.

Opal also includes a user-friendly interface that allows researchers and engineers to easily set up and run simulations, visualize the results, and analyze the behavior of the beam. It supports parallel computing, allowing for efficient simulation of large-scale beam systems (Fig. 13).

The physics behind Opal is based on fundamental principles of electromagnetism, classical mechanics, and statistical mechanics. It uses advanced mathematical techniques such as PIC methods, finite element methods, and other numerical approaches to accurately model the behavior of charged particle beams [25–27,58].

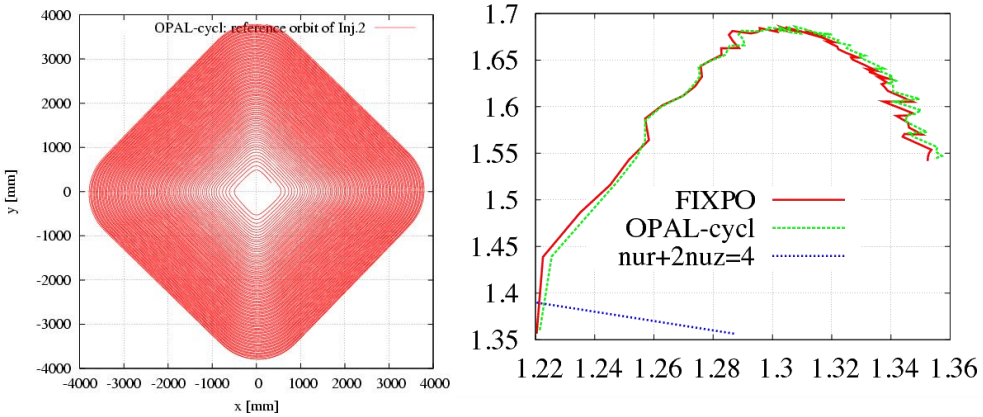

Fig. 13. Reference orbit(left) and tune diagram(right) in Injector II. [27]

SNOP

The SNOP program is designed for particle dynamics simulations in compact cyclotrons, from injection to extraction [31]. It uses 3D electric and magnetic field maps, calculates beam space charge effects, and analyzes beam losses. The program's user-friendly interface allows for easy control of parameters and visualization of results (Fig. 14).

SNOP uses the classical fourth-order Runge-Kutta method to solve equations of motion and supports 3D field maps from programs like OPERA/TOSCA. It also considers particle self-fields and allows for particle loss calculations on accelerator structure elements (Fig. 15). The program has been successfully applied to many accelerator facilities, demonstrating its effectiveness in beam dynamics analysis [31].

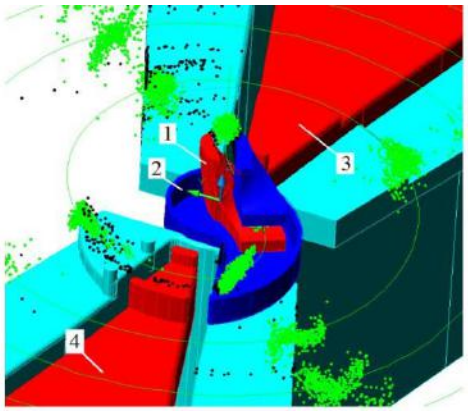

Fig. 14. Visualization of the central region of a cyclotron: (1) inflector, (2) inflector RF shield, (3) dee 2, (4) dee 1. [31]

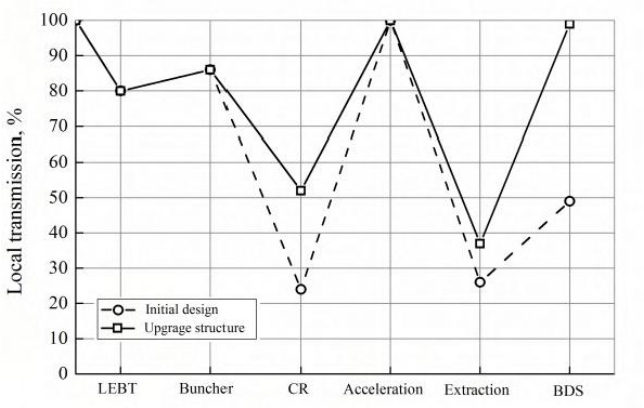

Fig. 15. Beam transmission efficiency at various structure elements of the cyclotron. [59]

CYCLONE

CYCLONE is a software package for beam dynamics simulation in cyclotrons. It is used for modeling and analyzing the behavior of charged particles as they are accelerated within a cyclotron accelerator [60]. Some of the main features and physics behind CYCLONE include:

1. Particle Tracking: CYCLONE enables precise monitoring of the movement of charged particles in the magnetic and electric fields of the cyclotron. This includes the consideration of relativistic effects and space charge interactions (Fig. 16).
2. Magnetic Field Modeling: The software incorporates detailed magnetic field modeling, which is crucial for accurately simulating the trajectories of particles as they spiral outward due to the increasing magnetic field strength [30].
3. Radiofrequency Cavities: CYCLONE can simulate the behavior of particles as they are accelerated by the radiofrequency (RF) cavities within the cyclotron, taking into account the interaction between the particles and the RF fields.
4. Space Charge Effects: The software can model space charge effects, which are crucial in high-intensity beams where mutual repulsion between particles can significantly impact their trajectories.
5. Nonlinear Effects: CYCLONE can handle nonlinear effects in the magnetic and electric fields, providing a more comprehensive simulation of the cyclotron's behavior.
6. Optimization and Design: CYCLONE can be used for optimizing the design and operation of cyclotrons, allowing for the exploration of different parameters to achieve desired beam characteristics.

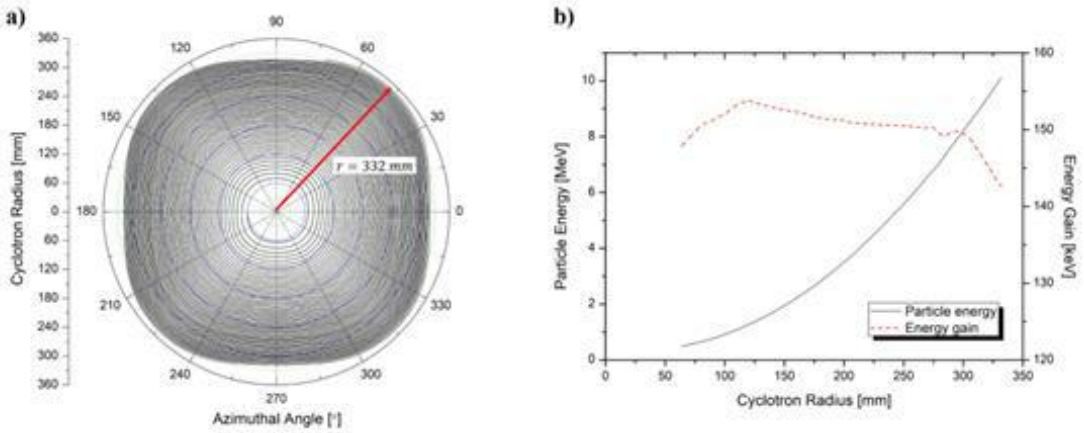

Fig. 16. Beam dynamic result: a) beam trajectory and b) particle energy and energy gain. [61]

ASTRA

ASTRA is a powerful software package used for simulating the dynamics of charged particle beams in accelerators and beamlines (Fig. 17). Some of the special features and physics behind ASTRA include; Particle Tracking-Accelerator Elements: The software incorporates a wide range of accelerator elements, such as quadrupoles, drift spaces, cavities, and bends, allowing for the modeling of various accelerator configurations and beamlines; Space Charge Effects, Collective Effects, Wake Fields, RF Cavities, and Optimization and Design. This software is widely used by accelerator physicists and engineers for the design and optimization of particle accelerators, including synchrotrons, storage rings, free-electron lasers, and linear accelerators. It is an essential tool for understanding and improving the performance of accelerator systems, and it has been instrumental in the development of numerous accelerator facilities worldwide [62].

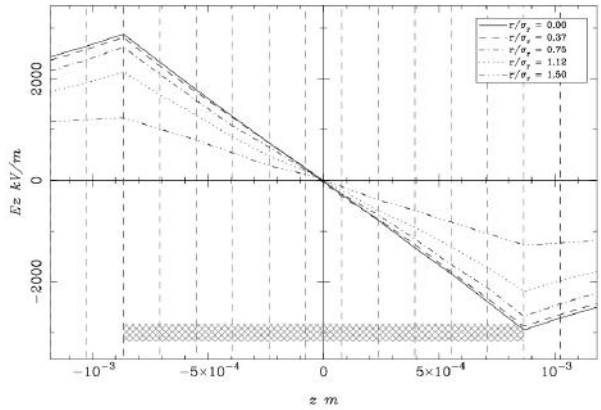

Fig. 17. Longitudinal electric field of a short bunch with an aspect ratio of 2, E_z along the z-axis calculated with MG. [63]

CST Studio Suite

CST Studio Suite is a robust 3D electromagnetic software that is employed for designing, analyzing, and optimizing electromagnetic structures [64]. The CST Particle Studio (PS) module is capable of analyzing interactions between charged particles and electromagnetic fields in the main components of a particle accelerator such as an ion source [65–67], electron gun [68–71], magnets [72–74], and RF cavities [75] as well as other involving elements [76,77]. Fig. 18 demonstrates the particle trajectories and energy distribution in a 9-sector compression magnet [72]. CST Particle Studio employs the finite integration (FIT)

method and adopts hexahedral/tetrahedral meshing to discretize the computational domain. It is possible to define particle sources on solid surfaces to emit particles based on predetermined emission models.

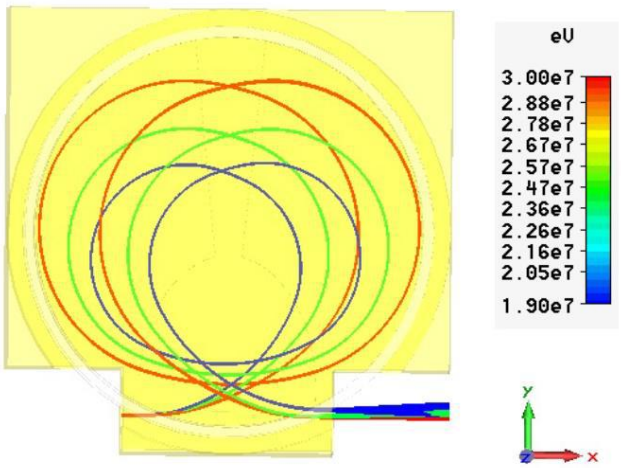

Fig. 18. Beam trajectory through a 9-sector magnet.

CST Particle Studio main solvers include Particle Tracking (TRK) Solver, PIC Solver, Electrostatic PIC (Es-PIC) Solver, and Wakefield Solver. The main responsibility of the TRK solver is to compute particle trajectories in electromagnetic fields. It also can calculate the space charge effect on electric field with the help of Gun iteration mode. Additionally, the solver allows for independent tracking of different particle types from user-defined sources. The PIC solver is a simulation technique used to compute both particle paths and electromagnetic fields in real time, considering space charge effects and the interaction between particles and fields. It is widely used in simulating devices involving particle-field interaction and for assessing electron multipacting risk in high-power devices [78–81]. The Es-PIC solver accurately models the dynamics of space charge using a transient approach that is not possible in the TRK solver. Unlike the PIC solver, it only focuses on electrostatic effects so there is no current and H-field induction. These made the solver well-suited for analyzing structures with large time scales. The Wakefield solver is a tool that calculates the electromagnetic fields around a particle beam, taking into account the wakefields generated by interactions with the irregularities in the surrounding structure. These methodologies are crucial for simulating and comprehending the behavior of particles in particle accelerators.

Moreover, the tool can calculate particle current, energy, emittance, and other beam dynamic parameters with high accuracy and efficiency. The CST Studio Suite with the help of its coupled thermal simulation is

also able to directly determine the heating process according to the due absorbed power of dumped particles [82].

The software is compatible with multiple platforms and offers a user-friendly interface that streamlines the simulation workflow and facilitates the interpretation of the simulation results. As discussed above, researchers have shown interest in utilizing the software for studying the beam dynamics in several accelerator facilities.

3. Techniques for evaluating the beam dynamics

There are various techniques available for assessing the beam dynamics such as; Particle tracking simulations, Phase space analysis, Emittance measurements, Beam stability analysis, Wakefield diagnostics, Beam-based imaging, Beam-based feedback, and Beam-based diagnostics. Some of the most important ones are outlined below.

In particle tracking simulations, the motion of particles within the beam is tracked to evaluate beam dynamics and identify potential issues. Phase space measurements are used to analyze the distribution of particle positions and momenta within the beam, providing insight into the overall dynamics of the beam. Emittance measurements assess the spread of particle trajectories, offering information on the overall quality of the beam dynamics. Monitoring the stability of the beam over time and under different operating conditions helps evaluate its overall dynamics and performance. Wakefield diagnostics are used to measure the electromagnetic fields and Wakefields generated by the beam, providing insight into the interaction of the beam with its surroundings. Imaging techniques, such as beam imaging or beam tomography, are employed to visualize the beam and its dynamics in real time, allowing for the identification of any irregularities or instabilities. Feedback systems are implemented that use measurements of the beam dynamics to actively adjust and control the beam parameters, ensuring optimal performance.

Beam-based diagnostics

Some important approaches for analyzing beam dynamics are using techniques such as beam-based alignment and beam-based feedback to actively adjust and control the beam dynamics based on real-time measurements.

Beam position monitoring: Installing beam position monitors along the beamline to measure the position and trajectory of the beam, providing real-time feedback on the beam dynamics [83–86] (Fig. 19).

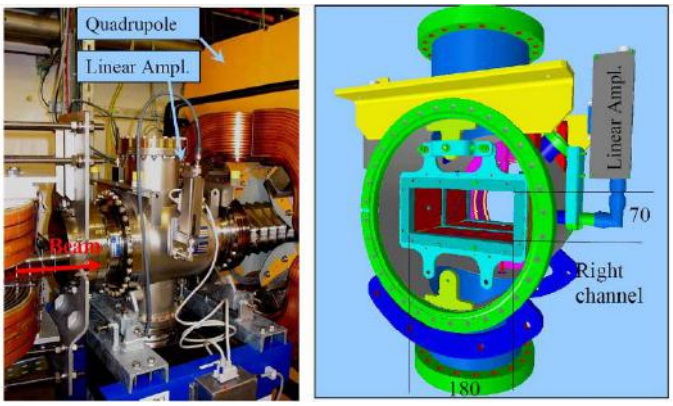

Fig. 19. Photo of a linear-cut BPM at the ion therapy facility HIT(left) and its technical drawing (right). [86]

Beam profile measurements: Using beam profile monitors to measure the transverse and longitudinal profiles of the beam, allowing for the evaluation of beam size, shape, and intensity [87–89] (Fig. 20).

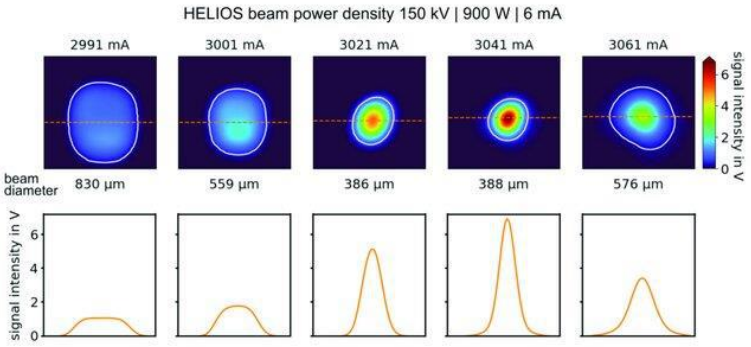

Fig. 20. Beam measurement on the HELIOS machine. In the under-focused state, the beam shows a top heat profile, while in the focused and over-focused state, the beam shows a Gaussian profile. [89]

4. **Machine Learning and Artificial Intelligence**

Machine learning and artificial intelligence can be applied to evaluating beam dynamics in several ways: 1. Predictive modeling, 2. Anomaly detection, 3. Optimization, 4. Pattern recognition, 5. Adaptive control, 6. Automated diagnostics, 7. Reinforcement learning, 8. Data-driven decision making.

1. Predictive modeling: Machine learning algorithms can be utilized to build predictive models that can forecast the behavior of the beam-based system on historical data. This can help identify potential issues or optimize beam parameters, as seen in the case of the Large Hadron Collider of CERN [2] (Fig. 21).

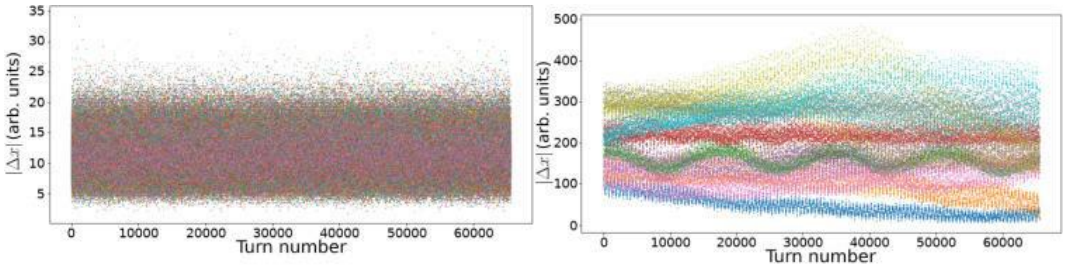

(a) Predicted inlier by Isolation Forest.

(b) Predicted outlier by Isolation Forest.

Fig. 21. Examples of signals for 108 nominal bunches from fill 6595 (a) and 10 anomalous ones from fill 7392 (b), as predicted by the IF. [2]

2. Anomaly detection: Machine learning algorithms can be trained to detect anomalies in the beam dynamics, such as unexpected changes in beam position, intensity, or shape, which can indicate potential problems [90] as demonstrated in (Fig. 22).

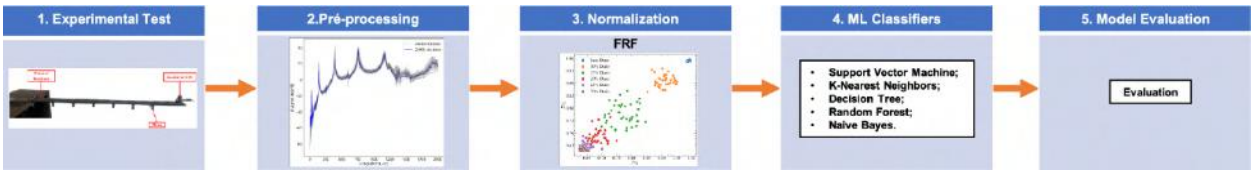

Fig. 22. Flowchart of damage assessment process using experimental dataset. [90]

3. Optimization: AI techniques can be used to optimize beam parameters and control systems in real time, ensuring that the beam dynamics are maintained at their optimal performance levels. Examples of such systems are IsoDAR RFQ [91] and National Synchrotron Light Source II in China [92] (Fig. 23 and Fig. 24).

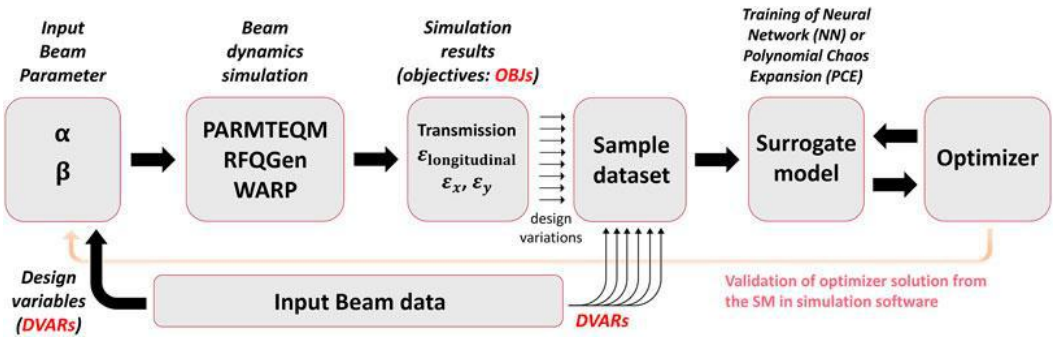

Fig. 23. General machine learning optimization scheme for RFQ beam dynamics. [91]

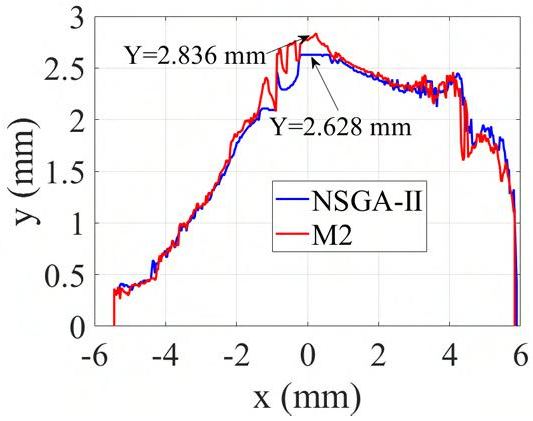

Fig. 24. DA for the HEPS lattice with the best solutions obtained by NSGA-II and M2 method. [92]

4. Pattern recognition: Machine learning algorithms can be used to recognize patterns in the beam dynamics data, helping to identify correlations and trends that may not be apparent through traditional analysis methods [93].

5. Adaptive control: AI-based control systems can adaptively adjust beam parameters based on real-time measurements, ensuring stable and efficient beam dynamics.

6. Automated diagnostics: AI algorithms are utilized to automatically analyze and interpret beam dynamics data, providing insights into the performance of the beam and identifying areas for improvement.

7. Reinforcement learning: AI techniques such as reinforcement learning can be used to train control systems to optimize beam dynamics based on feedback from the beamline.

8. Data-driven decision-making: Machine learning can help in making data-driven decisions for beamline operations, by analyzing large volumes of data to identify patterns and trends that can inform operational strategies [93] (Fig. 25).

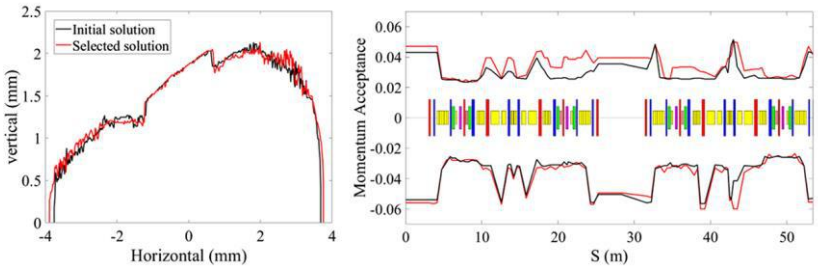

Fig. 25. The numerical tracking results of the DA(left) and local momentum acceptance (right) for the initial solution (black curve) and the selected solution(red curve). [93]

Overall, the application of machine learning and AI to beam dynamics can lead to more efficient and optimized beamline operations, as well as improved diagnostics and control of beam parameters.

Comparison of Beam Dynamic Analysis Methods, Software and Codes

Beam dynamic analysis methods, software, and codes are essential for understanding the dynamics of particle beams, including their trajectory, emittance, energy spread, and other properties. As mentioned before, there are several methods, software, and codes available for beam dynamic analysis, each with its advantages and limitations, and specific applications.

When comparing these methods, it is important to consider factors such as accuracy, computational efficiency, and the ability to handle complex beam dynamics phenomena. Additionally, user-friendliness and availability of support and documentation are also important considerations.

Comparing them involves evaluating their features, capabilities, and performance in various scenarios. This can help researchers and engineers choose the most suitable tool for their specific needs and applications. It is evident that addressing this issue requires separate research and should be tackled independently. So, only a few limited cases are briefly mentioned below.

Furman et al. [94] discussed a comparison of four beam-beam codes, TRS, BBTRACK3D, LIFE-TRAC, and TAIL, under specific conditions. The comparison includes turn-by-turn single particle tracking, tune shift with amplitude, and computation of 1-D and 2-D particle distributions. The simulations involve space-charge expansion and beam transport through an electrostatic lens. The results showed good agreement among the codes and with analytical calculations. They also described algorithms for slicing the opposing bunch longitudinally and for computing the complex error function. The beam-beam kick from one slice is also investigated [94].

Hanke et al. [95] discussed the comparison of simulation codes for the beam dynamics of low-energy ions at the CERN Laser Ion Source. Three simulation codes, KOBRA, IGUN, and CPO were compared using test cases and experimental data. The codes indicated good conformity with each other and with experimental data. The simulations included space-charge expansion and beam transport through an electrostatic lens. The results indicated that the codes are capable of estimating source parameters within acceptable tolerances. However, some discrepancies were observed when comparing the simulations with experimental data [95].

Also in related research, Ostroumov et al. [96] compared the TRACK code with some other code mentioned in Table 2. They considered the results of each code with TRACK and reported near outcomes for most of them. Some of the results related to the comparison of TRACK with other codes are illustrated in Fig. 26.

Table 2. Comparison of TRACK, IMPACT, PARMILA, and TRACEWIN [96]

TRACK	IMPACT	ASTRA	PARMILA	TRACEWIN
Ions & electrons	Ions & electrons	Electrons & (H^-)	Ions	Ions
Multi-beam	Multi-beam	Single beam	Single beam	Single beam
Support any element	Most elem. No RFQ	Less elem. No RFQ	Most elem. No RFQ	Most elem. Calls TOUTATIS
1D, 2D, 3D fields	1D, 2D, 3D fields	1D, (3D) fields	Hard-edge 2D fields	3D fields
3D Poisson	3D Poisson	3D Poisson	2D Poisson	2-3D Poisson
Fast	Fast	2-3x slower	Fast	Fast
Serial/Parallel	Serial/Parallel	Serial only	Serial only	Serial/-
Errors + corrections	Errors + corrections	Errors only	Errors only	Errors + corrections

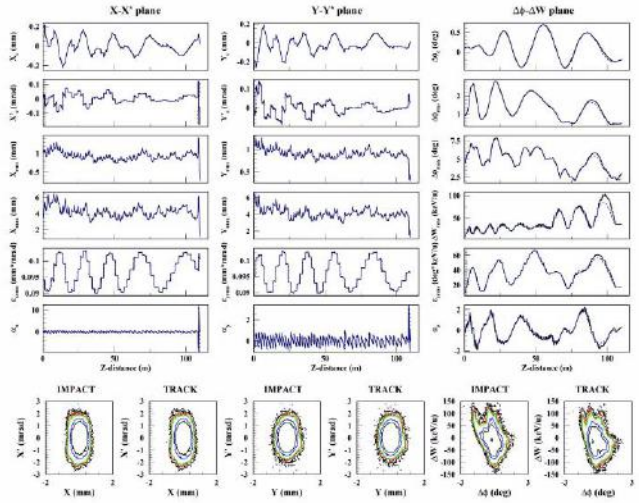

a) RIA driver Linac Beam Dynamics: TRACK (blue) vs IMPACT (black) [97]

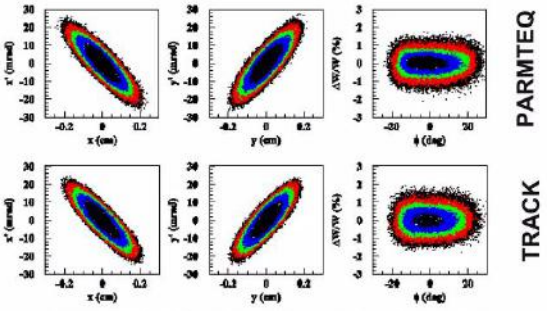

SNS-RFQ: 32 mA H-, 1M particles simulated

Emittance: N-RMS	Parmteq	TRACK
ε-x (mm-mrad)	0.213	0.204
ε-y (mm-mrad)	0.211	0.203
ε-z (deg-keV)	99.63	105.86

b) SNS RFQ Beam Dynamics: TRACK vs PARMTEQ [98]

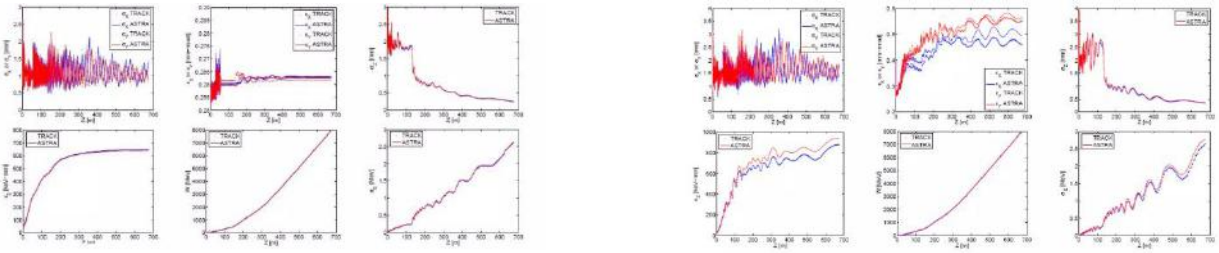

c) FNAL Proton driver Beam Dynamics: TRACK (Dotted curve) vs ASTRA (solid curve) [99]

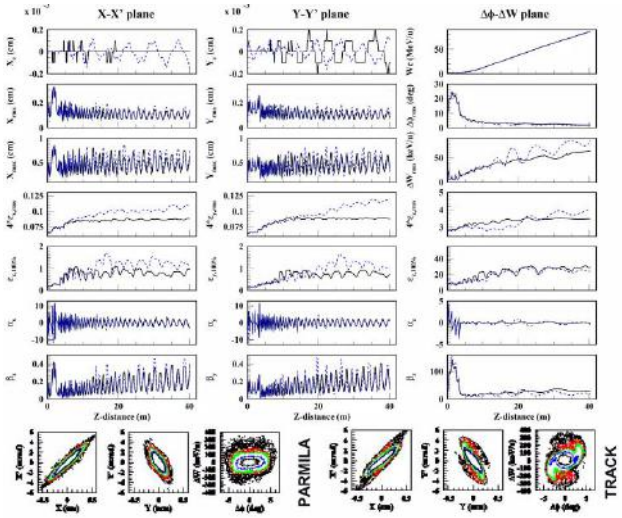

d) SNS Linac Beam Dynamics: TRACK (blue) vs PARMILA (black) [100]

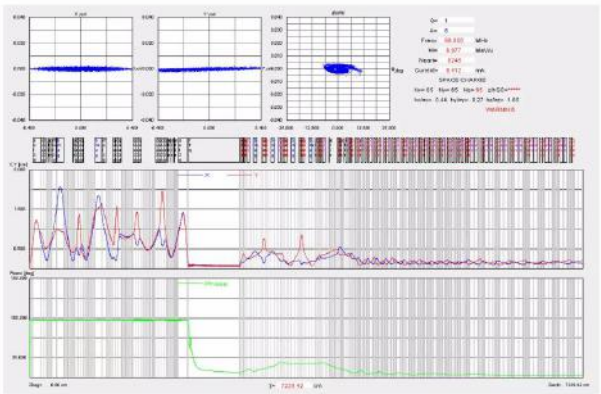

e) SPIRAL-2 Linac Beam Dynamics: TRACK vs TRACEWIN [96]

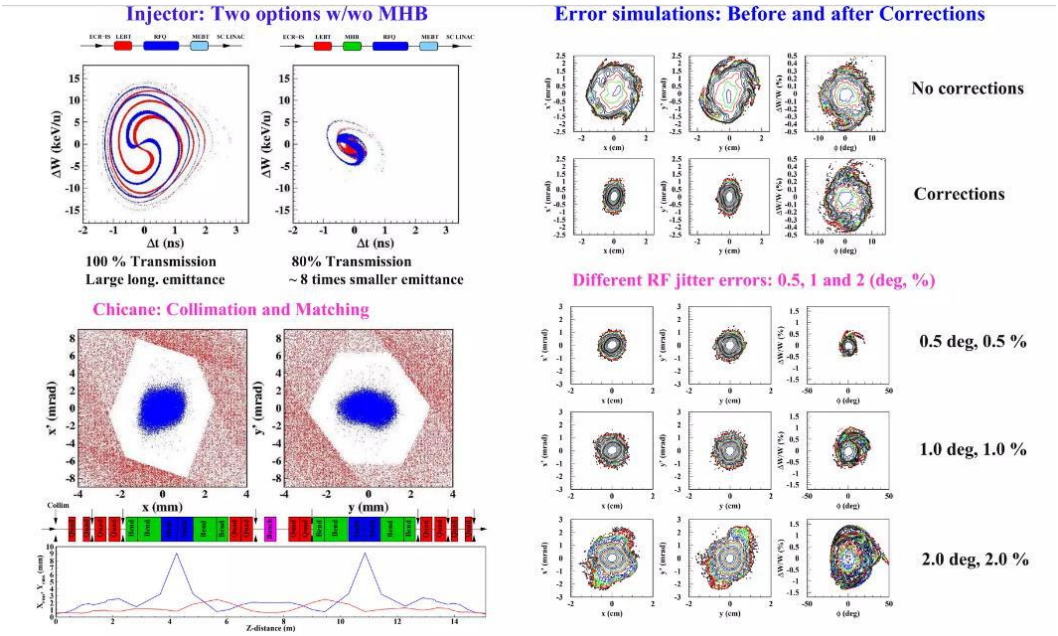

f) TRACK Application: Design of the FRIB Linac [96]

Fig. 26. Comparison of TRACK with other codes

References

[1] Nikolaev, E. N., Heeren, R. M. A., Popov, A. M., Pozdneev, A. V., and Chingin, K. S., 2007, "Realistic Modeling of Ion Cloud Motion in a Fourier Transform Ion Cyclotron Resonance Cell by Use of a Particle-in-cell Approach," Rapid Comm Mass Spectrometry, 21(22), pp. 3527–3546.

[2] Arpaia, P., Azzopardi, G., Blanc, F., Bregliozzi, G., Buffat, X., Coyle, L., Fol, E., Giordano, F., Giovannozzi, M., Pieloni, T., Prevete, R., Redaelli, S., Salvachua, B., Salvant, B., Schenk, M., Camillocci, M. S., Tomás, R., Valentino, G., Van der Veken, F. F., and Wenninger, J., 2021, "Machine Learning for Beam Dynamics Studies at the CERN Large Hadron Collider," Nucl. Instrum. Meth. A, 985, p. 164652.

[3] Batygin, Y. K., 2005, "Particle-in-Cell Code BEAMPATH for Beam Dynamics Simulations in Linear Accelerators and Beamlines," Nucl. Instrum. Meth. A, 539(3), pp. 455–489.

[4] Xiao, C., He, Y., Yuan, Y.-J., Lu, Y.-R., Liu, Y., Wang, Z.-J., Du, X.-N., Yao, Q.-G., Liu, G., Xu, M.-X., He, S.-B., and Xia, J.-W., 2012, "A Particle-in-Cell Mode Beam Dynamics Simulation of Medium Energy Beam Transport for the SSC-Linac," Chinese Phys. C, 36(1), pp. 84–90.

[5] Qiang, J., Ryne, R. D., Blind, B., Billen, J. H., Bhatia, T., Garnett, R. W., Neuschaefer, G., and Takeda, H., 2001, "High-Resolution Parallel Particle-in-Cell Simulations of Beam Dynamics in the Spallation Neutron Source Linac," Nuclear Instruments and Methods in Physics Research Section A: Accelerators, Spectrometers, Detectors and Associated Equipment, 457(1), pp. 1–11.

[6] Bruhwiler, D. L., Giacone, R. E., Cary, J. R., Verboncoeur, J. P., Mardahl, P., Esarey, E., Leemans, W. P., and Shadwick, B. A., 2001, "Particle-in-Cell Simulations of Plasma Accelerators and Electron-Neutral Collisions," Phys. Rev. ST Accel. Beams, 4(10), p. 101302.

[7] Salamin, Y. I., Zhao, Q., and Sun, T., 2023, "Investigation of the Collective Effects in the Cosmic Zevatron Based on Cyclotron Auto-Resonance by Preliminary Particle-in-Cell Simulations," Phys. Lett. A, 478, p. 128918.

[8] Winklehner, D., Adelmann, A., Gsell, A., Kaman, T., and Campo, D., 2017, "Realistic Simulations of a Cyclotron Spiral Inflector within a Particle-in-Cell Framework," Phys. Rev. Accel. Beams, 20(12), p. 124201.

[9] Fu, Y., Yang, J., Mou, H., Tan, R., Xia, X., and Gao, Z., 2022, "Integrative Simulation of a 2 Cm Electron Cyclotron Resonance Ion Source with Full Particle-in-Cell Method," Computer Physics Communications, 278, p. 108395.

[10] Yuan, Y.-S., Wang, N., Xu, S.-Y., Yuan, Y., and Wang, S., 2015, "Theoretical Study of a Dual Harmonic System and Its Application to the CSNS/RCS*," Chin. Phys. C, 39(12), p. 127002.

[11] Pardal, M., Sainte-Marie, A., Reboul-Salze, A., Fonseca, R. A., and Vieira, J., 2023, "RaDiO: An Efficient Spatiotemporal Radiation Diagnostic for Particle-in-Cell Codes," Computer Physics Communications, 285, p. 108634.

[12] Huang, C., An, W., Decyk, V. K., Lu, W., Mori, W. B., Tsung, F. S., Tzoufras, M., Morshed, S., Antonsen, T., Feng, B., Katsouleas, T., Fonseca, R. A., Martins, S. F., Vieira, J., Silva, L. O., Esarey, E., Geddes, C. G. R., Leemans, W. P., Cormier-Michel, E., Vay, J.-L., Bruhwiler, D. L., Cowan, B., Cary, J. R., and Paul, K., 2009, "Recent Results and Future Challenges for Large Scale Particle-in-Cell Simulations of Plasma-Based Accelerator Concepts," J. Phys. Conf. Ser., 180, p. 012005.

[13] Mori, W. B., 2002, "Recent Advances and Some Results in Plasma-Based Accelerator Modeling," AIP Conf. Proc., 647(1), pp. 11–28.

[14] C Huang, V K Decyk, M Zhou, W Lu, W B Mori, J H Cooley, T M Antonsen Jr, B Feng, T Katsouleas, J Vieira, and L O Silva, 2006, "QuickPIC: A Highly Efficient Fully Parallelized PIC Code for Plasma-Based Acceleration," Journal of Physics: Conference Series, 46(1), p. 190.

[15] Welch, D. R., Bennett, N., Genoni, T. C., Thoma, C., and Rose, D. V., 2020, "Fast Hybrid Particle-in-Cell Technique for Pulsed-Power Accelerators," Phys. Rev. Accel. Beams, 23(11), p. 110401.

[16] Lee, Y., Kim, E.-S., Hwang, J.-G., Lee, J., and Kim, J., 2024, "Beam Dynamics in the Booster Synchrotron of Korea-4GSR Project," Nuclear Instruments and Methods in Physics Research Section A: Accelerators, Spectrometers, Detectors and Associated Equipment, 1060, p. 169074.

[17] Wolski, A., 2014, *Beam Dynamics in High Energy Particle Accelerators*, IMPERIAL COLLEGE PRESS.

[18] Majernik, N., Andonian, G., Lynn, W., Kim, S., Lorch, C., Roussel, R., Doran, S., Wisniewski, E., Whiteford, C., Piot, P., Power, J., and Rosenzweig, J. B., 2023, "Beam Shaping Using an Ultrahigh Vacuum Multileaf Collimator and Emittance Exchange Beamline," Phys. Rev. Accel. Beams, 26(2), p. 022801.

[19] Kumar, V., and Sharma, A., 2023, *A REVIEW OF CALCULATION OF EMITTANCE GROWTH FOR SOME COMMON CASES IN ACCELERATOR PHYSICS*.

[20] "Phase Space Distributions and Emittance in 2D Charged Particle Beams | COMSOL Blog" [Online]. Available: https://www.comsol.com/blogs/phase-space-distributions-and-emittance-in-2d-charged-particle-beams/.

[21] Roussel, R., Edelen, A., Kennedy, D., Kim, S., Wisniewski, E., and Power, J., 2023, "Demonstration of Autonomous Emittance Characterization at the Argonne Wakefield Accelerator," Instruments, 7(3), p. 29.

[22] Deng, H., and Feng, C., 2013, "Using Off-Resonance Laser Modulation for Beam-Energy-Spread Cooling in Generation of Short-Wavelength Radiation," Phys. Rev. Lett., 111(8), p. 084801.

[23] Chao, A. W., Tigner, M., Weise, H., and Zimmermann, F., 2023, *Handbook of Accelerator Physics and Engineering; 3rd Ed.*, World Scientific, Singapore.

[24] Makino, K., and Berz, M., 2006, "COSY INFINITY Version 9," Nucl. Instrum. Meth. A, 558(1), pp. 346–350.

[25] Smirnov, V., 2017, "Computer Codes for Beam Dynamics Analysis of Cyclotronlike Accelerators," Phys. Rev. Accel. Beams, 20(12), p. 124801.

[26] Adelmann, A., Calvo, P., Frey, M., Gsell, A., Locans, U., Metzger-Kraus, C., Neveu, N., Rogers, C., Russell, S., Sheehy, S., Snuverink, J., and Winklehner, D., 2019, "OPAL a Versatile Tool for Charged Particle Accelerator Simulations," arXiv:1905.06654 [physics.acc-ph].

[27] "The OPAL Framework: Version 2022.1-Dev" [Online]. Available: https://amas.web.psi.ch/opal/Documentation/master/.

[28] Aseev, V. N., Ostroumov, P. N., Lessner, E. S., and Mustapha, B., 2005, "TRACK: The New Beam Dynamics Code," *Proceedings of the 2005 Particle Accelerator Conference*, IEEE, pp. 2053–2055.

[29] Rao, Y. N., and Baartman, R., 2013, "50 Years of Cyclotrons Designed Using CYCLOPS," Proceedings of FFAG'13, pp. 21–24.

[30] Milton, B. F., 1999, *CYCLONE VERS 8.4*, TRI-DN-99-4, TRIUMF, Vancouver, BC, Canada.

[31] Smirnov, V. L., and Vorozhtsov, S. B., 2012, "SNOP—Beam Dynamics Analysis Code for Compact Cyclotrons," *Proc. 23rd Russian Particle Accelerator Conf.(RuPAC'12)*, pp. 325–327.

[32] Onischenko, L. M., and Samsonov, E. V., 2001, "Code Phascol for Computation of Space Charge Effects in the Cyclotrons and Synchrocyclotrons," Вопросы атомной науки и техники.

[33] Milton, B. F., and Pearson, J. B., 1989, *Annual Report Scientific Acivities*, TRI-DN-89-19, Canada's National Meson Facility, TRUIMF.

[34] Pearson, J. B., Balden, R. J., Kleeven, W. J., Milinkovic, L. S., and Milton, B. F., 1991, "Aspects of Phase Space Dynamics in Spiral Inflectors," *12th International Conference on Cyclotrons and Their Applications*, p. G1.02.

[35] Sauret, J., Chabert, A., and Prome, M., 1984, "Multiparticle Codes Developed at GANIL," *Computing in Accelerator Design and Operation*, W. Busse, and R. Zelazny, eds., Springer Berlin Heidelberg, Berlin, Heidelberg, pp. 164–169.

[36] Gorelov, D., Johnson, D., and Marti, F., 2001, "NORTICA—a New Code for Cyclotron Analysis," *AIP Conference Proceedings*, American Institute of Physics, pp. 414–416.

[37] Van der Geer, S. B., De Loos, M. J., and Bongerd, D., 1996, "General Particle Tracer: A 3D Code for Accelerator and Beam Line Design," *Proc. 5th European Particle Accelerator Conf., Stockholm*.

[38] Yaramyshev, S., Barth, W., Lauber, S., Miski-Oglu, M., Rubin, A., Scheeler, U., Vormann, H., and Vossberg, M., 2023, "DYNAMION—A Powerful Beam Dynamics Software Package for the Development of Ion Linear Accelerators and Decelerators," Appl. Sciences, 13(14), p. 8422.

[39] "Madx.Web.Cern.Ch/Madx."

[40] Deniau, L., Burkhardt, H., De Maria, R., Giovannozzi, M., Gläßle, T., Jowett, J., Latina, A., Persson, T., Schmidt, F., Shreyber, I., and Skowroński, P., 2019, "Upgrade of MAD-X for HL-LHC Project and FCC Studies," *Proceedings of the 13th Int. Computational Accelerator Physics Conf.*, p. 7 pages, 0.785 MB.

[41] Deniau, L., Grote, H., Roy, G., and Schmidt, F., "MADX Program (Methodical Accelerator Design) Version 5.04.00 User's Reference Manual."

[42] Flowerdew, J., 2023, "Investigating Nonlinear Integrable Optics with a Paul Trap," PhD, University of Oxford.

[43] De Maria, R., Deniau, L., Dilly, J., Gray, J. M., Latina, A., Schmidt, F., Skowronski, P., Berg, J. S., and Gläßle, T., 2023, "Status of MAD-X V5.09," p. WEPL101.

[44] Fomin, A., Abukeshek, R., Bogacz, A., Bruni, C., Guyot, C., Michaud, J., and Perrot, L., 2023, "Lattice Design of 250 MeV Version of Perle," JACoW, IPAC2023, p. TUPL171.

[45] Berg, J., Palmer, R., and Witte, H., 2023, "Lattice Design for the Interaction Region of the Electron-Ion Collider," JACoW, IPAC2023, p. MOPL158.

[46] Streun, A., Aiba, M., Böge, M., Calzolaio, C., Ehrlichman, M., Negrazus, M., Riemann, B., and Vrankovic, V., 2023, "Swiss Light Source Upgrade Lattice Design," Phys. Rev. Accel. Beams, 26(9), p. 091601.

[47] Grote, H., and Schmidt, F., 2003, "Mad-X - an Upgrade from Mad8," *Proceedings of the 2003 Particle Accelerator Conference*, IEEE, Portland, OR, pp. 3497–3499.

[48] Herr, W., 2004, *Particle Tracking with MAD-X Including LHC Beam-Beam Interactions*, CERN, Geneva.

[49] Schicho, P., 2015, "Optimizing Simulation Times of SPS Slow Extraction Using MAD-X."

[50] Carver, L. R., Buffat, X., Li, K., Métral, E., and Schenk, M., 2018, "Transverse Beam Instabilities in the Presence of Linear Coupling in the Large Hadron Collider," Phys. Rev. Accel. Beams, 21(4), p. 044401.

[51] Park, C. S., Freemire, B., Chung, M., Stancari, G., and Stern, E., 2021, "Progress in Space Charge Compensation Using Electron Columns," JINST, 16(03), p. P03048.

[52] Paret, S., and Boine-Frankenheim, O., 2010, "SPACE CHARGE EFFECTS DURING MULTITURN INJECTION INTO SIS-18," p. 76.

[53] Nevay, L. J., Snuverink, J., Abramov, A., Deacon, L. C., Garcia-Morales, H., Lefebvre, H., Gibson, S. M., Kwee-Hinzmann, R., Shields, W., Walker, S. D., and Boogert, S., 2020, "BDSIM: An Accelerator Tracking Code with Particle-Matter Interactions," Comput. Phys. Commun., 252, p. 107200.

[54] Borland, M., 2000, "Elegant: A Flexible SDDS-Compliant Code for Accelerator Simulation," *6th International Computational Accelerator Physics Conference (ICAP 2000)*.

[55] Wang, Y., and Borland, M., 2006, "Pelegant: A Parallel Accelerator Simulation Code for Electron Generation and Tracking," AIP Conf. Proc., 877(1), pp. 241–247.

[56] King, J. R., Pogorelov, I. V., Amyx, K. M., Borland, M., and Soliday, R., 2019, "GPU Acceleration and Performance of the Particle-Beam-Dynamics Code Elegant," Comput. Phys. Commun., 235, pp. 346–355.

[57] Hanuka, A., Emma, C., Maxwell, T., Fisher, A. S., Jacobson, B., Hogan, M. J., and Huang, Z., 2021, "Accurate and Confident Prediction of Electron Beam Longitudinal Properties Using Spectral Virtual Diagnostics," Sci. Rep., 11(1), p. 2945.

[58] 2009, "Proceedings of International Computational Accelerator Physics Conference 2009," San Francisco, CA, USA.

[59] Humphries, S., 1990, *Charged Particle Beams*.

[60] Mohamadian, M., Afkhami, M., Solhju, R., and Afarideh, H., 2022, "Modify RF Cavity of 10 MeV Cyclotron to Improve the Beam Gain by Beam Dynamic Analysis," Iranian Journal of Science and Technology, Transactions A: Science, 46(2), pp. 677–688.

[61] Lee, J., Ghergherehchi, M., Namgoong, H., Kim, H., Ha, D., Yeon, Y. H., Kim, H. W., and Chai, J.-S., 2020, "Characterization of Beam Dynamics for SKKUCY-10 Cyclotron," Nucl. Instrum. Meth. B, 468, pp. 71–80.

[62] Iliakis, K., Timko, H., Xydis, S., Tsapatsaris, P., and Soudris, D., 2022, "Enabling Large Scale Simulations for Particle Accelerators," IEEE Trans. Parallel Distrib. Syst., 33(12), pp. 4425–4439.

[63] Pöplau, G., van Rienen, U., and Flöttmann, K., 2006, "New 3D Space Charge Routines in the Tracking Code Astra," *Proceedings of ICAP 2006 (Proceedings of the 9th International Computational Accelerator Physics Conference), Chamonix Mont-Blanc, France*, pp. 135–138.

[64] "CST Studio Suite" [Online]. Available: www.cst.com.

[65] Zhu, R., Chen, W., Li, H., Ouyang, H., Liu, S., Xiao, Y., Lü, Y., Cao, X., Li, F., Sun, J., Liu, S., and Xue, K., 2022, "Optimization of Transverse Emittance for RF-Driven Negative Hydrogen Ion Source Developed at China Spallation Neutron Source," Review of Scientific Instruments, 93(5), p. 053302.

[66] Ghergherehchi, M., Mu, X.-J., Yeon, Y.-H., and Chai, J.-S., 2014, "Simulation of Electron Behavior in PIG Ion Source for 9 MeV Cyclotron," Chin. Phys. C, 38(12), p. 127004.

[67] Hosseinzadeh, M., and Afarideh, H., 2013, "Optimization and Numerical Simulation for the Accelerator of the Commercial H-Cyclotron Ion Source," arXiv preprint arXiv:1306.0984.

[68] Adam, G., 2021, "Modulated Electron Beam Produced by a Thermionic Cathode Electron Gun for Particle Accelerator Applications."

[69] V. Goel, R. Chandra, A. Roy, and N. Maiti, 2020, "Electrostatically and Electromagnetically Focused 60kW Electron Gun for High Voltage Applications," *2020 International Conference on Convergence to Digital World - Quo Vadis (ICCDW)*, pp. 1–6.

[70] Spachmann, H., and Becker, U., 2006, "Electron Gun Simulation with CST PARTICLE STUDIO," Nuclear Instruments and Methods in Physics Research Section A: Accelerators, Spectrometers, Detectors and Associated Equipment, 558(1), pp. 50–53.

[71] Nazari, M., Abbasi, F., Ghasemi, F., and Jafarzadeh, M., 2016, "Design and Simulation of a Thermionic Electron Gun for a 1 MeV Parallel Feed Cockcroft-Walton Industrial Accelerator," *7th Int. Particle Accelerator Conf.(IPAC'16), Busan, Korea, May 8-13, 2016*, JACOW, Geneva, Switzerland, pp. 1976–1978.

[72] Dhavale, A. S., and Acharya, S., 2018, "9-Sector Compression Magnet Design," JINST, 13(12), p. P12025.

[73] Namgoong, H., Kim, H. S., Lee, J. C., Ha, D. H., and Chai, M. G. J.-S., 2020, "Design of High Sensitive Magnet and Beam Dynamics for AMS Cyclotron," mass spectrometry, 1, p. 2.

[74] Dhavale, A. S., Sarkar, S. G., Mittal, K. C., and Gantayet, L. M., 2014, "Beam Dynamics Study and Design of 348° Compression Magnet for Neutron Time of Flight (n-TOF) Facility," JINST, 9(01), p. T01003.

[75] Kurennoy, S., and Batygin, Y., 2022, "CST Modeling of the LANSCE Coupled-Cavity Linac," *JACoW*, JACOW Publishing, Geneva, Switzerland, p. MOPOGE17.

[76] Kurennoy, S. S., 2018, *Beam Dynamics Modeling of the Proton RFQ MEBT with CST Particle Studio*, Los Alamos National Lab.(LANL), Los Alamos, NM (United States).

[77] Parashar, S., Dhavale, A. S., and Sharma, A., 2021, "Design and Development of Particle Accelerator Components for a 10MeV Industrial Linac," *2021 22nd International Vacuum Electronics Conference (IVEC)*, IEEE, pp. 1–2.

[78] Dang, J. J., Kim, H. S., Kwon, H. J., and Lee, S., 2022, "Multipacting Simulation on Half-Wave Resonator for 200 MeV Energy Upgrade of Komac Proton Linac."

[79] Fan, M., Liu, H., Li, A., Wu, X., Wang, Y., Qu, P., Chen, Q., and Li, B., 2020, "Multipacting Study of Power Couplers for the CSNS DTL," Nuclear Instruments and Methods in Physics Research Section A: Accelerators, Spectrometers, Detectors and Associated Equipment, 953, p. 163067.

[80] Romanov, G., 2017, "Simulation of Multipacting with Space Charge Effect," American Journal of Physics and Applications, 5(FERMILAB-PUB-17-399-TD).

[81] Berrutti, P., Khabiboulline, T., Ristori, L., Romanov, G., Sukhanov, A., and Yakovlev, V., 2013, *Multipacting Simulations of SSR2 Cavity at FNAL.*, Fermi National Accelerator Lab.(FNAL), Batavia, IL (United States).

[82] Becker, U., 2007, "Recent Developments in 3D Electromagnetic and Charged Particle Simulation," *2007 IEEE International Vacuum Electronics Conference*, pp. 1–4.

[83] Maesaka, H., Otake, Y., Togawa, K., Shintake, T., Ego, H., Fukui, T., Hosoda, N., and Ohshima, T., 2007, "BEAM POSITION MONITOR AT THE SCSS PROTOTYPE ACCELERATOR."

[84] Trummer, S., 2017, "Beam Position Monitor for Electron Linear Accelerator."

[85] Wendt, M., 2021, "A Brief **Introduction** to Beam Position Monitors for Charged Particle Accelerators," IEEE Instrum. Measur. Mag., 24(9), pp. 21–32.

[86] Forck, P., Kowina, P., and Liakin, D., 2008, "Beam Position Monitors," CAS - CERN Accelerator School: Course on Beam Diagnostics, Dourdan, France.

[87] Gibson, S. M., Boorman, G. E., Bosco, A., and Holloway, R., 2013, "Overview of Laserwire Beam Profile and Emittance Measurements for High Power Proton Accelerators," *Proceedings of IBIC 2013*.

[88] Rosily, S., Kewlani, H., Mathew, J. V., Thomas, R., Dikshit, B., and Krishnagopal, S., 2023, "Gas Sheet Beam Induced Fluorescence Based Beam Profile Measurement for High Intensity Proton Accelerators," Nucl. Instrum. Meth. A, 1058, p. 168851.

[89] Reith, M., Franke, M., and Körner, C., 2023, "Robust γ-TiAl Dual Microstructure Concept by Advanced Electron Beam Powder Bed Fusion Technology," Crystals, 13(9).

[90] de Sousa, A. A. S. R., da Silva Coelho, J., Machado, M. R., and Dutkiewicz, M., 2023, "Multiclass Supervised Machine Learning Algorithms Applied to Damage and Assessment Using Beam Dynamic Response," Journal of Vibration Engineering & Technologies, 11(6), pp. 2709–2731.

[91] Koser, D., Waites, L., Winklehner, D., Frey, M., Adelmann, A., and Conrad, J., 2022, "Input Beam Matching and Beam Dynamics Design Optimization of the IsoDAR RFQ Using Statistical and Machine Learning Techniques," Front. in Phys., 10, p. 875889.

[92] Wan, J., Chu, P., Jiao, Y., and Li, Y., 2019, "Improvement of Machine Learning Enhanced Genetic Algorithm for Nonlinear Beam Dynamics Optimization," Nucl. Instrum. Meth. A, 946, p. 162683.

[93] Wan, J., Chu, P., and Jiao, Y., 2020, "Neural Network-Based Multiobjective Optimization Algorithm for Nonlinear Beam Dynamics," Phys. Rev. Accel. Beams, 23(8), p. 081601.

[94] Furman, M., Zholents, A., Chen, T., and Shatilov, D., "Comparisons of Beam-Beam Code Simulations."

[95] Hanke, K., Heising, S., Probert, G., and Scrivens, R., 2002, "Comparison of Simulation Codes for the Beam Dynamics of Low-Energy Ions," Rev. Sci. Instrum., 73, pp. 783–785.

[96] Ostroumov, P. N., Mustapha, B., and Carneiro, J.-P., 2009, "ESS-Bilbao Initiative Workshop. Beam Dynamics Codes: Availability, Sophistication, Limitations."

[97] Mustapha, B., Aseev, V. N., Ostroumov, P. N., Qiang, J., and Ryne, R. D., 2005, "RIA Beam Dynamics: Comparing Track to Impact," *Proceedings of the 2005 Particle Accelerator Conference*, pp. 2095–2097.

[98] B.Mustapha and P.N.Ostroumov, 2008, "End-to-End Simulation of the SNS Linac Using TRACK."

[99] Carneiro, J.-P., 2006, "Benchmarking of Simulation Codes TRACK and ASTRA for the FNAL High-Intensity Proton Source," *Proceedings of LINAC 2006*, Knoxville,Tennessee USA.

[100] Mustapha, B., and Aseev, V. N., 2006, "First TRACK Simulations of the SNS Linac," *Proceedings of LINAC 2006*, Knoxville,Tennessee USA.

ICNST 2024
International Conference on Nuclear Science and Technology
6- 8 MAY 2024 | Isfahan, Iran

Qualitative Study of the P¯ANDA Planar GEM-Tracker acceptance in the decay channel p¯p→Λ¯Λ→p¯pπ^+ π^- (Paper ID : 1055)

Divani N. Correspondent[1*]

[1] *Physics Department, University of Birjand, Birjand, Iran*

Abstract

The $\bar{P}$ANDA (anti-Proton ANnihilation in DArmstadt) experiment, which studies proton anti-proton annihilations, will be installed at the future facility for anti-proton and ion research in Darmstadt, Germany. $\bar{P}$ANDA detectors can cover a wide physics program which includes baryon and meson spectroscopy, studies of quantum chromodynamics, nucleon structure, electromagnetic processes, the study of hadrons in nuclei, and hypernuclear physics including the study of excited hyperon states. One specific feature of most hyperon ground states are long decay lengths of several centimeters. The central tracking detectors of $\bar{P}$ANDA are not completely optimized for these long decay lengths. Therefore, an upgrade option is proposed to use a set of the planar GEM trackers in forward region of interest. The current and conceptual designed $\bar{P}$ANDA GEM tracking stations contribute to measure particles emitted in the polar angles between about 2 to 22 degrees that are not covered by other kind of detectors in the $\bar{P}$ANDA setup. For this detector acceptance studies have been performed using the decay channel $\bar{p}p \rightarrow \bar{\Lambda}\Lambda \rightarrow \bar{p}p\pi^+\pi^-$.

Keywords: FAIR, $\bar{P}$ANDA, GEM-Tracking Detector, Hyperon

Introduction and Motivation

The standard model of particles physics describes the elementary particles and their interactions. Strong interactions of quarks and gluons are described by the theory of quantum chromodynamics (QCD) [1]. The motivation of $\bar{P}$ANDA is to explore the transfer region between perturbative and non-perturbative QCD [2]. One of its physics program is the study of hyperons and their excited states. Hyperons decay weakly and therefore this have a long life time and a mean decay length of several centimeters. To investigate the impact of the GEM-Tracking detector for hyperons in inner part of the $\bar{P}$ANDA setup, the simulations have been performed with $\bar{p}p \rightarrow \bar{\Lambda}\Lambda \rightarrow \bar{p}p\pi^+\pi^-$ decay channel. This channel has been chosen because Λ is the

[1] n_divani@birjand.ac.ir

lightest hyperon, which is easiest to produce and all the final-state particles are charged particles [3]. Simulations were carried out using the PandaRoot framework based on FairRoot [11].

The $\bar{P}$ANDA experimental setup

The $\bar{P}$ANDA [4] detector will be a part of the HESR[2] at FAIR facility for antiproton and ion research [5]. The HESR [6] will provide anti-protons with momenta from of 1.5 GeV/c up to 15 GeV/c, corresponding to center-of-mass energies of 2.0 up to 5.5 GeV. The $\bar{P}$ANDA is a fixed target experiment. It consists of two parts, the target spectrometer (TS) with a cylindrical geometry which is mounted around the interaction region in 2 T solenoid magnetic field and the forward spectrometer (FS) for the reconstruction of high-energy, forward-boosted particles in 1 T dipole magnetic field. This design allows the $\bar{P}$ANDA detectors to provide almost 4π acceptance for both charged and neutral particles. A property of hyperons is their long life time, and hence long decay length. For the tracks reconstruction of these particles a central tracking system is used. This central tracking system consists of the Micro Vertex Detector (MVD), the Straw Tube Tracker (STT) and the Gas Electron Multiplier (GEM) stations. The MVD is a silicon based high precision vertex detector and the innermost sub-detector enclosing the interaction point. The STT consists of gas filled drift tubes arranged in a cylindrical geometry around the beam axis. The GEM stations are also gas based detectors with planar geometry located directly downstream of the STT, and are thus important to reconstruct the trajectories of particles emitted in the forward direction within the target spectrometer. This central tracking system provides a high tracking resolution. In addition, the information from these detectors is combined with other components of $\bar{P}$ANDA to provide a good particle identification [7].

The $\bar{P}$ANDA Planar-GEM Tracking Detector

In the $\bar{P}$ANDA experiment, charged particles proceeding to the forward directions with the polar angles approximately between 2 to 22 degrees (that are not covered by other kind of detectors in the $\bar{P}$ANDA setup) [8] will be measured by a set of large-area planar gaseous micro-pattern detectors equipped with GEM foils as amplification stages. The current GEM-tracker has been implemented as a system of three GEM-disc stations as the conceptual technical design. Each station realizes a complex series of multi-layers with aluminized Kapton windows serving as screening, cathodes, a set of GEM foils, position sensitive pad

[2] High Energy Storage Ring

planes, an Argon/CO_2 mixture as the detector gas containers, cooling and support-structures as well as front-end electronic devices. Each of the GEM foils and pad planes is represented as a sandwich of three thin layers with a Copper-Kapton-Copper configuration. The double-sided read-out pad planes are located in the center of each GEM-disc station providing strip information about crossing particles in four projections: radial and circular in upstream, horizontal and vertical on the downstream side. In this presented design, the $\bar{P}$ANDA GEM-tracker stations are in form of circular planes (disk shape) with the same gap and holes in the middle. The entire thickness of the main part of each GEM station is about 6 cm in beam direction, and it consists of various kinds of materials for main layers and GEM foils such as Kapton, Aluminum and Copper. The holding and supporting structures are made from Carbon and Glass Fibers with total thickness of 2 cm and 4 cm per station, respectively. In addition, each GEM station contributes with segments for the electronic devices, cables and supplies conduit, gas containers and cooling support rings. The total radius and the position (Z) along the beam line (in the Cartesian coordinate originating from the interaction point) of each station respectively are 45 and 119.4 cm for the first station, 56 and 155.4 cm for the second station and 74 and 188.5 cm for the last one. The Riddle shell is a rigid and light-weight supporting structures made from Carbon Fibers which holds all the GEM-tracker stations in place has also been implemented. The entire GEM-tracker with three stations and the supporting structure is shown in Fig. 1. It is placed inside the target spectrometer of the $\bar{P}$ANDA setup.

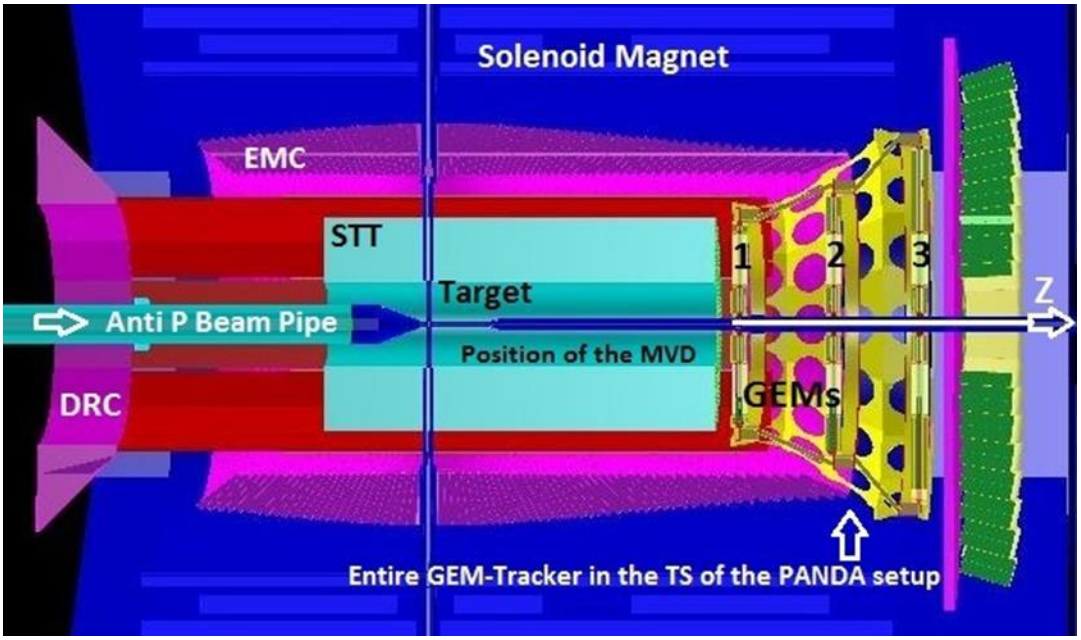

Fig. 1. The Monte Carlo simulation of the $\bar{P}$ANDA GEM-tracker assembly together with the detector systems surrounding the target in the target spectrometer (TS). The beam pipe along the Z-axis and the position of the

target, the micro vertex detector (MVD), the straw tube tracker (STT), the Cherenkov detection system (DRC) and the electromagnetic calorimeters (EMC) which are referred in the discussion in this text are also shown.

Acceptance Studies and Results for the $\bar{P}$ANDA GEM-Trackers

Acceptance studies have been performed for the $\bar{p}p \rightarrow \bar{\Lambda}\Lambda \rightarrow \bar{p}p\pi^{+}\pi^{-}\ decay$ channel using the $\bar{P}$ANDA GEM-Trackers at an incident beam momentum of 2 GeV/c which is near the production threshold. For the simulation of the $\bar{\Lambda}\Lambda$ decay the EvtGenDirect (forward peaking generator) event generator is used [9]. EvtGenDirect used the Lambda-LambdaBar model which is based on the angular distribution of Λ measured in the PS185 experiment [10]. Full $\bar{P}$ANDA detector setup including the $\bar{P}$ANDA GEM-Trackers has been used in the PandaRoot framework [11] which is based on FairRoot [12]. PandaRoot has been developed to perform the detector simulations and reconstructions code within the FairRoot software framework. Several kinds of event generators can be applied to create particles and several simulation engines can be used to transport them. The package contains reconstruction, tracking, particles identification, and physics analysis procedures.

Mass Resolution:

The full $\bar{P}$ANDA setup based on the PandaRoot framework has been used in two cases with the GEM-tracker (with contributions of the three inner trackers STT, MVD, and GEM together) and without GEM-tracker (with contributions of the two inner trackers STT and MVD only) in order to study and compare the behavior and the performance of the current designed GEM-tracker in this physics decay channel (using same simulastion criterias in two cases). The mentioned reaction was simulated at beam momenta of 2 GeV/c of the boosted anti-protons by generating one thousand events to study a real state of interaction as the forward peaking. The simulations have been done with the realistic pattern recognition for the track finding procedure [13]. The influence of the GEM-tracker in order to improve the invariant mass reconstruction in this channel are shown in Figs. 2 and 3. The Λ invariant mass reconstruction for all possible combinations of the Lambda decay products candidates which is clearly optimized by using GEM-tracker in forward direction.

Fig. 2 shows the invariant mass reconstruction and the polar angular distribution of the simulated Lambdas with (red) and without (black) GEM-tracker in the $\bar{P}$ANDA setup. The left panel of Fig. 2 demonstrates the Lambda mass reconstruction for all possible combinations of the related particles in this decay channel.

The right panel of Fig. 2 is also implied a big improvement using GEM-tracker to show the reconstructed Lambda in forward directions of interest (below 22 degrees) qualitatively. Fig. 3 shows the same plots for the reconstructed anti-Lambdas which are shown better enhancement using GEM-tracker in comparison with reconstructed Lambdas. Therefore, one can conclude that the present layout of the GEM-tracker is helpful to increase the invariant mass reconstruction of the mentioned particles. Although, the plots qualitatively can show good reconstruction efficiency for both particles, it is high for anti-Lambdas.

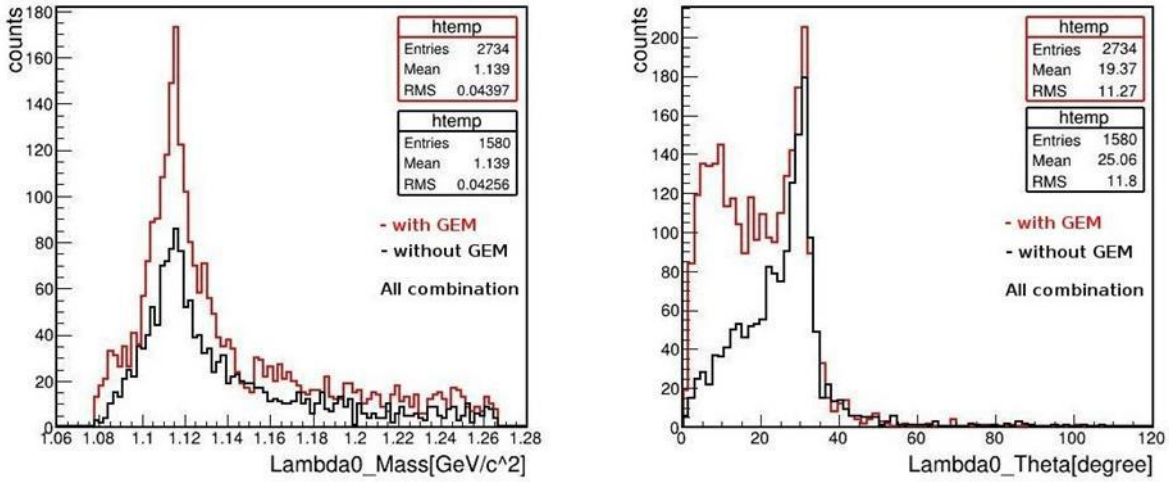

Fig. 2. The invariant mass reconstruction and the polar angular distribution of the simulated Lambdas with (red) and without (black) GEM-tracker in the $\bar{P}$ANDA setup.

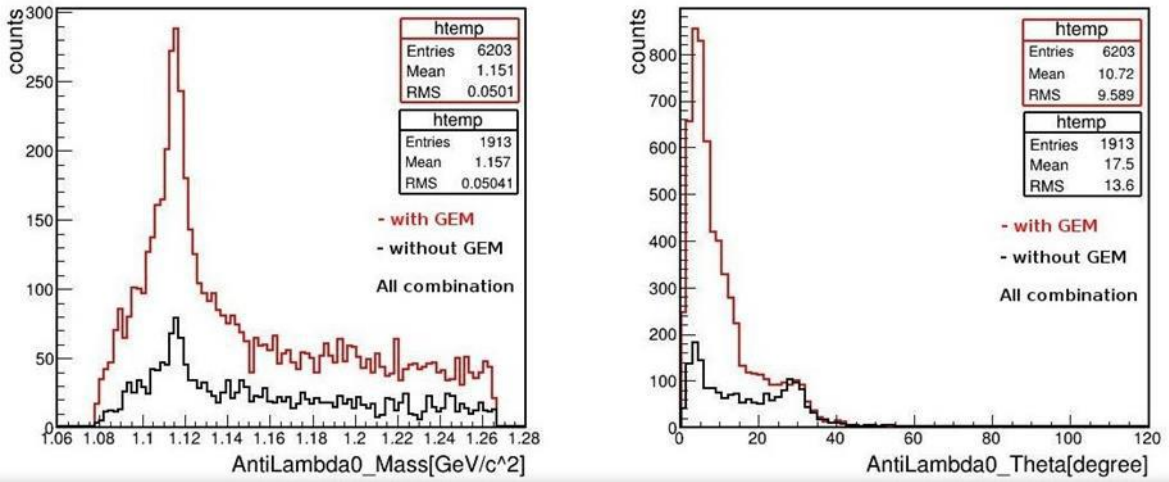

Fig. 3. The invariant mass reconstruction and the polar angular distribution of the simulated anti-Lambdas with (red) and without (black) GEM-tracker in the $\bar{P}$ANDA setup.

Angular distribution:

It is important to understand the angular distributions of all the final-state particles for the optimization of the detector position and its coverage. Fig. 4 shows the angular distributions for all final-state particles (p, $\bar{p}$, π^+, π^-) and also for the reconstructed Lambda and anti-Lambda. It has been observed that p and $\bar{p}$ have a maximum decay angle up to 42 degrees (shown in the left panel of Fig. 4). However, Pions (π^+, π^-) are distributed from zero to ninety degrees (shown in the middle panel of Fig. 4). The simulation was run by using entire setup of $\bar{P}$ANDA detections systems.

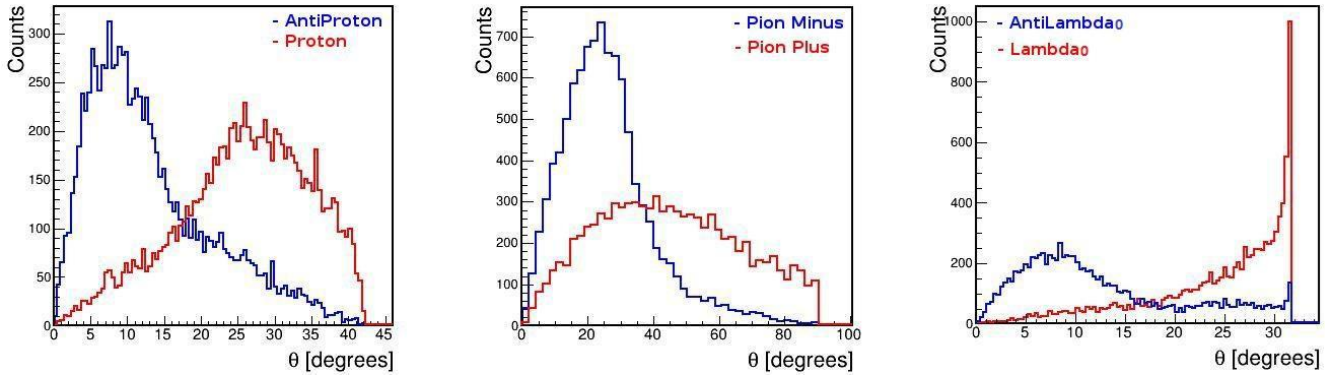

Fig. 4. The angular distributions for all final state particles (p, $\bar{p}$, π^+, π^-)

Anti-protons which came from high momentum tracks and pions minus can create more than hits in the angular coverage from 0 to 22 degrees (GEM region). Protons which came from low momentum tracks create less than hits in the angular coverage from 0 to 22 degrees as they travel up to 90 degrees and pions plus have a large angular distribution 0 to 90 degrees. Therefore, the right panel of Fig. 4 represents the angular distribution of Lambdas and anti-Lambdas as they travel up to 32 degrees. It is clear that most of the anti-Lambdas moved forward and are reached by GEM-Tracker (below 22 degree) truly. The angular distribution versus the momentum of the particles are also shown in Figs. 5 and 6.

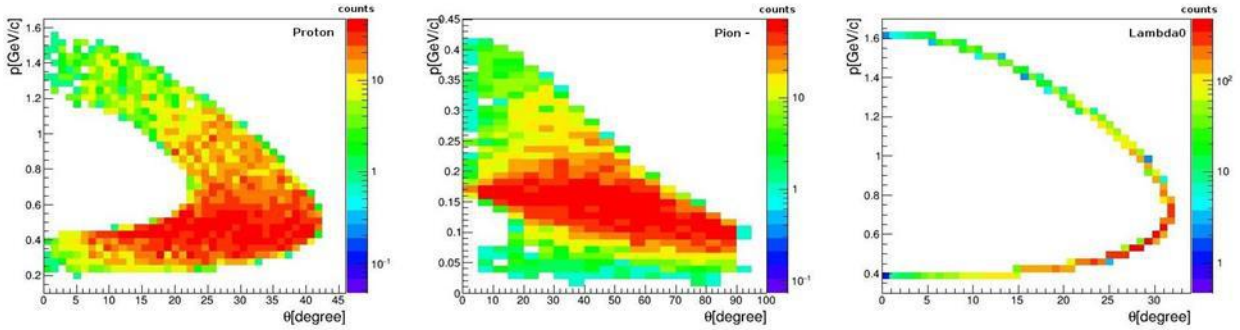

Fig. 5. The momentum versus polar angle theta for protons, pions minus and reconstructed Lambdas.

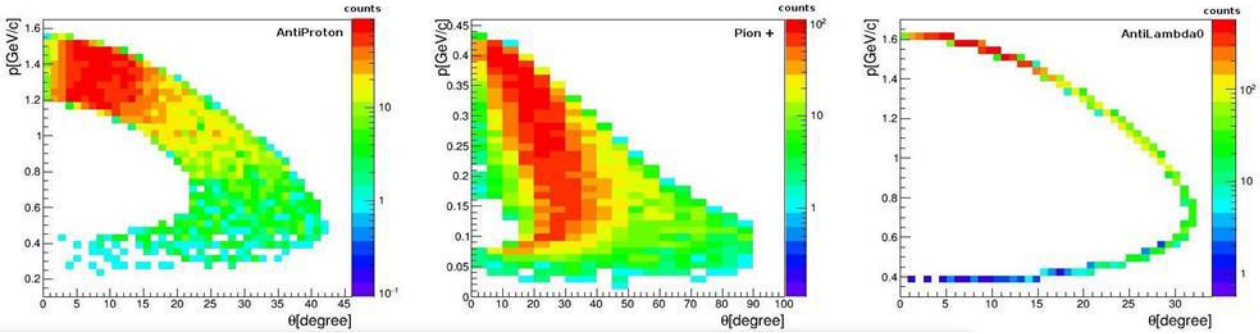

Fig. 6. The momentum versus polar angle theta for anti-protons, pions plus and reconstructed anti-Lambdas.

Fig. 5 shows the momentum versus polar angle (theta) of protons, pions minus and reconstructed Lambdas. It is implied that most of the Lambdas will appear in degrees between 15 to 32, and therefore the large polar distribution of the protons and pions minus. Similarly, Fig. 6 shows the momentum versus polar angle (theta) of the anti-protons, pions plus and reconstructed anti-Lambdas. It is implied that most of the anti-Lambdas will appear in degrees between 1 to 17, and therefore the anti-protons and pions plus are moved in forward directions truly. Therefore, the influence of the GEM-Tracker to improve mass reconstruction in this channel is considerable.

Summary and Conclusions

The simulation of the $\bar{p}p \rightarrow \bar{\Lambda}\Lambda \rightarrow \bar{p}p\pi^{+}\pi^{-}$ decay channel at an antiproton momentum of 2 GeV/c has been used to study the acceptance of the GEM-Tracking detector for the $\bar{P}$ANDA Experiment at FAIR. The decay vertex positions of Λ and $\bar{\Lambda}$ have been shown that $\bar{\Lambda}$ is strongly forward boosted in comparison to Λ in this simulation. Most of the $\bar{\Lambda}\Lambda$ events are decaying before the Lambda Disk Detector with two tracking layers positioned at 40 cm and 60 cm downstream of the interaction point [16]. The angular distribution of all final-state particles has been simulated. The number of hit points per track increase with the GEM-Tracking detector. In this simulation all parts of the GEM-Tracker geometry such as support structures, cables and cooling pipes are taken into account a real and current implementation are designed and located in the real geometry in the simulation. Therefore, all of the results show the performance of the full detector in forward directions [14-17].

Acknowledgment

Author would like to thank $\bar{P}$ANDA MVD group at IKP, Juelich Germany. This work is performed with the help and kind support of them. This research is part of the Ph.D. thesis of the author who was a member of the $\bar{P}$ANDA collaboration for several years at GSI.

References

[1] Fritzsch H et al., Phys. Lett. B47 365 (1971); Politzer H D, Phys. Rev. Lett. 30 1346 (1973); Gross D J and Wilczek F, Phys. Rev. Lett. 30 1343 (1973); Weinberg S, Phys. Rev. Lett. 31 494 (1973).

[2] EPJ web of conferences 241, 01015(2020), NUSTAR 2019, http://doi.org/10.1051/epjconf/202024101015.

[3] PS185 collaboration, Proposal PS185 'Study of Threshold Production of pbar p to antihyperon Hyperon at LEAR', CERN/PSCC/81-69/P49 (1981).

[4] $\overline{\text{P}}$ANDA Collaboration, Physics Performance Report for: $\overline{\text{P}}$ANDA -Strong Interaction Studies with Antiprotons, [http://arxiv.org/abs/arxiv:0903.3905].

[5] FAIR- An International Facility for Antiproton and Ion Research, Webpage: <www.fair-center.eu/puplic/experimentprogram/antiproton-physics/panda.html>.

[6] R. Toelleet al., HESR at fair: status of technical planning, Particle Accelerator Conference, 2007. PAC. IEEE, USA, DOI:10.1109/PAC.2007.4440783.

[7] Journal pf physics: conference series 742 (2016) 012028, doi:10.1088/1742-6596/742/1012028; Technical Design Report for the: $\overline{\text{P}}$ANDA Micro Vertex Detector (AntiProton Annihilations at Darmstadt) Strong Interaction Studies with Antiprotons, $\overline{\text{P}}$ANDA Collaboration, GSI, Darmstadt, November 2011, Webpage: <https://panda.gsi.de>.

[8] N. Divani Veis et al., Monte Carlo simulation for the $\overline{\text{P}}$ANDA GEM-tracker detector, GSI Scientific Report 2015, GSI, Darmstadt, p.92, DOI:10.15120/GR-20161-1.

[9] P̄ANDA Collaboration, Letter of Intent for: P̄ANDA, Strong Interaction Studies with Antiproton, 21/01/2004.

[10] P. D. Barnes et al., Phys. Rev. C 54, 1877, Oct 1996.

[11] S.Spataro 2008 J. Phys.: Conf. Ser. 119 032035.

[12] [https://fairroot.gsi.de].

[13] R. Karabowicz et al., GSI Scientific Report 2009(2010) 117.

[14] N. Divani Veis et al., Performance study of the conceptual implementation of the P̄ANDA GEM-tracking detector in Monte Carlo simulation, Iranian Journal of Physics Research ISI in Persian No. 2, Vol.19, Summer 2019, 471-478.

[15] N. Divani Veis et al., Performance qualitative study of the P̄ANDA GEM-tracker in the physics simulation, DOI: 10.22055/JRMBS ISC in Persian No.1, Vol.9, Spring 2019, 65-74.

[16] N. Divani Veis et al., Implementation of the P̄ANDA Planar-GEM tracking detector in Monte Carlo simulations, Nuclear Inst. And Methods in Physics Research A, 880 (2018), Doi: 10.1016/j.nima.2017.10.036. 201-209.

[17] N. Divani et al., Performance studies of the P̄ANDA planar GEM-tracking detector in physics simulations, NIM A, 884 (2018), Doi: 10.1016/j.nima.2017.11.096. 150-156.

ICNST 2024
International Conference on Nuclear Science and Technology
6- 8 MAY 2024 | Isfahan, Iran

Design and construction of magnetic sector mass spectrometer for analysis of stable isotopes (Paper ID : 1073)

Ebrahim teimoory[1]*, Mir Mohmmad hoseini[1]

[1]Atomic Energy Organization of Iran – Shahid Ahmadi Roshan Enrichment Complex - Isfahan – Iran

**Email: e.tunivesity@gmail.com*

Abstract

In recent years, the use of stable isotopes in the field of disease diagnosis and treatment has significantly expanded. Considering the localization and development of the stable isotope enrichment industry in the country, one of the most important needs of this industry is the identification, precise isotopic analysis, and examination of the impurity levels of enriched gases. In order to analyze, investigate, and study stable isotopes, a magnetic sector mass spectrometer called "IRANIUM" was designed and built. The IRANIUM magnetic sector has a 90-degree deflection angle and a 30-centimeter radius, which increases its effective radius to 60 centimeters with entrance and exit angles of 26.6 degrees. The ionization source of this device is designed as Nier type. To improve the alignment between the source plates, highly precision spherical insulators have been used for ionization source. To simultaneously measure different isotopes of gases, 9 Faraday cup and SEM detectors were used in the device. A user-friendly software has been designed and developed to control and monitor various parameters of the device. The device was tested with deuterium, helium, neon, krypton, and xenon gases to identify and evaluate their isotopic spectra. The results of this research show that the built device has a suitable resolution for mass separation of less than 1amu, high flatness peak amount and stability of mass scan to analyze and determine the purity of stable isotopes.

Keywords: Mass spectrometer, Magnetic sector, EI ionization source, stable isotope analysis, resolution.

Introduction

Mass spectrometry is a technique for mass study of elements, identification of molecular compounds and isotopic analysis of elements. This method is very efficient in various industries such as oil, pharmaceutical, aerospace, environment, air pollution monitoring and especially in the nuclear industry. One of the most important applications of this method in the enrichment industry is the quantitative analysis and isotopic ratiometry of gas samples such as deuterium, krypton, neon, xenon, sulfur hexafluoride and tellurium. Mass spectrometers are made as magnetic dipole, electrostatic quadrupole or a combination of them. One of the characteristics of the magnetic sector mass analyzer is accuracy, high resolution and simultaneous analysis of several isotopes. The source of ionization in this equipment is electron impact, heat, laser, secondary ion impact, or plasma. The detectors used in this equipment are usually of the Faraday cup type. But to measure isotopes whose values are insignificant, secondary electron multipliers, photomultipliers, etc. are usually used. Various researches have been conducted in the field of designing and manufacturing magnetic mass spectrometers in large and miniature dimensions. Miniature spectrometers, which usually have space and environmental applications, are usually designed to be portable and to analyze low-mass samples. Electron bombardment ionization source is one of the most widely used types for sample ionization in this equipment. In this equipment, the combination of magnetic and electrostatic analyzers is used to increase the resolution [1-9]. SIMS (Secondary Ion Mass Spectrometer) and AMS (Accelerator Mass Spectrometer) methods are used to analyze microgram samples. In research, the secondary ion mass spectrometer (SIMS) was combined with a single-stage accelerator mass spectrometer (SSAMS) to increase the very high and very specific resolution. The combination of these two devices, in addition to reducing the disadvantages of each, also achieves 10 times better sensitivity than the SIMS [10]. The design of different electromagnets has been done using Opera, SIMION, CST software. In order to create an accurate magnetic field, to an accurate current source where accurate resistors with very high temperature stability, DCCT sensors or Hall effect sensors are used for sampling. All kinds of cooling techniques, including air cooling, water cooling, etc., can be used depending on the cross section of the wire [11-17].

IRANIUM design

The design of different parts of the device, including the ionization source, mass analyzer and detector, was done first by theoretical calculations and using the relationships governing the transport of charged particles in the magnetic field, and then based on the simulation of different parts of the device in COMSOL and

CST software. The device includes an electron impact ionization source, a magnetic sector mass analyzer, and a Faraday cup and SEM detector. The main parts of the device are shown in Figure

1. The inlet system of the IRANIUM device is of gas type and has 3 expanding chambers for connecting different samples to the device. This system, which is shown in Figure 2, has a number of solenoid valves, expansion chamber and pressure gauge. The control of the valves and the display of all parameters related to pressure and temperature in the input system are done by the software. In order to reduce the dynamic tensions of the gas as well as its homogenization, the gas first enters the expanding chamber, then enters the ionization source through a capillary tube. In this design, a turbomolecular pump is used to empty the path and remove the memory effect in a short time. All connections and system enclosures are designed and built according to UHV standards. The pre-vacuum of the inlet system is provided by a scroll pump up to 5 x 10^{-2} mbar and a higher vacuum is provided by using one turbo molecular pump and four ion pumps up to 10^{-10} mbar.

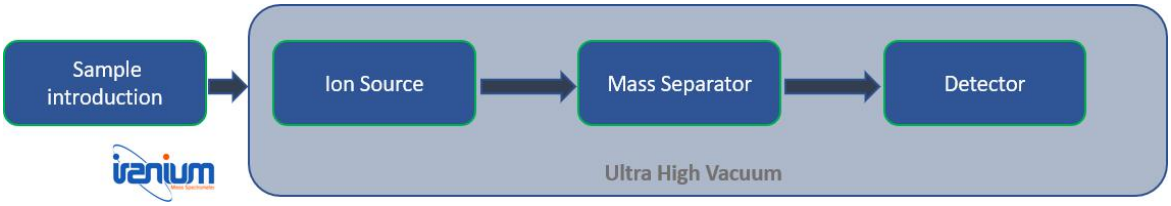

Fig.1. Schematic of magnetic sector mass spectrometer

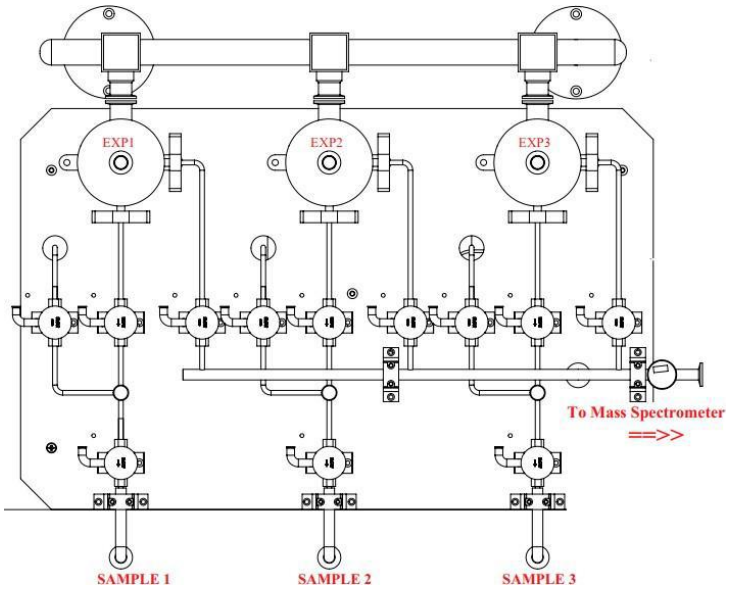

Fig.2. IRANIUM mass spectrometer input system

The ionization source of the IRANIUM device is an electron impact type. The electron beam is produced by a tungsten-rhenium filament. A magnetic field is used in the ionization source to spin the electrons. The amount of electron emission can be adjusted between 100 and 500 microamps and the electron beam energy can be adjusted between 50 and 150 electron volts. The accelerating voltage of the ionization source can be adjusted between 0 and 10 kV. This voltage is constant after the initial setting and mass scanning will be done with high precision by changing the magnetic field. The electrostatic lenses of the ionization source are designed in such a way that the most ions are transferred to the output. The plates of the electrostatic lenses are isolated from each other using spherical rubies.

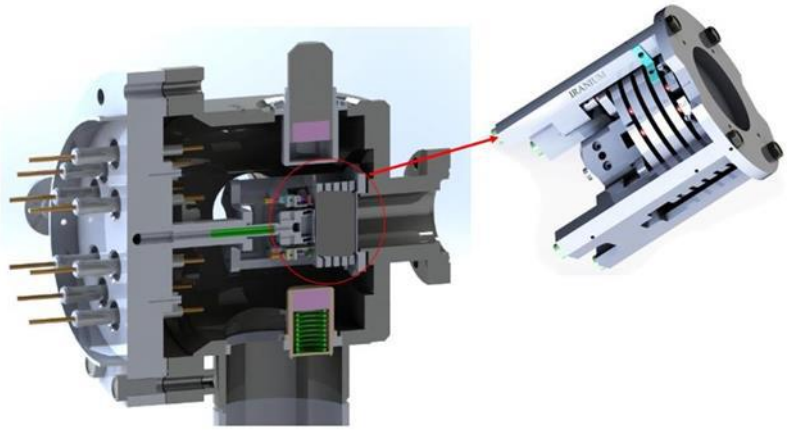

Fig.3. A section of the ionization source of the IRANIUM mass spectrometer

Finally, the ion beam exits from the ionization source through a slit with a width of 150 micrometers and accelerates towards the analyzer. Some of the parameters of the ionization source, such as adjusting the accelerator voltage and displaying it, controlling the temperature of the ionization source and displaying it, can be done through the software. Magnetic field analyzer of the IRANIUM is a C-shaped (magnetic dipole). The relationship governing the movement of a charged particle in a magnetic field is as follows.

$$m = \frac{B^2 r^2 Ze}{2V} \qquad [1]$$

B: Magnetic field density V: Accelerator voltage

r: Radius of the magnetic sector

m: ion mass

Z*e: electric charge of the ion

Usually, isotopic measurement of samples is performed on positively charged ions that are more abundant. Therefore, the value of Ze in the above relationship is equal to 1. The size of the accelerator voltage V for the analysis of stable gases is considered to be 5 kV with an accuracy of $\Delta V/V=3\times10\text{-}6$. The size of the radius of the magnetic sector (r) is very effective on the resolution of the device. According to the equation 1, the relationship between the mass of the particle and the magnetic field is non-linear, hence the resolution of the device decreases with the increase of the mass of the particle. The design of the radius analyzer of the IRANIUM device is done in a different way so that it can separate isotopes with a mass difference of 1amu in different masses (Figure 4). According to the calculations, the size of the radius of the magnetic sector was considered to be 30 cm. The maximum value of magnetic field density is 0.8 tesla with accuracy $\Delta B/B=10\text{-}4$.

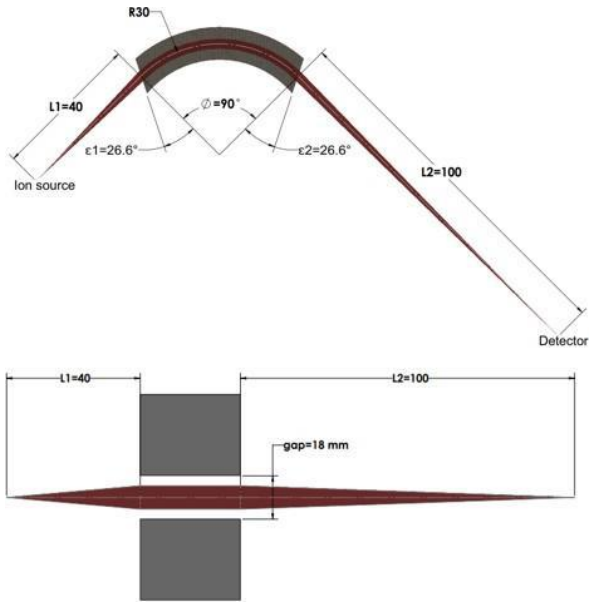

Fig.4. Ion entry and exit design with an angle of 26.6 degrees

The core is designed in such a way that the ion entry and exit angle is 26.6 degrees with respect to the magnetic field. The presence of this angle causes the ions that have the same mass and diverge in the perpendicular direction before entering the magnetic field, move parallel to each other under the magnetic field and converge after exiting the nucleus. The way of ion movement in IRANIUM device is according to Figure. To increase the resolution, the magnification of the device analyzer is set to 2. The distance of the output of the ion source to the magnetic field is 40 cm and the distance of the detector to the magnetic field is 100 cm. The magnetic sector is made of high purity iron and the air gap of the core is 18mm. The number of turns of the coil is 900 turns with a wire cross section of $10mm^2$, which is placed as two separate coils on both sides of the air gap of the core. To achieve a magnetic field density of 0.8 tesla, the coil current will be about 13 amps. The coil cooling system is water cooled. The magnetic field density feedback is entered into the control circuit by a Hall effect sensor with high accuracy and stability. In order to make the magnetic field more stable, the temperature of the Hall effect sensor is controlled with high precision.

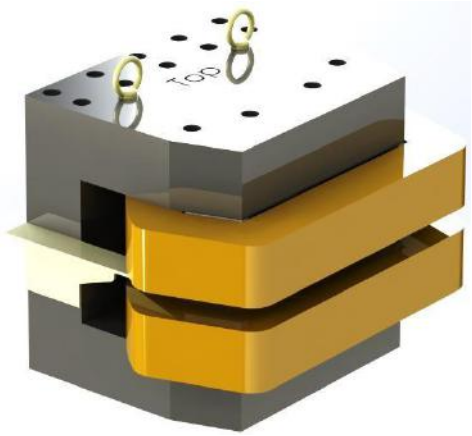

Fig.5. The design of the magnetic sector of the IRANIUM device

The detector of the device is designed as a multi-collector with a combination of Faraday cup and SEM. In order to perform preliminary tests and find the focal point in the output of the magnet, a single Faraday cup detector was used, which has the ability to move 20 cm in the direction of the particle movement. The detector chamber of the device is designed in such a way that it is possible to take samples and measure the ratio of 9 isotopes at the same time. At the time of writing this article, the detector set is being designed and the results presented in this report are related to a Faraday cup type detector. Figure 6 shows the schematic of IRANIUM design, also Figure 7 shows the built device with inlet system.

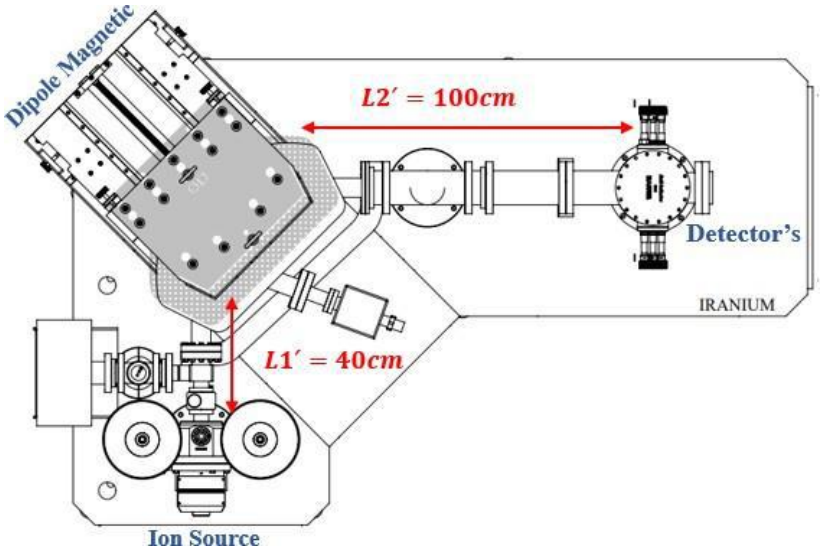

Fig.6. Complete design of IRANIUM magnetic sector mass spectrometer

Fig.7. IRANIUM magnetic sector mass spectrometer with inlet system

Experimental Results

To start working with the device, the stability of the different parts of the device must be ensured. The parts whose stability is of great importance are: accelerator voltage, ion source electron emission rate, magnetic field, detector amplifier electronics and also the device vacuum size. All the mentioned parameters were checked and measured, the results of which are shown in Table 1 below.

Table.1. Stability characteristics of IRANIUM mass spectrometer

Accelerator voltage stability	The stability of the electron emission rate of the ion source	Stability of the magnetic field	Stability of detector preamplifier output	Vacuum device
$\frac{\Delta V}{V} = 3 \times 10^{-6}$	$\frac{\Delta I}{I} = 3 \times 10^{-6}$	$\frac{\Delta B}{B} \cong 2 \times 10^{-4}$	$\frac{\Delta V}{V} = 8 \times 10^{-5}$	$5 \times 10^{-9} mbar^*$

*Vacuum of the device is reported for the case where the sample is not injected into the device.

One of the tests that is done to check the stability of different parts of the device is the scanning of the magnetic field on a certain spectrum in a relatively long period of time. If during this period the position of the desired peak shape and its intensity have not changed significantly, it can be said that the device has good stability. As mentioned in the table above, the stability of the device includes the stability of the magnetic field, the stability of the accelerating voltage, the stability of the electron emission and the amount of gas flow entering the ionization chamber. In the spectra related to the 136-xenon isotope, it is displayed in a period of 30 minutes. As it is clear in the figure, the corresponding spectrum during 30 minutes, the shift or the intensity change of the mass shift rate is less than 0.02amu.

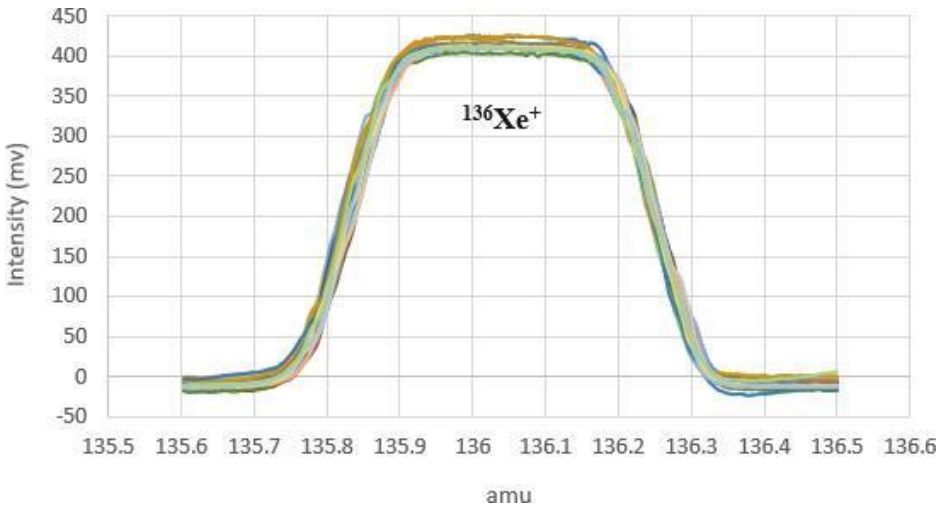

Fig.7. Spectra related to Xenon 136 isotope in 30 minutes (number of scans 30)

The practical results of the device with a number of Faraday cup detectors are reported. The gain used in the pre-amplifier part is 100 G. Samples of stable gases deuterium, helium, neon, krypton and xenon were tested with the device. It should be noted that the analyzed samples were unknown samples and there was no information about their isotopic ratio. Therefore, there may be a discrepancy between the isotopic ratio presented in the tables, which is the same as the isotopic ratio of the natural sample, and the isotopic ratio shown in the figures. In the following, the test results of the mentioned samples are presented. (In order to better display the isotopes in some figures, their intensities have been presented in logarithms.)

Deuterium Gas

Stable isotopes of natural hydrogen are shown in Table 2. The deuterium gas used for testing with IRANIUM mass spectrometer has a purity of 94% of D_2 isotope.

Tbale.2. Isotopes of natural hydrogen

Isotope	mass (amu)	abundance
^{1}H	1.00794	99.98
^{2}H or D	2.015	0.02

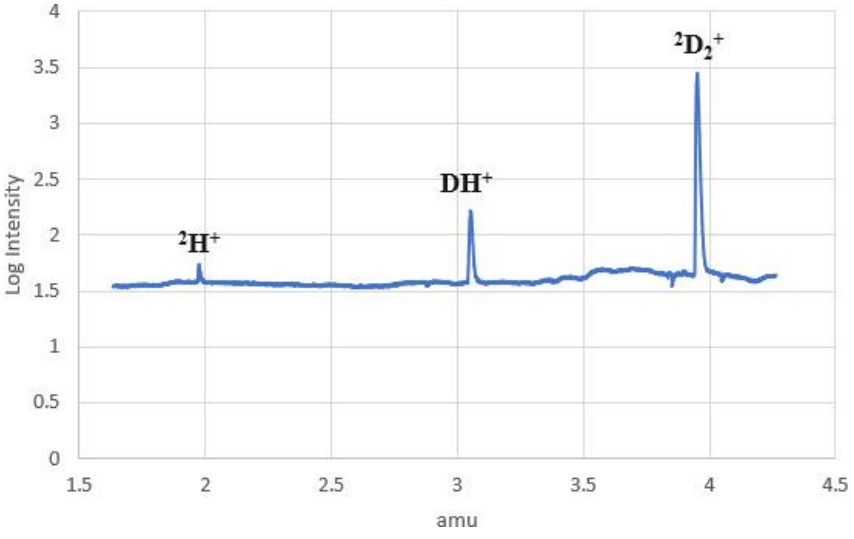

Fig.8. Spectrum related to deuterium analysis

Helium Gas

Helium has 2 isotopes with masses of ^{3}He and ^{4}He. The amount of isotope 3 is so small that it cannot be detected with the Faraday cup detector.

Table.3. Isotopes of natural helium

Helium	mass (amu)	abundance
^{3}He	3.016	0.0001
^{4}He	4.002	99.999

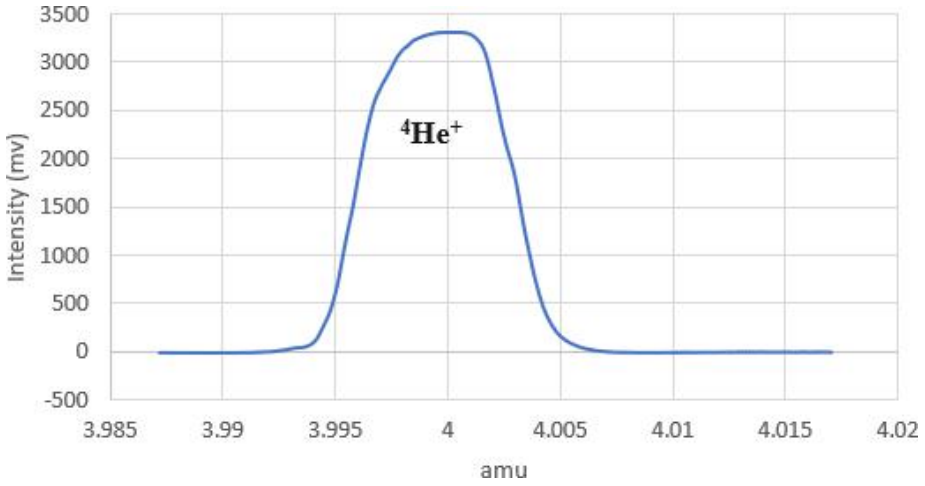

Fig.9. The spectrum related to isotope 4 of helium gas

Neon Gas

Neon has 3 isotopes ^{22}Ne, ^{21}Ne, ^{20}Ne according to table 4. Isotope 21 is less abundant than isotopes 20 and 22, so it can hardly be displayed without changing the gain in the pre-amplifier (Figure 11).

Table.4. Isotopes of natural Neon

Neon	mass (amu)	abundance
^{20}Ne	19.99	90.48
^{21}Ne	20.99	0.27
^{22}Ne	21.99	9.25

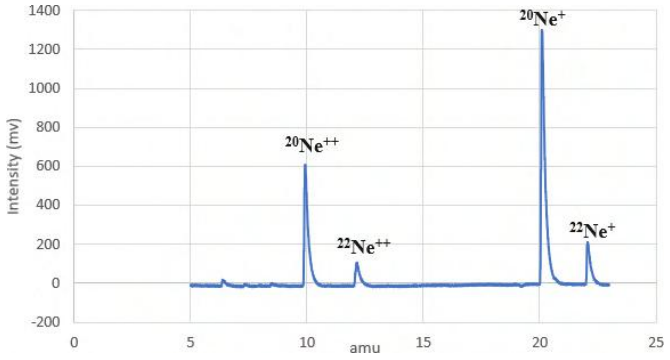

Fig.10. Spectrum of single positive and double positive isotopes of an unknown sample of neon gas

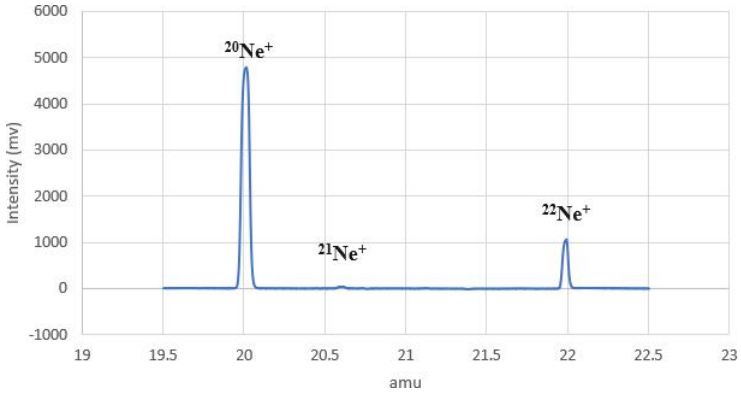

Fig.11. Spectrum of isotopes of 20,21 and 22 neon gas

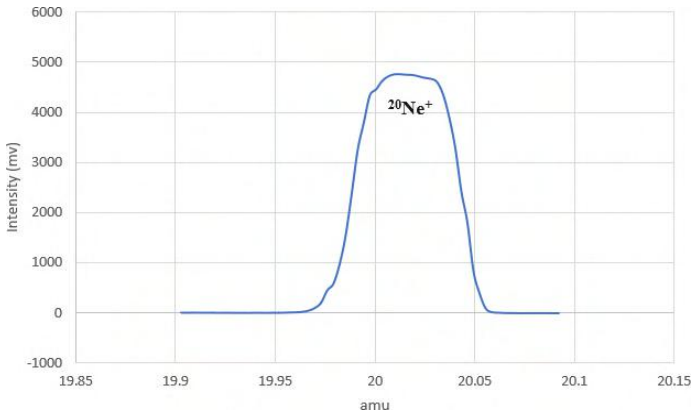

Fig.12. Spectrum related to isotope 20 of neon gas

krypton Gas

Krypton gas has 6 isotopes according to Table 4. The krypton gas capsule injected into the device also contains xenon gas, which is shown in Figure 14 of the spectrum of single positive and double positive isotopes of krypton and xenon gas.

Table.5. Isotopes of natural krypton

krypton	mass (amu)	abundance
^{78}Kr	77.92	0.35
^{80}Kr	79.91	2.28
^{82}Kr	81.91	11.58
^{83}Kr	82.91	11.49
^{84}Kr	83.91	57.00
^{86}Kr	85.91	17.30

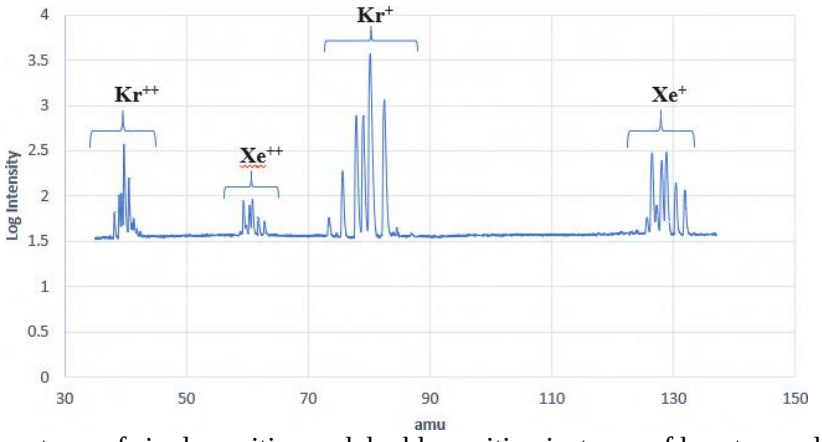

Fig.13. Spectrum of single positive and double positive isotopes of krypton and xenon gas

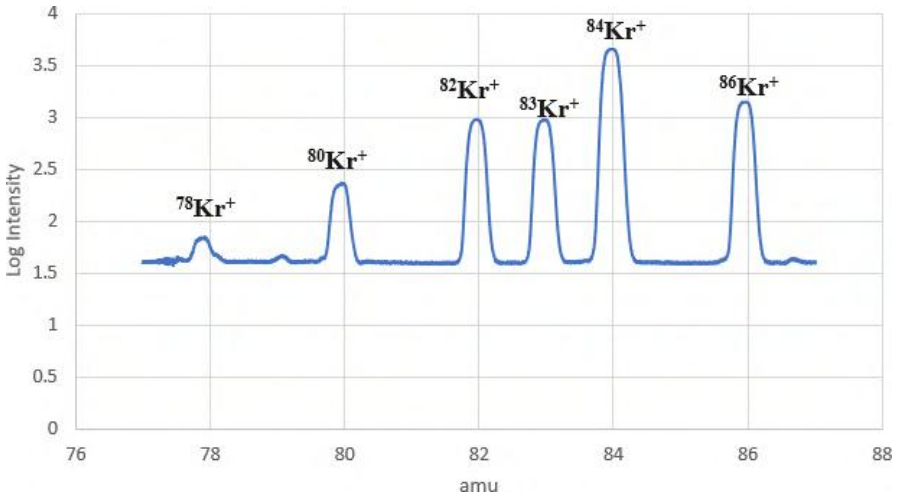

Fig.14. Spectrum of isotopes of an unknown sample of krypton gas

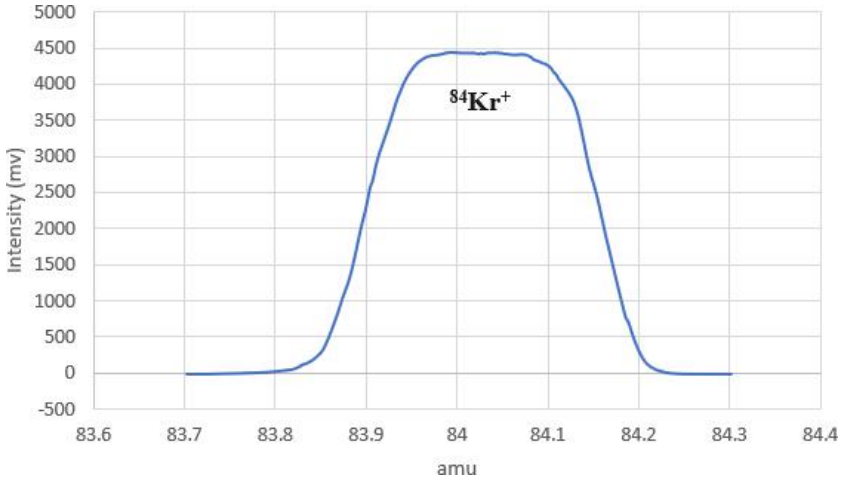

Fig.14. The spectrum related to isotope 84 of krypton gas

Xenon Gas

Xenon gas has 9 isotopes according to the table below

Table.6. Isotopes of natural Xenon

Xenon	mass (amu)	abundance
^{124}Xe	123.9	0.09
^{126}Xe	125.9	0.09
^{128}Xe	127.9	1.92
^{129}Xe	128.9	26.44
^{130}Xe	129.9	4.08
^{131}Xe	130.9	21.18
^{132}Xe	131.9	26.9
^{134}Xe	133.9	10.4
^{136}Xe	135.9	8.9

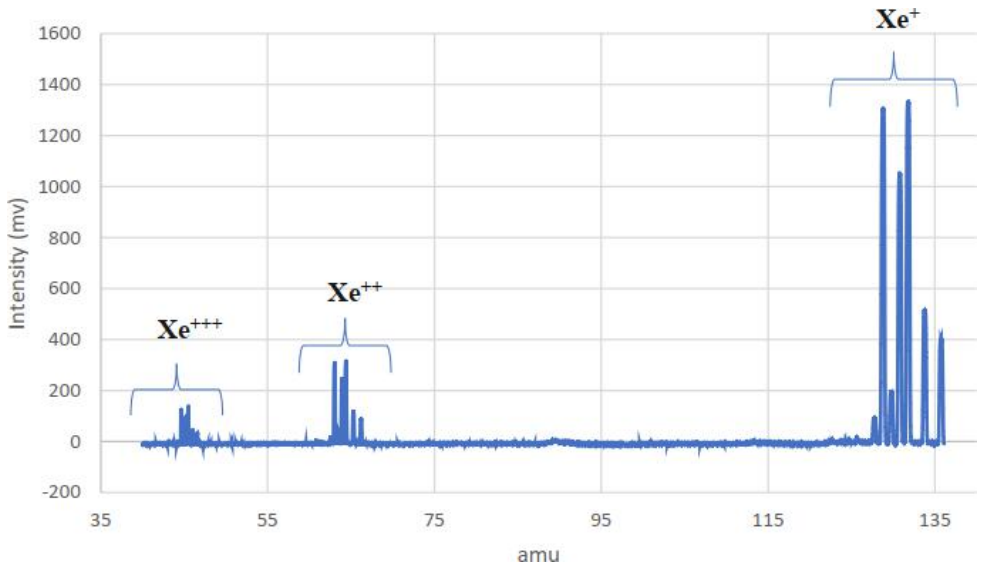

Fig.15. Spectrum of single positive, double positive and triple positive isotopes of an unknown sample of xenon gas

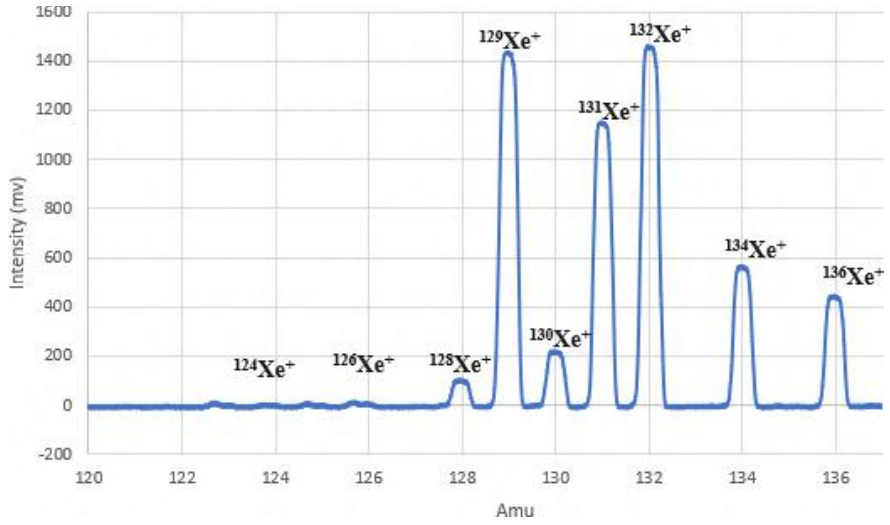

Fig.16. Spectrum of isotopes of an unknown sample of Xenon gas

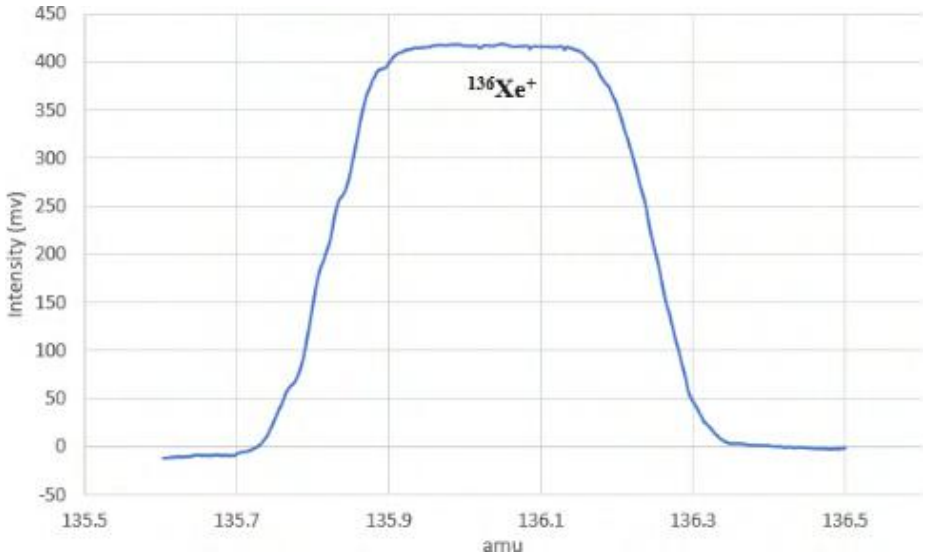

Fig.17. The amount of flat peak isotope 136 of xenon gas

Conclusion

In this article, we described the design and construction of IRANIUM magnetic sector mass spectrometer for measuring stable isotopes, according to the size of the radius of the magnetic sector and the design of the analyzer with 2 magnifications, the resolution of the device is such that it can be Also analyzed the higher mass of 200amu. The device was evaluated with deuterium, helium, neon, krypton and xenon gases and their spectra were processed in the software. All results presented in this paper are reported with a single Faraday Cup detector. The results presented in this report are qualitative and no quantitative analysis has been performed. Therefore, an analysis on precision, accuracy, as well as SD, RSD has not been done. The ultimate goal of designing and building this xenon sample analysis device is that currently the detector set includes 9 Faraday cups with separate pre-amplifiers for each cup being designed and built. Quantitative analysis information along with SD, RSD of xenon sample will be reported in future articles.

Reference

Brown, I. G. (Ed.). (2004). The physics and technology of ion sources. John Wiley & Sons.

Dennis, P. F., Vinen, S., Marca-Bell, A., & Rowe, P. J. MIRA: a new isotope ratio mass spectrometer for clumped isotope studies of CO2.

Jain, S. K., Malik, R., Sekar, K., Naik, P. A., & Hannurkar, P. R. (2010). Design, fabrication and measurement of 90 mass-analyzing magnet.

Hadjar, O., Schlathölter, T., Davila, S., Catledge, S. A., Kuhn, K., Kassan, S., ... & Verbeck, G. F. (2011). IonCCD detector for miniature sector-field mass spectrometer: investigation of peak shape and detector surface artifacts induced by keV ion detection. Journal of the American Society for Mass Spectrometry, 22(10).

Li, D., Guo, M., Xiao, Y., Zhao, Y., & Wang, L. (2011). Development of a miniature magnetic sector mass spectrometer. Vacuum, 85(12), 1170-1173.

Bhatia, R. K., Yadav, V. K., Mahadeshwar, V. M., Gulhane, M. M., Ravisankar, E., Saha, T. K., ... & Gupta, S. K. (2013). A novel variable dispersion zoom optics for isotope ratio sector field mass spectrometer. International Journal of Mass Spectrometry, 339, 39-44.

Qi, G., Tian, D., Gao, G., Liu, G., Qiu, C., & Long, T. (2020). Numerical Simulations and the Design of Magnetic Field-Enhanced Electron Impact Ion Source with Hollow Cylinder Structure. Journal of Analytical Methods in Chemistry, 2020.

Prohaska, T., Irrgeher, J., Zitek, A., & Jakubowski, N. (Eds.). (2014). Sector Field Mass Spectometry for Elemental and Isotopic Analysis. Royal Society of Chemistry.

Becker, S. (2008). Inorganic mass spectrometry: principles and applications. John Wiley & Sons.

Groopman, E. E., Willingham, D. G., Fahey, A. J., & Grabowski, K. S. (2020). An overview of NRL's NAUTILUS: a combination SIMS-AMS for spatially resolved trace isotope analysis. Journal of analytical atomic spectrometry, 35(3), 600-625.

Tanabe, J. T. (2005). Iron dominated electromagnets: design, fabrication, assembly and measurements. World Scientific.

Liebl, H. (2008). Applied charged particle optics (Vol. 2012). Berlin: Springer.

Aruev, N. N., Baĭdakov, E. L., & Mamyrin, B. A. (2007). Precision electromagnet for a mass spectrometer. Technical Physics, 52, 258-262.

Peters, A., Feldmeier, E., Schömers, C., Steiner, R., Eickhoff, H., Knapp, T., & Welsch, C. P. (2009). Magnetic field control in synchrotrons. In Proc. Part. Acc. Conf., Vancouver, Canada.

Kolobov, V. V., & Barannik, M. B. (2019). A Magnetic-Field Regulation and Stabilization System. Instruments and Experimental Techniques, 62, 646-652.

Wang, N., Li, Z., Zhang, Z., He, Q., Han, B., & Lu, Y. (2014). A 10-A high-precision DC current source with stability better than 0.1 ppm/h. IEEE Transactions on Instrumentation and measurement, 64(6), 1324-1330.

Kolobov, V. V., Selivanov, V. N., & Barannik, M. B. (2018). Development of a System for Measuring and Recording Ion Currents for an MI-1201IG Mass Spectrometer. Journal of analytical chemistry, 73, 1282-1291.

ICNST 2024 International Conference on Nuclear Science and Technology
6- 8 MAY 2024 | Isfahan, Iran

Design and Optimization of a Load-Sensitive Preamplifier for Detectors Neutron (Paper ID : 1074)

Foroogh Hatami*[1], Mohammad Ali Shafei[1],

[1] *Faculty of Physics, Yazd University, Yazd, Iran*

Abstract

This research, presents the design details of a load-sensitive preamplifier with a low-noise Op-Amp input, specifically designed for semiconductor neutron detectors with varying capacitances. The preamplifier consists of two layers; the first layer acts as a buffer to maintain the input signal's shape, while the second layer amplifies the signal with different coefficients. This preamplifier efficiently converts charge carriers generated during nuclear reactions into detectable pulses, which are initially weak and require amplification for detection. By Utilizing this preamplifier, pulse amplification factors can be adjusted by factors of 1, 1.2, 1.43, 1.62, 1.82, 2, 2.2, 2.5, 2.8, 3, 4, 5 and 6 using a designed potentiometer. The preamplifier circuit, enhances and optimizes the pulse significantly. Additionally, noise reduction strategies are discussed, along with advancements in count rate capabilities, which are crucial for sophisticated neutron detection systems.

Keywords: preamplifier, neutron detector, semiconductor, Op-Amp

Introduction

Neutron detectors have numerous applications, including tracking and detecting thermal neutrons, counting and imaging, determining nuclear neutron flux in reactors, medical imaging, hygrometry, internal security fields, nuclear shields, managing radioactive waste in disarmament nuclear plants, and more [1,2]. Silicon p-n junction detectors with converter materials such as 10B and 6LiF exhibit higher efficiency than conventional planar detectors. Neutrons, being neutral particles, are not detected directly; rather, they are detected in a multi-step process by converting a neutron into vector particles with high energy. 10B is a suitable choice as a neutron converter material due to its high neutron cross-section and compatibility with silicon. The neutron reaction with 10B is determined as follows:

$$10B + n \rightarrow \begin{cases} 7Li\ (at\ 1.015\ MeV) + \alpha\ (at\ 1.777\ MeV) \\ Reaction\ Q-value = 2.792\ MeV\ (at\ grand\ state)\ 7Li^{*}(at\ 840\ keV) + \alpha\ (at\ 1.470\ MeV) \\ Reaction\ Q-value = 2.310\ MeV\ (at\ 1st\ excited\ state) \end{cases}$$

^{2} α and $^{7}_{4}$Li ions are emitted in opposite directions and can escape from the micron-sized boron region, entering the silicon region with a fraction of their initial kinetic energy. The remaining energy is deposited in the p-n junction of the charge collector silicon. This subsequent enhancement of pulse shaping and signal differentiation provides the possibility of detecting neutron events where the pulse height is greater than the electronic noise level [3,4]. The noise level of the detection system directly affects the neutron yield. Therefore, designing special preamplifiers with minimal electronic noise leads to the development of detectors with high capacity and efficiency. Electronic readout systems suitable for detectors should be low noise, compact, and cost-effective. Although commercial preamplifiers such as Ortec and Canberra [5] are used for high-capacity detectors, they do not meet all the design criteria mentioned.

For instance, in the Ortec model 142A [6], a FET transistor is employed, and a very high resistance of 93 Ω must be applied at the input to prevent potential noise and reduce it with a gentle slope. Additionally, these types of transistors exhibit lower speed performance and are more cost-effective than their counterparts. The 142A preamplifiers are designed for detectors with an input capacity of 0 to 100 pF, and for higher capacities, the performance characteristics are slightly diminished. The energy range for normal applications in this model of amplifiers is from 0 to 200 MeV. Therefore, it is necessary to develop preamplifiers with specialized designs suitable for detectors. The second part of the article presents the design considerations of the main preamplifier. In the third part, it elaborates on the design of the load-sensitive preamplifier, and in the fourth part, it discusses the design results.

Research Theories

Recent advances in pulse shape detection in silicon detectors have sparked new studies in this field. The objective is to apply this technique to charge signals generated in both high- capacitance and low-capacitance planar silicon detectors, with the aim of determining the mass and charge of the reaction products. To achieve this goal, the preamplifier must preserve the charge collection time information, requiring a wide bandwidth and signal rise time without altering the output voltage amplitude. This process is known an impedance matching.

In this project, a buffer circuit is employed to mitigate the impact of loading on the amplifier circuit that affects the detector's output. The buffer circuit consists of an op-amp. In the circuit shown in Figure 1, the gain of circuit is set to one, and its input resistance is significantly high. As a result, the circuit prevents

introducing a loading effect on the detector output, thereby ensuring the distortion-free preservation of the detector output.

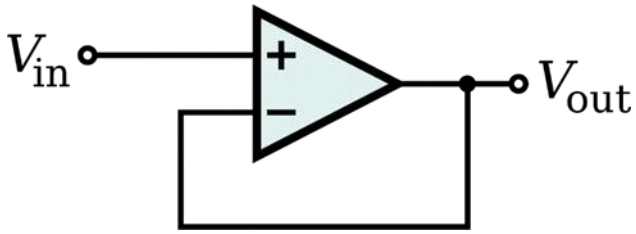

Fig.1. Buffer circuit

To eliminate the effect of op-amp input bias current on the output voltage and reduce its input current, a 20 kΩ resistor is placed in both the op-amp input and its feedback branch. A non-inverting amplifier configuration has been used to amplify the signal with an op- amp. This arrangement is shown in Figure 2.

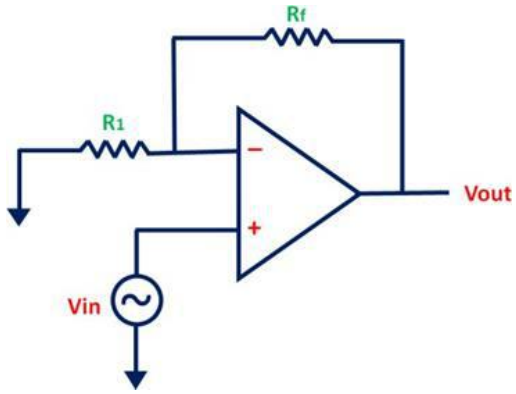

Fig.2. A non-inverting Amplifier configuration

The gain value of this amplifier is determined by the relationship Vout = (1 + Rf/R1)* Vin. If Rf = 0Ω, the gain of this amplifier equals one,making the minimum gain one. By choosing suitable values for R1 and Rf, the desired amplification factor can be attained. Additionally, to neutralize the impact of the op-amp inverter base's bias current, a resistance is included in this base.

Experimental

In this design, the OP249 component is used to implement the arrangements mentioned in the previous section [7]. This component contains two op-amps, each with JFET transistors as inputs. JFET input

transistors help minimize noise, making them ideal for applications requiring low noise level. Op-amps designed for very low noise typically incorporate JFET inputs.

In addition to JFET technology, there is also CMOS technology, which is cost-effective but also has some drawbacks. The primary drawback is its slower speed compared to BJT technology. Therefore, op-amps requiring high speeds are typically constructed using BJT technology. By using BJT technology, the amount of noise introduced into the circuit is minimized.

In the case of this op-amp, the minimum value of the product of bandwidth and gain, denoted by GBW, is equal to 3.5 MHz. This means that high-frequency signals can be easily amplified. Furthermore, the Total Harmonic Distortion (THD) parameter for this op- amp is 0.002%, indicating minimal impact on the input waveform. The noise density parameter for this op-amp is 75nV/√Hz (seventy-five nano-volts per square root of Hertz), suggesting very low noise in this op-amp.

Based on these parameters, it can be confidently asserted that if the frequency of the input signal is less than 3.5 MHz, the signal can be easily amplified without any distortion or noise, and the amplified output signal will be identical to the input signal in terms of shape. This amplifier preserves the collection time information. The minimum value of the product of bandwidth and gain for this op-amp is 3.5 MHz. For example, with a gain of 3.5 (which multiplies the signal by 3.5), the input signal can have a frequency of 1 MHz. It should be noted that the product parameter of bandwidth and gain is a minimum of 3.5 MHz, a guarantee provided by the op-amp manufacturer. Notably, in practice, this parameter often exceeds 3.5 MHz several times (and higher values are better). In the case of an op-amp, the time constant holds no significance; all speed limitations are expressed by the product parameter of bandwidth and gain. This amplifier consists of two layers: the first layer acts as a buffer, preventing the amplifier from altering the shape of the input signal, while the second layer handles the amplification. This amplifier processes a single input signal.

The designed preamplifier is immune to temperature changes and power supply fluctuations thanks to the OP249 op-amp. The OP249 op-amp can operate within a temperature range of -40 to +85 degrees Celsius, with only one microvolt of its offset voltage changing for every degree Celsius. However, this parameter is not significant for our project. Additionally, its supply voltage range is ±4.5V to ±18V, with has the highest efficiency achieved at ±15V and a temperature of 25 degrees Celsius.

The first floor of this preamplifier acts as the buffer circuit, while the second floor serves as the amplifier. Please refer to Figure 3 for the circuit diagram.

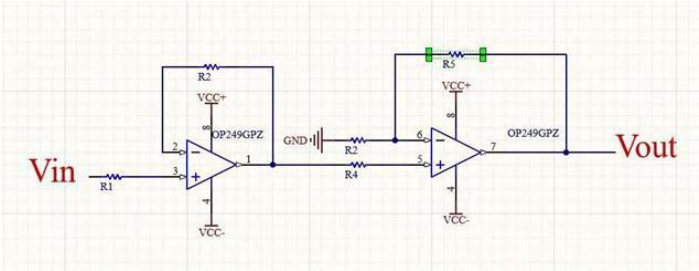

Fig.3. Preamplifier circuit

In Figure 4, the schematic of the amplifier is displayed. Two power sources are utilized in this circuit. The output of the detector is connected to the signal section, and the amplified signal is taken from the output section.

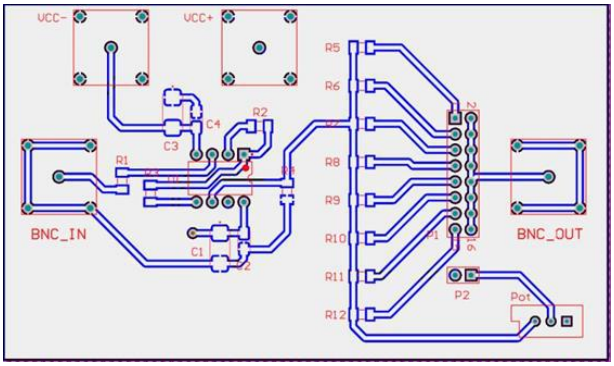

Fig.4. Designed schematic of pre-amplifier circuit

The output of the preamplifier on the oscilloscope with frequencies of 2.27 kHz and 3.08 kHz and input voltage of ±5V, ±10V and ±15V, is shown in the picture 5.

(a)

(b)

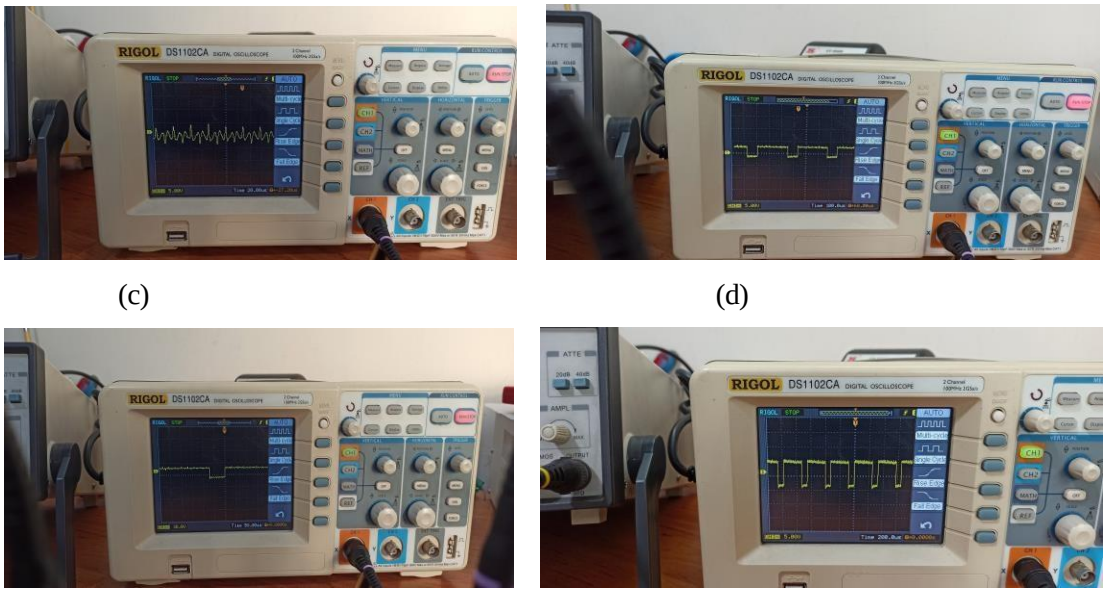

(c) (d)

(e) (f)

Fig5. (a) Voltage = 5V with 2.27 kHz frequencies, (b) Voltage = 5V with 3.08 kHz frequencies, (c) Voltage = 10V with 2.27 kHz frequencies, (d) Voltage = 10V with 3.08 kHz frequencies, (e) Voltage = 15V with 2.27 kHz frequencies, (f) Voltage = 15V with 3.08 kHz frequencies.

As is evident in the pictures, the best waveform was observed at ±10V and ±15V Voltages. Given that our goal is to design a preamplifier suitable for silicon detectors with low input voltages, it can be concluded that the op amp used in this design is completely suitable for such detectors. Additionally, it was observed that the best waveform with the least noise and distortion occured at an input voltage of ±15V for input signals less than 3.5MHz (images (e), (f)).

In the P1 section, by connecting the jumper from top to bottom, it creates amplification coefficients of 1.2, 1.43, 1.62, 1.82, 2, 2.2, 2.5, and 2.8. If the jumper is placed on the P2 connector, the amplification coefficients can be adjusted from 1 to 6 with the help of a potentiometer. However, there is a limitation in the use of jumpers because simultaneous use of several jumpers to increase the amount of amplification is not possible.

The maximum positive and negative voltage that can be used is ±15V. The voltage +15V is connected to +VCC, the voltage -15V is connected to -VCC, and the common ground must be connected to GND.

Conclusions

An op-amp is used to amplify the signal, making it a much more efficient component compared to a simple transistor. Essentially, each op-amp is a combination of forty to fifty transistors created with intricate and highly precise processes. As a result, it outperforms simple transistor circuits in terms of noise. Commercial models from Ortec and Canberra use FET transistors along with the buffer circuit. While these transistors may have lower performance speed and be more budget-friendly than the BJT transistors in the op-amp used in the designed circuit, the OP249 op-amp in the designed circuit allows for a wider operating temperature range (-40°C to +80°C) with minimal offset voltage changes for each Celsius degree. In contrast, the listed commercial models operate within a limited temperature range of 0°C to 50°C.

The superiority of the designed model over Ortec and Canberra models lies in its two-layer design. The first layer serves as a buffer, preventing the amplifier from altering the shape of the input signal, while the second layer performs the amplification. Pulse amplification is achieved through P1 and P2 connectors with coefficients of 1, 1.2, 1.43, 1.62, 1.82, 2,

2.2, 2.5, 2.8, 3, 4, 5, and 6. This allows for receiving and analyzing the output signal from the out connector with minimal noise and a bit of amplification using predetermined coefficients. In commercial models, only the first layer of the buffer is used, and no amplification is performed.

Furthermore, the designed model accommodates a maximum input voltage of ±15 V, whereas in commercial models, the operating voltage can go up to ±2000 V DC.

The measurement method and equipment used in this article are innovative method and designed and manufactured according to silicon detectors.

Acknowledgements

We will like to express our sincere gratitude to M. Qasemi of Shiraz Electronics Industries for his invaluable assistance in the design and construction of the preamplifier.

References

Kouzes, R.T., (2009). The 3He supply problem. Pacific Northwest National Lab (PNNL), Richland, WA (United States).

GAO, U. (2011). Neutron detectors, Alternatives to using helium-3. US GAO.

Danon, Y., et al. (2014). Large area zero bias solid-state neutron detectors. Proc. Trans. Amer. Nucl. Soc, 110.

English, E., et al. (2016). Low-noise preamplifier design considerations for large area high capacitance solid-state neutron detectors. IEEE Transactions on Nuclear Science, 63(1): p. 304-315.

https://www.directindustry.com/prod/canberra-industries/product-23661-555313.html

https://www.directindustry.com/industrial-manufacturer/signal-amplifier-81107.html

https://www.analog.com/media/en/technical-documentation/data-sheets/OP249.pdf

ICNST 2024
International Conference on Nuclear Science and Technology
6- 8 MAY 2024 | Isfahan, Iran

Theory of everything and nucleons (Paper ID : 1082)

Dr. alireza sadrejamaly M.D

Alirezasj1342@gmail.com

Tehran-Iran

Abstract

The development of nuclear technologies requires more understanding of nuclear physics and research in this field. The nuclear physics is based on interactions between nucleons (protons and neutrons) and their conversions inside atomic nucleuses. Therefore, in order to better understanding ,a clearer picture of the internal structure of nucleons should be created first. Considering that nucleons are composite particles which consist of three quarks. First I will try to construct a theory that explains how they form from fundamental particles, then based on the model derived from the theory, I will explain various nuclear phenomena such as the size of the atomic nucleus, types of nuclear decays and various binding of nucleons inside atomic nucleus and different isotopes which are the purposes of this research.

One of the most important results of this research is that the nucleons were formed as a result of leptons fusion (the only fundamental particles) inside quasars or active galactic nucleus as we see protons are decayed due to collision with each other in accelerators and each proton decays to two leptons (muons).

Key words: lepton, neutro, proton, quark, atomic nucleus

Introduction

How are nucleons formed from fundamental particles? The evidence needed to answer this question is scattered in three different branches of science. Observational evidences in cosmology means the place where nucleons are formed, experimental evidences in particles physics caused by collision of protons in accelerators, and experimental evidences of the nucleons behavior inside nucleus of the atoms and their decays in nuclear physics. The approach of this research is to select all relevant evidences from the mentioned sciences and then reasoning and conclusion to create a theory (theory of everything),then evaluating the theory in explaining the physical phenomena and many unsolved problems in physics with the existing theories. Considering that the strength of a theory depends on the variety of phenomena, it can explain and finally the description of nucleons behavior inside nucleus of atoms is based on the theory.

Baryon asymmetry problem

After the big bang , matter and antimatter must have been created in equal. In other words,as much as the matter is in hundreds of billions of galaxies (each of which has billions of stars) antimatter must have been created. But so far no trace of it has been found[1][2][3]. Considering that the existence of such a huge amount of antimatter must have traceable effects on astronomical observations due to annihilation with matter along the boundary between matter and antimatter regions. "But now deemed unlikely that any region within the observable universe is dominated by antimatter"[3] .The production of pairs of matter and antimatter due to the collision of high energy gamma rays occurs if these waves collide together face to face . Even if there was such high energy gamma rays after the big bang,they must be moving side by side and in the same direction, moving away from each other divergently and they didn't have the possibility of hitting together face to face even in the initial small space.On the other hand, the creation of matter and antimatter in equal amount after the big bang isn't logically acceptable, considering that they immediately destroy each other without building anything. However what is clear from the all evidences that is certain that only matter was created after the big bang, and all these galaxies and stars are its case.

Conclusion:After the big bang only matter has existed in cosmos based on all observational evidences.

Free quark problem

After the big bang only matter has existed in cosmos.The only fundamental and essential particles of matter are leptons and quarks from which all matters including protons, neutrons and atoms are made . But so far,no independent and separate free quark has been found in nature. Numerous experiments of colliding composite particles such as protons and atomic nucleuses in the most powerful accelerators had not led to finding a free and independent quark.

The fractional charge of quarks also explains their non-independent existence, so quarks only exist as combination form .Neutrons and protons as matter building units were made from quarks ,neutron spontaneously decays to lepton(electron) ,proton and energy. Protons when collide with each other in accelerator, each proton decays to two leptons(muons) and energy [4],[5] so a proton was made from two energetic leptons and a neutron was made from three energetic leptons, of course under influence of huge constricting power ,happened somewhere in cosmos.

As a result, based on the available evidences, it can be concluded that quarks are not elementary and fundamental particles , but originated and formed from energetic leptons. So the leptons are only type of fundamental particles which created after the big bang and quarks are only, their combination (entanglement of their innermost parts together) form , so as soon as separation from each other(as seen in accelerators) act as their original lepton behavior. Quarks inside nucleons of atomic nucleus can change their charge by capturing or releasing lepton (electron)that is another reason for their close structural relationship. So quark and lepton are different behaviors of one thing in two status and condition, combination or free states.

Conclusion: After the big bang only leptons have existed.

Expansion,isotropy

Electrostatic repulsion between super fast leptons caused expansion. Electrostatic repulsion caused maximum distance between each particle from adjacent particles . This process gradually caused uniform distribution so ,after reaching equilibrium , density of the particles became same and uniform in all directions (isotropy problem solution). Finally very huge fog of isotropic and homogenous leptons were formed .[6]

Cosmic microwave background (CMB)

In very huge fog of leptons which are expanding uniformly at a speed near light speed, magnetic forces formed around leptons groups more efficiently due to reaching isotropy. The adjacent magnetic forces combined together until they became so powerful enough to overcome the repulsion force between leptons which is very huge (the reason for excessive size of galactic nucleus). The magnetic forces caused activation of a process called pinch effect (electromagnetic pinch) [7][8] which led to condensing and compressing of leptonic clouds. Increasing heat due to compression generated emission of cosmic microwave background (CMB).As the leptons clouds became more compressed and dense CMB became more intense.So there are red central areas inside blue peripheral areas in CMB map as anisotropy[9]. CMB map has compression topography. Blue peripheral areas makes empty parts of cosmos (voids). Red central areas makes full parts of cosmos (quasars and galaxies). CMB originated from leptons with thermal black body spectrum due to compression and condensation of leptons certainly along with increasing temperature.Building of cosmos, large scale structures from primary

particles (leptons) started by CMB emitting because it is the first sign of compression and condensation inside the cosmos.

Quasars

It should be noted that CMB is a sign of abundance of leptons with electromagnetic force. This force is billion billion billion billion times stronger than the gravity force. Very weak gravity force of particles and atoms couldn't be creator of cosmic structures like galaxies and stars especially because all of them are in plasma form in space and only the magnetic force could counterparts with electrostatic repulsion force. [8]

Very huge magnetic forces formed around clouds of leptons then electromagnetic pinch ocurred (constriction magnetic field) which caused condensation of leptons inside them. Accumulation of huge amount of matter formed huge gravity force around them. Very weak gravity force formed in tremendous dimensions from beginning, because only in this case it could be effective in building of cosmos large scale structures.

Gravity force caused continuous compression and condensation of leptons in a structure called quasar and must be great enough to overcome huge repulsion between leptons (reason of high magnitude of remained super massive black holes). Inside the quasars under pressure of huge gravity force, leptons are compressed together and with initial start and spark by electromagnetic pinch, fusion took place and continued, so a neutron is made from each three energatic leptons(this is just opposite direction of neutron decay and proton decay in accelerator ,which the result is three leptons and energy).Fusion caused entanglement of innermost structures of each three leptons until chargon. Compressing of each two sides leptons to middle lepton converted its charge from negative to positive and consumed their one negative charge at all .

Strong force between quarks caused by entanglement and neutralization of a part of the remaining negative charges of sides leptons with a part of positive charge of middle positive charge which is the foundation of quantum chromodynamics . So the location of the missed baryons(missed baryons problem)are inside quasars and active galactic nucleuses (AGN) where baryons synthesis are occurring from leptons and this is the reason, why fermions are less numerous than photons (supersymmetry problem solution).

A particle behave like quark in entanglement state inside baryon, and behave like lepton in free and separate state.

That is a type of fusion which takes place between energetic leptons under pressure of huge gravity inside active galactic nucleus, during this process each three leptons convert to a neutron (baryon synthesis).Leptons don't have a tendency to react with neutrons .Neutrons inside huge gravity can't decay (like inside neutron star) so as a result of the lack of reaction with surrounding particles and under huge pressure of gravity, neutrons ejected and exited from quasar center as quasar jets .As soon as exiting ,neutrons decay to protons, electrons and neutrinos (origin of cosmic neutrino background) .This is the reason of why there's exactly the same numbers of electrons and protons in nature because both of them were created from decay of neutron,in exactly equal numbers.

Neutrons and protons inside quasars jets make light elements ,hydrogen, deuterium, helium,Lithium (Lithium problem solution).

"Baryogenesis via leptogenesis is an unavoidable consequence of SO(10) grand unified theories (GUTs) ".[10][11]

So there are two types of stars ,leptonic stars which are known as quasars or active galactic nucleuses and protonic stars like sun. Formation of protonic stars are like leptonic stars are by compression of protons with magnetic constriction fields around them (plasma pinch) and creation of gravity, because most hydrogens in space are in plasma form (protons) and in all different types of those stars in cosmos only fusion of protons occur.

Results of stars formation from charged particles are charged gravity so active galactic nucleus or leptonic stars have negative gravitomagnetic forces and protonic stars like sun have positive gravitomagnetic forces , so galaxies repel each other due to their identical negative charges (as known ,dark energy) and attract their stars strongly due to their non-identical charges (as known, dark matter). Remained black holes of them also charged ، so there are super massive black holes with negative gravitomagnetic force in centers of galaxies and ordinary black holes with positive gravitomagnetic forces are orbiting around them. Charged black holes are one of solutions of Einstein's field equation for a black hole which is both rotating and electrically charged (Kerr-Newman metric).[12][13]

Nucleons

Within a proton, down quark is placed between two up quarks .Up quarks aren't able to get close each other, and rotate around central down quark while keeping a distance from each other, due to repulsion between their positive electrostatic charges , so proton is stable. But inside a neutron up quark ,placed between two down quarks and because charges of down quarks completely neutralized so they can rotate around central up quark freely and without keeping distance with each other which cause impact between them and creation of weak force which cause decay of free neutron. But a neutron inside nucleus of atom is stable because its down quarks link to up quarks of adjacent protons which prevents them from rotating around the central up quark and keep the all quarks of neutron in a parallel line ,with line of quarks of adjacent proton,so neutron becomes stable inside nucleus especially when located between two protons but peripheral neutrons because link only at one side so are less stable as it is seen in different types of decays in isotopes of an element especially with a large number of neutrons compared to protons

It should be noted that all these linear nucleons inside atomic nucleus are on the same surface. All the nucleons inside the nucleus of an atom are located on the surface of one plane in which each up quark is linked to four adjacent down quarks and each down quark is linked to four adjacent up quarks except peripheral nucleons. (it seems very similar to a chess board with horizontal or vertical links)(Fig)

Three types of binding between nucleons inside nucleus

All following bonds are between down and up quarks of peripheral nucleons with nucleus except triquark bond which in addition to peripheral bonds it is also seen inside nucleus bonds.

Monoquark bond is only between down quark of a neutron and up quark located around a nucleus. Because it is only binding between neutron and nucleus, neutron separates as free neutron (neutron emission) like in isotopes of hydrogen with 4,5,6,7 mass numbers so most of these neutrons bind to nucleus with monoquark bond loosely and the reason of N emission of nucleus is its loose peripheral monoquark binding mostly.

Another monoquark bond is between up quark of a proton with down quark, located around a nucleus. Because it is only binding between proton and nucleus, it separates as free proton (proton emission) like in isotopes of Lithium with 3,4,5 mass numbers .

So monoquark bond is responsible for most nucleon (proton or neutron) emission of nucleus.

Diquark bond is between central and one of side quarks of a nucleon with two adjacent quarks located around a nucleus in a manner that up quark and down quark bind together so a side quark of them, remain free and without any binding, and it can rotate around central quark and cause negative beta decay in neutron or it can be close to central quark and cause positive beta decay in proton which convert a diquark binding to triquark binding.

So diquark bond is responsible for most beta decay (positive or negative) of nucleus.(Fig)

Beta decay causes movement of a nucleon by the size of a quark around nucleus. Three nucleons of Lithium isotope (atomic number=mass number=3) all are protons ,how these protons can form it in spite of their electrostatic repulsion? Only answer is diquark bond model.

Triquark bond is a binding which all three quarks of a nucleon bind to adjacent quarks in up-down bindings and responsible for bindings inside nucleuses and some of peripheral bindings. Triquark bond is dominant type of binding inside nucleus while monoquark and diquark bonds are located mostly in periphery. (Fig)

Excitation of nucleus means side quarks of nucleons get away from central quark (like getting away of energetic electron from atomic nucleus)due to receiving energy which will return to basic status by radiation of gamma ray, but before that, excited nucleons inside nucleus can alter stability of bindings between nucleons and may cause alpha decay or fission.

Distance between central quark and side quarks of a nucleon can alter by binding one of side quarks with a another quark in nucleus which cause sharing of binding force with it so a decline in its binding force with central quark ، so getting away from central quark. In fact this cause central quark displaces and getting closer the another side quark. This movement is important in formation of positive beta decay which start by that proximity, releasing positron, changing to down quark and rotation around other side quark and converting to neuron.

This model is alphabet of nucleon's world in this theory and with super computer simulation can improve our understanding about nuclear physics.

In fact a nucleus with these types of alteration in its bindings and variant types of decays can manage its shape , size and structure for reaching the most stable status.

Size and shape of nucleus

The nucleon radius for a free proton is equal to 0.8 femtometer in free status .[14]The distance between nucleons is also 0.8 femtometre inside the nucleus. Because inside the nucleon, in the free status, the side quarks rotate around the middle quark, but inside the nucleus, due to the bond with each other, they are fixed, as a result, the nucleons are next to each other at a distance equal to the radius of the nucleon. This makes the distance of each middle quark from its sides quarks to be equal approximately to its distance from the adjacent quark, this makes it possible to accommodate up to three hundred nucleons in the uranium nucleus with a diameter ten times of the diameter of the free proton and in area one hundred times larger than that by considering the reduction of common nucleons It reaches almost about 250 nucleons or lesser, which is close to the mass number of uranium (that is, placing five nucleons in an area twice the area of a free proton), of course, approximately.

This causes all the distances between the adjacent down and up quarks to be almost the same, which creates harmony, and the integrity and uniformity of the nucleus. Each up quark inside the nucleus may belong to two neutrons or four protons, and each down quark may belong to two protons or four neutrons . Another result is that, nucleons can bond with each other along the longitudinal and transverse axes because down-up distances are almost equal in that two axes . When a nucleus starts to decay , from the four connections of each quark with the neighboring quarks ,in the order of the weakest connections, separation begins, this allows the nucleus to maintain the most strongest bonds for reaching the most stable status.

Conclusions

It can be concluded that lepton is the unit and building block of matter and all atoms, on the other hand lepton has three ability:1,sensing motion and energy (sensor) 2,storing it as mass or kinetic energy (memory) 3,releasing it in various environments and contacts (action).These are exactly definition of intelligence and reveal why and how consciousness exists in universe, because building unit of matter in universe has a simplest form of intelligence . We see a clear example of it in computers and artificial intelligence, which all work with electrons (leptons).

It is obvious that by simulating complex mental models that are the basis of this theory, the concepts of this theory can be developed with supercomputers.

Supplementary information

Dark matter-Dark energy

Gravitational force is created in two ways, from leptons and protons. Both types are created by magnetic fields constriction around fast and parallel movement of particles (leptons, protons)during pinch effect. They form on the surface of space time plate, where magnetic forces rings are located and constricted around clouds of leptons or protons.

Because these particles have different electric charge, the resulting gravitational forces also have different spin and charge. Gravity force around leptons cloud is negative gravitomagnetic force and makes quasar and galactic nucleus. Gravity force around protons cloud is positive gravitomagnetic force and makes star. These forces have properties similar to electric charges of particles:1,Identical charges of them repel each other 2,Non-identical charges of them attract each other 3,Both of them pull and rotate space time plane (and of course everything without Gravitomagnetic charge inside it like planets) in which they are formed (accretion disc of seyfert galaxies and stars during formation) and then eject it from two sides along with their rotational axis (jets of quasars and stars during formation)like tornado but in two opposite sides rather than only one side . In fact accretion disc and jets show their interaction with surrounding space time.

After the formation of a star this gravitomagnetic pattern (accretion disc -jets)undergoes changes under the influence of nuclear explosions and turbulence of magnetic fields inside the star and becomes the current pattern of gravity (like sun) but at the end of a star's life by overcoming again of gravitomagnetic force that pattern return, which could be seen in supernova (exit from two sides) and if converted to black hole will have two jets of emission . In quasars and galaxies, disappearance of jets occurs at the end of baryons synthesis from leptons, although the emission of radiation continues along with those paths (like milky way galaxy).Both stars and quasars are neutralizing electrically charged particles (protons, leptons)by converting them to neutrons but the quasars gradually eject neutrons through its jets while the stars throw them out suddenly through supernova explosion.

Galaxies with negative gravitomagnetic forces move away from each other (as known dark energy) .A galaxy with negative gravitomagnetic force attracts it's stars with positive gravitomagnetic forces strongly (as known dark matter).Stars don't collide with each other inside a galaxy due to their positive gravitomagnetic forces repulsion despite very large numbers.

Some of the negative gravitomagnetic force of the center of each galaxy neutralized with positive gravitomagnetic forces of its surrounding stars. So primary quasars and galaxies without or very low stars are moving away from earth and each other faster than those with much more stars near earth (due to stronger repulsion) in recent galaxies.

The unneutralized negative gravitomagnetic force of center of a galaxy can interact with positive gravitomagnetic forces of the stars in neighbor galaxies and cause formation of satellite galaxies. In case of intensity of this interaction, collision between galaxies can occurred. Centers of two neighbor galaxies after being close to each other creates two separate focuses of gravity in a new elliptical galaxy.

Therefore the sequences of galaxies evolution and formation consists of:quasar, seyfert galaxy, spiral galaxy,irregular galaxy(galaxies collision), elliptical galaxy. Sequences of matters evolution and formation consists of:lepton,quark,baryon, hydrogen, helium. Sequences of forces evolution and formation consists of:negative electromagnetic force, negative gravitomagnetic force, strong force, weak force, positive electromagnetic force, positive gravitomagnetic force. The formation and evolution of the forces can explain well ,why electromagnetic, strong, and weak forces are so close to each other in terms of their relative strength. Why the strong force is limited to the inside of the nucleon. Why the gravity force and electromagnetic force are similar in terms of long distance behavior(which are proportional to the reverse of distance square)and range of influence (which are infinity).All bosons(carriors of forces)are special movement of space time which formed by particles, like sound ,wind,tornado which all of them are particular movement of air. Lepton is one ,proton is two and neutron is three of building units of matter in subatomic world. Then after creation of hydrogen atom , hydrogen is one ,deuterium is two ,tritium is three and helium is four in new atomic world.

Like world of atoms and molecules, interaction between negative gravitomagnetic force of galaxies and positive gravitomagnetic forces of stars in neighbor galaxies create various and complicated forms like cluster and so on. Also it causes stability in system. On the other hand because (unlike world of

atoms)negative charges are in the center of galaxies and positive charges orbiting around them, cause balance and equilibrium between galaxies and atoms world.

The negative gravitomagnetic force of center of each galaxy is at least three times stronger than the positive gravitomagnetic forces of total number of its stars because originated from leptons which are three times of all protons of a galaxy, so can react with other adjacent structures in cosmos.

Nature and essence of gravity:The existing reality is that the only matter in nature is this ordinary baryonic matter, and the invention of dark matter and dark energy is due to its unknown hidden properties of its charged gravity therefore, its repulsion is called dark energy and its additional attraction is called dark matter. While we know that this ordinary and stable matter is composed of two charged particles (proton and lepton)in which one rotates around the other, on the other hand, we know that there are two types of celestial bodies(active galactic nucleuses and stars)in the stable cosmos, where one of them rotates around the other and completely sure that at least one of them (star)is made from charged particles (protons).Also we know that the remnants of gravity of them make two completely different types of black holes(ordinary black hole and super massive black hole)which one of them(ordinary black hole)rotates around the other(super massive black hole) So far, no reasonable and acceptable explanation has been provided for how a super massive black hole was made. The only possible answer is to exist two types of gravity with different spins and charges.

Black holes

Black hole created by a star have positive gravitomagnetic force(positive black hole).Black hole created inside quasar have negative gravitomagnetic force(negative super massive black hole) . Both of them have similar pattern that could be seen as accretion disc and jets which represents interaction between a black hole with space time. The only difference between them is different spin and charge.

A quasar is actually a leptonic star. In the center of a quasar, leptons are converted to the neutrons and neutralized. A quasar has negative gravitomagnetic force. Material in the center of a quasar (neutrons)are expelled by the pressure of gravity gradually by its jets and created light elements which used in the formation of stars around the quasar. This process leads to separation of the gravity from its building materials gradually until the end of jets activity and a black hole is formed which is the pure gravity.This black hole has spin and negative charge .

A star is actually a protonic star. In the center of a star ,protons are converted to the neutrons (inside atoms nucleus).The star has positive gravitomagnetic force. The material in the center of the star are expelled by the pressure of the gravity abruptly by supernova explosion at the end of star's life and the created heavy elements are used in the formation of planets around the star.This process leads to separation of the gravity from its building material and a black hole is formed which is the pure gravity .This black hole has spin and positive charge.

Black holes ,as it is thought, does not arise from condensing matter, but from collapse of gravity force after expelled internal matters. Intensity and strength of gravity after conversion to black hole does not change. Matter can not enter inside black hole due to inertial force. If black holes were created by collapse and compression of material, it didn't remain any material for the production of stars (around galaxies)and planets (around stars).

Galaxy

A galaxy has five different parts which are formed in order:

1,Active galactic nucleus:which is actually a leptonic star where inside it leptons fusion occurs and a neutron is created from each three leptons . Neutrons are ejected by jets so central galactic nucleus is gradually compressed . Until the end of leptons, galactic nucleus remains active. Then galactic nucleus compresses and remnants of gravity converting to super massive black hole.

2,Jets: Neutrons are ejected inside two opposite jets(moving spirally) along the axis of galaxy rotation . As soon as releasing from pressure of gravity, neutrons decay to protons , electrons and neutrinos. Spiral compression by magnetic forces around protons causes plasma pinch and fusion inside this magnetic ropes . Result is production of various light elements and radiations. These light elements are origin of all materials and stars around each galaxy. This stream of light elements production continues until the end of galactic nucleus activity (Lithium problem solution).

3,Low density intragalactic region: The light elements that are spread in the space by the jets create the huge low density intragalactic region. The light elements are pulled by galactic gravity under guidance of magnetic lines emerging from the N poles located at end of the jets and finally reach to accretion disk which resemble S magnetic poles . This process takes long time. This region is like two huge polish doughnuts

(a fat torus with two narrow funnels along the rotation axis) above and below the accretion disc which their axis are along the jets.

4,Accretion disc:Rotation of the light elements, under the influence of the Gravitational force makes the accretion disc in which the light elements are condensed and their speed increases continuously . When the particles reach the innermost orbits their speed reaches the maximum and under the influence of centrifugal (inertial)force, they are thrown out parallel to the disc. These orbits are on the upper and lower levels of the magnetic spinning top's body which was created during electromagnetic pinch process. By scattering of particles, their radiations due to friction force also ends and galactic arms are formed. Since radiations have no mass and inertial force due to it ,if they enter smaller orbits, they no longer have the possibility to escape from gravity (event horizon) so they remain in the trap of gravity and rotate on the surface of symmetric magnetic spinning top until releasing by jets.

5,High density galactic arms: The thrown light elements, in two opposite directions ,on the upper and lower planes relative to the accretion disc create the high density galactic arms which are moving away from active galactic nucleus. Inside these arms stars are formed and their light, causing the illumination and clarification of total arms.

Nucleus of a galaxy has two phases:1,early phase:leptonic star or active galactic nucleus 2,super massive black hole Active galactic nucleus has three sections:1,symetric magnetic spinning top field 2,inside it 3,outside i

The magnetic field produced by electromagnetic pinch around the leptons has schematic like a spinning top. This symmetric spinning top is composed of a disc in the center with upper and lower cone and axis in such a way that the magnetic force rotates first around the central disc then around cones and axes in opposite direction, at the end it makes two N magnetic poles (magnetic monopole).Inside these structures leptons are converted into neutrons and are ejected at the end of axes .Outside of it there's negative gravitomagnetic force. No substances is able to enter this structure because after approaching and increasing its speed throw out from conical parts. Radiations also isn't able to enter this structure because after reaching the event horizon are trapped, but after moving through the path of the cones, at the end of the axes released as can observe in the milky way galaxy(two large areas of released radiations above and below the galactic nucleus).

Universe

Moment of big bang (zero moment)is an equal sign in an equation which two sides (before and after it)must be completely equivalent (thermodynamicly). After big bang ,there are leptons and space time so before it there must be a biggest negative black hole or a superparticle(condense form of particles)plus space quiescence (without time and motion)or frozen space (space at absolute zero of Kelvin).So big bang was decay (fragmentation)of that black hole as a result of confrontation with space quiescence(without time and motion)or a change at the state of superparticle and temperature of space. Superparticle or biggest black hole can only produce one type of particle (identical to itself).

Returning to the past should be accompanied by a reduction of complexity, so it should be reach the minimum complexity and maximum simplicity after big bang (one type of particle based on the theory is the simplest form). In philosophy, this is called the movement from uniy(singularity)to plurality(particles). Increasing of space time inside frozen space or space quiescence due to particles and energies ,created by big bang, lead to increase effect environment, for repulsion between leptons and galaxies leading to expansion in two phases:1,fast phase due to leptons 2,slow phase due to quasars and galaxies.

Evolutionary stages of large scale structures

0-Big bang 1- Leptons (rapid expansion) 2- Homogeneous leptonic fog 3- Leptons clouds constriction by electromagnetic pinch (emitting CMB) 4- Leptonic star (active galactic nucleus) 5- Active galactic nucleus and jets(protoquasar),these jets are the most distant visible objects at the end of dark ages 6- Protoquasar and low density intragalactic region (prequasar) 7- Prequasar and accretion disc (quasar) 8- Quasar and galactic arms (preseyfert galaxy) 9- Preseyfert galaxy and stars in arms (seyfert galaxy) 10 - Seyfert galaxy and inactivity of galactic nucleus (spiral galaxy-barred galaxy)in this stage first active galactic nucleus converts to super massive black hole, then jets fade ,it needs too time for evacuation of low density intragalactic region completely and the last phase is fading of accretion disc 11, a-With the arms gradually moving away first Hoag type galaxies then ring galaxies are formed (low interaction region between galaxies). 11,b- satellite galaxy ,Irregular galaxy due to collision between galaxies and after collision elliptical galaxy (high interaction region between galaxies).

Stars formation stages is similar:After formation of protonic clouds inside galactic arms, they are constricted by plasma pinch cause creation of protonic stars with jets ,accretion discs and protoplanetery

structures. There are some differences between star and quasar: Small size, low positive gravitomagnetic force ,no exiting of it's products during fusion activity after formation and its internal magnetic fields turbulence after formation,releasing products suddenly(supernova). Stars produce heavy elements while active galactic nucleuses produce light elements.

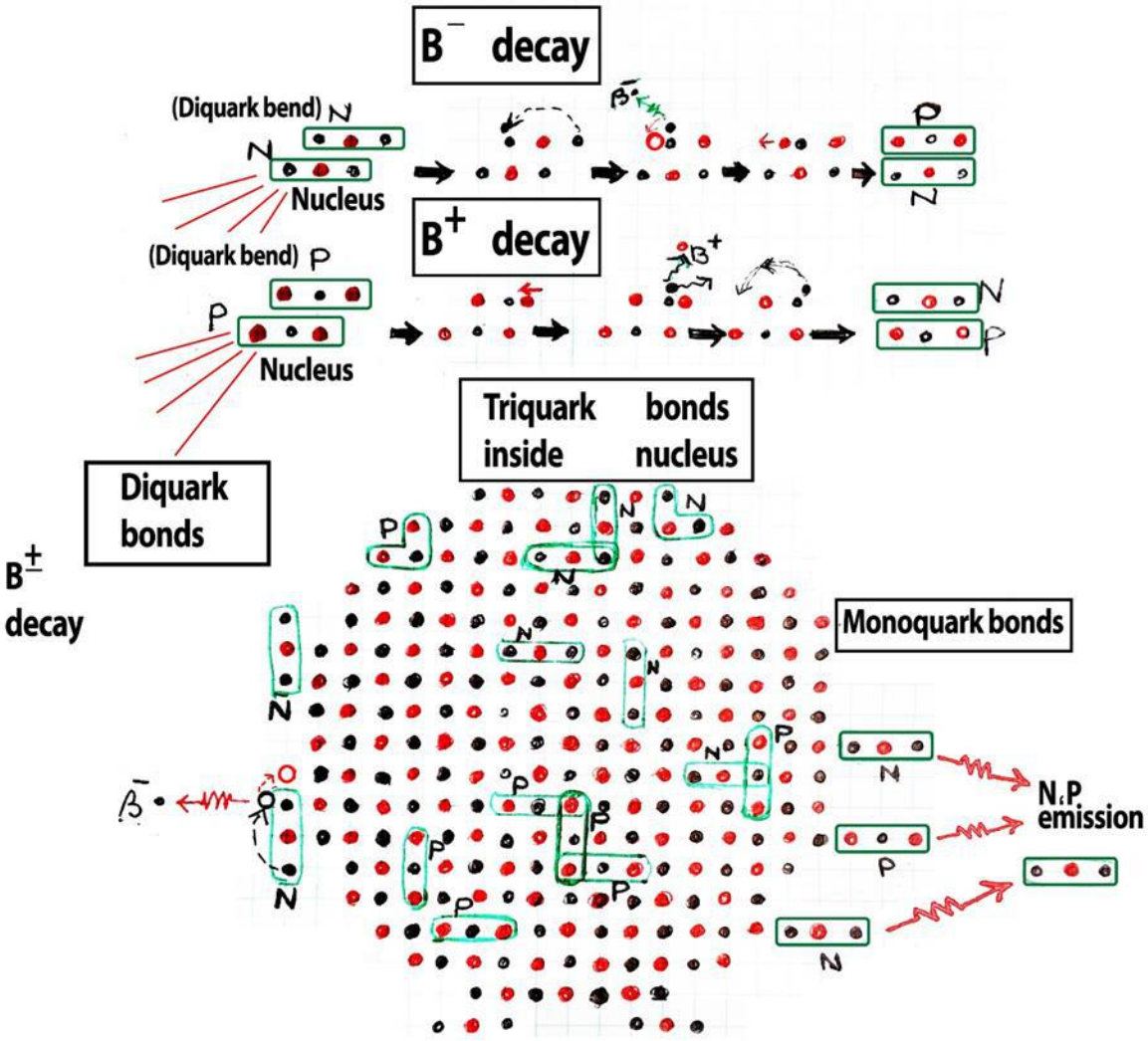
B⁻ decay
(Diquark bend) N
Nucleus
B⁺ decay
(Diquark bend) P
Nucleus
Diquark bonds
B± decay
Triquark bonds inside nucleus
Monoquark bonds
N,P emission

NUCLEUS

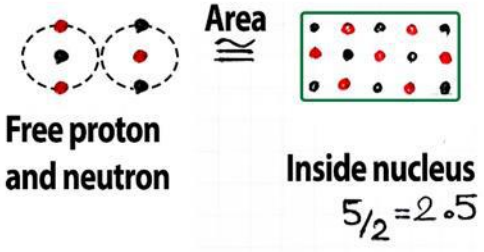
Area
Free proton and neutron
Inside nucleus
5/2 = 2.5

References

1. "The matter-antimatter asymmetry problem". CERN. Retrieved April 3, 2018.

2. Sather, Eric. "The Mystery of the Matter Asymmetry" (PDF). Vanderbilt University. Retrieved April 3, 2018.

3. Canetti, L.; Drewes, M.; Shaposhnikov, M. (2012). "Matter and Antimatter in the Universe". New J. Phys. 14 (9): 095012. arXiv:1204.4186. Bibcode:2012NJPh...14i5012C. doi:10.1088/1367-2630/14/9/095012. S2CID 119233888.

4. Ralston, John P., and Davidson E. Soper. "Production of dimuons from high-energy polarized proton-proton collisions." Nuclear Physics B 152.1 (1979): 109-124.

5. Usai, Gianluca, and NA60 collaboration. "Low mass dimuon production in proton-nucleus collisions at 400 GeV/c." Nuclear Physics A 855.1 (2011): 189-196.

6. Barrow, John D., and Richard A. Matzner. "The homogeneity and isotropy of the universe." Monthly Notices of the Royal Astronomical Society 181.4 (1977): 719-727.

7. Lee, S. (1983). "Energy balance and the radius of electromagnetically pinched plasma columns". Plasma Physics. 25 (5): 571–576. Bibcode:1983PlPh...25..571L. doi:10.1088/0032-1028/25/5/009.78

8. Peratt, Anthony L. "Evolution of the plasma universe: II. The formation of systems of galaxies." IEEE transactions on plasma science 14.6 (1986): 763-778.

9. Hu, Wayne, and Scott Dodelson. "Cosmic microwave background anisotropies." Annual Review of Astronomy and Astrophysics 40.1 (2002): 171-216.

10. Bernal, Nicolás, et al. "Rescuing high-scale leptogenesis using primordial black holes." Physical Review D 106.3 (2022): 035019.

11. P. Di Bari and A. Riotto, Successful type I leptogenesis withSO(10)-inspired mass relations, Phys. Lett. B 671, 462.(2009)

12.Newman, Ezra; Couch, E.; Chinnapared, K.; Exton, A.; Prakash, A.; Torrence, R. (1965). "Metric of a Rotating, Charged Mass". Journal of Mathematical Physics. 6 (6): 918–
.919. Bibcode:1965JMP.....6..918N. doi:10.1063/1.1704351

13. Newman, Ezra; Janis, Allen (1965). "Note on the Kerr Spinning-Particle Metric". Journal of
.Mathematical Physics. 6 (6): 915–917. Bibcode:1965JMP.....6..915N. doi:10.1063/1.1704350

14 . Antognini, Aldo, et al. "Proton structure from the measurement of 2S-2P transition frequencies of muonic hydrogen." Science 339.6118 (2013): 417-420.

ICNST 2024 International Conference on Nuclear Science and Technology
6- 8 MAY 2024 | Isfahan, Iran

Chemical Analysis of Iranian Glass Artifacts Using Micro-PIXE Technique: Insights from Van de Graff Laboratory of Tehran (Paper ID : 1100)

Agha-Aligol D.[1]*, Jafarizadeh M.[2], Moradi M.[1]

[1]Van de Graaff Laboratory, Physics and Accelerators Research School, Nuclear Science and Technology Research Institute (NSTRI), Tehran, Iran
[2]Moghaddam Museum, University of Tehran, Tehran, Iran

Abstract

In this research, the micro-PIXE technique was used to analyze 100 samples of glass artifacts from different historical periods ranging from the Parthian to the middle of the Islamic period. The main objective of this study is to identify the raw materials used to manufacture glass artifacts in various regions of Iran and during different historical periods. Another question that arises is the quality and purity of the silica and soda sources used in the production of Iranian glasses. Additionally, the research aims to determine the coloring and decoloring agents used in the manufacturing process and whether these materials were intentionally or unintentionally added during the making process. The findings indicate that a significant number of the examined glass objects fall into the category of plant-ash silica-soda-lime glasses. Additionally, within the analyzed collection, there are identifiable examples of natron glasses. Moreover, the elemental composition of the glasses shows that glasses from different regions can be classified based on the variations of MgO, K_2O, and CaO.

Keywords: ancient glass, micro-PIXE, elemental analysis, plant-ash, silica- soda-lime

INTRODUCTION

Elemental analysis of ancient glass artifacts demonstrates a direct link between the raw materials utilized in ancient glass production, the geographical origin, and the historical priode[1, 2]. Laboratory investigations have revealed that the elemental composition of the ancient glasses provides insights into both the raw materials employed and the manufacturing techniques used in the production procces[3]. By comparing the elemental compositions of glass samples from diverse historical sites worldwide, we can uncover economic, cultural, and commercial relationships across different historical epochs[4, 5]. The research for elemental analysis of historical glasses in Iran began in 2018 with the aim of identifying the challenges in this field at Van de Graaff Laboratory in Physics and Accelerators Research School, in Nuclear Science and Technology Research Institute (NSTRI). Upon resolving the identified challenges and implementing appropriate solutions, the research projects focusing on Iranian ancient glass commenced[6,

7]. In this study, about 100 glass samples(including glass vessels, bracelets and beads) from various historical sites in Iran, spanning from the Parthian period to the early Islamic era, were analyzed using the micro-PIXE technique to study the elemental composition and determine the type of glasses and to examine the raw materials used in the manufacture of glass objects found in Iranian historical sites. The results obtained from analyzing these glass objects will be discussed in the subsequent sections of this paper.

EXPERIMENTAL

Micro-PIXE or "Particle Induced X-ray Emission in micron-scale" was performed based on the Van de Graaff accelerator. In micro-PIXE, when high-energy protons interact with the analyzed samples, they lead to the emission of characteristic X-rays from the constituent elements within the samples[8, 9].The energy of X-rays of each element is specific, which can be used to detect the elements are presented in the sample. Also, the number of X-rays with specific energy determined the concentration of the elements within the sample[10]. In the present research work, the micro-PIXE analysis was performed with Oxford microprobe system using the 3 MV Van de Graaff accelerator in the Atomic Energy Organization of Iran[7]. The samples were analyzed using a beam of 2.2 MeV protons focused to a diameter less than 10 μm. The beam current was in the range of 30 to 50 pA. Characteristic X-rays were detected using a Si(Li) detector with an active area of 60 mm^2 positioned at an angle of 135° relative to the incident beam direction and with an energy resolution of 150 eV for Fe-K_α. Moreover, the spectra were processed using the GUPIXWIN package to obtain the elemental composition of the glass objects[11]. Because of the cover layer and the corrosion resulting from the glass fragments being buried in soil, we examined tiny samples from the cross-section of the glass objects. The key advantage of micro-PIXE over regular PIXE lies in its ability to utilize elemental distribution maps. By analyzing these maps, we extracted the spectrum associated with the uncorroded core of the glass fragments. This core represents the original and authentic composition of the glass, allowing us to evaluate its elemental composition. Furthermore, to evaluate the accuracy of the elemental composition and to estimate the uncertainty in measuring the constituent elements of the samples, standard glass samples of Corning Museum were simultaneously analyzed under the same conditions of the samples[12]. By considering the results of standard samples, it can be observed that, using micro-PIXE, we are able to determine the composition of the main constituents of ancient glasses with an uncertainty within 1–10%[6].

Results and discussion

The results obtained from the micro-PIXE analysis of ancient glasses show that the elements measured in all analyzed glasses from Iranian historical sites include: sodium oxide (Na_2O), magnesium oxide (MgO), aluminum oxide (Al_2O_3), silicon oxide (SiO_2), phosphorus oxide (P_2O_5), sulfur oxide (SO_3), chlorine (Cl), potassium oxide (K_2O), calcium oxide (CaO), titanium oxide (TiO_2), manganese oxide (MnO), and iron oxide (Fe_2O_3). Chromium oxide (Cr_2O_3), copper oxide (Cu_2O) zinc oxide (ZnO) and strontium oxide (SrO) also detected in the few analyzed samples. It is important to highlight that the micro-PIXE technique does not exhibit sensitivity to oxide states. The concentration of specific elements like Fe or Cu includes the entire of possible states for these elements. The main constituents of the examined glasses include SiO_2, ranging from 60wt.% to 74wt.%; Na_2O, ranging from 12wt.% to 20wt.%; and CaO, ranging from 3wt.% to 10wt.%. Hence, it can be concluded that all the analyzed samples are silica-soda-lime glass type[5]. Additionally, the content of MgO varies within the range of 0.1wt.% to 7.5wt.%, K_2O varies between 0.1wt.% and 5.5wt.%, and Al_2O_3 shows changes in the range of 1.1wt.% to 5.5wt.%. Furthermore, elements such as MnO and Fe_2O_3 were identified, with concentrations ranging from 0.03wt.% to 2wt.%.

To answer questions about determining the type of raw materials used in the glasses, to investigate the variation of the silica and soda sources in the different Iranian sites, as well as to determine the coloring and decoloring agents in manufacturing process, we use the 2D scatter plots of the indicator elements in elemental compositions of glassses obtainded by micro-PIXE. In our model for categorizing glass samples, we assume that alkali and alkali earth oxides (such as Na_2O, MgO, K_2O, and CaO) in the glass originate from plant ash or fluxes. Additionally, elements like SiO_2, Al_2O_3, Fe_2O_3, and TiO_2 are believed to come from the silica source. Therefore, variations in these elements' content indicate differences in fluxes and the use of various types of plant ash or silica sources during glass production.

Flux type and classification of glass

In general, the most important elements that are usually introduced into glass composition through the flux raw material include: sodium, potassium, lead, magnesium, phosphorus, chlorine, and sulfur[13]. As proposed by Sayre and Smith[14], we can utilize the MgO and K_2O concentrations to categorize the ancient glass based on its type[15, 16]. According to this scheme, if both MgO and K_2O concentration in the glass are less than 1.5 wt%, it falls into the category of natron glass. Conversely, when the content of these two

oxides exceeds 2.5 wt%, the glass is referred to as plant ash glass, as it utilizes ash obtained from plants grown in saline soils as a flux[14].

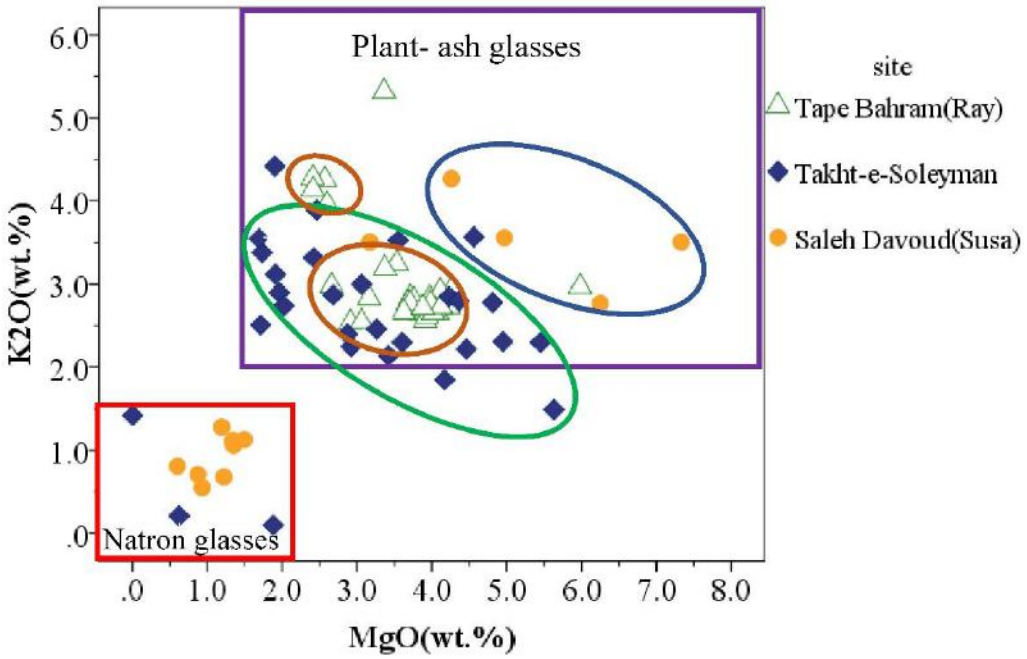

Fig. 1. Variation in wt.% of MgO versus K_2O in analyzed samples in this study

In Fig.1 variations of MgO relative to K_2O is demonstrated for all the analyzed samples in this study. As clearly observed in Fig.1, the analyzed glasses can be distinctly categorized into two groups, represented by red and pink rectangles. The first group, which includes colorful beads from Saleh Davoud and several samples from Takht-e Soleyman, consists of silica-soda-lime glasses with MgO and K_2O content less than 1.5wt.%, commonly referred to as "natron" glasses type[17]. Among the analyzed samples, the majority exhibit MgO and K_2O content exceeding 2.5wt.%. These glasses were produced using flux obtained from plant ashes and are commonly referred to as "plant-ash" glasses[18]. As shown in the Fig.1, the number of samples in the first group is relatively small compared to the second group. Moreover, in the second group, we can identify distinct sub-groups based on the varying levels of MgO and K_2O content, visually represented by colored ellipses. The presence of these distinct sub-groups suggests that various plant ashes were utilized as flux in the production of the glass artifacts discovered at Iranian archaeological sites[3, 19]. However, according to the literature, natron-based glasses were manufactured between 800 BCE and 800 AD within archaeological contexts in the eastern Mediterranean region[13, 20]. Hence, based on these findings, we can infer that there exist connections and long-distance trade involving raw materials and/or

completed glass artifacts between Iranian glassmakers and eastern Mediterranean region such as Syria, Palestinian and Egypt[21].

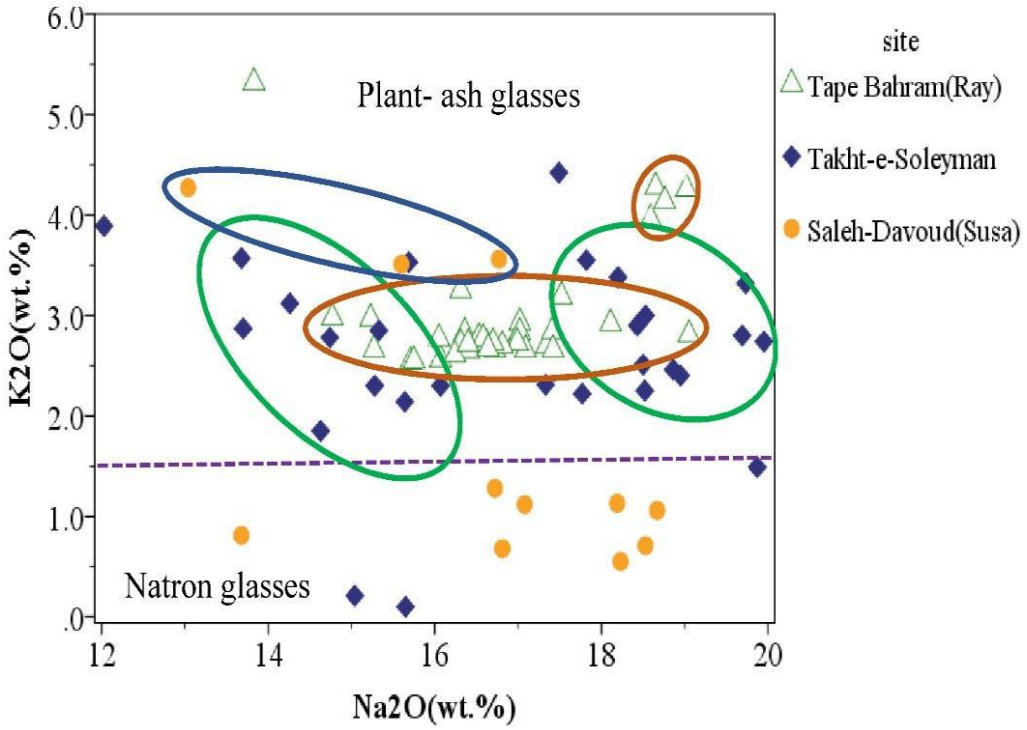

Fig. 2. Variation in wt.% of Na_2O versus K_2O in analyzed samples in this study

In Fig.2, variations in the weight percentage of Na_2O versus K_2O is depicted for all the analyzed glass samples from the studied sites. As observed in this figure, based on the variation of these two oxides, the analyzed samples are categorized into differnt distinct groups, represented by colored ellipses. Most of the Tape Behram samples are grouped together, indicated by brown ellipses. In the glasses from this site, the K_2O variation is minimal, with approximately 3wt.%. Nevertheless, the variations in Na_2O content in Tape Behram glasses are moderately elevated, in the range of 15wt.% to 19wt.%. However, four samples from Tape Behram stand apart from the remaining samples at this site due to their elevated concentrations of K_2O and Na_2O. On the other hand, according to Fig.2, it can be observed that the samples from Takht-e Soleyman, are divided into two separate groups, indicated by green ellipses. These two groups, characterized by differences in Na_2O content, and can be distinguished from each other. In one of the groups, the Na_2O content varies between approximately 17wt.% and 20wt.%, while in the second group, it ranges from 13wt.% to 16wt.%. Meanwhile, the K_2O content remains relatively consistent in both groups. Furthermore, in the case of natron glasses, the Na_2O concentration exhibits significant variations, ranging from 12wt.% to 19wt.%. According to extensive research and studies conducted on natron glasses, it has

been determined that this type of glass is classified into differnt subgroups based on the source of silica and flux used in its production[22]. The differences in the elemental compositions of natron glass found in Saleh-Davoud and Takht-e Solyman suggest that these glasses were made in distinct regions across the eastern Mediterranean.

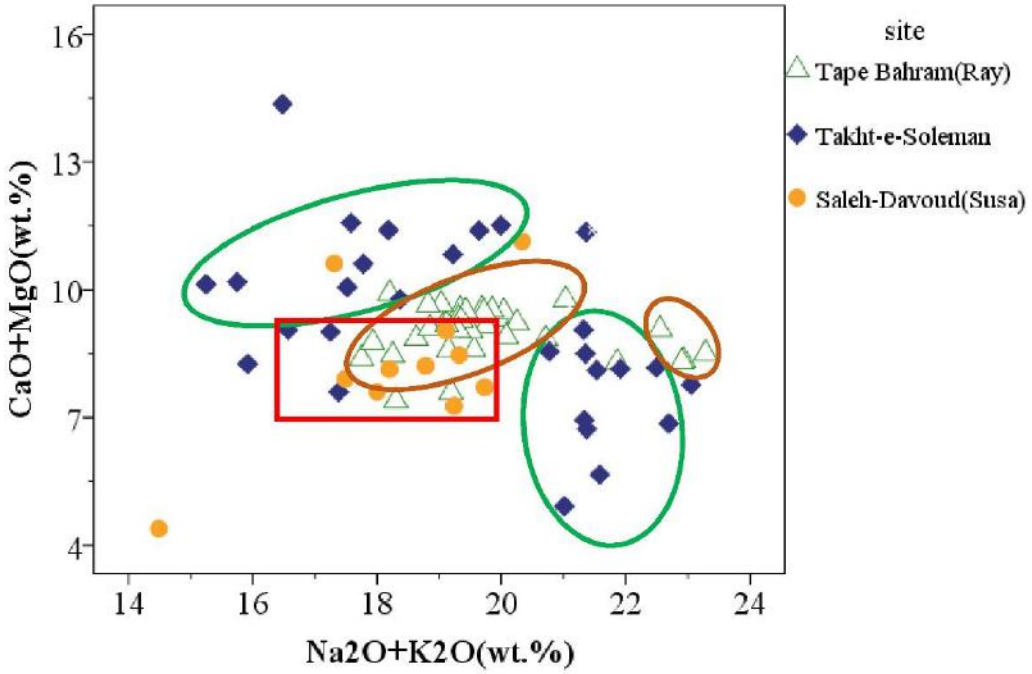

Fig. 3. variation of wt.% of total content of soda and potash (alkaline elements) versus total content of CaO and MgO (alkaline earth elements) in analyzed samples in this study

The Fig.3 illustrates the changes of the total concentration of sodium and potassium oxides in terms of the total weight parentage of magnesium and calcium oxides in all analyzed samples in this study. As observed in this figure, the distinct groups described earlier are clearly identified within these glass samples.

Hence, considering the concentration of elements like magnesium, potassium, sodium, and calcium introduced into the glass from raw flux materials, it can be deduced that various fluxes were utilized in manufacturing glasses at Iranian archaeological sites. Given that variations in ash elements are likely linked to the specific plant type used for ash preparation, these alterations imply that each site probably employed ash derived from a distinct plant species.

Silica raw materials

The quality and purity of silica sources used in glass production are studied by examining the concentration of elements such as SiO_2, Al_2O_3, Fe_2O_3, and TiO_2[3]. These elements are introduced into the glass composition from raw materials of silica. Silica-soda-lime glasses typically utilize sand, pebble, or pure quartz as their raw materials for silica[23]. In Fig. 4 the variation of SiO_2 versus Al_2O_3 in analyzed samples in this study is shown.

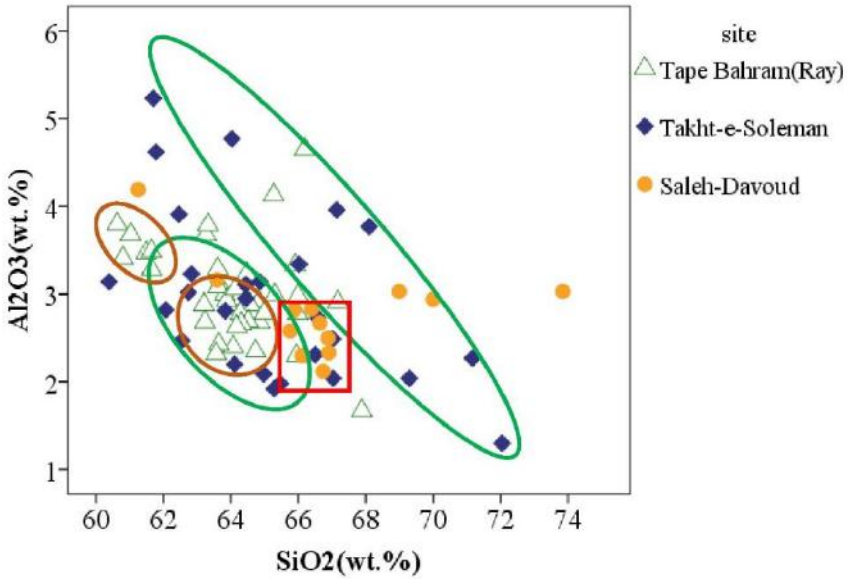

Fig. 4. Variation in wt.% of SiO_2 versus Al_2O_3 in analyzed samples in this study

The analyzed glasses exhibit varying concentrations of Al_2O_3, ranging from 1.20wt.% to 5.20wt.% as depicted in Fig. 4, while the concentration of SiO_2 varies between 60wt.% and 74wt.%. However, as shown in this figure, we can see an inverse linear correlation between SiO_2 and Al_2O_3 concentration.This correlation indicates that Al_2O_3, introduced as an impurity of the silica raw materials to the glass composition[24]. Morever, it can be inferred that the analyzed glasses were likely produced using relatively impure silica sources like river sand or pebbles[23]. This conclusion arises from the fact that when pure quartz serve as the source for silica raw materials, the glass composition typically contains less than 1wt.% of Al_2O_3 and less than 0.50wt.% of Fe_2O_3[23] . However**,** considering the varation in SiO_2 and Al_2O_3 content, it is highly probable that various types of sand were employed in the production of these glasses. In the case of samples from Takht-e Soleyman, notable differences exist in the concentrations of Al_2O_3 and SiO_2 and do not conform to a well-defined grouping.

Coloring and decoloring agents

Based on the elemental composition of the analyzed samples, it is evident that Fe_2O_3 and Cu_2O are elements that can play the most significant role as coloring agents in these samples. Morever, MnO is the only element that used as a decoloring agents. Fe_2O_3 and MnO are initially inter to glass composition as impurity from raw materials of silica[13]. Based on this fact, changes in the weight percentage of Fe_2O_3 in terms of MnO can provide useful information about the intentional or unintentional addition of coloring and decoloring agents during the manufacturing process[25].

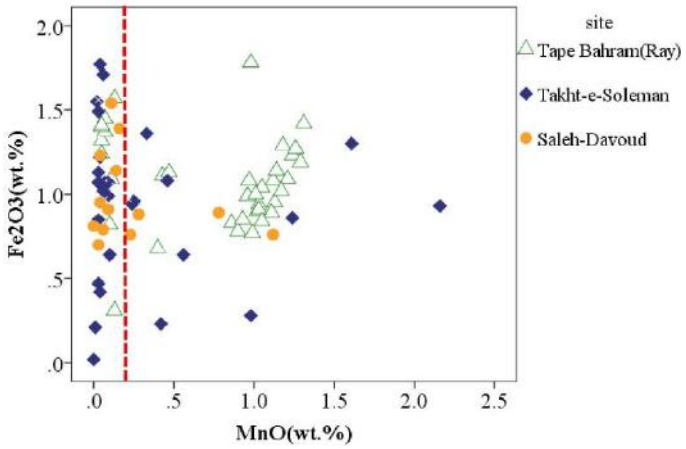

Fig. 5. Variation of a Fe_2O_3 in terms of MnO in analyzed samples in this study

In Fig. 5, the variation of Fe_2O_3 with respect to MnO is depicted for all the analyzed samples from the investigated sites. As observed in this figure, based on the changes of these oxides, the analyzed samples from these sites are divided into two main groups:

Group one: These samples exhibit MnO level ranging from 0.3wt.% to 2.25wt.%, along with Fe_2O_3 content varying between 0.2wt.% and 1.8wt.%.

Group two: This group includes samples where MnO is typically less than 0.25wt.%, and Fe_2O_3 content is similar to group One, ranging between 0.2wt.% and 1.8wt.%, exept one sample.

However, it is common that if MnO is unintentionally introduced into the glassmaking process from impurities present in silica, its concentration in the samples should be less than approximately 0.3wt.%[23]. Therefore, based on Fig. 5, it is evident that in many samples from Tape Bahram, as well as some samples from Takht-e Soleyman and Saleh Davoud (group one), the addition of MnO as decoloring agent

deliberately has been carried out. However, in the samples of group two, which mainly include samples from Takht-e Soleyman and Saleh Davoud, and some samples from Tape Bahram, MnO has unintentionally entered the manufacturing process. While, in these two groups the Fe_2O_3 has unintentionally and from impure silica entered to the manufacturing process and it cause to create green taint glasses.

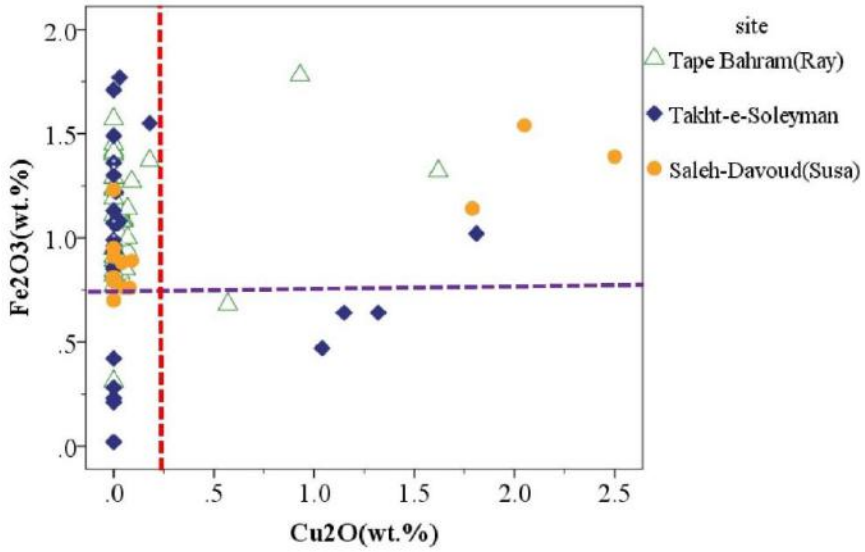

Fig. 6. Variation of a Cu_2O in terms of Fe_2O_3 in analyzed samples in this study

On the other hand, based on the variations of Cu_2O with respect to Fe_2O_3 as shown in Fig.6, it is evident that in the analyzed samples, only a few samples from Tape Bahram, Takht-e Soleyman, and Saleh, Cu_2O has intentionally been added as a coloring pigment to create dark green color in the glasses. As show in in the Fig.6 the content of Cu_2O is more than 0.10 wt.% and varies between 0.54 and 2.50 wt.%.

Conclusions

The examination of historical Iranian glasses indicates that the analyzed collection in this study comprises both plant-ash and natron glass types. By analyzing the MgO and K_2O levels, we identified two distinct groups, indicating the utilization of various flux types in glass manufacturing. Furthermore, differnt groups were identified in the plant-ash glasses based on elements originating from flux. This suggests the utilization of varying types or quantities of ashes as fluxes. Morever, the results show that sands served as vitrifying agents, while impurities in the sand, such as Fe_2O_3 and MnO, played roles in both coloring and decoloring the glass.

Acknowledgements

The authors would like to express their sincerest appreciation to all those who have made this article possible, in particular the beam line staff of the Van de Graaff laboratory of NSTIR, for their help during the experiments.

References

[1] T. Rehren, I.C. Freestone, Ancient glass: from kaleidoscope to crystal ball, Journal of Archaeological Science, 56 (2015) 233-241.

[2] I. Angelini, B. Gratuze, G. Artioli, Glass and other vitreous materials through history, The Contribution of Mineralogy to Cultural Heritage(2019).

[3] N. Schibille, J. Lankton, B. Gratuze, Compositions of early Islamic glass along the Iranian Silk Road, Geochemistry, (2022) 125903.

[4] F. Koleini, L.C. Prinsloo, W.M. Biemond, P. Colomban, A.-T. Ngo, J.C.A. Boeyens, M.M. van der Ryst, Towards refining the classification of glass trade beads imported into Southern Africa from the 8th to the 16th century AD, Journal of Cultural Heritage, 19 (2016) 435-444.

[5] N. Schibille, C. Klesner, D.R. Neuville, S. Stark, A.I. Torgoev, S.J. Mirzaakhmedov, Geochemical variations in early Islamic glass finds from Bukhara (Uzbekistan), Geochemistry, (2024) 126078.

[6] N. Salehvand, D. Agha-Aligol, A. Shishegar, M.L. Rachti, The study of chemical composition of Persian glass vessels of the early Islamic centuries (10^{th}–11^{th} centuries AD) by micro-PIXE; Case Study: Islamic collection in the National Museum of Iran, Journal of Archaeological Science: Reports, 29 (2020) 102034.

[7] D. Agha-Aligol, M. Mousavinia, V. Fathollahi, Micro-PIXE analysis of early Islamic (10^{th}–11^{th} century AD) glass vessels from the Tape-Bahram historical site in Ray, Iran, Archaeological and Anthropological Sciences, 15 (2022) 1.

[8] M. Nastasi, J.W. Mayer, Y. Wang, Ion Beam Analysis: Fundamentals and Applications, Taylor & Francis(2014).

[9] S.A.E. Johansson, J.L. Campbell, PIXE: a novel technique for elemental analysis, Wiley(1988).

[10] B. Schmidt, K. Wetzig, Ion Beams in Materials Processing and Analysis, Springer Vienna(2012).

[11] J.L. Campbell, N.I. Boyd, N. Grassi, P. Bonnick, J.A. Maxwell, The Guelph PIXE software package IV, Nuclear Instruments and Methods in Physics Research Section B, 268 (2010) 3356-3363.

[12] E.P. Vicenzi, S. Eggins, A. Logan, R. Wysoczanski, Microbeam Characterization of Corning Archeological Reference Glasses: New Additions to the Smithsonian Microbeam Standard Collection, Journal of Research of the National Institute of Standards and Technology, 107 (2002) 719-727.

[13] P. Degryse, A.J. Shortland, Interpreting elements and isotopes in glass: A review, Archaeometry, 62 (2020) 117-133.

[14] E.V. Sayre, R.W. Smith, Compositional Categories of Ancient Glass, Science, 133 (1961) 1824-1826.

[15] Y. Abe, R. Shikaku, I. Nakai, Ancient glassware travelled the Silk Road: Nondestructive X-ray fluorescence analysis of tiny glass fragments believed to be sampled from glassware excavated from Niizawa Senzuka Tumulus No. 126, Japan, Journal of Archaeological Science: Reports, 17 (2018) 212-219.

[16] T. Chinni, S. Fiorentino, A. Silvestri, S. Mantellini, A.E. Berdimuradov, M. Vandini, Glass from the Silk Roads. Insights into new finds from Uzbekistan, Journal of Archaeological Science: Reports, 48 (2023) 103841.

[17] S. Maltoni, A. Silvestri, A. Marcante, G. Molin, The transition from Roman to Late Antique glass: new insights from the Domus of Tito Macro in Aquileia (Italy), Journal of Archaeological Science, 73 (2016) 1-16.

[18] N. Kato, I. Nakai, Y. Shindo, Transitions in Islamic plant-ash glass vessels: on-site chemical analyses conducted at the Raya/al-Tur area on the Sinai Peninsula in Egypt, Journal of Archaeological Science, 37 (2010) 1381-1395.

[19] N. Schibille, B. Gratuze, E. Ollivier, É. Blondeau, Chronology of early Islamic glass compositions from Egypt, Journal of Archaeological Science, 104 (2019) 10-18.

[20] A. Shortland, L. Schachner, I. Freestone, M. Tite, Natron as a flux in the early vitreous materials industry: sources, beginnings and reasons for decline, Journal of Archaeological Science, 33 (2006) 521-530.

[21] D. Whitehouse, 'Things that travelled': the surprising case of raw glass, Early Medieval Europe, 12 (2003) 301-305.

[22] M. Phelps, I.C. Freestone, Y. Gorin-Rosen, B. Gratuze, Natron glass production and supply in the late antique and early medieval Near East: The effect of the Byzantine-Islamic transition, Journal of Archaeological Science, 75 (2016) 57-71.

[23] E. Gliozzo, The composition of colourless glass: a review, Archaeological and Anthropological Sciences, 9 (2017) 455-483.

[24] J. Henderson, S.D. McLoughlin, D.S. McPhail, Radical changes in Islamic glass technology: evidence for conservatism and experimentation with new glass recipes from early and middle Islamic Raqqa, Syria, Archaeometry, 46 (2004) 439-468.

[25] N. Schibille, A. Sterrett-Krause, I.C. Freestone, Glass groups, glass supply and recycling in late Roman Carthage, Archaeological and Anthropological Sciences, 9 (2017) 1223-1241.

ICNST 2024 International Conference on Nuclear Science and Technology
6- 8 MAY 2024 | Isfahan, Iran

Investigating the Deterioration and Corrosion of Ancient Iranian Manuscript Using Ion Beam Analysis Techniques (Paper ID : 1102)

Moradi M.[1], Agha-Aligol D.[1]*, Lamehi-Rachti M[1]

[1] *Van de Graaff Laboratory, Physics and Accelerators Research School, Nuclear Science and Technology Research Institute (NSTRI), Tehran, Iran*

Abstract

In this study, few number of pages from an ancient manuscript that have undergone significant damage, were analyzed using micro-ion beam techniques, including micro-PIXE, micro-RBS, and micro-STIM to identify the factors responsible for the deterioration of these manuscripts. The micro-PIXE results indicate that the yellow decoration ink that has suffered severe corrosion is composed of a combination of Cu and Zn pigments. Moreover, the micro-PIXE analysis reveals that copper is the main element that forms the decoration of this manuscript. The studying the various copper pigments, it was discovered that one of the copper pigment types, which is made up of copper mineral elements, is verdigris or copper acetate (II) with the chemical formula Cu $(CH_3COO)_2$. This pigment is highly susceptible to environmental moisture. As a result, favorable environmental conditions such as optimal humidity and elemental composition like copper can cause local oxidation of paper to destroys the paper substrate. Furthermore, the results demonstrate that the black ink used to write the text in this manuscript is carbon-based and does not contribute to the corrosion of the paper. However, the micro-RBS analysis indicates that the ink has fully permeated and diffused in the bulk of paper and it increased the corrosion effect.

Keywords: ancient manuscript, ink and paper, micro-PIXE, micro-RBS, pigment

Introduction

Throughout numerous years, paper has served as a prominent medium for documenting scientific and cultural accomplishments[1, 2]. Consequently, the significance of these manuscripts is evident to all. Paper primarily consists of cellulose, with the addition of minor quantities of mineral and organic additives like starch. A significant and critical issue that poses a threat to ancient paper documents, books, and manuscripts stored in libraries and personal collections is the gradual deterioration and erosion of the paper material[1, 3]. Numerous factors contribute to the deterioration and loss of paper documents. Some of these factors are associated with the composition of the paper itself or the chemicals applied to it, while others are influenced by environmental conditions like humidity and temperature[4]. Throughout history, soot or

carbon black[5, 6] and iron-gall inks have been extensively employed for writing and documenting human ideas[7]. The well-documented phenomenon of paper degradation and corrosion resulting from iron content in iron-gall inks is widely recognized[8]. Numerous studies have investigated this type of corrosion[8-10]. Recently, another factor contributing to the deterioration and loss of paper substrates in certain documents has been attributed to the presence of transition elements, such as iron and copper, in the compounds used[10-14]. An examination of handwritten documents in our country reveals that numerous paper manuscripts are corroded and face the risk of destruction. Given that the composition of paper and composite materials significantly influences corrosion, identifying the constituents of both is crucial for preventing this process[10]. Our research focuses on investigating the factors contributing to the deterioration of an ancient manuscript. We employ elemental analysis to determine the paper and composite components. By studying samples from damaged areas across different pages, using techniques like micro-PIXE, micro-RBS, and micro-STIM, we aim to uncover the relationship between corrosion causes and the chemical composition of the composite used in this manuscript.

Experimental

The Micro-Ion Beam analysis was performed with microprobe system manufactured by Oxford Instruments using the 3 MV Van de Graaff accelerators at the Nuclear Science & Technology Research Institute in Atomic Energy Organization of Iran[15-17]. The samples were analyzed in a vacuum chamber using a beam of 2.2 MeV protons focused to a diameter less than 10 μm. The beam current was in the range of 30 to 50 pA. Micro-PIXE or "Particle Induced X-ray Emission in micron-scale" was performed to measure the elemental composition of papers and inks. During the interaction of the high-energy proton with the analyzed samples, the characteristic X-rays of the constituent elements are emitted from the samples. The energy of X-rays of each element is specific, which can be used to detect the elements are presented in the sample. Also, the number of X-rays with specific energy determined the concentration of the elements within the sample[18, 19]. Characteristic X-rays were detected using a Si(Li) detector with an active area of 60 mm^2 positioned at an angle of 135° relative to the incident beam direction and with an energy resolution of 150 eV for Fe-K_α. Moreover, the spectra were processed using the GUPIXWIN package to obtain the elemental composition of the glass objects[20]. Scanning Transmission Ion Microscopy (micro-STIM) measurements were carried out using a surface barrier detector at angle of 20° to the incident beam direction. Morever, the Rutherford Backscattering Spectrometery(micro-RBS) was used to determine the

thickness and redistribution of the ink in the paper with a surface barrier detector placed at 160° scattering angle to the incident beam direction.

Results and Discussion

In this research, differnt samples from an ancient manuscript containing verses from the Holy Quran have been chosen for examination and analysis. The optical image of one of the manuscript pages is presented in Fig.1. As depicted in the figure, the manuscript features inclue dark yellow lines used for calligraphy and ornamentation across all pages. However, as clearly illustrated in the figure, the paper near these yellow lines has suffered from corrosion. In certain sections of the manuscript, this corrosion has advanced to the point of causing visible cracks, as evident in Fig.1b. The objective of this study is to explore the factors contributing to the deterioration and corrosion of the manuscript. Additionally, we aim to establish a connection between the causes of corrosion and the chemical composition of the pigments employed in the decoration lines within this manuscript.

Fig.1. An optical image of a page from this manuscript that shows a significant deterioration

The samples selected for this investigation were carefully chosen to minimize any potential harm to the pages. Consequently, these samples were taken from approximately less than 1 cm^2 within the manuscript, and various areas of these samples were subjected to analysis. Fig. 2 illustrates the elemental distribution maps for paper and the decoration line in analyzed sample. The optical image of sample displays various analyzed regions, marked by red squares. In this sample, three distinct regions were examined. Focusing

on region 1, the elemental distribution maps reveal that the decoration line mainly consist of copper (Cu) and zinc (Zn) elements. A comparison between the optical image of region 1 and the micro-PIXE elemental maps, confirms that copper and zinc are exclusively abundant within the area where the decoration lines are present, while they are absent outside these line. Furthermore, the elemental distribution maps depicted in Fig.3 reveal the presence of trace amounts of sulfur (S), titanium (Ti), and iron (Fe) within the decoration lines[21, 22]. An additional significant finding arising from the elemental maps distribution of non-uniform elemental maps of calcium (Ca) in the analyzed areas.The calcium X-ray map gives interesting information about the surface of the paper and also the fabrication process[15]. Usually, Ca concentration in the paper is not uniform and X-ray maps show islands of high calcium content. This effect is probably due to a Ca compound such as bone powder, which would have been used for filling and treating the paper[15]. The composition of the black ink was investigated by examining additional regions within the analyzed sample, specifically regions 2 and 3**.** The analysis findings indicate that iron is absent in the black ink. Instead, the black ink is likely composed of carbon soot[15, 23].

The X-ray spectra corresponding to the dark yellow ink and paper, specifically for region 1 within the analyzed sample shown in Fig. 2, have been displayed in Fig. 3. Clearly, when examining the two spectra in Fig.2, the elemental contrast between the decoration line and paper becomes fully evident that copper (Cu) and zinc (Zn) constitute the primary elements in the decoration lines, while other elements detected in the sample such as magnesium (Mg), aluminum (Al), silicon (Si), sulfur (S), chlorine (Cl), potassium (K), calcium (Ca), titanium (Ti), and iron (Fe), compose the paper substrate.

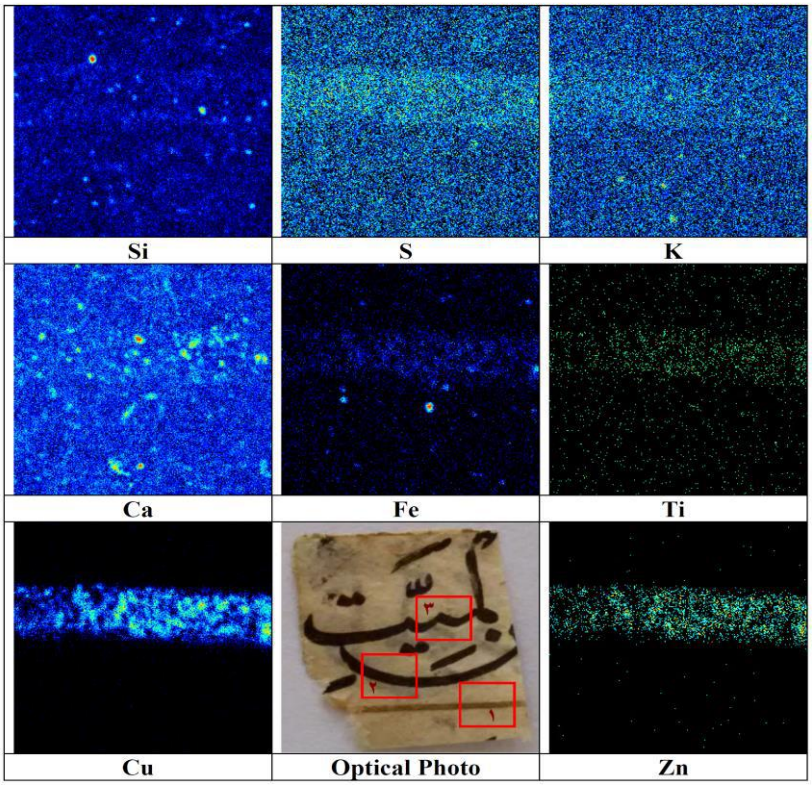

Fig. 2. The distribution of micro-PIXE elemental maps for a sample in the analyzed manuscript in area with/without ink (area 1). The optical image of the sample and different analyzed regions is shown in the figure. The dimensions of the analyzed regions are 2.5×2.5 mm^2.

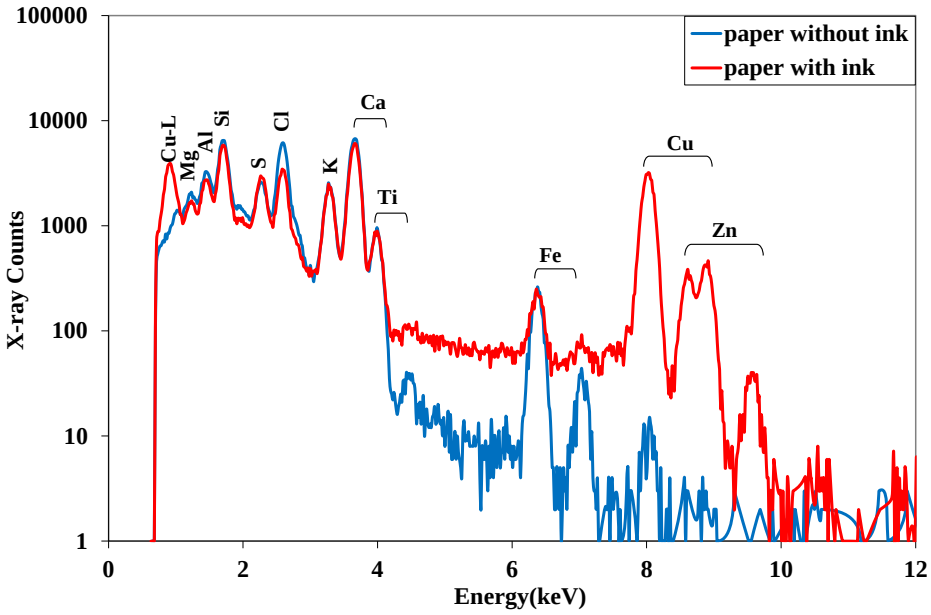

Fig. 3. The micro-PIXE spectra obtained for region 1 within the analyzed sample shown in Fig. 2.

In Fig.4**,** we observe the profile and distribution of copper**,** zinc**,** iron, and titanium within the sample under investigation**.** These distributions were obtained through linear scanning in the X direction. The figure is plotted based on the total number of characteristic X-rays recorded in the X direction, as depicted in the optical image of Fig. 4**.** Notably, this figure provides a clear differentiation between the elements present in the decoration lines and those constituting the paper substrate**.** Furthermore, it allows for a semi-quantitative analysis of the elemental composition of both the decoration lines and the paper substrate. Based on Fig. 4, the copper concentration in the decoration lines is approximately ninefold higher than the zinc content. The Cu element profile in the scanning line exhibits non-uniformity and significant fluctuations due to ink diffusion within the paper. The findings from semi-quantitative analysis of ink and paper in ancient manuscript, as demonstrated earlier, indicate that these methods are adequate for assessing the elemental composition and identifying inorganic pigments used in different manuscripts. Micro-PIXE mapping and the semi-quantitative analysis of pigments indicate that copper (Cu) predominantly constitutes the applied pigment within the decorition lines. Through analysis of various copper compounds, it becomes evident that one of the distinct types of copper pigments, composed of mineral elements, is verdigris or copper(II) acetate ($Cu(CH_3COO)_2$). This pigment exhibits high sensitivity to environmental moisture[14]. Hence, favorable environmental conditions, including humidity and an optimal copper chemical composition, can lead to localized oxidation of paper or cellulose- the primary paper component- resulting in complete destruction of the paper substrate. The findings from our study align with previously published reports. These articles highlight copper element as catalysts in the oxidation of cellulose and other related products. The observed corrosion, linked to copper pigments, is understood as the detrimental impact on ancient papers when adorned with pigments containing transition elements.

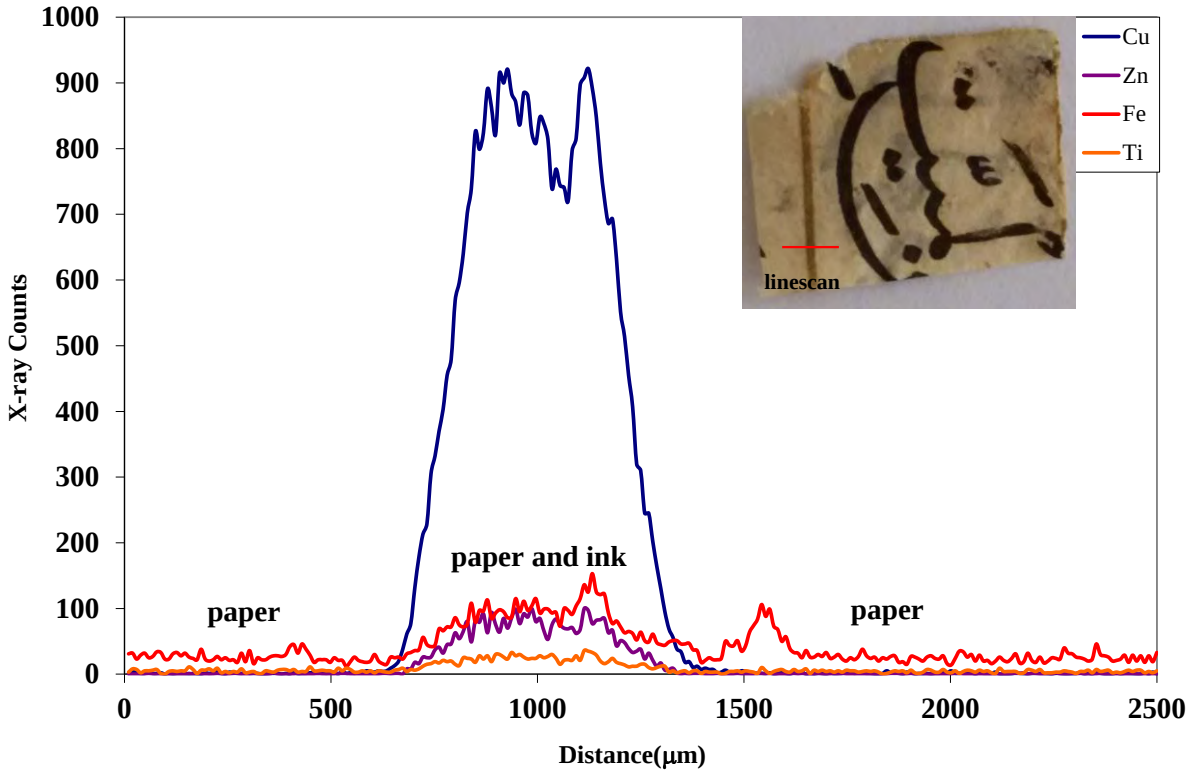

Fig. 4. The elemental profile of line scan in the X direction, for the analyzed sample

Furthermore, we employed the micro-RBS technique, to explore the penetration of the ink into the paper substrate and assess the depth of penetration, as well as to estimate the presence of light elements not measurable by micro-PIXE. Fig.5 displays the Rutherford backscattering spectrometry (RBS) spectrum (blue line) acquired from region 1 of the sample depicted in Fig.2, as well as the simulated spectrum (pink dash line) generated using SIMNRA software. The figure clearly indicates that the main elements within the paper are light elements, specifically carbon, oxygen and hydrogen. The atomic percentages obtained for these elements through fitting the experimental spectrum using SIMNRA.6 software are as follows: C (carbon): 29.3%, O (oxygen): 23.2% and H (hydrogen): 46.3%. Remarkably, these values closely align with the atomic composition of cellulose ($C_6H_{10}O_5$), and is consistent with it which constitutes the fundamental elements of paper[24]. Furthermore, Fig.5 illustrates the presence of heavier elements-specifically copper and zinc-in the decoration lines. The atomic percentages for copper and zinc are approximately 0.9% and 0.1%, respectively. Remarkably, these values consistent perfectly with the semi-quantitative findings from Fig. 4, where the copper-to-zinc ratio was approximately 9.

Furthermore, micro-RBS analysis reveals that the ink employed for decorating the manuscript has completely penetrated the paper substrate, seamlessly integrating with it. Had this not been the case, we

would have anticipated observing a distinct peak corresponding to the ink layer, with a thickness proportional to the peak's width in the Fig.5 spectrum. However, no such layer is evident.

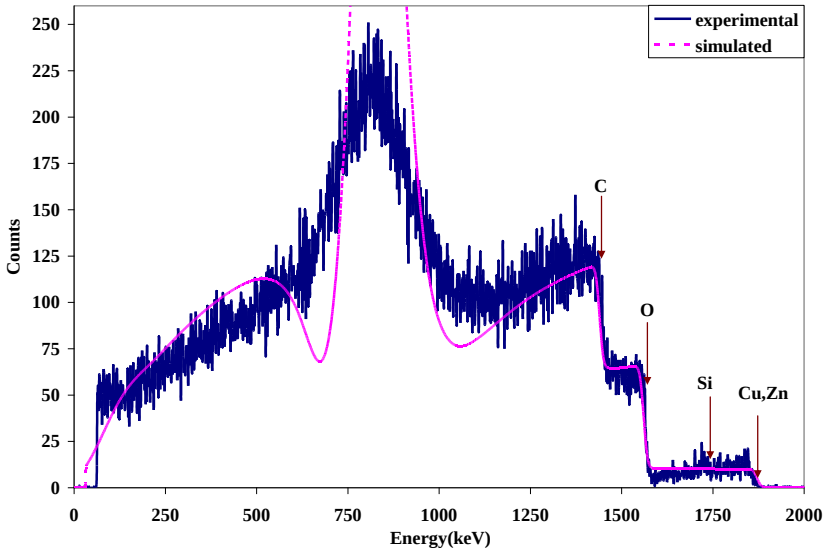

Fig.5. The RBS spectrum obtained from area 1 in the sample shown in Fig.2 along with the simulated spectrum obtained using SIMNRA.

By employing Micro-STIM technique, valuable insights into the mass density distribution at various depths within the thin sample like ancient manuscripts can be acquired**.** Fig.7 displays the result obtained from an additional sample of this particular manuscript. The sample analyzed using micro- PIXE, RBS, and STIM techniques, simultaneously. Furthermore, the figure displays both the optical image and the sampling location of analyzed from another page in the manuscript. Additionally, it includes an image of the analyzed area captured using a light microscope at a magnification of 16X. In this figure, it is apparent that the decoration line contains both copper and zinc elements, as indicated by the elemental distribution obtained from the analyzed area. Additionally, the two-dimensional distribution image obtained from the micro-STIM reveals the heterogeneity of the analyzed region. However, in the STIM map, the fiber tissue forming the paper substrate is fully visible. Considering the well-defined dimensions of the analyzed area, one can estimate the dimensions of the fibers constituting the paper[24].

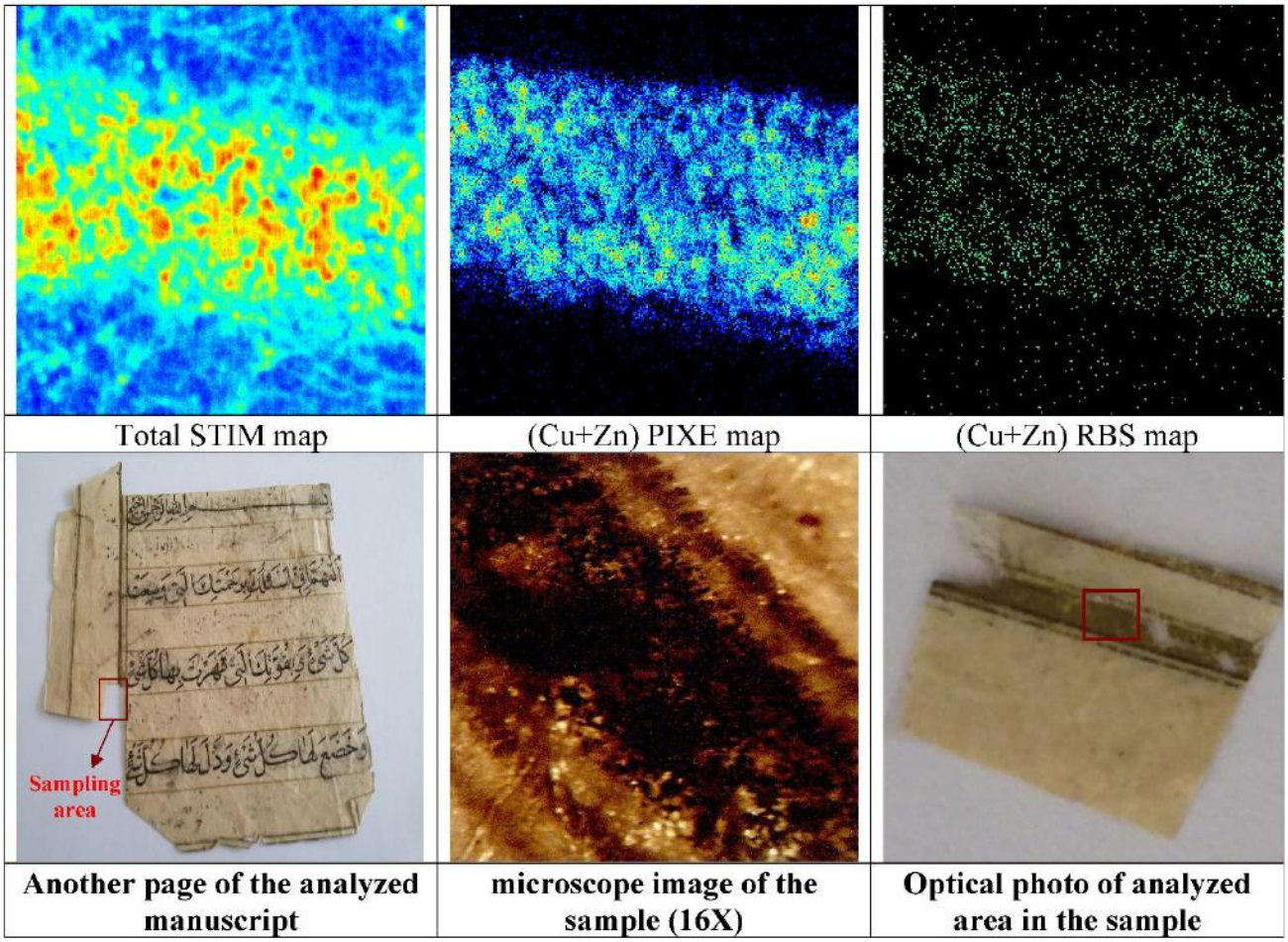

Fig.6. The micro-PIXE, micro-RBS, and micro-STIM maps for another analyzed sample in the manuscript. Also, the optical photo and microscope image with a magnification of 16X are shown in the figure.

Conclusions

The current study demonstrates that elemental mapping using Micro-Ion Beam Analysis provides valuable insights into the composition and depth profiles of inks and papers utilized in ancient manuscripts. Based on the findings from micro-PIXE analysis, copper is the predominant element constituting the decoration lines in this ancient manuscript. Under suitable conditions, such as humidity and with the presence of copper in the inks, local oxidation of paper or cellulose can occur to complete destruction of the paper substrate. However, the findings also indicate that the black ink employed for writing this manuscript does not belong to the iron-gall ink category. Furthermore, by employing complementary techniques such as micro-RBS) and micro-STIM, valuable insights regarding paper properties are ink profile inferred. Notably, it has been demonstrated that the paper exhibits non-uniform thickness.

Acknowledgements

We express our gratitude to Dr. F.B for providing ancient documents. Additionally, we extend our thanks to the technical staff at the Van de Graaff laboratory for their assistance during the experiments.

References

[1] O. Abdullatef, M. Helal, M. Soliman,H. Elmenshawy, Evaluation of the Conditions of a Calligraphy Manuscript and an Old Historical and Archaeological Legitimate Argument from the 18th Century, International Journal of Materials Technology and Innovation, 3 (2023).

[2] L. Idjouadiene, T.A. Mostefaoui, A. Naitbouda, H. Djermoune, D.E. Mechehed, M. Gargano, L. Bonizzoni, First applications of non-invasive techniques on Algerian heritage manuscripts: the lmuhub ulahbib ancient manuscript collection from Kabylia region (Afniq n Ccix Lmuhub), Journal of Cultural Heritage, 49 (2021) 289-297.

[3] W. Faubel, S. Staub, R. Simon, S. Heissler, A. Pataki, G. Banik, Non-destructive analysis for the investigation of decomposition phenomena of historical manuscripts and prints, Spectrochimica Acta Part B: Atomic Spectroscopy, 62 (2007) 669-676.

[4] M. Titubante, F. Giannini, A. Pasqualucci, M. Romani, G. Verona-Rinati, C. Mazzuca, L. Micheli, Towards a non-invasive approach for the characterization of Arabic/Christian manuscripts, Microchemical Journal, 155 (2020) 104684.

[5] D.M. Goltz, A Review of Instrumental Approaches for Studying Historical Inks, Analytical Letters, 45 (2012) 314-329.

[6] T. Christiansen, D. Buti, K.N. Dalby, P.E. Lindelof, K. Ryholt, A. Vila, Chemical characterization of black and red inks inscribed on ancient Egyptian papyri: The Tebtunis temple library, Journal of Archaeological Science: Reports, 14 (2017) 208-219.

[7] J. Duh, D. Krstić, V. Desnica, S. Fazinić, Non-destructive study of iron gall inks in manuscripts, Nuclear Instruments and Methods in Physics Research Section B: Beam Interactions with Materials and Atoms, 417 (2018) 96-99.

[8] M. Choat, G. Gloy, D.B. Gore, D.E. Jacob, Which elements are useful for understanding the composition of ancient papyrus inks?, Powder Diffraction, 32 (2017) S90-S94.

[9] M. Haddadi, M. Afsharpour, M. Azadi-Boyaghchi, M. Sadeghi, H. Javadian, Synthetic antioxidants as iron gall ink corrosion inhibitors in historical manuscripts, Journal of Cultural Heritage, 60 (2023) 12-21.

[10] G. Adami, A. Gorassini, E. Prenesti, M. Crosera, E. Baracchini, A. Giacomello, Micro-XRF and FT-IR/ATR analyses of an optically degraded ancient document of the Trieste (Italy) cadastral system (1893): A novel and surprising iron gall ink protective action, Microchemical Journal, 124 (2016) 96-103.

[11] S. Pessanha, M. Manso, M.L. Carvalho, Application of spectroscopic techniques to the study of illuminated manuscripts: A survey, Spectrochimica Acta Part B: Atomic Spectroscopy, 71-72 (2012) 54-61.

[12] B. Kanngießer, O. Hahn, M. Wilke, B. Nekat, W. Malzer, A. Erko, Investigation of oxidation and migration processes of inorganic compounds in ink-corroded manuscripts, Spectrochimica Acta Part B: Atomic Spectroscopy, 59 (2004) 1511-1516.

[13] V.S. Šelih, M. Strlič, J. Kolar, B. Pihlar, The role of transition metals in oxidative degradation of cellulose, Polymer Degradation and Stability, 92 (2007) 1476-1481.

[14] E. Fazio, C. Corsaro, D. Mallamace, Paper aging and degradation monitoring by the non-destructive two-dimensional micro-Raman mapping, Spectrochimica Acta Part A: Molecular and Biomolecular Spectroscopy, 228 (2020) 117660.

[15] D. Agha-Aligol, F. Khosravi, M. Lamehi-Rachti, A. Baghizadeh, P. Oliaiy, F. Shokouhi, Analysis of 18th–19th century's historical samples of Iranian ink and paper belonging to the Qajar dynasty, Applied Physics A, 89 (2007) 799.

[16] P. Oliaiy, D. Agha-Aligol, F. Shokouhi, M. Lamehi-Rachti, Analysis of Iranian postage stamps belonging to the Qajar dynasty (18th–20th century's) by micro-PIXE, X-Ray Spectrometry, 38 (2009) 479-486.

[17] F. Watt, The nuclear microprobe: a unique instrument, Nuclear Instruments and Methods in Physics Research Section B: Beam Interactions with Materials and Atoms, 130 (1997) 1-8.

[18] S.A.E. Johansson, J.L. Campbell, PIXE: a novel technique for elemental analysis, Wiley1988.

[19] M. Nastasi, J.W. Mayer, Y. Wang, Ion Beam Analysis: Fundamentals and Applications, Taylor & Francis2014.

[20] J.L. Russell, J.L. Campbell, N.I. Boyd, J.F. Dias, GUMAP: A GUPIXWIN-compatible code for extracting regional spectra from nuclear microbeam list mode files, Nuclear Instruments and Methods in Physics Research Section B: Beam Interactions with Materials and Atoms, (2017).

[21] K. Virro, E. Mellikov, O. Volobujeva, V. Sammelselg, J. Asari, L. Paama, J. Jürgens, I. Leito, Estimation of uncertainty in electron probe microanalysis: Iron determination in manuscripts, a case study, 2007.

[22] C. Remazeilles, V. Quillet, T. Calligaro, J. Claude Dran, L. Pichon, J. Salomon, PIXE elemental mapping on original manuscripts with an external microbeam. Application to manuscripts damaged by iron-gall ink corrosion, Nuclear Instruments and Methods in Physics Research Section B: Beam Interactions with Materials and Atoms, 181 (2001) 681-687.

[23] L. Burgio, Pigments, dyes and inks: their analysis on manuscripts, scrolls and papyri, Archaeological and Anthropological Sciences, 13 (2021) 194.

[24] V. Mathayan, M. Sortica, D. Primetzhofer, Determining the chronological sequence of inks deposited with different writing and printing tools using ion beam analysis, Journal of Forensic Sciences, 66 (2021) 1401-1409.

ICNST 2024 International Conference on Nuclear Science and Technology
6- 8 MAY 2024 | Isfahan, Iran

Determination of a Wave Function of the Pauli Equation with Deng-Fan Potential under Aharonov-Bohm Effect (Paper ID : 1106)

H.Nezampour[1,*], S. M. Motevalli[1], S. S. Hosseini[1]

[1] *Department of Nuclear Physics, Faculty of Science, University of Mazandaran, Babolsar, Iran*

Abstract

In this work, an analytical approximate solution of the Pauli equation with a Deng-Fan potential under the influence of the Aharonov-Bohm effect has been studied using the generalized Nikiforov-Uvarov (NU) parametric method. In this research, mathematical and physical methods are employed to calculate the wave function for different states of the system. After obtaining the wave functions, special energy values can be computed for regions where r>R and r<R by considering boundary conditions and continuity in the region r=R. This research employs the NU method, a versatile tool for solving second-order differential equations. The Pauli equation, crucial in describing fermions with spin ½, is explored within the context of the Deng-Fan potential and the Aharonov-Bohm effect. Originating from the non-relativistic limit of the Dirac equation, the Pauli equation has historical significance in quantum theory's development. This study addresses its application in two dimensions with the Deng-Fan potential and the Aharonov-Bohm effect, considering a constrained and non-zero magnetic field. Eigenenergy values and eigenfunctions are obtained using the NU method, revealing wave functions for different regions. Results illustrate the wave function's behavior, showcasing its decrease with increasing radial distance and increase with angular momentum. The Deng-Fan potential emerges as an intriguing option for theoretical physicists studying molecular systems. Qualitatively resembling the Morse potential, it proves compatible with quantum requirements and is suitable for investigating physical systems alongside Coulomb or linear potentials. The study contributes an approximate analytical solution for the Pauli equation's eigenwave functions, enhancing understanding of quantum systems under molecular potentials and advancing quantum physics knowledge.

Keywords: Pauli Equation, Deng-Fan Potential, Aharonov–Bohm effect, Wave function

Introduction

The wave equation used to describe fermions with spin ½ is called the Pauli equation. This equation represents a crucial domain in the field of physics, elucidating the non-relativistic characteristics of fermions and recognized as one of the intriguing concepts in this scientific discipline [1]. This is related to explaining experimental results [2]. The Pauli equation has been presented as a non-relativistic limit of the

Dirac equation [3, 4]. In 1927, Pauli introduced his spin matrices for the first time and addressed the modification of the non-relativistic Schrödinger equation. When Dirac introduced the relativistic free-wave equation, it not only provided a minimal equation for incorporating electromagnetic interactions but also revealed that his equation includes a term associated with interaction with a magnetic field – a Term manually added to the Pauli equation. Since then, it became apparent that the electron's angular momentum, as a relativistic phenomenon, should be considered, and the term related to spin-½ could be substituted into the relativistic Schrödinger equation. The Pauli equation is a fundamental equation in quantum mechanics that describes the behavior of particles with spin-½ in a magnetic field. The Deng-Fan potential is a model potential used to study wave properties. The Aharonov-Bohm effect is a quantum mechanical phenomenon describing the interaction between charged particles and a magnetic field. In this paper, we delve into the examination of analytical solutions of the Pauli equation under the influence of the Deng-Fan potential and the Aharonov-Bohm effect.

The NU (Nikiforov-Uvarov) method:

The generalized Nikiforov-Uvarov method has found applications in solving many second-order differential equations in various branches of physics. The equations are considered in the following form [5]:

$$\psi''(s)+\frac{\tilde{\tau}(s)}{\sigma(s)}\psi'(s)+\frac{\tilde{\sigma}(s)}{\sigma^2(s)}\psi(s)=0 \qquad (1)$$

In which σ(s) and σ˜(s) are polynomials, at most of the second degree, and τ˜(s) is a first-degree polynomial. The parametric form of this method is given as follows:

$$\{\frac{d^2}{ds^2}+\frac{\alpha_1-\alpha_2 s}{s(1-\alpha_3 s)}\frac{d}{ds}+ \frac{1}{[s(1-\alpha_3 s)]^2}[-\xi_1 s^2+\xi_2 s-\xi_3]\}\psi=0 \qquad (2)$$

In which αi and ξi, for i=1,2,3, are all parameters [5].

The Pauli equation with the Deng-Fan potential

The Pauli equation, also known as the Schrödinger-Pauli equation, was formulated by Wolfgang Pauli in 1927. In other words, this equation is a formulation of the Schrödinger equation for particles with spin-½, addressing the interaction of particle spins with the electromagnetic field. Additionally, this equation is essentially the non-relativistic limit of the Dirac equation and is applicable at speeds where relativistic effects can be neglected. Bohm was a theoretical physicist with innovative ideas in philosophy and quantum theory. He was recognized as one of the most important theoretical physicists of the 20th century. Bohm, along with Mr. Aharonov, discovered the "Aharonov-Bohm effect," demonstrating how a magnetic field with a non-zero vector potential could influence regions of space that are inaccessible To the magnetic field. The Aharonov-Bohm effect, named after David Bohm and Yakir Aharonov, illustrates how a magnetic field, despite having a non-zero vector potential, can exert an influence on regions of space that lack direct access to the field [6]. The Aharonov-Bohm effect is a quantum mechanical phenomenon. When a particle is prohibited from accessing a magnetic field directly, but its wave function is influenced by a magnetic flux confined to a solenoid, experimental confirmations have been conducted. In this work, we study the Pauli equation for a relativistic particle with spin-½ confined in two dimensions and under the influence of the Deng-Fan potential in the presence of the Coulomb problem, taking into consideration the Aharonov-Bohm effect [7]. The vector potential in the Coulomb gauge is considered as follows:

$$e\vec{A}=\begin{cases}-\dfrac{\rho}{r}\hat{u}_{\varphi} & r>R\\ 0 & r<R\end{cases} \qquad (3)$$

Where $\rho=-e\int_0^{\infty}H(r)rdr$ is the system flux, which is constrained and non-zero. The parameter H represents the magnetic field perpendicular to the x, y plane. Initially, we analyze the Aharonov-Bohm effect for the Pauli equation in the Coulomb gauge.

$$\left[\frac{1}{2M}[\vec{\sigma}\cdot\Pi]^2+V(r)-E_{n,l}\right]\Psi_{n,l}(\vec{r})0, \qquad (4)$$

Where p is the canonical momentum operator, and the wave function is considered to have two components as follows:

$$\Psi_{n,l}(\vec{r}) = \begin{pmatrix} \psi_{n,l}^{(1)}(r) \\ \psi_{n,l}^{(2)}(r) \end{pmatrix} e^{il\varphi} \tag{5}$$

In this work, we have studied the Deng-Fan potential [8].

$$V_{D-F}(r) = V_0 + \frac{V_1}{e^{\alpha r}-1} + \frac{V_2}{(e^{\alpha r}-1)^2} \tag{6}$$

Here r represents the radial distance, and α, V_0, V_1, and V_2 are constant coefficients. By substituting it into equation (5) and solving, we obtain the eigenenergy values and eigenfunctions using the NU method. For the regions where r>R, we have:

$$\begin{aligned} \phi_{n,l}^{(1)}(r>R) = & \left(\frac{1}{e^{\alpha r}-1}\right)^{-\sqrt{\xi}} \left(\frac{e^{\alpha r}}{e^{\alpha r}-1}\right)^{\sqrt{\zeta}} \\ & \left[\frac{(1+a)}{n!}\, {}_2F_1\left(-n, 1-a+n; 1+b; \frac{-1}{e^{\alpha r}-1}\right)\right. \\ & + \frac{(1+a)}{n!}\left(\frac{1}{e^{\alpha r}-1}\right)^{2\sqrt{\xi}} {}_2F_1(-n, 1-a+n; 1 \\ & \left. + b; \frac{-1}{e^{\alpha r}-1}\right)] \end{aligned} \tag{7}$$

And for the regions where r<R:

$$\begin{aligned} \phi_{n,l}^{(1)}(r<R) = & \left(\frac{1}{e^{\alpha r}-1}\right)^{\sqrt{\eta}} \left(\frac{e^{\alpha r}}{e^{\alpha r}-1}\right)^{-\sqrt{\mu}} \\ & \frac{(1+d)}{n!}\, {}_2F_1\left(-n, 1-c+n; 1+d; \frac{-1}{e^{\alpha r}-1}\right) \end{aligned} \tag{8}$$

Equations (7) and (8) represent the eigenwave functions in the region r>R and r<R. In addition, the coefficient of ${}_2F_1(a, b, c, \rho)$ are the usual hypergeometric series in Eqs. (7) and (8).

Results and discussion

As we know, the splitting of a spectral lines into several parts in the existence of a magnetic field (is so called the Zeeman effect) is significant in physics. It is interesting to study of the Deng-Fan potential in the

presence of a particular magnetic field, like the AB field effect, especially on the energy levels and eigenvalues.

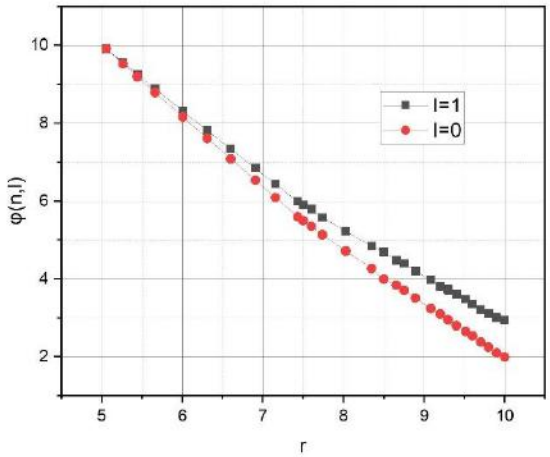

Fig1. Wave function for l=0 and l=1 in the region r>R.

The graph of wave function as a function of the variable r for the region r>R in Figure 1. In this diagram, at a stable r value, the graph of the wave function will increase with an increase in l.

In this paper, an approximate analytical solution of the Pauli equation in the presence of a Deng-Fan potential under the influence of the Aharonov-Bohm field has been considered using the generalized Nikiforov-Uvarov (NU) method. The results of calculations for the wave function in the region where r>R are shown in Fig1. As observed, the wave function decreases with increasing r and increases with increasing l at a constant r. Additionally, it is motivating to indication that the presentation of the AB field lifts the degeneracy of the energy levels.

Conclusions

The Deng-Fan potential provides an intriguing option for theoretical physicists, especially in the study of molecular systems. This potential qualitatively resembles the Morse potential and is compatible with quantum requirements. It can be a suitable choice for investigating physical systems alongside Coulomb or linear potentials, taking into account the effects of Aharonov-Bohm fields. In this research, we have explored an approximate analytical solution for the eigenwave functions of the Pauli equation with the Deng-Fan potential in the presence of the Aharonov-Bohm effect using the Nikiforov-Uvarov (NU) method. This can contribute to a deeper understanding of the behavior of quantum systems under the influence of molecular potentials and advance the field of quantum physics effectively.

References

[۱] Greiner, W. and W. Greiner, *Spin*. (2001): Springer.

[۲] Hodge, W., S. Migirditch, and W.C. Kerr, *Electron spin and probability current density in quantum mechanics.* American Journal of Physics, (2014). 82(7): p. 681-690.

[۳] Haouam, I. and L. Chetouani, *The Foldy-Wouthuysen transformation of the Dirac equation in noncommutative Phase-Space.* Journal of Modern Physics, (2018). 9(11): p. (2021).

[۴] Sakurai, J.J., *Advanced quantum mechanics*. (1967): Pearson Education India.

[5] Berkdemir, C., *Application of the Nikiforov-Uvarov method in quantum mechanics.* Theoretical Concepts of Quantum Mechanics, (2012). 225.

[6] Ehrenberg, W. and R.E. Siday, *The refractive index in electron optics and the principles of dynamics.* Proceedings of the Physical Society. Section B, (1949). 62(1): p. 8.

[7] Deng, Z. and Y. Fan, *A potential function of diatomic molecules.* Shandong Univ. J, (1957). 7: p. 162.

[8] Hassanabadi, H., et al., *Deng-Fan potential for relativistic spinless particles—an Ansatz solution.* Communications in Theoretical Physics, (2012). 57(3): p. 339.

ICNST 2024
International Conference on Nuclear Science and Technology
6- 8 MAY 2024 | Isfahan, Iran

Study of various decay half-lives for 290-293Lv super heavy isotopes (Paper ID : 1115)

Aghakouchacki Z.[1*], Pahlavani M. R.[1]

[1]Department of Physics, faculty of Basic Science, University of Mazandaran, Babolsar, IRAN
[*] Corresponding author E-Mail: aghakuchakizahra2266@gmail.com

Abstract

Various decay half-lives of different isotopes of Livermorium super heavy nucleus are studied. α-decay half-lives of under consideration isotopes are obtained using semi-empirical formula produced by Royer [J. Phys. G: Nucl. Part., 26, 1149(2000)]. Cluster decay half-lives of these isotopes for decay of ^{9}Be, $^{10-11}$B, ^{12}C, ^{16}O, ^{19}F, $^{20-22}$Ne, ^{23}Na, $^{24-26}$Mg, ^{27}Al, $^{28-30}$Si, ^{31}P, $^{32-34}$S, ^{35}Cl, $^{36-40}$Ar, $^{39-41}$K and $^{40-48}$Ca clusters are predicted using a phenomenological relation constructed by Manjunatha [Mod. Phys. Lett. A, 35(6), 2050016(2020)] based on tunneling of cluster through decay barrier. Also spontaneous fission half-lives of these isotopes are calculated based on semi-empirical relation constructed by Santhosh et al. [Nucl. Phys. A, 832, 220 (2010)], following Gamow penetration probability through fission barrier. Calculated half-lives are compared with each other as well as available experimental data. Satisfactory agreement is achieved between predicted and measured data. This type of study has been done to predict possible decay modes of super heavy isotopes which helps experimental scientists to arrange their experiments.

Keywords: α-decay, cluster decay, spontaneous fission, half-life, semi-empirical-formula, super heavy isotopes.

1. INTRODUCTION

Most super heavy isotopes synthesized artificiality in excited state and decay through spontaneous fission in competition with α and cluster radioactivity. The superiority decay mode closely related to neutron number of decay products. Furthermore, for super heavy isotopes with higher atomic number (Z), α-decay is one of the prominent emission channel beside spontaneous fission. Cluster radioactivity is a rare decay mode of super heavy isotopes compared with α-decay and spontaneous fission. Cluster decay is an emission type located between α-decay and spontaneous fission which is emission of particles heavier than α and lighter than the lightest fission fragment with considerable occurrence probability (A ~ 70). Today, elements with $Z \geq 104$ are known as super heavy elements. Recently, by development of nuclear microscopic theories and manufacturing of new generations of accelerators and detectors, the prediction of

the stability island located in the super heavy region have made the study of super heavy element both theoretically and experimentally one of the hot and popular fields of nuclear physics.

α-decay was discovered in 1899 just before determining a part of an atom as a nucleus after a series of experiments conducted by Sir Ernest Rutherford to investigate the properties of this particle. The quantum tunneling theory of α-decay was first developed and quantitatively explained in 1928 independently by George Gamow, Edward Condon, and Ronald Wilfred Gurney. While classical mechanics forbid the escaping of α-particles with kinetic energy less than the Coulomb barrier, quantum mechanics allow that to happen. According to quantum mechanics, microscopic particles, including α-particles, have a small, nonzero probability of tunneling through a finitely high potential barrier, even if it doesn't have enough kinetic energy to do so as required by classical mechanics. It is assumed that the α-particles are formed in a quasi-bound state before decay, i.e., two neutrons and two protons from the highest energy levels combine to form an α-particle inside the nucleus. Its formation lowers energy inside the parent nucleus because of the higher stability of α-particles. Cluster radioactivity has been predicted for first time in 1980 by Sandulescu, Poenaru, and Greiner [1]. Rose and Jones [2] arranged an experiment for observing ^{14}C emitted from ^{223}Ra, which identified the realistic existence of this novel type of radioactivity in 1984. Wei and his co-authors, Poenaru et al. and Sandulescu used sophisticated experimental setup to measure the heavier clusters such as ^{20}O, ^{24}Ne, ^{28}Mg, ^{32}F and ^{34}Si emitted from isotopes located at Transe-lead rigion [3,4]. Although the Gamow's quantum tunneling effect was initially introduced to explain α-decay, it was successfully applied to obtain the cluster decay probability. Theoretical methods for calculating cluster decay half-life classified into two groups, α like and fission like. The preformed α like models suppose that the emitted cluster is previously shaped in the parent nucleus with a certain formation probability, that determined by the overlapping region of both the parent and the daughter nucleus wave functions before it could penetrate the barrier produced between α-particle and daughter nucleus with its available energy. While the fission like models assume that the parent nucleus undergoes continuous deformation until overcoming the confining interaction barrier to release the cluster. According to α like assumptions, Santhosh and his research group [5] used the Coulomb and proximity potential model (CPPM) to evaluate the α and cluster-decay half-lives of $^{248-254}$Cf isotopes. In addition to these microscopic approaches, numerous semi-empirical formulas with some adjustable parameters have also been proposed to obtain the α and cluster-decay half-lives. In spontaneous fission an unstable heavy or super heavy isotope divided into two fragments with roughly comparable masses accompanied by neutrons and γ-rays. However, in low

excitation energies, asymmetric fission (fragments with different masses) is more likely than symmetric fission (fragments with approximately the same masses) and neutron emission has a very low probability so that it can be ignored. The energy produced in spontaneous fission is equal to the difference in the mass of the parent and fission fragments in unit of energy and appears as the kinetic energy of fragments. Generally, fission may take place spontaneously [6,7] or induced by neutrons [8,9], protons and α-particles [10,11], heavy charged particles (fusion-fission reaction) [12,13] and energetic electromagnetic radiations [14,15]. Also, the conversion of a heavy or super heavy isotopes into three fragments (ternary fission) is a rare process with low probability compared with binary fission (one in a few Hundreds binary fission) [16,17]. A set of theoretical methods used to predict α-decay, cluster radioactivity and spontaneous fission half-lives by considering a mixed potential combined nuclear, Coulomb and centrifugal terms. Barrier penetration probability is calculated based on Wentzel-Kramer-Briluwin (WKB) approximation [18]. Some phenomenological methods have been constructed based on some observed facts and physical laws to estimate spontaneous fission half-life. The adjustable parameters of these formula have been obtained through fitting with available experimental data in the desired region.

This paper continued as follows: The theoretical approach to calculate α-decay, cluster radioactivity and spontaneous fission half-lives are discussed in section 2. In section 3, the theoretical results are analyzed and compared with the available experimental data. The paper is concluded in section 4.

2. THEORETICAL FRAMEWORKS

One of the most important decay modes of heavy and super heavy excited isotopes is α-decay that is occurred in competition with cluster decay and spontaneous fission of heavy and super heavy isotopes. There are many theoretical methods to calculate decay half-life which are classified into two categories. Direct calculation of α-decay, cluster radioactivity and spontaneous fission half-lives have been done based on quantum mechanical tunneling of decaying particles through barrier using WKB approximation. In these approaches by supposing pre-production of particles inside the parent nucleus, selection of a proper mean-field potentials (usually consist of nuclear and Coulomb potentials and centrifugal term), the probability of tunneling is calculated by WKB approximation. Then by considering other realities, the decay constant and decay half-life can be predicted. In other groups, by considering efficient quantities, a phenomenological formula with some adjustable parameters are constructed. Usually, these undetermined coefficients are obtained through list square fitting with the experimental data observed in the region near to understudy

region. There are numerous semi-empirical formulas constructed by different scientists considering different efficient quantities with various adjustable parameters to obtain α-decay, cluster radioactivity and spontaneous fission half-lives. In this paper we attempt to study different decay modes of $^{290-293}_{116}Lv$ (Livermorium) super heavy isotopes. For achieving this goal, we aim to discuss these decay modes separately.

2.1. α-DECAY HALF-LIFE

There are many semi-empirical-formula in order for calculating α-decay half-life [19,20]. One of these formula has been constructed by Royer based on Geiger-Nuttall experimental low. Geiger and Nuttall showed that the logarithmic α-decay half-life related to speed of emitted α-particles inversely. Considering conservation principle of energy and linear momentum, the kinetic energy of α-particle is almost equal to energy released in α-decay. The Q-value of α-decay for a parent nucleus with mass m_p, daughter nucleus produced after α-decay with mass number m_d is obtained using,

$$Q_\alpha(Z.N) = m_p(Z.N) - m_d(Z-2.A-2) - m_\alpha(2.2)\,. \quad (1)$$

Where, $m_\alpha(2.2)$ is mass of emitted α-particle and all masses measured in unit of energy [21]. Based on conservation lows of energy and momentum, following relation obtained for kinetic energy of α-particle,

$$K_\alpha = \left(\frac{A-4}{A}\right) Q_\alpha \qquad and \qquad v_\alpha \propto \frac{1}{\sqrt{Q_\alpha}} \quad (2)$$

Royer [22] constructed following semi-empirical formula for calculating α-decay half-life,

$$\log T_{\frac{1}{2}}(s) = a + bA^{\frac{1}{6}}Z^{\frac{1}{2}} + \frac{cZ}{\sqrt{Q_\alpha}} \quad (3)$$

where, $A.Z\ and\ N$ are in order mass, atomic and neutron numbers of parent nucleus. Three adjustable coefficients are obtained equal to $a = -66.44.\ b = -0.048\ and\ c = 1.8852.$ The α-decay halters $a.b\ and\ c$ are obtained by list square fitting with experimental data in super heavy region. Half-lives of $^{290-293}_{116}Lv$ super heavy isotopes are predicted using this semi-empirical relation.

2.2. CLUSTER RADIOACTIVITY HALF-LIFE

As indicated in section 1, emission of particles heavier than α and lighter than the lightest fission fragment is classified as cluster radioactivity. The emission probability of heaviest cluster related to mass number of parent nucleus. This means that by increasing mass number of parent nucleus, the probability of emission for heavy cluster is increase. Different clusters with various half-lives can be considered for emission from super heavy isotopes. In this research, we have been calculated the half-lives of ^{9}Be, $^{10\text{-}11}$B, ^{12}C, ^{16}O, ^{19}F, $^{20\text{-}22}$Ne, ^{23}Na, $^{24\text{-}26}$Mg, ^{27}Al, $^{28\text{-}30}$Si, ^{31}P, $^{32\text{-}34}$S, ^{35}Cl, $^{36\text{-}40}$Ar, $^{39\text{-}41}$K and $^{40\text{-}48}$Ca clusters supposed to emitted from isotopes of Livermorium super heavy nucleus. There are a few semi-empirical-formula with different undetermined coefficients for calculating cluster radioactivity half-life [19,20]. Among different semi-empirical formula for calculating cluster-decay half-life, following complicated phenomenological formula that has been produced by Manjunathan et al. [20] is used to predict cluster radioactivity half-lives,

$$\log T_{\frac{1}{2}} = \left\{\left(Z_c A_c^{-\frac{1}{3}}\right)^2 \sum_{i=0}^{2} Z^i A_{2i} + \left(Z_c A_c^{-\frac{1}{3}}\right)^1 \sum_{i=0}^{2} Z^i A_{1i} + \sum_{i=0}^{2} Z^i A_{0i}\right\} \frac{Z_d}{2\sqrt{Q_c}}$$

$$+ \left\{\left(Z_c A_c^{-\frac{1}{3}}\right)^2 \sum_{i=0}^{2} 0.53 Z^i B_{2i} + \left(Z_c A_c^{-\frac{1}{3}}\right) \sum_{i=0}^{2} 0.53 Z^i B_{1i} + \sum_{i=0}^{2} Z^i A_{0i}\right\} \qquad (4)$$

In the above equations, 18 adjustable coefficients $A_{2i}.A_{1i}.A_{0i}.B_{2i}.B_{1i}$ and B_{0i} are determined using fitting with the experimental data. Also, A_c and Z_c are in order the mass and the atomic numbers of emitted cluster, Z_d and Z are the atomic number of daughter and parent nucleus, respectively and Q_c is the energy released in cluster radioactivity. The fitting parameters are presented in Table 1 [20].

Table 1. Adjustable parameters of semi-empirical formula

i	A_{2i}	A_{1i}	A_{0i}	B_{2i}	B_{1i}	B_{0i}
0	-5.8946	61.40271	-79.2567	110.7946	-862.417	1037.946
1	0.135994	-1.11765	1.4145	-1.9446	14.48453	-180.0448
2	-6.19E-04	4.43E-03	-6.17E-03	8.41E--03	-6.28E-02	7.73E-02

This formula produces logarithmic half-lives for α and cluster decay from parent super heavy nuclei in the super heavy region. This complicated formula is used to calculate logarithmic cluster decay half-lives of 9Be, 10-11B, 12C, 16O, 19F, 20-22Ne, 23Na, 24-26Mg, 27Al, 28-30Si, 31P, 32-34S, 35Cl, 36-40Ar, 39-41K and 40-48Ca clusters emitted from $^{290-293}_{116}Lv$ super heavy isotopes.

2.3. SPONTANEOUS FISSION HALF-LIFE

Spontaneous fission reaction is a process that usually happened in heavy and super heavy isotopes in competition with particle-decay. Because of its complicity, the analytical calculation of its half-life is need sophisticated knowledge about nuclear force and various conjugate fragments produced in fission. On the other hand, some semi-empirical formulas were constructed to evaluate spontaneous fission half-life. It is well known today that the fissionability parameter ($\frac{Z^2}{A}$) and relative neutron excess ($I = \frac{N-Z}{N+Z}$) are two effective parameter in calculating spontaneous fission half-life. Santhosh and his co-authors constructed a semi-empirical formula for logarithmic half-life of spontaneous fission based on these quantities as a power series of them. This formula contains five adjustable parameters that can be obtained by least square fitting with measured data in the super heavy region. This semi-empirical relation is defined as follows [20]:

$$log_{10}(yr) = a\frac{Z^2}{A} + b\left(\frac{Z^2}{A}\right)^2 + c\left(\frac{N-Z}{N+Z}\right) + d\left(\frac{N-Z}{N+Z}\right)^2 + e\,. \quad (5)$$

Where, five undetermined coefficients are $a = -43.25203$, $b = 0.49192$, $c = 3674.3927$, $d = -9360.6$ and $e = 580.75058$. These constants are obtained by least square fitting with the available experimental data in the super heavy region. Also, the logarithmic half-life is calculated in unit of year and A and Z are in order the mass and atomic numbers of fissioning isotope.

3. Results and discussion

Calculated α-decay half-lives of four of Livermorium super heavy isotopes are compared with the available experimental data and also with the spontaneous fission half-lives in Table 2. As it is clear from this table, the calculated α-decay half-lives correspond with experimental data. Moreover, except for $^{293}_{116}Lv$ for other three isotopes the spontaneous fission half-lives are more than the α-decay half-lives, this means the α-decay is dominant decay mode for these isotopes.

Calculated logarithmic cluster decay half-lives for emission of ^{9}Be, $^{10\text{-}11}$B, ^{12}C, ^{16}O, ^{19}F, $^{20\text{-}22}$Ne, ^{23}Na, $^{24\text{-}26}$Mg, ^{27}Al, $^{28\text{-}30}$Si, ^{31}P, $^{32\text{-}34}$S, ^{35}Cl, $^{36\text{-}40}$Ar, $^{39\text{-}41}$K and $^{40\text{-}48}$Ca clusters from $^{290-293}_{116}Lv$ super heavy isotopes are indicated in table 3. As it is clear from this table, the half-lives for emission of various isotopes of each cluster from super heavy isotopes, by increasing the mass number of clusters is increased. Also, for producing of a closed shell magic or near magic daughter nuclei, the cluster decay half-life is induced

because the corresponding cluster decay Q-value is increased which is lower the efficient potential barrier high. This fact highlight the role played by shell effects.

The logarithm of α-decay half-lives for $^{290-293}_{116}Lv$ super heavy isotopes are plotted as a function of $\frac{1}{\sqrt{Q}}$. The linear behavior of this plot shows good adherence to the semi-empirical Geiger-Total law.

Table2. Q-values, calculated & experimental half-lives and spontaneous fission half-lives for $^{290-293}_{116}Lv$**.**

Parent nuclei	Q_α(MeV)	Alpha decay half-lives (s) (Experimental)	Alpha decay half-lives (s) (Calculated)	Spontaneous fission Half-lives (s) (Calculated)
$^{290}_{116}Lv$	10.995	0.015	0.01523	7.830987
$^{291}_{116}Lv$	10.885	0.063	0.03269	1.972769
$^{292}_{116}Lv$	10.785	0.018	0.06612	0.392052
$^{293}_{116}Lv$	10.675	0.053	0.14513	0.049473

Table 3. Q-values and calculated cluster radioactivity half-lives of different clusters emitted from $^{290-293}_{116}Lv$ super heavy isotopes

Parent nuclei	Cluster	Daughter nuclei	Q_c(KeV)	$\left(\text{Log}_{T_{\frac{1}{2}}}(s)\right)$(Calcuted)
$^{290}_{116}Lv$	^{9}Be	$^{281}_{112}Cn$	15731.45	8.58425
	^{10}B	$^{280}_{111}Rg$	19089.38	19.54288
	^{11}B	$^{279}_{111}Rg$	24642.29	7.95047
	^{12}C	$^{278}_{110}Ds$	38780	7.02398
	^{16}O	$^{274}_{108}Hs$	56357	12.28512
	^{19}F	$^{271}_{107}Bh$	60657.44	15.85095
	^{20}Ne	$^{270}_{106}Sg$	70641.93	19.88586
	^{21}Ne	$^{269}_{106}Sg$	71071.78	17.29032
	^{22}Ne	$^{268}_{106}Sg$	76254.71	11.98843

	^{23}Na	$^{267}_{105}Db$	80549.83	19.37313
	^{24}Mg	$^{266}_{104}Rf$	88823.57	24.29251
	^{25}Mg	$^{265}_{104}Rf$	89532.78	21.67699
	^{26}Mg	$^{264}_{104}Rf$	95164.54	16.44845
	^{27}Al	$^{263}_{103}Lr$	98556.86	23.82308
	^{28}Si	$^{262}_{102}No$	106422.79	28.56739
	^{29}Si	$^{261}_{102}No$	108465.08	25.31492
	^{30}Si	$^{260}_{102}No$	113852.96	20.50865
	^{31}P	$^{259}_{101}Md$	115910.54	28.05970
	^{32}S	$^{258}_{100}Fm$	120615.53	34.19351
	^{33}S	$^{257}_{100}Fm$	123025.85	30.79774
	^{34}S	$^{256}_{100}Fm$	129476.69	25.49029
	^{35}Cl	$^{255}_{99}Es$	129954.53	33.44302
	^{36}Ar	$^{254}_{98}Cf$	133920.54	39.53740
	^{38}Ar	$^{252}_{98}Cf$	143710.23	30.42843
	^{40}Ar	$^{250}_{98}Cf$	148899.6	24.66571
	^{39}K	$^{251}_{97}Bk$	143609.19	38.24156
	^{41}K	$^{249}_{97}Bk$	150743.24	30.99246
	^{40}Ca	$^{250}_{96}Cm$	146886.40	44.25097
	^{42}Ca	$^{248}_{96}Cm$	156184.59	35.48991
	^{43}Ca	$^{247}_{96}Cm$	157905.87	32.96916
	^{44}Ca	$^{246}_{96}Cm$	163881.8	28.53691
	^{46}Ca	$^{244}_{96}Cm$	169717.8	23.11982
	^{48}Ca	$^{242}_{96}Cm$	174451.16	18.64536
$^{291}_{116}Lv$	^{9}Be	$^{282}_{112}Cn$	17061.55	6.41192
	^{10}B	$^{281}_{111}Rg$	19859.38	18.11826
	^{11}B	$^{280}_{111}Rg$	24682.22	7.90214
	^{12}C	$^{279}_{110}Ds$	38220	7.50463
	^{16}O	$^{275}_{108}Hs$	55487	12.92427
	^{19}F	$^{272}_{107}Bh$	59937.44	16.38623

	^{20}Ne	$^{271}_{106}Sg$	69661.93	20.58535
	^{21}Ne	$^{270}_{106}Sg$	71541.78	16.97463
	^{22}Ne	$^{269}_{106}Sg$	75574.71	12.39018
	^{23}Na	$^{268}_{105}Db$	79709.85	19.91502
	^{24}Mg	$^{267}_{104}Rf$	87733.57	24.99992
	^{25}Mg	$^{266}_{104}Rf$	90292.78	21.21111
	^{26}Mg	$^{265}_{104}Rf$	94764.54	16.66787
	^{27}Al	$^{264}_{103}Lr$	98056.86	24.12240
	^{28}Si	$^{263}_{102}No$	105602.79	29.06510
	^{29}Si	$^{262}_{102}No$	109035.08	24.99035
	^{30}Si	$^{261}_{102}No$	113212.96	20.84173
	^{31}P	$^{260}_{101}Md$	115130.54	28.50470
	^{32}S	$^{259}_{100}Fm$	119555.53	34.82955
	^{33}S	$^{258}_{100}Fm$	123395.85	30.58896
	^{34}S	$^{257}_{100}Fm$	128581.69	25.95134
	^{35}Cl	$^{256}_{99}Es$	129063.53	33.94837
	^{36}Ar	$^{255}_{98}Cf$	132661.54	40.28883
	^{38}Ar	$^{253}_{98}Cf$	142652.83	30.97351
	^{40}Ar	$^{251}_{98}Cf$	148144.9	25.02062
	^{39}K	$^{252}_{97}Bk$	142507.19	38.86327
	^{41}K	$^{250}_{97}Bk$	149847.54	31.44499
	^{40}Ca	$^{251}_{96}Cm$	145438.40	45.11039
	^{42}Ca	$^{249}_{96}Cm$	155036.59	36.08834
	^{43}Ca	$^{248}_{96}Cm$	158256.17	32.79375
	^{44}Ca	$^{247}_{96}Cm$	163175.7	28.86716
	^{46}Ca	$^{245}_{96}Cm$	169375.1	23.26668
	^{48}Ca	$^{243}_{96}Cm$	174282.96	18.71235
$^{292}_{116}Lv$	^{9}Be	$^{283}_{112}Cn$	15441.55	9.09429
	^{10}B	$^{282}_{111}Rg$	18339.38	21.01560
	^{11}B	$^{281}_{111}Rg$	24132.29	8.57948
	^{12}C	$^{280}_{110}Ds$	37810	7.86322

	^{16}O	$^{276}_{108}Hs$	54677	13.53305
	^{19}F	$^{273}_{107}Bh$	58937.44	17.14589
	^{20}Ne	$^{272}_{106}Sg$	68651.93	21.32186
	^{21}Ne	$^{271}_{106}Sg$	69241.78	18.55029
	^{22}Ne	$^{270}_{106}Sg$	74724.71	12.90021
	^{23}Na	$^{269}_{105}Db$	78509.85	20.70428
	^{24}Mg	$^{268}_{104}Rf$	86583.57	25.76103
	^{25}Mg	$^{267}_{104}Rf$	87882.78	22.70892
	^{26}Mg	$^{266}_{104}Rf$	94204.54	16.97733
	^{27}Al	$^{265}_{103}Lr$	97096.86	24.70366
	^{28}Si	$^{264}_{102}No$	104612.79	29.67374
	^{29}Si	$^{263}_{102}No$	106895.08	26.22201
	^{30}Si	$^{262}_{102}No$	112462.96	21.23561
	^{31}P	$^{261}_{101}Md$	113990.54	29.16351
	^{32}S	$^{260}_{100}Fm$	118375.53	35.54744
	^{33}S	$^{259}_{100}Fm$	121015.85	31.94897
	^{34}S	$^{258}_{100}Fm$	127631.69	26.44626
	^{35}Cl	$^{257}_{99}Es$	127743.53	34.70712
	^{36}Ar	$^{256}_{98}Cf$	131321.54	40.10064
	^{38}Ar	$^{254}_{98}Cf$	141503.83	31.57304
	^{40}Ar	$^{252}_{98}Cf$	147135.3	25.49954
	^{39}K	$^{253}_{97}Bk$	141007.19	39.72103
	^{41}K	$^{251}_{97}Bk$	148461.54	32.15316
	^{40}Ca	$^{252}_{96}Cm$	143916.40	46.02750
	^{42}Ca	$^{250}_{96}Cm$	153687.29	36.80066
	^{43}Ca	$^{249}_{96}Cm$	155788.17	34.04173
	^{44}Ca	$^{248}_{96}Cm$	162206	29.32466
	^{46}Ca	$^{246}_{96}Cm$	168652.7	23.57818
	^{48}Ca	$^{244}_{96}Cm$	173903.06	18.86432
$^{293}_{116}Lv$	^{9}Be	$^{284}_{112}Cn$	16801.55	6.81606

^{10}B	$^{283}_{111}Rg$	19139.38	19.44748
^{11}B	$^{282}_{111}Rg$	24162.29	8.54190
^{12}C	$^{281}_{110}Ds$	37300	8.31754
^{16}O	$^{277}_{108}Hs$	53927	14.10895
^{19}F	$^{274}_{107}Bh$	58297.44	17.64232
^{20}Ne	$^{273}_{106}Sg$	67691.93	22.03717
^{21}Ne	$^{272}_{106}Sg$	69781.78	18.17324
^{22}Ne	$^{271}_{106}Sg$	73974.71	13.35743
^{23}Na	$^{270}_{105}Db$	77699.85	21.24726
^{25}Mg	$^{268}_{104}Rf$	88282.78	22.45610
^{26}Mg	$^{267}_{104}Rf$	93344.54	17.45802
^{27}Al	$^{266}_{103}Lr$	96106.86	25.31212
^{29}Si	$^{264}_{102}No$	107455.08	25.89619
^{30}Si	$^{263}_{102}No$	111872.96	21.54849
^{31}P	$^{262}_{101}Md$	113340.54	29.54342
^{33}S	$^{260}_{100}Fm$	121385.85	31.73496
^{34}S	$^{259}_{100}Fm$	126801.69	26.88348
^{35}Cl	$^{258}_{99}Es$	126883.53	35.20777
^{38}Ar	$^{255}_{98}Cf$	140474.83	32.11596
^{40}Ar	$^{253}_{98}Cf$	146307.99	25.89545
^{39}K	$^{254}_{97}Bk$	139987.19	40.31210
^{41}K	$^{252}_{97}Bk$	147589.54	32.60378
^{42}Ca	$^{251}_{96}Cm$	152469.29	37.45142
^{43}Ca	$^{250}_{96}Cm$	155988.87	33.93932
^{44}Ca	$^{249}_{96}Cm$	161288	29.76137
^{46}Ca	$^{247}_{96}Cm$	168176.6	23.78467
^{48}Ca	$^{245}_{96}Cm$	173790.36	18.90949

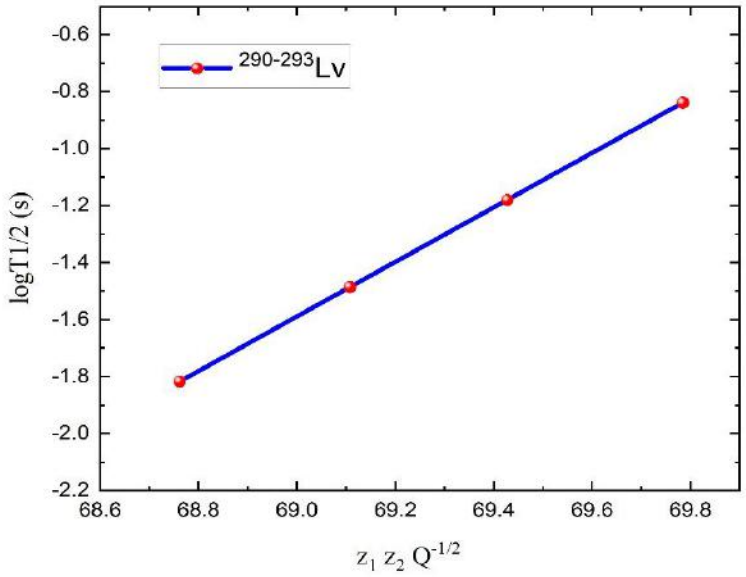

Fig. 1. Geiger-Nuttall plot of logarithmic α-decay half-lives as a function of $\frac{1}{\sqrt{Q}}$

Conclusions

In this research, we studied the stability of four super heavy isotopes of Livermorium nucleus by calculating the half-life of their α-decay, spontaneous fission and cluster decay. The results show that the probability of α emission from these isotopes is more likely than other decays. Also, the role of closed shell in the stability of isotopes is well evident. This type of research helps scientists to detect and discover these isotopes by identifying the dominant mode, so that they know what type of decay they should consider before conducting experiments. Also, calculating the half-life of α-decay and comparing it with measured data shows the accuracy of calculations. Following the Geiger-Nuttall law is well shown by the linear behavior of the logarithm of the half-life of α-decay in terms of the square root of the energy of α particles as indicated in Figure 1.

References

1. Sandulescu, A., Poenaru, D. N. and Greiner, W. (1980). Soviet Journal of Particles and Nuclei. 11:528.

2. Rose, H. J. and Jones, G. A. (1984). A new kind of natural radioactivity. Nature, 307: 245-247.

3. Sandulescu, A. (1989). A new radioactivity. Journal of physics G: Nuclear and particle, 15:529-554.

4. Poenaru, D. N. and Greiner, W. (1991). Rare decay modes by cluster emission from nuclei. Journal of physics G: Nuclear and particle, 17: S443-S451.

5. Santhosh, K. P. and Biju, R. K. (2013). Stability of $^{248-254}_{98}Cf$ isotopes against alpha and cluster radioactivity. Annal of physics, 334: 280-287.

6. Pahlavani, M. R. and Karimi Gazafroodi, H. (2022). Isotopic yields and spontaneous fission half-lives of $^{279}_{110}Ds$ and $^{281}_{110}Ds$ superheavy isotopes. International journal of modern physics E, 31(12):2250103-1-2250103-12.

7. Pahlavani, M. R. and Joharifard, M. (2019). Isotopic yield and spontaneous fission half-life of spontaneous fission for $^{284}_{112}Cn$ and $^{284}_{114}Fl$ super heavy isotopes using direct method and semiempirical formula. Physical review C, 99: 044601-1-044601-12.

8. Pahlavani, M. R. and Mirfathi, S. M. (2015). Dynamics of neutron-induced fission of $^{235}_{92}U$ using four-dimensional Longevin equations. Physical review C, 92: 024622-1-024622-5.

9. Pahlavani, M. R. and Mirfathi, S. M. (2016). Dynamical simulation of neutron-induced fission of Uranium isotopes using four-dimensional Langevin equations. Physical review C, 93: 044617-1-044617-8.

10. Pahlavani, M. R. and Gazmeh, M. (2022). Simulation of fragments mass distribution of $^{237}_{93}Np$, $^{241-243}_{95}Am$ and $^{239-242-244}_{94}Pu$ isotopes in proton-induced fission. International journal of modern physics E, 31(01): 2250008-.

11. Rathan, S. S., Ramaswami, R. J. and Prakash, Satya (1991). Alpha particle induced fission of $^{209}_{83}Bi$ at 55.7 and 58.6 MeV. Radiochimical acta, 55: 169-172.

12. Pahlavani, M. R., Naderi, D. and Mirfathi, S. M. (2011). Dynamical simulation of fission fragments kinetic energy in heavy-ion fusion-fission reaction. Modern physics letter A, 26(13): 975-985.

13. Mirfathi, S. M. and Pahlavani, M. R. (2008). Dynamical simultaion of energy dissipation in asymmetric heavy-ion induced fission of $^{200}_{82}Pb$, $^{213}_{87}Fr$ and $^{251}_{99}Es$. Physical review C, 78: 064612-1-64612-5.

14. Pahlavani, M. R. and Mehdipour, P. (2018). Product yields for the photo fission of $^{232}_{90}Th$, $^{234-238}_{92}U$, $^{237}_{93}Np$ and $^{239-240-242}_{94}Pu$ actinides at various photon energies. Nuclear science and technology, 29: 146-1-146-8.

15. Pahlavani, M. R. and Mehdipour, P. (2018). Study of photo fission fragments mass distribution of $^{232}_{90}Th$, $^{238}_{92}U$, $^{237}_{93}Np$ and $^{240}_{94}Pu$ isotopes in various γ-ray energies. International journal of modern physics E, 27(03): 180018-1-180018-13.

16. Pahlavani, M. R., Ghodsi, O. N. and Zadehrafi, M. (2017). ${}^{4}_{2}He$, ${}^{10}_{5}Be$, ${}^{14}_{6}C$ and ${}^{16}_{8}O$ light fragments acompanied cold ternary fission of the ${}^{250}_{96}Cm$ isotope in an equaterial three-cluster model. Physical review C, 96: 054612-1-54612-8.

17. Pahlavani, M. R. and Zadehrafi, M. (2018). ${}^{4}_{2}He$, ${}^{10}_{5}Be$, and ${}^{34}_{12}Mg$ accompanied ternary fission of the ${}^{242}_{94}Pu$ isotope in the touching equitorial configuration. European physical journal A, 54: 128-1-128-8.

18. Miller, S. C. and Good, R. H. (1953). A WKB-type approximation to the Schrodinger equation. Physical review, 91(01): 174-179.

19. Manjunatha, H. C. and Sridhar, K. N. (2017). New semi-empirical formula for α-decay half-lives of the heavy and super heavy nuclei. The european physical journal A, 53: 156-1-156-9.

20. Manjunata, H. C., Sowmya, N. and Nagaraja, M. (2020). Semi-empirical formula for alpha and cluster decay half-lives of super heavy nuclei. Modern physics letter A, 35(06): 2050016-1-2050016-8.

21. Audi, G., Wapstra, A. H. and Thiboult, C. (2003). The Ame2003 atomic mass evaluation: (II). Tables graphs and References. Nuclear physics A, 729(01): 337-676.

22. Wang, Y. Z., Wang, S. J., Hou, Z.y. and Gu, J. Z. (2015). Systematic study of α-decay energies and half-lives of super heavy nuclei. Physical review C, 92: 064301-1-064301-9.

ICNST 2024 International Conference on Nuclear Science and Technology
6- 8 MAY 2024 | Isfahan, Iran

Study of level density and thermodynamic quantities for 256 98 and 290 114 axially symmetric deformed heavy and superheavy isotopes using the back sifted Fermi gas model (Paper ID : 1116)

Khooy A.[1*] Pahlavani M. R.[1]

[1] Department of Nuclear Physics, Faculty of Basic Science, University of Mazandaran, Iran

* Corresponding author E-mail: asghar.khooy@gmail.com

Abstract

The level density and the thermodynamic quantities for $^{256}_{98}Cf$ heavy, and $^{290}_{114}Fl$ super heavy isotopes have been calculated using an improved version of the back sifted Fermi gas model including the temperature dependent level density parameter, the pairing energy, and the shell effects. The single-particle level density parameter for $^{256}_{98}Cf$ heavy and $^{290}_{114}Fl$ super heavy isotopes have been calculated using a semi-classical method, taking into account the Woods-Saxon potential for the interaction of nucleons inside the nucleus based on the single-particle Fermi gas model. A power series up to third degree are considered for energy as a function of temperature instead of square of temperature in the simple back shifted Fermi gas model. The calculated level density parameters are used to obtain the level density and the thermodynamic quantities of these isotopes such as the entropy, the temperature, and the heat capacity. The obtained results for these isotopes as a function of excitation energies were compared. The variation of the heat capacity as a function of the excitation energy shows the breaking of the first nucleon pair, which occurs at energies $E = 2.948\ MeV$ and $E = 3.04\ MeV$ for $^{256}_{98}Cf$ heavy and $^{290}_{114}Fl$ super heavy isotopes, respectively.

Keywords: Level density, back shifted Fermi gas model, temperature, entropy, heat capacity, excitation energy.

Introduction

The first theoretical attempts to explain the nuclear level density was performed by Bethe in 1936 [1]. In analogy with the classical thermodynamic, he defined that the thermodynamic quantities of nuclei like the temperature, the entropy, the heat capacity are closely related to the nuclear level density. Bethe arranged some experiments to investigate the dependence of nuclear reaction rate on the nuclear level density [2]. The measured nuclear level density has been collected in the energy region close to the nuclear ground level or Fermi energy [3] using the neutron resonance spacing data [4]. A new method to extract level density and γ-ray strength function from primary γ-ray spectra has been reported by Oslo experimental

group [5]. One of the most important applications of nuclear level density is the calculations of nuclear reaction cross sections based on the Hauser-Feshbach method [6]. This method is applied especially for calculation of interaction cross-section associated to the stellar evolution like the supernovae, neutron stars and destruction of compact binary stars [7].

Different methods such as the Fermi gas model(FGM) [8], the back-shifted Fermi gas model (BFGM) [9, 10], the constant temperature (CT) model [11, 12], the shell model Monte Carlo approach (SMMC) [13, 14], the Bardeen Cooper Schrieffer (BCS) model [15, 16], the static path plus random phase approximation (SPA+RPA) algorithm [17, 18], and the generalized super fluid model (GSM) [19–22] have been developed to calculate the nuclear level density parameter. Among these models, the BFGM is commonly used for direct evaluation of the nuclear level density. This method contains two adjustable parameters including the back shift energy, E1, and the single-particle level density parameter a. The single-particle level density can also be obtained through the semi-classical method [23–25] using a proper nuclear mean field potential [26, 27]. Therefore, the BFGM can be parameterized only with one parameter, E1. Then the level density is calculated using the basic relation of the single-particle level density parameter, as a function of the single particle level density at the Fermi energy. Finally, the thermal quantities of nuclei such as the entropy, the nuclear temperature and the heat capacity are predicted using the nuclear level density.

One of the most important applications of nuclear physics is the nuclear energy generation which is performed using the fission and the fusion reactions. These reactions require accurate knowledge of nuclear reaction rates that is related sensitively on the thermal properties of nuclei. Also, simulations of astrophysical processes and formation of neutron-reach isotopes that are happened in distant galaxies and stars require theoretical information about thermodynamic behavior of nuclear reaction, because some of such reactions were not occurred in the earth. Efforts to produce highly neutron-rich super-heavy isotopes using rare-isotope accelerator facilities are directly related to theoretical knowledge about decay of these highly excited isotopes which is related to their level densities and thermodynamic quantities. Also, the breaking of the first nucleon pair can be seen by plotting the nuclear heat capacity versus excitation energy. The macroscopic GSM [28] is constructed based on behavior of a super fluid at low energy which shows the nuclear phase transition or the pair breaking well.

The atomic nucleus is a complex many-body quantum mechanical system. A complete description of the nuclear structure requires solution of the Schrodinger equation with a suitable mean field potential in order

to obtain the nuclear wave functions and their corresponding energy levels. Although the strong nuclear interaction is not known well, we still need nuclear models that describe the fundamental properties of the nucleus. The mean field shell model [29] and its extended versions for deformed nuclei and models based on the many-body theory [30] are two important groups for extracting single-particle energy levels and wave functions of nucleons inside the nucleus, and studying the collective behaviors of nuclei. For light nuclei that are small enough, by solving the Schrodinger differential equation with suitable boundary condition, its energy levels and corresponding wave functions can be determined. But for heavy nuclei with high mass number, it is not possible to solve the resultant differential equation. Therefore, the statistical microscopic methods combined with the spectral explanation and the numerical approximations are required to extract the level density.

In order to avoid the complexity of the nuclear level density problem, based on the FG model, some assumptions were used that are not compatible with reality. In other words, effects such as coupling, pairing, shell effect, etc., were not taken into account, while considering these effects are necessary to accurately determine the nuclear level density. Nevertheless, to account for these interactions, the interacting fermions model with the BCS potential for pairing effect or the semi-empirical relations of the BFGM is used. The models that deal with the pairing energy require its temperature dependence.

To validate the results obtained from the calculations of the level density for these nuclei, the experimental data of the Oslo group is used. However, due to the lack of experimental level density, for $^{256}_{98}\mathbf{Cf}$ heavy and $^{290}_{114}\mathbf{Fl}$ superheavy isotopes, the back shifted energy parameter as the only adaptable parameter of the level density relationship is determined.

THEORETICAL METHOD

The nuclear level density in the fundamental BFGM model is expressed as follows [31].

$$\rho_{BFGM}(U) = \frac{1}{12\sqrt{2}\sigma} \times \frac{Exp(2\sqrt{(aU)}}{a^{\frac{1}{4}}U^{\frac{5}{4}}} \quad . \tag{1}$$

With

$$U = E(T) - \Delta(T) - E_{shell}(T) - E_1 \tag{2}$$

where $a, \sigma, U,\ E(T), E_1, \Delta(T)$, and $E_{shel}(T)$ are the level density parameter, the spin cutoff parameter, the effective excitation energy, the excitation energy, the energy back shift parameter, the nuclear pairing energy, and the shell effects, respectively. The spin cutoff parameter can be calculated using the following equation [32]:

$$\sigma^2 = 0.0146A^{\frac{5}{3}} \frac{1 + \sqrt{1 + 4a(U)}}{2a} \quad (3)$$

The temperature dependent shell effects can be calculated using the following equation [33].

$$E_{shell} = M_{Exp} - M_{LDM} \quad (4)$$

Where M_{Exp} is the measured nuclear mass and M_{LDM} is the calculated nuclear mass in the liquid drop model (LDM). The pairing energy is obtained as follows [33]:

$$\Delta_0 = \begin{cases} \Delta_{0n} + \Delta_{0p} & for\ Z\ and\ N\ even \\ \Delta_{0p} & for\ Z\ even\ and\ N\ odd \\ \Delta_{0n} & for\ N\ even\ and\ Z\ odd \\ 0 & for\ Z\ and\ N\ odd \end{cases} . \quad (5)$$

Where Δ_{0n}, Δ_{0p}, and Δ_0 are the neutron single-particle pairing energy in the Fermi energy, the proton single-particle pairing energy and total single-particle pairing energy, respectively. These quantities are defined as follows:

$$\Delta_{0n} = \frac{r}{N^{\frac{1}{3}}} Exp\left[-s\left(\frac{N-Z}{A}\right) - t\left(\frac{N-Z}{A}\right)^2\right]$$

$$\Delta_{0p} = \frac{r}{Z^{\frac{1}{3}}} Exp\left[s\left(\frac{N-Z}{A}\right) - t\left(\frac{N-Z}{A}\right)^2\right], \quad (6)$$

Where $N, Z,$ and A are in order the neutron number, the atomic number and the mass number of the nucleus and

$$\Delta(0) = \Delta_{0n} + \Delta_{0p}$$

The temperature-dependent pairing energy, Δ (T) has a relationship with its value in the Fermi energy, Δ (0) as follows [34]

$$\Delta(T) = \frac{\Delta(0)}{1 + e^{\left(\frac{T}{0.3} - \frac{7.37}{0.03\sqrt{A}}\right)}} \quad (7)$$

The relation between the nuclear excitation energy and the nuclear temperature can be obtained by considering the temperature dependent pairing energy and shell effect as follows:

$$\frac{1}{T} = \left(\sqrt{\frac{a}{U}} - \frac{3}{4U}\right)\left[1 - \left(\frac{d\Delta(T)}{dT} + \frac{dE_{shell}(T)}{dT}\right)\right]\frac{dT}{dE} \quad . \quad (8)$$

Then by considering a polynomial set up to power 3 between nuclear energy and temperature [31]

$$E(T) = a_0 + a_1 T + a_2 T^2 + a_3 T^3 \quad (9)$$

The coefficients a_0, a_1, a_2, and a_3 are obtained by substituting E(T) from equation (9) into equation (8) in each small interval of temperature. Then, using these coefficients, nuclear energy becomes a function of temperature. The level density parameter in the Fermi energy is obtained using the following relation,

$$\tilde{a} = \frac{\pi^2}{6} g \quad (10)$$

Where g is the single-particle level density that is equal to sum of level densities for neutrons and protons. The single- particle level density parameter in the Fermi energy, g can be obtain using the semi-classical method or through fitting with the experimental data. The following semi-classical formula is used to calculate the single-particle level density [33]

$$g = \frac{2}{\pi}\left(\frac{2m}{\hbar^2}\right)^{\frac{3}{2}} \int dr r^2 \sqrt{\varepsilon - V(r)}\ \theta(\varepsilon - V(r)). \quad (11)$$

Where m and ε are mass and the single-particle energy levels of neutrons and protons, respectively. θ(X) is the well-known step function. V(r) is the effective mean field potential of nucleons inside the nucleus that is equal to the nuclear potential between neutrons and protons and the Coulomb potentials between protons. Here, Woods-Saxon potential ($V_{WS}(r)$) is considered for interaction of nucleons inside the nucleus. This potential for the axially symmetric deformed nuclei is defined as follows:

$$V_{WS}(r,\theta) = \frac{-V_0}{1 + e^{\frac{(r - R(\theta))}{d}}} \quad (12)$$

WhereV_0, d, and R(θ) are respectively the dept of potential, the diffuseness parameter, and the radius of deformed nucleus. The dept of nuclear potential is obtained using the following semi-empirical formula [35]

$$V_0 = 49.6\left[1 \pm 0.86\left(\frac{N-Z}{A}\right)\right], \quad (13)$$

Where + (−) sign is used for protons (neutrons). The diffuseness parameter is a constant varied in the region [0.5, 1], which can be evaluated using the following semi-empirical relation [36],

$$d = 0.5 + 0.33\left(\frac{N-Z}{A}\right). \quad (14)$$

$R(\theta)$ is defined by the following semi-classical relation

$$R(\theta) = 1.17 + (1 + \beta_2 Y_{20})R_h \quad (15)$$

with

$$R_h = \left[1 + 0.39\left(\frac{N-Z}{A}\right)\right]A^{\frac{1}{3}}.$$

Where β_2 and Y_{20} are respectively the quadrupole deformation parameter of nucleus and the special function related to the quadrupole deformation. The attractive Coulomb potential between protons inside the axially symmetric deformed nucleus is defined as follows:

$$V_C(r,\theta) = \frac{1}{4\pi\varepsilon_0}\frac{Ze^2}{r}\left[1 + \frac{3R^2(\theta)}{5r^2}\beta_2 Y_{20}\right]. \quad (16)$$

The temperature dependent level density parameter, $a(U)$ is defined as follows [37]:

$$a(U) = \tilde{a}\left[1 + \frac{1 - Exp(-\gamma U)}{U}E_{shell}(T)\right], \quad (17)$$

with $\gamma = \frac{0.35}{A^{\frac{1}{3}}} MeV^{-1}$.

The level density parameter is obtained in a given excitation energy. Then by substitution in equation (1), the level density, $\rho(U)$ is obtained. The entropy of nucleus is related to the level density by the following relation,

$$S = K_B \, Ln \, \frac{\rho}{\rho_0}, \tag{18}$$

Where K_B is the Boltzman constant and ρ_0 is the normalization constant that can be evaluated using the third law of thermodynamics. The nuclear temperature has a relationship with its entropy as follows:

$$T = \left(\frac{\partial S}{\partial E}\right)^{-1} \tag{19}$$

and finally, the heat capacity can be calculated using the following formula

$$C_V = \left(\frac{\partial T}{\partial E}\right)^{-1} \tag{20}$$

The necessary optimal quantities used to calculate the level density parameters are listed in Table1.

Table 1. The optimal values obtained for the parameters in the back shifted Fermi gas model (BFGM)

Isotope	ã	Δ_0	E_{shell}	β_2	E_1
$^{256}_{98}$Cf	24.644	1.474	0.882	0.240	0.346
$^{290}_{114}$Fl	29.88	1.52	-0.0611	-0.011	1.355

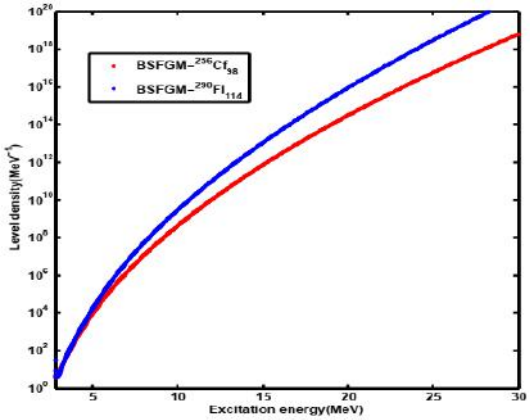

Fig. 1. The level density of the axially symmetric deformed $^{256}_{98}Cf$ heavy and $^{290}_{114}Fl$ super heavy isotopes using the BFGM with the temperature-dependent level density parameter, the temperature-dependent pairing energy and the temperature-dependent shell effect as a function of the excitation energy are compared together.

In Figure 1, the variation of the level density of the axially symmetric deformed $^{256}_{98}$Cf heavy and $^{290}_{114}$Fl super heavy isotopes have been calculated using the BFGM with the temperature-dependent level density

parameter, the temperature-dependent pairing energy and the temperature-dependent shell effect in terms of excitation energy are compared to each other. It can be seen that the level density of the heavy isotope $^{256}_{98}$Cf is higher than the $^{290}_{114}$Fl superheavy isotope. According to this figure, one can see the variation protocol of level density are same for two isotopes. Also, the difference between them is smaller in lower excitation energies.

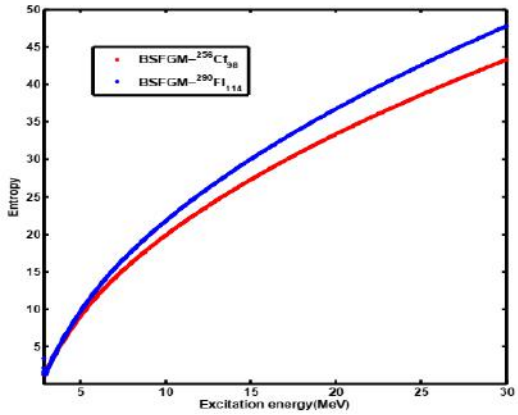

Fig. 2. The calculated entropy of the axially symmetric deformed $^{256}_{98}$Cf heavy and $^{290}_{114}$Fl super heavy isotopes in the BFGM with the temperature-dependent level density parameter, the pairing energy, and the shell effect as a function of the excitation energy are compared.

In Figure 2, the variation of the entropy for $^{256}_{98}Cf$ heavy and $^{290}_{114}Fl$ super heavy isotopes calculated based on the BFGM with the temperature-dependent level density parameter, the pairing energy and the shell effect modifications in terms of excitation energy are compared to each other. It can be seen that the entropy of the $^{256}_{98}Cf$ heavy isotope is much higher than the $^{290}_{114}Fl$ superheavy isotope, whoever in lower energies the difference is reduced. This figure shows the same procedure of variation for both isotopes.

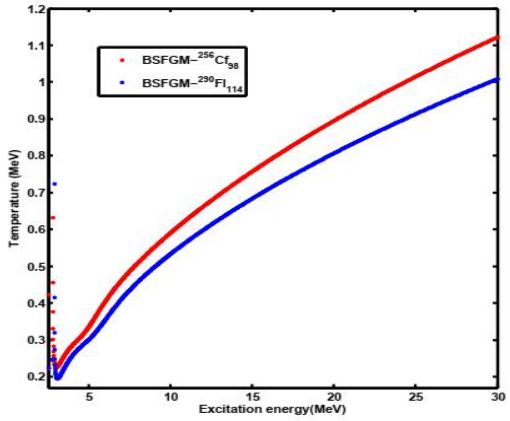

Fig. 3. The calculated temperature of the $^{256}_{98}$Cf heavy and the $^{290}_{114}$Fl superheavy isotopes using the BFGM with the temperature-dependent level density parameter, the pairing energy and the shell effect as a function of the excitation energy are compared.

In Figure 3, the variation of the entropy of $^{256}_{98}Cf$heavy and $^{290}_{114}Fl$ super heavy isotopes that have been calculated based on the BFGM with the temperature-dependent level density parameter, the pairing energy and the shell effect in terms of the excitation energy are compared to each other. It can be seen that the temperature of the $^{256}_{98}Cf$ heavy isotope $^{290}_{114}Fl$ is higher than the $^{290}_{114}Fl$ superheavy isotope while the variation procedure for both isotopes is same.

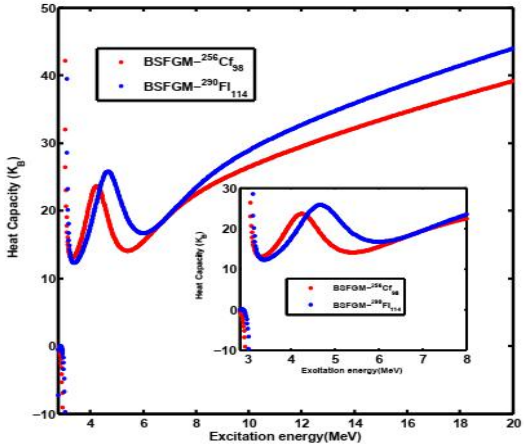

Fig. 4. The calculated heat capacity of the $^{256}_{98}Cf$ heavy and the $^{290}_{114}Fl$ superheavy isotopes using the BFGM with the temperature-dependent level density parameter, the pairing energy and the shell effect as a function of the excitation energy are compared.

In Figure 4, variation of the heat capacity of the $^{256}_{98}Cf$heavy and the $^{290}_{114}Fl$ superheavy isotopes have been calculated using the BFGM with the temperature-dependent level density parameter, the pairing energy and the shell effect in terms of the excitation energy are compared to each other. It can be seen that the Heat capacity of the super heavy isotope $^{290}_{114}Fl$ is higher than the heavy isotope $^{256}_{98}Cf$, however their protocol of variation are same. According to this figure, there is an inconsistency in the diagram for both isotopes in the lower energies which is show the breaking of the first nucleons pair for $^{256}_{98}Cf$ heavy and $^{290}_{114}Fl$ isotopes, that are observed at E=2.948 MeV and E=3.04 MeV, respectively. Also, the first pair breaking is occurred at $E = 2\Delta_0$, which is conformed the validity of the theoretical model.

Conclusions

In this research, the level density and the thermodynamic quantities of the $^{256}_{98}Cf$ heavy and the $^{290}_{114}Fl$ superheavy isotopes have been calculated using the BFGM with the temperature-dependent level density parameter, the pairing energy and the shell effect modifications. The results of calculations are presented and compared in figures 1 to 4 for the level density, the entropy, the temperature, and the heat capacity of $^{256}_{98}Cf$ heavy and $^{290}_{114}Fl$ superheavy isotopes, respectively. Due to the lack of the experimental data, the

comparison with observed data is not possible. According to the heat capacity diagram, the breaking of first nucleons pair are observed at $E = 2\Delta_0$ which is consistent with the theoretical concepts of the method and confirmed its validity. These types of calculation help scientist especially for synthesized of the unmeasured super heavy isotopes.

References

1. Bethe, H. A. (1936). an attempt to calculate the number of energy levels of a heavy nucleus, phys. 50(4):332.
2. Bethe, H. A. (1937). nuclear physics, B. nuclear dynamics, theoretical, Rev. Mod. Phys, 9(2):69.
3. Firestone, R. B. and Shirly, V. S. (1996). Table of isotopes, 8th edition, Vol. Π, New York, John Wiley and sons.
4. Iljinov, A. S. Mebel, M. V. Bianchi, N. et al. (1992). phenomenological statistical analysis of level densities, decay width and lifetimes of excited nuclei, Nucl. Phys. A, 543(3):517-57.
5. Schiller, A. B. Bergholt, L. Guttormsen, M. et al. (2000). extraction of level density and γ strength function from primary γ spectra, Nucl. Inst. Meth. Phys. Res. A, 447(3):498-511
6. Hauser, W. and Feshbach, H. (1952). the inelastic scattering of neutrons, Phys. Rev, 87 (2): 366--373.
7. Raucher, K. L. Thieleman, F. K. and Kratz, K. L. (1997). nuclear level density and the determination of thermonuclear rates for astrophysics, Phys. Rev. C, 56:1613-1625
8. Bohr, A. and Mottelson, B. R. (1998). nuclear structure, World Scientific, Vol. 1.
9. Egidy, T. V. and Burner, D. (2005). systematics of nuclear level density parameters, Phys. Rev. C, 72(4): 04431.
10. Koning, A. G. Helaire, D. and Goriely, S. (2008). global and local level density models, Nuc. Phys. A, 810(1-4):13–76.
11. Gilbert, A. and Cameron, A. G. W. (1965). a composite nuclear-level density formula with shell cprrection, Can. J. Phys, 43(8):1446-1496
12. Zelevinsky, V. Karanpagia, S. Berlaga, A. (2018). constant temperature model for nuclear level density, Phys. Lett. B, 783: 428-433
13. Koonin, S. E. Dean, D. J. and Langanke, K. (1997). shell model Monte Carlo methods, Phys. Rep, 278(1):1-77

14. Alhassid, Y. Bertsch, G. F. and Fang, L. (2003). nuclear level statistics: Extending shell model theory to higher temperature, Phys Rev. C, 68(4):044322.
15. Moretto, L. G. (1972). statistical description of a paired nucleus with the inclusion of angular momentum, Nucl. Phys. A, 185(1):145-165
16. Karegar, Z. and Dehghani, V. (2013). statistical pairing fluctuation and phase transition in $^{94}_{42}$Mo, J. Phys. G: Nucl. Parti. Phys. 40(4): 045108.
17. Rossignall, R., Canosa, N. and Ring, P. (1998). thermal and quantal fluctuations for fixed particle number in finite superfluid system, Phys. Rev. Letts, 80(9):1853-1856
18. Kaniko, K. and Hasegawa, M. (2005). quenching gap at finite temperature in $^{184}_{74}$W, Phys, Rev. C, 72(2):4307.
19. Nikjou, A. and Sadeghi, M. (2018). overview and evaluation of different level density modes for the $^{123}_{53}$I radionuclide production, App. Radi. Isot., 136: 45-58
20. Soltani,M. and Jafari, S. (2014). generalized superfluid model in calculating the nuclear level density parameters, J. Radi. Nucl. Tech., 1(1): 17-23
21. Ignatyuk, A. V. Istekov, K. K. and Smirenkin, G. N. (1979). role of the collective effects in a systematic of nuclear level density, Yadernaya Fizika, 29(4):875-883
22. Shlomo, S. (1992). energy level density of nuclei, Nucl. Phys. A, 539(1):17-36.
23. Dehghani, V. and Alavi, S. A. (2016). nuclear level density of even-even nuclei with temperature dependent pairing energy, Eur. Phys. J. A, 52(10):306.
24. Bhagawat, A. Vinas, X. Centelles, M. Schuck, P. and Wyss, R. (2010). microscopic- approach for binding energies with the Wigner-Kirwood method, Phys. Rev. C, 81(4):4321.
25. Pahlavani, M. R. Alavi, S. A. and Farhadi, F. (2014). nuclear level density of heavy nuclei $Z \geq 90$ through semiclassical method, Mod. Phys. Lett. A, 29(3):1450017.
26. Handloser, G. and Stocker, W. (1985). mean field description of nuclear level densities, Nucl. Phys. A, 441(3):491-500
27. Shlomo, S. Kolomietz, V. M. and Dejbaksh, H. (1997). single particle level density in a finite depth potential well, Phys. Rev. C, 55(4):1972-1981.
28. Zhang, Y. Bjeicic, A. et al. (2022). many-body approach to superfluid nuclei in axial symmetry, Phys. Rev. C, 105(4):4326.
29. Pan, F. Xiaoxue, D. Launey, K. D. et al. (2016). an exactly solvable spherical mean-field plus extended monopole pairing model, Nucl. Phys. A, 947: 234-247.

30. Pahlavani, M. R. and Alavi, S. A. (2012). solution of Woods-Saxon potential with spin-orbit and centrifugal terms through Nikiforo-Uvarov method, Comm. Theo. Phys., 58(5):739 -743
31. Pahlavani, M. R. and Masoumi dinan, M. (2019). thermal properties of $^{172}_{70}$Yb and $^{162}_{66}$Dy isotopes in the back shifted Fermi gas model with temperature-dependent pairing energy, Pramana, 93(3).
32. Bucurescu, D. and Egidy, T. V. (2005). systematics of nuclear level density parameter, J. Phys. G: Nucl. Parti. Phys, 31(10):S1675- S1680.
33. Madland, D. G. and Nix, J. R. (1988). new model of the average neutron and proton pairing gaps, Nucl. Phys. A, 476(1):1-38
34. Ivanyuk, F. A. Ishizuka, C. Usang, M. D. and Chiba, S. (2018). temperature dependence of shell corrections, Phys. Rev. C, 97(5):4331.
35. Patyyk, Z. and Sobiczewski, A. (1991). ground-state properties of the heaviest nuclei analyzed in a multidimensional deformation space, Nucl. Phys. A, 533(1):132-152.
36. Suhanen, J. (2007). from nucleon to nucleus, Springer- verlag.
37. Hilaire, S. (2004). Energy dependence of the level density parameter, Phys. Lett. B, 583(3-4):264-268

ICNST 2024
International Conference on Nuclear Science and Technology
6- 8 MAY 2024 | Isfahan, Iran

Insights into Two-Proton Emitters Half-Life: The Influence of Nuclear Shape and Potential Barriers (Paper ID : 1163)

Yazdankish, Enayatolah[3]

Applied Chemistry Department, Faculty of Gas and Petroleum, Yasouj University, Gachsaran, Iran

Abstract

The precise determination of the half-life of two-proton emitters (2P-emitters) is crucial for understanding nuclear stability, ensuring safety in nuclear applications, optimizing medical treatments, and investigating astrophysical phenomena. This study calculated the half-life of 2P-emitters in certain nuclei using the proximity potential. Furthermore, the Wentzel-Kramers-Brillouin approximation was utilized to assess the penetration probability through the potential barrier, which includes nuclear, Coulomb, and centrifugal potentials. The findings demonstrate that the penetration probability and, therefore, the half-life of 2P-emitters, are influenced by the shape of the total potential. Two semi-empirical half-life calculations - Gamow's relation and Hatsukawa's- were presented and compared with the obtained results to validate the results. Additionally, laboratory results for the relevant nuclei were incorporated for comparison. The data from this study exhibit a closer fit with experimental results than the semi-empirical relationships. Moreover, the methodology employed here suggests that alpha decay and two-proton decay share a common explanation. A table of 2P-emitters half-lives for various nuclei is presented, indicating stronger agreement with experimental data than semi-empirical values.

Keywords: two-proton emitter nuclei, diproton, proximity potential, the half-life of two-proton emitter nuclei, semi-empirical half-life calculations.

Introduction

Enhancing the precision of decay half-life calculations for nuclei carries significant implications. It facilitates a deeper comprehension of nuclear stability and the behavior of matter at atomic and subatomic scales. Moreover, it plays a pivotal role in ensuring the safety of nuclear technology and mitigating the risk of radioactive contamination. Furthermore, an accurate understanding of the decay half-life of nuclei is indispensable for determining optimal dosage and formulating strategic approaches to medical interventions reliant upon particle-emitting radionuclides [1-5].

[3] mailto:enayat.yazdankish@gmail.com

While alpha and beta decay are the predominant decay modes exhibited by various unstable nuclei, it is noteworthy that other decay modes also contribute to the overall decay process. Specifically, emissions such as Deuteron, Carbon, and Oxygen from certain unstable nuclei play a role in the decay phenomenon. Of particular interest are proton and neutron decay, as they are fundamental particles constituting the nuclei. Notably, although a nucleus containing two protons is inherently unstable, certain nuclei exhibit simultaneous two-proton decay. The theoretical discussion of two-proton decay dates back to the early sixties with Goldansky's work [6], and this decay mode is now well-documented in light proton-rich nuclei. Mechanistically, the process can be visualized as depicted in Figure 1, wherein the simultaneous emission of two protons can be attributed to the subsequent splitting of a ^{2}He (diproton) particle or as a genuine three-body decay. Furthermore, the decay of two successive one-proton emissions represents an entirely distinct mechanism [7-9].

Branching ratio estimates made using the R-matrix approximation have indicated that diproton (^{2}He) emission, corresponding to decay via protons correlated in a ^{1}S state, might dominate [10-13].

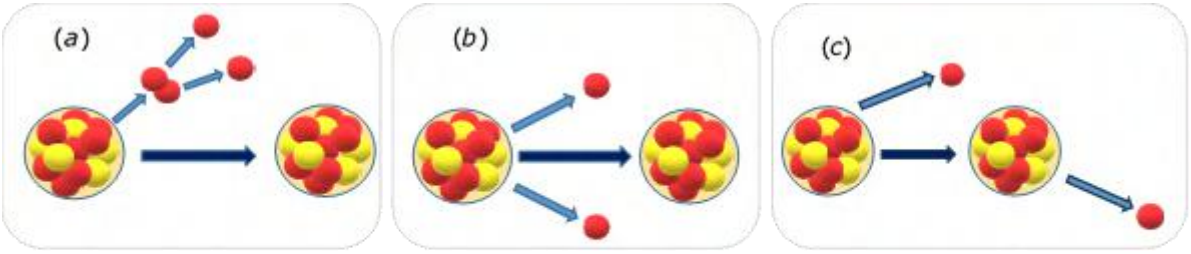

Figure 1: (a) Two- proton or diproton emmision, (b) A genuine three-body decay, and (c), The decay of two successive one-proton emissions.

Since the introduction of the phenomenological proximity potential by Blocki et al. in 1977, researchers have extensively developed, modified, and generalized this potential to elucidate the fusion process of nuclei, as well as the Alpha and other cluster decay of nuclei [14, 15]. This practical potential consists of two components; one is contingent upon the geometry of colliding nuclei, the radius of nuclei, surface energy [16], and surface width or thickness, while the other component is a universal function dependent upon the surface distance of the colliding nuclei. Various modifications have been employed over time to adapt this potential and its coefficients for the model's generalization [17, 18]. However, many proximity potentials exist, wherein some modifications are not substantial. In this study, the total potential of nuclei, encompassing nuclear, Coulomb, and centrifugal potentials, is considered to calculate the half-life of two-proton emitter nuclei. The Wentzel-Kramers-Brillouin (WKB) approximation is employed for this purpose

[19]. The proximity potential is selected as the nuclear potential, allowing for the consideration of the effect of nuclear shape. Subsequently, the fundamental theoretical framework is presented in section 2. Section 3 is devoted to the results and discussion, and finally, the conclusion is provided in section 4.

Theory

Proximity Potential and WKB Approximation

The calculation of the half-life of unstable nuclei is a crucial area of study as it contributes to our comprehension of the behavior of matter at the subatomic level and ensures the safety of nuclear technology, among other factors. This includes deriving the half-life of cluster decay of nuclei, encompassing alpha, proton, diproton, carbon, oxygen, and other cluster decays. The half-lives of nuclei can be derived as [20, 21]:

$$T_{1/2} = \frac{\ln 2}{\lambda} = \frac{\ln 2}{\upsilon P_{2p}} \tag{1}$$

where, λ is the decay constant, and υ is assault frequency which can be obtained as:

$$\upsilon = \frac{1}{2R_p}\sqrt{\frac{2E_K}{M_{2p}}} \tag{2}$$

where, $E_K = Q\left[1 - \left(M_{2p}/M_p\right)\right]$ wherein Q is the total energy released in the decay reaction, M_{2p} is the mass of diproton or two-proton, and M_p and R_p are the mass and the radius of the parent nuclei, respectively [22]. P_{2p}, the penetration probability of the diproton through the potential barrier, is given based on the Wentzel-Kramers-Brillouin (WKB) as:

$$P_{2p} = exp\left(-\frac{2}{\hbar}\int_{R_{in}}^{R_{out}} dr\sqrt{2\mu(V_T(r) - Q)}\right) \tag{3}$$

where, r is the distance from the center of the nucleus, μ is the reduced mass of the diproton and daughter nuclei, and by considering M_{2p} and M_d as diproton and daughter nuclei mass, respectively, then:

$$\mu = \frac{M_{2p}M_d}{M_{2p} + M_d} \tag{4}$$

The $R_{in}(r)$ and $R_{out}(r)$ are the inner and outer points of potential that recoil the particle and are given by solving the equation: $V_T(r) - Q = 0$. The total potential V_T is given as:

$$V_T = V_N + V_C + V_L \quad (5)$$

where, V_N, V_C, and V_L are nuclear, coulomb, and centrifugal potential, respectively, and are given as follows.

The centrifugal potential:

$$V_L = \hbar^2 \frac{l(l+1)}{2\mu r^2} \quad (6)$$

where, l is the angular momentum and as said before μ is the reduced mass of two-proton and daughter nuclei.

The coulomb potential:

$$V_C(r) = \frac{Z_{2p} Z_d}{r} e^2 \begin{cases} \frac{1}{r} & r > R_C \\ \frac{1}{2R_C}\left[3 - \left(\frac{r}{R_C}\right)^2\right] & r \le R_C \end{cases} \quad (7)$$

In this context, Z_{2p} and Z_d denote the atomic numbers of the diproton and daughter nuclei, respectively. The proton charge is represented by *e*, and the distance between the centers of the daughter nucleus and the diproton is illustrated by *r*. Additionally, the total charge radii of the diproton and daughter nucleus are denoted as $R_C = R_d + R_{2p}$wherein

$$R_i = 1.28A_i^{1/3} - 0.76 + 0.8A_i^{-1/3} \quad (8)$$

where, R_i and A_i stands for the radius and mass number of diproton or daughter nuclei.

a. The nuclear potential:

$$V_N(s) = 4\pi\gamma b\left[\frac{C_{2p}C_d}{C_{2p}+C_d}\right]\phi(s/b) \quad (9)$$

where, the potential is made of two parts, one which is dependent on nuclear shape only is $4\pi\gamma b\left[C_{2p}C_d/(C_{2p}+C_d)\right]$, and the other is a universal function, $\phi(s/b)$. In this regard, γ is the surface tension coefficient; *b* is the penetration width of the nuclear surface and is almost equal to unity $(b \approx 1fm)$; C_i are called Sassman central radii, which depend on the radius of the diproton or the daughter nucleus and are expressed based on relations (8) and (10); $\phi(s/b)$ is the universal function of the proximity potential, and s is the distance between the surface of the diproton and the surface of the daughter nucleus.

$$\gamma = 0.9517\left[1-1.7826\left(N-Z\right)^2/A^2\right] MeV/\,fm^2 \quad (9)$$

$$C_i = R_i - \left(b/R_i\right), \quad (10)$$

In these relationships; N, Z, and A are the neutron, proton, and mass number, respectively, and R_i expressed based on equation (8) for diproton or daughter nuclei. The universal function $\phi\left(\xi = s/b\right)$, is expressed by the following relation:

$$\phi\left(\xi\right) = \begin{cases} -1.7817 + 0.9270\xi + 0.143\xi^2 - 0.09\xi^3 & \xi \le 0.0 \\ -1.7817 + 0.927\xi + 0.01696\xi^2 - 0.05148\xi^3 & 0.0 \le \xi \le 1.9475 \\ -4.41\exp\left(-\xi/0.7176\right) & \xi \ge 1.9475 \end{cases} \quad (11)$$

Semi-experimental Relation

Gamow-like model

Similar to alpha decay, diproton emission from the nucleus is understood as a tunneling phenomenon, and the probability of tunneling from the potential barrier is described by equation (3). In this context, the nuclear potential is a spherical well with radius R_{in}. Outside the spherical well, the nuclear potential is zero, so the potential barrier is the sum of the Coulomb and centrifugal potentials, and the spherical potential affects the potential barrier only through R_{in}. By considering the probability of penetration in the barrier, the decay half-life can be determined using equation (1). The radius of the potential well is expressed by the following relationship.

$$R_{in} = r_0(A_{2p}^{1/3} + A_d^{1/3}) \quad (12)$$

In this relationship, A_{2p} and A_d are the atomic number of the diproton and the daughter nucleus, and $r_0 = 1.224\,fm$ is a constant value.

Hatsukawa model

The Hatsukawa relation was presented to express the half-life of alpha decay. Then this relationship was expanded to calculate the half-life of diproton emission. Based on this [23, 24]:

$$\log_{10} T_{1/2} = 0.2746 Z_{2p} Z_d \left[\frac{A_{2p} A_d}{AQ}\right]^{1/2} \left[\arccos\sqrt{X} - \sqrt{X(1-X)}\right] - 20.446 \quad (13)$$

here, $X = r_0 (A_{2p}^{1/3} + A_d^{1/3}) Q / Z_{2p} Z_d e^2$.

Result and Discussion

Two-proton emission is possible when the amount of reaction energy Q is positive. This energy is expressed by the following relationship.

$$Q = \Delta M - \left(\Delta M_d + \Delta M_{2p}\right) \quad (14)$$

In this regard, ΔM , ΔM_d , and ΔM_{2p} are the excess mass of the mother nucleus, daughter nucleus, and the excess mass of the emitted diproton, respectively.

In Figure 2, the Q-value with the total potential, nuclear potential, Coulomb potential, and centrifugal potential are shown. In this figure, the horizontal axis is the distance to the center of the nucleus, which is plotted in femtometers, and the vertical axis is plotted in terms of energy. At small distances from the center of the nucleus, the dominant potential is the nuclear potential, which is absorbing. At greater distances, the nuclear potential tends to zero and the repulsive Coulomb potential dominates. Centrifugal potential has the greatest effects in short distances. In addition to these potentials, the amount of energy released in the reaction, (Q-valve) which is a line without slope, is also shown.

The angular momentum, spin, and parity of the nuclei involved in the reaction follow the following relationship.

$$\left|j_p - j_d\right| \le j_{2p} \le \left|j_p + j_d\right| \quad (15)$$

$$\pi_p / \pi_d = (-1)^{l_{2p}} \quad (16)$$

here, j_p, π_p, j_d and π_d are the angular momentum and parity of the parent and daughter nuclei, respectively. The l_{2p} and j_{2p} are the orbital angular momentum and the total angular momentum of the emitted diproton. Spin of proton is ½, therefore, the spin of diproton is one or zero. On the other hand, as said before, the spin of diproton must be one [10-13]. Notably, the deuteron, which is the most similar nucleus to the diproton, also has spin one. By considering $S_{2p} = 1$ for diproton, $j_{2p} = l_{2p} + S_{2p}$, equations

(15) and (16), and total angular momentum of parent and daughter nuclei the orbital angular momentum of diproton can be obtained.

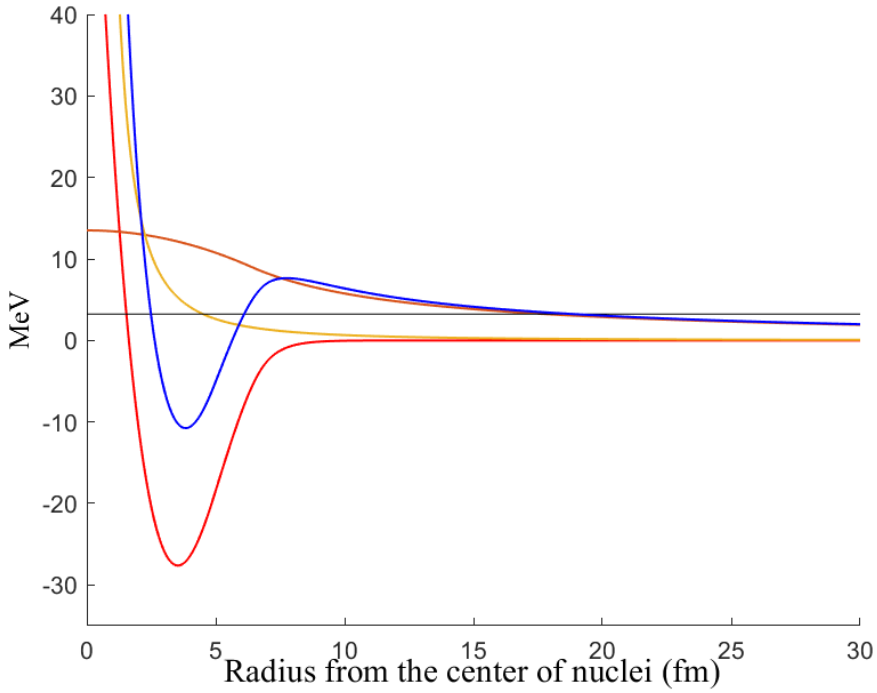

Figure 1: The proximity nuclear potential, coulomb potential, centrifugal potential, the total potential and the Q-value or the amount of energy released in the decay versus the distance from the center of the nucleus (in Mev) for ^{38}Ti.

In Table 1, the half-life of 15 diproton emitters in the ground state is given. Compared to alpha decay, in the case of diproton emission, the Coulomb force has a lower value, but the centrifugal potential has a higher value (according to the relation (6) for a certain angular momentum, it has a greater centrifugal potential, because of the smaller reduced mass.) Consequently, the half-life of the diproton-generating decay is more sensitive to the angular momentum. The experimental values of angular momentum are selected from the reference [25]. To compare the half-life of diproton decay from Gamow's model, the results obtained from Hatsukawa's semi-empirical relationship, and the laboratory data are also included in the table for comparison. Hatsukawa's model is a semi-empirical relationship that initially derives the half-life of alpha emitters and therefore, as can be seen from Table 1, does not work well for two-proton emitters.

In order to better compare the data with the laboratory data, the root mean square of the obtained data was compared with other models. The root mean square is expressed by the following relation.

$$\sigma = \left\{ \frac{1}{n-1} \sum_{i=1}^{n} \left(\log_{10} T_i^{cal} - \log_{10} T_i^{\exp} \right)^2 \right\}^{1/2} \quad (17)$$

here, n is the number of samples, and $T_i^{\exp}$ and T_i^{cal} are the experimental and computational half-lives, respectively. Table 2 presents the root mean squares of the difference between the logarithm of the calculated half-life of diproton decay and its experimental value, as calculated based on equation (17), for all three models.

Table 1: Comparison of the calculated half-life of diproton emitting nuclei with theoretical models of Gamow and Hatsukawa and experimental data.

No	**Nucleus**	**Q in MeV [26]**	$\log_{10} T_{1/2}(s)$			
			This paper	Gamow	Hatsukawa	Exp. Data [25]
1	^{11}O	4.250	-20.7134	-20.687	-18.4950	-21.7033
2	^{12}O	1.737	-18.7728	-19.848	-11.2221	-20.0506
3	^{15}Ne	2.520	-19.2135	-17.772	-17.7432	-21.1135
4	^{16}Ne	1.401	-20.1287	-19.057	-10.5282	> -20.2441
5	^{19}Mg	0.760	-12.2401	-12.320	-9.9968	-11.301
6	^{26}S	2.360	-8.8075	-9.459	-1.2272	< -7.10237
7	^{29}Ar	5.900	-6.4515	-8.183	-4.9276	> -7
8	^{30}Ar	3.420	-13.0907	-13.275	-1.0823	< -11
9	^{38}Ti	3.240	-6.4091	-7.085	-3.4264	< -6.92082
10	^{45}Fe	1.800	-4.28513	-3.742	-0.7669	-2.60206
11	^{48}Ni	2.390	-4.1761	-4.890	3.6077	-2.55284
12	^{54}Zn	2.280	-5.65098	-6.882	1.5275	-2.74473
13	^{58}Ge	3.230	-12.401	-13.526	-1.9612	-
14	^{67}Kr	2.890	-3.3168	-3.842	1.3604	-2.13077
15	^{90}Pd	0.050	-5.72903	-6.853	2.8807	-2 > -6.36794

Table 2: displays the root mean square of the difference between the logarithm of the half-life of two-proton decay and its experimental value. The calculations and comparisons are performed for all three models and for eight nuclei.

model	This paper	Gamow	Hatsukawa
σ	1.789862	2.392995	4.972147

Conclusion

Two-proton emission is one of the rare decays among unstable nuclei and it usually happens in proton-rich nuclei. In addition, this decay is not possible in nuclei with an odd atomic number. Because in this case, proton decay is more likely. But in nuclei with an even atomic number, due to the existence of the pairing force between protons, they form a bound system, and therefore the probability of diproton decay increases.

The WKB approximation and the proximity potential were presented to explain the alpha decay for the first time, and then it was used for the decay of other nuclear clusters. Here also the WKB approximation and the proximity potential were used to explain the diproton decay, which showed that like the alpha decay, The WKB approximation and proximity potential are suitable for explaining diproton decay and the half-life of diproton decay can be obtained based on that. The effect of orbital angular momentum on the height of the potential barrier and therefore on the probability of the particle penetrating the potential barrier is greater when a diproton is emitted than when an alpha particle or other heavier particles are emitted, on the other hand, the effect of the Coulomb force is relatively less. In addition to proximity potential, Hatsukawa's semi-empirical relations and Gamow's model were used to calculate the logarithm of the decay half-life of diproton emission. The calculations of the root mean square of the half-life difference with their experimental values showed that the use of proximity potential and WKB approximation is better than semi-empirical models.

References

1. Cui, J., Y. Zhang, S. Zhang, and Y. Wang, *α-decay half-lives of superheavy nuclei.* Physical Review C, 2018. 97(1): p. 014316.

2. Hosmer, P., et al., *Half-Life of the Doubly Magic r-Process Nucleus N 78 i.* Physical review letters, 2005. 94(11): p. 112501.

3. Wang, Y., S. Wang, Z. Hou, and J. Gu, *Systematic study of α-decay energies and half-lives of superheavy nuclei.* Physical Review C, 2015. 92(6): p. 064301.

4. Manjunatha, H. and K. Sridhar, *New semi-empirical formula for α-decay half-lives of the heavy and superheavy nuclei.* The European Physical Journal A, 2017. 53(7): p. 156.

5. Qi, L.-J., et al., *Systematic calculations of cluster radioactivity half-lives in trans-lead nuclei.* Chinese Physics C, 2023. 47(1): p. 014101.

6. Goldansky, V., *On neutron-deficient isotopes of light nuclei and the phenomena of proton and two-proton radioactivity.* Nuclear Physics, 1960. 19: p. 482-495.

7. Delion, D. and S. Ghinescu, *Two-proton emission systematics.* Physical Review C, 2022. 105(3): p. L031301.

8. Zhou, L., S.-M. Wang, D.-Q. Fang, and Y.-G. Ma, *Recent progress in two-proton radioactivity.* Nuclear Science and Techniques, 2022. 33(8): p. 105.

9. Pathak, D., et al., *Quest for two-proton radioactivity.* The European Physical Journal Plus, 2022. 137(2): p. 272.

10. Jänecke, J., *The emission of protons from light neutron-deficient nuclei.* Nuclear Physics, 1965. 61(2): p. 326-341.

11. Kryger, R., et al., *Two-Proton Emission from the Ground State of O 12.* Physical review letters, 1995. 74(6): p. 860.

12. KeKelis, G., et al., *Masses of the unbound nuclei Ne 16, F 15, and O 12.* Physical Review C, 1978. 17(6): p. 1929.

13. Brown, B.A., *Diproton decay of nuclei on the proton drip line.* Physical Review C, 1991. 43(4): p. R1513.

14. Yazdankish, E. and M. Nejatolahi, *Improved calculation of alpha decay half-life by incorporating nuclei deformation shape and proximity potential.* Physica Scripta, 2023. 98(11): p. 115309.

15. Santhosh, K., *Two-proton radioactivity within a Coulomb and proximity potential model for deformed nuclei.* Physical Review C, 2022. 106(5): p. 054604.

16. Gharaei, R. and S. Mohammadi, *Study of the surface energy coefficient used in nuclear proximity potential of the α-nuclei systems from density-dependent nucleon-nucleon interactions.* The European Physical Journal A, 2019. 55(7): p. 119.

17. Ghodsi, O. and A. Daei-Ataollah, *Systematic study of α decay using various versions of the proximity formalism.* Physical Review C, 2016. 93(2): p. 024612.

18. Gharaei, R., O. Ghodsi, and M. Kafash, *Study of the surface energy coefficient used in nuclear proximity potential from density-dependent nucleon–nucleon interactions.* Annals of Physics, 2020. 419: p. 168236.

19. Ramzan, M., et al., *Generalized fractional Wentzel–Kramers–Brillouin approximation for electron tunnelling across rough metal interface.* Proceedings of the Royal Society A, 2023. 479(2270): p. 20220600.

20. Denisov, V.Y. and A. Khudenko, *α-decay half-lives, α-capture, and α-nucleus potential.* Atomic Data and Nuclear Data Tables, 2009. 95(6): p. 815-835.

21. Denisov, V.Y. and H. Ikezoe, *α-nucleus potential for α-decay and sub-barrier fusion.* Physical Review C, 2005. 72(6): p. 064613.

22. Ismail, M., A. Ellithi, A. El-Depsy, and O. Mohamedien, *Correlation between alpha preformation probability, decay half-life and barrier assault frequency.* International Journal of Modern Physics E, 2017. 26(05): p. 1750026.

23. Zdeb, A., M. Warda, C. Petrache, and K. Pomorski, *Proton emission half-lives within a Gamow-like model.* The European Physical Journal A, 2016. 52: p. 1-6.

24. Hatsukawa, Y., H. Nakahara, and D.C. Hoffman, *Systematics of alpha decay half-lives.* Physical Review C, 1990. 42(2): p. 674.

25. Kondev, F., et al., *The NUBASE2020 evaluation of nuclear physics properties.* Chinese Physics C, 2021. 45(3): p. 030001.

26. Wang, M., et al., *The AME 2020 atomic mass evaluation (II). Tables, graphs and* ***References****.* Chinese Physics C, 2021. 45(3): p. 030003.

ICNST 2024 International Conference on Nuclear Science and Technology
6- 8 MAY 2024 | Isfahan, Iran

Simulation of the breakdown threshold electric field in the electrostatic quadrupole of the 200 keV Cockcroft-Walton Accelerator (Paper ID : 1207)

Mansouri.H M.M[*1], Mirzaei H.R.[2], Feghhi S.A.H.[3], Sanaye.Hajari S.[4]

[1,3]*Radiation Application Department, Shahid Beheshti University, Tehran, Iran*

[2,4] *Department of Physics and Accelerators, Nuclear Science and Technology Research Institute, Tehran, Iran*

Abstract

The main use of the 200 keV Cockcroft-Walton accelerator is neutron generation, so it is necessary to focus the deuterium beam at a distance of less than one meter on a circular surface with a diameter of less than 2 cm. An electrostatic quadrupole was chosen for this purpose. With considering different geometries (Bar, Curved and Hyperbolic) for each quadrupole, the characteristic parameters such as tolerable voltage and focal length will be different. One of the most important challenges faced by the construction of electrostatic quadrupole for beam convergence is the issue of electrical breakdown and spark between electrodes close to each other. Therefore, there are limitations in the applied voltage and determining the focal length. It is very important to study and check this tolerance threshold before construction. In this research, the electric field profile has been simulated using COMSOL Multiphysics software in different electrostatic quadrupole structures and geometries. Considering the electric field threshold limit for breaking, focal length and beam diameter were investigated and evaluated. Finally, according to the existing limitations for the 200 keV electrostatic accelerator, quadrupole geometry and voltage were determined.

Keywords: Electrical Breakdown, Quadrupole, Electrostatic Accelerator, Focal point, Beam Envelope

Introduction

One of the applications of the Cockcroft-Walton 200 kV accelerator is neutron generation by colliding a deuterium beam on a tritium target [١]. In this accelerator particles have been produced by a RF ion source and the accelerate to the energy of 200 keV. The beam doesn't move in an ideal trajectory and diverges. it will cause particles lost and reduce the output efficiency of accelerator. To compensate this problem, beam control instruments like bending magnets, steers, Einzel lens, immersion lens and quadrupoles lens are used. Quadrupoles are one of the most widely used lenses in beam convergence, which are used in both electrostatic and electromagnetic types.

Using a doublet electrostatic quadrupole lens for beams with relatively low energies is a more appropriate choice. Although electromagnetic quadrupoles are more widespread, but electric samples have several advantages: 1. they can be made much smaller than electromagnetic lenses, 2. electrostatic lenses do not suffer from hysteresis effects, 3. negligible current is drawn from the power supply, 4. stable voltage is more readily achieved than stable current in electromagnetic systems [2].

One of the most important problems that limit the use of this lens for high energy beams is the problem of electrical breakdown. This electric discharge will limit the performance of the quadrupole and cause damage to it. Breakdown occurs when the dielectric between two electrodes cannot tolerate the applied electric field and its charge carriers are released from the atom and cause an electric current between the two electrodes. Breakdown voltage in gases will be described by Paschen's low [2, 3] . The particles move in vacuum because the beam will be scattered and lost by colliding the air particles. With using vacuum pumps, the air pressure inside the beam tube is reduced to about $10^{-7} - 10^{-4}$ Torr, considering that the quadrupole is placed in this vacuum chamber, the breakdown voltage will be higher for it. Based on the experimental tests, it has been observed that the breakdown voltage for the pressure ranges of $10^{-5} - 10^{-3}$ Torr is independent of the vacuum pressure and will change only with the distance between the electrode plates [4-7]

In this paper, the main is to investigate the quadrupole performance in applied threshold breakdown voltage for different quadrupole structures and the nearest focal point of this maximum voltage is determined. The parameters like length, distance and radius of aperture are same for each structure. According to the results of this research, it is possible to determine the appropriate place target in such a way that the breakdown does not occur and the beam collide it with the highest efficiency. The parameters like focal point and magnification in transvers axis have been investigated and finally, using these results, the most appropriate geometric shape for the quadrupole will be selected.

200 keV Cockcroft-Walton accelerator (ES-200)

A 200 keV Cockcroft-Walton accelerator is under development and installation the laboratory of the Physics and Accelerator Research School (Nuclear Science and Technology Research Institute- NSTRI) Iran [8]. This accelerator was used to develop the beam diagnostic, transport systems and neutron generation. The specification of each part of the 200 keV accelerator are described and shown in Table 2.

The main purpose of this work is to describe the construction and operation of the low energy Cockcroft-Walton accelerator with energy in range of zero to 200 keV. The accelerator is shown in Fig 2.

Table 2. The specification of the 200 keV electrostatic accelerator

Ion Species	Gases ions (proton, He, O, N, etc.)
Acceleration Voltage	< 200 kV
Beam Current Max.	< 1mA
Energy Stability	< 0.5%
Operation Time without Maintenance	> 2000 h

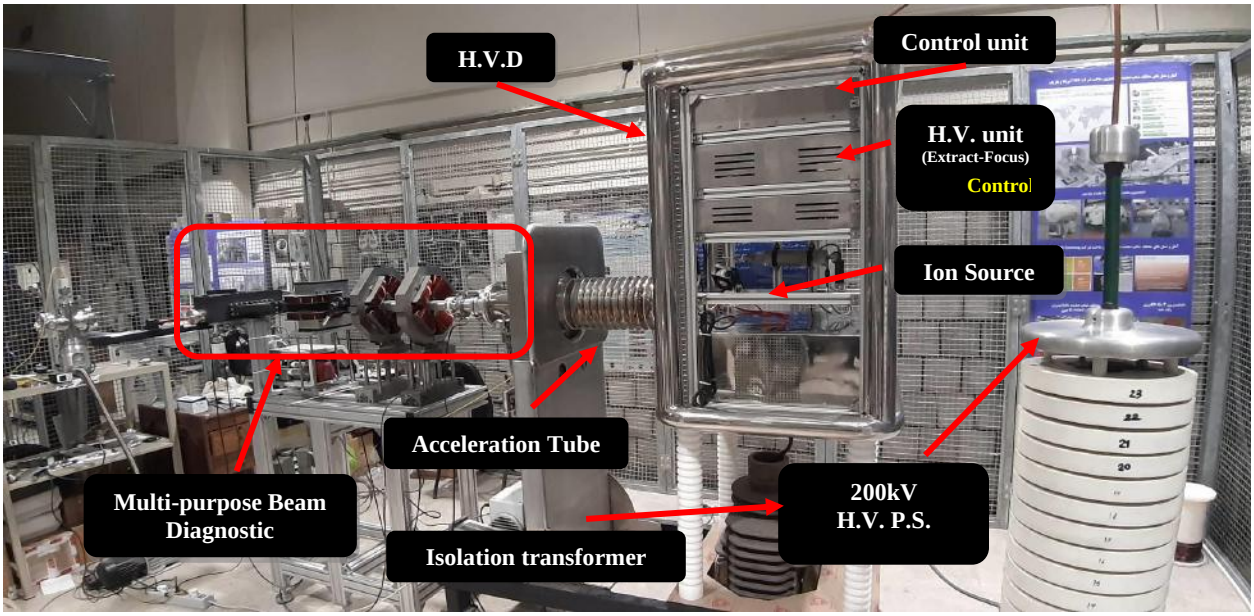

Fig 2. Picture of the 200 keV Cockcroft-Walton accelerator is installed in laboratory of the physics and accelerator research school

Models

Geometry is important to electric field profile in quadrupole and its performance, so three examples of the most used structures of electrodes have been selected. The

Fig **3** shows the geometry of model's structures. Usually, electrodes are made of steel, and in this study, steel is considered for the electrodes. The length of the electrodes is 10 cm and the radius of their inner circle is 3 cm.

The profile of the field in each of these structures is somewhat different, and accordingly, the threshold electric field will depend on the type of structure. The focal point and the magnification of beam will also be determined separately for each geometry and electric field.

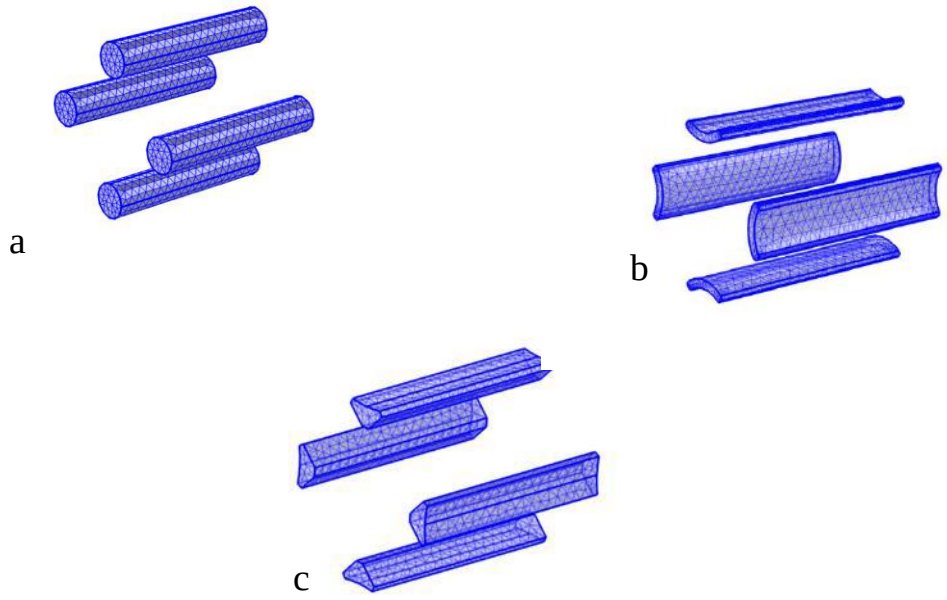

Fig 3. Structure of models (a) Bar electrode structure (b) Curved electrode structure and (c) Hyperbolic electrode structure.

The electric field is intense near the sharp points and the effect of this intensity can be reduced to some extent by changing the curvature of these points. Other quadrupole parameters such as the radius of the inner circle and the length of the electrodes and the distances between the quadrupoles are fixed in this study, and the changes of each of these characteristics can change the breakdown voltage and the focal point.

Simulations

The electric field and particle trajectory are simulated by using COMSOL Multiphysics software. In this simulation, two modules AC-DC and Charged Particle Tracing are used. AC-DC module determines the electric field by solving Laplace's equation for meshing the space, and by defining the input particles in AC-DC module and the solved electric field, the behavior of the particles can be studied. In each quadrupole, the two electrodes facing each other are ground and the others are in applied voltage, and in the next quadrupole, these applied voltages are switched. The initial beam has 1000 protons with an initial energy of 200 keV and a diameter of 2 cm.

Tetrahedral meshes are used, the size of the largest element is 7.15 cm and the smallest element is 0.52 cm. Numbers of meshes for Bar, Curved and Hyperbolic is 131035, 127179, 153437 respectively.

The diameter of beam is 2 cm and enters the quadrupole in parallel. The spatial and angular distribution considered for the particles is the KV distribution, it mostly implies the uniform behavior of particles inside its phase space ellipse [9].

Electric Field Simulation

After providing the simulation conditions, the field is studied for each structure and its maximum value is determined. Due to the fact that the field is more intense at the sharp points, the maximum point of the field is also located near the electrodes and in their initial or end plates.

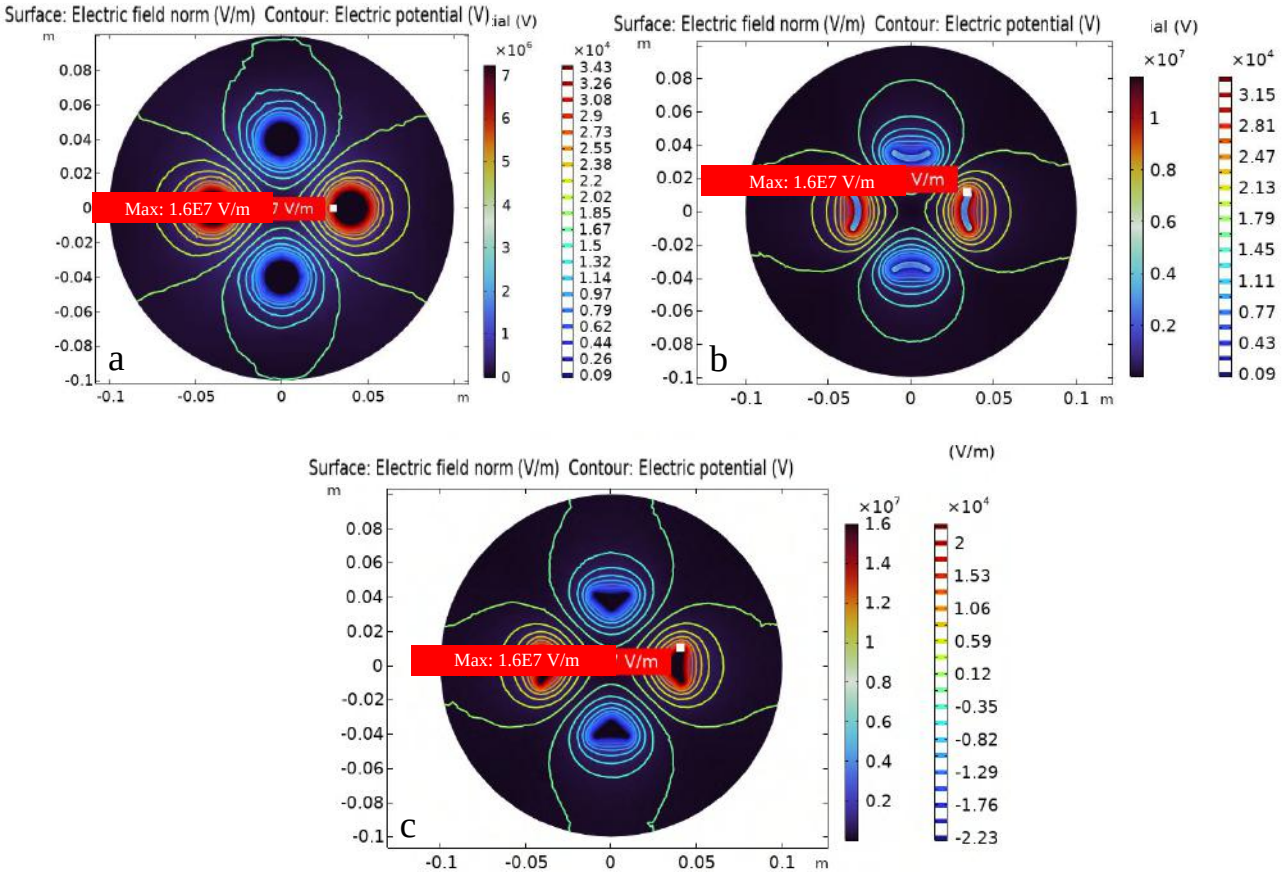

Fig 4. Profile of equipotential lines and maximum field in the planes of (a) Bar (b) Curved (c) Hyperbolic structures

Based on theoretical studies and experiments, the breakdown field for vacuum with pressure range of$10^{-5} - 10^{-3}$, $1.6 \times 10^{7} V/m$ determined. To finding threshold of voltage, the applied voltages to electrodes (V_1, V_2) changes. Due to the maximum of electric field that was considered as threshold of field, V_1, V_2 are found in such a way that the maximum field is equal to the determined threshold.

Fig 3 shows the transvers profile of equipotential lines in these three structures. The voltages applied to each quadrupole are in the Table 3.

Table 3. Breakdown voltage for different structures of quadruples.

	V_1 (kV)	V_2 (kV)
Bar Electrodes	37	35.2
Curved Electrodes	35	34.11
Hyperbolic Electrodes	47	46.47

1. Beam Profile and Focal Point Simulation

After determining the threshold of voltage, the performance of the beam is studied in the presence of maximum voltage applied quadrupoles. Due to the fact that the presence of astigmatism is inevitable in all lenses, the focal points of the x-y and x-z plates will be different. In this situation, the focal point is considered at a place where the shape of the beam is closest to the circle. So, the focal point is determined by Circle of Least Confusion [10].

To compare the beam size two location defined, one plane shows a beam profile before entering the quadrupole and the other shows the beam profile at the focal point.

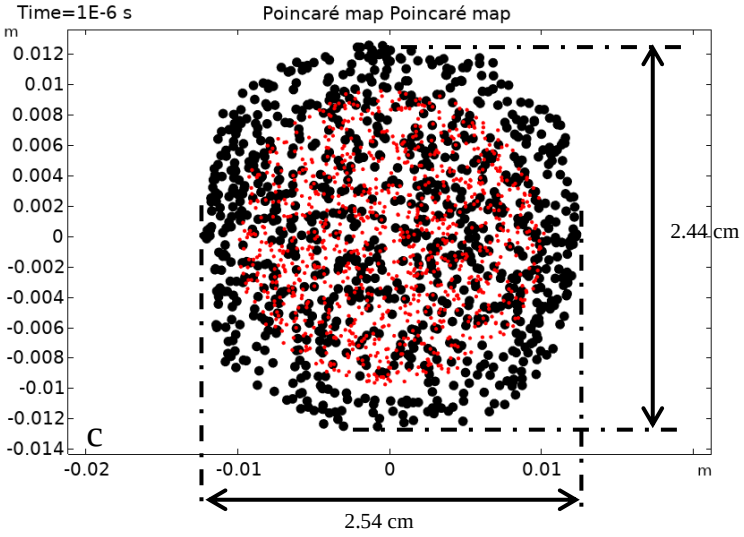

Fig 5. Beam Envelope in (a) x-y (b) x-z (c) transverse profile of beam in initial (small red points) and focal plane (large black points) in Bar structure

The breakdown voltage for the Bar structure is estimated to be higher than the Curved geometry and lower than the Hyperbolic one, and according to the simulation results, one of the focal points is located inside the quadrupole, and this leads to the fact that the beam is diverging in one direction when leaving the quadrupole, and the circle of least confusion that considered as the focal point have a larger radius than the initial beam. This structure can be used in cases where the diameter of the target is larger than the diameter of the beam or the intensity of the beam to collided the target is high.

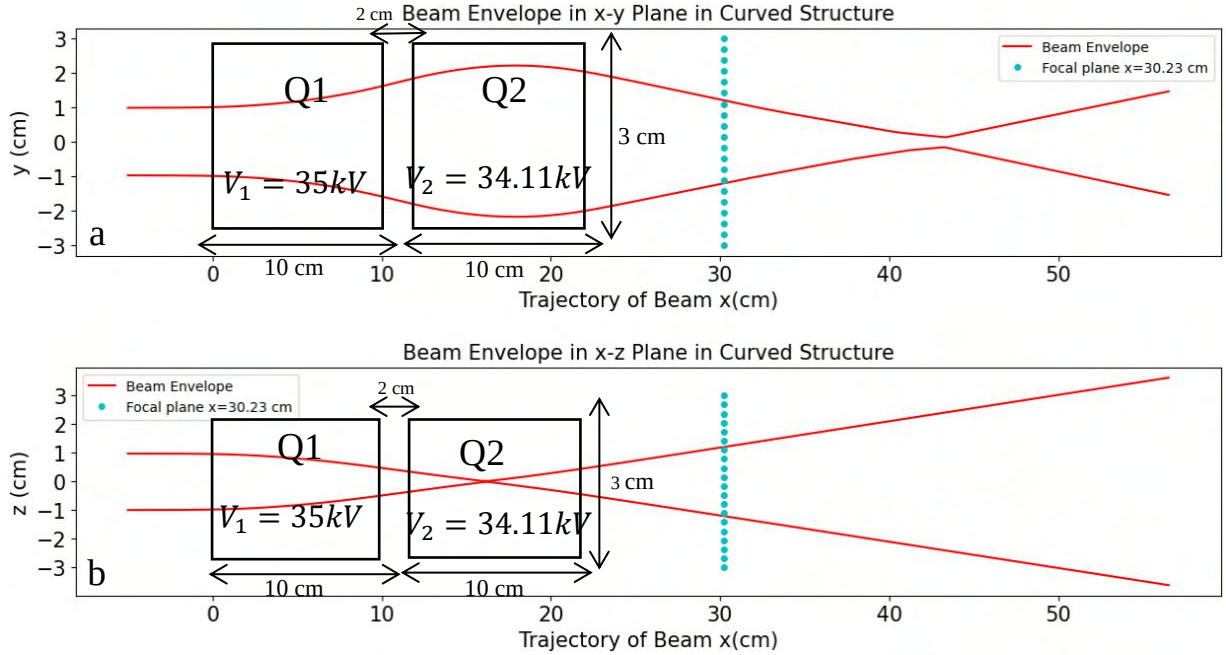

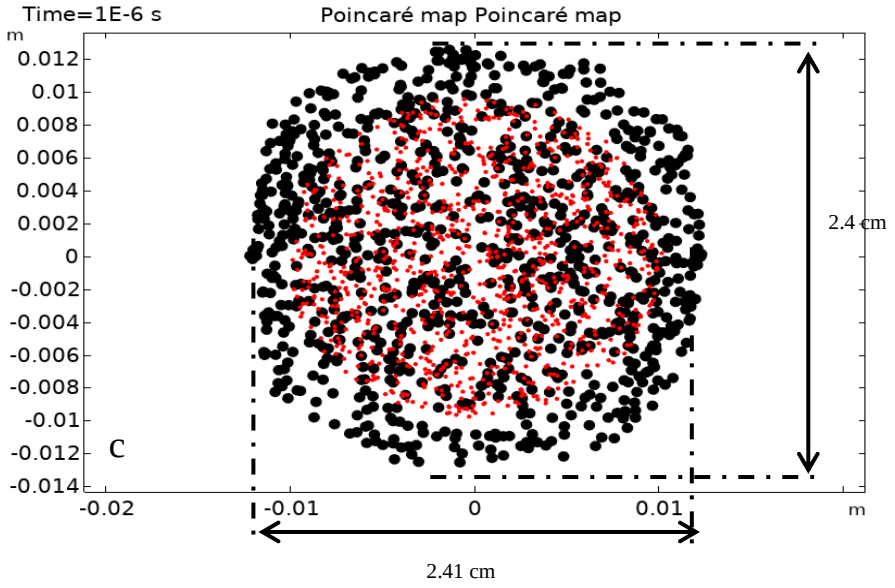

Fig 6. Beam Envelope in (a) x-y (b) x-z (c) transverse profile of beam in initial (small red points) and focal plane (large black points) in Curved structure

Curved geometry is not a good choice in the limit of low-breakdown voltages. This model also has a focal point inside the quadrupole, like the Bar model, and this will cause the magnification to be greater than 1 and the beam will diverge more. The use of this sample is limited in applications that require a beam with a lower intensity and larger diameter.

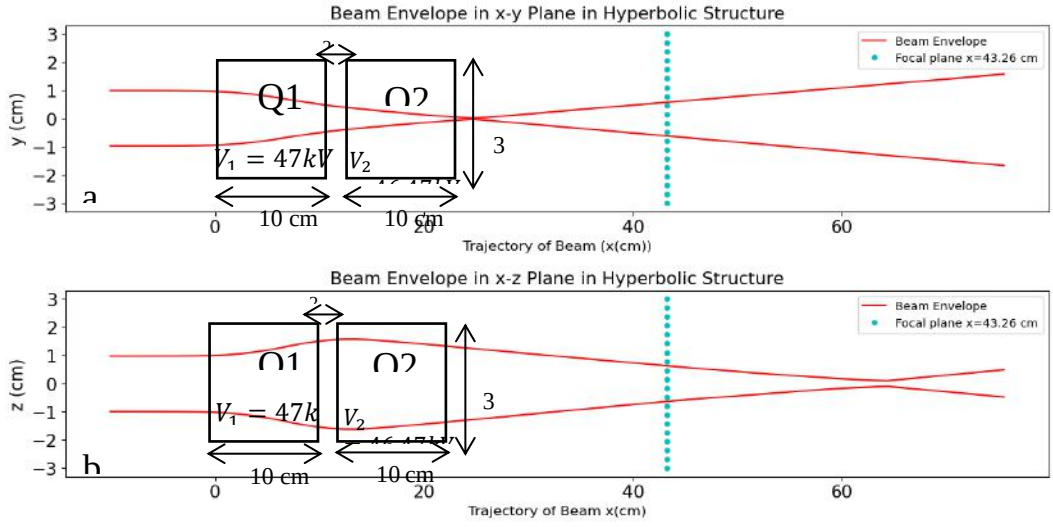

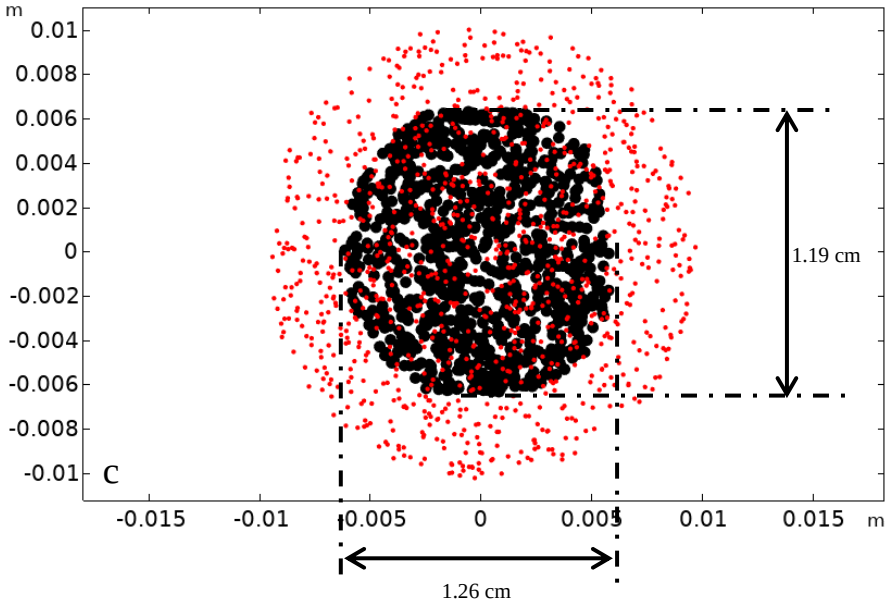

Fig 7. Beam Envelope in (a) x-y (b) x-z (c) transverse profile of beam in initial (small red points) and focal plane (large black points) in Hyperbolic structure

The choice of Hyperbolic geometry will be a suitable choice for high-energy beams due to the high threshold tolerable of the voltage, and on the other hand, considering that the profile of the beam is not a point in the focal plane, it is the best option for neutron generation applications, which needs a uniform beam with size of target.

Table 4. Focal point and magnification in both transverse axis y and z

	Focal point (cm)	y Magnification $\Delta y'/\Delta y$	z Magnification $\Delta z'/\Delta z$
Bar Electrode	30.7	$\frac{2.44}{2} = 1.22$	$\frac{2.54}{2} = 1.27$
Curved Electrode	30.23	$\frac{2.4}{2} = 1.2$	$\frac{2.41}{2} = 1.2$
Hyperbolic Electrode	43.26	$\frac{1.19}{2} = 0.59$	$\frac{1.26}{2} = 0.63$

Conclusion

The purpose of this research is to investigate the limit of electrical breakdown in the electrostatic quadrupole lens, according to which, different quadrupole structures can be classified based on the beam energy and the application of the accelerator device.

The voltage tolerance threshold of the Hyperbolic structure $V1 = 47\ kV, V2 = 46.47$ is higher than other structures, and on the other hand, its focal plane, which is located at $x = 43.26\ cm$, is further away from other structures, and its uniform beam profile makes it suitable for neutron production applications, in contrast the voltage tolerance of the Curved structure $V1 = 35\ kV, V2 = 34.11$ is less than other structures and its focal point at $x = 30.23\ cm$ is the closest point between these three structures. On the other hand, the diameter of the beam in the focal plane is greater than the diameter of the primary beam like Bar structure, which can be used in cases where the less intensity is required. The focal point of the Bar structure with medium voltage tolerance threshold $V1 = 37\ kV, V2 = 35.2$ is located at $x = 30.7\ cm$.

The main purpose of this accelerator is neutron generation and output beam from the hyperbolic structure is the most appropriate choice for this application. In addition to preventing beam divergence, it can be uniformly adjusted to the size of the target diameter and had the highest neutron generation efficiency. Due to the higher voltage tolerance of this structure, it can be used for more energetic beams, and with more freedom of action can determine the target location in less energetic beams.

References

[1] M. Moslemipoorkani, E. Ebrahimibasabi, and M. Sohani, "Design and simulation of the parameters affecting the ion beam characteristics from a penning ion source," *Iranian Journal of Physics Research,* vol. 20, no. 1, pp. 103-116, 2020.

[2] A. D. Dymnikov and G. A. Glass, "Comparison Of Electromagnetic, Electrostatic And Permanent Magnet Quadrupole Lens Probe-Forming Systems For High Energy Ions," in *AIP Conference Proceedings*, 2011, vol. 1336, no. 1: American Institute of Physics, pp. 248-252.

[3] G. Francis, *The glow discharge at low pressure*. 1956.

[4] R. Hackam and G. G. Raju, "Electrical breakdown of a point-plane gap in high vacuum and with variation of pressure in the range 10− 7− 10− 2 Torr of air, nitrogen, helium, sulphur hexafluoride, and argon," *Journal of Applied Physics,* vol. 45, no. 11, pp. 4784-4794, 1974.

[5] R. Hackam and L. Altcheh, "ac (50 Hz) and dc electrical breakdown of vacuum gaps and with variation of air pressure in the range 10− 9− 10− 2 Torr using OFHC copper, nickel, aluminum, and niobium parallel planar electrodes," *Journal of Applied Physics,* vol. 46, no. 2, pp. 627-636, 1975.

[6] L. Cranberg, "The initiation of electrical breakdown in vacuum," *Journal of Applied Physics,* vol. 23, no. 5, pp. 518-522, 1952.

[7] P. G. Slade, *The vacuum interrupter: theory, design, and application*. CRC press, 2018.

[8] A. Fathi, S. Feghhi, S. Sadati, and E. Ebrahimibasabi, "Magnetic field design for a Penning ion source for a 200 keV electrostatic accelerator," *Nuclear Instruments and Methods in Physics Research Section A: Accelerators, Spectrometers, Detectors and Associated Equipment,* vol. 850, pp. 1-6, 2017.

[9] R. Bailey, "Proceedings, CAS-CERN Accelerator School: Ion Sources," 2013.

[10] L. S. Pedrotti, "Basic physical optics," *Fundamentals of Photonics,* vol. 1, pp. 152-154, 2008.

ICNST 2024
International Conference on Nuclear Science and Technology
6- 8 MAY 2024 | Isfahan, Iran

Resonant Frequency and E-Field Profile Improvement in Traveling-Wave Accelerating Cavity using Machine Learning (Paper ID : 1212)

Malekpour A.[1*], Khorsandi M.[\], Sadeghipanah A.[2,3], Ahmadian namin S.[2,3]

[1]*Radiation Application Department, Shahid Beheshti University, Tehran, Iran*
[2]*Institute for Research in Fundamental Sciences (IPM), Tehran, Iran*
[3]*Iranian Light Source Facility (ILSF), Qazvin, Iran*
[*]*Email: afarin_malekpour@yahoo.com*

Abstract

In this research, supervised learning algorithms were used to optimize the output parameters of the acceleration structure. These algorithms were utilized in two sections: adjusting the $\pi/2$ mode resonant frequency of an S-band 9-cell traveling wave structure and enhancing the profile of the $3\pi/8$ mode's longitudinal electric field obtained by Bead-pull measurement. The first section involved the implementation and evaluation of a Multi Feature Polynomial Regression model using simulation data. The experimental data is then used for final verification. When applied to experimental data, the model with this algorithm showed an excellent performance with 95% accuracy of prediction of true values. In the second part, using poor accuracy measurements of the $3\pi/8$ mode field profile, a K Neighbors Regressor (KNR) model was developed and evaluated. This model is then used to predict the values, improving the accuracy of the field profile. The predicted values of field profile produced by KNR algorithm showed an accuracy of 96% compared to the field profile obtained through accurate measurements. The overall result revealed that the proposed algorithm significantly improved the accuracy of field profile specially when compared to a poor measurement data.

Keywords: Acceleration Structure, Bead-pull Measurement, Machine Learning, Optimization, Resonance Frequency, Supervised Learning.

1. INTRODUCTION

The optimization of a linear acceleration structure to achieve optimum values of specific parameters such as resonance frequency, coupling coefficient, and field amplitude is a time-consuming and challenging task. The development of artificial intelligence and its applications in various fields, especially for particle accelerators, has significantly improved the optimization process and control of these devices [1]. In this study, machine learning algorithms were used to optimize the output parameters of the traveling wave acceleration structure. Specifically, the focus was on tuning the resonance frequency of the $\boldsymbol{\pi/2}$ mode and

improving the accuracy of the $\mathbf{3\pi/8}$ mode longitudinal electric field profile measured by the bead-pull method.

When it comes to acceleration structures, the primary mode's resonance frequency is usually adjusted after construction by working on its inner surface [2]. This study introduces a novel approach by leveraging machine learning algorithms to intelligently adjust the resonance frequency of the main mode in traveling wave acceleration structures. The algorithm is designed to predict frequency changes of the main mode when a bulge with specific radius and volume is introduced. By inputting the desired projection's radius and volume into the algorithm, one can intelligently set the resonant frequency.

Following the construction of the acceleration structure, the axial electric field profile is typically extracted using the bead-pull method [3]. To streamline and expedite the field extraction process, machine learning algorithms were employed in this study. Several relevant studies in this area are referenced [4-8].

2. **Research Theories**

2-1. Polynomial Regression Algorithm

Polynomial regression is a supervised learning algorithm that predicts target labels using input features. It is a type of regression analysis in which the independent variable (feature) and the dependent variable (label) is modeled as an nth degree polynomial. The general form of the polynomial regression model with one feature is given in Equation 1 [9].

$$\mathbf{y = b_0 + b_1 x_1 + b_2 x_2 + \ldots + b_n x_n} \qquad (\mathbf{1})$$

Where y is dependent variable, x is independent variable, $\mathbf{b_0}$ to $\mathbf{b_n}$ represent coefficients of the polynomial terms, and n is the degree of the polynomial. The goal of polynomial regression is to find the coefficients that best fit the data. This is typically done by minimizing the sum of squared differences between the actual values and the predicted values. Figure 1 shows the steps of second-degree polynomial regression. Initially, the input features are transformed into second-order polynomial features. Subsequently, the model is fitted using one of the fitting methods, such as linear regression or ordinary least squares. Once the model is trained, it is ready for prediction. Finally, the model's performance is evaluated by calculating metrics such as mean squared error or R-2 score [9].

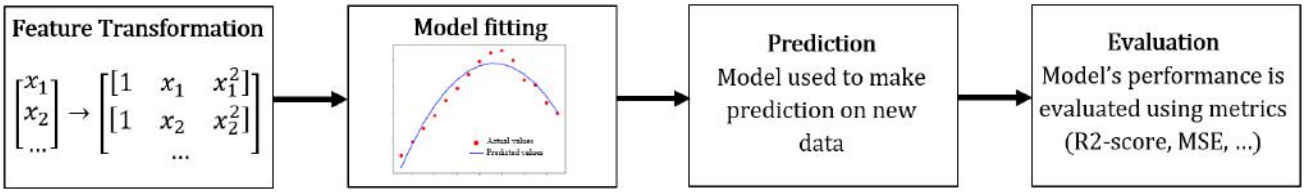

Fig. 1. Second-degree polynomial regression diagram

2-2. K Neighbors Regressor Algorithm

The K Nearest Neighbors (KNN) algorithm can be used for both classification and regression tasks. In the context of regression, it is called K Neighbors Regressor. It belongs to the family of instance-based or memory-based learning, where the algorithm memorizes the training data and uses them to make predictions for new unseen data [10].

Figure 2 shows the steps of the K Neighbors Regressor. Initially, the algorithm stores all the training data and corresponding target labels. Next, for a new data point, the algorithm finds the K nearest labels (neighbors) from the training set based on a distance metric, typically the Euclidean distance. The predicted value for the new data point is then computed as the mean (or weighted mean) of the target labels of its K nearest neighbors. Finally, the model's performance is evaluated by calculating metrics such as mean squared error and R-2 score [10].

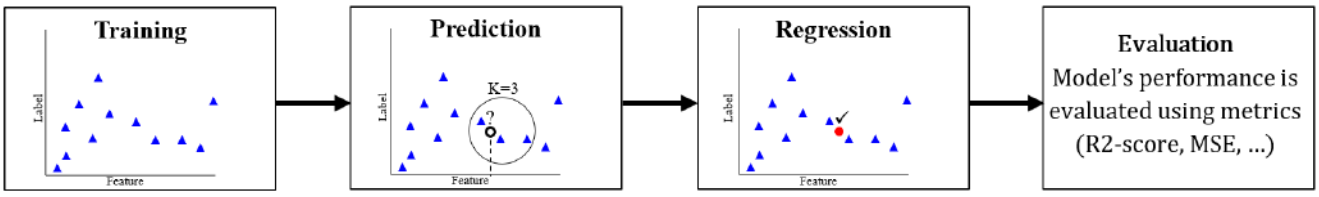

Fig. ۲. K Neighbors Regressor diagram

3. 9-Cell Traveling Wave Radio Frequency Accelerating Structure

In a constant impedance traveling wave radio frequency accelerating structure, an RF electromagnetic wave travels along the accelerator, interacting with particles to accelerate them. The wave is then absorbed at the end of the structure into a resistive load. The impedance of the structure remains constant, ensuring a stable acceleration gradient. This design minimizes RF wave reflections and ensures efficient energy transfer to the particles [3].

The 9-cell laboratory sample of this accelerator structure is created using the contraction method and features 9 resonance modes. The main mode of operation is $\boldsymbol{\pi/2}$ with a resonance frequency of 3.022 GHz, and the total length of the structure is 200 mm. Achieving desired changes in the output parameters of this structure, such as resonance frequency, requires precise adjustments to its dimensions. However, altering these dimensions is challenging and sensitive due to the irreversible nature of dimensional changes after creation [3]. Figure 3 shows the image of the 9-cell cavity and the electric field profile of $\boldsymbol{\pi/2}$ mode.

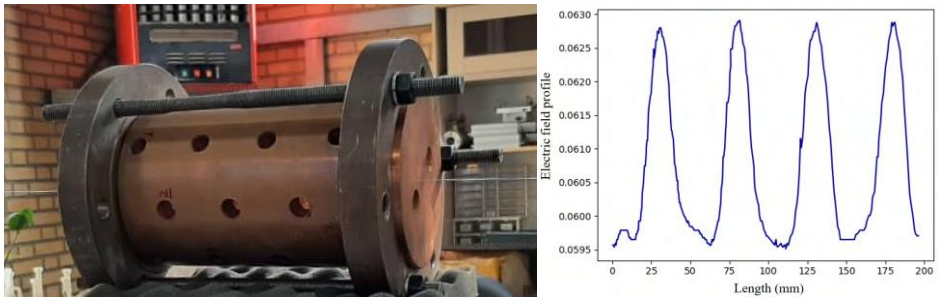

(a) (b)

Fig. 3. (a) 9-cell Traveling Wave cavity, (b) $\pi/2$ mode electric field profile

4. Machine Learning-Based Resonant Frequency Optimization

4-1. Simulation

To utilize supervised learning algorithms for adjusting the resonance frequency, we first compiled a dataset derived from simulation of an acceleration structure with 5 cells, including 3 full cells and two half cells around, using the high frequency module in the CST studio software package. Figure ٤ simply illustrates the simulated structure.

The dataset was constructed by inserting electrically conductive balls with varying radii into the cells and recording their impact on the resonance frequency of different modes. the data set have been given in Table 1 which consists of 13 columns containing information such as the radius, volume, resonance frequency of 5 resonance modes, the cell number where the ball was placed and frequency fluctuations compared to the situation without the ball.

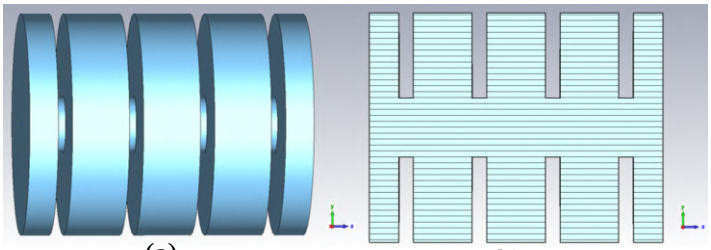

(a) (b)

Fig. 4. Layout of a 5-cell Traveling-Wave acceleration structure simulated in the CST software (a) full 3D model, (b) cropped view

Table 1. Simulation dataset

Bead specifications		Resonant frequency of the modes (MHz)					5-Cell	Frequency oscillations (MHz)				
Radius (mm)	Volume (mm^3)	f_{r_0}	$f_{r_{\pi/4}}$	$f_{r_{\pi/2}}$	$f_{r_{3\pi/4}}$	f_{r_π}	$Cell_n$	Δf_0	$\Delta f_{\pi/4}$	$\Delta f_{\pi/2}$	$\Delta f_{3\pi/4}$	Δf_π
0	0	2980.586	2985.725	2997.977	3009.953	3014.833	0	0	0	0	0	0
0.5	0.523599	2980.436	2985.579	2997.8134	3009.734	3014.593	1	0.15	0.1465	0.1636	0.2194	0.2404
1	4.18879	2980.436	2985.625	2997.7879	3009.788	3014.589	1	0.1497	0.0997	0.1891	0.1654	0.2444
…	…	…	…	…	…	…	…	…	…	…	…	…

After importing the necessary libraries (pandas, numpy, pylab, matplotlib.pyplot), the simulation dataset were preprocessed and their relationships were evaluated. A subset of the data was then selected, focusing on the presence of the ball in the middle cell of the simulated structure. This subset was chosen due to its significant impact on the resonant frequency of the main mode and the observed correlation between the frequency changes of this mode and the changes in the ball volume, as depicted in Figure 5(a). With the evidence presented in Figure 5(a), The second-degree polynomial regression algorithm was deemed suitable for fitting this subset of data.

The second-degree polynomial regression algorithm allows for the prediction of continuous values by fitting a curve with Equation (2) to the data. In this equation, y represents the dependent variable (label), x represents the independent variable (feature), $\mathbf{b_1}$ and $\mathbf{b_2}$ denotes the fit coefficients and $\mathbf{b_0}$ signifies the fit intercept. Increasing the number of features can enhance the algorithm's accuracy.

$$\mathbf{y = b_0 + b_1 x + b_2 x^2} \qquad (\mathbf{2})$$

To build the model, the volume and radius of the ball were selected as features and the frequency changes of the $\boldsymbol{\pi/2}$ mode were selected as label, then the data were divided into training and test sets. The 'Polynomial Features' from the preprocessing section of the sklearn library and the 'linear_model' from

that library were utilized. The model was evaluated using the prediction values for the test dataset and calling the 'r2_score' from the metrics section of the sklearn library.

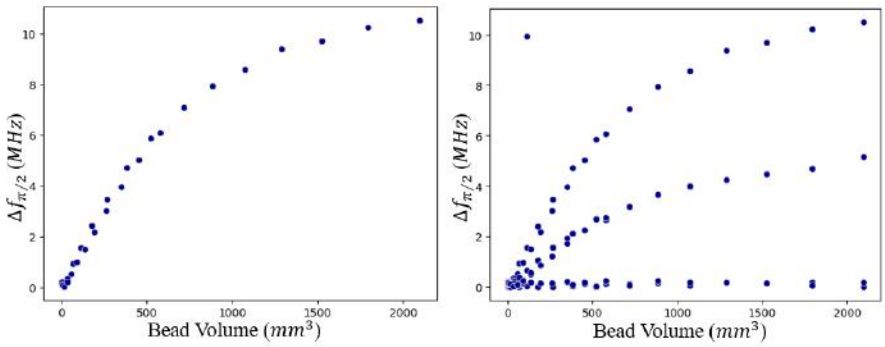

(a) (b)

Fig. 5. Resonant frequency oscillation of the $\pi/2$ mode per bead volume change (a) in cell 3, (b) in all cells

4-2. Experimental Measurement of the Main Mode Resonant Frequency Oscillation

Once the model's precision was sufficient, final validation of the algorithm was performed with experimental measurement data. This measurement was conducted on a constructed sample of a 9-cell traveling wave acceleration structure. Metal balls of varying sizes were placed in the middle cell of the structure, and the changes in the resonant frequency of the main mode were recorded using a network analyzer equipped with two ports and antennas. The measured data including the ball's radius and volume, the cell number where the ball was placed, the resonance frequency of the main mode of the structure, and the frequency fluctuations relative to the base state (without balls). Figure 6 shows a scatter diagram of the resonance frequency changes according to the change in the pellet volume. Validation of the algorithm was performed by rebuilding the model and evaluating it using the experimental data.

Table 2. Experimental dataset

Radius (mm)	Volume (mm^3)	$f_{r_{\pi/2}}$(MHz)	Cell	$\Delta f_{\pi/2}$(MHz)
0	0	3021.92	5	0
0.5	0.523599	3021.886	5	0.0337
1	4.18879	3021.886	5	0.0339
1.5	14.13717	3022.17	5	0.2499
2	33.51032	3022.305	5	0.3852
…	…	…	…	…

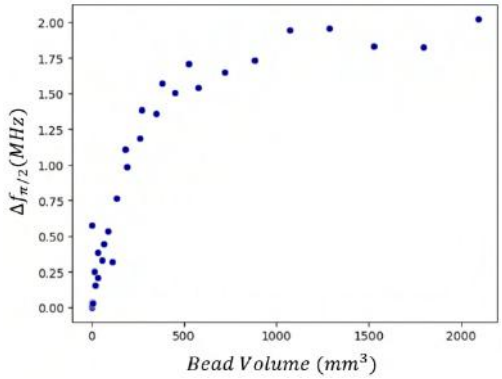

Fig. 6. Resonant frequency oscillation of the $\pi/2$ mode per bead volume change in cell 5

5. Enhancing Electric field profile

Bead-pull method involves moving a dielectric bead incrementally along the length of the structure and recording the changes in resonance frequency of different modes. The axial electric field profile is then derived from the recorded data and Equation (3). In this equation, E represents the electric field domain, f_0 represents the resonance frequency in the absence of the bead and f represents the resonance frequency in the presence of the bead in the longitudinal coordinates.

$$E = \sqrt{\frac{|f - f_0|}{f_0}} \qquad (3)$$

However, achieving an accurate profiled field requires extremely small longitudinal movements of the bead, which made the extraction process a highly time-consuming work. The goal is to enhance the accuracy of the electric field profile of the structure using a dataset derived from experimental measurements of changes in $3\pi/8$ mode resonance frequency. These experimental measurements were initially characterized by low accuracy, prompting the use of machine learning to improve the profile extraction process.

After preprocessing the data, it was observed based on Figure 7 that there is no relationship between the changes in the resonance frequency and the changes in the bead placement length. Therefore, a simple fit to the data was not feasible. To overcome this challenge, alternative algorithms including Radius Neighbors Regressor (is a non-parametric algorithm that uses a fixed radius to find the neighbors of a data point. It calculates the average of the labels of all the neighbors within the specified radius.), Random Forest Regressor (Constructs a multitude of decision trees during training. Each tree in the forest predicts the

output value, and the final prediction is the average of all the tree predictions.), Gradient Boosting Regressor (Builds models sequentially. Each new model corrects errors made by the previous ones, focusing on the residuals (the differences between the actual and predicted values). The final prediction is the sum of the predictions from all the models.), Voting Regressor (Combines the predictions from multiple machine learning algorithms (in this research linear regression, RFR, and GBR). It takes the average of the predictions from each individual regressor.), and K Neighbors Regressor were employed to construct the model. Among these algorithms, the K Neighbors Regressor showed good accuracy in predicting frequency fluctuations.

Table 3. Low accuracy Bead-pull measurement data

Longitudinal coordinate of presence of bead (mm)	Resonant frequency of $3\pi/8$ Mode (GHz)
2.1	3.0143
3.7	3.01424
6	3.01418
…	…

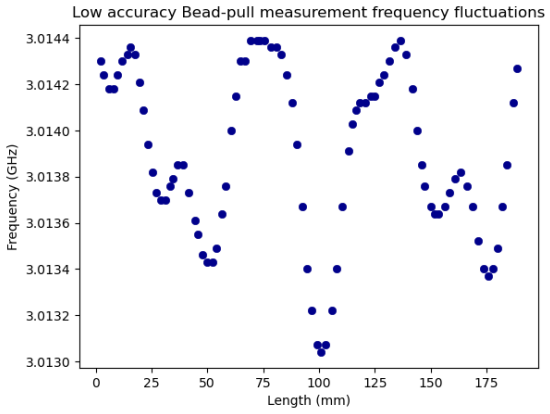

Fig. 7. Frequency fluctuation per position of bead scatter plot.

The ‘K Neighbors Regressor’ algorithm was employed from the neighbor’s section of the sklearn library to predict frequency changes for missing longitudinal coordinates. Through the expansion of the dataset and the application of Equation (3), the characteristics of the electric field were effectively calculated, overcoming the challenges posed by the absence of a relationship in the data. To verify the results, the resulting field profile was compared with the profile obtained from precise experimental measurements.

6. Results and Discussion

Table 4 summarizes the results of the section 4, focusing on the accuracy of the algorithms used. In Figure 8, the second-degree polynomial regression is plotted on the data to assess the possibility of overfitting. As evident from this figure, no overfitting is observed. The second-degree polynomial fitting algorithm with several features demonstrated the best performance, achieving an accuracy of 95% when evaluated using data from experimental measurements. This algorithm worked effectively in predicting frequency fluctuations of the main mode that indicates its suitability for optimizing acceleration structures.

Table 4. Results of Machine Learning-Based Resonant Frequency Optimization

Second order polynomial regression algorithm	
$y = b + \theta_1 x + \theta_2 x^2$	
Accuracy	Data type
98%	Simulation
Multi feature second order polynomial regression algorithm	
$y = b + \theta_1 x_1 + \theta_2 x_1^2 + \theta_3 x_2 + \theta_4 x_2^2 + \cdots$	
Accuracy	Data type
99%	Simulation
95%	Experimental

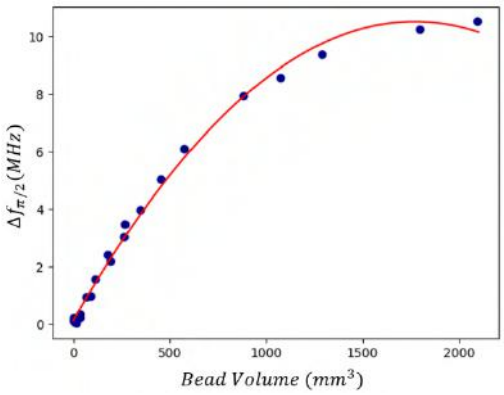

Fig. 8. Second-degree polynomial regression applied to the dataset.

Moving to the second part of the research, Table 5 and Figure 9 present the outcomes of section 5. The K Neighbors Regressor algorithm achieved the highest reported accuracy for predicting missing values, indicating its effectiveness. Figure 10 displays the algorithm's performance in predicting frequency

fluctuations for non-existent length values. Additionally, the figure shows a number of test data points whose labels are predicted by the algorithm, plotted against the actual values of the labels. These data points were used to calculate the performance accuracy of the model built with the K Neighbors Regressor algorithm.

Table 5. Results of Enhancing Electric Field Profile

Accuracy	Data type	Algorithm
96%	Experimental	K Neighbors Regressor
94%	Experimental	Radius Neighbors Regressor
93%	Experimental	Random Forest Regressor
83%	Experimental	Voting Regressor
78%	Experimental	Gradient Boosting Regressor

Figure 9 illustrates the electric field profile of the acceleration structure. The dark blue curve indicates the field profile obtained from experimental measurements with low precision, while the red curve depicts the improved field profile using the machine learning algorithm. The black curve also displays the profile of the electric field obtained from accurate experimental measurements. A comparison between the red and black curves proves the improvement of the profile. Furthermore, the improved profile eliminates low-amplitude noise present in the experimental measurement, enhancing the accuracy of the electric field profile.

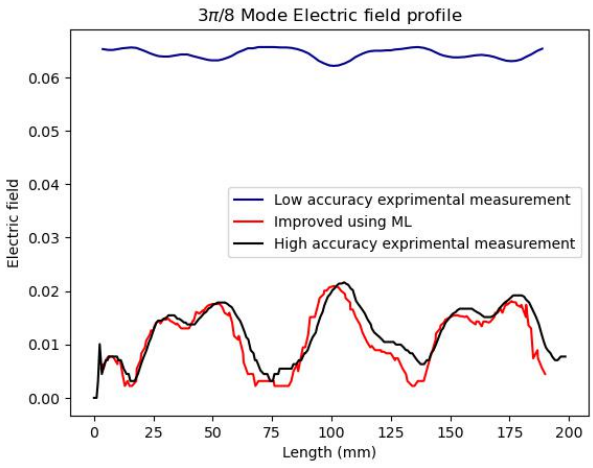

Fig. 9. Electric field profile

Prediction	y
3.0137	3.0138
3.0135	3.0137
3.0137	3.0137
3.0144	3.0144
3.0137	3.0136
3.0137	3.0137
3.0134	3.0134
3.0141	3.0142
3.0139	3.0139
3.0141	3.0141

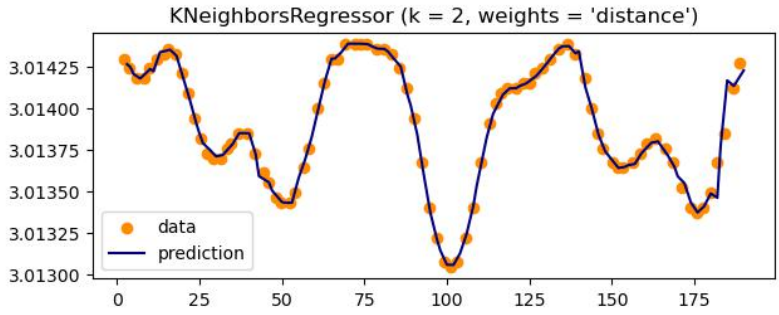

Fig. 10. K Neighbors Regressor (KNR) model constructed and utilized for predicting frequency oscillation for unknown data input.

Conclusions

The present research demonstrates the effectiveness and application of machine learning algorithms in optimization of the output parameters of acceleration structures post-construction. In addition, the algorithms proved successful work on adjusting the resonant frequency of the $\pi/2$ mode and enhancing the profile of the axial electric field of the $3\pi/8$ mode. With an accuracy of 95%, the algorithms can adjust the resonance frequency, while achieving an accuracy of 96% allows for an increase in the number of frequency fluctuation data and improvement in the resulting electric field profile. Besides the algorithm's optimal performance, they also contribute to increased optimization speed and the attainment of specific parameters. Finally, the positive effect of the removal of low-amplitude noises have been also observed in the results.

References

[1] Edelen, A. and et al. (2022). Optimization and machine learning for accelerators. USPAS_ML.

[2] Lamehi Rashti, M. and Sanaye Hajari, Sh. and et al. (2022). Design and construction of a traveling wave electron linear accelerator at Institute for Research in Fundamental Sciences (IPM). Iranian Journal of Physics Research.

[3] Ghasemi, F. (2015). Design and construction of electron linear accelerator TW-tube and measurement of it's parameters. PhD Thesis. Shahid Beheshti University.

[4] Kazemi, K. and Moradi, Gh. (2021). Employing machine learning approach in cavity resonator sensors for characterization of lossy dielectrics. IJICTR, volume13-number3.

[5] Wan, J. and Jiao, Y. and et al. (2021). Current study of apping machine learning to accelerator physics at IHEP. IPAC, ISSN:2673-5490.

[6] Zhang, Zh. and Song, M. and et al. (2021). Online accelerator optimization with a machine learning-based stochastic algorithm. Machine Learning: Science and Technology, Sci. Technol. 2 015014.

[7] Liu, Y. and Luo, T. and et al. (2023). Detecting Resonance of Radio-Frequency cavities using fast direct integral equation solvers and augmented bayesian optimization. IEEE, physics.acc-ph. 2305.05918v2.

[8] Daniil nimara, D. and Malek mohammadi, M. and et al. (2023). Model-based reinforcement learning for cavity filter tuning. Proceeding of machine learning research, vol 211:1-11.

[9]github.com/KonuTech/Machine-Learning-with-Python/blob/master/ML0101EN-Reg-Polynomial-Regression-Co2-py-v1.ipynb

[10] scikit-learn.org/stable/modules/generated/sklearn.neighbors.KNeighborsRegressor.html

ICNST 2024 International Conference on Nuclear Science and Technology
6- 8 MAY 2024 | Isfahan, Iran

RF transmission line of a 2.45 GHz ECR ion source (Paper ID : 1231)

Asadi Aghbolaghi M.[1], Abbasi Davani F.[1*], Yarmohammadi Satri M.[2], Riazi Mobaraki Z.[2], Ghasemi F.[2]

[1]*Department of Radiation Application, Faculty of Nuclear Engineering, Shahid Beheshti University, P.O. Box 19839-69411, Tehran, Iran*

[2]*School of Physics and Accelerators, Nuclear Science and Technology Research Institute, P.O. Box 14395-836, Tehran, Iran*

Abstract

Microwave coupling plays an important role to energize the electrons in an electron cyclotron resonance ion source (ECRIS) plasma. Several components are hired for wave transition from a magnetron to the ECR plasma chamber. In this work, DC break, pressure window, ridged waveguide and plasma chamber have been designed and simulated by COMSOL Multiphysics to transmit the microwave power. The power and frequency are 1 kW and 2.45 GHz, respectively. The results show the 9.9 mm quartz pressure window maximize the forward transmission power to the cavity and TE_{111} mode gets excited. The DC break is based on utilizing the insulating rings along the WR-284 waveguide, which has low wave return loss for a wide range of frequencies. A four-ridged waveguide is considered for impedance matching and electric field focusing. The amplification of the electric field in the middle of cylindrical plasma chamber is satisfied with dimensions of Ø9 cm×10 cm.

Keywords: ECRIS, RF transmission line, DC break, Pressure window, Ridged waveguide, Plasma chamber

Introduction

ECRIS as the front-end for the most useful applications is hired to produce different ion current in research and medical institute, and industries such as: ion beam etching, ion beam doping, micro-machining and semiconductor fabrication [1]. For accelerators and ion beam applications that require high-current mono-charge state ion currents, the 2.45 GHz ECRIS has a wide range of applications, due to its advantages of long lifespan, high beam current and good beam quality. This source is based on the resonance, heating and increasing the energy of plasma electrons. For the 2.45 GHz microwave power injection which is equal to the Larmor frequency of rotating electrons around the field lines, the resonance magnetic field is obtained by $B = \frac{m_e \omega}{q} = 875$ G [3]. The main parts of this plasma source are: RF power supply (magnetron), RF line, plasma chamber, magnet structure and extraction system [2]. RF line typically consist of directional coupler, circulator, three-stub tuner, DC break, pressure window, ridged waveguide [3]. In this work, The RF frequency and power values are chosen of 2.45 GHz and 1 kW, respectively.

Research Theories

Plasma Chamber:

Since the desired resonance frequency in this research is equal to 2.45 GHz, the desired diameter and length for exciting TE_{111} mode in the aluminum cylindrical cavity is about 9 cm and 10 cm, respectively, to produce at least the high electric field of 10^4 V/m, Figure 1. By applying the ridged waveguide, the field in the center of the chamber increases to 1.1×10^5 V/m, which is almost twice the case without it (see Figure 1). Also, the different values of diameter and length can be chosen, but it should be noted that by choosing a large length, the distance between the plasma and the extraction electrode is large and it prevents the extraction of the beam quality. Also, choosing a short length result in a small volume of plasma. Since the inner diameter of the cavity is equal to 9 cm, the remaining space between chamber and coil is assigned to the flanges and the cooling system, which keeps the temperature of the chamber at 20˚C to avoid the volume expansion of the chamber and thus prevent the change of resonance frequency (Figure 2).

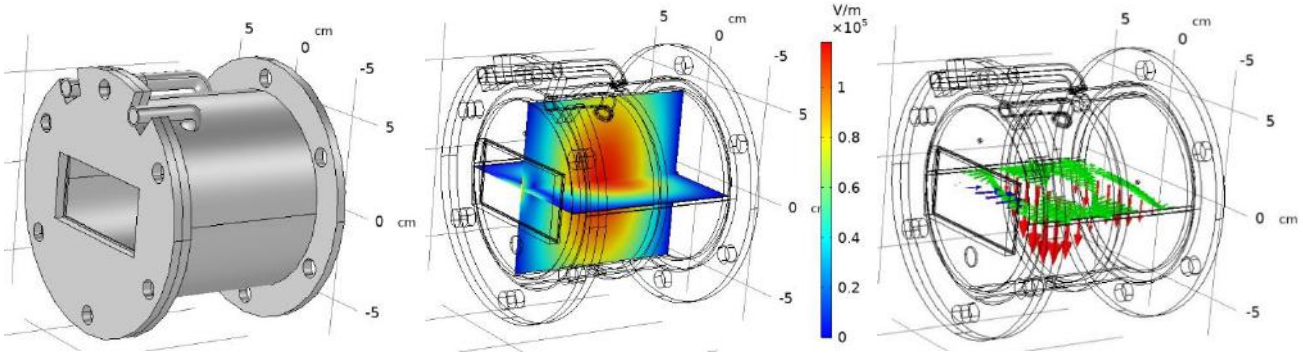

Fig. 1. Left) Shematic of simulated plasma chamber, center) the electric field in the plasma chamber due to the presence of the ridged waveguide and right) Direction of electric field (red arrow), magnetic field (green arrow) and power flux (blue arrow)

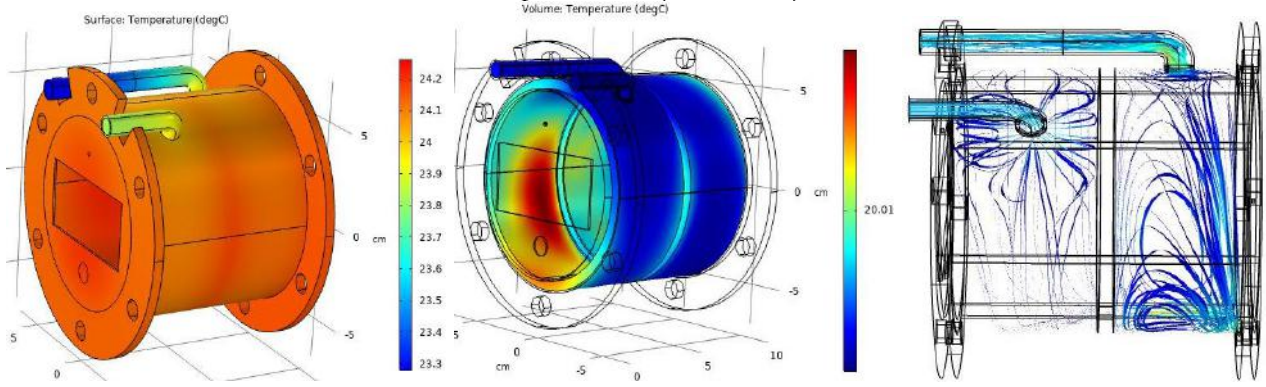

Fig. 2. Left) The cavity temperature without cooling, center) cavity with water cooling and right) the water circulating path around the cavity.

Ridged Waveguide:

Coupling of microwave power to the plasma plays an important role to produce a high axial plasma density and improves the output current from the ion source. Since the plasma impedance is equivalent to a complex dynamic quantity whose value changes with the change of various plasma parameters such as magnetic field, gas pressure, incident microwave wave power, etc., so an automatic tuner is also needed. The ridged waveguide is designed by considering the standard waveguide WR-284 with dimensions of 7.2136 cm and 3.4036 cm, which matches the impedance of the waveguide with the plasma impedance (around 50-150 ohms). These waveguides are usually used for: 1- optimizing the coupling between the microwave wave source and the plasma chamber and 2- Focusing the electric field on the central axis of the chamber. The schematic of a four-step ridged waveguide is shown in Figure 2.

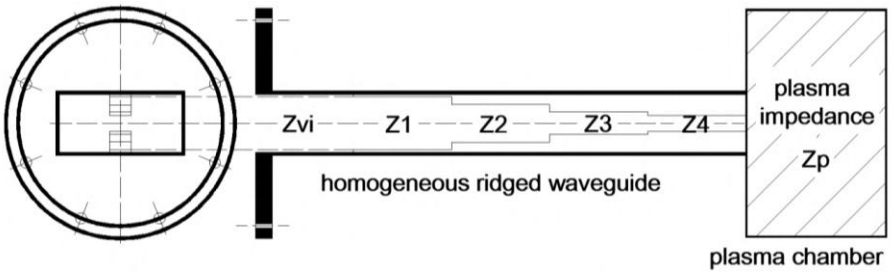

Fig.2. Schematic of the ridged waveguide with four steps coupled to the plasma chamber

Here, Z_1, Z_2, Z_3, and Z_4 are the impedances of each step of the waveguide, Z_{vi} is the wave impedance (or voltage-current impedance) of the standard WR-284 waveguide, and Z_p is the plasma impedance. The wave impedance of the standard waveguide is obtained from equation (1):

$$Z_{vi} = \frac{2b\pi\eta}{2a}\left[1 - \left(\frac{\lambda_0}{\lambda_c}\right)^2\right]^{-\frac{1}{2}}, \quad (1)$$

where η, b, a, λ_0 and λ_c are the impedance of free space (377 Ω), the height and width of the waveguide, the free space wavelength and cutoff wavelength, respectively. As a result, the value of wave impedance for standard rectangular waveguide WR-284 in TE_{10} mode and frequency of 2.45 GHz is equal to 527 Ω. The length of each step is equal to a quarter of the wavelength at the working frequency of 2.45 GHz, and the impedance of each part of the ridged waveguide is determined by the equation (2):

$$\frac{Z_{n+1}}{Z_n} = \exp\left[2^{-N} C_n^N \ln\frac{Z_n}{Z_0}\right] \quad (2)$$

Here n and N are the number of steps, the total number of steps. The determined values for the impedance and the distance between the ridges in each step of the waveguide are shown in Table 1. The designed four-step ridged waveguide is shown in Figure 5.

Table 1. Impedance values and the distance between the ridges in each step of the waveguide

Number	Distance(cm)	Impedance(Ω)
1	3.2	483
2	2.2	341
3	1.3	203
4	0.9	144

Pressur Window:

The microwave vacuum or pressure window is widely used to keep the vacuum (Figure 3-left). The thickness of the window should transmit the wave power and stop the energetic electrons towards the wave transmission line and magnetron. In this work, a single-layer quartz window which is cheap and available, was designed. The thickness of the window was checked from 1 to 20 mm and it was observed that the return wave loss (S11) with a thickness of 9.9 mm is the lowest and equal to 51 dB, and the transmission loss (S21) is equal to 0.01, Figure 4.

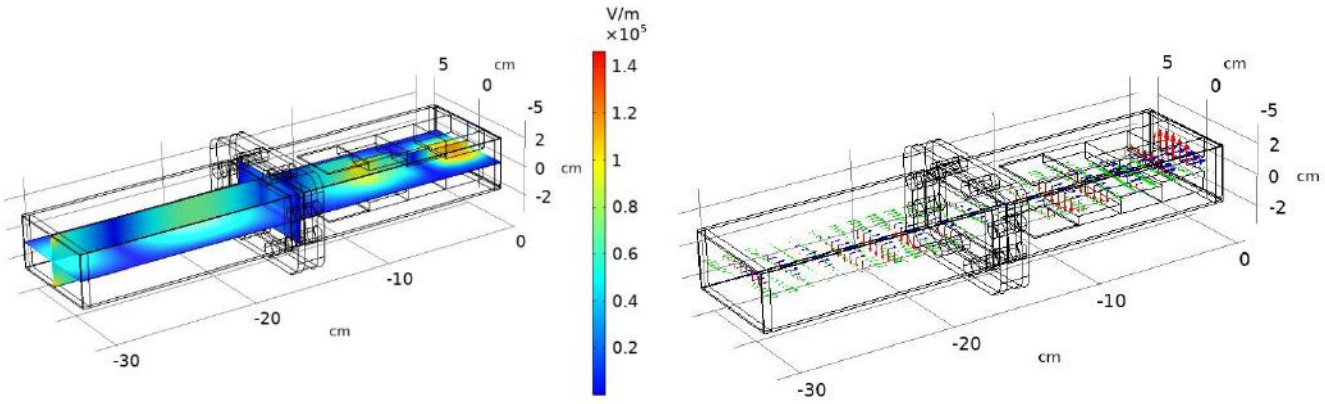

Fig. 3. Left) The electric field released in the system with the presence of the vacuum window and right) electric, magnetic fields and electric power density released with the presence of vacuum window

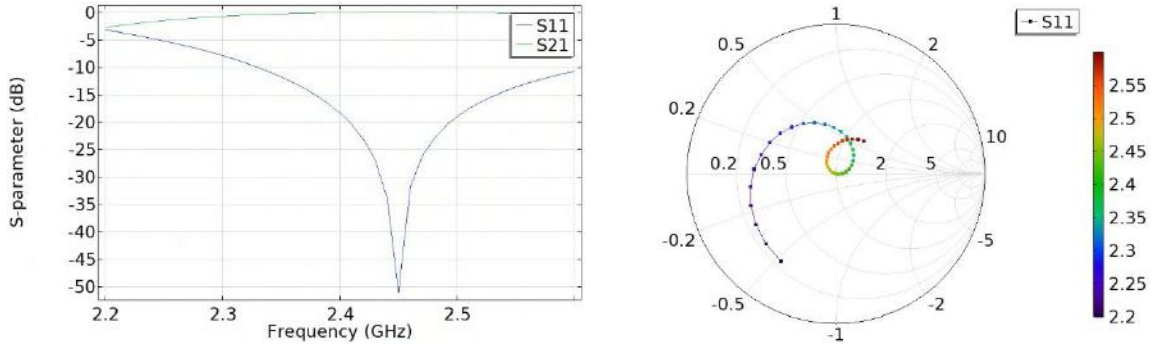

Fig. 4. Left) Variations of wave return loss (S11) and transmission loss (S21) of a quartz window with a thickness of 9.9 mm and right) Polar display of return wave loss (S11) as a function of frequency

As it can be seen in Figure 5, the temperature of the chamber increases to about 27˚C. In this figure, the green arrows represent the magnetic field and the blue arrows represent the electric field.

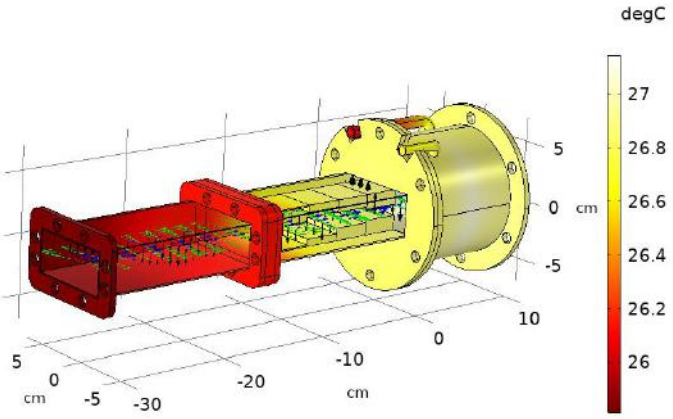

Fig. 5. Temperature distribution and electric field (black arrow), magnetic field (green arrow) and electric power density (blue arrow) in the system with the presence of vacuum window

Dc Break:

DC break is required to isolate the RF generator (magnetron) from the high voltage applied to the plasma chamber (50 kV in this design). So, mechanical strength and low wave loss are the important features that should be considered. Teflon, high density polyethylene, and polypropylene are the most widely used materials for this purpose. As described in Ref. [4], by considering 6 insulating washers (or rings) such as G-10CR resin with a thickness of 5 mm (in the waveguide connection with thickness of 2 mm) are placed

in the path of the waveguide. Also, the width of each piece of waveguide is equal to 2.5 cm. Figure 6 shows how the transmission and return loss changes for the DC break. As seen, at the frequency of 2.45 GHz, the value of S_{11} is equal to 43 dB. Since the high voltage break is not placed in front of the wave, all the investigated frequencies pass through the center of the Smith-Chart (Figure 7) with little loss.

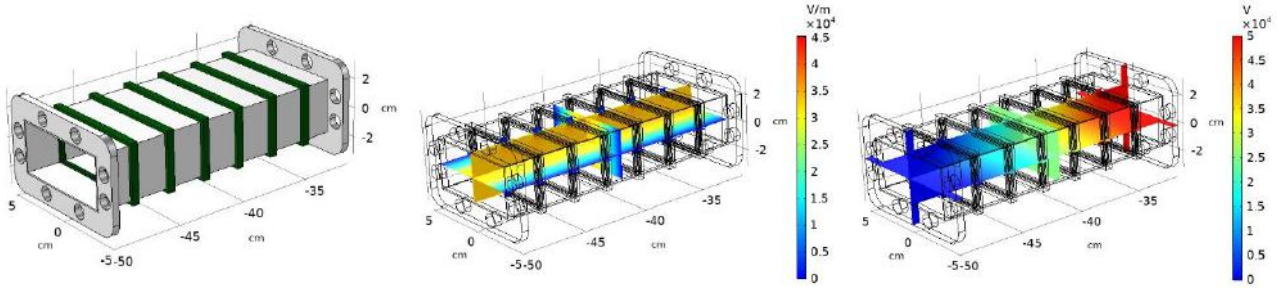

Fig. 6. Left) Schematic of high voltage barrier using G-10CR resin, center) variation of electric field and right) variation of electric potential.

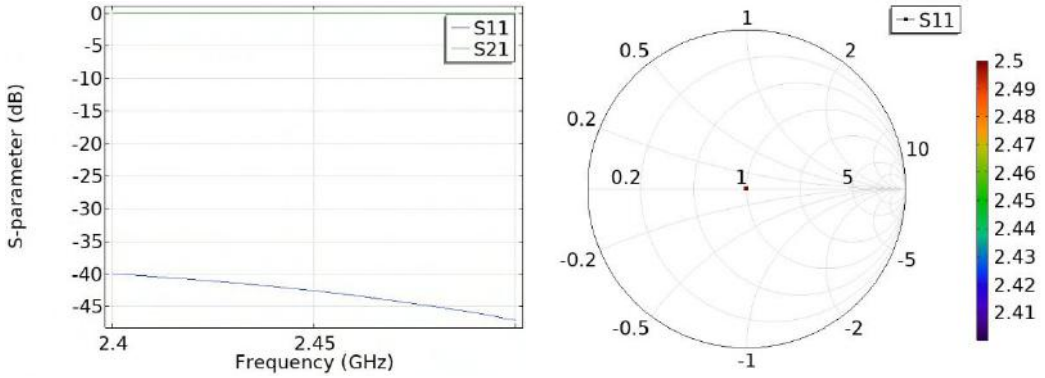

Fig. 7. Left) Changes of wave return loss (S11) and transmission loss (S21) of the high voltage barrier with a thickness of 5.8 mm and right) Polar display of return wave loss (S11) as a function of frequency

Conclusions

In this work, DC break, pressure window, ridged waveguide and plasma chamber have been designed and simulated by COMSOL Multiphysics to transmit the microwave power. The results show the 9.9 mm quartz pressure window maximize the forward transmission power to the cavity. The DC break is based on utilizing the insulating rings along the WR-284 waveguide, which has low wave return loss for a wide range of frequencies. A four-ridged waveguide is considered for impedance matching and electric field focusing.

The amplification of the electric field in the middle of cylindrical plasma chamber is satisfied with dimensions of Ø9 cm×10 cm.

References

[1] Jin, Q. Y., Liu, Y. G., Zhou, Y., Wu, Q., Zhai, Y. J. and Sun, L. T. (2021). RF and Microwave Ion Sources Study at Institute of Modern Physics.

[2] Jain, S. K., Sharma, D., Senecha, V. K., Naik P. A. and Hannurkar, P. R. (2014). Study of microwave components for an electron cyclotron resonance source: Simulations and performance. Sadhana. 39: 901–920.

[3] Roychowdhury, P. (2014). Design, Development and Characterization of High Current Electron Cyclotron Resonance Ion Source. Bhabha atomic research centre, Mumbai.

[4] Asadi Aghbolaghi, M., Abbasi Davani, F. et al. (2023). Design and comparing of high voltage break in wave transferring line of an ECR ion source. The 29th Iranian Nuclear Conference.

Investigating the effect of distance of e-1H two spin system on dynamic nuclear polarization by DNPSOUP (Paper ID : 1262)

Yadollahzadeh B.[1*], Razavinejad R. [1], Shahamat Y.[1], Mirzaei H.R. [2]

[1] Department of Physics, Faculty of Science, Imam Hossein Comprehensive University, Tehran, Iran
[2]Physics & Accelerators Research School, Nuclear Science and Technology Research Institute, Tehran, Iran

Abstract

The advantage of Nuclear Magnetic Resonance (NMR) over other spectroscopic methods is that it provides atomic-resolution for determining structures and is non-invasive; however, NMR spectroscopy is generally disrupted by poor sensitivity or low polarization. In an NMR experiment (1 GHz ,23.5 T magnet at room temperature), approximately polarization of protons is less than 0.01%. By contrast, for the same temperature and magnetic field strength, electrons have a polarization 658 times that of protons. Dynamic Nuclear Polarization (DNP) is a sensitivity enhancement technique used to enhance (NMR) signals by transferring polarization from unpaired electrons to nuclei of interest via microwave irradiation. Temperature, external magnetic field, distance between e-1H two spin and microwave field strength are the

important parameters on DNP mechanism. In this work, the effect of distance between e-1H two spin system on dynamic nuclear polarization was investigated by DNPSOUP.

Keywords: Nuclear Magnetic Resonance, Dynamic Nuclear Polarization, Microwave

Introduction

In 1953 Overhauser proposed that the large polarization of unpaired electrons could be transferred to neighboring nuclei by saturating the corresponding electron paramagnetic resonance (EPR) transition. The result of this process would be an enhancement of the signal intensities of the associated nuclear magnetic resonance (NMR) signals by a factor of (γ_e/γ_H) ~660 in the case of protons. The validity of this suggestion was vigorously debated until Carver and Slichter reported an experiment in which they polarized ^{7}Li [1]. The first DNP mechanism reported in insulating solids was the SE and was described by Jeffries [2, 3], and Abragam et al.[4]. Five years later, the mechanism of the cross-linking effect of DNP was observed by Kesnich [5] and subsequently discussed in more detail by Huang and Hill [6, 7] and Whelan [8, 9]. In the 1980s and early 1990s, efforts to incorporate DNP into magic angle spinning (MAS) and other solid-state NMR experiments were initiated by Wind et al [10].

There wasn't microwave sources operating above 40–50 GHz, these experiments were limited to low fields. In 1993 Becerra et al [11] introduced a gyrotron as a microwave source for DNP experiments at 5 Tesla (140 GHz for electrons), with the specific aim of developing an experimental approach that allows DNP at higher magnetic fields for new NMR experiments.

There are several simulation packages to the nuclear magnetic resonance. SPINEVOLUTION [12] is a software package for high performance NMR simulations, and in recent years DNP simulation capabilities were added to it. Second, SPINACH [13] is a broad collection of specific purposed simulation scripts within the MATLAB eco-system. The library of this code not only deals with DNP simulations but also covers NMR, EPR, MRI, etc. SIMPSON [14] is an excellent solid-state NMR simulation program, that performance and usability was good. Its DNP simulation features are currently being developed. GAMMA [15], a powerful magnetic resonance C++ library, provides basic tools to build any magneti resonance simulation software. It currently does not provide any DNP-ready functionalities. There also exists code developed for case-by-case DNP simulations using fixed parameters [16-20]. SPINEVOLUTION and SPINACH provide DNP simulation capabilities. However, SPINEVOLUTION, due to its proprietary

nature, the underlying assumptions and simulation logic are not available for customization, making it difficult to complement DNP theory developments. On the other hand, SPINACH requires a user to have former knowledge of MATLAB. Dynamic Nuclear Polarization Simulation Optimized with a Unified Propagator (DNPSOUP) was developed by Chen Yang et al at Massachusetts Institute of Technology. DNPSOUP is a command line software written in C++, and it is supplemented with a JavaScript graphical user interface for input file generation. [21].

The important effective parameters on DNP are temperature, external magnetic field, distance between e-^{1}H two spin and microwave field strength. In this work, the effect of distance between e-^{1}H two spin system on dynamic nuclear polarization was investigated by DNPSOUP. For this purpose, we investigate the Zeeman and microwave field profiles of OE, SE on contemporary continuous wave (CW). This paper was presented as follow: 1. DNP theory, 2. DNPSOUP details, 3. Simulation results and at last the conclusion were presented.

Theories

The general principle of DNP is that a higher level of polarization of the electron spins can be transferred to the surrounding nuclear spins upon microwave irradiation at or near the electron paramagnetic resonance (EPR) transitions. However, polarization transfer from electrons to nuclei is a complex phenomenon and can be broadly classified based on the number of coupled electron spins participating in the polarization transfer process to OE, SE Cross Effect (CE), Thermal Mixing (TM) (Fig.1). These mechanisms can occur alone or simultaneously, depending on the substance's properties.

These mechanisms divided into coherent and incoherent processes, which depending on the relative strengths of the terms in the Hamiltonian of the system and their contributions to the spin relaxation rates. In a coherent mechanism, μw pulses are used to drive a particular transition in the e-n system, such that the corresponding polarization oscillates between e and n spins. However, utilizing such coherent mechanisms requires high power and pulse phase control in microwave system to be implemented at high B_0 field . Incoherent DNP is achieved by saturation of selected EPR transitions of the polarizating agent (PA) to achieve a steady-state nuclear spin polarization that is higher than at thermal equilibrium.

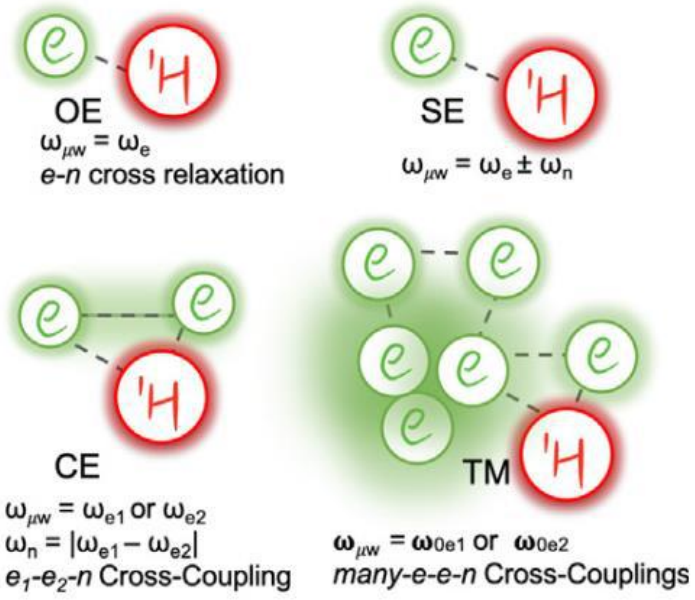

Figure. 8. Model system for four general DNP mechanisms: SE (e; n), OE (e; n), CE (2e; n) and TM (multi-e; n) with corresponding μw irradiation conditions [22]

Now, we will discuss DNP mechanisms within the incoherent regime. As shown in fig 1, the earliest known mechanism is the OE that involves saturation of the allowed single quantum electron spin transition in a coupled e-n spin system followed by e-n cross-relaxation. Another mechanism for enhancing nuclear spin polarization is the SE that relies on driving an e-n (forbidden) double quantum (DQ) or zero quantum (ZQ) transition, as illustrated in Fig. 1B, and is applicable to many different types of solids. However, these forbidden DQ and ZQ transitions become less probable at higher B_0, rendering SE inefficient [22, 23]

To explain in detail we focus on DNP in liquid free radicals, and then we present only a summary of the OE . As shown in Figure 2, the OE for two spins (an electron spin S = 1/2 and ^{1}H proton spin I = 1/2) is typically described by a Four-level energy diagram. Here, p is the electron spin relaxation rate, w_1 the proton spin relaxation rate, w_2 the double quantum relaxation rate and w_0 the zero quantum relaxation rate. The basic theory of the Overhauser enhancement is as follows: an RF alternating field (of angular frequency ω_e) saturates the electron spin relaxation, which creates a non-equilibrium population distribution of the electron spins. The electron spin polarization transfer to the proton spin by the electron-proton cross-relaxation. The proton magnetization is also enhanced.

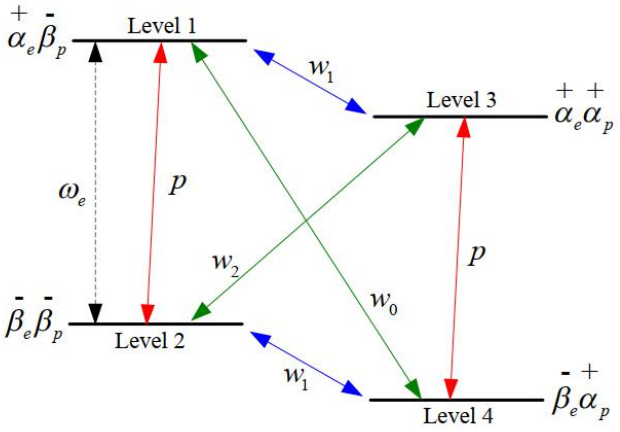

Figure. 9. Four-level energy diagram for an electron spin S = 1/2 coupled to a 1H proton spin I = 1/2.

The enhancement of the proton polarization, E, is defined as:

$$E = \frac{\langle I_z \rangle}{\langle I_0 \rangle} \approx 1 - \rho f s \frac{\gamma_e}{\gamma_p}$$

where $\langle I_z \rangle$ is the expectation value of the DNP, $\langle I_0 \rangle$ is its thermal equilibrium value, γ_e is the electron gyromagnetic ratio and ρ and f are, respectively:

$$\rho = \frac{\omega_2 - \omega_0}{\omega_2 + 2\omega_1 + \omega_0}$$

$$f = 1 - \frac{T_1}{T_{10}}$$

The coupling factor **ρ** is understood as the ratio of the electron-proton spin cross-relaxation rate (w_2 - w_0) and the proton spin relaxation rate due to the electrons (w_2 + 2w_1 + w_0). **ρ** expresses the efficiency of coupling between the electron and proton spins and ranges from -1 (pure scalar coupling) to 0.5 (pure dipolar coupling). For free radicals dissolved in solution, the coupling of the electron spins to solvent protons can be either scalar or dipolar, and hence, **ρ** can be safely assumed to be one.

The leakage factor **f** relates to the electron's ability to relax the proton spin and can be expressed in terms of the longitudinal relaxation times T_1 and T_{10} of the solvent in the presence and absence of the free radical, respectively. When a leakage factor is one that shows all relaxations of the protons are caused by electrons, whereas a leakage factor is zero, that shows all relaxations of the protons are from other sources. The saturation factor **S** is the degree of saturation of ESR, and varies from 0 to 1, depending on the power of

the applied RF electromagnetic field. Ideally, $S_{max} = 1$ and $f_{max} = 1$ can be safely assumed; therefore, $E_{max} = 1 + \frac{\gamma_e}{\gamma_p} \cong 660$. In other words, the amplitude of the FID signal can in theory be increased by 660 times. However, the theoretical increase E_{max} cannot be achieved for several reasons, one being that other paths of relaxation are present [24].

Dnpsoup

Dynamic Nuclear Polarization Simulation Optimized with a Unified Propagator (DNPSOUP) is a program which is an open source numerical software, it simulates spin dynamics for DNP. The software package utilizes a direct numerical approach using the inhomogeneous master equation to treat the time evolution of the spin density operator under coherent Hamiltonians and stochastic relaxation effects. DNPSOUP is a command line software written in C++, and it is supplemented with a JavaScript graphical user interface for input file generation. The code doesn't need any prior programming knowledge to running and also is open-sourced and fast. The code was developed using C++ for performance. The DNPSOUP code is consist of three modules: matrix, dnpsoup_impl, and dnpsoup_cli . Matrix is a linear algebra library. Dnpsoup_impl contains all the quantum mechanical calculations. Dnpsoup_cli is a command_line executable that handles input interpretation, task delegation, and then writing results to files. We chose JavaScript Object Notation (JSON) as input syntax. JSON is a lightweight data-interchange format. It is easy both for users to read and write, and for machines to parse and generate [25].

Simulations

In order to demonstrate the utility of the DNPSOUP software package, we provide examples of simulations of the Zeeman and microwave field profiles of several different CW DNP experiments. These include the SE and OE.

The most elementary spin system that will exhibit DNP is a simple e-^{1}H two spin system. Simulated field profile of solid effect and OE for an e-^{1}H two spin system illustrated in Fig. 3 That shows ^{1}H DNP-MAS enhancement field profiles obtained from sample containing the polarizing agents BDPA, at 9.4 T using 0.5 MHz Microwave field strength. The field profiles clearly show the expected SE enhancements at $\omega_{0S} \pm \omega_{0I}$ for BDPA radical. Note that the two SE DNP peaks are negative and positive SE corresponding to the zero quantum and double quantum SE transitions, respectively separated by twice the nuclear Larmor

frequency ($2\omega_{0I}$ = 800 MHz). A strong positive enhancement at the center of the field profile due to the OE with ZQ relaxation dominating and yielding a positive enhancement was observed. To simulate, we used $T_1^{ZQ} = 10s$ and $T_1^{DQ} = 10{,}6s$ to represent the ZQ and DQ double quantum relaxation timescales, respectively. Note that the magnitude and sign of the OE enhancement are affected by the difference between the ZQ and DQ relaxation rates $(\frac{1}{T_1^{ZQ}} - \frac{1}{T_1^{DQ}})$ as predicted by theory.A g-tensor of (2.00263, 2.00259, 2.00234) was used to estimate the electron in BDPA. The electron and ^{1}H were located at (0, 0, 0) and (0, 0, 5) in Å in Cartesian coordinate. T_{1e} and T_{2e} are 5 ms and 1µs, whereas T_{1n} and T_{2n} are 10 s and 5 ms respectively.

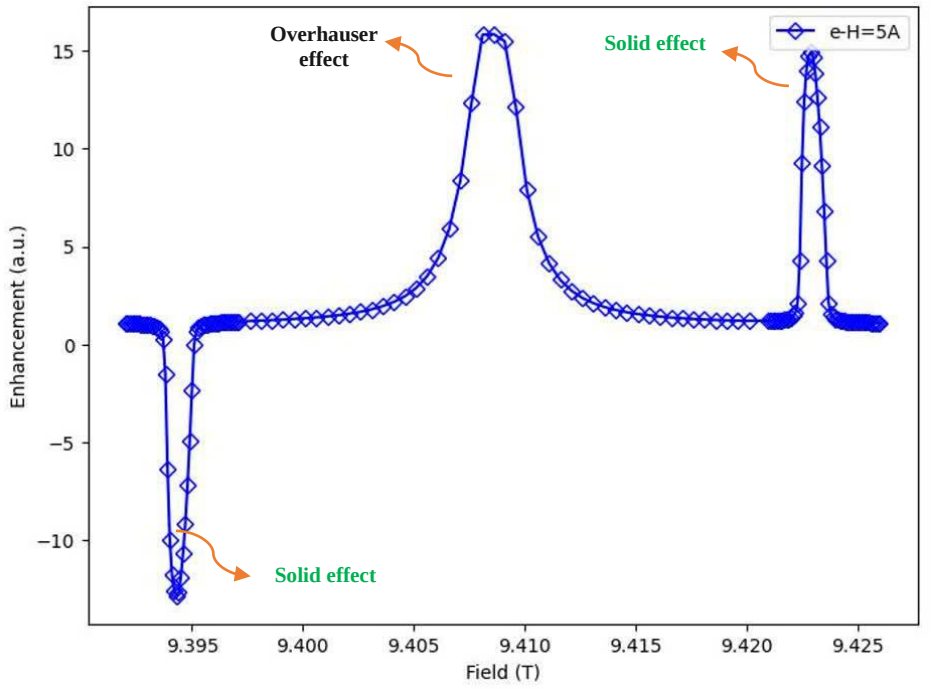

Figure.10. Simulated field profile of SE and OE for an e-^{1}H two spin system. ZQ relaxation constant of $T_1^{ZQ} = 10s$ and DQ relaxation constant of $T_1^{DQ} = 10.6s$ were used to demonstrate the OE. A 5-second CW microwave irradiation with $\frac{\omega_{1S}}{2\pi} = 0.5$MHz and 263.7 GHz center frequency was applied at MAS frequency of $\frac{\omega_r}{2\pi} = 8K$Hz.

In the following, in order to investigate the effect of the distance between e-^{1}H two spin system in 0.5 MHz Microwave field strength on the enhancement of the proton polarization in the OE and SE, three positions in Cartesian coordinates for proton and electron have been simulated. The electron was located at (0, 0, 0) and ^{1}H were located at three position (0, 0, 4) ,(0, 0, 5) and (0, 0, 6) in Å in Cartesian coordinate. Simulated field profile of solid effect and Overhauser effect illustrated in Fig. 4.

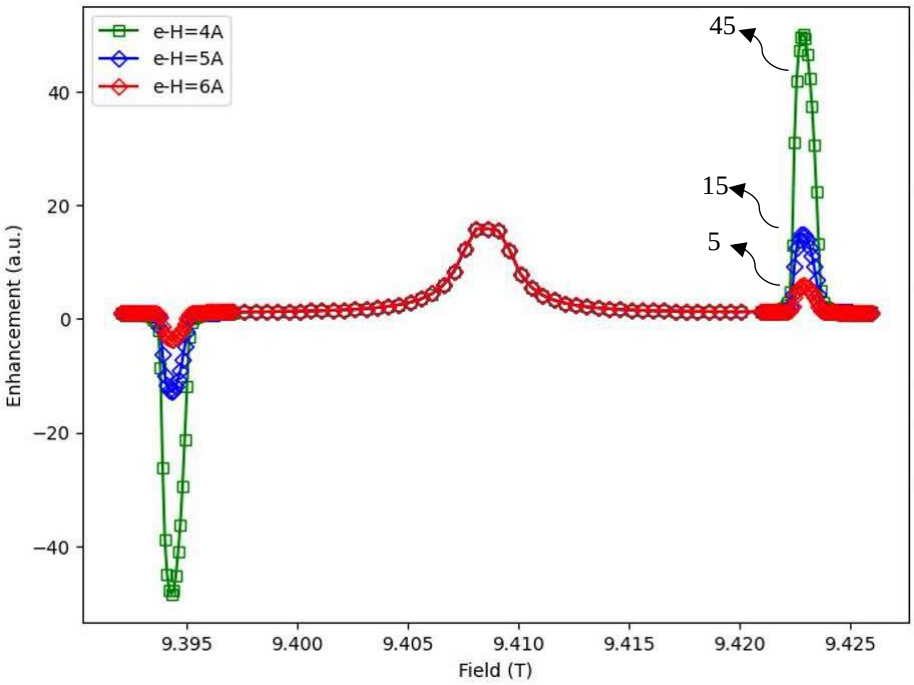

Figure. 11. Simulated field profile of SE and OE for an e-1H two spin system in three distances between the e-^{1}H. ZQ relaxation constant of $T_1^{ZQ} = 10s$ and DQ relaxation constant of $T_1^{DQ} = 10.6s$ were used to demonstrate the OE. A 5-second CW microwave irradiation with $\frac{\omega_{1S}}{2\pi} = 0.5$MHz and 263.7 GHz center frequency was applied at MAS frequency of $\frac{\omega_r}{2\pi} = 8K$Hz.

As it can be seen from the diagram in Figure 4, with the decrease of the distance between the e-^{1}H, there was no change in the enhancement of the proton polarization in the OE, but in the SE, with the decrease of the distance, we see an increase in the enhancement of the proton polarization.

For a distance of 6A between the e-^{1}H two spins, the enhancement of the proton polarization in the SE is about 6, and for a distance of 5A, this value is about 15, and for a distance of 4A, this value increases significantly and reaches 45.

Conclusions

In summary, The DNP effect was introduced in order to enhance (NMR) signals by transferring polarization from unpaired electrons to nuclei of interest via microwave irradiation. For the study and investigation of this effect, the DNPSOUP code was used. One of the important effective parameters, distance between e-^{1}H two spin system on dynamic nuclear polarization was simulated.

From the examination of Simulated field profile of SE and OE in three distances between the e-^{1}H, it was observed that with the decrease of the distance between the e-^{1}H, there was no change in the enhancement of the proton polarization in the OE, but in the solid effect, with the decrease of the distance, 6A, 5A and 4A we see an increase in the enhancement of the proton polarization 5,15 and 45 respectivly. This is because the OE was the first DNP mechanism proposed for systems with mobile electrons, such as metals and liquids, and also microwave power-dependent studies show that OE saturates at much lower power levels than SE in the same samples.

Acknowledgements

Acknowledgements of people, grants, funds, *etc.* should be placed here. The names of funding organizations should be written in full.

References

[1] T. Maly *et al.*, "Dynamic nuclear polarization at high magnetic fields," *The Journal of chemical physics,* vol. 128, no. 5, 2008.

[2] C. Jeffries, "Polarization of nuclei by resonance saturation in paramagnetic crystals," *Physical Review,* vol. 106, no. 1, p. 164, 1957.

[3] C. Jeffries, "Dynamic orientation of nuclei by forbidden transitions in paramagnetic resonance," *Physical Review,* vol. 117, no. 4, p. 1056, 1960.

[4] E. Erb, J.-L. Motchane, and J. Uebersfeld, "Effet de polarisation nucléaire dans les liquides et les gaz adsorbés sur les charbons," *Comptes Rendus Hebdomadaires Des Seances De L Academie Des Sciences,* vol. 246, no. 14, pp. 2121-2123, 1958.

[5] C. Whitehead, S. Tornabene, and G. Stafford, "The Polarization in Neutron-Proton Scattering at 77 MeV," *Proceedings of the Physical Society,* vol. 75, no. 3, p. 345, 1960.

[6] C. F. Hwang and D. A. Hill, "Phenomenological Model for the New Effect in Dynamic Polarization," *Physical Review Letters,* vol. 19, no. 18, pp. 1011-1014, 10/30/ 1967, doi: 10.1103/PhysRevLett.19.1011.

[7] C. F. Hwang and D. A. Hill, "New Effect in Dynamic Polarization," *Physical Review Letters,* vol. 18, no. 4, pp. 110-112, 01/23/ 1967, doi: 10.1103/PhysRevLett.18.110.

[8] D. S. Wollan, "Dynamic nuclear polarization with an inhomogeneously broadened ESR line. I. Theory," *Physical Review B,* vol. 13, no. 9, pp. 3671-3685, 05/01/ 1976, doi: 10.1103/PhysRevB.13.3671.

[9] D. S. Wollan, "Dynamic nuclear polarization with an inhomogeneously broadened ESR line. II. Experiment," *Physical Review B,* vol. 13, no. 9, pp. 3686-3696, 05/01/ 1976, doi: 10.1103/PhysRevB.13.3686.

[10] R. A. Wind, M. J. Duijvestijn, C. van der Lugt, A. Manenschijn, and J. Vriend, "Applications of dynamic nuclear polarization in 13C NMR in solids," *Progress in Nuclear Magnetic Resonance Spectroscopy*, vol. 17, pp. 33-67, 1985/01/01/ 1985, doi: https://doi.org/10.1016/0079-6565(85)80005-4.

[11] L. R. Becerra *et al.*, "A Spectrometer for Dynamic Nuclear Polarization and Electron Paramagnetic Resonance at High Frequencies," *Journal of Magnetic Resonance, Series A,* vol. 117, no. 1, pp. 28-40, 1995/11/01/ 1995, doi: https://doi.org/10.1006/jmra.1995.9975.

[12] M. Veshtort and R. G. Griffin, "SPINEVOLUTION: A powerful tool for the simulation of solid and liquid state NMR experiments," *Journal of Magnetic Resonance,* vol. 178, no. 2, pp. 248-282, 2006/02/01/ 2006, doi: https://doi.org/10.1016/j.jmr.2005.07.018.

[13] H. J. Hogben, M. Krzystyniak, G. T. P. Charnock, P. J. Hore, and I. Kuprov, "Spinach – A software library for simulation of spin dynamics in large spin systems," *Journal of Magnetic Resonance,* vol. 208, no. 2, pp. 179-194, 2011/02/01/ 2011, doi: https://doi.org/10.1016/j.jmr.2010.11.008.

[14] M. Bak, J. T. Rasmussen, and N. C. Nielsen, "SIMPSON: A general simulation program for solid-state NMR spectroscopy," *Journal of Magnetic Resonance,* vol. 213, no. 2, pp. 366-400, 2011/12/01/ 2011, doi: https://doi.org/10.1016/j.jmr.2011.09.008.

[15] S. A. Smith, T. O. Levante, B. H. Meier, and R. R. Ernst, "Computer Simulations in Magnetic Resonance. An Object-Oriented Programming Approach," *Journal of Magnetic Resonance, Series A,* vol. 106, no. 1, pp. 75-105, 1994/01/01/ 1994, doi: https://doi.org/10.1006/jmra.1994.1008.

[16] F. Mentink-Vigier, Ü. Akbey, H. Oschkinat, S. Vega, and A. Feintuch, "Theoretical aspects of Magic Angle Spinning - Dynamic Nuclear Polarization," *Journal of Magnetic Resonance,* vol. 258, pp. 102-120, 2015/09/01/ 2015, doi: https://doi.org/10.1016/j.jmr.2015.07.001.

[17] F. Mentink-Vigier, A.-L. Barra, J. van Tol, S. Hediger, D. Lee, and G. De Paëpe, "De novo prediction of cross-effect efficiency for magic angle spinning dynamic nuclear polarization," *Physical Chemistry Chemical Physics,* vol. 21, no. 4, pp. 2166-2176, 2019.

[18] K. R. Thurber and R. Tycko, "Theory for cross effect dynamic nuclear polarization under magic-angle spinning in solid state nuclear magnetic resonance: The importance of level crossings," *The Journal of chemical physics,* vol. 137, no. 8, 2012.

[19] K. O. Tan, C. Yang, R. T. Weber, G. Mathies, and R. G. Griffin, "Time-optimized pulsed dynamic nuclear polarization," *Science Advances,* vol. 5, no. 1, p. eaav6909, 2019, doi: doi:10.1126/sciadv.aav6909.

[20] K. O. Tan, M. Mardini, C. Yang, J. H. Ardenkjær-Larsen, and R. G. Griffin, "Three-spin solid effect and the spin diffusion barrier in amorphous solids," *Science Advances,* vol. 5, no. 7, p. eaax2743, 2019, doi: doi:10.1126/sciadv.aax2743.

[21] C. Yang, K. O. Tan, and R. G. Griffin, "DNPSOUP: A simulation software package for dynamic nuclear polarization," *Journal of Magnetic Resonance,* vol. 334, p. 107107, 2022.

[22] A. Equbal, S. K. Jain, Y. Li, K. Tagami, X. Wang, and S. Han, "Role of electron spin dynamics and coupling network in designing dynamic nuclear polarization," *Progress in Nuclear Magnetic Resonance Spectroscopy,* vol. 126, pp. 1-16, 2021.

[23] K. Nowak, "The gyrotron for DNP-NMR spectroscopy: A review," *Bulletin of the Polish Academy of Sciences Technical Sciences,* vol. 70, no. 1, pp. e140354-e140354, 25.02.2022 2022, doi: 10.24425/bpasts.2022.140354.

[24] J. Ge *et al.*, "Overhauser geomagnetic sensor based on the dynamic nuclear polarization effect for magnetic prospecting," *Sensors,* vol. 16, no. 6, p. 806, 2016.

[25] C. Yang, K. Ooi Tan, and R. G. Griffin, "DNPSOUP: A simulation software package for dynamic nuclear polarization," *Journal of Magnetic Resonance,* vol. 334, p. 107107, 2022/01/01/ 2022, doi: https://doi.org/10.1016/j.jmr.2021.107107.

ICNST 2024 International Conference on Nuclear Science and Technology
6- 8 MAY 2024 | Isfahan, Iran

Feasibility study of neutron kinematic reconstruction using the time-of-flight data of BINA scintillators (Paper ID : 1263)

Ramazani-Sharifabadi R. Correspondent[1*], Mahjour-Shafiei M. Co-Author[2], Ramazani-Moghaddam-Arani A. Co-Author[3]

[1]*Physics & Accelerator School, NSTRI, PO Box 14395-836, Tehran, Iran*

[2]*Department of physics, Uiversity of Tehran, North-Kargar St., Tehran, Iran*

[3]*Department of nuclear physics. Faculty of Physics, University of Kashan, Kashan, Iran*

Abstract

Neutrons leave only a trace in the BINA detection system, and therefore, extracting neutron kinematic parameters through ADC signals are practically not feasible. The MWPC detector can also detect only the hit position of charged particles. In this article, a new approach is presented based on the time-of-flight information of neutrons originated from the three-body break-up channel of deuteron-deuteron scattering at 130 MeV to extract neutron kinematic parameters. To achieve this, the X and Y coordinates, and subsequently, scattering angles (polar and azimuthal) of neutrons are extracted using the hit position of particles in scintillator bars along with their time-of-flight (TOF) information. Having the information of the scattering angles of neutrons and kinematical parameters of one of the charged particles, one can extract the neutron energy using momentum and energy conservation laws. To validate the proposed approach, the kinematics of protons obtained through the aforementioned approach were compared with those obtained using merely ADC signals. Identifying and reconstructing the kinematics of final-state neutrons allows us to analyze different hadronic channels of *dd* scattering process in which neutrons are detected as a final-state particle. As a result, Coulomb effects and isospin dependency of nuclear potential can be investigated.

Keywords: Neutron detection, Deuteron-Deuteron scattering, Three-Body break-up channel, Time-of-Flight information

Introduction

The strong nuclear force is a fundamental building block in nuclear physics. As the Van der Waals force is an effective Coulomb interaction acting between molecules, the nuclear force is similarly an effective interaction acting between nucleons. It is common to interpret the interactions between nucleons by the exchange of mesons. Analog to the exchange of massless photons describing successfully the electromagnetic interaction, the meson-exchange theory developed by Yukawa in 1935 successfully

describes the interaction between two nucleons with the exchange of virtual mesons between them [1]. To date, several phenomenological nucleon-nucleon (NN) potentials have been derived based on Yukawa's model. Some of them are successfully linked to the fundamental theory of quantum chromodynamics (QCD) through chiral perturbation theory (χPT). Precision measurements obtained from NN scattering data are strikingly well described by these modern NN potentials, albeit with several parameters of the potentials fitted to the data.

Applying high-precision NN potentials to describe systems composed of at least three nucleons shows some discrepancies between theoretical calculations and experimental data. Rigorous Faddeev calculations based on high-precision NN potentials for the binding energy of triton underestimate the experimental data [2] by 10%. *Ab-initio* calculations of the differential cross sections in elastic nucleon-deuteron scattering show large discrepancies with experimental data in the minima of the cross sections. These observations indicate the presence of the thre-nucleon force (3NF) effect. Green's function Monte Carlo calculations based on the AV18 NN potential complemented with the IL7 three-nucleon potential give a better description of the experimental data for the binding energies of light nuclei [3]. The inclusion of 3NF effects can partly resolve the deficiencies observed in the differential cross section in elastic N*d* scattering as well [4-6]. Results of polarization observables after inclusion of 3NFs essentially do not change in the line of covering the discrepancies implying that spin-dependent parts of 3NF effects are not yet well understood [7]. In the last two decades, a systematic study of 3NFs has been initiated through a Dutch-Polish collaboration providing an extended experimental database for testing theoretical models [8-16].

Identifying final-state particles e.g. neutrons and charged particles and reconstructing their kinematics allows us to study isospin dependencies as well as Coulomb effects in four-nucleon systems. This paper presents the results of a dedicated analysis performed to study feasibility of the neutron detection in the plastic scintillators of BINA, and consequently, establish a novel approach to register events in which neutrons are detected as final-state particles. Each step is validated using the protons of the three-body break-up in the role of neutrons in this channel. Once neutron information is extracted, one can extend the analysis of four-body systems to parts of the phase space where neutrons are involved. Knowing neutron kinematics makes it possible also to study isospin and Coulomb effects directly.

Experimental Setup

The BINA, Big-Instrument for Nuclear-Polarization Analysis, is nearly a 4π detection system invested for studying dynamical properties of few-nucleon systems like 3NF effects. The BINA setup is shown in Fig. 1. The setup consists of two parts, the forward wall and the backward ball. The forward wall consists of a multi-wire proportional chamber (MWPC) to determine the scattering angles of the charged particles, twelve vertically-mounted plastic ΔE scintillators with the thickness of 2 mm, and ten horizontally-mounted E scintillators with the thickness of 12 cm. The E scintillators are mounted in a cylindrical shape with the center of the cylinder matching the interaction point of the beam with the target. The particle identification was done using the time-of-flight (TOF) information of the E scintillators. Photomultiplier tubes (PMTs) were mounted on both sides of each E scintillator. ADC and TDC Signals from these PMTs are used to extract the energy and TOF of the scattered particles. The resolution of TOF is around 0.5 ns. Also, a small offset of 0.28 ± 0.13 pA in the readout of the current was observed.

Fig. 1. BINA detection system with 12 cm-thick scintillators mounted on a sylinrical shape pointing the target position and the backward ball including 149 phoswich scintillators.

Since neutrons are not seen by MWPC, time-of-flight information of the charged particles was used to construct a virtual MWPC to extract the position of the neutrons left a trace in the E scintillators. In this case, MWPC was used as a veto-detector to discriminate neutrons from charged particles. Also, the majority of final-state neutrons deposit only a fraction of their energy in the E scintillator bars, and therefore, the amplitude of corresponding ADC signals are not sufficient to show actual energy of neutrons. An alternative

solution is using conservation laws to reconstruct the neutron energy. A detailed description of the BINA including all elements involved in the experiment was given in [17].

Analysis method

In the analysis of the three-body break-up channel, we would like to find the correlation between the energy of the deuteron and the proton for the desired configuration, (θ_d, θ_p, φ_{12}). All in all, there are nine variables involved in the three-body break-up process, namely θ_i, φ_i, and E_i where i refers to the deuteron, proton, and neutron. Considering the momentum and energy conservation laws, measuring five variables of two particles are enough to obtain the other kinematical variables unambiguously. The energy, polar and azimuthal angles of the deuteron is measured using the BINA detection system, but, the kinematical parameters of neutron can not be measured directly using BINA.

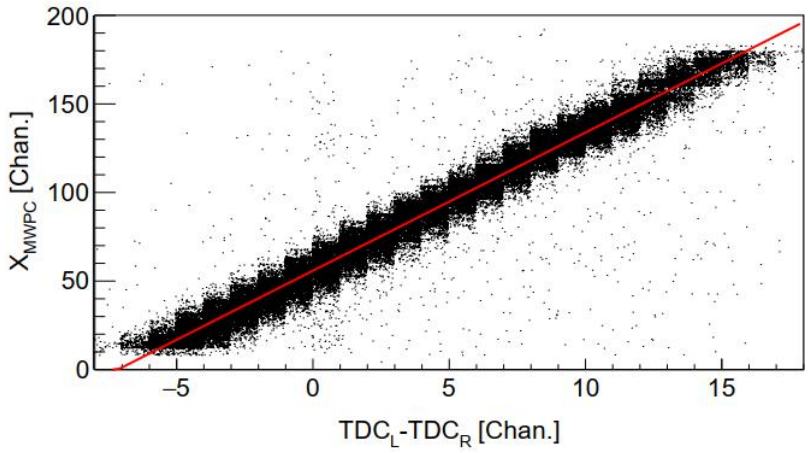

Fig. 2. The X coordinate of the MWPC versus the difference between the left (TDC_L) and the right (TDC_R) of the E scintillator number 1. The solid line is a line fit through the spectrum.

The MWPC can not detect the neutron particles, and therefore, their position (X and Y coordinates) are extracted using the TOF data and the hit positions registered in the E scintillators of the forward wall. The X coordinate is obtained using the difference between the right TDCs (TDC_R) and left TDCs (TDC_L) obtained from the mounted PMTs in both sides of each scintillator. Then, we define the variable $\Delta TDC = TDC_L - TDC_R$ which is proportional to the X coordinate. Measured X coodinates of MWPC is used to find this proportionality. A typical correlation between the X coordinate using the MWPC for the charged particles and that using ΔTDC for E scintillator number 1 is presented in Fig. 2. The solid line which is obtained by a line fit through the middle of the spectrum is used to extract the X coordinate of the detected

particles. The resolution of the reconstructed X coordinate has been found to be around 2.9 cm. To extract the Y coordinate, the middle of the Y position of each scintillator is used as the Y coordinate of the hit that was detected in that scintillator. Since the width of the horizontal *E* scintillators is 9 cm, the resolution of the Y coordinate should be 4.5 cm.

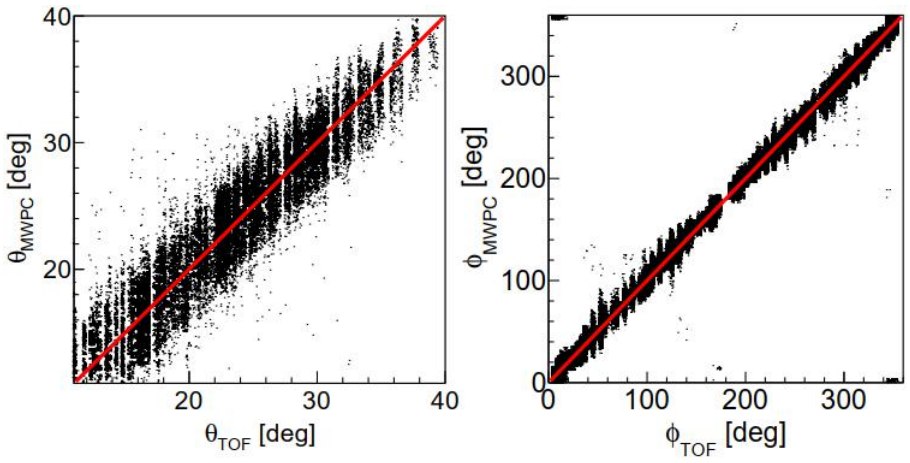

Fig. 3. Left (Right) panel, comparison between the measured polar (azimuthal) angle using the TOF information of the *E* scintillators of the forward wall and those measured by the MWPC. The solid lines are the bisector line.

Having the X and Y coordinates of each hit, one can calculate the polar and azimuthal angles of the particles detected in the forward wall. The procedure of extracting scattering angles is validated via comparing the results with the hit information of the charged particles obtained from the MWPC, Fig 3. This figure illustrates the consistency of the two approachs (using the TOF information and the the MWPC) in measuring the polar angle (left panel) and the azimuthal angle (right panel. The solid lines show the bisector line. The angular resolution of both reconstructed polar and azimuthal angles are around 2°. The agreement between the two methods for charged particles is very good, lending confidence to apply the TOF-based method for position determination of neutrons.

To exclude MWPC inefficiencies for charged particles, we are interested in the energy correlation between the particles seen by MWPC (Y-axis) and those particles which had no trace in the MWPC (X-axis), see Fig. 4. It shows that the majority of events involve neutrons since the spectrum peaks towards lower neutron energies corresponding to events for which a small fraction of energy is deposited and not registered by the MWPC. Only a few percent of all candidate neutron events deposited a large energy in the *E* scintillator. These events correspond to charged particles for which the MWPC was inefficient. Therefore, by utilizing

a graphical cut we can exclude most of the misidentified charged particles not seen by the MWPC for further analysis.

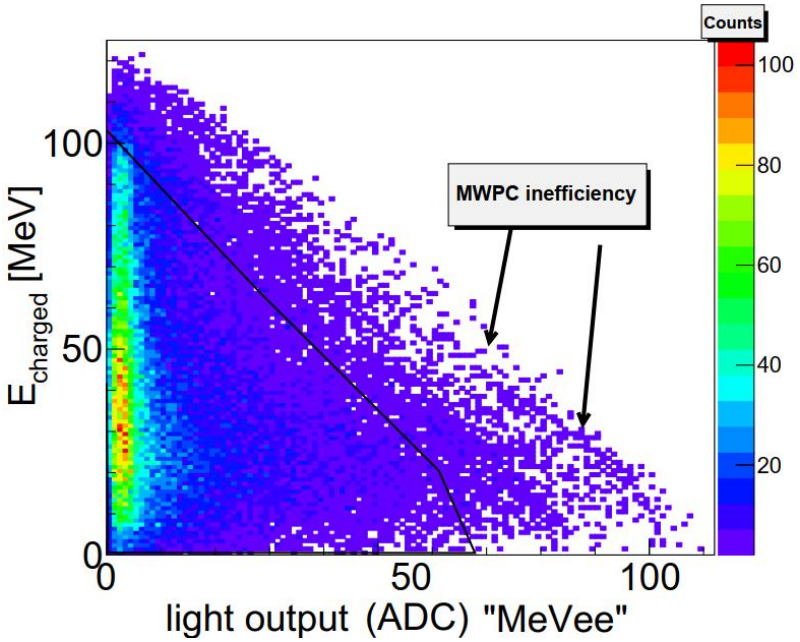

Fig. 4. The energy correlation between the particles seen by MWPC (Y-axis) and those particles which had no trace in the MWPC (X-axis). The solid line shows the graphical cut used to exclude misidentified charged particles not seen by the MWPC. "MeVee" indicates that the X-axis is proportional to the light output.

Results and discussion

In this reaction, the kinematical variables (energy and scattering angles) of the deuteron are measured directly using the detector components of BINA. Also, the polar and azimuthal angles of the neutron are obtained using the reconstruction of the neutron position, as discussed before. Solving the four equations, corresponding to the four conservation laws, using the numerical package, TMinuit, in ROOT gives the other kinematical variables such as the energy of the neutron. This procedure is also evaluted using the protons of the three-body break-up ignoring their MWPC information. Figure 5 shows the energy of the proton at the target position (E_p) measured by BINA after energy calibration versus the reconstructed energy of the proton ($E_{p,Rec.}$) using the conservation laws. It indicates that the reconstructed energy is compatible with the measurement done by BINA.

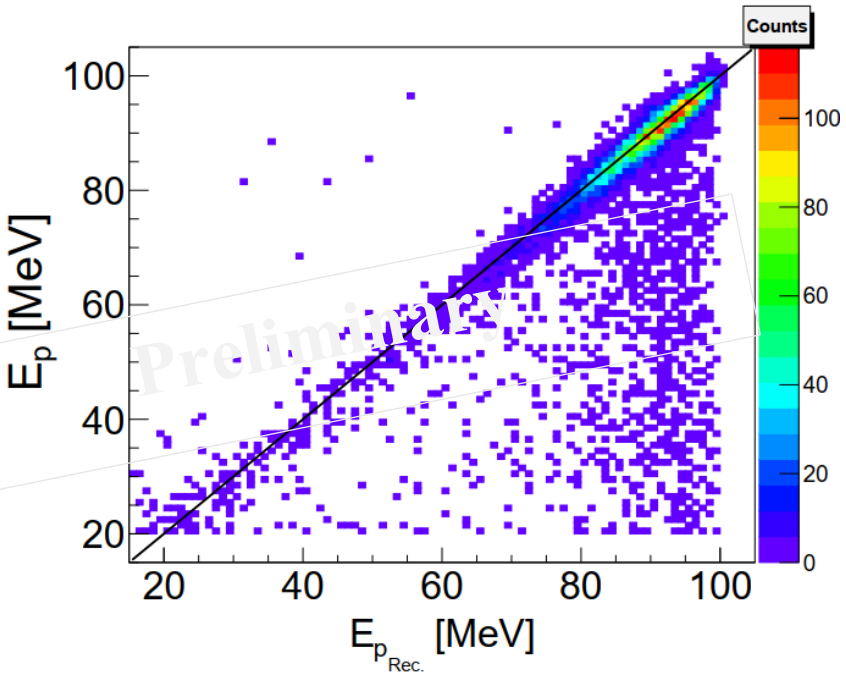

Fig. 5. The energy of the proton at the target position (E_p) measured by BINA after energy calibration versus the reconstructed energy of the proton ($E_{p,Rec.}$) using the conservation laws. The solid line is the bisector line. The tail under the bisector line belongs to events in which particles have undergone hadronic interactions.

The S-curve is defined based on the correlation between the energies of two particles. For convenience in the analysis, the energies of the deuteron and neutron are also expressed by two new variables, namely *S* and *D*. The variable *S* is the arclength along the *S*-curve with the starting point at the minimum energy of the deuteron. The variable *D* is the distance between the point (E_d, E_n) and the kinematical *S*-curve. The S-curve of the deuteron-neutron case is constructed using the rconstrcuted energy of neutron. As a cross check, protons of the three-body break-up is used again to act as a neutron. The right panel in Fig. 6 represents the reconstructed *S*-curve of the configuration ($\theta_d = 28^\circ$; $\theta_p = 28^\circ$; $\varphi_{dp} = 180^\circ$) for the ^{2}H(***d***; *dp*)*n* reaction. The solid line shows the expected kinematical locus for this configuration. In this case, the energy of the deuteron (E_d) is measured by BINA after energy calibration and the energy of the proton ($E_{p,Rec.}$) is obtained using the conservation laws. The left panel of Fig. 6 shows the conventional *S*-curve of the ^{2}H(***d***; *dp*)*n* reaction for the same configuration that the energy of both deuterons and protons are measured by BINA. The results shown in the right panel of Fig. 6 demonstrate that we correctly applied energy and momentum conservation laws to each event. Also, note that the data do not perfectly fall on top of the expected *S*-curve (solid line). This is because the data are selected for a finite bin in each configuration whereas the conservation laws are applied for each event. With this energy-reconstruction method, we are also able to extract *S* for each event.

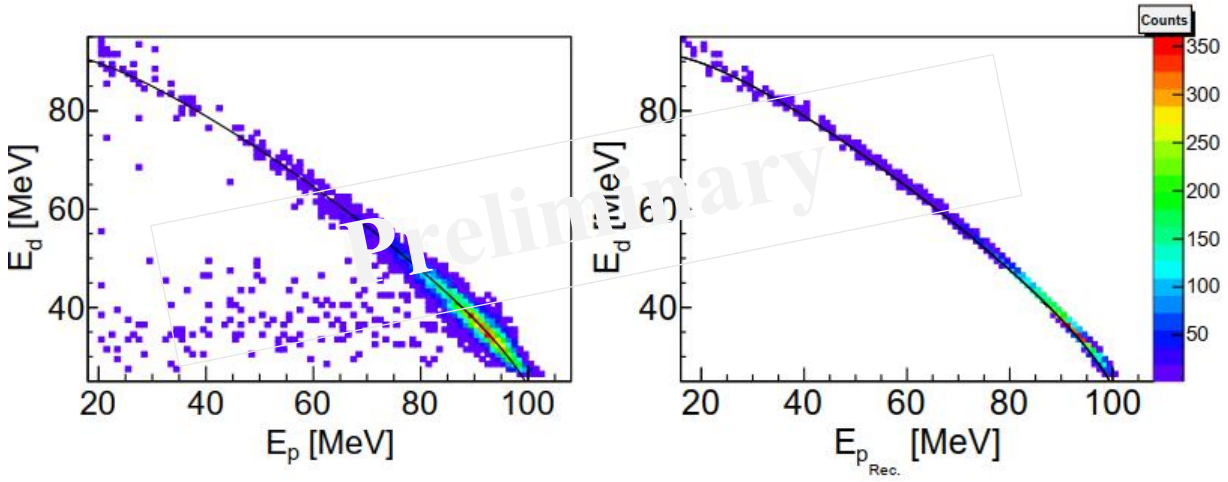

Fig. 6. The left panel shows the normal *S*-curve of the configuration (θ_d = 28°; θ_p = 28°; φ_{dp} = 180°) for the ^{2}H(***d***; *dp*)*n* reaction where both energies of the proton and deuteron are measured with BINA. The solid line shows the expected kinematical locus for this configuration. The right panel shows the corresponding reconstructed *S*-curve. In this case, the energy of the deuteron (E_d) is measured by BINA after energy calibration and the energy of the proton ($E_{p,Rec.}$) is obtained using the conservation laws.

Conclusions

Neutron-detection feasibility was investigated by plastic scintillators of BINA. Since the neutron-detection efficiency of the thick *E* scintillators of BINA was around 10%, a novel approach was exploited to reconstruct the neutron kinematics using Time-of-Flight information of the particles detected in the forward wall of BINA. A virtual MWPC was constructed by finding a correlation between the measurements of the MWPC of BINA and the corresponding hit-position information of the particles obtained by their TOF information. Then, the position and the scattering angle of the neutron was measured by the virtual MWPC. Since the ADC signals of PMTs obtained from the trace of neutrons in the scintillators were not sufficient to measure the actual energy of the neutron, the TOF information of the particles, and the momentum and energy conservation laws were used to reconstruct the energy of the final-state neutron, and subsequently, the corresponding S-curve.

Acknowledgements

The authors acknowledge the work by the cyclotron and ion-source groups at KVI for delivering a high-quality beam used in these measurements. The present work has been performed with financial support from the "Nederlandse Organisatie voor Wetenschappelijk Onderzoek" (NWO).

References

[1] Yukawa, H. (1935). *Proc. Phys. Math. Soc. Jpn. 17,* p. 48.

[2] Witala, H. (2010). *Few Body Syst. 49, 61*.

[3] Pieper, S. (2001). *Phys. Rev. C 64, 1*.

[4] W. H. a. G. W, (2008). *Eur. Phys. J. A 37 87*.

[5] Witala, H. (1998). *Phys. Rev. Lett. 81, 11*.

[6] Ermisch, K. (2005) *Phys. Rev. C 71, 064004*.

[7] Kalantar-Nayestanaki, N. (2012) *Rep. Prog. Phys. 75*.

[8] Ermisch, K. (2001) *Phys. Rev. Lett. 86, 5862*.

[9] Ciepal, I. (2019) *Phys. Rev. C 100, 024003*.

[10] Mohammadi-Dadkan, M. (2020) *Eur. Phys. J. A 56, 81*.

[11] Ramazani-Moghaddam-Arani, A. (2008). *Phys. Rev. C 78, 014006*.

[12] Ramazani-Moghaddam-Arani, A. (2011). *Phys. Rev. C 83, 024002*.

[13] Ramazani-Sharifabadi, R. (2019). *Eur. Phys. J. A 55, 177*.

[14] Ramazani-Sharifabadi, R. (2020). *Eur. Phys. J. A 56, 221*.

[15] Ramazani-Sharifabadi, R. (2021). *Eur. Phys. J. A 57, 119*.

[16] Tavakoli-Zaniani, H. (2020). *Eur. Phys. J. A 56, 62*.

[17] Mardanpour, H. (2008). Ph.D. thesis, University of Groningen.

ICNST 2024 International Conference on Nuclear Science and Technology
6- 8 MAY 2024 | Isfahan, Iran

Developing a 6 MeV linear electron accelerator (Paper ID : 1267)

H. Sayyar[1], H. Noori[1], M. Yahaghi[1], M. Khosravani[1], M. Monshizadeh[1], H. Saravani[1], A. Ghalehasadi[1], R. Roozehdar Mogaddam[1], E. Javadi[1], O. Haghighi[1], M. S. Islami[1], A. Farokhizadeh[1], A. Taheri[1,2*] and S.P. Shirmardi[1,2]

[1]Iran Radiation Application Development Company (IRAD Co.) – Atomic Energy Organization of Iran, Tehran – I.R. of Iran, PO Box: 14395-836
[2]Radiation Application Research School, Nuclear Science and Technology Research Institute, Tehran, Iran, PO Box: 14395-836

Abstract

The electron linear accelerator, known as LINAC, is one of the most widely used accelerators. The LINAC have made significant contributions to various fields such as basic sciences, applied sciences, medicine, and security. This article discusses the successful testing of an indigenously designed and constructed S-band 6 MeV linear electron accelerator. The designed LINAC components include a modulator (LINAC starter), RF radio frequency power source (magnetron), waveguide components to transmit RF power to the accelerator part, including circulator, adapter, waveguides, and dummy load, the accelerator tube (including electron gun, target, and ion pump), cooling system and insulating gas system, control system, and display. The system and its components, such as modulator signal shape, forward and reflected waves and other parameters for cold test, were thoroughly tested and the successful results are described in detail. The main objective behind designing and fabricating this LINAC is to develop an X-ray non-destructive testing (NDT) system.

Keywords: Linear electron accelerator, RF waves, magnetron, circulator, waveguide.

Introduction

The linear electron accelerator, commonly known as LINAC, is a widely utilized accelerator in various industries [1], medical fields [2], and research applications [3]. LINACs are used for purposes such as cancer treatment, production of radiopharmaceuticals, sterilization of medical equipment, and non-destructive testing (NDT) [3]. There are over 30,000 particle accelerators in operation globally across these sectors [4]. Radiofrequency (RF) linear accelerators typically operate within a frequency range of 100 MHz to several GHz [5]. In medical and industrial settings, LINACs primarily operate in the S-band frequency range of 2-4 GHz [6].

The concept of sequentially-pulsed drift tubes, which is fundamental to the development of LINACs, was introduced by Ising in 1924 [7]. Nassiri et al. provide a detailed account of the construction history of these accelerators [8]. Initial efforts in constructing a LINAC in Iran were reported by Ghasemi et al., utilizing a klystron-based RF source with a maximum power of 2.5MW [9]. Klystrons, known for their high frequency and high-power capabilities, are ideal for generating necessary energy in particle accelerators through enhancement of RF signals using resonant cavities and electron manipulation within a vacuum [10].

X-band LINACs have been the focus of research due to their compact size and higher frequencies [11, 12]. Some studies have explored the design of LINACs for use in cargo x-ray inspection systems [13, 14]. Ongoing experiments aim to develop proton LINACs for various applications, including material processing and medical uses [15, 16].

The current project is centered on developing a laboratory LINAC with a standing-wave (SW) structure operating at a frequency of 2998 MHz in $\pi/2$ mode. The objective is to achieve a beam energy of 6 MeV.

MATERIALS AND METHODS

The LINAC design includes components such as a modulator (the accelerator starter), RF power source (magnetron), waveguide elements (circulator, adapter, waveguides, dummy load) for RF power transmission to the accelerator part, the accelerator tube (comprising electron gun, target, ion pump), cooling system, insulating gas system, control system, and display. A schematic and image of these components are illustrated in Figure 1. Additional components of the accelerator encompass peripheral equipment like an appropriate electrical panel, grounding, workbench, safety features, and industrial necessities.

In LINACs, electron acceleration initiates from the modulator, serving as a pulse generator to convert three-phase electricity into suitable pulses for powering the magnetron. The magnetron, when stimulated by the input pulse, generates RF waves at a frequency of 2998 Hz with a maximum power of 2.5 MW. These waves are conveyed to the accelerating tube via the circulator, enhancing the energy of electrons emitted from the cathode within the tube. Subsequently, when these electrons collide with the target in the tube, X-rays are produced. Apart from the acceleration tube, the other components in the linear electron accelerator are largely similar.

Two types of LINACs exist based on accelerating tubes: traveling-wave accelerators (TW) and standing-wave accelerators (SW). Due to the absence of a suitable shield, the modulator underwent testing by substituting an equivalent resistance with a 3 MW capacity instead of the accelerator tube, with parameters such as forward and reflected waves being evaluated. Following the establishment of an appropriate biological shield, an active test (hot test) for the accelerator will be conducted in the near future. Cold tests include measuring some of the parameters, signal shape of the magnetron and reflected wave measurements.

Fig. 1. Schematic view and picture of the completed radio frequency line.

In the following section, the components of the designed electron accelerator are described:

The modulator converts AC line power into high voltage pulse power, involving a control module, external power supplies, power charging module, and switching section. The charging module, a PFN circuit, stores electrical power using capacitors and inductors. The final output pulse is 10 kV square, with adjustable PRF period (40 to 400 Hz).

The magnetron is a vacuum tube that produces high-power electromagnetic wave pulses with frequencies ranging from a few hundred megahertz to several gigahertz. Its anode is a copper cylinder, while the cathode is a hollow cylinder of emitting materials, mainly barium oxide. In this study, an e2v MG5193 magnetron was used. The output is a radio frequency pulse with a maximum power of 2.5 megawatts and a frequency of 2998 MHz. The connection between the magnetron and the modulator is shown in figure (2).

Fig. 2. Connections between the magnetron and the modulator

Magnetron operation requires a permanent magnetic field for electron movement, which can be adjusted by an electromagnet. The intensity of the magnetic field increases with intensity, and water is used as cooling agent for LINAC's electromagnets. A 1500 Gauss electromagnet can adjust the required magnetic field.

- The automatic frequency adjustment system ensures the radio frequency wave output from the magnetron remains at the tube resonance frequency, preventing temperature and waveguide impedance changes from affecting the resonant frequency and resulting in a stable standing wave in the accelerator.

- The electron gun power supply generates the electron beam, with current passing through the filament affecting the number of electrons emitted. Other power sources include the vacuum ion pump, electromagnet of the magnetron, and filament magnetron. The cathode voltage is 10-15 kV in pulse form with a frequency corresponding to PRF. Other sources of System power supplies are as follows, the power source of the vacuum ion pump is 3.5 to 4.2 kV DC (adjustable), The power source of the electromagnet of the magnetron is 20 volts DC and 20 amps, Filament magnetron 9-Volt DC 8.5-Amp power supply.

- Pulse transformer: The main pulse voltage output from the modulator must be increased in a transformer. This work is done in a pulse trans. The transformer output is the main power supply of a 48 kV pulsed magnetron with a current of 110 amps and a maximum width of 4.2μs.

- The circulator is a crucial component in telecommunications, transmitting signals in one direction and preventing signal return to the original generator. It injects output waves into the acceleration tube, preventing damage to the magnetron.

- Dummy load: dummy load is a modified and tapering waveguide system used to effectively absorb the power of the radio frequency wave returned from the circulator. In this system, carbon is cemented and is used with other carbon compounds such as silicon carbonate as a radio frequency wave absorber.

- Cooling system: An air-cooled compression chiller is used to cool the equipment in the LINAC system. After cooling in the chiller, the water is pumped to a collector with eight outlets for use in the heat sources of the device (magnetron, electromagnet, transformer, dummy load, circulator, ceramic, electron gun, and target). After cooling the heat sources, water is collected in the outlet collector and pumped to the chiller. To ensure the constant flow of water, flow switches have been placed in the water paths.

- Gas injection system: Due to the use of high voltages in the LINAC system and to prevent sparking inside the structure of the radio frequency power transmission, waveguides, adapter, dummy load, and circulator of the accelerator are filled with sulfur hexafluoride gas at a pressure of about 26 psi.

The intended vacuum for the designed accelerator is in the range of$10^{-8}mbar$.To revive and maintain it, an ion pump has been used.

Results and discussion

A magnetron equivalent resistance was used to perform the modulator test. The magnetron equivalent resistance (figure 3) was connected to the system according to the diagram in figure (4). According to the signal measured on the oscilloscope, the voltage value is about 35 kV, and the current is about 80 amperes.

Fig. 3. Constructed magnetron equivalent resistance

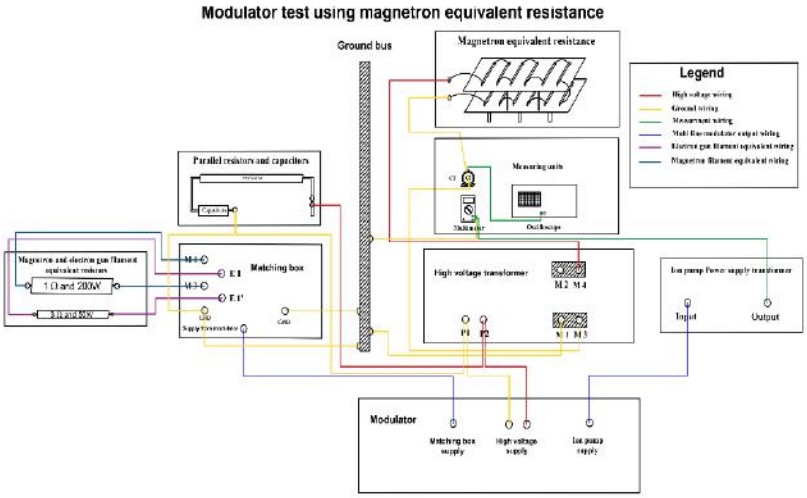

Fig. 4. Modulator using constructed magnetron

In Figure (5), the output pulse of the modulator is shown on the equivalent resistance load, where the green line is read by the high voltage probe and the yellow line is read by the Current Transformer.

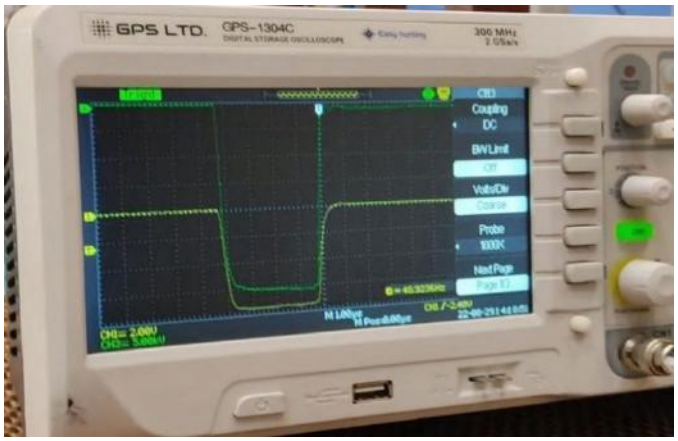

Fig. 5. Shape of the output pulse of the modulator on the equivalent resistance load. Green channel read by the high voltage probe and yellow line read by the Current Transformer

As can be seen in the figure (5), the modulator output is 35 kV with a current of 80 amps. Accelerator output results for the cold test are given in Table 1. The results of the cold test show that the modulator is capable of feeding the magnetron.

Table 1. Parameters of accelerators for cold test

parameters	value
Heater voltage	**7.2-10.8V**
Cathode voltage	**35 kV**
Cathode current	**80A**
Duty Cycle	**0.001**
Magnetron filament current	**9A**
Magnetron filament voltage	**8.5V**
Pulse width	**2~5 µs**
PRF	**40~400 Hz**

The acceleration tube is the main part of a radio frequency accelerator. It can be said that all the parts of a LINAC are peripheral tools for starting and ensuring the correct operation of this part. In the commercial radio frequency electron accelerator, all stages of electron generation, acceleration, and conversion to X-rays are done in this part. The electron in the electron gun is produced with energy of several tens of kilo-electron volts, and it gains energy along the cavities of the acceleration tube, and after impacting the target, it produces X-rays through the bremsstrahlung process. The exact design of the holes, the material of the target, and the electron gun are the most important challenges in making this part.

In the next step, to test the waveguide line along with the magnetron, and due to the lack of a proper shield, a 3 MW resistance load was used instead of the tube. The signal of the magnetron and the forward and reflect wave in the waveguide line were observed and reported as shown in figure (6).

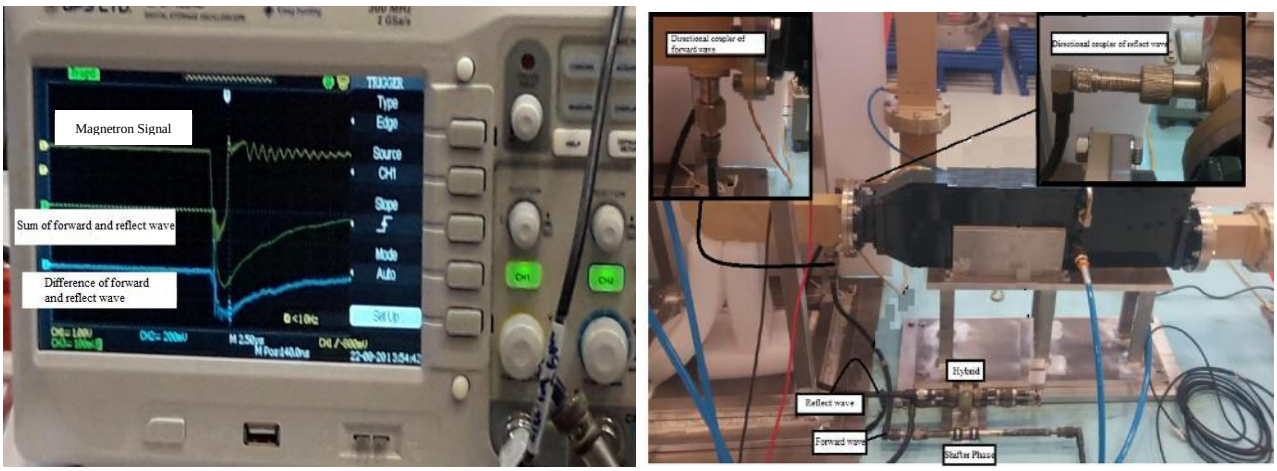

Fig. 6. Shape of the output pulse of the modulator on the equivalent resistance load. Green channel read by the high voltage probe and yellow line read by the Current Transformer.

The signal on the equivalent resistance load shown in figure (5) and the signals on the waveguide line shown in figure (6) show that the test was successful. As can be seen in figure (5), the shape of the signal is rectangular and from figure (6), it can be seen that the sum of forward and reflected waves and difference of forward and reflected waves have the same magnitude, so the reflected wave is ignorable. It shows that all forward waves are absorbed in the dummy load. The results have been tested repeatedly and in several time periods to ensure stability of the system. In the next steps of the project, and after providing the appropriate protection to extract X-rays and also the design and construction of a suitable collimator, imaging, and radiography (industrial CT scan) will be done.

Conclusions

To address the demand for electron accelerators in the country, we have designed and constructed a linear electron accelerator. Extensive cold tests have been successfully carried out, evaluating the modulator pulse, magnetron pulse, forward and backward waves, and synchronization between the gun and magnetron. These tests, along with other measured parameters, have confirmed that the LINAC meets all essential performance criteria for operation. In the near future, following the implementation of proper safety protocols for X-ray extraction and the setup of an appropriate collimator, imaging and radiography procedures will be performed.

References

[1] Kutsaev SV, Agustsson R, Arodzero A, et al (2021). Linear accelerator for security, industrial and medical applications with rapid beam parameter variation, Radiation Physics and Chemistry 183:109398.

[2] Ghalehasadi A, Şahiner E, Ashrafi S, et al (2021). Photoneutron dose and flux determination of a typical LINAC by MCNP simulation. Radiation Detection Technology and Methods 5:627–632.

[3] Kutsaev S V. (2021). Novel Technologies for Compact Electron Linear Accelerators (Review), Instruments and Experimental Techniques 64:641–656.

[4] Lim H, Kang SK, Kim HC, et al (2020). Compact Integration and RF Commissioning of the C-Band 9-MeV Electron Linear Accelerator at the Dongnam Institute of Radiological & Medical Sciences. Journal of the Korean Physical Society 76:622–627.

[5] Seeman, J. (2013). 7.1 General Introduction on Linear Accelerators: Design and Principles of Linear Accelerators and Colliders. Accelerators and Colliders, 183-185.

[6] Hanna SM Applications of X-band technology in medical accelerators. In: Proceedings of the 1999 Particle Accelerator Conference (Cat. No.99CH36366). IEEE, pp 2516–2518.

[7] Ising G (1924). Arkiv för Matematik, Astronomi och Fysik 18 (1).

[8] Nassiri A, Chase B, Craievich P, et al (2016). History and Technology Developments of Radio Frequency (RF) Systems for Particle Accelerators. IEEE Trans Nucl Sci 63:707–750.

[9] Ghasemi F, Abbasi Davani F, Lamehi Rachti M, et al (2015). Design, construction and tuning of S-band coupler for electron linear accelerator of institute for research in fundamental sciences (IPM E-linac). Nucl Instrum Methods Phys Res A 772:52–62.

[10] Min S-H, Kwon O, Sattorov M, et al (2019). Low-level RF control of a klystron for medical linear accelerator applications. AIP Adv 9 (2).

[11] Kutsaev SV, Agustsson R, Arodzero A, et al (2021). Compact X-Band electron linac for radiotherapy and security applications. Radiation Physics and Chemistry 185:109494.

[12] Mishin A V (2005). Advances in X-band and S-band linear accelerators for security, NDT, and other applications. In: Proceedings of the 2005 Particle Accelerator Conference. IEEE, pp 240–244.

[13] Mittal KC, Yadav V, Bhattacharjee D, et al (2011). Performance of the 9 MeV RF linac for cargo scanning. In: Proceedings of the DAE-BRNS Indian particle accelerator conference.

[14] Chae MS, Lee BN, Kim JH, et al (2019). Characterization of a Radiation Source for a Container Inspection System Based on a Dual-Energy RF Linac, Journal of the Korean Physical Society 74:642–648.

[15] Chan KCD, Lawrence GP, Schneider JD (1998). Development of RF linac for high-current applications, Nucl Instrum Methods Phys Res B 139:394–400.

[16] Zhang Y, Fang W-C, Huang X-X, et al (2021). Radio frequency conditioning of an S-band accelerating structure prototype for compact proton therapy facility, Nuclear Science and Techniques 32:64.

ICNST 2024 International Conference on Nuclear Science and Technology
6- 8 MAY 2024 | Isfahan, Iran

Enhancement of proton energy in target normal sheath acceleration for the rear concave target (Paper ID : 1328)

Somayeh Rezaei[1*], Mohammad Jafar Jafari[1]

[1]Plasma and Fusion Research School, Nuclear Science and Technology Research Institute, Tehran, Iran

Abstract

The most common and experimentally convenient approach for proton laser acceleration is the target normal sheath acceleration (TNSA) mechanism. Tuning the laser and target parameters can lead to achieve optimal conditions for proton acceleration. In this regard, changing the target geometry is another way in which can somehow help to improve the acceleration performance. In this work, by focusing on the single-layer target and changing the behind geometry of the target, where the sheath field is formed; the performance of proton acceleration in mechanism TNSA has been studied. For this purpose, two-dimensional particle in cell (PIC) simulation code has been used to compare the energy spectrum in two cases of the target with rear flat surface and with rear shaped one. Al target is used with thickness range of micrometer and the laser intensity is near$10^{20}W/sm^2$ for the Gaussian pulse shape. The simulation results show an increase in the proton cutoff energy when the target rear side has concavity compared to the normal state.

Keywords: Proton acceleration- TNSA- Target rear side- sheath field

INTRODUCTION

After the first observations of laser proton beam acceleration up to energies of several megaelectron volts, extensive research has been done in this field[1] . Considering the acceptable and desirable characteristics of the accelerated proton beam, including the brightness of energy distribution and short pulse width, as well as its applications in homogeneous heating[2], neutron production[3], fast ignition[4] and proton therapy[5]; It is very important to improve this method as much as possible. In particular, the required energy of the proton beam for use in hadron therapy is 80-260 MeV, which currently the minimum required energy (80 MeV) can be provided by the proton laser acceleration mechanism[6]. So far, various models have been presented to describe the physics of laser interaction with the target[7-9]. In the simplest and most common model called target normal sheath field acceleration (TNSA), first hot electrons are produced during the interaction of the laser pulse with the target[10]. This electron population moves along the target with a temperature of several megaelectron volts and causes ionization of the target[11]. By separating the electron

population from the target ions, a charge separation field is formed, and protons are accelerated in this field. The amount of proton beam energy depends on the amplitude of the formed electrostatic field, density distribution and energy distribution of hot electrons[12]. The models governing proton acceleration by TNSA method were widely developed numerically between 2000-2010. For example, the isothermal plasma expansion model[7], the adiabatic plasma expansion[8], the quasi-static model[13] and the layered target model [14] have been investigated that in all cases, the goal was determining the dependence of the maximum proton energy and the shape of the energy spectrum on the primary parameters. With the development of models, its results became closer to experimental results, however, due to the limitations of analytical methods in recent years, computational codes have been used to approximate and predict experimental results.

So far, many simulation[15] and experimental[16] studies have been carried out on investigating the effect of laser parameters, such as energy, intensity, pulse width, spot size, and also target parameters [17, 18]. Still, further development is needed to improve the quality of the proton beam as well as its cut- off energy in order to be efficient in its applications. In this work, we have investigated the effect of the target behind geometry on the acceleration performance in the TNSA acceleration scheme using 2D particle-in-cell (PIC) simulations. A target with a concave geometry in behind has been considered and its results is compared with the reference case of a flat target. In the second part, the basic of TNSA theory and in the third part, the simulation results are discussed. Finally at the end the conclusion is summed up.

Research Theory

During the interaction of the high-intensity laser pulse with the target, hot electrons with the energy of several megaelectron volts are produced and spread along the target. After the electrons are removed from the behind surface of the target, an electrostatic potential is created at the boundary between the vacuum and the target. This leads to the ionization of the target, and thus the acceleration of the protons from the back surface of the target in the electrostatic field. Due to the formation of a sheath field perpendicular to the target behind surface, this mechanism is called TNSA. A schematic of electron cloud formation and proton acceleration with TNSA mechanism is shown in Figure 1.

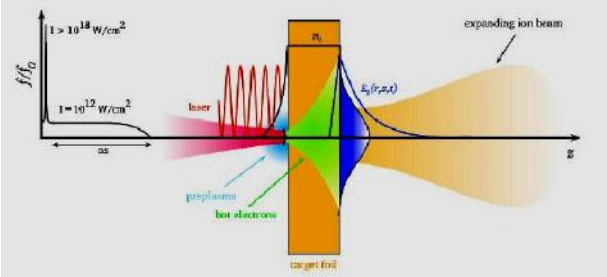

Figure 1. Schematic of the TNSA mechanism. A thin target foil with a thickness of 5-50 μm is subjected to high intensity

laser radiation. [6].

Various models have been proposed to describe ion laser acceleration. In the first and simplest model presented by Mora in 2003, the effects of charge separation in collisionless plasma expansion into vacuum have been investigated[7]. In this model, the temperature of the particles is considered constant during expansion (isothermal model), the plasma is placed in a semi-infinite space at the start time (t=0) and its boundary conditions are as follows.

$$t=0:\begin{cases} n_i = n_{i0} & x<0 \\ n_i = 0 & x>0 \end{cases} \qquad (1)$$

In this relation, ni is the ion density at each moment and ni 0 is the ion density at the first time. In addition, ions are considered cold and electrons with Boltzmann temperature distribution.

$$n_e = n_{e0} \exp\left(\frac{-e\phi}{k_B T_e}\right) \qquad (2)$$

Here, n_e is the electron density and n_{e0} is the same in the initial conditions, T_e electron temperature, e electron charge, k_B Boltzmann's constant and ϕ electrostatic potential. Also, plasma is neutral

($n_{e0} = Zn_{i0}$) and at infinity the conditions $\phi(-\infty = 0)$, $n_e(-\infty) = n_{e0}$, are established. In this approach, by numerically solving the continuity equations:

$$(\frac{\partial}{\partial t} + v_i \frac{\partial}{\partial x}) n_i = -n_i \frac{\partial v_i}{\partial x}$$
$$(\frac{\partial}{\partial t} + v_i \frac{\partial}{\partial x}) v_i = -\frac{Ze}{m_i} \frac{\partial \phi}{\partial x} \quad (3)$$

and Poisson's equation:

$$\varepsilon_0 \frac{\partial^2 \phi}{\partial x^2} = e(n_e - Zn_i) \quad (4)$$

The electric field in the ion front and the maximum velocity of ions is equal to:

$$E_{front} = \sqrt{2} k_B T_e / e\lambda_D \quad (5)$$

$$v_{max} \simeq 2c_s \ln(\tau + \sqrt{\tau^2 + 1}) \quad (6)$$

In the above relations T_e, n_{e0} are temperature and electron density, v_i is the ion velocity, $c_s = (Zk_B T_e / m_i)^{1/2}$ ion sound velocity, $\tau = \omega_{pi} t$, $\omega_{pi} = (n_{e0} Ze^2 / m_i \varepsilon_0)^{1/2}$ plasma ion frequency and $\lambda_D = \sqrt{\frac{\varepsilon_0 k_B T_e}{n_e e^2}}$ [7].

As can be seen from equation (5), the amplitude of electrostatic field depends only on the temperature and electron density. This field as long as the temperature of the electrons is high and in other words, during the time period of the laser pulse; will persist and decrease as the ion front expands behind the target. The important result of this model is the energy spectrum and the cutt-off energy of the ions, which is predicted by the following relations[7].

$$E_P \simeq 2k_B T_e.[\ln(\frac{\omega_{pp}\tau_L}{\sqrt{2e_E}} + \sqrt{1+\frac{\omega_{pp}^2\tau_L^{22}}{2e_E}})]^2 \quad (7)$$

$$\frac{dN_p}{dE_p} = \frac{n_{i0}t}{\sqrt{m_p}}\frac{1}{\sqrt{E_p}}.\exp(-\sqrt{\frac{2E_p}{k_B T}}) \quad (8)$$

Where, E_P the maximum of proton energy, $\omega_{pp} = \sqrt{\frac{n_e e^2}{\varepsilon_\circ m_p}}$ proton frequency of plasma, τ_L laser duration m_p proton mass e_E Napier's constant.

According to equation (7), the speed of ions diverges logarithmically with time, which is not consistent with the experimental results. In fact, in this model (isothermal), the temperature of the electrons is considered constant, while this assumption is reasonable only during the time of the laser pulse duration, and not valid in the later times. So that, the electrons lose their energy and get cold. Therefore, in a more complete model, the adiabatic expansion of plasma was investigated by Mora in 2005 [29]. In this model, instead of considering the semi-infinity of the plasma, a finite slab with length L is considered for the plasma. The boundary conditions in this model are as follows:

$$\begin{cases} n_i = n_{i\circ} = \frac{n_{e0}}{Z} & -\frac{L}{2} < x < \frac{L}{2} \\ n_i = \circ & x > \frac{L}{2} \ \ \& \ \ x < -\frac{L}{2} \end{cases} \quad (9)$$

The governing equations in this model are the same as before (equations 2-4) with the difference that the electron energy transfer equation has also been added. Herer unlike the isothermal model, the ion velocity does not increase to infinity with time and reaches a saturation value depending on the plasma thickness as follow:

$$v_{final} = 2c_s(0.32\,L/\lambda_{D0} + 4.2) \quad (10)$$

Where, L is the plasma thickness, cs the ion sound speed and λD0 is the deby length at the initial moment of the plasma. As can be seen from equations (5) and (10), the created electrostatic field and the final energy of the ions depend on the density profile and the initial electron temperature of the target. Therefore, the initial conditions of the target during the interaction of the main pulse have a decisive role in the acceleration performance, especially the cut-off energy (maximum energy) and the energy spectrum of the proton beam. On the other hand, due to the presence of pre-pulse in laser facilities, which interacts with the solid target before the arrival of the main pulse; the main factor of changing target parameters is the laser pre-pulse. Although, with the pre-pulse interaction, the front surface of the solid target is ionized and forms a plasma, which increases the absorption of electron energy, it should be noted that depending on the energy, intensity and width of the pre-pulse; the rear side of the target can be destroyed. In this case, it will weaken the field created behind the target and ultimately reduce the acceleration efficiency [30]. On the other hand, the rear density profile of the target may improve the acceleration process. In order to investigate this idea, in this work, by changing the initial rear geometry of the target from normal shape to the concave, the characteristic of the accelerated beam has been examined. In the follow section, two-dimensional simulation results have been analyzed.

Simulation

In this work, the two-dimensional version of the particle simulation code, Smilei [19] is used. The parameters used in the code are as follows: The laser pulse of wavelength 0.8μm is p-polarised with intensity 2.1×10^{20} W/cm ^{2} . The Gaussian profile is used both in space and time, with the focal spot at the waist w_0 = 5 μm and pulse duration (FWHM) =40 fs. The simulations are performed with a fully ionized quasi-neutral Al target comprising of Al^{+9} ions, protons & electrons, localized between 0 and 6 μm along the x-axis and 0 to 30 μm along the y-axis. The number density of Al and H are $40n_c$ and $4n_c$, respectively. Becouse of getting close to the reality a performed exponential density gradient has been considerd in front surface of the target for two cases of rear sharp density and rear conccave density (see figure 2). The simulation box extends from 0 μm to 100 μm along the x-axis (i.e. direction of laser propagation) and from 0 μm to 30 μm along the y-axis.

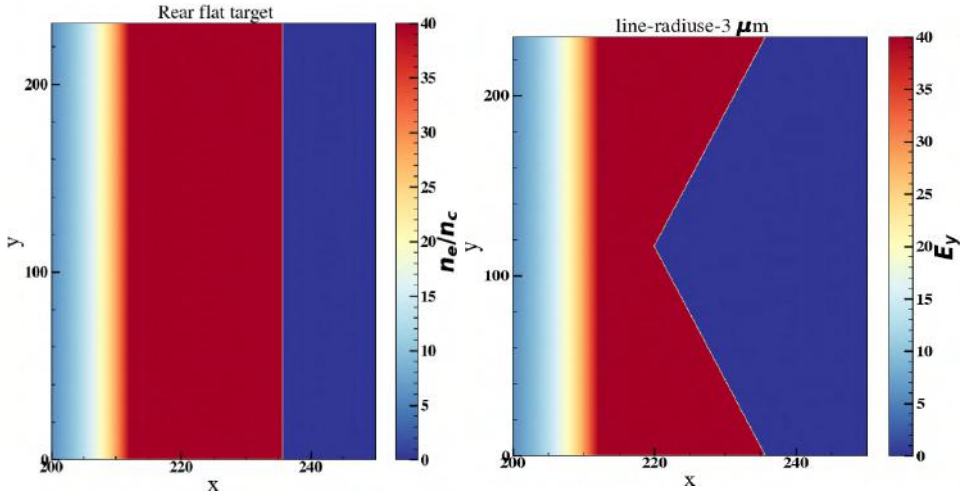

Fig. 2. Target geometries for flat rear side, and for concave rear sides with different groove and height (parameter d and h represent groove and height respectively)

In order to investigate the effect of the rear density gradient of the target on the acceleration of the proton beam, by changing this parameter and performing simulations, the results have been compared. Figure 2 shows the initial profile of the targets. As can be seen from Figure 2, the front of the target reaches the maximum density with an exponential profile (with 0.81 μm scale length) for both targets. And the back side of the target is considered flat and concave. The proton energy spectrum for different initial conditions of the target and laser intensities are shown in Figure 3.a

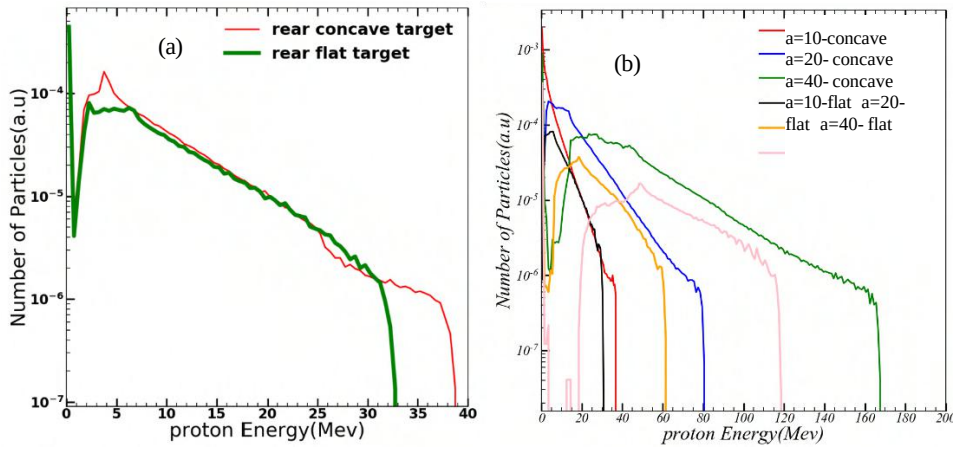

Fig. 3. Proton energy spectrum distribution of flat and for concave target for a) a=10 and b) a=10, a=20 and a=40

It can be seen from Figure 3.a that by changing the gradient behind the target from a flat surface to a concave form, the proton cut-off energy changes from 33 to 40 MeV, which is a significant change. However, the shape of the energy distribution of both cases is approximately the same. This is due to the same parameters of the target in front side, which causes the production of hot electrons with the same energy and density. While, the gradient at the rear side of the target causes a change in the longitudinal electric field (see Figure 4), resulting in the acceleration of protons. The difference in proton cut-off energy in two targets with rear flat and concave surface will increase with enhancing the laser intensity (see figure 3.b)

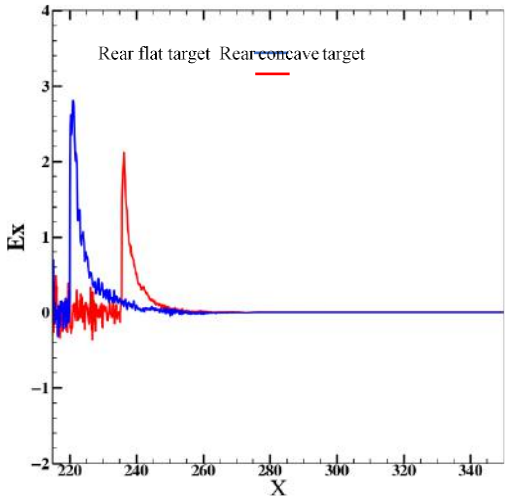

Fig. 4. Electrostatic field (E_x)for rear flat and concave targets

Conclusions

Considering the wide range of laser accelerated proton beam applications, research is still going on to improve the acceleration performance. In this regard, the efficiency of the acceleration process can be improved by changing the parameters of the laser as well as target. In this work, by changing the geometry of target rear side from flat shape to concave shape, the trend of the proton energy spectrum has been investigated and the results have been compared. The 2D-simulations show that by changing the density gradient to concave form, the amplitude of the electric field can be increased, and this leads to an increase about 20% in the proton cut-off energy. The results of this work show that by changing the target parameters, the acceleration efficiency can be improved without enhancing initial laser energy.

References

[1] Snavely, R., et al., Intense high-energy proton beams from petawatt-laser irradiation of solids.

[2] Physical review letters, 2000. 85(14): p. 2945.

[3] Patel, P., et al., Isochoric heating of solid-density matter with an ultrafast proton beam. Physical review letters, 2003. 91(12): p. 125004.

[4] McKenna, P., et al., Broad energy spectrum of laser-accelerated protons for spallation-related physics. Physical review letters, 2005. 94(8): p. 084801.

[5] Roth, M., et al., Fast ignition by intense laser-accelerated proton beams. Physical review letters, 2001. 86(3): p. 436.

[6] Bulanov, S. and V. Khoroshkov, Feasibility of using laser ion accelerators in proton therapy.

[7] Plasma Physics Reports, 2002. 28: p. 453-456.

[8] Roth, M. and M. Schollmeier, Ion acceleration-target normal sheath acceleration. arXiv preprint arXiv:1705.10569, 2017.

[9] Mora, P., Plasma expansion into a vacuum. Physical Review Letters, 2003. 90(18): p. 185002.

[10] Mora, P. Thin-foil expansion into a vacuum. in AIP Conference Proceedings. 2006. American Institute of Physics.

[11] Grismayer, T. and P. Mora, Influence of a finite initial ion density gradient on plasma expansion into a vacuum. Physics of Plasmas, 2006. **13**(3).

[12] Wilks, S., et al., Energetic proton generation in ultra-intense laser–solid interactions. Physics of plasmas, 2001. **8**(2): p. 542-549.

[13] Wilks, S., et al., Absorption of ultra-intense laser pulses. Physical review letters, 1992. **69**(9): p. 1383.

[14] Hatchett, S.P., et al., Electron, photon, and ion beams from the relativistic interaction of Petawatt laser pulses with solid targets. Physics of Plasmas, 2000. **7**(5): p. 2076-2082.

[15] Passoni, M. and M. Lontano, Theory of light-ion acceleration driven by a strong charge separation. Physical review letters, 2008. **101**(11): p. 115001.

[16] Albright, B., et al., Theory of laser acceleration of light-ion beams from interaction of ultrahigh- intensity lasers with layered targets. Physical review letters, 2006. **97**(11): p. 115002.

[17] Wang, D., et al., Enhanced proton acceleration from an ultrathin target irradiated by laser pulses with plateau ASE. Scientific reports, 2018. **8**(1): p. 2536.

[18] Zimmer, M., et al., Analysis of laser-proton acceleration experiments for development of empirical scaling laws. Physical Review E, 2021. **104**(4): p. 045210.

[19] Margarone, D., et al., Laser-driven proton acceleration enhancement by nanostructured foils.

[20] Physical review letters, 2012. **109**(23): p. 234801.

[21] Neely, D., et al., Enhanced proton beams from ultrathin targets driven by high contrast laser pulses. Applied Physics Letters, 2006. **89**(2).

[22] Derouillat, J., et al., Smilei: A collaborative, open-source, multi-purpose particle-in-cell code for plasma simulation. Computer Physics Communications, 2018. **222**: p. 351-373.

ICNST 2024
International Conference on Nuclear Science and Technology
6- 8 MAY 2024 | Isfahan, Iran

Electrostatic field evolution of different rear triangular targets in TNSA mechanism (Paper ID : 1331)

Mohammad Jafar Jafari[1], Somayeh Rezaei[1*]

[1]*Plasma and Fusion Research School, Nuclear Science and Technology Research Institute , Tehran, Iran*
*corresponding e-mail: somayeh.rezaei@gmail.com

Abstract:

The first and most feasible developed model for proton laser acceleration is target normal sheath acceleration (TNSA) mechanism. The effective factors in the formation of the sheath field and its amplitude are the density and temperature of hot electrons. In addition, the gradient of the rear surface of the target can affect the acceleration duration time as well as the quality of output beam. Since the sheath field formed behind the target is responsible for forward accelerated proton, therefore, the density gradient can play an important role in the proton acceleration performance. In this work, by changing the curvature target rear side from a flat surface to a concave surface, the space-time pattern of the sheath field formed behind the target has been investigated and simulated. For this purpose, two-dimensional particle simulation code (PIC) has been applied. The amplitude of the sheath field for different parameters of depth and height of concavity has been analyzed and plotted in space-time coordinates. The simulation results confirm the existence of an optimal point for the gradient behind the target.

Keywords: Proton acceleration- TNSA- Rrear side density gradient- Electrick field space-time profile

INTRODUCTION

The use of chirp pulse amplification (CPA) technology in high-power laser systems has made a huge leap in the field of laser interaction with matter [1]. By increasing the laser intensity up to order 1018 W/cm2 and applying to the target, the electron motion in the electromagnetic field becomes relativistic which will open a new field of physical phenomena. Today, the laser systems that have been launched or are being built around the world during the last few years have provided pulses with a maximum power of one PW [2, 3]. The laser intensity that can be achieved with such laser power reaches more than1021W/cm2. At such high intensities, the amplitude of rising edge of laser pulse is large enough to convert the solid material into the plasma state before the laser pulse reaches its peak. Then the main part of pulse interacts with fully ionized and heated plasma. Due to the collective effects of released electrons, such a plasma can produce electric fields with an amplitude of more than 1012 V/m in which is several times stronger compared to the electric field of normal accelerators (108 V/m) and as a result, the length of the particle acceleration path

to reach the energy of several hundred megaelectron volts is about one millimeter [4]. This is significantly reduced compared to common accelerators, which reach several tens of meters in length. Therefore, high-intensity lasers are expected to be a suitable alternative to conventional RF linear accelerators. During the last decade, a significant increase in the energy of accelerated particles has been observed in experiments conducted in the field of laser-plasma interaction. In this process, the laser pulse energy is effectively used to produce electron beams with kinetic energy in the range of several 100 kV to more than 200 MeV [5]. In the second stage, the gamma ray with energy a few MeV[6], proton beam [7] and heavy ions [8] up to energies of several MeV are produced. The generation of proton beams with energy of several megaelectron volts during the interaction of high- intensity laser pulses with thin solid targets has attracted much attention due to the unique properties of such beams. In fact, independent of the target species, a strong proton signal is observed in these experiments [9]. The origin of these protons is water vapor and hydrocarbon pollution on the target surfaces. So far, a lot of research has been done with the aim of improving the characteristics of the proton beam and experimental setup with controllability and high reproducibility. In addition various mechanisms for ion laser acceleration, including target normal sheath acceleration (TNSA), radiation pressure-induced acceleration (RPA) and Coulomb explosion (CE) on solid targets have been proposed. In many of these methods, target geometry and pulse shaping have been addressed to improve ion energy and beam quality. The interaction regime depends on the characteristics of the laser pulse (such as wavelength, time width of the pulse, energy, the size of the beam radius and its intensity) as well as the characteristics of the irradiated material (such as the type of material, its density profile and thickness). furthermore, the sheath field can be enhanced by increasing the temperature or density of electron. So the acceleration performance can be improved by properly adjusting the target and laser parameters. Many reports and articles of experimental data are available in the investigation of the TNSA acceleration method with different thicknesses of the target as well as the laser pulse with medium (1019Wcm -2) and high (1021Wcm -2) intensities [10-13]. Currently, research is ongoing on to improve the proton cut-off energy by changing the target geometry. In this work, by changing the rear side profile target from flat form to a triangular one, the space-time evolution of the electrostatic field has considered using a two- dimensional simulation tool, and the results have been compared for different groove and base of the triangle.

SIMULATION RESULTS

In this work, the two-dimensional version of particle simulation code, Smilei [14] is used. The parameters used in the code are as follows: The laser pulse of wavelength 0.8μm is p-polarised with intensity 2.1×10^{20} W/cm ^{2} . The Gaussian profile is used both in space and time, with the focal spot at the waist w_0 = 5 μm and pulse duration(FWHM) =40 fs. Simulations are performed with a fully ionized quasi-neutral Al target comprising of Al^{+9} ions, protons & electrons, localized between 0 and 6 μm along the x-axis and 0 to 30 μm along the y-axis. The number density of Al and H are $40n_c$ and $4n_c$, respectively. The targets used in this work include a rear flat target and targets with a concave rear side (with different hollow and height). To get close to the reality a performed exponential density gradient has been considerd in front surface of the target for all cases (see figure 2). The simulation box extends from 0 μm to 100 μm along the x-axis (i.e. direction of laser propagation) and from 0 μm to 30 μm along the y-axis.

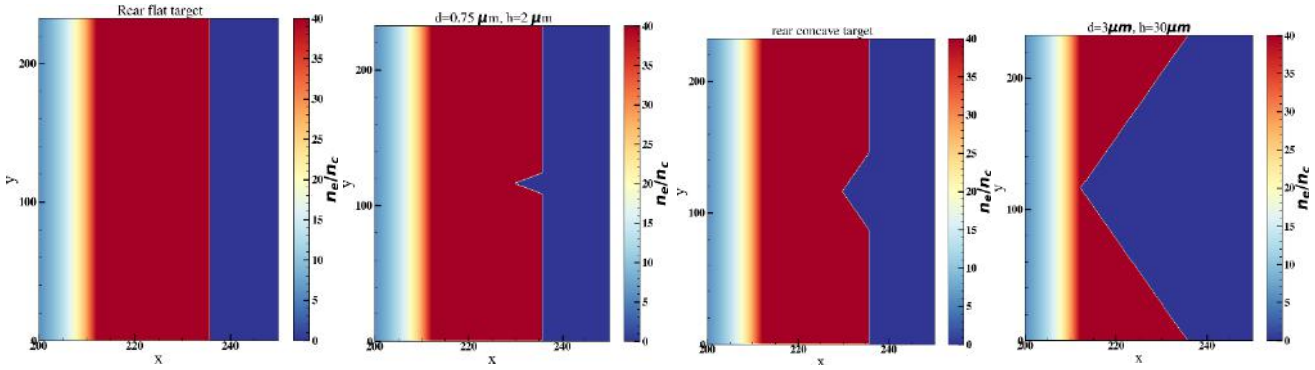

Fig. 1. Target geometries for flat rear side, and for concave rear sides with different groove and height (parameter d and h represent groove and height respectively)

In order to investigate the effect of the rear density gradient of the target on the acceleration of the proton beam, by changing this parameter and performing simulations, the results have been compared. Figure 1 shows the initial profile of the targets. As can be seen from Figure 1, the front of the target reaches the maximum density with an exponential profile (with 0.81 μm scale length) for all targets.

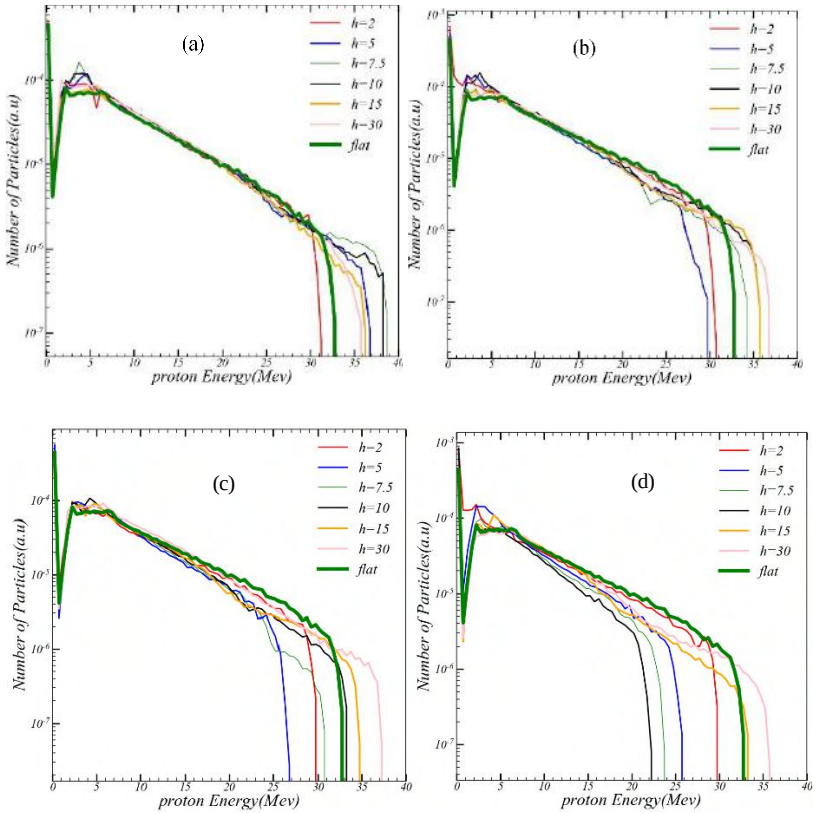

Fig. 2. Proton energy spectrum distribution for flat target and for concave one with a) d=0.75 μm, b) d=1.5 μm, c) d=2 μm and d) d=3 μm

In order to find the optimal geometry and investigate the dependence of the cut-off energy on the height and the amount of depth of the groove, the changes of the proton cut-off energy for targets with and different heights and groove are plotted in Figure 2. It can be seen from Figure 2 that by changing the density gradient behind the target from a flat surface to a concave form, the proton cut-off energy will change. According to the trend of the energy spectrum from Figure 2, the optimum point is at a height of

7.5 for d=0.75 μm. This means that with suitable targetery, the proton cut-off energy can be improved from 33 MeV (the rear flat target) to 40 MeV, without spending any extra energy. Since the electrostatic field created behind the target is responsible for the acceleration of the proton, therefore, in Figure 3, the time-space changes of the electrostatic field have been shown for several cases. One can see from Figure 3, in a fixed depth, the amplitude of the field becomes stronger as the height increases. Also, the intensity of the field does not change much with the change of depth for a fixed height.

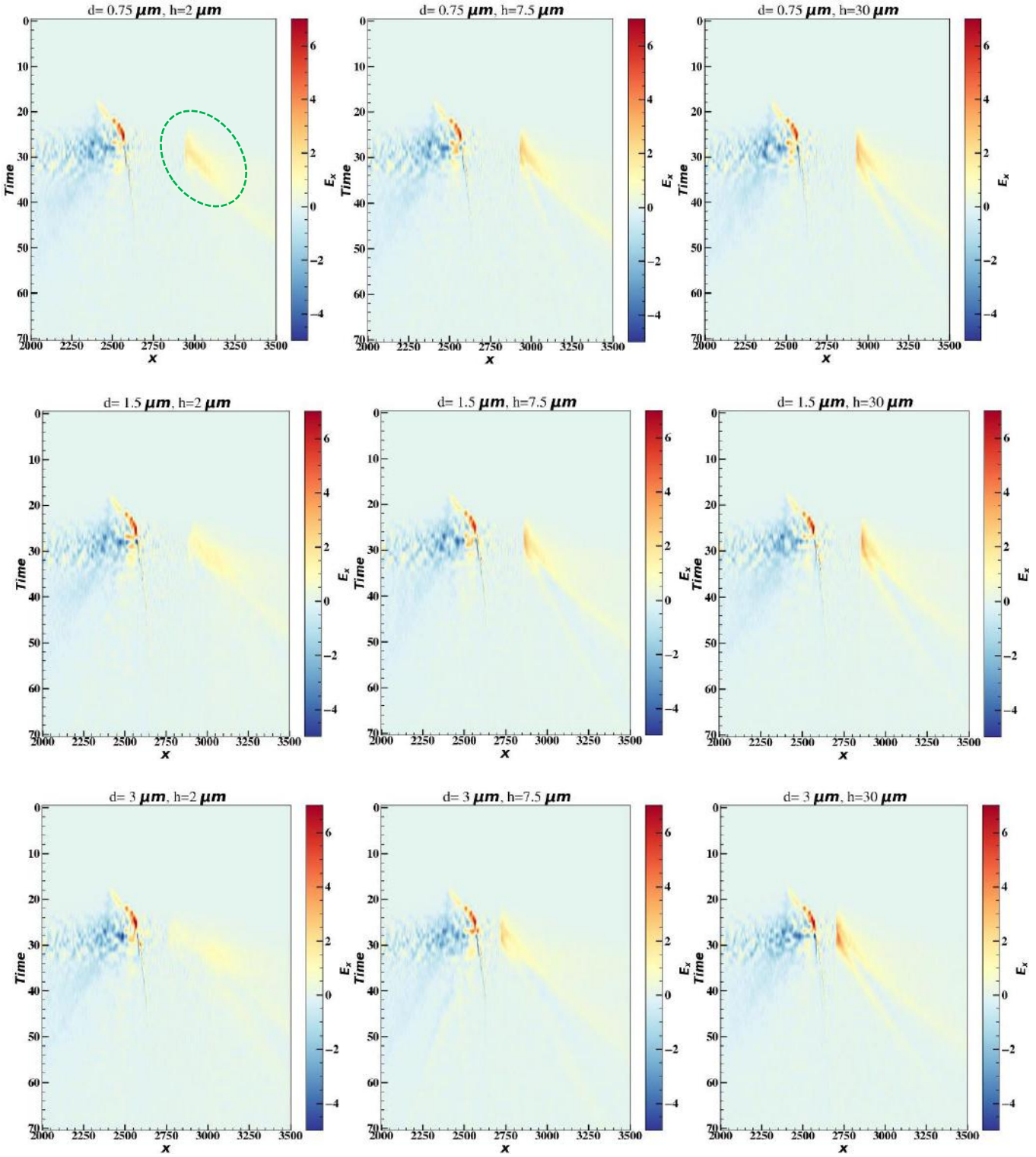

Fig. 3. Space-time variations of the electrostatic field (E_x) for rear concave targets. The area marked in the circle represents the electric field(E_x) produced behind the target.

Conclusions

Considering the importance of improving the energy of the accelerated proton beam in the TNSA mechanism, in this work, the changes in the energy of proton beam have been investigated by changing the target rear side geometry. By applying the different concave targets for initial conditions in the two-dimensional simulation Smilei code, the changes in the longitudinal electric field as well as the distribution of proton energy were investigated. According to the simulation results, there exits an optimum point for the concavity (depth and height of the target behind triangular geometry), at which point the cut-off energy reaches its maximum value. In addition, according to the time-space changes of the electrostatic field, it was found that the longer the base of the triangle behind the target, the stronger field (E_x) can be created.

References

[1] Strickland D, Mourou G. Compression of amplified chirped optical pulses. Optics Communications. 1985;55(6):447-449.

[2] Edwards C. Vulcan Petawatt Upgrade Overview. CLF/RAL Annual Report, URL: http://www. clf. rl. ac. uk/Reports/2001-2002/pdf/75. pdf, 2002.

[3] Kitagawa Y, et al., Prepulse-free petawatt laser for a fast ignitor. IEEE Journal of Quantum Electronics, 2004;40(3):281-293.

[4] Malka V, et al., Electron acceleration by a wake field forced by an intense ultrashort laser pulse. Science, 2002;298(5598):1596-1600.

[5] Esarey E, et al., Overview of plasma-based accelerator concepts. IEEE Transactions on Plasma Science. 1996;24(2):252-288.

[6] Gahn C, et al., MeV γ-ray yield from solid targets irradiated with fs-laser pulses. Applied Physics Letters. 1998;73(25):3662-3664.

[7] Maksimchuk A, et al., Forward ion acceleration in thin films driven by a high-intensity laser. Physical Review Letters. 2000;84(18):4108.

[8] Hegelich M, et al., MeV ion jets from short-pulse-laser interaction with thin foils. Physical Review Letters. 2002;89(8):085002.

[9] Gitomer S, et al., Fast ions and hot electrons in the laser–plasma interaction. The Physics of Fluids. 1986;29(8):2679-2688.

[10] Derouillat, J., et al., Smilei: A collaborative, open-source, multi-purpose particle-in-cell code for plasma simulation. Computer Physics Communications, 2018. 222: p. 351-373.

[11] Margarone D, et al., Laser-driven proton acceleration enhancement by nanostructured foils. Physical Review Letters. 2012;109(23):234801.

[12] Dollar F., et al., High contrast ion acceleration at intensities exceeding 10 21 W cm^{-2}. Physics of Plasmas. 2013;20(5):056703.

[13] Roth M, et al., Energetic ions generated by laser pulses: A detailed study on target properties. Physical Review Special Topics-Accelerators and Beams. 2002;5(6):061301.

[14] Derouillat, J., et al., Smilei: A collaborative, open-source, multi-purpose particle-in-cell code for plasma simulation. Computer Physics Communications, 2018. 222: p. 351-373.

ICNST 2024 International Conference on Nuclear Science and Technology
6- 8 MAY 2024 | Isfahan, Iran

Investigation and optimization of beam emittance of the radio frequency electron gun of pre-injector of Iranian Light Source Facility. (Paper ID : 1367)

Rafiei Hossein[1*], Sadeghipanah Arash[2], Dayyani Kelisani Mohsen[2], Kalantari Seyed Zafarollah[1]

[1]Isfahan University of Technology, Isfahan, Iran
[2]Institute for Research in Fundamental Sciences(IPM), Tehran, Iran

Abstract

The Iranian Light Source Facility(ILSF) is a fourth-generation low-emittance synchrotron light source under development in Iran. This synchrotron needs an electron pre-injector for producing, focusing, and injecting the energetic electron beam into the booster ring. Then a chain of s-band linear accelerators increases the beam energy. The energy of every linac is 50 MeV and the energy of the beam in the booster ring rises to 3 GeV.

The ILSF gun is a standing wave thermionic radio frequency gun. The extracted electron beam of the electron gun has an energy of about 2.5 MeV and the beam's emittance after crossing of alpha-magnet equals 1.5 micrometer-rad.

Decreasing the emittance of the electron beam in the electron gun, optimize the cost of maintaining process the electron beam, further.

In this paper, we investigate the RF and beam dynamics design of the gun cavity through optimization of some features like frequency, electric field, scattering and the beam emittance. We investigate the effect of the changes of different parameters like cathode radius and amplitude of electric field on the beam emitance and try to optimize it.

Keywords: Iranian Light Source Facility-radio frequency electron gun- emittance-CST studio suite-SPIFFE code-beam dynamics

INTRODUCTION

Iranian Light Source Facility (ILSF) is a new 3 GeV third-generation synchrotron radiation laboratory in the design stage and will be built in Iran. It will provide super bright synchrotron radiation desired for cutting-edge science in several fields and will serve as a significant impetus for multi-disciplinary research. Within the injector an electron gun produces an electron beam and the Focusing of the electron beam is done by alpha-magnet and multipole magnets in longitudinal and transverse directions, respectively. To

have efficient beam injection and extraction processes through the ILSF accelerators, a low emittance (less than 10 mm-mrad normalized) pre-injector is designed for the ILSF. Also, low emittance results in decreasing the cost of construction of the storage ring. Emittance is a parameter that indicates the quality of the electron beam. Emittance is a measure of the parallelism of a beam.

This paper introduces an overview of the electromagnetic design of the electron gun cavity and then the optimization of electron beam emittance will be investigated. The related beam dynamics issues and particle tracking simulation results are explained at the end. It should be noted that the CST microwave studio software is used to design and optimize the main pre-injector cavity components. The SPIFFE simulation code is employed for particle tracking and beam dynamics studies. The design and construction of the ILSF RF electron gun were done by Dr. Arash Ssadeghipanah and others and here we want to optimize this design [1].

RESEARCH THEORIES

The ILSF pre-injection system consists of an RF electron gun with a thermionic cathode, an alpha magnet for longitudinal compression, three accelerating linac tubes, and quadrupole and steering magnets for transverse beam control. A layout of the pre-injector of ILSF is displayed in Fig.1 [1].

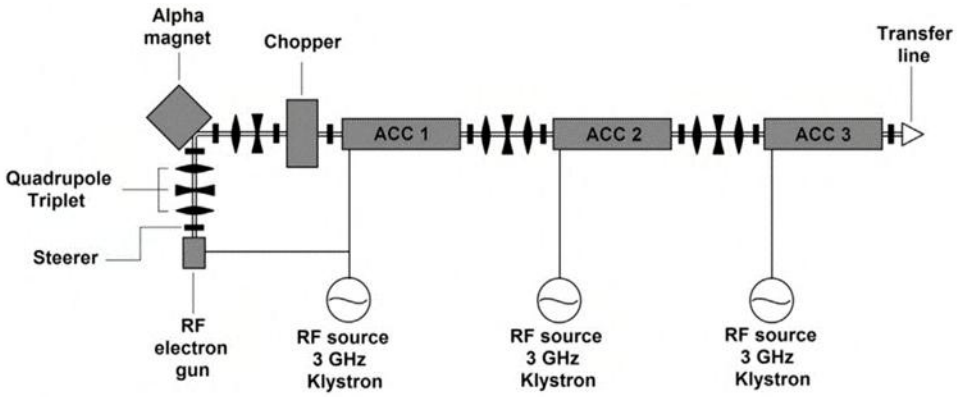

Fig.1. The layout of pre-injector of ILSF [1].

The early design for the RF electron gun is a $\pi/2$ mode structure which generates the initial electron bunches. The coupling in between the cells is done by a side coupling cavity that a waveguide transports the power produced by a klystron to it. RF electron gun has a 1.5-cell structure operating at 2998 MHz. A flat pill thermionic cathode with a diameter of 6 mm is placed on the half-cell wall. The half-cell to full-cell field ratio is set at 30 to 40 percent to minimize the electron back-bombardment on the cathode surface. At full

power, the accelerating gradient of the full-cell cavity is around 80 MV/m for a peak RF input power of 4 MW. The frequency and input power of the electron gun form this accelerating gradient. The acceleration gradient produces an energy-chirped electron bunch with a maximum energy of 2.5 MeV. In simulation, the maximum cathode emission is set to 1.4 A (corresponding to 5 A/cm2 current density), and the electrons leaving the cathode are considered to have uniform radial distribution within a maximum radius of 3 mm. A layout of the RF electron gun of ILSF is displayed in Fig.2 [1].

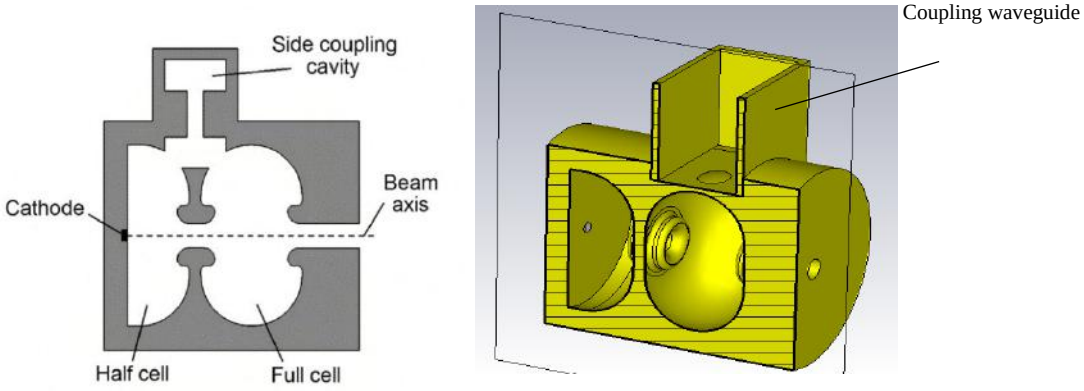

Fig.2. The layout of the RF electron gun of ILSF. The side coupling cavity is shown on the left and the wave guide and the coupling hole are shown on the right [1].

The low-energy electrons leaving the RF gun will be filtered in the alpha magnet downstream, leaving a bunch with an energy spread of no more than 10 percent. The electron bunches have an energy-chirped shape at the exit of the RF electron gun which means that the low-energy electrons are located at the tail of the bunches. To eliminate the undesired low-energy electrons after the RF gun and before they gain more energy in the Linac tubes, an energy filter is employed inside the alpha magnet to allow passing only 40% of the high-energy electrons with a 10% energy spread. A chopper magnet is employed to pass three consecutive bunches of electrons. The bunched electrons go through the three traveling wave Linac tubes each with a length of 3.5 m. They reach the target energy of 150 MeV. Each Linac tube provides the energy of 50 MeV with an accelerating RF phase near the crest. At the end of three accelerators, the energy of the beam reaches to 150MeV [2].

Emittance is the figure of merit, quality and parallelism of a beam. if x is the transverse place and p_x is the transverse momentum of the beam, we can define the emittance, as below [3]:

$$\epsilon = \mathrm{N}\sqrt{\langle x^2\rangle\langle {p_x}^2\rangle - \langle x\, p_x\rangle^2} \qquad (1)$$

where N is the normalization coefficient. On the other hand, emittance is the area of phase space configuration of a beam. The importance of emittance is that the magnitude of force should apply to the beam for focusing it is proportional to the square of emittance.The lower the emittance of the electron beam in the electron gun, the lower the cost of focusing and maintaining the electron beam. If $F_r(r)$ is the focusing force of the beam, R is the maximum radius of beam emittance, γ is the relativistic factor, then for a beam with a mass of m_0 and axial velocity of v_z, the focusing force is [3]:

$$F_r(r) = \frac{{\epsilon_r}^2}{R^3}(\gamma m_0 {v_z}^2) \tag{2}$$

If q is the particle charge, σ is the root mean square(RMS) radius of the beam, I_b is the current of the beam, P_{av} is the average momentum of the beam and ΔU_b is the free energy of the beam (The amount of difference between the existing beam energy and the corresponding uniform beam energy), then the difference of beam emittance on its emit direction is corresponded to [4]:

$$\frac{\partial {\epsilon_r}^2}{\partial z} = -\frac{q\sigma^2}{2I_b P_{av}}\frac{\partial}{\partial z}\Delta U_b \tag{3}$$

According to this relation, these actions are useful for minimizing the beam emittance: reducing the beam radius, reducing the free energy of the beam, and growing the average momentum of the beam. In the following, we investigate the effect of beam radius and average momentum on beam emittance.

The emittance right on the cathode has a thermal distribution and is in the form:

$$\epsilon_n = \frac{r_c}{2}\sqrt{\frac{k_b T}{mc^2}} \tag{4}$$

Where r_c is the cathode radius, k_b is the Boltzmann constant, T is the cathode temperature, and mc^2 is the electron's rest mass.

Due to equation.3 and equation.4, the cathode radius has an optimized value that decreases the emittance and doesn’t destroy the emittance on the cathode. Therefore optimizing the cathode radius is more important than minimizing it.

In the following, first, we optimize the RF gun electric field by CST studio suite [5] and then investigate the effect of cathode dimension and amplitude of electric field on the emittance of beam. CST is a high-performance 3D EM analysis software package for designing, analyzing, and optimizing electromagnetic (EM) components and systems.

The design of the electric field of the RF electron gun cavity was done by the CST studio suite. The field ratio of half-cell to full-cell is set at about 1:3 and the S-parameter of this cavity is set at about -28dB. The default power in CST is 1 MW and at this power, The acceleration field gradient in half-cell and full-cell is $12_{/}5\ \frac{MV}{m}$ and $20\ \frac{MV}{m}$ respectively. As input power grows, the field gradient grows too. Also, the electric field profile should be in a form that the acceleration and bunching of the beam are done effectively. The electron field, S-parameter, and the ratio of half-cell to full-cell fields of the RF electron gun are shown in Fig.3.

Note that a lot of frequency modes may be formed in a cavity. Each mode has a special frequency and peak in the S-parameter diagram. Since the cavity of the electron gun resonates in a specified frequency, other resonance peaks were damped by changing the dimension and size of cavity components. So in Fig. 3.a, only one dominant peak is seen and other peaks are dismissed or are very small. We remind that if there is any difference between the desired value and the simulated frequency value, this difference will be solved by the tuning process.

a b c

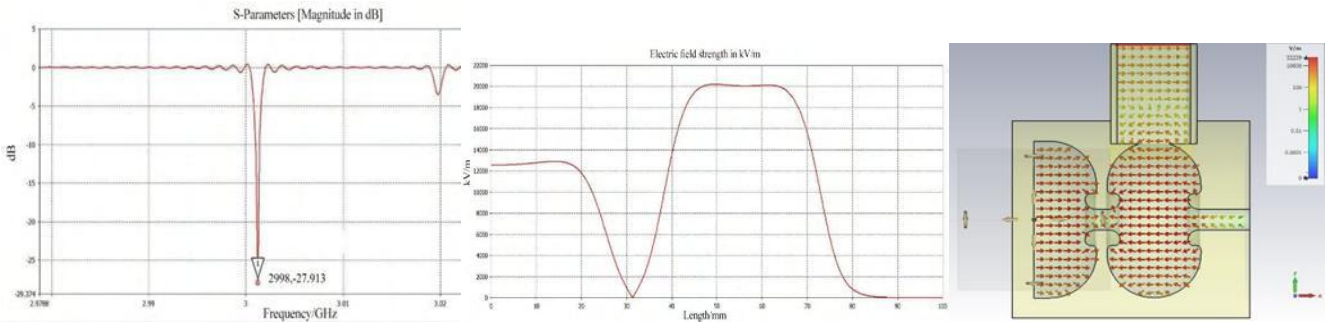

Fig.3. Design of RF electron gun. a: S-parameter of RF electron gun cavity, b: ratio of half-cell to full-cell fields, and c: the profile of electric field resonates in π/2 mode.

After designing and optimizing the electric field of the ILSF RF electron gun, since the accuracy of CST for beam dynamics calculation is low, and it can't mesh the beam-like structure, There are two ways to

investigate the dynamics of the beam: increase the number of meshes in CST or use the beam dynamics codes. An increase in the meshes in CST causes an increase in the time of the simulation. Therefore we use the SPIFFE (SPace charge and Integration of Forces For Electrons) code [6] for this object.

Spiffe is a fully electromagnetic 2-1/2 dimensional particle-in-cell code for the simulation of RF guns and similar systems with cylindrical symmetry. Here for optimizing the emittance of electron beam, we investigate the effect of changes in beam parameters on beam emittance. according to equation.3, we select the beam radius and the amplitude of the electric field.

First, for a fixed electric field, we change the radius of the cathode and calculate the beam emittance. Note that the results of SPIFFE code are in terms of a text file, so the drawing of emittance in phase space configuration would done by inserting the SPIFFE results in Python code. The profile of the electric field simulated by SPIFFE is shown in Fig.4. Then by using this electric field, the phase space of the electron beam is drawn. Fig.5 shows the phase space of the electron beam in 6 different radiuses of the cathode.

a b

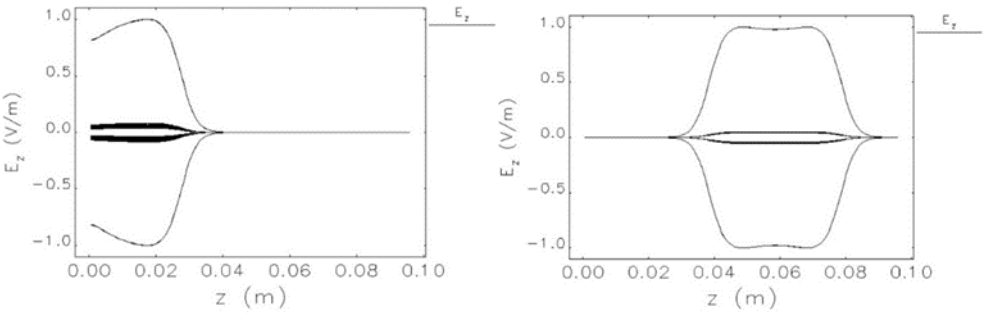

Fig.4. Electric field along the length of the electron gun, a: half cell and b: full cell.

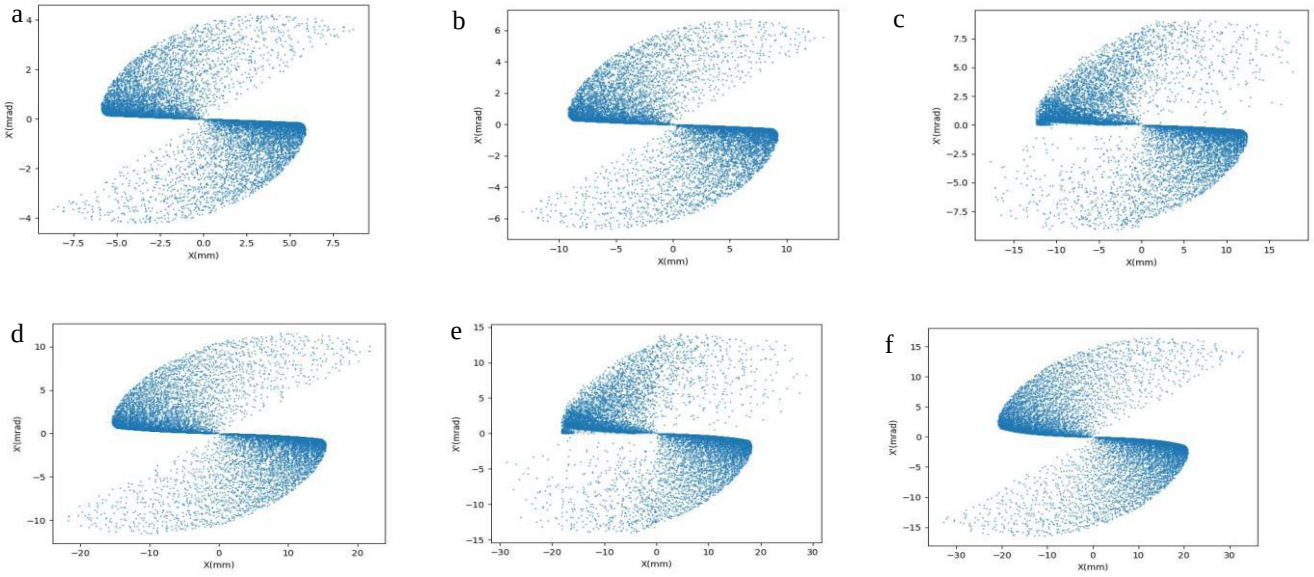

Fig.5. The changes of phase space and emittance of the electron beam at the discharging of RF electron gun for a fixed electric field and different radiuses of cathode: a:1mm, b:1.5mm, c:2mm, d:2.5mm, e:3mm, f:3.5mm.

In order to evaluate the effect of the electric field on emittance, we adopt the radius of 2.5 mm and change the magnitude of the electric field for 5 steps related to a maximum amplitude of electric field. Note that based on the S-parameter in the minimum value, these different amplitudes of electric fields aren't far from the first electric field so no problem in choosing them for effect on the electron beam. Fig.6 shows the phase space of the electron beam in 6 different electric fields

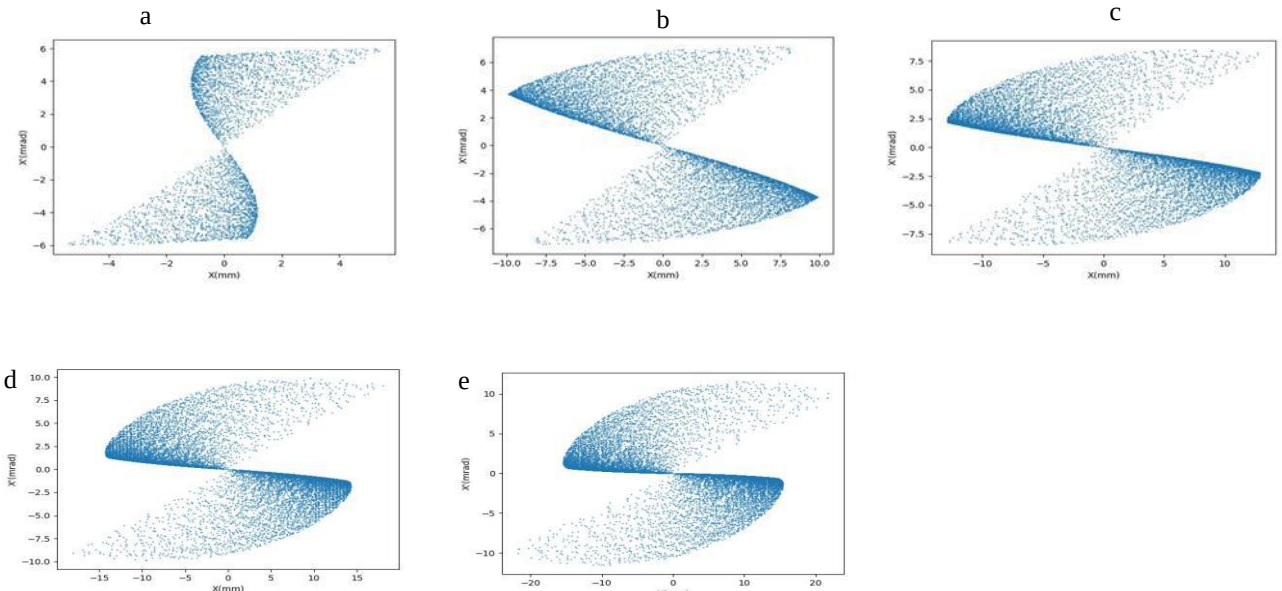

Fig.6. The changes of phase space and emittance of the electron beam at the discharging of RF electron gun for a fixed radius of cathode and different magnitude of electric fields: a:0.5E, b:0.62E, c:0.75E, d:0.87E, e:1E.

The electrons at the head of the generated bunches from the RF gun have a higher energy than electrons at the tail. The bunch length will increase longitudinally in drift sections between the RF gun and the first Linac tube. Therefore, the alpha magnet is employed to serve as a longitudinal phase space spinner. The alpha magnet has a magnetic field gradient of 324 G/cm. the bunch that comes out from the alpha magnet will be compressed longitudinally. The energy filter inside the alpha magnet is utilized to allow the passing of 40% of the highest energy electrons with a 10% energy spread. So here we investigate the momentum spread and distribution of time(histogram) for a bunch. Also, we did this for different electric fields. These spreads are shown in Fig.7 and Fig.8 respectively.

As it is seen in Fig.7 and Fig.8, about 90 percent of particles in a beam are under the maximum energy of the beam. So we eliminate these particles to enhance emittance and localize the bunches. The layout of the phase space of the electron beam after passing the alpha magnet for different radii and different electric fields is presented in Fig.9 and Fig.10.

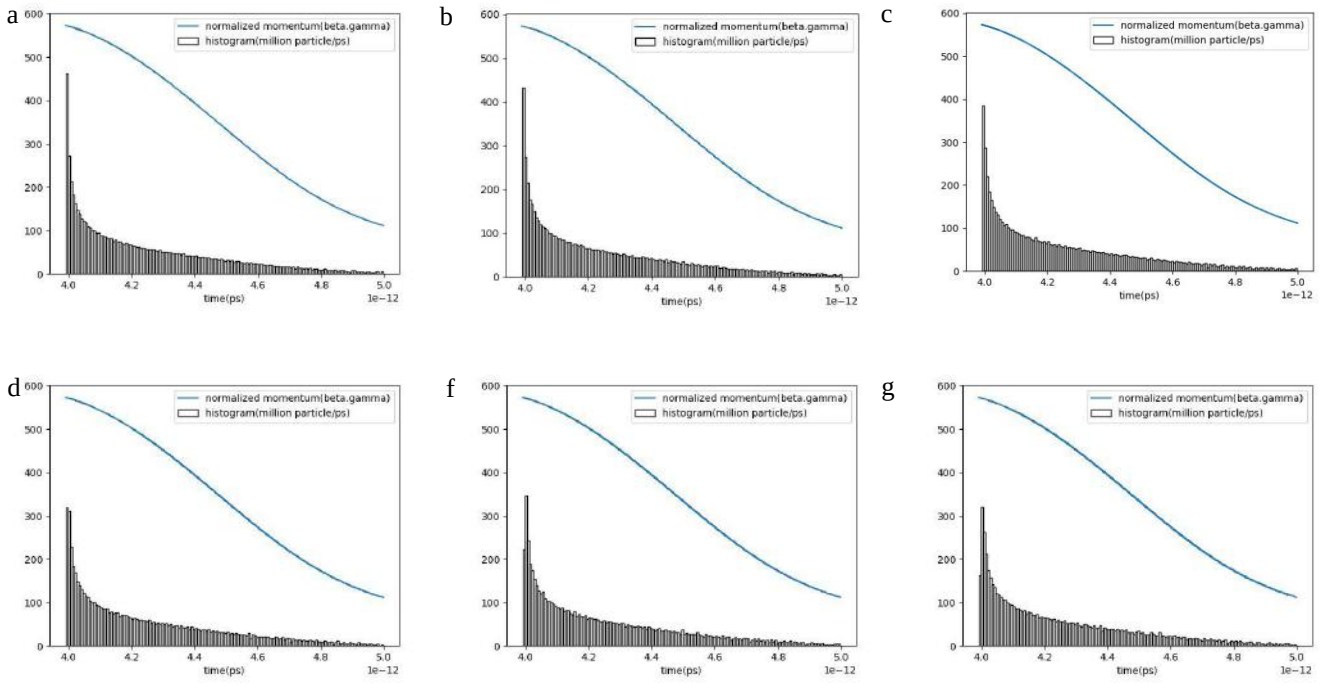

Fig.7. Energy spread and time distribution of particles in an electron beam at the discharging of RF electron gun for a fixed electric field and different radiuses of cathode: a:1mm, b:1.5mm, c:2mm, d:2.5mm, e:3mm, f:3.5mm.

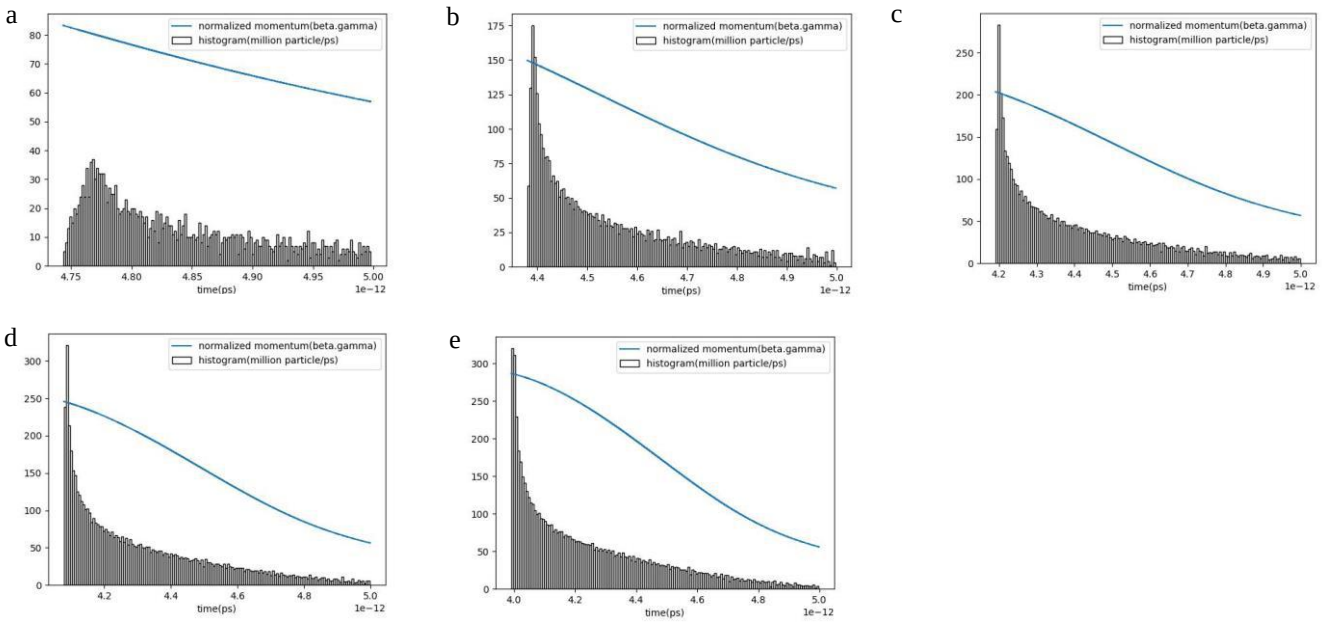

Fig.8. Energy spread and time distribution of particles in an electron beam at the discharging of RF electron gun for a fixed radius of cathode and different magnitude of electric fields: a:0.5E, b:0.62E, c:0.75E, d:0.87E, e:1E.

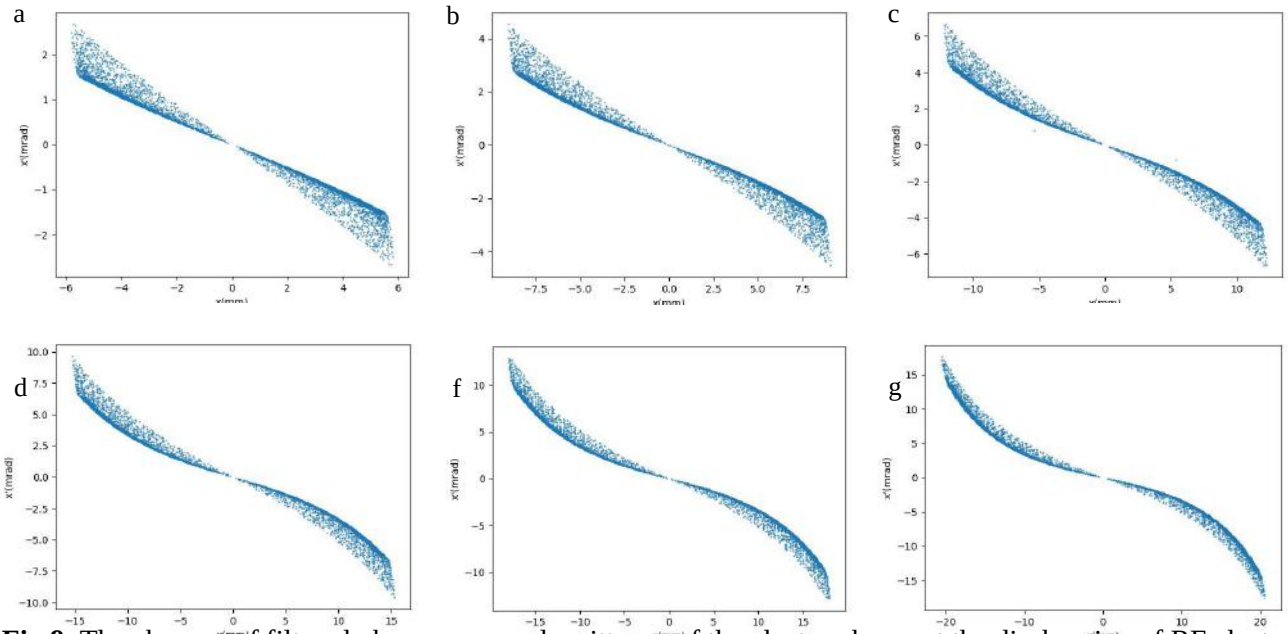

Fig.9. The changes of filtered phase space and emittance of the electron beam at the discharging of RF electron gun for a fixed electric field and different radiuses of cathode: a:1mm, b:1.5mm, c:2mm, d:2.5mm, e:3mm, f:3.5mm.

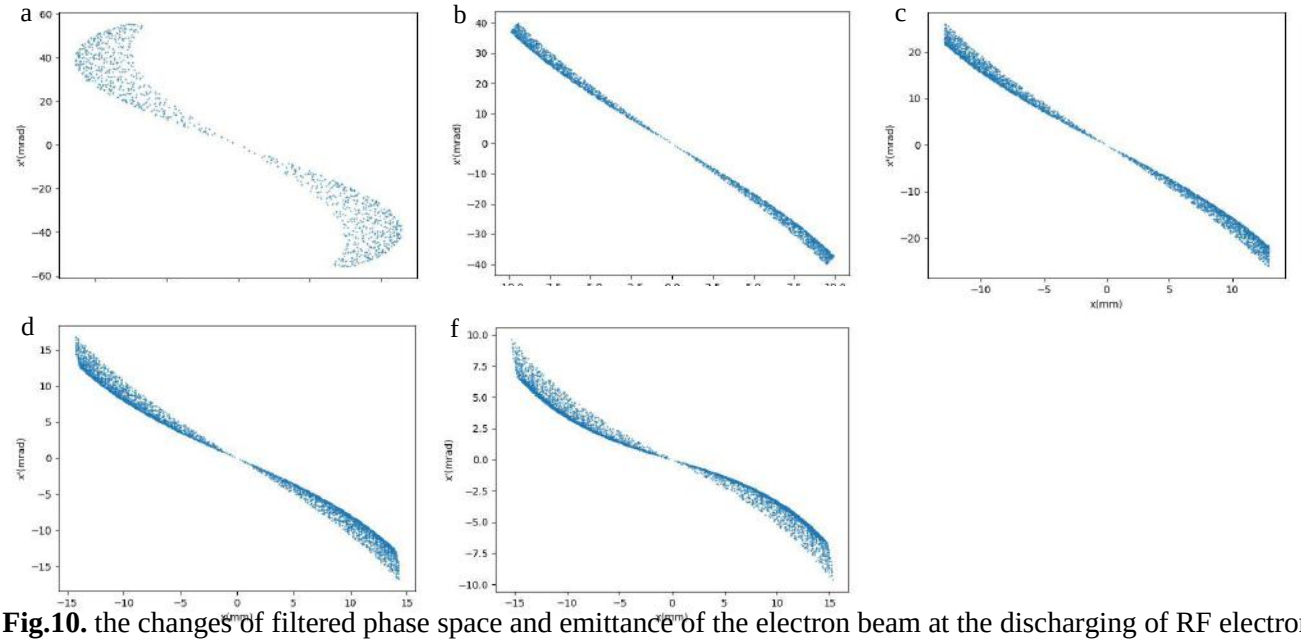

Fig.10. the changes of filtered phase space and emittance of the electron beam at the discharging of RF electron gun for a fixed cathode radius and different magnitude of electric fields: a:0.5E, b:0.62E, c:0.75E, d:0.87E, e:1E.

Results and discussion

The relation of cathode size and magnitude of electric field on differences of electron beam emittance was investigated. For different cathode sizes, the electric field was fixed and in the mode of different electric fields, the radius of the cathode was fixed. We can also calculate the value of emittance from equation.1 for this state. These values are reported in Table.1.

Table.1. the values of emittance based on equation.1 for different states.

state	**Fixed electric field and different radiuses of cathode(mm)**						**Fixed cathode radius($2/5\ mm$) and different values of electric fields.**				
Value of variable	$1\ mm$	$1/5\ mm$	$2\ mm$	$2/5\ mm$	$3\ mm$	$3/5\ mm$	$0/5\ E$	$0/62\ E$	$0/75\ E$	$0/87\ E$	$1\ E$
Emittance before filtering by alpha magnet ($\mu m - rad$)	$4/12$	$10/12$	$18/72$	$30/04$	$43/46$	$59/88$	$1/56$	$7/36$	$14/31$	$21/43$	$30/04$
Emittance after filtering by alpha magnet ($\mu m - rad$)	$0/0911$	$0/229$	$0/457$	$0/861$	$1/59$	$2/84$	$0/267$	$0/58$	$0/842$	$0/941$	$0/861$

Also, we draw the diagram of the table.1 in fig.11:

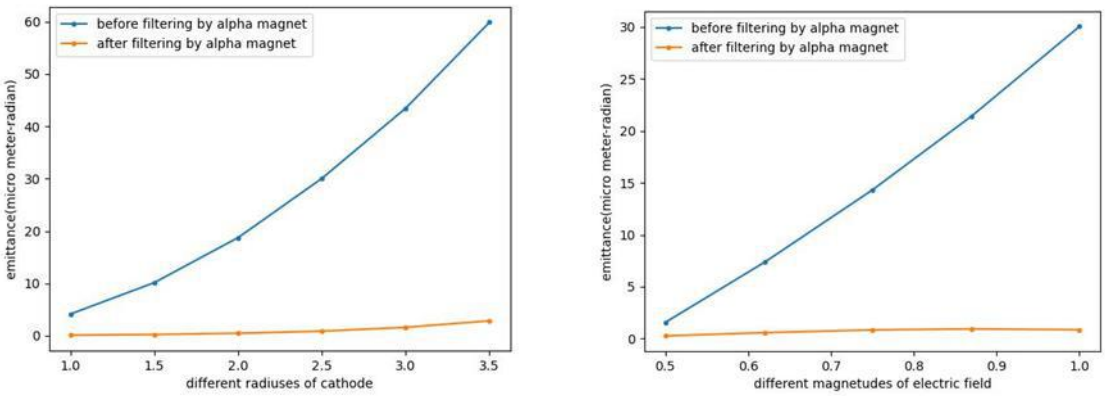

Fig.11. Diagram of the emittance changes by different cathode radiuses (left plot) and different magnitudes of electric field (right plot) based on Table.1.

Conclusions

In this paper, we check the RF electron gun of ILSF and redesign and optimize it. Then we investigate the effect of changing the cathode radius on beam emittance and the effect of change in electric field in parallel. It results that by enhancing the radius of the cathode the emittance increases. But as mentioned the minimizing the value of cathode radius has a limitation and we don't have decrease it in any extent. Also, minimizing the electric field results the reducing the emittance. But this rule is special to conservative fields. Since the RF electric field isn't a conservative field, by increasing it the emittance grows. so as much as we can reduce the cathode radius and conservative electric field, it is more useful to reducing the electron beam emittance.

References

[1] A Sadeghipanah, AH Feghhi, J Rahighi, and H Ghasem. Low emittance preinjection system for iranian light source facility. Nuclear Instruments and Methods in Physics Research Section A: Accelerators, Spectrometers, Detectors and Associated Equipment, 806:340–347, 2016.

[2] A Sadeghipanah, S Ahmadiannamin, M Ostovar, J Roohi, M Bahrami, and Z Pouyanrad. A new design for the rf electron gun of the iranian light source facility (ilsf). Nuclear Instruments and Methods in Physics Research Section A: Accelerators, Spectrometers, Detectors and Associated Equipment, 1051:168198, 2023.

[3] Stanley Humphries. Charged particle beams. Courier Corporation, 2013.

[4] M Dayyani Kelisani, S Doebert, and M Aslaninejad. Low emittance design of the electron gun and the focusing channel of the compact linear collider drive beam. Physical Review Accelerators and Beams, 20(4):043403, 2017.

[5] CST Microwave Studio Tutorial, CST GmbH (2006).

[6] M. Borland, Summary of Equations and Methods Used in SPIFFE, APS/IN/LINAC/92- 2, USA, 1992.

ICNST 2024 International Conference on Nuclear Science and Technology
6- 8 MAY 2024 | Isfahan, Iran

Measurement and calculation of gas pressure in a test-bed electrostatic accelerator (Paper ID : 1385)

Masoumzadeh A.[1*], Habibi M.[1], Mirzaei H.R.[2], Yadollahzadeh B.[2]

[1]*Department of Energy Engineering and Physics, Amirkabir University of Technology - Tehran Polytechnic, Tehran, Iran*

[2]*Department of Physics and Accelerators, Nuclear Science and Technology Research Institute (NSTRI), Tehran, Iran*

Abstract

In this work, a small-scale electrostatic accelerator as a test-bed ion source is simulated by COMSOL to compute the gas pressure, and compare the results with measured data. The accelerator already has been constructed and correctly operated. We aim to equip it with a gas-target neutralizer in the future. To perform the new optimal design before the construction, the simulation model must be validated. For this purpose, we evaluate the simulation results of the available setup by comparing them with the experimental measurement data. The electrostatic accelerator consists of a plasma source, extraction and acceleration tube, and vacuum vessel. The plasma source, which is filled with a flow rate of 0.3-1 SCCM of H_2 gas, is pressurized about 1 Pa (the highest-pressure level of the accelerator), and the vacuum vessel, which is equipped with a 200 lit/s turbo-molecular pump, is pressurized about 0.001 Pa (the lowest-pressure level of the accelerator). This pressure difference is formed by a 1.8 mm aperture. The effect of pump speed and gas injection value on the gas pressure is separately investigated. In addition to H_2, the gas distribution is computed for other gas species of D_2, He, N_2 and Ar. The results show that the increase of gas injection increases the pressure throughout the accelerator, while the increase in pump speed only decreases the pressure in the vacuum vessel. The results also acknowledge that heavier gases lead to higher pressure in the plasma source because of lower gas conductance.

Keywords: Accelerator, Ion source, Gas pressure, Gas distribution, COMSOL.

INTRODUCTION

Electrostatic accelerators are used to energize charged particles in a straight line [1, 2]. An electrostatic accelerator usually consists of three main sections: A plasma source, Extraction and acceleration tube and vacuum vessel, which are installed sequentially [3, 4]. Charged particles are produced in the high-pressure plasma source, then extracted by an extraction electrode toward vacuum vessel. A few electrodes are located just after extraction electrode to focus and accelerate the extracted particle beam. Energetic particles are widely used in scientific works such as advance surface processing [5, 6], fusion plasma heating [7], etc.

Gas pressure distribution along the accelerator is important for the best performance of the accelerator [8, 9, 10]. The pressure in plasma source must be high enough (about 0.1 to 5 Pa), while in the beam pass (acceleration tube and vacuum vessel) the pressure must be very low (about 1E-2 to 1E-5 Pa). This pressure difference is created using a small aperture (beam extraction aperture) that exists between two vacuum sections; plasma tube, which the gas is injected into it, and the vacuum vessel, which is evacuated by a pump. An aperture decreases gas conductance in a vacuum system, resulting in pressure difference between two vessels connected by the aperture [11, 12]. In the free molecular regime, the conductance does not depend on pressure. It depends only on the mean molecular speed, molar mass of gas and the vacuum system geometry [13].

To design and construct complicated accelerators, we need validated simulation to have a near approximation of the pressure. Some codes [14-16] and computer software [17] are available for modeling and calculation of the pressure. We chose the COMSOL because of our foresight. It is a multi-physics software. This software can couple the physics of free molecular flow with physics of beam optics and beam-gas interaction. This multi-physics model was used in our previous work [18], and also will need for our future works. There are two common methods to calculate the pressure: The Monte Carlo method [16, 19] and angular coefficient (or view-factor) method [14, 20, 21]. The COMSOL applies the angular coefficient method to compute the pressure, density and particle flux of a model [20].

EXPERIMENTAL

A test-bed electrostatic accelerator has been constructed at NSTRI. Figure 1 shows the experimental setup.

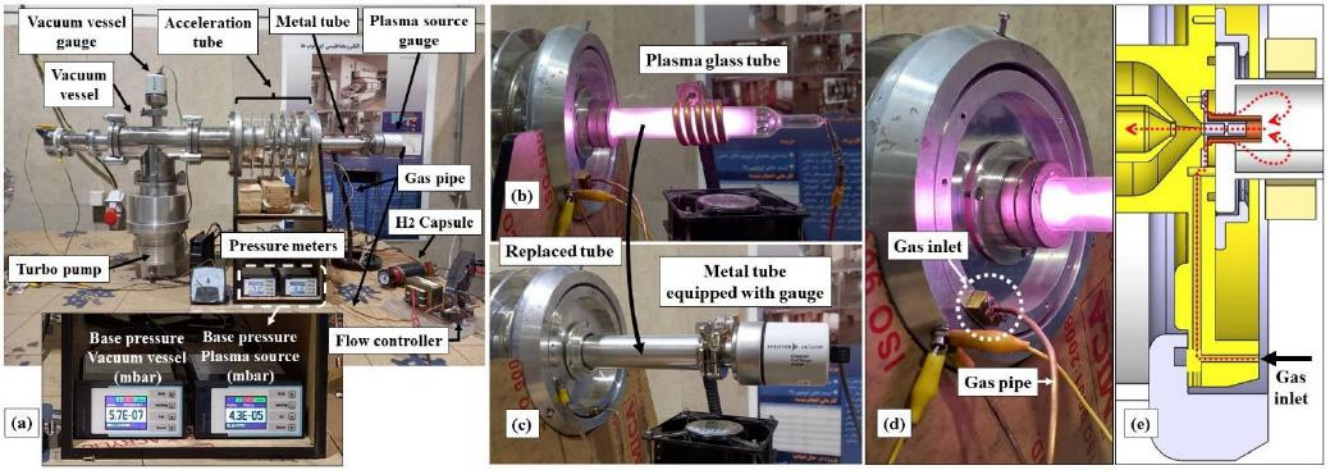

Fig. 1. (a) The experimental setup of the test-bed electrostatic accelerator, (b) plasma glass tube, (c) replaced metal tube equipped with pressure gauge, (d) gas pipe and inlet location, and (e) gas route from inlet to vacuum vessel.

The setup includes a metal tube which is replaced with the plasma glass tube to make it possible to install the pressure gauge (Fig. 1b and 1c), an acceleration tube with one plasma electrode, three lens electrodes and two acceleration electrodes, and a vacuum vessel. The equipment is the TURBOVAC TW290 drive TD400, a thermal-leak flow controller, a hydrogen capsule and two pressure gauges. The location of the gas inlet (Fig. 1d) and the gas route from the inlet to the vacuum vessel (Fig. 1e) are also shown in the figure.

Design and simulation

3D CAD design

The engineering and mechanical 3D CAD model of the accelerator is designed by the SOLIDWORKS software. Figure 2a shows the perspective view of the accelerator and Fig. 2b shows the side cross-section view in detail.

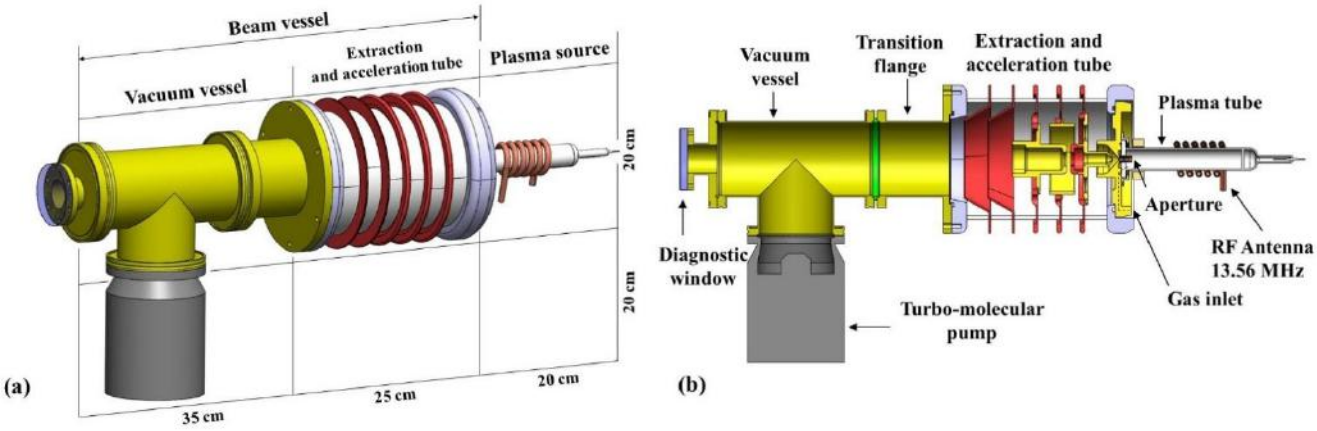

Fig. 2. The SOLIDWORKS 3D CAD model of the accelerator. (a) The perspective view and (b) the detailed cross-section view.

COMSOL model

The detailed 3D CAD is imported to the COMSOL for the computation of the steady-state pressure. For this purpose, the Free Molecular Flow module is used and solved by using the stationary study. The input parameters of the COMSOL model are presented in Table 1. The model is divided into five domains to define different mesh sizes for optimizing the meshing and decreasing the simulation time. The meshing is shown in Fig. 3. A leak is defined about 0.006 SCCM (Standard Cubic Centimeter per Minute). This value is acquired by matching computational base pressure with measured base pressure.

Table 1. The input parameters of the COMSOL model

Parameter	Value [unit]
Hydrogen molar mass: H_2	2.016 [g/mol]
Surface temperature	293.15 [K]
Gas temperature	293.15 [K]
Standard Pressure	1 [atm]
Gas injection flow rate	0 to 1 [SCCM]
Leak and outgassing	0.006 [SCCM]
Pump speed of H_2	200 [lit/s]
Mesh type	Free Tetrahedral
Number of mesh regions	5
Min. mesh size Region 1 to 5	8, 0.2, 1, 5, 14 [mm]
Max. mesh size Region 1 to 5	20, 1, 5, 18, 50 [mm]
Max. element growth rate Region 1 to 5	1.45, 1.3, 1.35, 1.5, 1.5

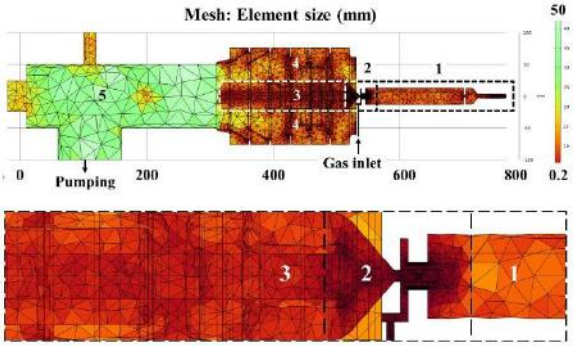

Fig. 3. The meshing of the interior volume of the imported CAD model in COMSOL. The largest mesh is shown with light green, and the smallest is shown with dark red. There are five regions of meshing with different element sizes respect to importance.

Results and discussion

The pressure of the plasma source and vacuum vessel were measured at different injection flow rates, and the data is plotted in Fig 4. The plot shows a direct relation between injection flow rate and pressure. Theoretically, the pressure of both sections must reach zero at the 0 SCCM flow rate, however, the zero pressure is not possible in practice, because of the leak and outgassing [22]. The optimal pressure of our

plasma source for the best plasma-RF matching is about 1 to 4 Pa. Therefore, the measurements are limited in this pressure range. The corresponding flow rate for this pressure range is 0.3 to 1 SCCM.

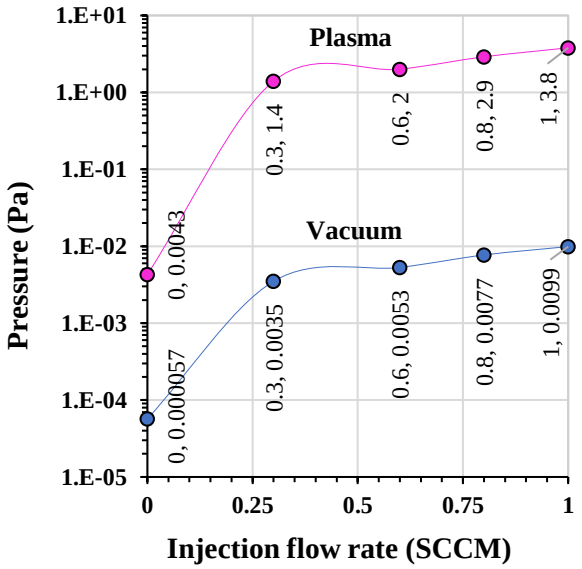

Fig. 4. The measured pressure versus the injection flow rate.

The experimental condition was simulated to compute the H_2 pressure along the central axis of the accelerator. The results are presented in Fig. 5a. To validate the simulation results, the related experimental data are simultaneously plotted. Figure 5b clearly shows the pressure drop along the aperture and acceleration tube.

The results show a 2 to 3-order differential pressure between the plasma source and the vacuum vessel, which is necessary. This pressure difference is formed using the aperture of the plasma electrode with 1.8 mm diameter and 1.15 mm length. The other electrodes are designed with large holes to easily pump throughout the acceleration tube. Therefore, the pressure quickly falls right after the aperture. The cross-section view of the CAD model is presented in top of the plot to show the pressure of each point of the accelerator axis. The other finding is the independence of pressure difference to gas injection. The simulation was performed for injection of 0 (with 0.006 SCCM leak), 0.3 and 1 SCCM. (The simulation revealed that the outgassing and leakage must be collectively equivalent to 0.006 SCCM to lead to the measured base pressure.) Increasing the injection leads to the gas enhancement throughout the accelerator so that the pressure difference remains constant.

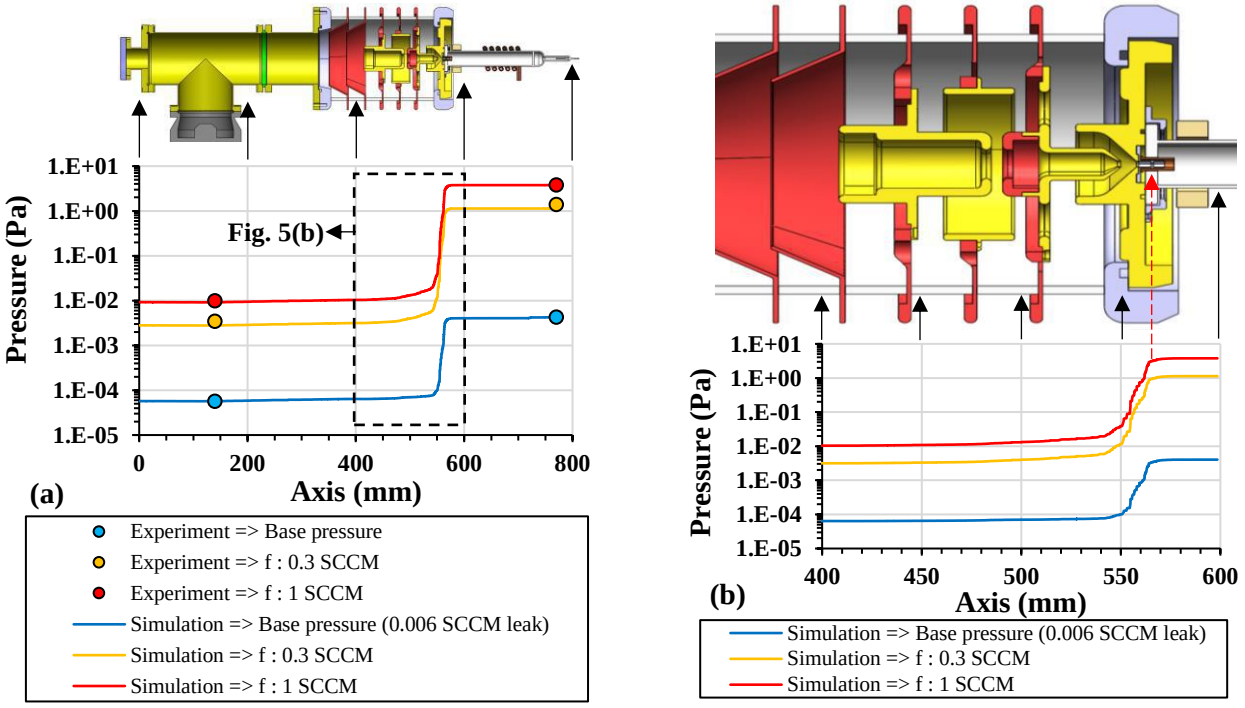

Fig. 5. The distribution of the gas pressure (a) along the accelerator and (b) extraction and acceleration region for injection flow rates of 0.006 (leak), 0.3 and 1 SCCM. The solid lines present the simulation results, and the circular markers present the measured data of the experiments.

To have a high-quality beam, the beam vessel (acceleration tube and vacuum vessel) must be in a high vacuum, while the plasma pressure must remain in a low vacuum. The main way is the use of a high-speed turbo pump. The effect of the installation of different turbopump brands with different pump speeds was investigated by simulation. Figure 6 shows the results for pump speeds of 200, 280, 350, 600 and 850 lit/s, without injection (only 0.006 SCCM leak) and with injection of a 0.3 SCCM H_2. The pump speeds of H_2 for each turbo pump brand were obtained from their manuals and used in the simulation.

The results show that the plasma source pressure seems unchanged, while the pressure of the beam vessel decreases with the increase in pump speed. The changes in the pressure of the plasma source will be visible for ultra-high-speed pumps. The plot shows a decrease in vacuum pressure above the pump from 0.0028 Pa to 0.0007 Pa for speeds between 200 and 850 lit/s with the same injection of 0.3 SCCM. Therefore, it is concluded that one way to increase the pressure difference is the increase of the pump speed.

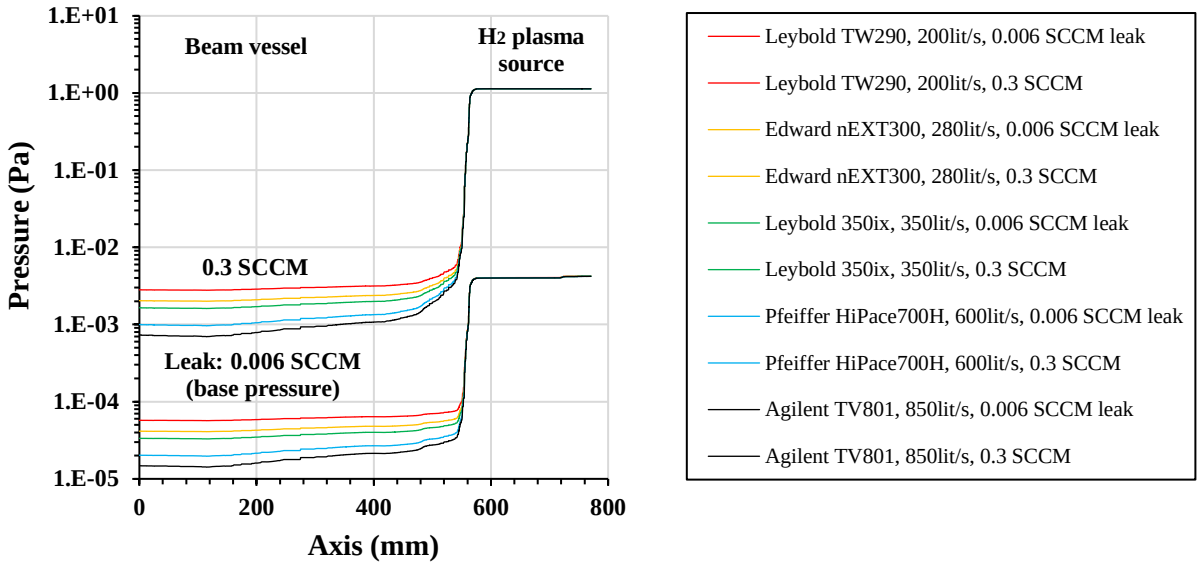

Fig. 6. The effect of different pump speeds on the distribution of the H_2 gas pressure along the accelerator. Injection flow rates: a 0.006 leak (base condition) and 0.3 SCCM.

The pressure difference depends on pumping speed values, aperture dimensions and gas type. In the previous section, the effect of pump speed was illustrated. The effect of gas type is also illustrated as follows. The gases of H_2, D_2, He, N_2 and Ar were studied and the results are compared in Fig. 7. These gases are different in molar mass. Heavier gases due to large molecular dimensions have lower conductance in vacuum. These gases hardly pass through the small apertures, so the pressure is increased upstream (plasma source), with a negligible increase in downstream (vacuum vessel). Both graphs Fig. 7(a) and (b) show an increase in plasma source pressure concerning the weight of the gases. The plasma source pressures, corresponding to H_2, D_2, He, N_2 and Ar, are 1.13, 1.59, 1.59, 4.2 and 5.02 Pa. Table 2 reports molar mass and the conductance of the gases from ref. [3]. The conductance ratios with respect to H_2 are presented and compared with the plasma source pressure ratios acquired from this work. By comparing the conductance ratio and pressure ratio, it is concluded that the plasma source pressure has a direct relation with gas conductance, however, considering the same pump speed for all gas types, the pressure around the pump does not change with gas type (Fig. 7a). In this work, a real situation was also investigated by considering the real pump speeds of installed Leybold TURBOVAC TW290 for each gas type. The evacuation speed of this pump is only reported for N_2. Therefore, we have to estimate the evacuation speed for other gases. The results are presented in Fig 7b. This investigation shows small changes only in vacuum pressure that are insignificant.

The other main finding is that the pressure drop along the beam vessel slowly occurs for heavier gases, while the pressure of lighter gases falls quickly. According to Fig. 7, The gas distribution along the beam vessel for H_2 (light gas) is almost flat, while, for Ar (heavy gas) has a slope. This behavior of distribution is referred to the gas conductance.

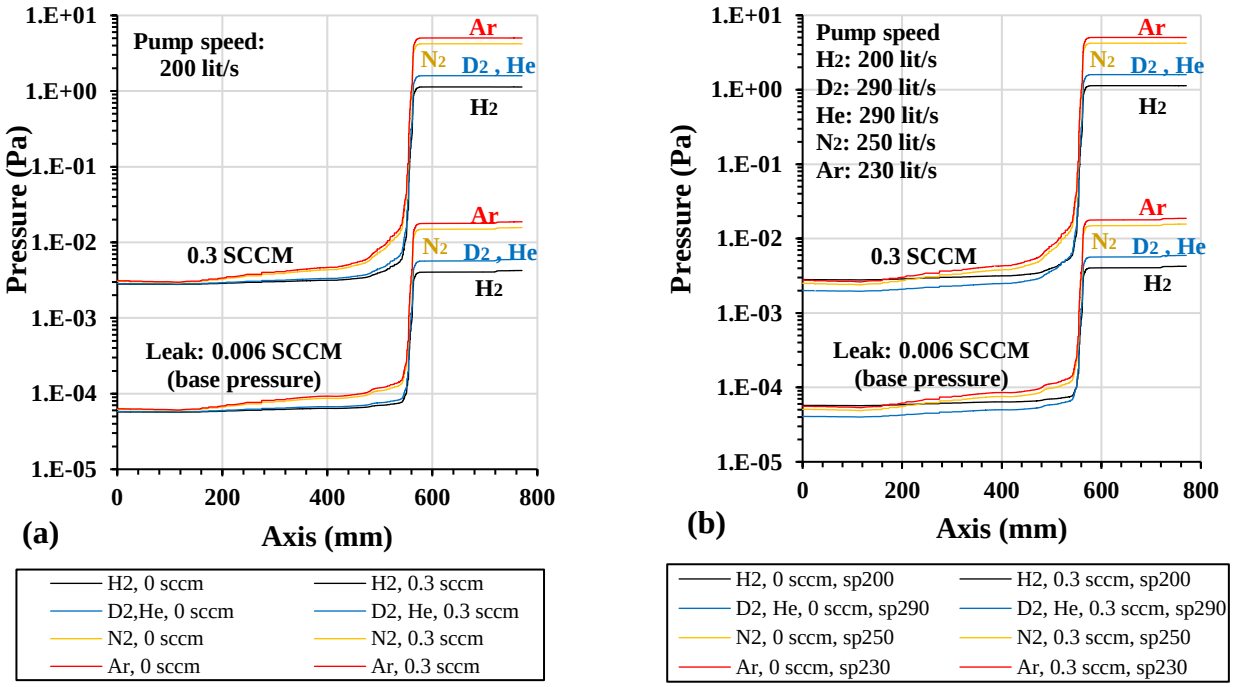

Fig. 7. The gas distribution of the H_2, D_2, He, N_2 and Ar along the accelerator for the injection flow rates of 0.006 (leak) and 0.3 SCCM. (a) with the same pump speed of 200 lit/s for all species, (b) with vacuum vessel equipped with Turbovac TW290 drive TD400 with specifications of approximated pump speed as H_2:200 lit/s, D_2 and He:290 lit/s, N_2:250 lit/s, Ar:230 lit/s.

Table 2. Molar mass, gas conductance [13], plasma source pressure (from this work), conductance ratio and plasma source pressure ratio respect to H2.

Gas	Molar mass [g/mol]	Conductance [lit/s.cm^2]	Plasma source pressure [Pa]	Conductance ratio	Plasma source pressure ratio
H_2	2.016	44	1.13	1	1
D_2	4.0028	31.1	1.59	$C(H_2) / C(D_2)$: 1.41	$p(D_2) / p(H_2)$: 1.40
He	4.0026	31.1	1.59	$C(H_2) / C(He)$: 1.41	$p(He) / p(H_2)$: 1.40
N_2	28.0134	11.75	4.21	$C(H_2) / C(N_2)$: 3.74	$p(N_2) / p(H_2)$: 3.72
Ar	39.96	9.85	5.02	$C(H_2) / C(Ar)$: 4.47	$p(Ar) / p(H_2)$: 4.44

Conclusions

The H_2 gas pressure in the test-bed electrostatic accelerator, which was constructed at NSTRI, is the subject of this work. The pressure was measured at two points of the accelerator; at the plasma source and the vacuum vessel. Then, the computational pressure along the accelerator was acquired by COMSOL simulation. The simulation acknowledged the experiment, which is a validation for our simulation model.

After model validation, the simulation was extended to investigate the effect of pump speed on the pressure. According to the results, the vacuum vessel pressure decreases with the increase of pump speed. However, the plasma source pressure was unchanged with changing the pump speed.

Another study investigated the effect of gas type on the pressure. In addition to H_2, the gases of D_2, He, N_2 and Ar were studied. This study shows that the gas type affects the pressure value and distribution. Heavier gases present higher pressure in the plasma source because of lower conductance. Also, the changes of the pressure along the beam vessel slowly occur for heavier gases, but the pressure above the pump almost is the same for all gases.

References

[1] Wiedemann, H. (2015). Particle accelerator physics. Springer Nature.

[2] De Esch, H. P. L., Kashiwagi, M., Taniguchi, M., Inoue, T., Serianni, G., Agostinetti, P., ... & Cavenago, M. (2015). Physics design of the HNB accelerator for ITER. Nuclear Fusion, 55(9), 096001.

[3] Agostinetti, P., Aprile, D., Antoni, V., Cavenago, M., Chitarin, G., De Esch, H. P. L., ... & Zaccaria, P. (2015). Detailed design optimization of the MITICA negative ion accelerator in view of the ITER NBI. Nuclear Fusion, 56(1), 016015.

[4] Hemsworth, R. S., Boilson, D., Blatchford, P., Dalla Palma, M., Chitarin, G., De Esch, H. P. L., ... & Zaccaria, P. (2017). Overview of the design of the ITER heating neutral beam injectors. New Journal of Physics, 19(2), 025005.

[5] Farahani, M., Kozák, T., & Pajdarová, A. D. (2023). Plasma diagnostics in high-power impulse magnetron sputtering of compound NbC target.

[6] Farahani, M., Kozák, T., Pajdarová, A. D., Bahr, A., Riedl, H., & Zeman, P. (2023). Understanding ion and atom fluxes during HiPIMS deposition of NbCx films from a compound target.

[7] Kazakov, Y. O., Nocente, M., Mantsinen, M. J., Ongena, J., Baranov, Y., Craciunescu, T., ... & Weisen, H. (2020). Plasma heating and generation of energetic D ions with the 3-ion ICRF+ NBI scenario in mixed HD plasmas at JET-ILW. Nuclear Fusion, 60(11), 112013.

[8] Sartori, E., Dal Bello, S., Serianni, G., & Sonato, P. (2013, February). Distribution of the background gas in the MITICA accelerator. In AIP Conference Proceedings (Vol. 1515, No. 1, pp. 121-128). American Institute of Physics.

[9] Sartori, E., Serianni, G., & Dal Bello, S. (2015). Simulation of the gas density distribution in the large vacuum system of a fusion-relevant particle accelerator at different scales. Vacuum, 122, 275-285.

[10] Sartori, E., Fincato, M., Siragusa, M., Pimazzoni, A., Grando, L., Tollin, M., & Serianni, G. (2020). Simulation and measurement of rarefied gas flow and neutral density profiles through a large multiaperture multigrid negative ion accelerator. Fusion Engineering and Design, 151, 111398.

[11] Siragusa, M., Sartori, E., Bonomo, F., Heinemann, B., Orozco, G., & Serianni, G. (2020). Simulation of the gas density distribution in the accelerator of the ELISE test facility. Review of Scientific Instruments, 91(1).

[12] Pavei, M., Dal Bello, S., Gambetta, G., Maistrello, A., Marcuzzi, D., Pimazzoni, A., ... & Tollin, M. (2020). SPIDER plasma grid masking for reducing gas conductance and pressure in the vacuum vessel. Fusion Engineering and Design, 161, 112036.

[13] Chiggiato, P. (2014). Vacuum technology for ion sources. arXiv preprint arXiv:1404.0960.

[14] Sartori, E., & Veltri, P. (2013). AVOCADO: A numerical code to calculate gas pressure distribution. Vacuum, 90, 80-88.

[15] Sartori, E., Dal Bello, S., Fincato, M., Gonzalez, W., Serianni, G., & Sonato, P. (2014). Experimental validation of the 3-d molecular flow code avocado. IEEE Transactions on Plasma Science, 42(9), 2291-2297.

[16] Kersevan, R., & Pons, J. L. (2009). Introduction to MOLFLOW+: New graphical processing unit-based Monte Carlo code for simulating molecular flows and for calculating angular coefficients in the compute unified device architecture environment. Journal of Vacuum Science & Technology A, 27(4), 1017-1023.

[17] COMSOL Multiphysics® v. 6.1. www.comsol.com. COMSOL AB, Stockholm, Sweden.

[18] Masoumzadeh, A., Habibi, M., & Mirzaei, H. R. (2024). Analytical solution versus the Monte Carlo simulation for studying the H+ beam neutralization in H_2 gas target neutralizer. International Journal of Hydrogen Energy, 57, 481-490.

[19] Luo, X., & Day, C. (2010). 3D Monte Carlo vacuum modeling of the neutral beam injection system of ITER. Fusion engineering and design, 85(7-9), 1446-1450.

[20] Free Molecular Flow Module User's Guide, pp. 64-80. COMSOL Multiphysics® v. 6. COMSOL AB, Stockholm, Sweden. 2022

[21] Wu, Z., Lian, C., Chundong, H., & Liqun, H. (2005). Analysis on pressure distribution in HT-7 neutral beam injection system. Plasma Science and Technology, 7(2), 2719.

[22] Chiggiato, P. (2020). Outgassing properties of vacuum materials for particle accelerators. arXiv preprint arXiv:2006.07124.

ICNST 2024 International Conference on Nuclear Science and Technology
6- 8 MAY 2024 | Isfahan, Iran

Investigation of Factors Influencing the Field Quality of a Synchrotron Bending Magnet using the Poisson Code (Paper ID : 1389)

F. Khodadadi Azadboni[1*], Elham Lotfizadeh[2] and Mahmoud Sadatagatizadeh[2]

[1] Department of Physics Education, Farhangian University, P.O. Box 14665-889, Tehran, Iran
F.khodadadi@cfu.ac.ir
[2]Department of Physics, K.N. Toosi University of Technology, P.O. Box 15875-4416, Tehran, Iran

Abstract

Bending magnets play a critical role in accelerator systems as they are responsible for bending the trajectory of charged particle beams. The design process involves optimizing the magnetic field parameters to ensure effective beam control and manipulation. In this study, a bending magnet is designed to generate a magnetic field with strength of 1.42 T and a gradient of 656.5 T/m. These parameters are carefully chosen to meet the specific requirements of the accelerator, enabling precise beam focusing and steering. The Poisson code plays a vital role in this research by enabling accurate and detailed simulations of the bending magnet. By inputting the magnet's geometry, material properties, and desired field parameters into the code, the resulting magnetic field distribution can be analyzed and visualized. This comprehensive assessment ensures the field remains stable, uniform, and properly shaped along the beam path. Furthermore, this paper explores the selection of alloy material for the bending magnet. The choice of alloy is crucial as it impacts various magnet properties, including magnetic permeability, mechanical strength, and thermal stability. By carefully considering material characteristics and conducting thorough analysis, the chosen alloy can meet the demanding requirements of the bending magnet design. The findings of this study contribute to the advancement of accelerator technology by providing valuable insights into the design and optimization of bending magnets using the Poisson code. Improving the performance and control of the magnetic field enhances the overall efficiency and reliability of high-energy accelerators. This has significant implications for applications such as particle physics research, medical imaging, and industrial processes requiring high-energy beams.

Keywords: Bending Magnet, Synchrotron, Poisson Code.

INTRODUCTION

Synchrotrons serve as powerful and effective tools for research in various scientific and medical fields, providing the ability to study the properties and behavior of particles at high energies [1-3]. Synchrotrons are devices used to accelerate particles to high energies for the study of their behavior and properties.

Constructing and operating a synchrotron involves significant costs, and increasingly complex models are being built every day. More powerful synchrotrons are constructed using larger radius paths and stronger microwave cavities to accelerate particles to very high speeds in bends and curves. Particles are initially injected into the central ring of the synchrotron, which is accomplished by an intermediate synchrotron or a linear accelerator with an initial energy [4-5]. The energy of the particles is then increased along the path. The particles pass through a high-voltage electrostatic accelerator. When the particle velocity is not close to the speed of light, the frequency associated with the voltage increase can be approximately synchronized with the cyclical magnetic field. The frequency control circuit operates using a servo loop sensitive to the passage of the moving particle group. As the particle velocity approaches the speed of light, the frequency practically approaches a constant value, and the current in the bending magnetic field increases continuously. The energy of such synchrotrons is limited by the strength of their magnetic field. The maximum energy to which particles can be accelerated (for a given ring size and a specific magnetic field strength) is determined by the saturation point in the magnetic field core, where increasing the current does not contribute to a stronger field.

Radiating particles such as electrons lose a significant fraction of their energy during rotation, so they need to be continuously accelerated. For this purpose, synchrotrons utilize strong magnetic fields. These fields guide the particles toward the center of the synchrotron ring and keep them on a curved trajectory to continuously increase their energy [6-8]. When particles approach the speed of light, the increase in particle energy is limited due to the increasing current in the bending magnetic field. In this regime, there is a need for a larger and more powerful synchrotron with a stronger magnetic field to accelerate particles to higher energies. Synchrotrons are used in various scientific disciplines. One way to increase the power of a synchrotron is to use larger radius bends and more magnets to create stronger magnetic fields. This allows the particles to require less change in direction during saturation, resulting in less energy loss [9].

Figure 1: Schematic diagram of electron acceleration in synchrotron and how synchrotron radiation is emitted

There are different types of magnets used in accelerators, each with its specific application. Dipole magnets are used to bend the particle beam in accelerators. Quadrupole magnets are used to focus the beam or create beam confinement. Sextupole magnets, on the other hand, are used for chromatic correction in accelerators. Dipole magnets are one of the fundamental types of magnets. They create a uniform magnetic field between two poles, allowing the particle beam to be deflected and follow an arc of a circle. Dipole magnets are constructed in three different shapes: C-shaped dipole magnet, H-shaped dipole magnet, and window-frame dipole magnet. The cross-sectional view of dipole magnets shows the particle beam moving in a small space between the two poles. The magnetic field direction is perpendicular to the electron's trajectory, causing the particles to move along an arc of a circle. Many of these magnets are required to complete a full circular path for the particleS [5-7].

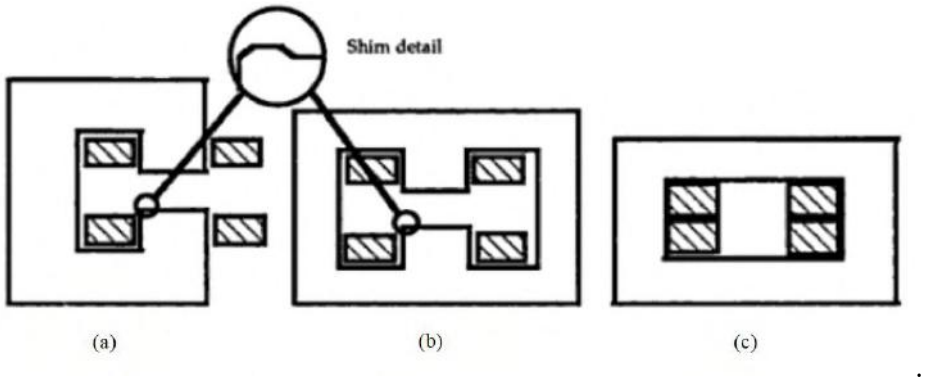

Figure 2: Cross section of a) C-core, b) H-core bipolar core and c) Window frame.

The magnetic field observed around iron poles is a known magnetic field and is part of a low to medium energy accelerator system used for transporting low to medium energy charges [4]. In iron poles, the highest field levels are below the maximum saturation levels, which are induced through current transfer in wire coils. Understanding the function of this magnet requires understanding the forces and their directions affecting the trajectory of charged particles, which is commonly modeled [7]. In a circular particle accelerator or a curved beamline in a transfer line, dipole magnets are the most commonly used elements. A dipole magnet creates a uniform field between its poles, generated by alternating current induced in the wire coils. In other words, an alternating current flowing clockwise around the poles creates a downward uniform magnetic field, which aims to bend and guide the trajectory of charged particles.

The creation of a three-dimensional magnet starts with a two-dimensional design. Designing a two-dimensional magnet requires determining the path of the poles to achieve a specified and uniform field

strength using non-ideal boundary conditions determined by the induction and physical dimensions and location of the wire coils and the physical boundary conditions of the steel cores. The design process involves defining a primary path for the pole, analyzing its behavior, improving the pole by modifying its shape, and iteratively repeating the processing steps until the desired two-dimensional and uniform field strength is achieved. Therefore, in this research, the Poisson code software has been used to simulate the bending magnet of a synchrotron. The quality of the field and the field gradient and the type of alloy used in the design of the bending magnet for the optimization of the Poisson code[10] are investigated.

RESEARCH THEORIES

This article presents a research study focused on the design of a dipole magnet used for bending ion beams in a synchrotron. The specific design approach involves a combination of magnets with a focusing element. The bending magnet is utilized in the accelerator, which operates at 3 GeV energy. The storage ring consists of 32 dipole magnets with a maximum field strength of 1.42 Tesla and a gradient of 656.5 T/m. The magnet used in this design is of the C-shape type, with a bending angle of 11.25 degrees and a bending radius of 0.0477 m. The magnet gap measures 36 mm, and the desired field quality is specified as $\Delta B/B_0 \leq \pm 10^{-4}$. These parameters are crucial for the successful design of the bending magnet. In the dipole magnet design, the most important parameters that we need are listed in Table 1.

Table 1: Parameters of the Bending Magnet

parameter	value
Beam energy	3 GeV
Magnet type	C- shape dipole
1/42 T	Central field (B_0)
5/656 T/M	Field gradient (G_0)
7/047 M	Bending radius
11/25 Degrees	Bending angle
36 mm	Gap (g)

Magnetic gradient includes bending and focusing vertically. Magnetic gradient requires central field B_0 and gradient (slope) B', half the height of the gap h, and cut-off center (transverse) x = 0. To determine the appropriate equation for the magnet pole tip gradient, the following expression is used:

$$Y_{Gradiant} = B_0 h / (B_0 + B_x^{'}) \quad (1)$$

Here, h represents half of the gap height is h = ±g/2 = ±18 mm. Therefore, the pole equation for the magnetic gradient was used equation 1.The next step involves calculating the excitation current. Each coil requires a total current, which can be computed using the following equation:

$$NI = B(h + l_{iron}/\mu_r) / \mu_0 \quad (2)$$

In the equation 2, NI represents the excitation current, B denotes the magnetic induction, μ_r is the relative permeability, and μ_0 is the permeability of free space. The ideal coil shape is illustrated in Figure (3), consisting of four loops, with each loop comprising ten turns. The bending magnet is designed in a rectangular shape. This geometric shape is commonly used for bending magnets and can be made of copper or aluminum. The bending magnet is equipped with a complete water cooling system. This water pipe serves as a cooling mechanism to maintain the temperature of the bending magnet within an acceptable range. To provide insulation, the bending magnet is coated with a glass covering. This glass coating acts as an insulator to prevent direct contact between the bending magnet and the external environment. The design of the bending magnet involves specifying the current-turns. This refers to determining the current passing through the bending magnet, which determines the rotation rate of the magnet. The total conducting space and the number of turns in the bending magnet have two degrees of freedom. This means that the current-turns and rotation rate can be determined to optimize the efficiency and performance of the bending magnet. The currents and twisting of the bending magnet can cause perturbations. To minimize the impact of perturbations on the performance of the bending magnet, precise calculations, modeling, and necessary corrections are required.

The conductor size is 16.6 × 10.75 mm, and the maximum excitation current is 527 A, resulting in a total current of approximately 21000 A-turns. The l_{iron}/μ_r factor represents the magnetic resistance of the alloy, which depends on the core material. The magnetic permeability in the 1.5 T field is precisely 1999. Additionally, the magnetic field line length inside half of the magnet measures 746.5 mm, resulting in a magnetic resistance of 0.373 A/T. Therefore, the excitation current for a dipole magnet is approximately 772.52 A-turns, while for the specified B_0 = 1.42 T field at the magnet center, it is approximately 20746.60 A-turns.

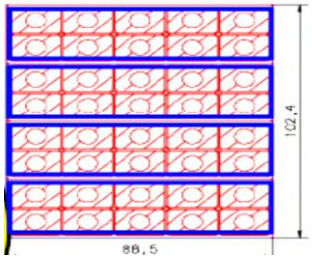

Figure (3): Four-layer torus

In this design, the field quality in the central pole region is evaluated for a combined magnet configuration. The field quality is determined by the following equation:

$$\Delta B/B_0 = [(B_y(x) - B_y(0) - gx]/ B_y(0) \quad (3)$$

Where g represents the central gradient. To analyze the magnetic properties of the magnets, the permeability of the alloy is utilized.

Results and discussion

In the design of the bipolar magnet, with millimeter changes of the points of the bending magnet, we can reach the desired design with the desired characteristics. The results obtained for the design of the pole tip coordinates are given in Table 2. The final points for better magnet design that are required are shown. Based on the provided intervals and field quality requirements, the field quality can be represented as follows:

For the range $-10 \leq X \leq 10$, the field quality is given by $\Delta B/B_0 = \pm 7\times10^{-5}$

For the range $-20 \leq X \leq 20$, the field quality is given by $\Delta B/B_0 = \pm 5\times10^{-5}$

To meet the field quality requirements for a dipole magnet, $\Delta B/B_0$ should be $\leq 10^{-4}$.

Considering both intervals, we can see that the field quality of ±20 is more suitable than the initial value and satisfies the field quality requirement. Therefore, we can choose the field region of ±20 as the appropriate field region. With the simulation of a bending magnet using the Poisson code, after completing the design, it can display the Poisson output and the cross-sectional profile of the bending magnet. Figure 4 shows a view of the tip of the designed pole. The design of the bending dipole magnet with the required magnetic field and magnet gradient in the accelerator has been completed. The cross-sectional profile of the

upper half of the dipole magnet, with the field range at x=0, y=18mm and a field strength of 42/1 T, is shown in Figure 4. This software is capable of plotting field curves and field gradients. Additionally, it can plot the magnetic field in both vertical and horizontal directions and the gradient using the same program. The figure 5 shows a complete view of the magnetic and of bending magnet design. depict the field curve and field gradient in the region $-30 \leq X \leq 30$.

Table 2: The final coordinates of the designed pole tip

NO	X	Y	NO	X	Y	NO	X	Y
1	-30/376	20/220	31	5/000	17/647	61	87/339	85/554
2	-24/029	19/810	32	6/000	17/580	62	88/000	90/251
3	-22/863	19/770	33	7/000	17/511	63	104/000	153/000
4	-22/053	19/733	34	8/000	17/442	64	109/000	158/000
5	-21/000	19/642	35	9/000	17/375	65	-51/000	240/645
6	-20/000	19/542	36	10/000	17/311	66	-51/000	151/400
7	-19/000	19/471	37	11/000	17/242	67	-51/000	27/745
8	-18/000	19/387	38	12/000	17/176	68	-50/116	25/450
9	-17/000	19/307	39	13/000	17/114	69	-47/929	23/584
10	-16/000	19/224	40	14/000	17/048	70	-45/185	22/150
11	-15/000	19/141	41	15/000	16/984	71	-40/599	21/042
12	-14/000	19/061	42	16/000	16/922			
13	-13/000	18/983	43	17/000	16/854			
14	-12/000	18/904	44	18/000	16/795			
15	-11/000	18/823	45	19/000	16/731			
16	-10/000	18/742	46	20/000	16/650			
17	-9/000	18/69	47	21/023	16/561			
18	-8/000	18/91	48	21/993	16/481			
19	-7/000	18/16	49	23/253	16/361			
20	-6/000	18/41	50	25/372	16/061			
21	-5/000	18/366	51	27/944	15/715			
22	-4/000	18/291	52	30/863	15/482			
23	-3/000	18/218	53	33/105	15/555			
24	-2/000	18/145	54	36/000	16/406			
25	-1/000	18/072	55	37/944	17/104			
26	0/000	18/000	56	39/428	17/879			
27	1/000	17/929	57	40/000	18/411			
28	2/000	17/858	58	41/178	19/264			
29	3/000	17/787	59	45/222	22/878			
30	4/000	17/718	60	51/733	27/740			

Considering the field quality relationship in the range $-20 \leq x \leq 20$, the desired quality is given by $\pm 5 \times 10^{-5}$ $\Delta B/B_0$, indicating that this design has a very low error percentage and is an ideal design. Figure 5.(b) shows the plot of $B_y(x)$-gx, which represents the suitable range for the field quality. Figure 6 displays the plot of magnetic permeability as a function of field for the magnet alloy used in the design. Additionally, Figure 6 show the B-H and H-μ curves, respectively. Furthermore, in Figure 7 (a) and (b), the permeability plot for the two matrial alloy is presented. By overlapping these two curves and comparing of two matrial, we can observe that the permeability of the material of steel ALBA is higher than that of the steel 1010 material.

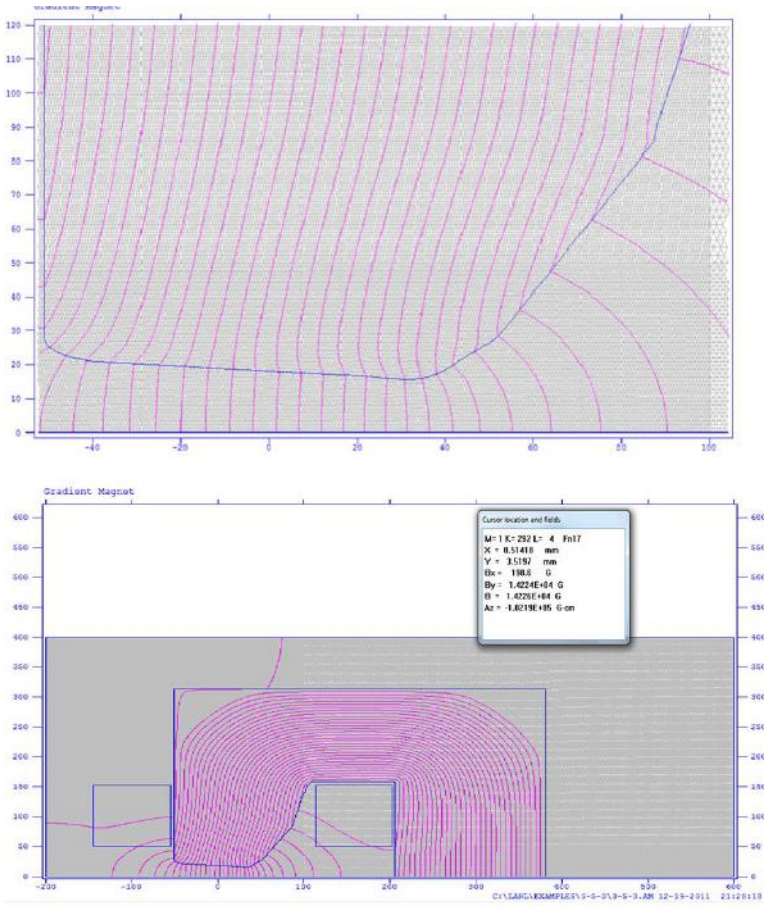

Figure 4: Cross-section of the pole with half of the 18mm hole in the center of the magnet

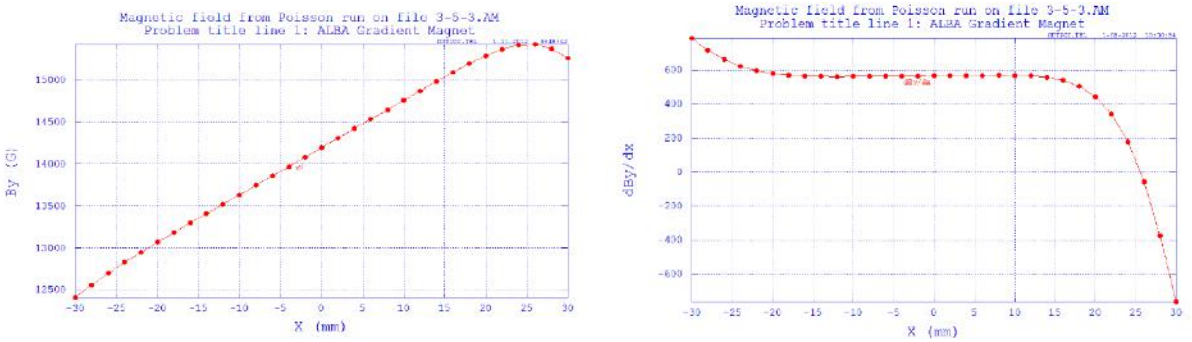

Figure 5. field in the area inside the gaff (a)Vertical field in the region 30≤X≤-30 (b) Field quality, Magnetic field gradient in the area of 30≤X≤-30

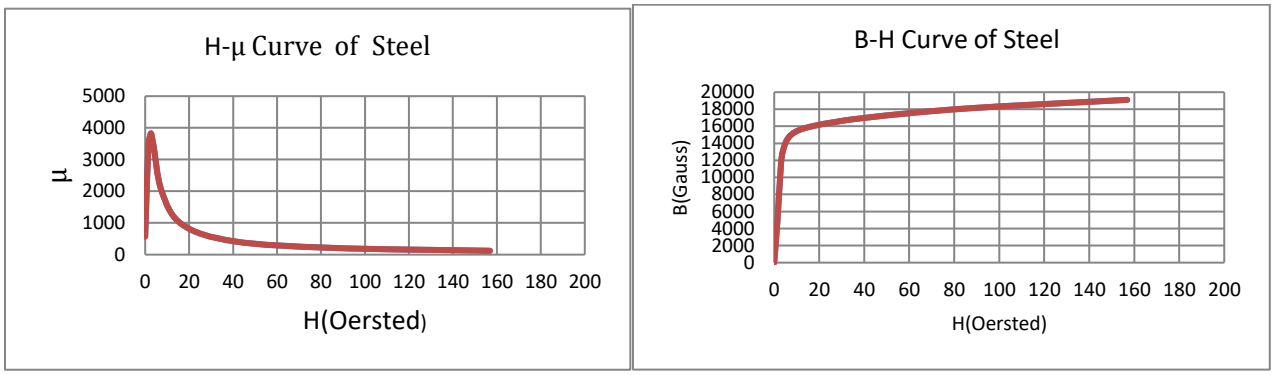

Figure **6**. B-H and H-μ curves

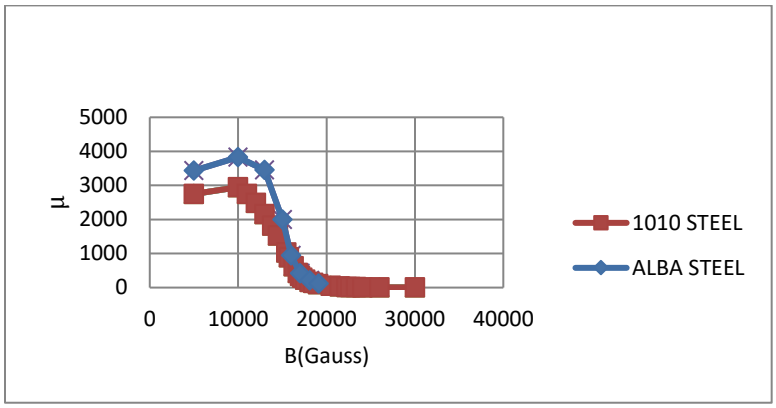

Figure 7. μ-B curve of two types of alloys used in the bending magnet

Conclusions

Bending magnets are used to steer charged particles, such as electrons or protons, in circular paths within synchrotron accelerators. These magnets generate a strong magnetic field perpendicular to the particle trajectory, causing the particles to curve and follow a circular path. The design of the bending dipole magnet has been completed, achieving the desired magnetic field and magnet gradient required for the accelerator. The design shows a very low error percentage, with a desired field quality of $\pm 5\times10^{-5}$ $\Delta B/B_0$ in the range $-20 \leq x \leq 20$. This indicates that the design is ideal and meets the required field quality criteria. Generally, a higher permeability is beneficial for magnetic materials used in magnets. A higher permeability material allows for a stronger magnetic field to be generated within the magnet. This is crucial for bending magnets as it determines the curvature and radius of the particle trajectory. Higher permeability materials enable the generation of stronger magnetic fields with a given amount of magnetic material. This allows for more efficient use of the magnet's volume and reduces the amount of material required, which can be important for space and cost considerations. Materials with higher permeability can help improve the homogeneity of the magnetic field within the bending magnet. This is desirable for maintaining precise control over the

particle trajectories and minimizing beam dispersion. With a higher permeability material, it is possible to achieve the desired magnetic field strength using lower excitation currents. This can result in reduced power consumption and heat generation, contributing to the overall efficiency of the accelerator. Considering these factors, the selection of a higher permeability material for the bending magnet in the synchrotron accelerator is beneficial in terms of achieving desired magnetic field strength, efficiency, and control over particle trajectories.

References

[1] Mondal, S. S. (2019). *design optimization of a support for the storage ring quadrupole magnet in a synchrotron radiation facility* (Doctoral dissertation, University of Saskatchewan).

[2] Chertok, I., Michailov, S., & Sukhina, B. The magnet system for the BESSY II injector synchotron.

[3] Livet, F., Bley, F., Létoublon, A., Simon, J. P., & Bérar, J. F. (1998). Coherent small-angle scattering on a bending-magnet beamline at the ESRF. *Journal of Synchrotron Radiation*, *5*(6), 1337-1345.

[4] Krzywinski, J., Saldin, E. L., Schneidmiller, E. A., & Yurkov, M. V. (1997). A new method for ultrashort electron pulse-shape measurement using synchrotron radiation from a bending magnet. *Nuclear Instruments and Methods in Physics Research Section A: Accelerators, Spectrometers, Detectors and Associated Equipment*, *401*(2-3), 429-441.

[5] Newborough, A., Buzio, M., & Chritin, R. (2013). Upgrade of the CERN proton synchrotron booster bending magnets for 2 GeV operation. *IEEE transactions on applied superconductivity*, *24*(3), 1-4.

[6] Zhang, H., Li, W. M., Feng, G. Y., Wang, L., Zhang, S. C., Li, W., & Liang, J. J. (2012). The magnet design for the HLS storage ring upgrade project. *Chinese Physics C*, *36*(1), 91.

[7] Khachatryan, V., Martirosyan, Y., & Petrosyan, A. (2004). Magnets for the CANDLE Booster Synchrotron, Design and Prototyping.

[8] Saeidi, F., Razazian, M., Rahighi, J., & Pourimani, R. (2016). Magnet design for an ultralow emittance storage ring. *Physical Review Accelerators and Beams*, *19*(3), 032401.

[9] Razazian, M., Saeidi, F., Yousefnejad, S., & Rahighi, J. (2020). Magnet design for Iranian Light Source Facility storage ring. *Journal of Instrumentation*, *15*(08), P08002.

[10] POISSON/SUPERFISH group of codes, Los Alamos National Laboratory Report No. LA-UR-87-126 (1987).

ICNST 2024
International Conference on Nuclear Science and Technology
6- 8 MAY 2024 | Isfahan, Iran

A study on a setup including scintillation detectors with the purpose of muon imaging using cosmic muons (Paper ID : 1401)

Fazlalizadeh M.[1], Bahmanabadi M.[2]

[1]Department of Physics, Payame Noor University, Tehran, Iran
[2] Department of Physics, Sharif University of Technology, Tehran, Iran

Abstract

A setup consist of scintillation detectors was designed based on available equipment in the cosmic ray laboratory of Physics Department at Sharif University of Technology. This paper studies the capability of this setup to be applied for muon imaging using cosmic muons. Two $10\times10cm^2$ scintillation detectors (Scin.A & Scin.B) as a muon tracer and a coincidence electronic circuit was applied to record data.

At first, a $100\times15cm^2$ scintillator was considered as an object and was divided into 10 regions. All regions were scanned by Scin.B and coincidence spectra of all these regions were recorded. General characteristics of this setup were studied. Next, a number of lead blocks were used as an object between Scin.A and Scin.B while they were all along. The Merit Factor of count rate in the absence and presence of different lead thicknesses shows this setup can be used to distinguish lead as a dense object.

Keywords: Muon Imaging, Cosmic Rays, Scintillation Detector

Introduction

Since muon imaging has experienced impressive developments, this method has been widely used in different fields. For instance, archeology [1], geology [2], security [3], etc. Muon imaging studies muon energy reduction or direction deflection in dense materials and massive elements to image structures with different dimensions and thicknesses. Energetic muons are more preferable to be used in muon imaging.

Cosmic rays are safe, available and free sources to produce energetic muons. When high energy primary cosmic particles (mostly protons) arrive the atmosphere, they interact with it and start showers of energetic secondary particles. Among produced secondary particles, muons are most likely to pass through the atmosphere and reach the ground [4], so cosmic muons with high penetration depth that are naturally made in the atmosphere are suitable particles to be used in muon imaging.

As muons pass through the material, energy reduction or direction deflection will occur. These two electromagnetic effects will lead to two types of muon imaging techniques: absorption imaging and muon scattering imaging [5].

Absorption muon imaging technique is based on muon energy loss (ionization and bremsstrahlung) in matter. By increasing the energy loss in a target, the muon crossing probability decreases. This technique is applied to large structures and dense materials. Improving spatial and angular resolution of muon detection makes determination of the muon path in the object more precise. Cavity or high dens region in the object can be found by comparing the absorption rate in different directions. As energy loss depends on integration of density over the path length, density can be estimated by knowing the average thickness of the object [6].

Muon direction is deflected in the matter due to multiple scattering, which leads to other techniques of muon imaging. By increasing the atomic number and density of a substance, the deviation angle is also increasing. To reconstruct muon direction and determine the deflection angle, the object needs to be placed between two sets of detectors. Identifying massive or dense areas in the object is obtained by studying deflection angles [6].

As our first attempt, we used available plastic scintillator detectors at the Cosmic Ray Laboratory (CR lab) of Sharif University of Technology's Physics department to find out if this equipment is appropriate to be used for muon tracking.

Experimental Setup

We used coincidence method between two $10\times10cm^2$ scintillators (Scin.A and Scin.B). Scin.A and Scin.B play the role of muon tracer. To make sure that the recorded coincident event by tracer scintillators is related to a particle that passes through the object, we select $100\times15cm^2$ scintillator as an object (Scin.C). In order to record its coincidence with Scin.A and Scin.B, Scin.C was placed on a table and divided into ten $10\times15cm^2$ regions. Scin.A was placed parallel to Scin.C at a distance of 1m from it, so that its center was just above the center of the first region of Scin.C. Scin.B is movable and was placed on Scin.C and moved in 10 regions. When Scin.B is in the first region, the center of Scin.B and the center of Scin.A are on the same vertical line.

Four photomultiplier tubes (PMT, 9813B with diameter of 5cm) were used in this experiment. PMT1 and PMT2 are respectively connected to Scin.A and Scin.B via plastic light guides. As shown in Fig. 1, PMT3 and PMT4 are connected to the two ends of Scin.C (Fig. 1).

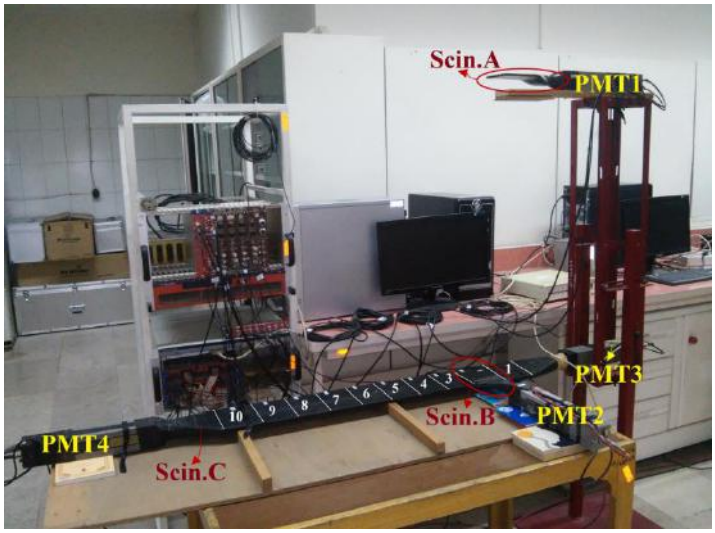

Fig. 1. Experimental setup. Various detectors and photomultipliers are indicated.

The signals produced by the PMTs are entered into a fast discriminator (CAEN N413A) where all channels are set at 25mV as the threshold level. The output of the discriminator channel related to PMT1 has been sent to the start inputs of TAC1, TAC3 and TAC4 (Time to Amplitude Converter, ORTEC 566). The outputs of other channels of the discriminator related to PMT2, PMT3 and PMT4 have been sent to the stop inputs of the mentioned TACs by different delay cables (Fig. 2). Finally, the outputs of the TACs, with a gate width of 200ns, are sent to a multichannel analyzer (MCA) via an analogue to digital converter unit (ADC, KIAN AFROUZ Inc.). The time lag between PMT2 and PMT3 was also recorded just for check. In this electronic circuit, the existence of a coincident event between Scin.A & Scin.B is considered as a trigger condition to record other signals.

We recorded the time coincidence between PMT1 and other PMTs which, from now on, we call these coincidences $T_{1\&2}$, $T_{1\&3}$, $T_{1\&4}$ and $T_{2\&3}$.

To find a suitable data acquisition time, at first a 5-day interval is chosen, then statistical analysis lead us to shorter data-taking intervals, so we reduced data acquisition time to 46 hours. All experiments in this report start at a certain time of the day for 46 hours.

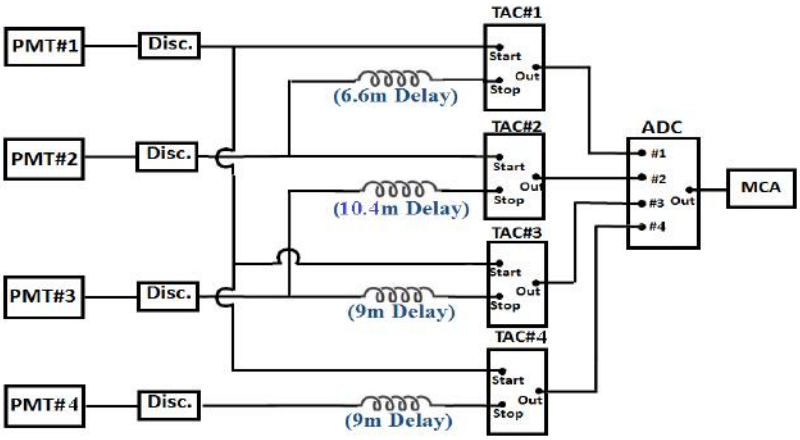

Fig. 2. Schematic view of electronic circuit.

Setup Examination (Experiment & simulation)

First to study the outcomes of the set up described above, we conducted an experiment and a simulation. In the designed experiment, we displaced Scin.B from region 1 to 10 and coincidence spectra of each region were recorded. Obtained coincidence spectra were fitted by Gaussian function ($f(t) = \boldsymbol{N} \exp(-(t-\boldsymbol{\tau})^2/2\boldsymbol{\sigma}^2)$). The peak position of the coincidence spectrum (τ) and half width of half maximum of the coincidence spectrum (σ) of each region is shown in Fig. 3 (left). As can be seen in it small changes occurred for the peak position of coincidence spectrum related to Scin.A and Scin.B, because their distance change in comparison of muon speed is negligible. In the case of our long detector (Scin.C) it took a longer time to form coincidence spectrum ($T_{1\&3}$) by moving Scin.B to regions farther from PMT3, for $T_{1\&4}$, τ has almost the reverse behavior. It should be mentioned that in this figure and some of the next figures error bars are smaller than the dimensions of the data points.

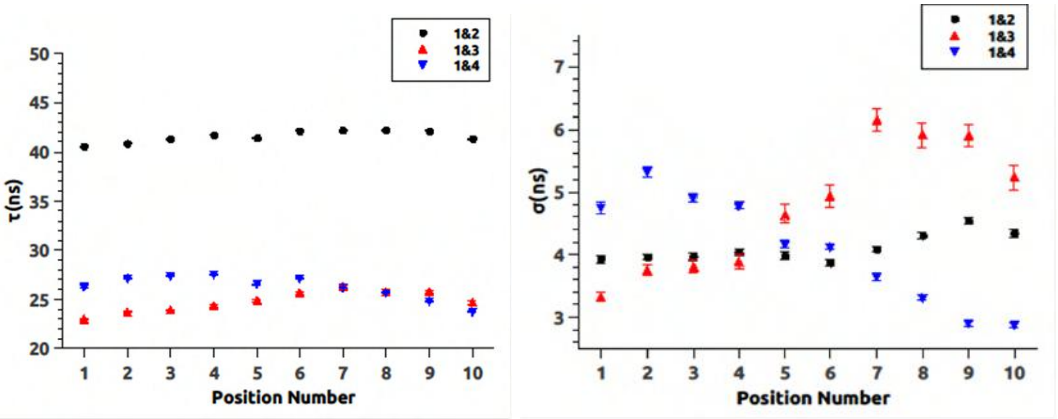

Fig. 3. The peak position of coincidence spectrum (left) and half width of half maximum of the coincidence spectrum (right) obtained from Gaussian function fit via number of region.

Fig. 3 (right) illustrates HWHM of three coincidence spectrums for different coincidences in all regions. For $T_{1\&2}$, by going to further regions, the effective area of detection decreases and particles traverse along longer path. The convolution of these two effects results in what can be seen in the plot. For $T_{1\&3}$ and $T_{1\&4}$ respectively, increasing and decreasing the distance from PMT3 and PMT4 is also effective.

The number of detected particles (count) is shown for each region in Fig. 4. Counts of $T_{1\&2}$ are decreased by moving Scin.B along Scin.C. As PMT3 and PMT4 are placed on two opposite sides of Scin.C, by moving Scin.B along Scin.C they show the reverse behavior, because of the distance of Scin.B from each PMT.

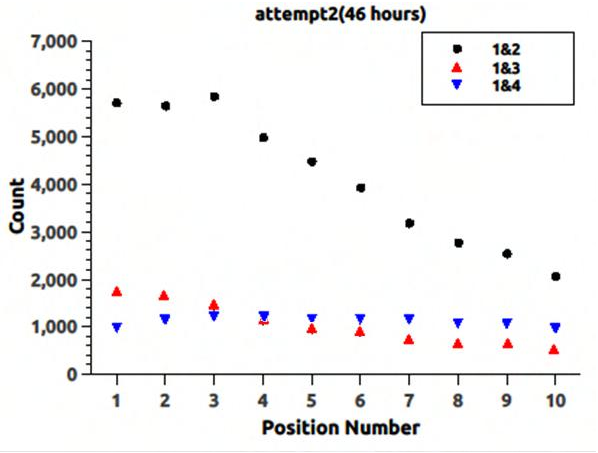

Fig. 4. Number of detected particles (count) for each region on Scin.C.

Next, we simulate our setup with GEANT4 toolkit [7]. Because we use cosmic muons as traversed particles in our setup, the outputs of the CORSIKA simulation [8] were used as input data in the simulation.

CORSIKA (Cosmic Ray Simulations for Kascade; version 74000) is used to simulate extensive air showers, initiated by proton, alpha, and different atomic nuclei as primary particles. Various models of Hadronic interaction are available in this program. The QGSJET (qgsjet01.f package) model [9] for hadronic interactions above *Elab* = 80GeV, and the GHEISHA [10] model for below *Elab* = 80GeV are used. These simulations were carried out at Tehran's level ($35^{\circ}43'N, 51^{\circ}20'E, 1200m\ a.s.l = 897g/cm^2$), and the components of the geomagnetic field are B_x = 27.97μT, B_z = 39.45μT at this site, which are taken from NOAA's National Centers for Environmental Information (NCEI) [11].

In Geant simulation, a muon source is considered as a 10×10cm^2 square which is divided into 25 equal sections, right above Scin.A. 10^6 muons are emitted from the center of each section of the source with

energy spectrum and angular distribution obtained from CORSIKA. It is worth mentioning that $\frac{\mu^+}{\mu^-} = 1.2$ [12] which is extracted from CORSIKA's outputs is also applied for source.

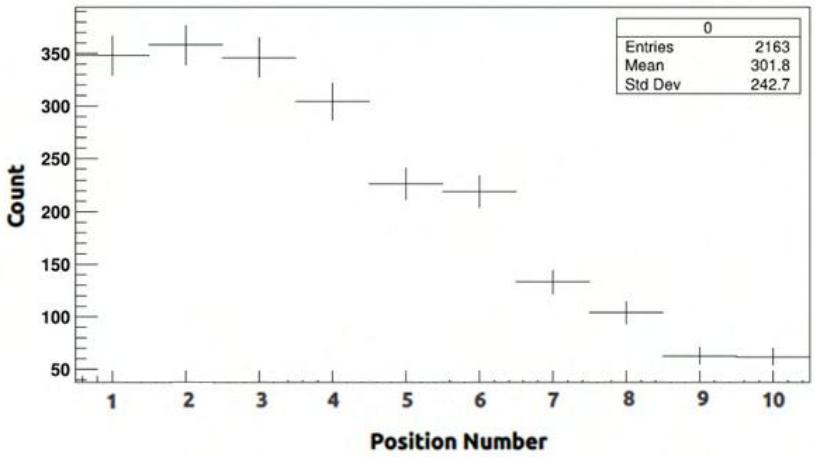

Fig. 5. The number of detected particles for each region on Scin.C obtained from simulation.

Fig. 5 shows the number of detected particles (count) for each region on Scin.C, it can be seen that simulated and experimental results have the same behavior.

In Fig. 4 and Fig. 5, by going farther from region 1 on Scin.C further effective detection area of Scin.A and Scin.B which triggers other PMTs decreases. At this point, calculating the acceptance is necessary.

In simulation, the initial condition for each region are constant and only geometry has been changed.

So the acceptance in each region only depended on the geometry of how Scin.B is placed in respect of Scin.A. We divided each scintillator area into 100 elements, which each element of the upper detector (Scin.A) is considered as a point source (*dA*) for all elements of lower one (Scin.B) (Fig. 6).

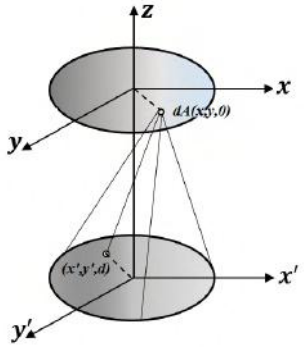

Fig. 6. Each element of the upper detector is considered as a point source (*dA*) for all elements of the lower one.

Using the following formula, the acceptance was calculated for each region in figure 6.

$$A = \int_{A_u} dA_{up} \int dA_{bottom} \frac{cos\theta}{r^2} \quad , \quad \frac{\hat{n}.\vec{r}}{r} = cos\theta$$

For rectangular areas, the formula converts to

$$A = \int_{-a_1}^{a_1} \int_{-b_1}^{b_1} dxdy \int_{-a_2}^{a_2} \int_{-b_2}^{b_2} dx'dy' \frac{d}{(d^2 + (x - x')^2 + (y - y')^2)^{\frac{3}{2}}}$$

Calculated acceptance of Scin.A and Scin.B for each region in Scin.C is reported in Table1.

Table 5. Acceptance of Scin.A and Scin.B for each region in Scin.C.

Number of region	1	2	3	4	5	6	7	8	9	10
Acceptance	0.99	0.98	0.94	0.87	0.80	0.71	0.63	0.55	0.48	0.41

By applying this method and enforcing the acceptance for each region, the plots of Fig. 4 are converted to Fig. 7. After enforcing the acceptances, the count of $T_{1\&2}$ in different regions is almost the same. The reverse behavior of $T_{1\&3}$ and $T_{1\&4}$ is more obvious now.

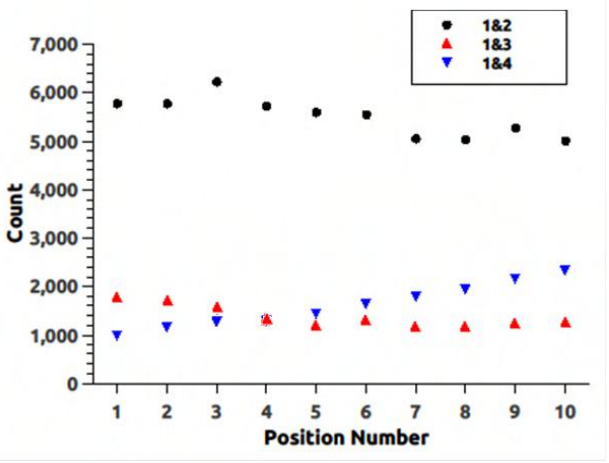

Fig. 7. Number of detected particles (count) for each region after enforcing the acceptance.

Possibility of imaging lead blocks by means of the defined setup

In the next step, we used some lead blocks (each 5×15×15cm^3) as an object between Scin.A and Scin.B while they were all along in the above-mentioned setup. Lead is a dense matter and has some influences on the count of traversed particles. As can be seen in Fig. 7, by adding more blocks as an object, the count of record particles was reduced due to the absorption and deflection. To omit low energy particles, we placed lead blocks above Scin.A as a shield. Now each particle for reaching Scin.A has to traverse these lead blocks, and it is more likely to be a muon. When just one block (5cm Pb) was placed above Scin.A count for various thicknesses of objects has different trends. It could be due to cascade formation in the lead above Scin.A, so we decided to add more blocks. Fig. 8 also shows the count versus the thickness of the object for the different thicknesses of Pb shield above Scin.A. When the thickness of Pb shield above Scin.A increases, the count decreases for the same Pb object thickness.

The Merit Factor (MF) was calculated to figure out if we are capable of distinguishing the presence of the lead object located between Scin.A and Scin.B by means of the number of detected cosmic particles. $MF_{a,b}$ is defined as below:

$$MF_{a,b} = \frac{|a-b|}{\sqrt{\sigma_a^2 + \sigma_b^2}}$$

where a and b are the number of detected particles and σ_a and σ_b are their errors.

The number of detected particles in the experimental setup with different thicknesses of Pb shield above Scin.A in the presence and absence of Pb object is reported in Table 2. $MF_{0,5}$ was calculated by using counts the absence and presence of a 5cm Pb object and is shown in this table too. As it can be seen, the presence of a 5cm Pb object is distinguishable for all Pb shield thicknesses expected for the 10cm Pb shield. This exception may be caused by experimental uncertainties. Therefore, $MF_{0,10}$ was also calculated by using counts in the absence and presence of a 10cm Pb object. All MFs are more than 1, and it makes us sure that this setup is able to distinguish the presence of a Pb object with 10cm thickness and more by using cosmic muons.

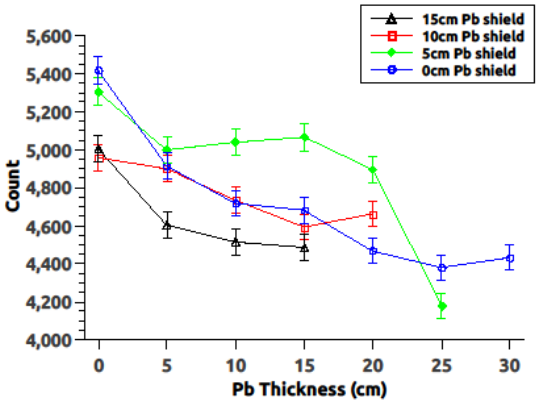

Fig. 8. Count versus thickness of object for different thicknesses of Pb shield above Scin.A.

Table 2. The particles counts in the experimental setup with different thicknesses of Pb shield in the presence and absence of Pb object and the calculated Merit Factors ($MF_{0,5}$ and $MF_{0,10}$) related to them.

		Object Thickness (cm)			Merit Factor	
		0	5	10	$MF_{0,5}$	$MF_{0,10}$
Shield Thickness(cm)	0	5416±73.59	4914±70.10	4717±68.68	4.94	6.94
	5	5304±72.83	4998±70.70	5038±70.98	3.01	2.62
	10	4956±70.40	4898±69.98	4734±68.80	0.58	2.26
	15	5005±70.75	4603±67.84	4513±67.16	4.10	5.04
	20	4857±69.69	4415±66.44	4155±64.46	4.59	7.39
	25	4782±69.15	4425±66.52	----------	3.72	-----

Event Rate

For all experiments in previous sections, $\bar{t} = \frac{time}{count}$ is calculated and reported in Table 3. It means that we detect 1 event per $\bar{t}(s)$. Since we assume that these events are random, it is expected that the time-spacing distribution of successive recorded events in each experiment follows an exponential decay function ($N = N_0 + A \exp(-t/T)$). The event rate (T) is also reported in Table 3. As it expected T and $\bar{t}$ are almost the same and recorded events are completely random.

Table 3. Compering time factor T and $\bar{t}$ for each experiment.

	0cm Pb shield		5cm Pb shield		10cm Pb shield		15cm Pb shield	
Thickness of object	T(s)	$\bar{t}$(s)	T(s)	$\bar{t}$(s)	T(s)	$\bar{t}$(s)	T(s)	$\bar{t}$(s)
0 cm	30.67	30.58	29.68	31.22	33.30	33.41	32.73	33.09
5 cm	32.45	30.70	32.12	33.13	33.61	33.81	34.93	35.98

10 cm	35.24	35.11	32.38	32.87	32.20	34.98	37.22	36.69
15 cm	35.69	35.38	32.70	32.70	36.12	36.05	36.29	36.92
20 cm	36.63	37.08	33.33	33.85	34.08	35.52		
25 cm	38.82	37.81	40.58	39.64				
30 cm	37.77	37.37						

Conclusion

In this work we use available equipment to study the possibility of muon imaging using cosmic muons by two $10\times10cm^2$ scintillation detectors as muon tracer (Scin.A & Scin.B) and coincidence circuit to record data.

To evaluate the performance of this setup, a $100\times15cm^2$ scintillation detector is used as an object. The number of detected particles, peak position and HWHM of the Gaussian function fitted to coincidence spectra in all regions of the object were studied. This setup is simulated by Geant4 and characteristics of input muons are obtained from CORSIKA. The reduction of count in $T_{1\&2}$ that can be seen in the experiment is also seen in the simulation results. This reduction is only depend on the geometry of the tracers' position. After applying the acceptance correction to the experimental data, the count of $T_{1\&2}$ shows uniform behavior.

Next, we placed different thicknesses of lead blocks as an object between tracers while Scin.B is in position No.1 and the count is recorded. Calculating the Merit Factors of counts shows that the presence of the lead object with thickness 10cm and more is distinguishable by our setup.

Reference

[1] Morishima, K. et al. (2015). Discovery of a big void in Khufu's Pyramid by observation of cosmic-ray muons. Nature, 24647

[2] Zhang, Z. et al. (2020). Muography and Its Potential Applications to Mining and Rock Engineering. Rock Mechanics and Rock Engineering. 53, 4893–4907.

[3] Barnes, S. et al. (2023). Cosmic Ray Muography for Border Security. Instruments 7(13)

[4] Grieder, P. (2010) Extensive Air Showers. Springer.

[5] Bonechi, L. et al. (2020). Atmospheric muons as an imaging tool. Rev. Phys. 5, 100038

[6] Sebastien Procureur, S. (2018). Muon imaging: Principles, technologies and applications. Nucl. Inst. Meth. A, 878:169.

[7] The GEANT4 Collaboration. GEANT4 – a simulation toolkit. NIM A 506 (2003).

[8] D. Heck, J. Knapp, J.N. Capdevielle, G. Schatz, T. Thouw. "CORSIKA". 1998.

[9] N. N. Kalmykov, and S. S. Ostapchenko, Yad. Fiz 56, 105 (1993), Phys. At. Nucl. 56 N3, 346(1993), N. N. Kalmykov and S. S. Ostapchenko and A. I. Pavlov, Izv. RAN Ser. Fiz. 58 N12, 21(1994), N. N. Kalmykov and S. S. Ostapchenko and A. I. Pavlov, Bull. Russ. Acad. Science (Physics) 58, 1966(1994), N. N. Kalmykov and S. S. Ostapchenko and A. I. Pavlov, Nucl. Phys. B (Proc. Suppl.) 52B, 17(1997).

[10] H. Fesefeldt, (GHEISHA), RWTH Aachen, Germany Report No. PITHA-85/02 (1985 (unpublished)).

[11] https://www.ngdc.noaa.gov/geomag-web/.

[12] Bahmanabadi, M. et al. (2019). The muon charge ratio using the CORSIKA simulation code. Physical Review D,

ICNST 2024 International Conference on Nuclear Science and Technology
6- 8 MAY 2024 | Isfahan, Iran

The role of nucleus-nucleus potential in the alpha decay half-life (Paper ID : 1418)

Mohamadi S.[a] ,Gharaei R.[a,b*]

[a] *Department of Physics, Sciences Faculty, Hakim Sabzevari University, P. O. Box 397, Sabzevar, Iran*
[b]*Department of Physics, Faculty of Sciences, Ferdowsi University of Mashhad, P. O. Box 91775-1436, Mashhad, Iran*

Abstract

Alpha decay half-lives of 222 parent nuclei (Z=66-105) were calculated using Zhang 2013 and Guo 2013 potential models and compared with experimental data. We know that the role of the nucleus-nucleus potential is very important. Therefore, with the aim of studying this potential, we performed calculations. Zhang 2013 and Guo 2013 potential models have the same formalism with different universal functions $\varphi(s_0)$, then the $\varphi(s_0)$ parameter can cause differences in the results of Zhang 2013 and Guo 2013 models. By examining the behavior of the total potential in terms of the separation distance and the behavior of the calculated half-lives in terms of the neutron number of the daughter nucleus, as well as the calculation of the rms deviation, it was found that the universal function has an important role in the proximity model formalism and the calculations of the half-life of alpha decay. these results can be a motivation for research on the role of the different universal functions introduced in the phenomenological proximity potential model.

Keywords: Alpha decay- Nucleus nucleus potential- Half-lives-Proximity potential

1. INTROUDUCTION

The alpha decay is one of the most interesting topics of nuclear physics in both theoretical and experimental studies. Alpha decay gives valuable information about structure of nuclei [1-5]. Theoretical mechanism of alpha-decay is considered as a quantum mechanical tunneling through the potential barrier between alpha cluster and the daughter nucleus [6-8]. Knowledge of the nucleus-nucleus (NN) interaction potential is a required part in the analysis of alpha decay process. Information about the NN potential is essential to explain and evaluate the alpha decay half-life. However, the precise definition of NN interaction potential is still difficult. The interaction potential consists of an attractive nuclear force, a repulsive long-range Coulomb force and a centrifugal force. Since the Coulomb and centrifugal forces can be calculated with great accuracy, the main remaining task is to calculate the nuclear potential. Many phenomenological and microscopic models have been made to provide a simple and correct form of the nuclear part of the interaction potential [9-29]. The proper selection of the nuclear potential is very important since it must

have a good experimental correlation. Moreover, this potential is expected to explain well the properties of alpha decay.

Among the various nuclear potentials presented, there is a potential model that is based on the "proximity theory". The proximity potential provides a simple formula for the NN interaction energy as a function of the separation between the surfaces of the approaching nuclei [20]. The proximity potential is a result of the geometrical factor (depending on the mean curvature of the interaction surface) and the universal function (depending on the distance of separation between two nuclei.). The universal function is independent of shapes of two nuclei and geometry of nuclei. The idea of universal function is fundamental advantage of proximity potential. Phenomenological proximity potential was first presented by Blocki et al. [20] for heavy-ion reactions. Shi and Swiatecki [30] applied proximity potential as the nuclear potential for the first time. After that, various versions of proximity potential were introduced, which have been used in alpha decay studies.

Y.J. Yao et.al [5] calculated the half-lives of α decay of even-even nuclei using fourteen different versions of proximity potentials. They compared the calculated half-lives with corresponding experimental data. The results show that the generalized proximity potential 1977 are in agreement with the experimental data. In comparison with the distributions of nuclear potentials at small distances and the distributions of total potentials above the released energy Qα, it is found that at small distances the distributions of nuclear potentials have large difference and the distributions of total potentials are different among the listed proximity potentials. The different potential distributions affect the penetration probability of α, which is related to the half-life of the α decay for each nucleus.

Zhang 2013 [31] and Guo 2013 [32] potential models are two recent versions of proximity formalism based on the combination of proximity theory and the microscopic Double-folding [33] approach with the density-dependent nucleon-nucleon interaction of CDM3Y6.

L. Zheng et al [31] calculated the half-lives of cluster decays using proximity potential model with a new universal function, and compared to the experimentally measured values and the theoretical ones of liquid drop model. The results of the calculations show reasonable agreement with the experimental data as well as the half-life calculations of liquid drop model. It shows that proximity potential model with the new universal function can be used successfully to calculate the half-lives of cluster decays for heavy nuclei.

In 2013, the universal function of proximity potential model is systematically studied from the double folding model with density-dependent nucleon–nucleon interaction (CDM3Y6) by analyzing several hundreds of fusion reaction systems with mass numbers from light nuclei to heavy nuclei by Guo et al [32]. The analytical formula of universal function is obtained at $s_0 > -1$ by fitting all of the calculated values. Using this formula, they calculate the Coulomb barrier heights for fusion reactions in comparison with the values of the experimental data and Prox77. It is shown that obtained universal function in proximity potential model can reproduce the Coulomb barrier heights.

In the present work, we intend to investigate the role of the nucleus-nucleus potential in the alpha decay process. This work is organized as follows. In the next section, the theoretical framework of the α-decay half-life and the selected potential models formalism is briefly presented. The detailed calculations and discussions are given in Sec. 3. Sec. 4 is a brief summary.

2. THEORETICAL FRAMEWORK

The half-life is given by,

$$T_{1/2} = \left(\frac{\ln 2}{\nu P}\right) \quad (1)$$

where $\nu = (\frac{2E_\nu}{h})$ represents the number of assaults on the barrier per second. The empirical vibration energy, is taken from Ref. [27].

Using the one-dimensional WKB approximation, the barrier penetrability P_α is given as,

$$P_\alpha = \exp\left\{-\frac{2}{h}\int_{R_a}^{R_b}\sqrt{2\mu(V-Q)}dr\right\} \quad (2)$$

Here μ the reduced mass is equal to $\mu = \frac{mA_1A_2}{A}$. m is the nucleon mass and A_1, A_2 are the mass numbers of the daughter nucleus and emitted cluster, respectively. The turning points R_a and R_b are determined as $V(R_a) = V(R_b) = Q_\alpha$.

Total interaction potential $V_T(r)$ between the α cluster and the daughter nucleus is consists of three parts: the Coulomb potential $V_C(r)$, the nuclear potential $V_N(r)$, and the centrifugal potential $V_l(r)$,

$$V_T(r) = V_C(r) + V_N(r) + V_l(r) \quad (3)$$

The Coulomb potential can be calculated by following the simple relation,

$$V_C(r) = \frac{Z_d Z_\alpha e^2}{r} \quad (4)$$

Where Z_i denote the Alpha cluster and daughter nucleus atomic numbers. The centrifugal potential can be defined as,

$$V_l(r) = \frac{\hbar^2 l(l+1)}{2\mu r^2} \quad (5)$$

Here *l* is the orbital angular momentum carried away by alpha cluster. Moreover, $\mu = \frac{m_d m_\alpha}{m_d + m_\alpha}$ is the reduced mass of the alpha- daughter system.

2.1. Description of the nuclear potential formalism

The proximity formalism can be used to calculate the nucleus-nucleus interaction potential. According to the Guo 2013 [31] and Zhang 2013[32], the nuclear potential can be calculated as follows,

$$V_N(r) = 4\pi b \overline{R} \gamma \varphi(s_0) \quad (6)$$

With the mean curvature radius R, reads as,

$$\overline{R} = \frac{R_d R_\alpha}{R_d + R_\alpha} \quad (7)$$

Here $R_{d(\alpha)}$, the effective sharp radius is as follows,

$$R_{d(\alpha)} = 1.28\, A_{d(\alpha)}^{1/3} - 0.76 + 0.8\, A_{d(\alpha)}^{-1/3} \quad (8)$$

Where A_α and A_d are the mass numbers of the α cluster and the daughter nucleus, respectively, The diffuseness of nuclear surface b is considered close to unity (b ≈ 1 fm). The surface energy coefficient γ has the following form,

$$\gamma = 0.9517\left(1 - 1.7826\left(\frac{N-Z}{A}\right)^2\right) \quad (9)$$

With $N = N_\alpha + N_d$, $Z = Z_\alpha + Z_d$, and $A = A_\alpha + A_d$. N_i. Z_i and A_i denote the neutron, proton and mass numbers of alpha cluster and daughter nucleus, respectively. The universal function $\Phi(s_0)$ is given by,

$$\Phi(s_0) = \frac{p_1}{1+e^{\frac{s_0+p_2}{p_3}}} \tag{10}$$

s_0 is obtained by $s_0 = \frac{r-R_d-R_\alpha}{b}$, where R_i is calculated by using Eq. 8. The values of parameters p_1, p_2, p_3 are −17.72, 1.30 and 0.854 for Guo 2013 model, respectively. For Zhang 2013 model the parameters are equal to p_1= −7.65, p_2= 1.02 and p_3= 0.89, respectively.

3. RESULTS AND DISCUSSION

The aim of the present work is the study of the nucleus-nucleus potential effect on the alpha decay process. A comparative study is provided using Guo 2013 and Zhang 2013 potential models. We have calculated the half-lives of 222 alpha decays with Z=66-105 by taking the interaction potential as the sum of Coulomb potential, centrifugal potential and nuclear potential. To calculate the centrifugal potential, it is necessary to know the value of the *l* angular momentum of the emitted α particle. The α-particle emission from nuclei follows the spin-parity selection rule. Thus the angular momentum of the emitted α particle satisfies the conditions,

$$\left|I_i - I_j\right| \le l_\alpha \le I_i + I_j . \qquad \frac{\pi_i}{\pi_j} = (-1)^{l_\alpha} \tag{11}$$

because the α-particle spin and parity are πα = +1 and Iα = 0, respectively. Here, $I_{j\,(i)}$, $\pi_{j\,(i)}$ are the spin and parity values of the parent nucleus in state j (and the spin and parity values of the daughter nucleus in state i). The Q-value for the α-decay and the experimental half-lives are evaluated using the Refs [34-35].

Using the formulas presented in the previous section, we calculated the nuclear potential. Fig. 1 shows the nuclear potentials behavior of the alpha decay of $^{212}_{91}$Pa . It can be seen that the difference between the Guo 2013 (dash-dotted line) and Zhang 2013 (straight line) models appears in $r \lesssim 13$ fm. This difference is more obvious in smaller r. In addition, it was found that the Zhang 2013 model has a lower attractive force than the Guo 2013 model, which leads to an increase in the potential barrier height. As a result, the penetration probability P_α of alpha particle decreases. According to the WKB approximation, the interaction potential between the alpha - daughter system is an important part in alpha decay calculations. Hence, we plot in Fig. 2 the total interaction potentials behavior between the alpha - daughter system using Guo 2013 (dash-dotted

line) and Zhang 2013 (straight line) potentials for alpha decay of $^{212}_{91}$Pa with $Q_\alpha = 8.42$ MeV (dotted line). as an example.

As expected, it can be seen that the Zhang 2013 model (with $V_B = 14.92$ MeV) has a higher potential barrier than the Guo 2013 model (with $V_B = 14.2$ MeV). In the Guo 2013 potential, due to the decrease in the height and width of the potential barrier the penetration probability of alpha particles increases. Therefore, the half-lives calculated through this model have smaller values than the Zhang 2013 model. This result can be confirmed by examining the logarithmic behaviors of alpha particle penetration probability P_α and alpha decay half-lives $\log_{10}T^{cal}_{1/2}$ (see Fig. 3). According to Fig. 3(a), P_α determined by Zhang 2013 has lower values than the Guo 2013. Fig. 3(b) shows that the half-life values calculated through Zhang 2013 are larger than other model.

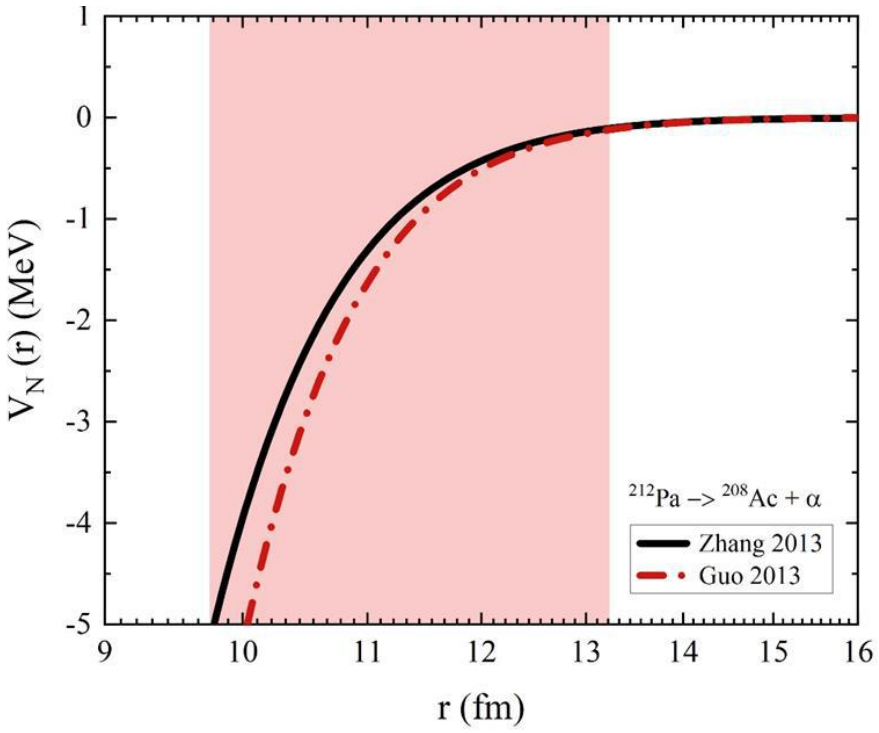

Fig. 1: *The nuclear potentials for alpha-decays from ^{212}Pa* parent nucleus using Zhang 2013 (straight line) and Guo 2013 (dash-dotted line) models.

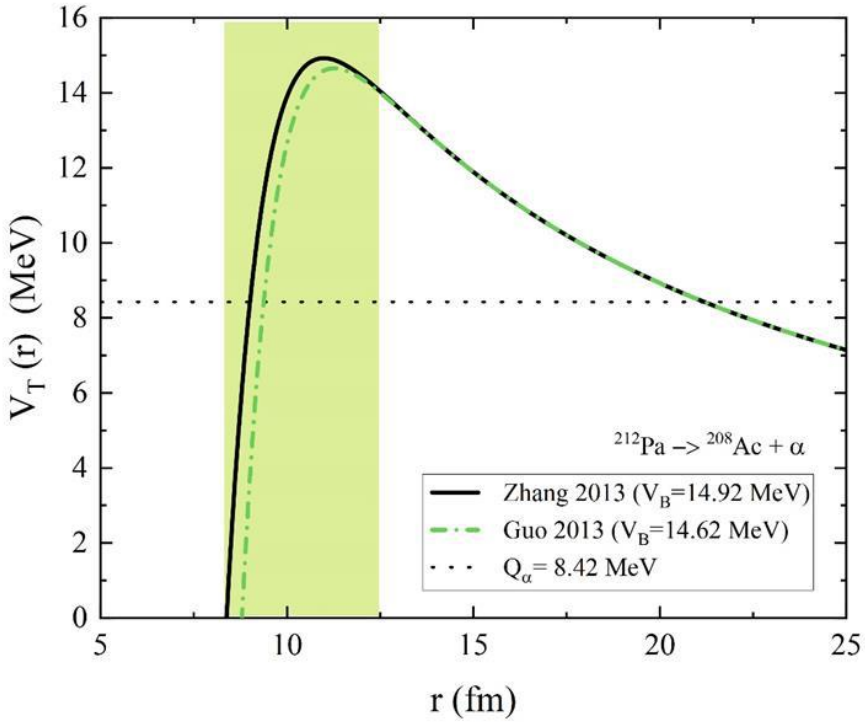

Fig. 2: The interaction potentials for alpha-decays from 212Pa parent nucleus using Zhang 2013 (straight line) and Guo 2013 (dash- dotted line) models. The Q_α is shown by dotted line.

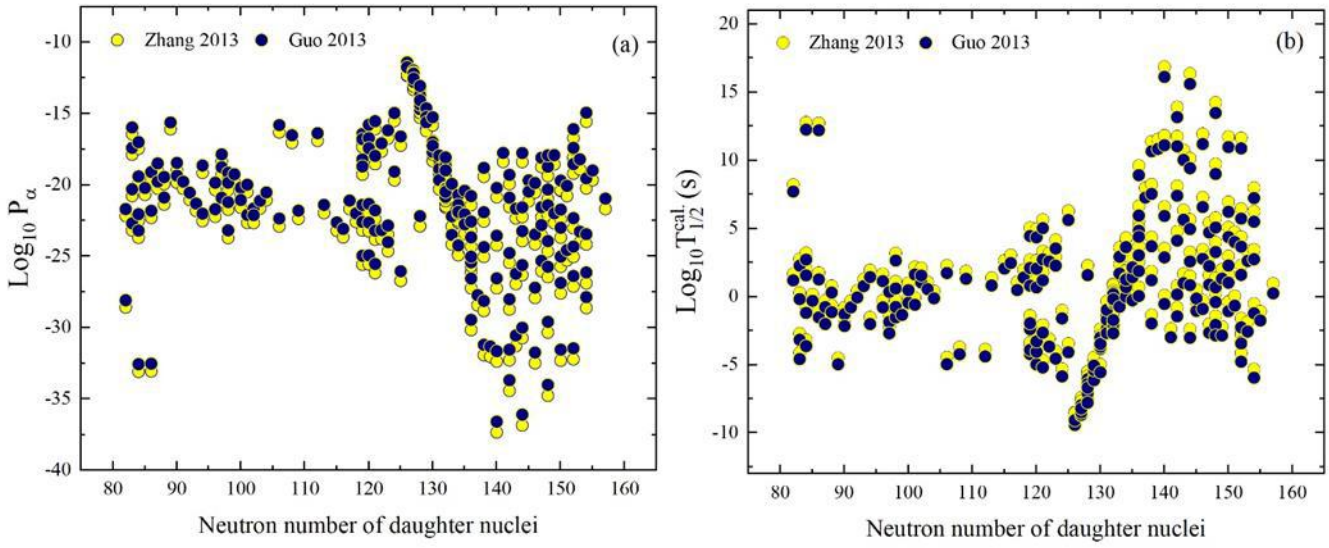

Fig. 3. The behavior of the logarithmic values of (a) the calculated penetration probability of the alpha particle and (b) the calculated half-lives using Zhang 2013 and Guo 2013 model.

In the following, the logarithmic difference of the calculated half-lives with the corresponding experimental data was presented in Fig. 4. The results show that the calculation of alpha decay half-lives using Zhang 2013 potential is closer to the corresponding experimental data than Guo 2013 potential.

For a better review, the standard deviation values σ were calculated as

$$\sigma = \sqrt{\frac{1}{N}\sum_{i=1}^{N}\left(\log_{10}T^{Cal}_{(\frac{1}{2})} - \log_{10}T^{Exp}_{(\frac{1}{2})}\right)^2}. \quad (12)$$

where N is the number of parent nuclei used for evaluation of the σ value. The evaluated value σ is 1.4576 for Zhang 2013 model and 1.9879 for Guo 2013 model. The evaluation shows that Zhang 2013 potential is more suitable for calculations in the alpha decay process compared to the other potential model. The important result obtained from these investigation is that the correct selection of the universal function can be effective in calculations and evaluations. Here, the only factor that leads to decrease or increase and generally changes in the important characteristics of alpha decay is the universal function of the selected models.

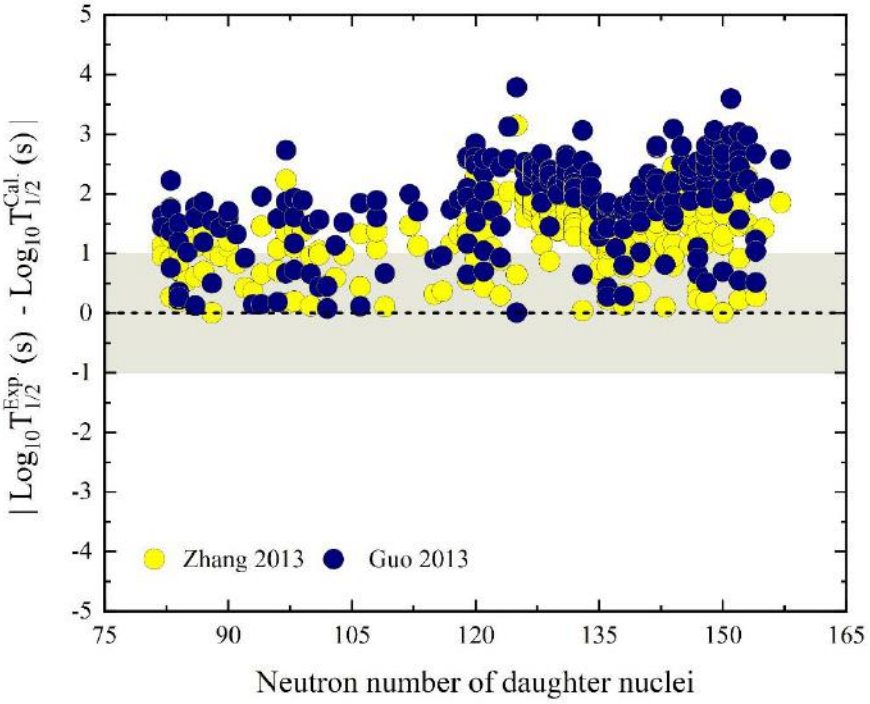

Fig. 4. The absolute difference between the predicted alpha half-lives and the experimental data using the Zhang 2013 and Guo 2013 potentials against the neutron number of daughter nuclei.

4. CONCLUSIONS

In order to investigate the effect of nucleas-nucleas potential on the alpha decay process, a comparative study using the potential models of Guo 2013 and Zhang 2013 has been presented. We have calculated the half-lives of 222 alpha decays with Z=105-66. The behavior of nuclear and total potentials was evaluated.

In addition, we investigated the behavior of alpha particle penetration probability and the calculated half-lives. We found that half-live values obtained through Zhang 2013 model are in better agreement with experimental data than Guo 2013 model. In addition, we found that the correct choice of universal function can be effective in calculations and evaluations. These results can be a motivation for research on the role of the different universal functions introduced in the phenomenological proximity potential model.

5. REFERENCE

[1] Delion, D. S. and Peltonen, S. and Suhonen, J. (2006). Systematics of the α-decay to rotational states. Physical Review C, 73:014315.

[2] Chowdhury, P.R and Samanta, C. and Basu, D.N. (2006). α decay half-lives of new super heavy elements. Physical Review C, 73:014612.

[3] Seif, W.M. (2006). α decay as a probe of nuclear incompressibility. Physical Review C, 74:034302.

[4] Basu, D.N. (2004). Lifetimes of the α decay chains of super heavy element Z = 115. Journal of Physics G: Nuclear and Particle Physics, 30: B35.

[5] Yao, Y. J, Zhang, G. L, Qu, W.W. and Qian, J.Q. (2015). Comparative studies for different proximity potentials applied to α decay. The European Physical Journal D, 51:122.

[6] Gamow, G.Z. (1928). Physics 51:204.

[7] Condon, E.U. and Guerney, R.W. (1928). Wave Mechanics and Radioactive Disintegration. Nature 122:439.

[8]. Condon, E.U. and Guerney, R.W. (1929). Quantum Mechanics and Radioactive Disintegration. Physical Review, 33:127.

[9] Poenaru, D.N. et al. (1986). Calculated half-lives and kinetic energies for spontaneous emission of heavy ions from nuclei. Atomic Data and Nuclear Data Tables, 34:423.

[10] Buck, B, Merchant, A.C. and Perez, S.M. (1993). Half-Lives of Favored Alpha Decays from Nuclear Ground States. Atomic Data and Nuclear Data Tables, 54:53.

[11] Xu, C. and Ren, Z.Z. (2005). Nuclear Physics A, 753:174.

[12] Xu, C. and Ren, Z.Z. (2005). Nuclear Physics A, 760:303.

[13] Basu, D.N. (2003). Role of effective interaction in nuclear disintegration processes. Physics Letters B 566:90.

[14] Zhang, H. F, Zuo, W, Li, J. Q, and Royer, G. (2006). α decay half-lives of new super heavy nuclei within a generalized liquid drop model Physical Review C, 74:017304.

[15] Zhang, H. F, and Royer, G. (2007). Theoretical and experimental α decay half-lives of the heaviest odd -Z elements and general predictions. Physical Review C, 76:047304.

[16] Chowdhury, P.R, Basu, D.N. and Samanta, C. (2007). α decay chains from element 113. Physical Review C, 75:047306.

[17] Gupta, R.K. et al. (2009). Fusion–evaporation cross-sections for the 64Ni+100Mo reaction using the dynamical cluster-decay model. Journal of Physics G: Nuclear and Particle Physics, 36:075104.

[18] Manhas, M. and Gupta, R. K. (2005). Proximity potential for deformed, oriented nuclei: “Gentle” fusion and “hugging” fusion. Physical Review C, 72:024606.

[19] Gupta, R.K. Singh, N. and Manhas, M. (2004). Generalized proximity potential for deformed, oriented nuclei. Physical Review C, 70:034608.

]20] Blocki, J. Randrup, W.J. and Swiatecki, C.F. (1977). Proximity forces. Annals of Physics,105:427.

[21] Myers, W.D. and Swiatecki, W.J. (2000). Nucleus-nucleus proximity potential and superheavy nuclei. Physical Review C, 62:044610.

[22] Möller, P. and Nix, J.R. (1981). Nuclear Physics A, 361:117.

[23] Dutt, I. and Puri, R.K. (2010). Analytical parametrization of fusion barriers using proximity potentials. Physical Review C, 81:064608.

[24] Dutt, I. and Puri, R.K. (2010). Comparison of different proximity potentials for asymmetric colliding nuclei. Physical Review C, 81:064609.

[25] Zhang, G.L. et al. (2007). Chinese Physics C, 31:634.

[26] Xu, C. and Ren, Z.Z. (2006). Global calculation of α-decay half-lives with a deformed density-dependent cluster model. Physical Review C, 74:014304.

[27] Royer, G. and Moustabchir, R. (2001). Nuclear Physics A, 683:182.

[28] Zhang, H.F. and Royer, G. (2008). α particle preformation in heavy nuclei and penetration probability. Physical Review C, 77:054318.

[29] Shi, Y.J. and Swiatecki, W.J. (1985). Nuclear Physics A, 438:450.

[30] Myers, W. D. and Swiatecki, W. J. (1967). ANOMALIES IN NUCLEAR MASSES. Ark. Fys. 36:343.

[31] Zhang, G.L. Zheng, H.B. and Qu, W.W. (2013). Study of the universal function of nuclear proximity potential between α and nuclei from density-dependent nucleon-nucleon interaction. The European Physical Journal A, 49:10.

[32] Guo, C.L. Zhang, G.L. and Le, X.Y. (2013). Study of the universal function of nuclear proximity potential from density-dependent nucleon–nucleon interaction. Nuclear Physics A, 897.

[33] Khoa, D. T. and Satchler, G. R. (2000). Nuclear Physics A, 668:3.

[34] Wang, M. et al. (2017). The Ame2016 atomic mass evaluation. The AME2016 atomic mass evaluation (II). Tables, graphs and references. Chinese Physics C Vol. 41(3):030003.

[35] Audi, G.(2017).The NUBASE2016 evaluation of nuclear properties. Chinese Physics C 41(3):030001.

ICNST 2024
International Conference on Nuclear Science and Technology
6- 8 MAY 2024 | Isfahan, Iran

Imaging a Lead Block Using Cosmic Muons: a Simulation Study with Geant4 (Paper ID : 1436)

Fazlalizadeh M.[1*], Bahmanabadi M.[2], Pezeshkian Y.[3]

1Department of Physics, Payame Noor University, Tehran, Iran
2 Department of Physics, Sharif University of Technology, Tehran, Iran
3 Department of Physics, Sahand University of Technology, Tabriz, Iran

Abstract

The cosmic muons are safe, free, and penetrating charged particles available around the Earth. Muons penetrating features make them a good candidate for imaging dense and massive structures when X-rays are not applicable.

We simulated the passage of cosmic muons through the lead blocks using Geant4 toolkit and counted muons passing the pixels of an ideal detector under the object. Images of 18 different thicknesses of the lead blocks were constructed. Results show that the borders can be seen due to the deflection of muons. For the thickness of the lead block up to 20cm, deflection is the dominant interaction. For the higher thicknesses, absorption is also considerable. Other aspects like optimum exposure time, detection of different geometrical shapes, the electron and positron's share in detected particles and the role of pixel size are also studied.

Keywords: Muon Imaging, Cosmic Rays, Simulation, CORSIKA, Geant4

INTRODUCTION

Imaging massive structures and dense materials has always been a challenge. The cosmic muons are good candidates for imaging these objects because of the small interaction cross-section in matter and high penetration depth. Cosmic muons are a safe and available source that are abundantly and freely produced in the interactions of primary cosmic rays with the upper atmosphere. These muons with several GeV mean energy arrive at the Earth's surface due to relativistic effects, with a flux of about $1\,\frac{particle}{min.cm^2}$ and can pass through thick layers of materials [1].

Muon imaging relies on measuring the change in the flux of muons due to the absorption or scattering of muons inside the object. This technique is applied in various fields, including archaeology, industrial controls, homeland security and civil engineering [2-5]. The drawback of this method is the long time required for imaging due to the low flux of muons. Overall imaging time depends on the size and material of the object under study on one hand and the size and resolution of the detection system on the other hand.

Therefore, simulation is the best approach to find out optimum conditions before designing any experimental setup. In this paper, we want to investigate the quality of images and the time required to image small-sized (~2250cm^3) dense objects with cosmic muons. For this purpose, a Geant4 code is developed to simulate the passage of muons through the blocks of Lead with different sizes and shapes. Geant4 is a toolkit to simulate passages of particles through the matter developed in CERN [6], it can be applied in high energy, nuclear and accelerator physics. Muons energy, obtained by CORSIKA Monte Carlo simulation [7], is given as an input parameter to our Geant4 code. CORSIKA is another simulation toolkit to simulate extensive air showers created by interacting the high energy primary cosmic rays with the atmospheric particles.

Image Construction of Different Geometrical Shapes

In the Geant4 environment, we designate a 50×50 cm² plane as a muon source. The geometry is as follows: a 15×15×10cm^3 lead block is positioned at the center, the muon source is located at the top, and a detector (detection surface) is situated at the bottom of the block. 2.5×10^6 muons are emitted downward vertically from random points on a source. The detection surface is divided into 2500 pixels, and the number of reached muons to each pixel (count) is recorded. The energy of muons is selected 3GeV and the muon ratio ($\frac{\mu^+}{\mu^-}$) is determined 1.2 which they are obtained from CORSIKA simulation [8].

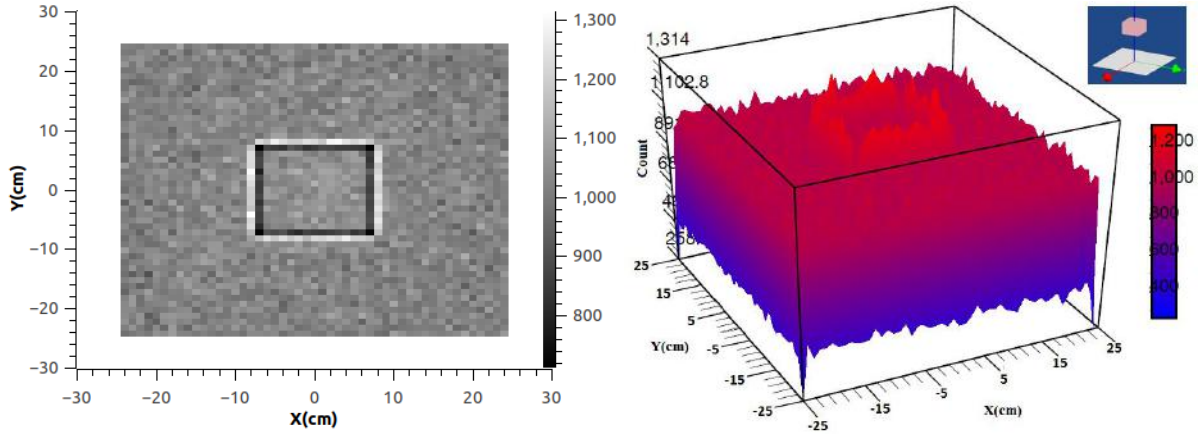

Fig. 1. 2D and 3D constructed images of a 15×15×10cm^3 lead block in 2500 pixels. Only the edges of block are distinguishable.

In Fig. 1, we can see that the edges of the block can be distinguished easily, while the count of muons in the pixels inside the block shape is similar to the count of pixels on the outside of the block. We can explain

the indistinguishability of pixels inside and outside of the objects boundaries by considering that the scattering of muons inside the object is the only prominent phenomenon and absorption is negligible.

Due to the scattering of the muons in the block, their coordinates in x-y plane changes from the source to the detector. If the coordinates of an emitted muon on the source plane are (x_0, y_0) and its coordinates in the detection surface are (x, y), the displacement will be $\Delta r = \sqrt{(x - x_0)^2 + (y - y_0)^2}$. The average displacement of the detected muons in each pixel is shown in Fig. 2. The average displacement of the muons for all pixels is about 0.58 cm which is at the order of the pixels dimension. Some muons, originally intended to strike a specific pixel, scatter and end up hitting neighboring pixels. Conversely, some muons initially directed toward neighboring pixels deviate and ultimately reach the intended pixel. So, a decrease in the quantity of muons is offset by a corresponding increase in their number. However, the scenario changes for border pixels. Scattering occurs in the pixels immediately below the lead block, while adjacent pixels lacking a block above them do not experience scattering. Consequently, we observe a decrease in the count of border pixels within the shape and a corresponding increase in the count of border pixels outside the shape.

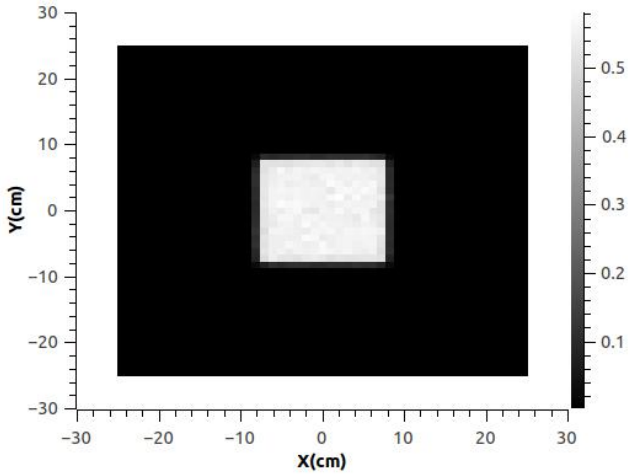

Fig. 2. The average displacement of muons due to the deflection in each pixel. The deflection mostly occurs for muons that pass through the lead block. The average displacement for these muons is 0.58 cm.

To observe the impact of varying the number of muons in border pixels for objects with non-cubic geometric shapes, we replicated the simulation using six lead pieces with diverse geometric configurations but comparable sizes (Fig. 3). Our original block is placed among the objects for comparison. In Fig. 4, the edges of the elliptical cylinder, cylindrical shell and parallelepiped are seen in the constructed image. The sphere is not as clear as other objects, and the image of the cones is not visible at all.

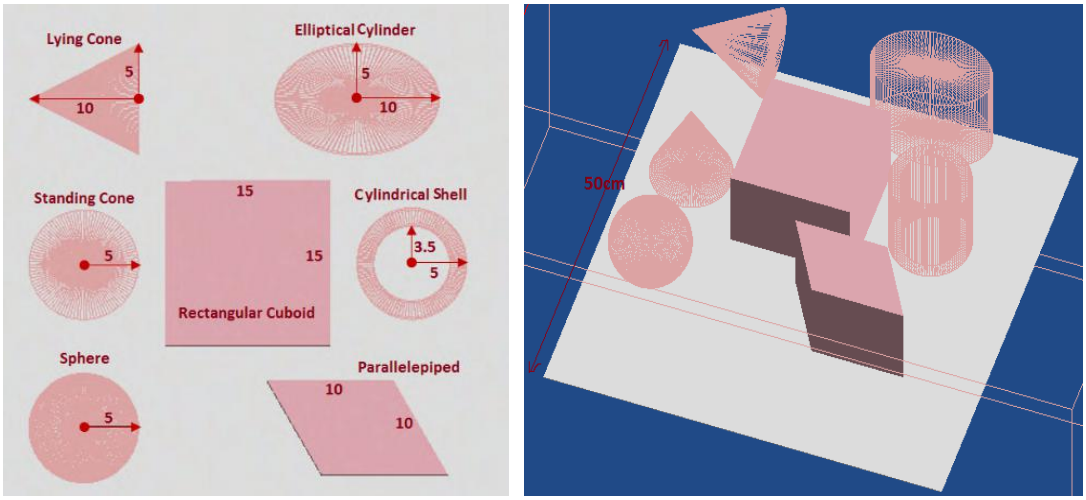

Fig. 3. Geometrical shapes used as objects and their dimensions (cm). All lead objects are homogenous solids.

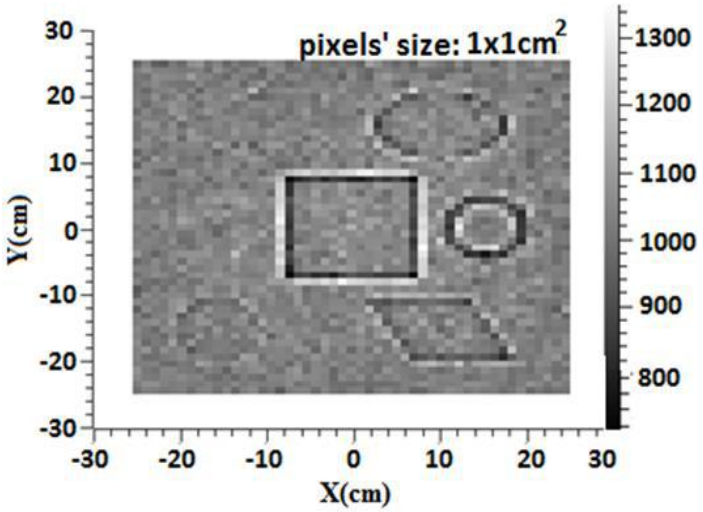

Fig. 4. Constructed image of different geometrical shapes with 10cm thickness in 2500 pixels.

Optimum Detection Time

Detection time (exposure time) is one of the important aspects of imaging. While increasing detection time can indeed improve image resolution, it is essential to minimize the detection time as much as possible. Various research groups utilize muons for imaging objects of different sizes. The size of objects affects the imaging time [9-11]. We change the number of emitted particles to find the optimum detection time for a fixed setup. Cosmic muon flux is $1\frac{particle}{min \times cm^2}$ at sea level. Since each pixel's size is considered $1\times1cm^2$, in N minutes N muon will pass a pixel. In other words, the count of muons in a pixel is the same as the detection time in minutes. In the literature, an accepted signal-to-noise ratio (SNR) value is typically 10:1 [12, 13].

Table 1. Number of detected muons, exposure time and signal-to-noise for each pixel in different runs of simulation with various numbers of emitted muons

Number of emitted muons	count	$\frac{count}{cm^2} \equiv time(min)$	Signal-to-noise
2.5×10^6	2499792	≈1000	31.62
1×10^6	999821	≈400	20
5×10^5	499970	≈200	14.14
2×10^5	199988	≈80	8.94
1×10^5	99990	≈40	6.32
5×10^4	49975	≈20	4.47

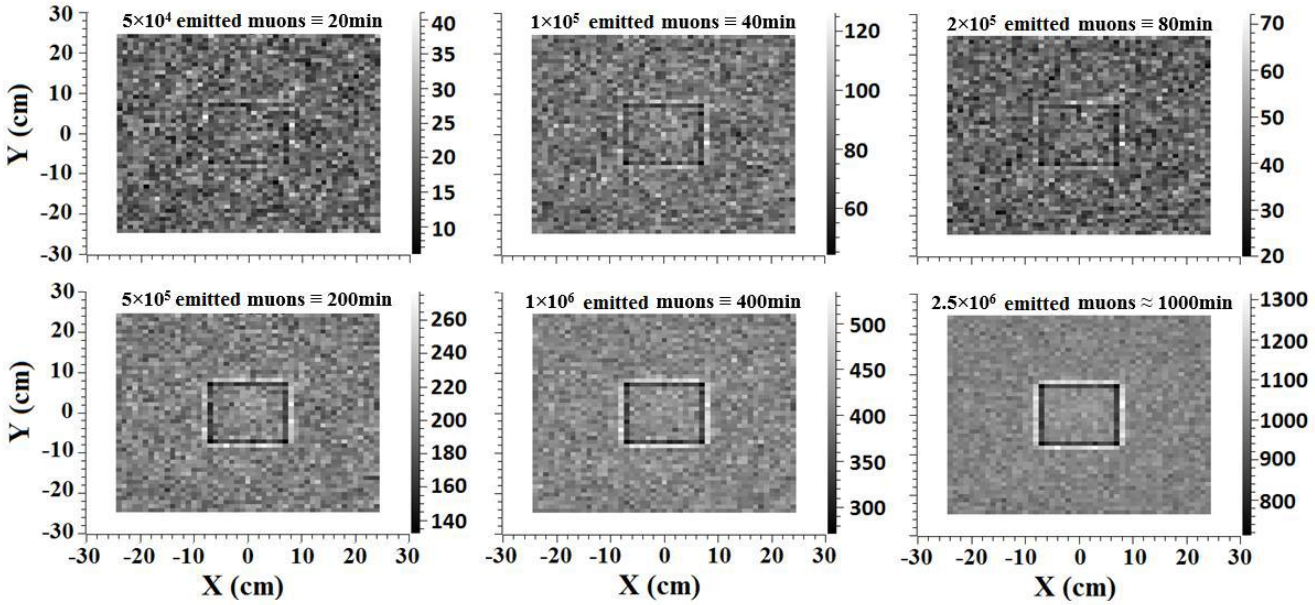

Fig. 5. Constructed images of a 15×15×10cm^3 lead block for different numbers of emitted muons at 2500 pixels. By increasing the exposure time (or number of emitted muons) the image resolution increases.

Referring to Figure 5, in order to construct an image of a lead cube with dimensions of 15×15×10 cm³ using a detector featuring 1×1 cm² pixels, we need a minimum emission of 10^5 muons with an energy of 3 GeV from the source. According to Table 1, approximately 80 minutes are required for 2×10^5 muons to traverse the surface area of 50×50 cm². During this 80-minute interval, the SNR reaches 8.94 (as indicated in Table 1). Throughout the remainder of the article, we adhere to the SNR condition of 9, effectively setting the number of source muons equal to 2×10^5.

Image Construction Results of Different Lead Block Thicknesses

We saw that 10 cm of a lead block cannot stop 3 GeV muons. In order to find the thickness in which the absorption of muons occurs, we repeat the simulation for 18 different thicknesses of lead blocks from a few

cm to 75cm. The lead blocks were placed 25cm above the detection surface and the source was placed 100cm above the detection area. In Fig. 6, we plot the sum of counted muons in pixels of the detector as a function of the lead block's thickness. Below a thickness of 20 cm, the number of muons reaching the detector remains constant. However, as the thickness of the lead block increases, the muon count decreases steadily.

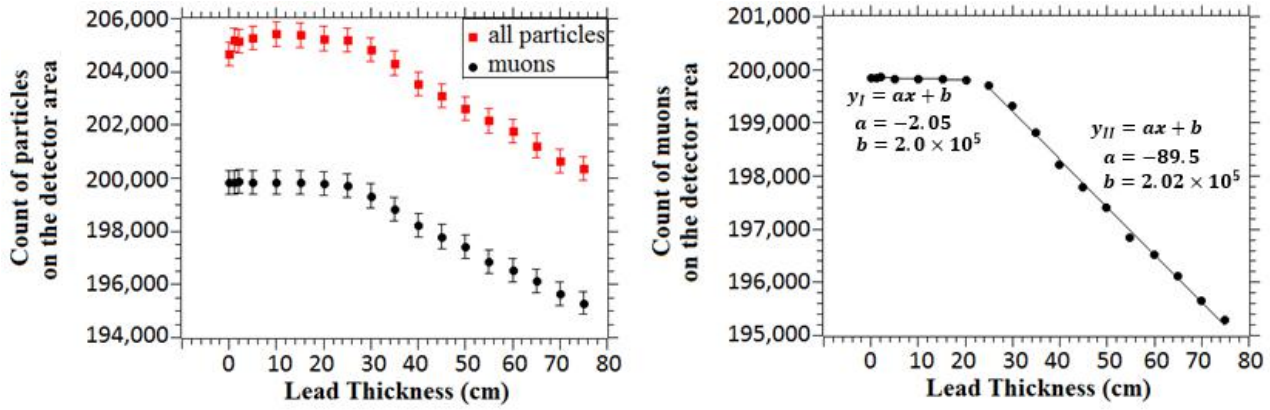

Fig. 6. (Left) Number of detected particles and detected muons versus lead thickness. (Right) Two linear functions are fitted on two parts of the diagram.

The number of detected particles in the detection area is more than the number of emitted muons (upper square points in the figure) due to the interaction of muons with lead atoms and the production of electrons and positrons. The number of all particles at the detector is ~(2.6±0.1) % more than the number of muons and remains almost constant for all thicknesses. While the interactions resulting in the production of electrons and positrons increase with thicker lead, their contribution to the overall particle count reaching the detector remains nearly constant. This phenomenon occurs because $e^{\pm}$ are rapidly absorbed within the lead material. As a result, the electrons detected originate primarily from the bottom of the lead block, having travelled only a short distance within the material.

To explore how pixel size impacts image resolution, nine lead objects of varying thicknesses, as depicted in the Fig. 7, were positioned between the source and the detection surface for investigation. Three images with pixel sizes of 1cm×1cm, 0.5cm×0.5cm and 0.1cm×0.1cm were constructed (Fig. 7). It is worth mentioning that in order to simulate nine 15×15cm^2 blocks simultaneously, the detection area is increased to 70×70cm^2. In constant exposure time, by shrinking the size of pixels, the edges become clearer. However, the image contrast decreases due to the reduction of count and consequently, an increase in statistical fluctuation in each pixel occurs. Choosing the appropriate pixel size for different applications depends on

the aim of the study. In the case of these three images, 0.5cm×0.5cm pixel size has better resolution and contrast than the other two.

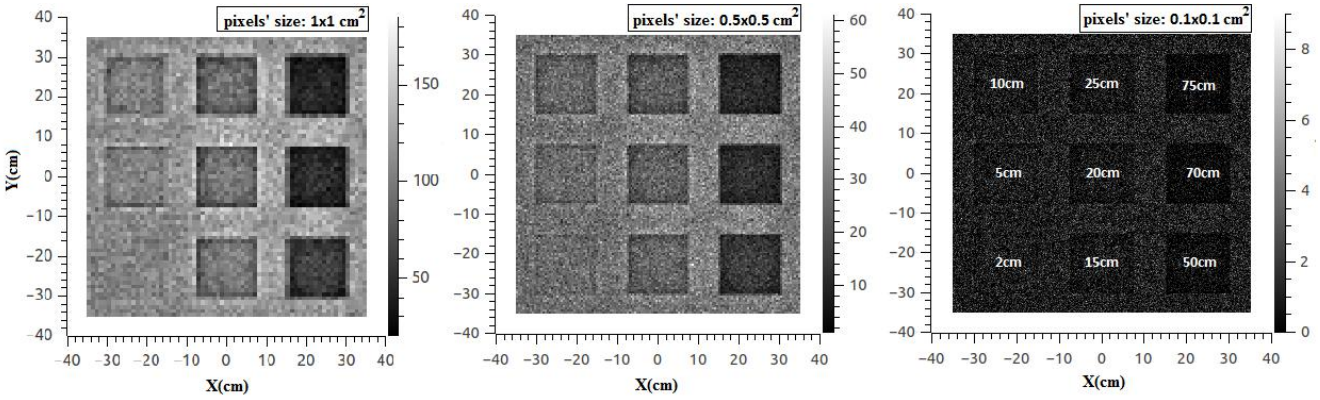

Fig. 7. Images of 9 lead blocks with different thicknesses (shown in the right image) constructed in 1cm×1cm, 0.5cm×0.5cm and 0.1cm×0.1cm pixel sizes.

Conclusions

In this study, Geant4 was used to simulate imaging a lead block as a dense matter using cosmic muons. The muon energy and muon ratio ($\frac{\mu^+}{\mu^-}$) are obtained by CORSIKA Monte Carlo simulation and entered as source characteristics in Geant4. This study shows that only borders of the lead block sized 15×15×10cm^3 are distinguishable in the image because of deflection. In the following, the image construction of different geometric shapes of lead with the same thickness (10cm) shows that only borders can be seen.

Cosmic muon flux at sea level is $1\frac{particle}{min.cm^2}$. Therefore, achieving a clear image of the object under study necessitates an exposure time of at least 80 minutes. It is evident that the imaging time is intricately linked to both the object's size and the dimensions of the detector's pixels.

Simulated images were generated for different thicknesses of lead blocks (ranging from 0 to 75 cm). The fitted curves indicate that, for 3 GeV muons passing through the lead blocks with thicknesses up to 20 cm, deflection remains the dominant interaction. As the thickness of the lead block increases, absorption also becomes more pronounced, occurring alongside deflection.

The impact of pixel size on image quality has also been studied. To determine the optimal size, we considered three different pixel dimensions. Among these, the 0.5×0.5 cm² pixels were deemed suitable for our initial conditions, taking into account the convolution of image border resolution and statistical fluctuations.

References

[1] Grupen, C. and Boris Sh. (2008). Particle detectors (2nd edition). Cambridge university press.

[2] Morishima, K. et al. (2015). Discovery of a big void in Khufu's Pyramid by observation of cosmic-ray muons. Nature, 24647

[3] Ruiz-del Arbol, P. et al.(2019). Non-destructive testing of industrial equipment using muon radiography. Philos. Trans. R. Soc. 377 (2137)

[4] Barnes, S. et al. (2023). Cosmic Ray Muography for Border Security. Instruments 7(13)

[5] Das, S. et al. (2022). Muography for Inspection of Civil Structures. Instruments 6 (77)

[6] The GEANT4 Collaboration. (2003). GEANT4 – a simulation toolkit. NIM A 506

[7] Heck, D. (1998). CORSIKA: A Monte Carlo code to simulate extensive air showers.

[8] Bahmanabadi, M. et al. (2019). The muon charge ratio using the CORSIKA simulation code. Physical Review D 100 (8)

[9] Procureur, S. (2018). Muon imaging: Principles, technologies and applications. Nucl. Instrum. Methods A, 878 169-179.

[10] Bouteille, S. et al. (2016). A Micromegas-based telescope for muon tomography: The WatTo experiment. Nucl. Instrum. Methods A. 834. 223.

[11] Alvarez,L.W. et al. (1970). Search for hidden chambers in the pyramids. Science, New Series 167 832.

[12] Schroeder, D. J. (1999). Astronomical Optics (2nd edition). Academic Press. p. 278. ISBN 978-0-12-629810-9, p 27.

[13] Bushberg, J. T., et al. (2006). The Essential Physics of Medical Imaging, (2e). Philadelphia: Lippincott Williams & Wilkins. p. 280.

ICNST 2024 International Conference on Nuclear Science and Technology
6- 8 MAY 2024 | Isfahan, Iran

Validity range of Vaughan's iterative method in electron gun design (Paper ID : 1460)

R. Panahi[1], S.A.H. Feghhi[1*], S. Sanaye Hajari[2], M. Khorsandi[1], A. Sadraii[3]

[1]Department of Radiation Application, Shahid Beheshti University, Tehran, Iran
[2]Physics and Accelerators Research School, Nuclear Science and Technology Research Institute, P.O.Box:11365-8486, Tehran-Iran
[3]Laser and Plasma Research Institute, Shahid Beheshti University, Tehran 1983969411, Iran

Abstract

The electron gun is an essential component of any vacuum electronic device, electron accelerator, electron microscope, etc. Before fabrication of the gun, it is necessary to design and optimize the gun geometry. Vaughan's iterative synthesis technique is widely used for the preliminary design of Peirce electron guns. The estimation of the geometrical parameters of the electron gun is given as the output of Vaughan's method. The validity of the iterative method over a wide range of convergence is a primary question in this design process. In this paper, the validity range of the iterative method has been studied. The CST studio software has been utilized to simulate the beam dynamics of the electron gun. The result shows that the validity of the iterative model improves as convergence increases.

Keywords: Electron gun; Vaughan's iterative synthesis technique; Perveance; Convergence; CST studio software

INTRODUCTION

An electron gun is a device that produces, concentrates, and directs an electron beam[1]. It is an essential component of any vacuum electronic device, electron accelerator, electron microscope, etc. The name gun is indicative of the function of the device in that it shoots off a stream of electrons [2]. Depending on the methods of extracting electrons from metals, the guns are also different, namely thermionic, photocathode, and field emission [1]. Among these, the thermionic electron gun stands out as one of the most widely used, particularly in klystrons and traveling wave tubes. For electron guns working in the space charge limited mode, peveance (P) is one of the important parameters that relates the beam current to the applied voltages and is defined by:

$$P = \frac{I}{V^{(3/2)}} = 14.67 \times 10^{-6} \frac{1-\cos(\theta)}{(-\alpha)^2} \quad (1)$$

Where I represents the beam current, V denotes the anode-cathode potential difference, θ represents the beam convergence angle, and $(-\alpha)$ corresponds to the Langmuir-Blodget parameter. The perveance is

completely dependent on the geometric feature [1]. Another parameter in the electron gun is convergence, which is defined as the ratio of the cathode to the waist of the beam cross-section area [3].

Most of the electron guns are designed following guidelines established by Pierce and are known as Pierce guns. To save time and cost, it is necessary to design and optimize the gun geometry before construction. So different synthesis techniques have been employed for the preliminary design of the Pierce gun. The synthesis of electron guns leads to the geometry of electron guns. At first, the design of the electron gun was based on a graphical method [4]. Then, the iterative and non-iterative synthesis techniques were proposed for the design of the Pierce electron gun. In these methods, the design of the electron gun is based on four input parameters: beam voltage, beam current, waist radius, and cathode current density. The estimation of the electron gun's geometrical parameters is provided as the output of these techniques[5, 6]. After the presentation of both iterative and non-iterative methods, several improved approaches for these methods have been presented by authors [7, 8]. The iterative method was proposed by Vaughan in 1981. Vaughan's iterative method is one of the most popular methods for the design of an electron gun. In this method, the geometrical parameters of the electron gun are calculated by iterative procedure. This paper investigates the validity range of Vaughan's iterative method. The CST studio software was used for electron gun simulation. The electron gun simulation in CST has been validated with the electron gun presented in ref [4].

RESEARCH THEORIES

Vaughan presented an iterative method of synthesizing Peirce electron guns with a curved cathode [5]. Fig. 1 illustrates the geometrical configuration of the Pierce electron gun. The input parameters of Vaughan's iterative method are beam voltage (V), current (I), waist radius (r_w), and cathode emission density (J_c). The geometry of the electron gun is given as the output in the iterative procedure which typically converges to 0.1°. This method assumes that the focus electrode makes an angle of 67.5° with the normal at the cathode edge. In this method, the slope of the beam edge trajectory in the anode plane is calculated from two points of view. Initially, the slope of the beam edge ($\tan(\phi_1)$) is calculated by considering the effect of the anode lens. Alternatively another approach calculates the slope of the beam edge based on the universal beam spread in the anode tunnel ($\tan(\phi_2)$). For continuity of the trajectory, these two slopes of the beam edge must be brought to equality. In Vaughan's iterative method, an initial estimation is made for convergence half angle (θ), which typically is $30\sqrt{\mu P}$. The equality of slope of the beam edge can be satisfied by adjustment of θ.

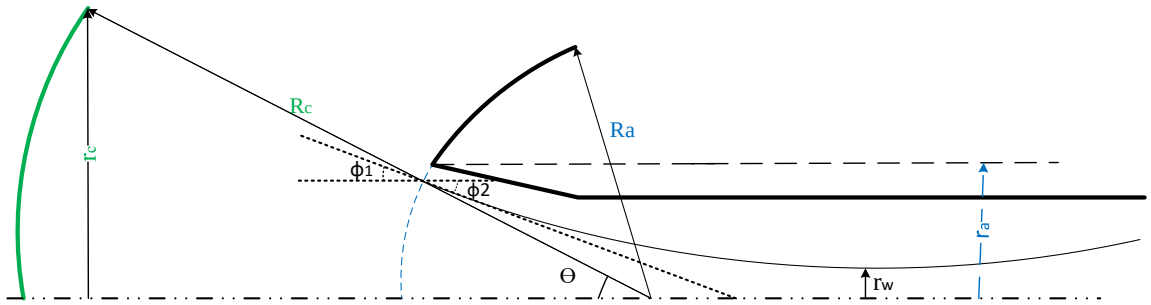

Fig. 1. Geometrical view of Pierce electron gun

An effective procedure involves multiplying the previous value of θ by $\left(\tan(\phi_2)/\tan(\phi_1)\right)^{1/2}$ and then recalculating the $\tan(\phi_1)$ and $\tan(\phi_2)$. The iterations can be stopped when $\tan(\phi_2)/\tan(\phi_1)$ falls within 1.0 ± 0.005, which corresponds roughly to 0.1°. When θ has been found to the desired accuracy, the geometrical parameters of the gun can be obtained from

$$R_c = r_c / \sin(\theta) \quad (2)$$

$$R_a = R_c e^{-\gamma} \quad (3)$$

$$r_b(z_a) = r_c e^{-\gamma} \quad (4)$$

$$r_a = 1.2 r_b(z_a) \quad (5)$$

$$z_{ac} = R_c - R_a \quad (6)$$

Where R_c is cathode spherical radius, r_c is cathode disk radius, $r_b(z_a)$ is beam waist, r_a is anode aperture radius, R_a anode spherical radius, z_{ac} is cathode to anode distance, and $\gamma = Ln\ \frac{R_c}{R_a}$.

For correction of spherical aberration, the values of θ and R_c be corrected and replaced by θ_T and R_{cT}. The values of θ_T and R_{cT} are defined as

$$\sin(\theta)/\sin(\theta_T) = k \quad (7)$$

$$R_{cT} = kR_c \quad (8)$$

Where k is the empirical constant less than unity (typically 0.905).

Validation of CST simulation

Ref [4] contains both dimensional drawings of the guns and measurements of the exit beam. To validate the CST simulation, the 5B type electron gun was simulated using CST software. When the potential difference between the cathode and anode is 4000 V, the perveance is 2.2 $\mu perv$ in experimental studies. In simulations, the perveance is found to be 2.08 $\mu perv$. Based on the results, the simulation exhibits a good agreement with the experimental data. The perveance diagram and trajectory of the beam are shown in Fig. 2.

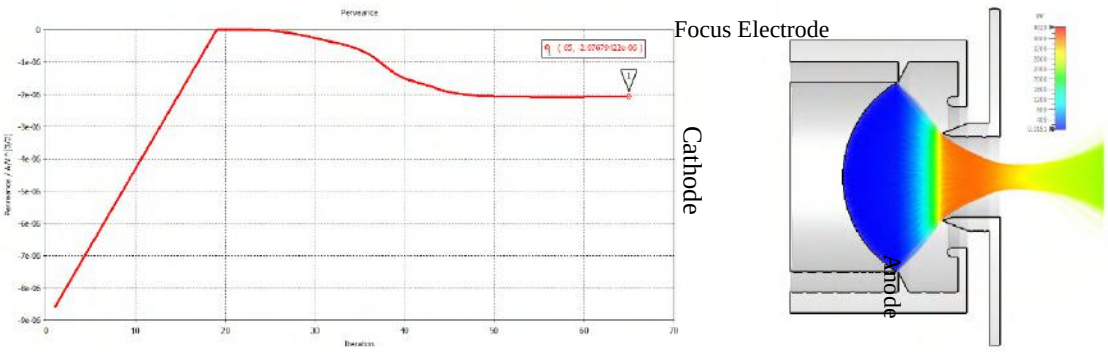

a b

Fig. 2. Perveance diagram (a) and the beam trajectory (b) of a 5B-type electron gun was simulated using CST software.

Material and method

The calculation flowchart of Vaughan's iterative method is shown in Fig. 3. In this study, the iterative method was employed to derive various gun geometries by altering input parameters. Several gun geometries were designed with constant perveance and varying convergence. The obtained geometries were simulated in CST software. In all geometries, the focus electrode makes an angle of 67.5° with the normal at the cathode edge. The initial setting parameters of CST are outlined in Table 6. We do not claim these parameters are optimal, but their results are reliable.

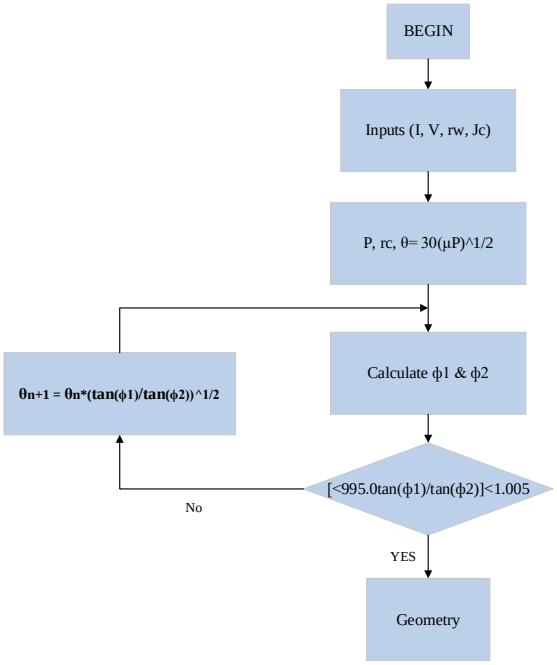

Fig. 3. Vaughan's iterative Flowchart

Table 6. Initial input parameters of CST

Parameter	value
Mesh type	Tetrahedral (model:40, background:30)
Tracking emission model	Space charge
Angle spread	89
Emission distance	0.03 mm
Solver	Particle tracking
Relative accuracy	-40 dB

Results and discussion

The height of the focus electrode is one of the important parameters that has often been overlooked in the iterative method. Fig. 4 shows the effect of electrode height on the perveance for a gun with theoretical perveance equal to 3 $\mu perv$. In this figure, the horizontal axis represents the ratio of electrode height to the distance between the cathode end and the center of the anode (anode plane). The vertical axis denotes the perveance. Fig. 4 illustrates that increasing the electrode height is correlates with a decrease in the perveance value. As the height of the electrode increases, the perveance value tends to stabilize at a certain limit.

Consequently, the resulting perveance value becomes independent of the height of the focus electrode. To standardize our simulations, we adopt a guideline where the electrode height is set to 0.7 times the distance to the anode plane.

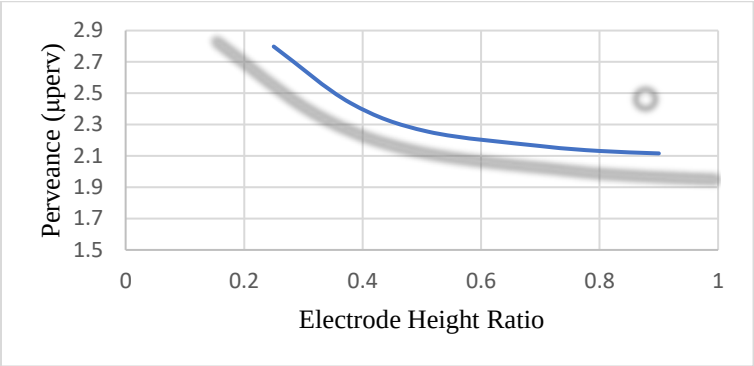

Fig. 4. Prveance for different heights of the focus electrode

Ref [5] indicated that the iterative method did not perform satisfactorily for the low-perveance gun. So, the gun with a perveance of 3 $\mu perve$ as typically high perveance was selected for our study. Several electron guns with different convergence values (10 to 300) were designed. Table 7 shows the input design parameters of these guns and their corresponding outputs. In all cases, the potential difference between the cathode and the anode is 5000 volts.

Table 7. Results of an iterative method for p= 3$\mu perv$ and V= 5000 V

Case number	convergence	r_w (mm)	r_c (mm)	R_c (mm)	R_a (mm)	r_a (mm)	θ	R_{cT} (mm)	θ_T
1	10	1.837	5.81	9.70	4.50	3.23	36.75	8.78	41.39
2	100	0.581	5.81	7.28	2.62	2.50	52.88	6.59	61.77
3	200	0.411	5.81	6.88	2.32	2.35	57.52	6.23	68.77
4	300	0.335	5.81	6.68	2.17	2.26	60.26	6.05	73.63

The obtained geometries for the electron gun were simulated by CST software. The simulation results are listed in Table 8. The table presents the relative difference between theoretical and output perveance as the ΔP. As can be seen, increasing the convergence leads to perveance being closer to its theoretical value. At higher convergence, the cathode has a more concave shape which results in the cathode playing a more important role in focusing than the focus electrode. So, it is reasonable that by increasing the convergence of the electron gun, the perveance value can be closer to its theoretical value.

Table 8. Results of CST simulation

Case number	convergence	Perveance ($\mu perv$)		ΔP (%)
		Theoretical	simulation	
1	10	3	2.16	28
2	100	3	2.34	22
3	200	3	2.70	10
4	300	3	2.97	1

Conclusions

This paper investigates the validity range of Vaughan's iterative method by designing various electron guns using this method. The focus electrode in all geometry makes an angle of 67.5° with the normal at the cathode edge. The CST software was used for the simulation of the electron gun. The simulation results indicate that increasing the height of the focus electrode leads to a decrease in the perveance value. When the height of the electrode is increased, the perveance value tends to a certain limit. Also, the simulation results show that the validity of the iterative model improves as convergence increases.

References

1. Gharaati, A. and D. Mardani, *Electrostatic design and fabrication a new tunable perveance pierce electron gun.* IEEE Transactions on Electron Devices, 2020. 68(1): p. 318-323.
2. Lewis, B.M., et al., *Design of an electron gun using computer optimization.* IEEE transactions on plasma science, 2004. 32(3): p. 1242-1250.
3. Cheng, Y., et al., *Low perveance confined-flow Pierce gun for a 0.14 THz broadband folded waveguide traveling wave tube.* Vacuum, 2011. 86(3): p. 335-339.
4. Frost, R., O. Purl, and H. Johnson, *Electron guns for forming solid beams of high perveance and high convergence.* Proceedings of the IRE, 1962. 50(8): p. 1800-1807.
5. Vaughan, J.R.M., *Synthesis of the Pierce gun.* IEEE Transactions on Electron Devices, 1981. 28(1): p. 37-41.
6. Tiwary, U. and B. Basu, *Noniterative method for the synthesis of convergent pierce electron guns.* IEEE transactions on electron devices, 1987. 34(5): p. 1218-1222.
7. Sharma, R., A. Sinha, and S. Joshi, *An improved method for the synthesis of anode aperture for Pierce guns.* IEEE Transactions on Electron Devices, 2001. 48(2): p. 395-397.
8. Yang, C., B. Jia, and Z. Zhu, *Improved noniterative method for the synthesis of convergent pierce electron guns.* IEEE transactions on electron devices, 2006. 53(11): p. 2849-2852.

ICNST 2024
International Conference on Nuclear Science and Technology
6- 8 MAY 2024 | Isfahan, Iran

Simulation of extraction of deutron beam from neutron generator ion source (Paper ID : 1469)

Hoseinzade M. Correspondent*

Physics and Fusion Energy Department, Atomic Energy Organization of Iran, Tehran, Iran

Abstract

Plasma and nuclear fusion research institute in nuclear science and technology research institute (IAEOI) is designing and building a neutron generator with the ability to produce 107 neutrons per second with the possibility of research and practical uses such as neutron radiography and element detection by gamma spectrometry. Induction is caused by neutron activation. One of the basic elements of the neutron generator is the ion source and, accordingly, the ion source accelerator for the acceleration and exit of the ion beam. The ion source used in this neutron generator is of the electron cyclotron resonance type, in which microwave waves with a frequency of 2.45 2.45 MHz are used to produce dense plasma. Taking into consideration the cooling power of the target for this type of neutron generator with this special purpose, the diameter of the beam with dimensions of about 5 mm is considered. In this article, the goal is to design and optimize the ion source accelerator using CST software to receive a beam with these dimensions at the exit. With the optimizations made with the working voltage of 60 kV and the distance between the first and second electrodes of 60 mm and the second and third electrodes of 91 mm and the aperture diameter of 3 mm, a strip with a diameter of about 5 mm is obtained.

Keywords: Neutron generator, Ion source, Accelerator, CST, Extrcation system

INTRODUCTION

The ion source is, mechanically and functionally, composed of two main parts: the plasma generator and the ion beam accelerator[1].

In the development of an ion source extraction physics are one of the critical problems that researchers in this field must face. Thus, a new extraction system has been designed for neutron generator in which the triode extraction system (also called the three electrode extraction system or the accel-decel extraction system) is a key component.

In order to reduce angular divergence and increase the transported beam current from the neutron generator ion source, improvements to the extraction system are required. This paper describes the simulation studies

to find the optimized design features of the new ion source and the possible electrode geometry modifications needed to extract the highest quality beam.

Due to the importance of the triode extraction system for a high current density plasma ion source, the operation principle of the ion source is carefully examined, and the triode extraction system is designed and optimized by using CST software (for Particle Beam Simulations)[2]. A detailed simulation process and the key parameters of the system are presented in this paper.

ION BEAM EXTRACTION

A thorough experimental analysis of extraction optics for a single circular aperture is given by Coupland [3]. For uniform emission from an infinite plane, the Child–Langmuir law [4] gives the current density, J, of singly ionized hydrogen as

$$(1) J = \left(\frac{1{,}74}{d_2}\right) V^{\frac{3}{2}} \quad mA\text{mm}^{-2}$$

where V is the applied extraction potential in kilovolts and d is the separation between the aperture and the extraction electrode in millimeters. For an emission from a concave surface with radius of curvature RM, for small values of d/RM it can be shown that Eq.(1) is multiplied by a factor

$$(2) \left(1 - 1{,}6\frac{d}{R_M}\right)$$

which is smaller than unity. The total beam current is found by multiplying the current density by the area of the emission aperture. For the cylindrical aperture of the ion source, the current is:

$$I = J\pi r^2 = 1{,}74\pi V^{\frac{3}{2}} S^2 \left(1 - 1{,}6\frac{d}{R_M}\right) \qquad (3)$$

where S =r/d is the aspect ratio, r is the radius of the hole in the plasma electrode, and F =πr^2 is the emitting area.

Space charge effect in beams is conveniently characterized by the perveance, taking into account the magnitudes of the beam current and the accelerating voltage. Beam perveance has been studied and calculated in order to define the beam trajectory and beam boundaries. The perveance, P, of an ion beam is defined as

$$(4) P = \frac{I}{V^{3/2}} = \left(1 - 1{,}6\frac{d}{R_M}\right) P_0 \;\; mAkV^{-3/2}$$

This is a function only of the geometry of the system.

The divergence angle ω at the exit of the extraction system is caused by: the shape of the plasma meniscus, the defocusing forces of the second aperture (as described above), the temperature of the ions (as we will see below), and by repulsive forces of the particles on themselves. The divergence angle has been calculated by Coupland [3],

$$\omega = 0{,}29S\left(1 - 2{,}14\frac{P}{P_0}\right) \qquad (5)$$

where S=r/d as above, and P is the perveance in the extraction gap, P =I/V3/2 , and P0 is the Child-Langmuir space-charge limited perveance for the one dimensional diode of length d with no electrons,

$$P_0 = \left[\left(\frac{4}{9}\right)\pi\right]\left(\frac{r^2}{d^2}\right)\varepsilon_0\left(\frac{2e}{M}\right)^{1/2} \qquad (6)$$

where ε_0 is the permittivity of the vacuum.

Equation (5) predicts that the divergence can be reduced to zero at a perveance equal to $0.47P_0$. In practice, the divergence does not decrease to zero and the perveance at the minimum divergence is less than $0.47P_0$.

OPTIMIZATION OF NEUTRON GENERATOR EXTRACTION SYSTEM

Fig 1 shows the 3D view of the extraction system of neutron generator. This system is composed of 3 electrodes. The first electrode is called plasma electrode. The second electrode is accelerator electode which accelerated the ion beam and the third electrode that here is target.

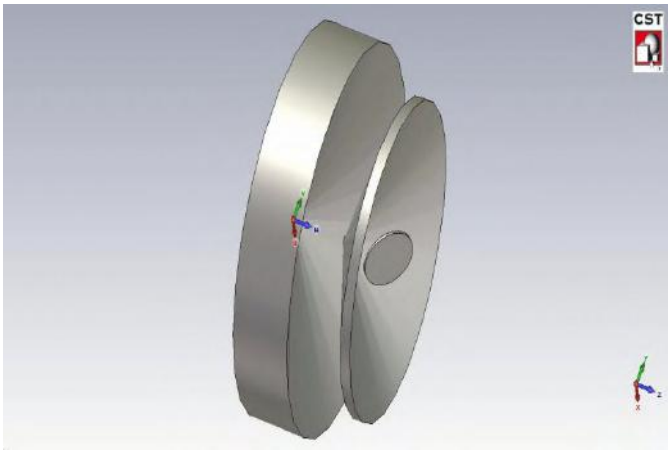

Fig. 1. 3D view of ion source extrcation system.

To optimize the beam extraction from a triode extraction system CST code is used. The following figure shows the simulated electrodes and extracted beam using CST computer code.

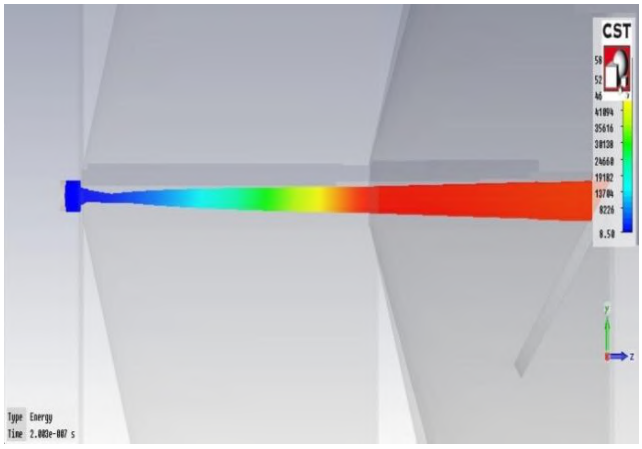

Fig. 2. The simulated ion beam extraction system of neutron generator.

The first electrode (plasma electrode) plays an important role in beam quality. The angle of this electrode affects the divergence of the beam. It has been accepted that shaping the plasma electrode, in general, is helpful to extract a beam at a low divergence angle. Also the diameter of the first electrode affects the beam current. The bigger the electrode diameter the more extracted current that can be diagnosed in the Faraday cup. In each ion source depending on its application, one parameter is important. In this ion source which is used for neutron generator the extracted beam diameter is important. The applied voltage on electrode to accelerate the beam, the distance between second and third electrode and plasma electrode diameter are parameters that affect the extracted beam diameter.

Figure 3 is a cross section of the beam from plasma electrode to target in tracking simulation. I was going to show it is elliptical. Also the beam diameter can be followed in this picture. For instance, in z= -3 mm the beam diameter in x position (the big blue elliptical) is roughly 2 mm.

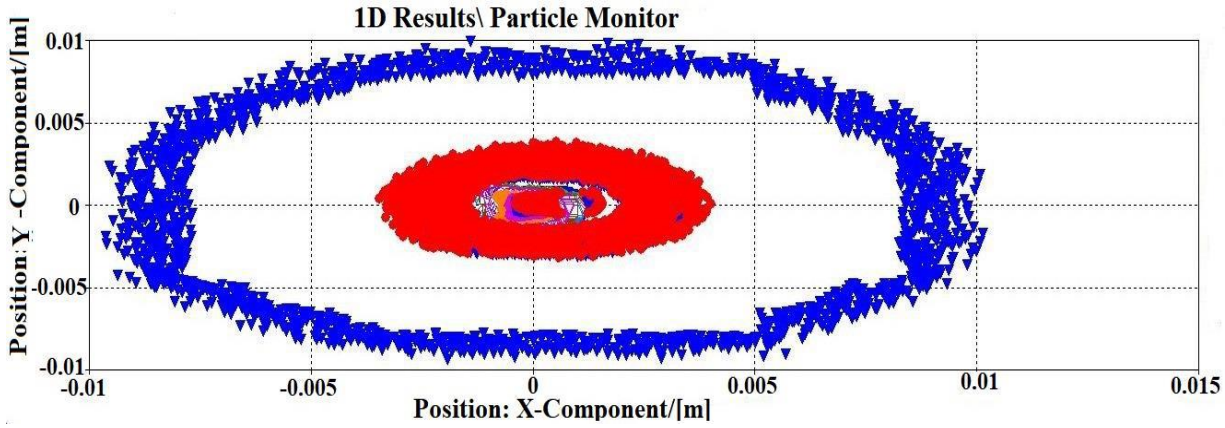

Fig. 3. The beam cross section in different positions from plasma electrode to target .

THE BEAM DIAMETER DEPENDENCE ON VOLTAGE

The applied voltage on second electrode is changed to monitor the beam diameter. As is shown in following figure as the voltage is increased the beam diameter is reduced. When the voltage is 60 kV the beam diameter is about 2 mm.

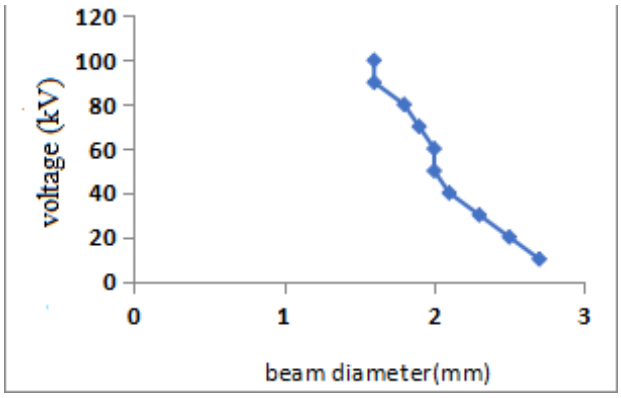

Fig. 4. The infuence of the voltage on beam diameter.

THE INFLUENEC OF VOLTAGE AND THE DISTANCE BETWEEN ELECTRODES ON BEAM DIAMETER

As is shown in the figure below with the change of second electrode and as a result the third electrode from the plasma electrode the extracted beam diameter is changed. From technical and laboratory point of view

the 60 kV voltage is a reasonable voltage to run the system. To get a beam with the considered diameter, the distance of 60 mm for second electrode and 91 mm for third electrode for the future simulations is chosen. The figure 5 is for this part of simulation.

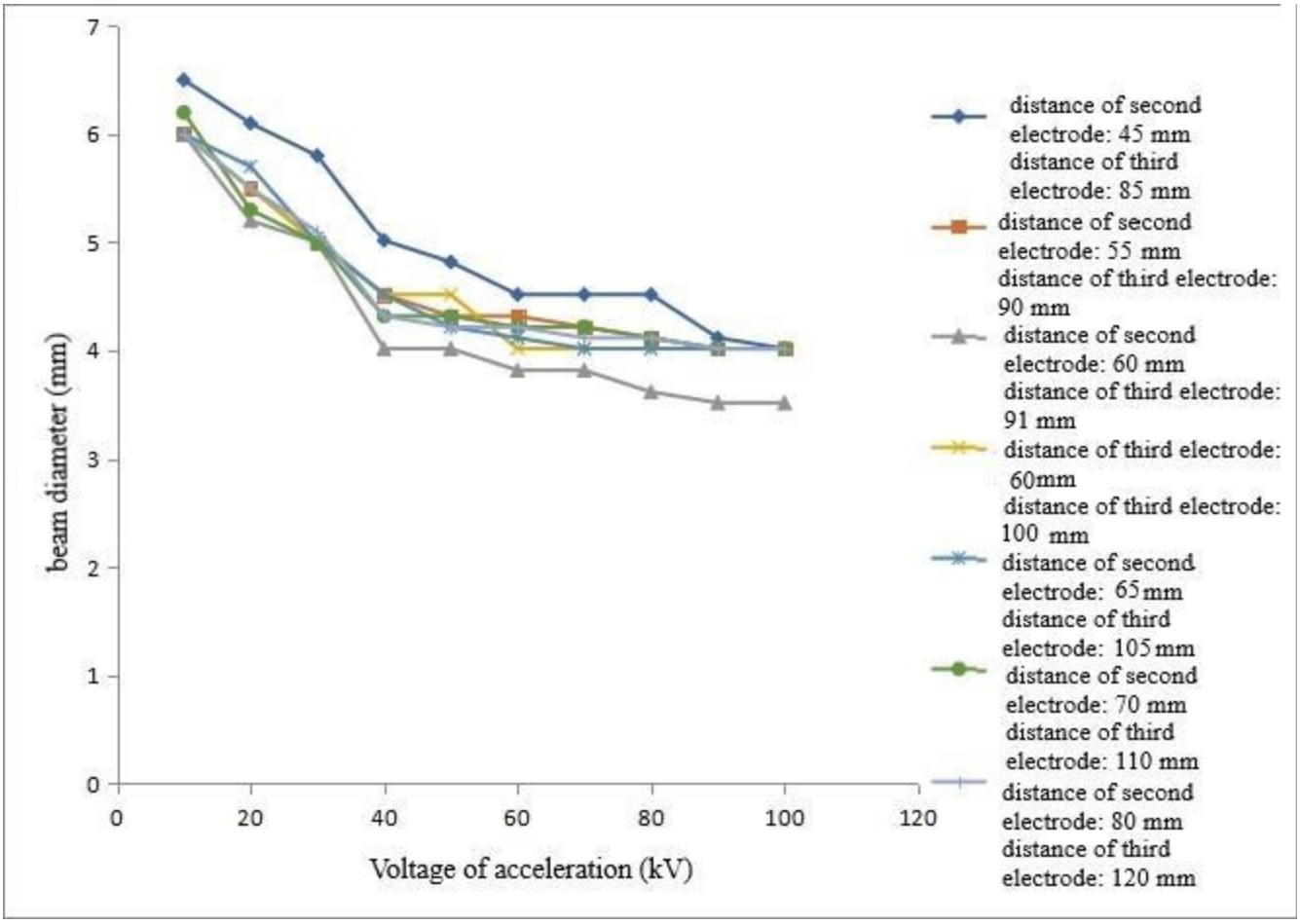

Fig. 5. The influence of the voltage and distances of second and third electrode from plasma electrode on beam diameter .

THE BEAM DIAMETER DEPENDENCE ON PLASMA ELECTRODE DIAMETER

The other parameter that has an influence on beam diameter is plasma electrode aperture. As is illustrated in figure below as the plasma electrode aperture is increased the beam diameter is increased too. Our aim is to get a beam of 5mm diameter which this goal is obtained with the aperture diameter of 3mm.

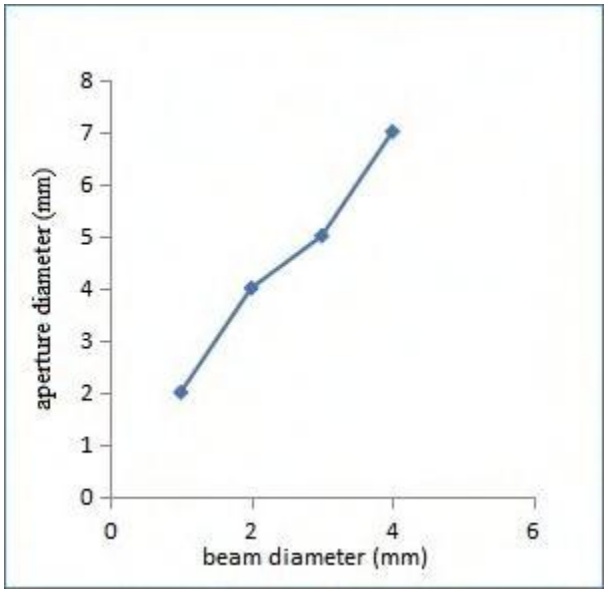

Fig. 6. The infuence of the aperture diameter on beam diameter .

Results and discussion

Fortunately in this paper the final goal that is beam of 5 mm diameter is acquired. To this end. First of all we applied voltage to accelerate the beam is modulated to 60 kV. The the distance of second and this electrode is set to 60 and 31 mm respectively to gain a beam of 4.2 mm and in the final stage with the change of plasma electrode aperture we get a beam with 5 mm diameter.

All these simulations has been performed with CST code. The final results and beam tracking of this simulations is shown in 2D following figure. The results of this simulation is used in the construction of the neutron generator that is currently under construction in the IECF lab.

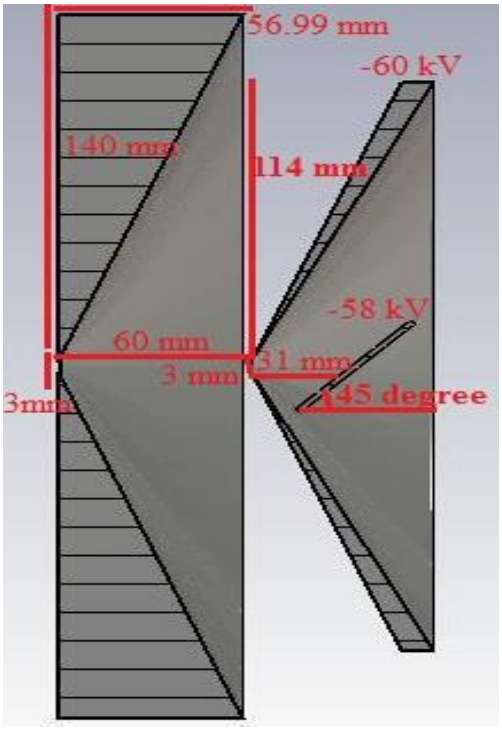

Fig. 7. 2D view of the neutron generator ion source accelerator .

References

Tondare V N, Vac J. Sci. Technol. A, 2005, 23(6): 1498

[2] CST. http:www.cst.com.

[3] Coupland J R, Green T S, Hammond D P, Riviere A C. Rev. Sci. Instrum., 1973, 44: 1258.

[4]Child C D. Phys. Rev., 1911, 32: 492.

ICNST 2024
International Conference on Nuclear Science and Technology
6- 8 MAY 2024 | Isfahan, Iran

Comparison of beam delivery system in wastewater treatment facillity using electron accelerator (Paper ID : 1470)

Safahani Z[1]. Afarideh H[1]. GHasemi F[2]. Aghayan M[2]

[1]amirkabir university, Department of Faculty of Physics and Energy Engineering, Tehran, Iran

[2]Nuclear Science and Technology Research Institute (NSTRI), Tehran, Iran

Abstract

Limited access to freshwater resources and the need for wastewater reuse have underscored the importance of different wastewater treatment methods. With the increasing number of suppliers of industrial electron accelerator and the successful implementation of new industrial wastewater irradiation centers, the use of this method has garnered attention in Iran, a semi-dry country. Industrial electron accelerator utilized in this application typically have an energy range of 1-2 MeV and a power range of 50 to 150 kW. The ELV and Dynamitron accelerators have been reported to be used in this application, with various beam delivery systems in different centers. Selecting the appropriate specifications for an accelerator for this application depends on factors such as the required dose, wastewater volume, the location of the irradiation in the typical wastewater treatment plant cycle, and the delivery system. This paper aims to review the different methods and compare their advantages and disadvantages, ultimately selecting and suggesting a sample for the project currently being implemented in Iran.

Keywords: Wastewater treatment, Industrial electron accelerator, Beam delivery system, Dynamitron

INTRODUCTION

Managing water resources in every country is considered one of the important and strategic issues that has a significant impact on the level of economic, social, and health indicators. Considering Iran's location in the dry and semi-dry belt of the world, as well as global trends of climate change and decreasing available water resources, attention to this issue in the country is of paramount importance. Simultaneously with the rapid expansion of industry and the increasing population growth, the need for water (industrial, agricultural, and drinking) has also significantly increased. Providing water through various methods, including treating urban and industrial wastewater, is one of the solutions that has received considerable attention in many countries, including Iran. Wastewater treatment plays a crucial role in addressing water scarcity and ensuring sustainable water resources management. By treating and reusing wastewater, we can reduce the pressure on freshwater resources and protect the environment [1]. Generally, wastewater

treatment involves various stages. The initial stages include adjusting the pH, removing colloidal particles, and in some cases, reducing the required oxygen from the effluent chemically [2]. The next stage involves physical, chemical, and biological methods that may be carried out separately or in combination. The third stage is employed to remove very small amounts of pollutants that may remain in the treated wastewater.

Wastewater treatment with electron beams is an efficient method for treating industrial and municipal wastewater. This method, with significant advantages such as high efficiency, predictable results, and environmental compatibility, is applicable in various fields including food industries, medicine, chemical industries, textiles, petrochemicals, rubber, and wastewater treatment [3]. In the process of treating wastewater using irradiation, the main objective is to remove non-biodegradable pollutants by converting them into mineral compounds and biodegradable organic compounds, as well as eliminating microbial contaminations.

The stages of wastewater treatment with electron beams consist of three steps. The first stage is pre-treatment, where suspended particles and large contaminants are removed from the wastewater. The next stage involves electron beam irradiation, where the wastewater is directly exposed to high-energy electron beams. The third stage is secondary treatment, where biological and chemical methods are used to remove remaining pollutants from the wastewater. Wastewater treatment requires continuous monitoring of various pollutants, including determining organic substances, which poses a significant challenge due to the diverse nature of organic compounds. Electron beam treatment provides cost-effective and efficient ways to address COD, BOD, and TOC in wastewater. Traditional methods for measuring organic substances include Chemical Oxygen Demand (COD) and Biochemical Oxygen Demand (BOD) tests. However, Total Organic Carbon (TOC) analysis is increasingly being used as a potential alternative, as it is faster, more accurate, more sensitive, and environmentally friendly. High levels of COD indicate pollution and can impact aquatic ecosystems. In electron beam treatment, the reduction of COD occurs due to the breakdown of pollutants by highly reactive species formed during the Radiolysis decomposition of water [4, 5, 6]. Reducing BOD is crucial for maintaining healthy water. Electron beam treatment can increase the biodegradability of non-biodegradable compounds by converting them [7]. TOC analysis helps in assessing the total organic load. Interestingly, electron beam treatment may not significantly reduce TOC levels but improves subsequent treatment stages [8].

Another application of ionizing radiation that can be used in water purification is the removal of microorganisms. For this purpose, the irradiation system is installed at the last stage of treatment. Ionizing radiations such as UV, X-rays, and electron beams are effective forms of energy that can destroy biological organic pollutants [9]. Ultraviolet radiation is used for disinfecting water by damaging the DNA of microorganisms, rendering them unable to reproduce. It is effective against bacteria, viruses, and some parasites [10]. Gamma rays emitted from radioactive isotopes (such as cobalt-60) penetrate water and disrupt microbial cells. This method is effective for sterilization and pathogen reduction. X-rays can be used for water treatment, although they are less common compared to other methods. They are mainly used for research purposes.

Industrial accelerators play a crucial role in wastewater treatment. Industrial accelerators are devices used to accelerate charged particles such as electrons or ions to very high energies [11]. Particle accelerators come in various types categorized into three main groups based on the acceleration mechanism: electrostatic accelerators, RF accelerators, and inductive accelerators. Accelerators are equipped with high-end technology and consist of various components such as electron guns, cavities, radiofrequency generators, bending magnets, vacuum systems, cooling systems, control systems, and beam transport lines [12, 13].

INTRODUCTION OF DIFFERENT RADIATION GEOMETRIES

Electron beam irradiation as a novel and efficient method for wastewater treatment is currently under development and expansion. The geometry of flow configuration refers to the positioning of the radiation source and wastewater flow in radiation systems. The selection of appropriate geometry plays a key role in the efficiency and effectiveness of the wastewater treatment process. In wastewater treatment using electron accelerators, there is a proportionality between accelerator parameters and radiation geometry, which is essential for achieving maximum efficiency and effectiveness. Key parameters involved in the design of electron beam irradiation units for water treatment include the coordination of electron beam characteristics and water flow parameters, crucial for ensuring effective and efficient treatment. Parameters such as beam energy, power, dimensions, scan frequency, and direction, along with water flow width, linear velocity, distance from the beam, wastewater thickness or volume, electron penetration depth, and absorbed dose of the target, are all vital factors that need to be carefully considered and optimized. These parameters are all interrelated and must be optimized together to design a large-scale electron beam water treatment system. In Figure 1, some of the important parameters are shown [14, 15].

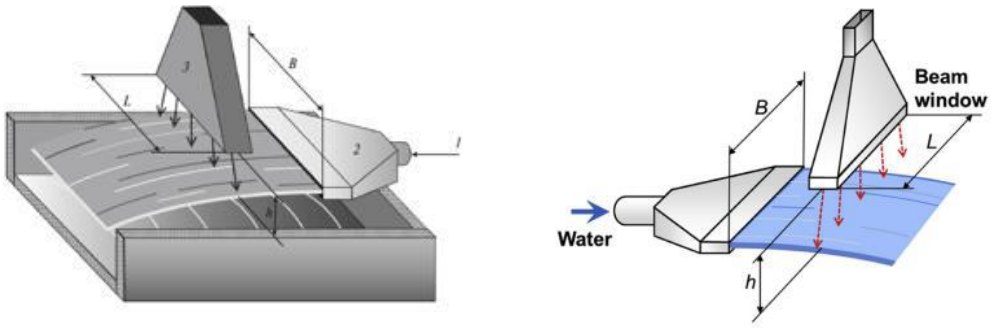

Fig. 1 Relative positions of an accelerator and a wide jet of water. Designations: (1) water supply, (2) nozzle forming a water jet, and (3) accelerator beam window.

To achieve the appropriate thin layer thickness and ensure uniform and effective irradiation of the wastewater stream, different geometrical configurations and specialized nozzle designs are utilized. Figure 2 depicts the categorization and explanation of various irradiation geometries that are commonly employed for electron beam wastewater treatment [16].

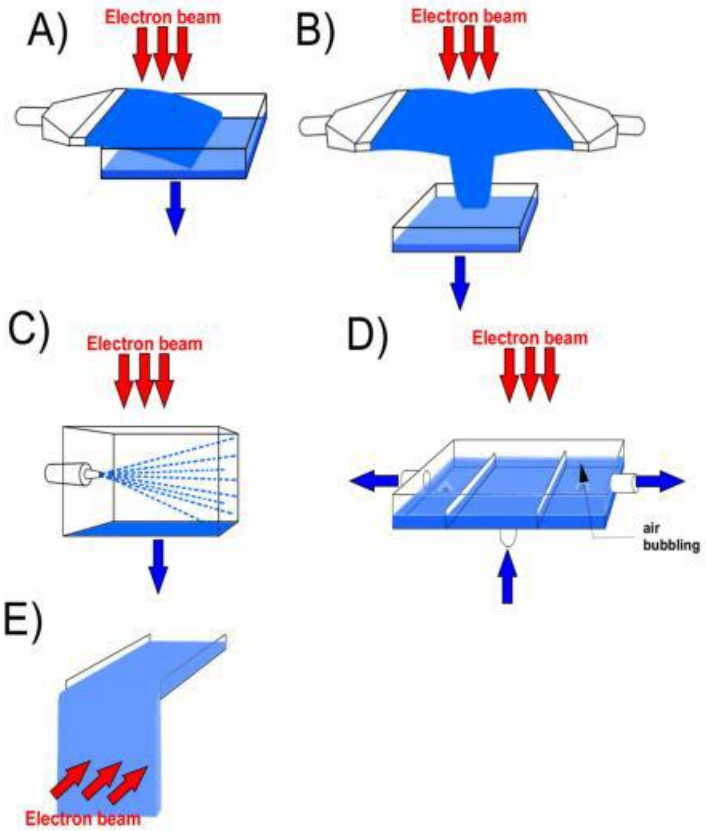

Fig. 2. . Different geometry of stream configuration for wastewater irradiation: (A) jet injection, (B) two opposite jets injection, (C) sprayer, (D) up-flow system with air bubbling, (E) natural flow

A) The jet injection geometry for electron beam wastewater treatment involves forming a continuous wastewater jet with its width adjusted to match the scanning width of the accelerator beam. A key aspect of this configuration is that the thickness of the irradiated wastewater layer is directly correlated to the penetration depth of the accelerated electrons, which in turn depends on the energy of the accelerator itself. This jet injection configuration is considered the most efficient and cost-effective method for electron beam water treatment as it maximizes the utilization of the electron beam while simultaneously maintaining the necessary thin layer thickness required for effective irradiation.

B) Two opposing jets injection: Similar to jet injection, but with two wastewater jets injected from opposite directions to increase synchronization and ensure uniform exposure to the electron beam irradiation [17].

C) Sprayer: Water is sprayed in fine droplets which are irradiated by the electrons. This configuration increases the water surface area exposed to the beam, but also increases electron losses due to scattering and absorption by air.

D) Upflow system with air bubbling: In this system, the wastewater flows upwards through a chamber while air is bubbled into it from the bottom [18].

E) Natural Flow: This option refers to the natural flow of wastewater through the radiation chamber without any additional mixing mechanism. This is typically not preferred as it may lead to uneven exposure and reduced treatment efficiency.

Comparing methods and presenting suggestions

Among ionizing radiations, gamma rays, and electron beams have the potential for treating wastewater. Most laboratory research is conducted using gamma rays, especially from cobalt-60 source. But due to the lower dose rate of gamma rays compared to electron beam and the costs associated to replace gamma source, the use of electron accelerators in an industrial scale is more cost-effective. In the process of electron beam irradiation, energy is transferred from the beam to the material. The higher the energy of the accelerated electrons, the greater penetrating into the material. Electrons present in the material, upon absorbing this energy, are excited to higher energy levels or ionized. This process leads to the production of strong reducing species such as hydrated electrons and hydrogen atoms, as well as strong oxidizing species such as hydroxyl radicals and hydrogen peroxide in the solution. For the purification of wastewater using electron beam irradiation, high-energy electron accelerators are required. Lower energy electron beams result in less

penetration into the wastewater stream. Therefore, for effective irradiation, the use of a thin liquid layer is essential. To ensure the appropriate thickness of the thin liquid layer and uniform irradiation, various geometries and injection systems are utilized. These geometries include jet injection, counter-current double jet injection, spray system, up flow bubble column system, and natural flow. The aim of this variety in configurations is to create a thin and uniform layer of wastewater for effective penetration and purification by electron beam irradiation. The most common configuration involves continuous injection of wastewater using a nozzle injector. The jet width is adjusted to match the width of the electron beam accelerator scan. After electron beam irradiation, the wastewater is collected in a tray. The thickness of the irradiated wastewater layer depends on the depth of penetration of the accelerated electrons and, therefore, is dependent on the accelerator energy. The configuration with wastewater jet and lateral electron beam is the most common as it establishes a good relationship between the wastewater and the beam.

Industrial electron accelerators come in two types: electrostatic and radiofrequency. ELV and dynamitron accelerators are types of electrostatic accelerators, while linear accelerator, Rhodotron and ILUs, are common types of industrial radiofrequency accelerators.

Today, dynamitron accelerator, as a type of electrostatic accelerator, is widely used in industries for modification of polymer materials, sterilization of medical equipment and wastewater treatment due to high efficiency and cost-effectiveness. In recent years, significant activities regarding the design and construction of Dynamitron industrial accelerator have been carried out in Nuclear science and technology research institute(NSTRI). In this project, useful experiences have been gained regarding the operation of this system and the design and construction of its components and subsystems, and also specialized human resources have been trained in this field. Also, Dynamitron accelerator has been used in the projects of wastewater treatment by electron beam that have been implemented in the world in recent years [19]. Figure 3 shows a view of the Dynamitron accelerator built in NSTRI.

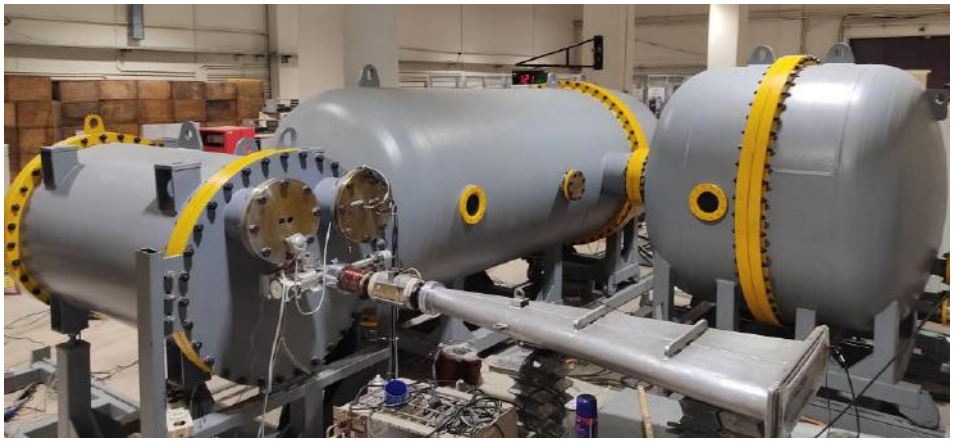

Fig. 3. a view of the Dynamitron accelerator built in NSTRI

Conclusions

The rapid population growth along with industrialization, urbanization, and high-water consumption lifestyle has led to serious challenges in wastewater management. Pilot factories and industrial applications demonstrate that radiation-based treatment processes can play a significant role in the future. The expansion of this process can improve environmental protection and have a fundamental impact on industrial development. Electron beam, as an advanced treatment process, can effectively aid in wastewater treatment. Considering the types of radiation geometries commonly used for electron beam wastewater treatment, jet injection, where water forms a broad jet under the accelerator window, is the most prevalent configuration as it provides good mixing and contact between wastewater and the beam. Nowadays, the dynamitron accelerator from the electrostatic accelerator group is utilized in this field due to its high efficiency and reasonable price.

References

[1] HEGAZY, „Radiation treatment of wastewater for reuse with particular focus on wastewaters containing organic pollutants and removal of heavy metals from wastewater," 2018.

[2] B. H. S.M. Kim, „APPLICATION OF HIGH POWER ELECTRON ACCELERATOR IN WASTEWATER TREATMENT," 2006.

[3] B.Nayak, „1 MeV,10 KW DC electron accelerator for industrial applicactions," 2016.

[4] J.Wang, „Treatment of hospital wastewater by electron beam technology: Removal ofCOD, pathogenic bacteria and viruses,” 2022.

[5] S. Wang, „First full-scale application of electron beam technology for treating dyeing wastewater (30,000 m3),” 2022.

[6] B. Han, „Electron Beam Treatment of Dyeing Wastewater,” 2005.

[7] Y. A. Maruthi, „Disinfection and reduction of organic load of sewage waterby electron beam radiation,” 2011.

[8] B.Han, „Combined electron-beam and biological treatment of dyeingcomplex wastewater. Pilot plant experiments,” 2002.

[9] B. Han, „Electron beam treatment of textile dyeing wastewater:operation of pilot plant and industrial plantconstruction,” 2005.

[10] Y. A. Maruthi, „Disinfection and reduction of organic load of sewage waterby electron beam radiation,” 2011.

[11] A. A. Bryazgin, „Industrial electron accelerators developed at the Budker Institute ofNuclear Physics, SB RAS,” 2018.

[12] محمد لامعی رشتی،فرشاد قاسمی و همکاران, ‘‘معرفی پروژه طراحی و ساخت شتاب دهنده خطی الکترون پژوهشگاه دانش های بنیادی,’’ ۱۳۹۴.

[13] محمد لامعی رشتی ،فرشاد قاسمی و همکاران, ‘‘بررسی اهمیت و کاربرد شتاب دهنده ها در دنیای امروز,’’ ۱۳۹۴.

[14] A. Ponomarev, „High-speed electron-beam water treatment: A technological consideration,” 2022.

[15] Y. Kim, „Features and Ways to Upgrade Electron-Beam Wastewater Treatment,” 2022.

[16] U. Gryczka, „Advanced Electron Beam (EB) Wastewater Treatment Systemwith Low Background X-ray Intensity Generation,” 2021.

[17] B. Han, „Operation of industrial-scale electron beam wastewater treatment plant,” 2012.

[18] P. Rela, „Development of an up-¯ow irradiation device for electronbeam wastewater treatment,” 2000.

[19] J. Wang, „Treatment of hospital wastewater by electron beam technology: Removal ofCOD, pathogenic bacteria and viruses,” 2022.

ICNST 2024 International Conference on Nuclear Science and Technology
6- 8 MAY 2024 | Isfahan, Iran

An overview of the implementation steps in dose calculation using the Collapsed Cone Convolution Superposition algorithm (Paper ID : 1494)

Zarepour A.[1*], Hadad K.[2]

[1]*Department of Nuclear Engineering, School of Mechanical Engineering, Shiraz University, Shiraz, Iran*
[2]*Department of Nuclear Engineering, School of Mechanical Engineering, Shiraz University, Shiraz, Iran*

Abstract

Nowadays, external or internal radiation therapy or treatment using charged particles and ions are used in different methods and techniques to treat different types of cancer. In a general view, the device/machine that is used in all these methods and techniques consists of two general parts, hardware and software.

In the software section, the most important components are the treatment planning systems and one of the most significant of their parts is the dose calculation engine used in them. This dose calculation engine is used to accurately and precisely calculate and estimate the amount of dose in different parts of the tumor, vital and radiation-sensitive organs of the body (OARs), and its normal and healthy tissues and then, using these dose amounts to plot the percent depth doses, the isodose curves, the lateral dose profiles, and the orthogonal transverse dose profiles of them.

In this dose calculation engine, various and different types of algorithms are used to calculate the dose, and one of the most important and widely used algorithms is the Collapsed Cone Convolution Superposition algorithm. In brief and simple, in this algorithm, the radiant energy or the charged particle energy is released, transported, and attenuated only along the axis of collapsed cones. Based on this assumption, in this algorithm, the dose consists of two parts, which include the TERMA and the energy dose kernels, by combining these two parts with the convolution operator, the dose amount is calculated. The TERMA acts as an impact function, in which the energy dose kernels are used to determine the effect of the TERMA value of each voxel on its neighboring voxels.

To achieve this goal that seems simple at first glance, a complete and comprehensive plan is needed. However, the process of implementing the CCCS dose calculation algorithm itself can be briefly divided into seven steps.

About the results, the implemented CCCS algorithm, when utilizing the 11x11 lattice of energy transport lines to perform dose calculations, has exhibited the lowest error compared to the results obtained using the

Monte Carlo method. In addition, of all the lattices of energy transport lines, the 5x5 configuration required the shortest time to perform dose calculations.

In addition, when comparing the time required for dose calculations using the two methods, it was observed that the Monte Carlo method necessitated several thousand minutes, whereas the implemented CCCS algorithm completed the task in a mere few tens of seconds to several minutes. Remarkably, despite these disparate computation times, the final results from both methods exhibited only minor differences.

Keywords: Treatment planning systems, Collapsed cone convolution superposition algorithm, TERMA, Primary and Scatter energy dose kernels, Lattice of energy transport lines, Interaction point of view

Introduction

There are various and different algorithms available for dose calculation. However, they can generally be classified into the following two groups:

Correction-Based Algorithms

Model-Based Algorithms

b-1) Convolution/Superposition Methods b-2) Direct Monte Carlo

In the dose calculation method employing algorithms from the first group, the initial step involves measuring the dose within a water phantom under reference and standard conditions. Then, using various correction coefficients, each applied for specific purposes, the dose value measured under reference conditions is changed into the dose value calculated for the desired arbitrary conditions.

The main weakness and limitation of algorithms in the first group arise when they are applied to newly invented and developed clinical methods and techniques in photon radiotherapy or hadron radiotherapy because these new innovative techniques are more complicated to have both higher precision for calculating the dose and more adaptation to the optimal treatment conditions, therefore their implementation is very challenging, boring, demanding and in many cases almost impossible.

However, the remarkable advantage of calculating the dose using algorithms from the second group lies in their ability to effectively handle and manage complex situations and conditions.

Among the two subgroups of the algorithms of the second group, the second subgroup, i.e., the direct Monte Carlo simulation method, has more limited applicability due to the constrained computing power of current processors and being time-intensive dose calculation process. Instead, the first subgroup, which comprises model-based algorithms utilizing convolution-superposition methods, demonstrates both high precision and an acceptable calculation speed for dose calculation.

The convolution-superposition methods are a family of models with roots in the image world and basically, they have been developed using energy deposition kernels, which were previously calculated with the help of the Monte Carlo method.

In convolution-superposition methods, the absorbed dose comprises two distinct components, which are combined using the convolution operator:

The TERMA, which describes the transport of primary photons.

The Kernel, which describes the energy transport and dose deposition of secondary particles resulting from the interaction of primary photons.

In summary, the absorbed dose is equal to the convolution of the TERMA and Kernel. This concept is shown in Fig. 1.

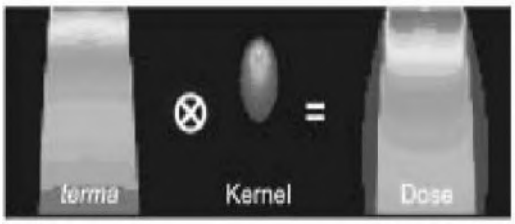

Fig. 1. The absorbed dose is equal to the convolution of TERMA and Kernel.

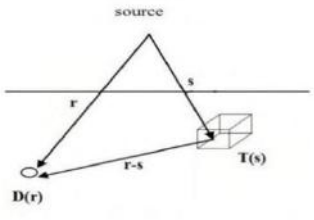

Fig. 2. The schematic representation of the basic geometry for calculating the absorbed dose

The schematic representation of the basic geometry upon which the extracted equations for the convolution-superposition methods are based is shown in **Fig. 2**. According to this geometry, the equation expressing the absorbed dose inside a three-dimensional homogeneous absorption medium, in integral form, is:

$$D(r) = \int \iiint T_E(s)\, h(E, r-s)\, d^3s\, dE \qquad (1)$$

Finally, by correcting this equation based on the radiological distance, i.e. the length corrected in terms of the electron density of the material of the irradiated medium compared to water, an equation is derived which is called the convolution-superposition relation:

$$D(r) = \int \iiint T(s) \frac{\rho(s)}{} c^2 h \quad [c(r-s)]\, d^3s\, dE \qquad (2)$$

To solve this equation, it is necessary to change it from continuous space to discrete space, considering both the appropriate energy spectrum resolution of the device's output beam and the suitable spatial resolution for the absorbent medium. To accomplish this change, various methods are available, which some of them can be listed as follows:

Collapsed Cone Convolution/Superposition-CCCS

Anisotropic Analytical Algorithm-AAA

Fast Fourier Transform-FFT

Among these methods, the Collapsed Cone Convolution/Superposition (CCCS) calculation algorithm has been widely used. This algorithm was introduced by Anders Ahnesjö in 1989.

In this algorithm, the following equations can be used to express the TERMA in its simplest form

$$T_E(r) = \frac{\mu}{\rho}(E,r)\, \boldsymbol{\Psi}_E(r) \qquad (3)$$

$$\boldsymbol{\Psi}(r) = \boldsymbol{\Psi}(r)\left(\frac{r_0}{}\right)^2 exp\left(-\left[\int_r \mu(E,r)\rho(l)dl\right]\right) \qquad (4)$$

Additionally, in this algorithm, the kernel itself, which is also referred to as the energy deposition kernel or dose kernel, is divided into two categories: one is the primary energy deposition kernel (Primary EDK), and the other is the scatter energy deposition kernel (Scatter EDK). The Primary EDK describes the energy transport of initial charged particles released by the first interaction of the primary photons. Additionally, it accounts for the secondary charged particles generated by these initial charged particles. The Scatter EDK describes the energy transport of initial charged particles released by the secondary photons, which include scattered photons, bremsstrahlung photons, and annihilation photons.

Here, it is useful to acknowledge that in the context of proton beam therapy, several dose calculation algorithms have been developed. Based on the basic formalisms used, they fall into three major categories: (a) pencil beam, (b) convolution/superposition, and (c) Monte Carlo.

Material and method

Generating the EDK

The initial step in implementing the CCCS algorithm involves generating energy deposition kernels. Therefore, the specific geometry employed for generating these EDKs such that they can be used later in this algorithm is the spherical geometry.

The process of meshing and voxelizing this spherical geometry, while considering its natural and inherent symmetry, is accomplished based on varying values of the two variables: the radius r and the polar angle θ. Based on this method of meshing and division, the internal space will be visualized as shown in Fig. 3. The shape of each of these voxels resembles a conical shell, as shown in Fig. 4.

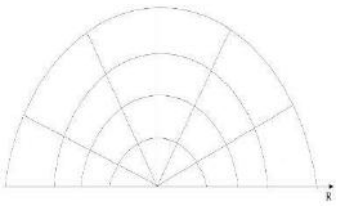

Fig. 3. The method of meshing and division the internal space of spherical geometry based on varying values of the radius r and the polar angle θ.

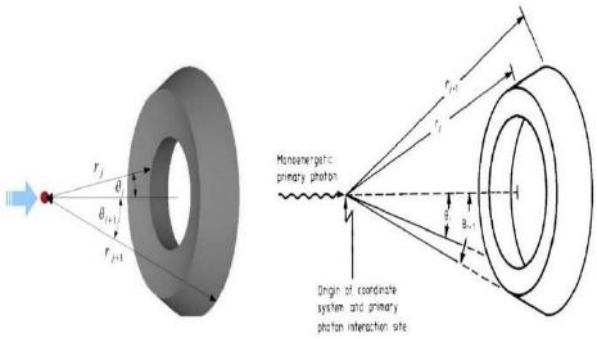

Fig. 4. The shape of each voxel resembles a conical shell.

The kernel calculation process begins with the constraint that the primary single-energy photons interact exclusively in the center of the spherical geometry, without any interactions occurring before reaching this central point, then the information and data relating to the energy absorption in each of these conical shell voxels are stored separately.

The kernels that are generated and calculated under these conditions are called Point Kernels. It is important to acknowledge that there exist various types of energy deposition kernels. However, the two most prevalent types today are Point Kernels and Pencil Beam Kernels.

The EDKnrc code, a subset of the EGSnrc software, is a nuclear code specifically designed for kernel generation. It facilitates the process of both generating and calculating these point kernels, as previously described.

It is important to clarify that the EDKnrc code reports the values of the energy deposition kernels as two distinct components in its output: the Total value and the Primary value. The Scatter value is obtained by calculating the difference between these two components.

To generate the kernels utilized in the CCCS algorithm, the default mode of the EDKnrc code has been used. In the default mode, the internal space of the spherical geometry is partitioned into 24 radial intervals and 48 angular intervals. The radial intervals and the angular intervals are expressed in centimeters and degrees, respectively.

In the context of photon beam therapy, the size of radial intervals near the point of photon interaction, specifically at the center of the spherical geometry, is small because the variations are severe. However, in the distant regions, the variations become slight, and therefore, their size is larger. However, in the context of proton or ion beam therapy, the size of radial intervals near the Bragg peak must be small due to pronounced variations. Conversely, in more distant regions where variations are slight, the size of these intervals can be larger.

Calculating the four coefficients A_θ, a_θ, B_θ, and b_θ

After the energy deposition kernels have been generated and calculated, it is time to assign an appropriate mathematical function to them. In the context of photon beam therapy, the following two mathematical functions are associated with the Primary EDK and the Scatter EDK, respectively:

$$h_P(r,\theta_m) = \frac{A_{\theta_m} e^{-a_{\theta_m} r}}{r^2} \quad (5)$$

$$h_S(r,\theta_m) = \frac{B_{\theta_m} e^{-b_{\theta_m} r}}{r^2} \quad (6)$$

By utilizing the values of Primary EDKs and Scatter EDKs generated by the EGSnrc software, and employing curve fitting techniques, it is possible to determine these four coefficients based on the following two equations.

One of the available tools for performing curve fitting is the Curve Fitting Toolbox provided by MATLAB software. In addition, for the obtained coefficients to be in the best possible state in terms of statistical correlation, it is advisable to select the Levenberg-Marquardt method.

The process of accomplishing curve fitting can be summarized as follows:

The values of the Primary EDKs or the Scatter EDKs, which belong to all 24 radial intervals, all of them situated along only one of the 48 angular intervals, are plotted on a graph. Subsequently, a curve corresponding to either equation (5) or (6) is fitted through these 24 data points.

By performing this procedure, two coefficients A_θ and a_θ are calculated exclusively for each of the 48 angular intervals. The bisector of each of the 48 angular intervals is represented as a collapsed cone and each pair of these two coefficients represents the dose contribution associated with that collapsed cone during the calculation of the Primary Dose. Additionally, two coefficients B_θ and b_θ are similarly calculated for each collapsed cone. Each pair of these two coefficients represents the dose contribution associated with that collapsed cone during the calculation of the Scatter Dose.

In the context of photon beam therapy, which is performed using linear accelerator machines, the output beam exhibits a spectrum of energy. Therefore, these two groups of EDKs can be generated using the EDKnrc code of the EGSnrc software, employing the direct or indirect method.

In the direct method, the energy spectrum of the linear accelerator machine should be defined according to the instructions provided in the user manual guide of the EDKnrc code. Upon executing this code, the Primary EDKs and Scatter EDKs values necessary for calculating the coefficients A_θ, a_θ, B_θ, and b_θ corresponding to the machine's energy spectrum are generated.

In the indirect method, the difference between the lowest and highest energies (E_{min} and E_{max}) in the machine's energy spectrum should be divided into separate energy intervals based on the desired suitable energy resolution, which means the continuous spectrum of energy is discretized into distinct energy intervals. Subsequently, the EDKnrc code is executed independently for each energy interval, corresponding to these intervals. Each of these executions generates the values of the Primary EDKs and the Scatter EDKs, which are necessary for calculating the coefficients A_θ, a_θ, B_θ, and b_θ associated with each of these energy intervals. At the time of code execution, the weight of each energy interval is uniform and equal to one. But

by asserting the weight of each energy interval within the energy spectrum of the machine under investigation and subsequently applying this weight to the coefficients A_θ, a_θ, B_θ, and b_θ corresponding to that specific energy interval, one can determine the coefficients associated with the energy spectrum of the machine.

Voxelizing irradiated medium

To perform dosimetry calculations using the CCCS algorithm, the irradiated medium must undergo voxelization.

The medium defined for the implementation of the CCCS dose calculation algorithm is as follows. A homogeneous rectangular cubic phantom made of water with dimensions of 50x50x40 cm^3 where a single-energy photon source is placed at a distance of 80 cm from its upper surface. In addition, a lead block is placed on top of this phantom to collimate the isotropic radiations emitted from the point source. This ensures that the field size created on the upper surface of the phantom varies, including field sizes of 4x4 cm^2, 5x5 cm^2, and 10x10 cm^2. The energy of the point source is chosen in such a way that all the photons emitted from it, under three different and distinct conditions, during each execution, have only specific values: 1.25 MeV, 3 MeV, and 6 MeV.

Calculating the TERMA

At this phase, the value of the TERMA for all the desired voxels, necessary for performing dosimetry calculations, should be computed according to equations (3) and (4). A schematic of this aim is shown in Fig. 5.

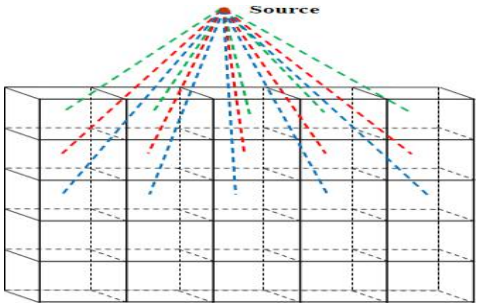

Fig. 5. A schematic of the calculating of the TERMA according to the equations (3) and (4).

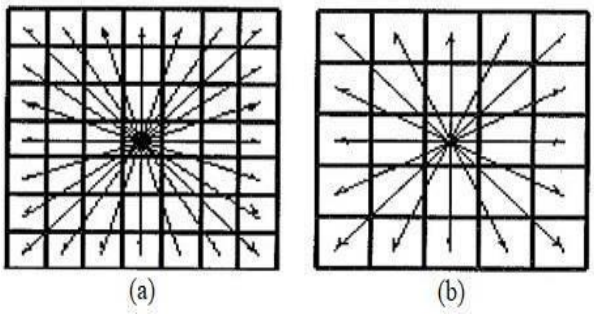

Fig. 6. The lattice of energy transport lines consists of (a) 7×7 and (b) 5×5 configurations, respectively.

Choosing the lattice of energy transport lines

Since the EDKs that can be used in the CCCS algorithm are obtained in spherical coordinates, while the voxels belonging to the irradiated medium are defined and specified in Cartesian coordinates, it is necessary to establish a suitable relationship between these two coordinate systems.

To achieve this goal, a lattice of energy transport lines is utilized. This lattice can take on configurations of 5×5, 7×7, 9×9, or 11×11. For instance, the first two patterns are depicted in Fig. 6. In Fig. 7, it is shown that if someone intends to use the lattice of 5×5 energy transport lines to transport the TERMA belonging to the voxel specified by the index (i,k), how its pattern can be.

The lattice of 5×5 energy transport lines consists of 16 independent and distinct transport lines for transmitting TERMA. In Fig. 7, it is assumed that the position of the point source is above the upper side of this slice. Therefore, according to this assumption, the line that transports the TERMA belonging to the voxel (i,k) to the voxel (i,k+2Δk), is called transport line #1 and the line that transports the TERMA belonging to the voxel (i,k) to the voxel (i,k-2Δk), it is called transport line #9. The transport lines on the right side of this figure, which are positioned between transport lines #1 and #9, are referred to as transport lines #2 to #8, respectively. Additionally, each transport line on the left side of this figure is equivalent to its corresponding symmetrical transport line. Finally, each of the transport lines in this lattice includes collapsed cones that have the smallest difference from that line.

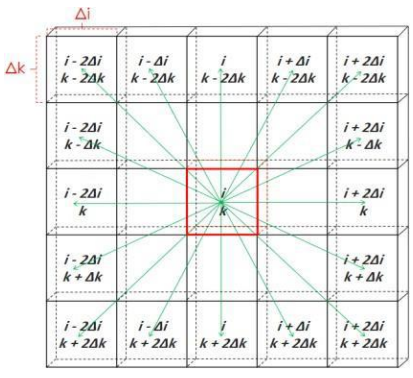

Fig. 7. Illustrating the implementation of the lattice of energy transport lines configured as 5×5.

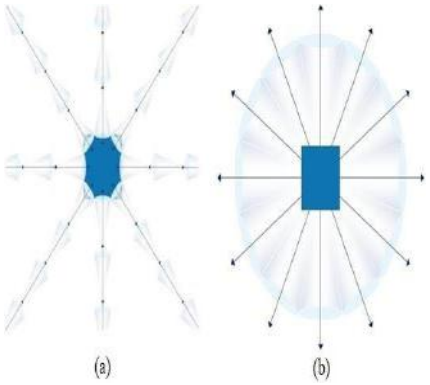

Fig. 8. (a) Dose Deposition Point of View and (b) Interaction Point of View, respectively.

Choosing the Point of View

It is possible to combine the dose contributions from each voxel using any of the four lattice configurations of energy transport lines (5×5, 7×7, 9×9, or 11×11), either following the Interaction Point of View approach or the Dose Deposition Point of View approach. Both of these approaches are illustrated in Fig. 8.

To enhance the compatibility with the conditions under which the EDKs were generated and calculated—i.e., the spherical geometry and the interaction of photons at the center of this spherical geometry—it is better to implement the CCCS algorithm based on the first approach.

Calculating the amount of Absorbed Dose

By utilizing the TERMA values associated with individual voxels, it becomes feasible to compute the Primary Dose and Scatter Dose for each voxel using equations (7) and (8), respectively. Subsequently, by summing these two values within each voxel, the total dose across all voxels is determined.

$$D^{P}_{mn}(r_i) = D^{P}_{mn}(r_{i-1})e^{-a_{\theta_m}\eta_i\Delta r} + T_i\Omega_{mn}\frac{A_{\theta_m}}{a_{\theta_m}}\left(1 - e^{-a_{\theta_m}\eta_i\Delta r}\right) \quad (7)$$

$$D^{S}_{mn}(r_i) = D^{S}_{mn}(r_{i-1})\left(1 - b_{\theta_m}\eta_i\Delta r\right) + T_i\Omega_{mn}B_{\theta_m}\eta_i\Delta r \quad (8)$$

The CCCS algorithm, which performs dose calculations based on these two equations and for instance, is adjusted to utilize the 5x5 lattice of energy transport lines, it can be described with the explanation provided below.

As mentioned in the fifth step, the 5x5 lattice of energy transport lines comprises sixteen independent transport lines for transporting the TERMA. For each of these transport lines, the dose calculation algorithm is rewrote based on the number of collapsed cones included in each line.

For instance, if transport line #1 includes four collapsed cones, each with its unique values of A_θ, a_θ, B_θ, and b_θ, it becomes essential to develop an algorithm. Initially, this algorithm places the coefficients A_θ and a_θ from the first collapsed cone into equation (7) to calculate the Primary Dose due to the first collapsed cone based on transporting TERMA from voxel (i,k) to voxel (i,k+2Δk). Subsequently, this process is repeated by replacing the coefficients associated with the other three collapsed cones. When calculating the Scatter

Dose, a similar approach is followed, but with the distinction that instead of A_θ and a_θ coefficients, B_θ, and b_θ coefficients are utilized, and equation (8) is employed in place of equation (7).

Results and discussion

In Figs. 9 and 10, two examples of dose profiles are shown. These dose profiles were obtained using the dose values calculated by dose calculations performed with the CCCS algorithm. Additionally, in both of these figures, the dose values obtained using the CCCS algorithm are compared with their corresponding dose values obtained using the Monte Carlo method, which is employed by MCNP software.

The CCCS algorithm, when utilizing the 11x11 lattice of energy transport lines to perform dose calculations, has exhibited the lowest error compared to the results obtained using the Monte Carlo method. In addition, of all the lattices of energy transport lines, the 5x5 configuration required the shortest time to perform dose calculations.

Furthermore, when comparing the time required for dose calculations using the two methods, we observed that the Monte Carlo method necessitated several thousand minutes, whereas the CCCS algorithm completed the task in a mere few tens of seconds to several minutes. Remarkably, despite these disparate computation times, the final results from both methods exhibited only minor differences.

The two obvious distinctions observed between the results of the two methods are associated with the buildup region and penumbra regions of the radiation field. Notably, the implemented CCCS algorithm has exhibited less effectiveness in delineating these two regions.

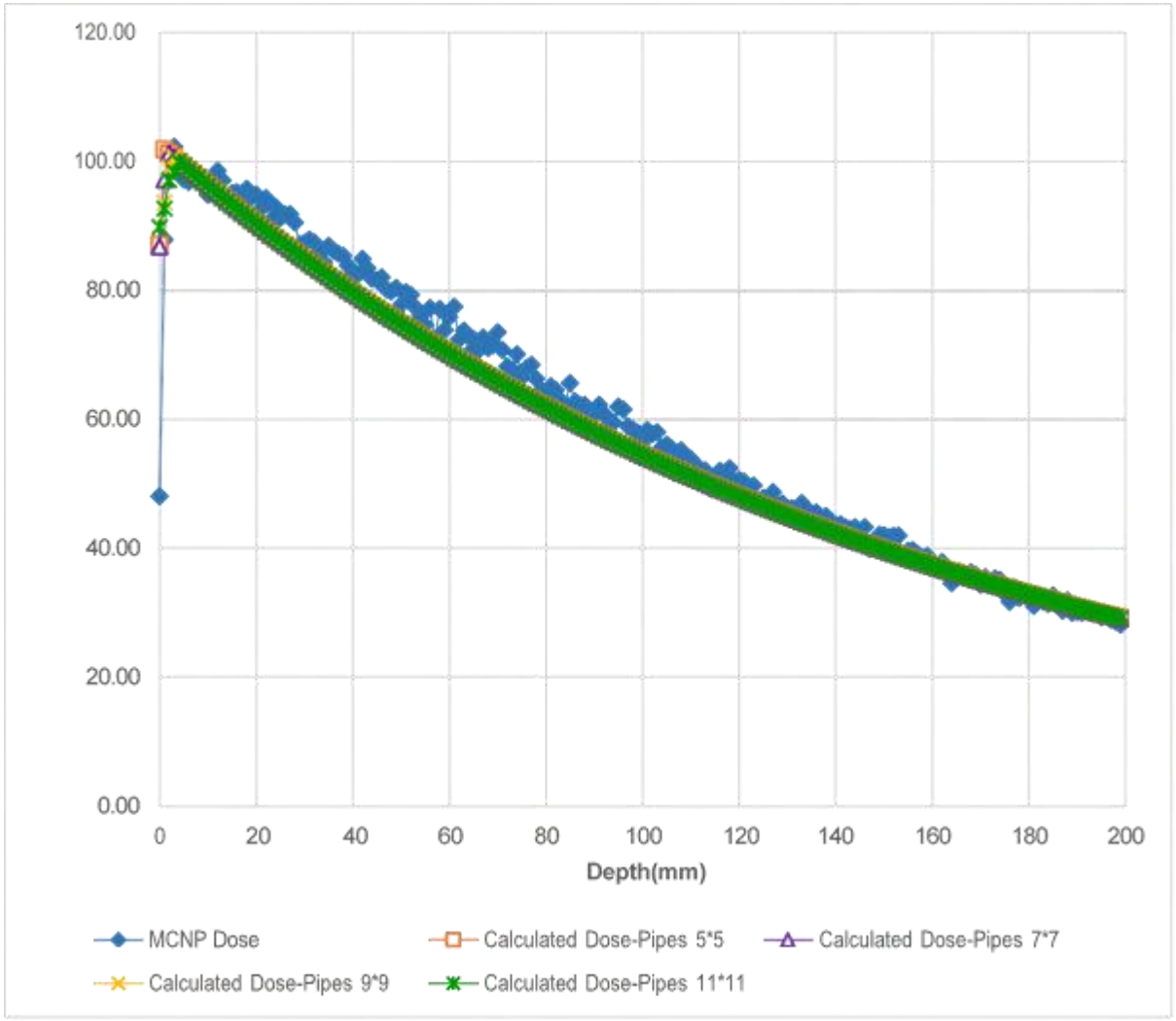

Fig. 9. Central axis percent depth for photon beam energy = 1.25 MeV, Field size = 10x10 cm^2, source to surface distance (SSD) = 80 cm and voxel spatial resolution = 1 mm.

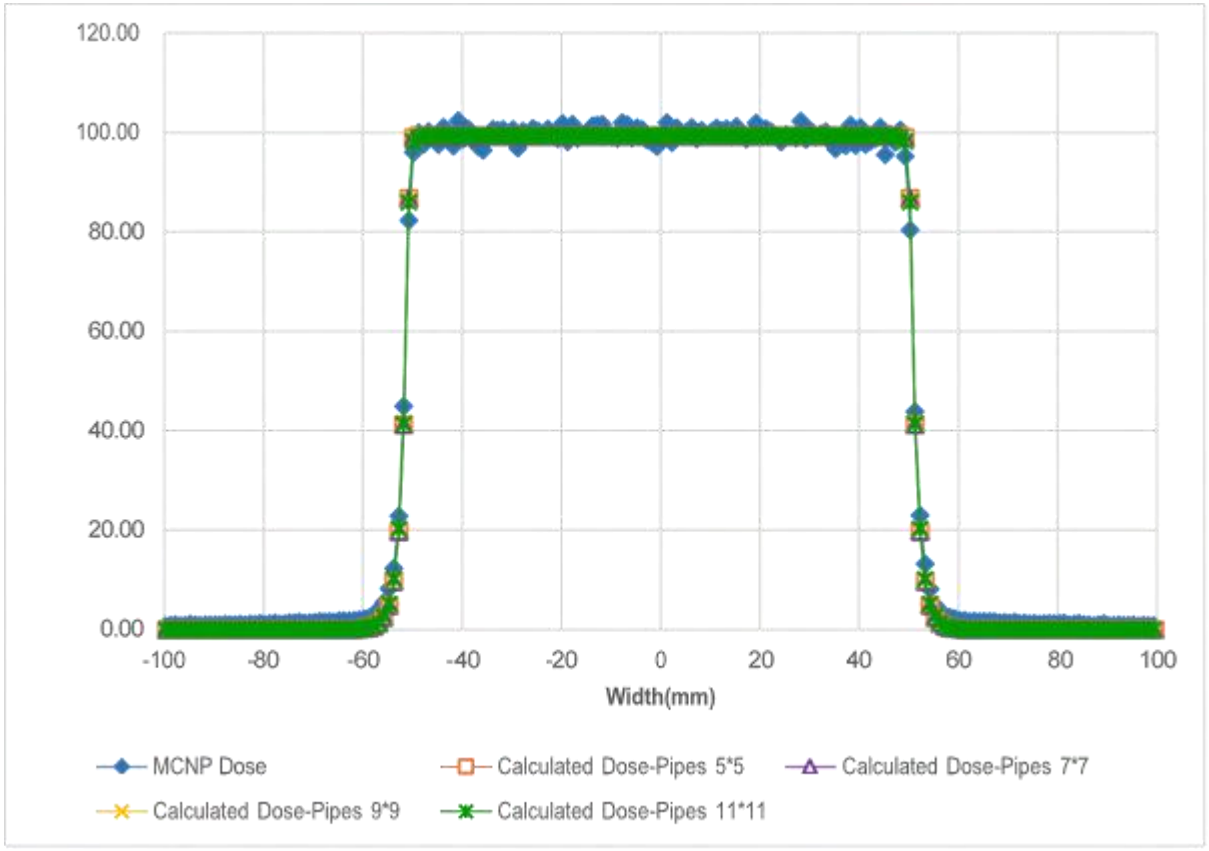

Fig. 10. Relative dose profile at depth = 5 mm for photon beam energy = 1.25 MeV, Field size = 10x10 cm^2, source to surface distance (SSD) = 80 cm and voxel spatial resolution = 1 mm

Conclusion

The utilization of the CCCS algorithm offers a significant advantage by allowing the use of the artful Monte Carlo method during the pre-production phase. This method enables precise transport simulations of photons, electrons, neutrons, or protons, which are generally computationally intensive and time-consuming. As a result, this method contributes to the creation of a robust support library containing the essential information and data necessary for CCCS algorithm implementation.

Then, during the clinical treatment planning stage, where the patient's presence time in the radiotherapy room is limited, this algorithm is employed within the treatment planning software. It serves as one of the options and alternatives integrated into the dose calculation engine that accomplish the dosimetry calculations, very fast, accurately, and precisely.

Acknowledgment

None. Funding None.

References

[1] Zarepour A. (2017). Implementation and parameter study of collapsed cone convolution algorithm used in radiotherapy dosimetry. [Master's thesis, Shiraz University]. IranDoc.

[2] Ahnesjö, A. 1989 Collapsed cone convolution of radiant energy for photon dose calculation in heterogeneous media Med. Phys. 16 577–92

[3] Ahnesjö, A. (1991). Dose calculation methods in photon beam therapy using energy deposition kernels. [PhD thesis, University of Stockholm].

[4] Ahnesjö, A. and Aspradakis, M. M. 1999 Review: dose calculations for external photon beams in radiotherapy Phys. Med. Biol. 44 R99–R155

[5] Ulmer, W and Harder, D. 1995 A triple Gaussian pencil beam model for photon beam treatment planning Z. Med. Phys. 5, 25–30

[6] Ulmer, W and Harder, D. 1996 Applications of a triple Gaussian pencil beam model for photon beam treatment planning Z. Med. Phys. 6, 68–74

[7] Sievinen, J., Ulmer, W. and Kaissl, W. 2005 AAA photon dose calculation in Eclipse Varian documentation RAD #7170B

[8] Ulmer, W., Pyyry, J. and Kaissl, W. 2005 A 3D photon superposition/convolution algorithm and its foundation on results of Monte Carlo calculations Phys. Med. Biol. 50, 1767–1790

[9] Liu, H., Mackie, T. R. and McCullough, E. C. 1997 A dual source photon beam model used in convolution/superposition dose calculations for clinical megavoltage x-rays beams," Med. Phys. 24, 1960–1974

[10] Murray, D. C., Hoban, P. W., Metcalfe, P. E. and Round, W. H. 1989 3-D superposition for radiotherapy treatment planning using fast Fourier transforms Australas. Phys. Eng. Sci. Med. 12 128–3

ICNST 2024 International Conference on Nuclear Science and Technology
6- 8 MAY 2024 | Isfahan, Iran

Rich-Dot-Protons as targets for spectral shaping of laser-driven proton acceleration (Paper ID : 1526)

Vosoughian H1*, Hajiesmaeilbaigi F1, Bostandoust E1, Razaghi H1, Motamedi A1.

[1]Photonic and Quantum Technologies Research School, Nuclear Science and Technology Research Institute, NSTRI, Iran.

Abstract

Here, the energy spectrum of high-energy protons generated in High-intensity lasers interacting with solid foils has been studied using the 2D Particle-In-Cell (PIC) simulations. Target Normal Sheath Acceleration (TNSA), is the dominant mechanism of proton acceleration. The dependency of the TNSA mechanism on the position of the microdot proton layer at the rear surface of the solid target indicates that for a microdot layer located away from the laser spot center, low energetic protons bunch with a broad energy spectrum is produced whereas, in the case of microdot at the center of laser spot, high energy protons with a quasi-monoenergetic spectrum is achieved. Outcomes reveal that, in the case of the proton-rich dot at the center, the proton-rich dot should have a smaller diameter than the scale of inhomogeneity of the electron sheath such that all protons experience the same potential. This configuration limits the transverse extension of protons and so improves the TNSA mechanism.

Keywords: Target Normal Sheath Acceleration; Particle-In-Cell; High-intensity lasers; TNSA mechanism.

INTRODUCTION

In recent years, the invention of the chirped pulse amplification technique to produce multi-terawatt laser pulses has opened up a new way to generate ultra-short and monoenergetic particle bunches with low emittance and high brightness that are comparable to conventional accelerators [1-8]. The method is based on the high-intense laser pulses interacting with matter. By the incident of the intense laser pulse (of the order of $I>10^{19}$ Wcm^{-2}) on the surface of a thin metal foil, the fast electrons are accelerated in the forward direction, penetrate the foil, and ionize the atoms along their path. Within a picosecond, the electrons that leave the target on the back surface create a quasi-static electric field perpendicular to the target surface. This field has cylindrical symmetry and its intensity decreases in the transverse direction. Due to the very short width of the bunch of fast electrons and its high charge, the size of this electric field near the axis reaches the values of several teravolts (10^{12}V) per meter, which corresponds to the potential of several tens of megaelectron volts. Protons and positively charged ions on the back surface of the foil can be accelerated by this field in a process called "Target Normal Sheath Acceleration (TNSA)", which continues until the

electron charge distribution is neutralized [9-11]. In most cases, the origin of the accelerated ions has been detected from the hydrocarbon contamination layer on the surface behind the target. Since the acceleration duration is very short and the ions are at rest before the acceleration and contain a very small volume of the phase space, the transverse emission of the proton beam reaches values less than 10 for 10 MeV protons However, the accelerated ion beams, while having a large longitudinal emittance, also exhibit an exponential energy spectrum extended to a specific cutoff energy.

This can be explained by the inhomogeneous transverse distribution of electrons in the sheath, which will create an inhomogeneous acceleration field in the transverse direction on the target surface. For a flat and unstructured target, the transverse distribution of the electric field and thus the size of the source of accelerated protons is much larger than the focal spot of the laser. Therefore, the protons of the target surface experience a wide range of potentials, which results in a wide distribution of energies. To investigate this effect, in this article, with the help of two-dimensional particle-in-cell simulations using EPOCH code [12], we have shown that the energy spectrum of the produced protons is strongly related to their spatial distribution on the target surface. To produce a high-quality proton beam with single- energy characteristics, we have proposed a micro-structured target, which consists of a thin metal sheet with a high atomic number and a small rich-proton spot on the back surface of the target. The transverse dimension of such proton dots is chosen to be smaller than the acceleration envelope so that the protons are only affected by the central part - that is, the uniform field region. In this configuration, the protons all experience the same acceleration potential and the resulting beam will contain protons with an almost single energy spectrum.

RESEARCH THEORIES

In general, the TNSA ion acceleration mechanism is interpreted as an accelerating scheme that benefits from a sheath electrostatic field generated by the hot-electrons component. For the standard TNSA mechanism (Fig. 1), the intense laser pulse well exceeding 10^{18} W/cm^2 is focused on a solid thin foil target.

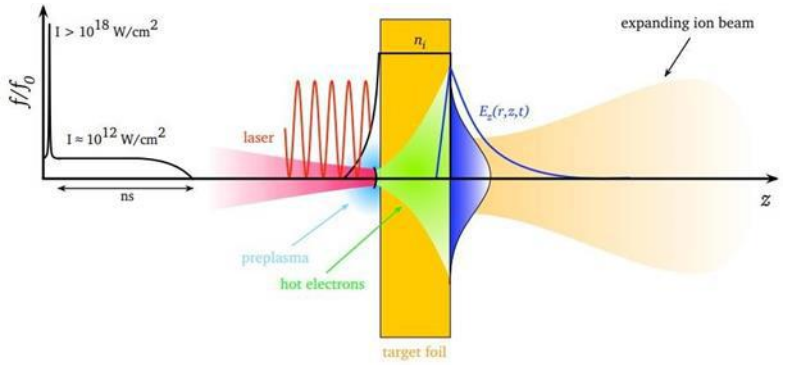

Fig. 1. Target normal sheath acceleration scheme. A thin target foil is irradiated by an intense laser pulse. The laser pre-pulse creates a pre-plasma on the target's front side. The main pulse interacts with the plasma and accelerates megaelectronvolt electrons, mainly in the forward direction. The electrons propagate through the target, where collisions with the background material can increase the divergence of the electron current. The electrons leave the rear side, resulting in a dense sheath. An electric field due to charge separation is created. The field is of the order of the laser electric field (~ TV/m), and ionizes atoms at the surface. The ions are then accelerated in this sheath field, pointing in the target normal direction[13].

At the primary stages of interaction, the laser pre-pulse, an unwanted and preceding laser light to the main pulse, arises from amplified spontaneous emission in regenerative amplifiers, excites a plasma that is expanding towards the incoming main pulse. A source of hot electrons is constituted in the laser focal spot where the main pulse interacts with the preformed plasma. The generated hot electrons penetrate the foil and so the binary collisions (multiple small-angle scattering) with the background material tend to broaden the electron distribution in a cone-shaped distribution [14]. The electron density at the rear side (neglecting recirculation), can be estimated as [13, 15]:

$$n_{0,rear} = \frac{\eta E_L}{c\tau_L \pi (r_0 + \mathrm{dtan}\,(\theta/2))^2 k_B T_{hot}}$$

$$\approx 1.5 \times 10^{19} \frac{r_0^2}{(r_0 + \mathrm{dtan}\,(\theta/2))^2} \frac{I_{18}^{7/4}}{\sqrt{1 + 0.78 I_{18} \lambda_{\mu m}^2} - 1} [cm^{-3}] \qquad (1)$$

where $r0$ denotes the laser spot radius, d the target thickness, and θ the broadening angle of the distribution [16]. The I_{18} indicates that the intensity has to be taken in units of 10^{18} W/cm^2. As evidence, the electron density at the rear side of the target strongly scales with the laser intensity and is inversely proportional to the square of the target thickness. When the electrons escape into the vacuum behind the target, The charge separation leads to an electric potential, Φ, in the vacuum region, according to Poisson's equation. In one dimension, it is given as:

$$\varepsilon_0 \frac{\partial^2 \Phi}{\partial z^2} = e n_{sheath} \quad (2)$$

To solve Eq. (2), it is assumed that the solid matter in one half-space ($z \leq 0$) perfectly compensates for the electric potential, whereas for $z \to \infty$ the potential goes to infinity. The derivative($\partial\Phi\ \partial z$)vanishes for $z \to \pm\infty$ .In the vacuum region ($z \to \pm\infty$), the field can be obtained analytically [17]. The electron density is taken as

$$n_{shaeth} = n_{0,rear} \exp\left(\frac{e\Phi}{k_B T_{hot}}\right) \quad (3)$$

where the electron kinetic energy is replaced by the potential energy, $-e\Phi$. The resulting potential is

$$\Phi(z) = -\frac{2k_B T_{hot}}{e} \ln\left(1 + \frac{z}{\sqrt{2}\lambda_D}\right) \quad (4)$$

and the corresponding electric field reads

$$E_z = \frac{2k_B T_{hot}}{e} \frac{1}{z+\sqrt{2}\lambda_D} \quad (5)$$

$\lambda_D = \left(\frac{\varepsilon_0 k_B T_{hot}}{e^2 n_{0,rear}}\right)^{1/2}$ is the electron Debye length that is defined as the distance over which significant charge separation occurs [18]. The maximum electric field is obtained at z =0:

$$E_{max}(z=0) = \frac{\sqrt{2}k_B T_{hot}}{e\lambda_D}$$

$$\approx 5.2 \times 10^{11}\, V/m \frac{r_0}{r_0 + d\tan\theta/2} I_{18}^{7/8}, \quad (6)$$

that is proportional to the laser intensity, depends on target thickness(d), and the laser spot radius.

SIMULATION RESULTS

To demonstrate the dependence of the accelerating field in the TNSA mechanism on the target properties, the series of two-dimensional simulations of the TNSA mechanism are done using the 2D Particle-In- cell code. Here, the fully ionized Aluminum target is initially

$a_0 = \sqrt{\frac{I_L \times \lambda_L^2}{1.37\times 10^{18}}} = 5.11 = \frac{1.11\times 10^{21}\left(\sqrt{1+a_0^2}\right)}{\lambda_L^2}.cm^{-3}$ $a_L = a_0\, exp\left(\frac{-y^2}{w_L^2}\right) sin^2\left(\frac{\pi t}{\tau_0}\right)$

located between $x = 20\mu m$ to $x = 30\mu m$. The target is defined as two sections; an exponential ramp with a scale length of $8\mu m$ located in front of the Al target that its density increased up toshows the critical density for the laser pulse and hereis defined as the normalized vector potential); the Al target with the constant density of $n_e = 100n_c, n_i = 0.076n_e$ and 5 μm $thick$. Moreover, a thin proton rich layer is inserted at the rear side of target from $x = 30\mu m$ to $x = 30.20\mu m$ as a contamination layer. The incident laser pulse has a transversely Gaussian profile with a normalized intensity of spot size of $wL = 10\mu m$, and a pulse duration of $\tau L = 45fs$ where, e and me are the electron charge and mass, EL and ω are the laser electric field and frequency and c is the speed of light in vacuum. The laser pulse with a wavelength of $\lambda = 0.8\mu m$ and an intensity of about $I = 5.6 \times 10^{19} \frac{W}{cm^2}$ enters the simulation box from the left boundary and interacts with the aluminum target. The simulation box is $60\mu m(x) \times 30(\mu m)$ which corresponds to a window with 1500×1500 cell. The proton rich target is defined by 200 particle per cell and main target is defined by 10 particle per cell. Boundary conditions both for particles and EM fields have been chosen as an absorbent surface to remove the escaped particles from the simulation process.

the interaction of a high-power laser pulse with the target has been shown in Figs (2). As evidence, the laser pulse penetrates the plasma ramp, and the hot electrons are generated by the $J \times B$ mechanism [19] so they are confined in a Deby sheath after escaping to the vacuum region (FiG.2(c)). Due to charge separation, a highly intense electric field (Ex) normal to the target surface, is induced in the vacuum region according to Figs (2(d-e)). The evolution of the normal electric field at the rear side is shown in Fig.(4a). As seen, at the time of 160 fs, the maximum field strength is about$Ex = 2 \times 10_{12}(V/m)$, that is only slightly smaller than the laser electric field strength of $E_L = 1 \times 10_{13}(V/m)$!. The hot electron's temperature distribution is also shown in Figs. 3(a-c). As obvious, the hot electron distribution isexpanded when passing through the target in a near cone shape such that the rear side temperature increased up 1٠ٰkelvins at a time of 160 fs (Fig. 4b), where the electric field is maximum at the rear surface. The conversion efficiency from laser energy to hot electrons is not perfect, and only a fraction η is converted. The total number of electrons is $n_{0,hot} = \frac{\eta E_L}{c\tau_L \pi r_0^2 k_B T_{hot}}$ following a scaling with intensity as $\eta = 1.2 \times 10^{-15} I^{0.74}$For ultra-high intensities, η can reach up to 60% for near-normal incidence and up to 90% for irradiation under 45 ◦ [20].

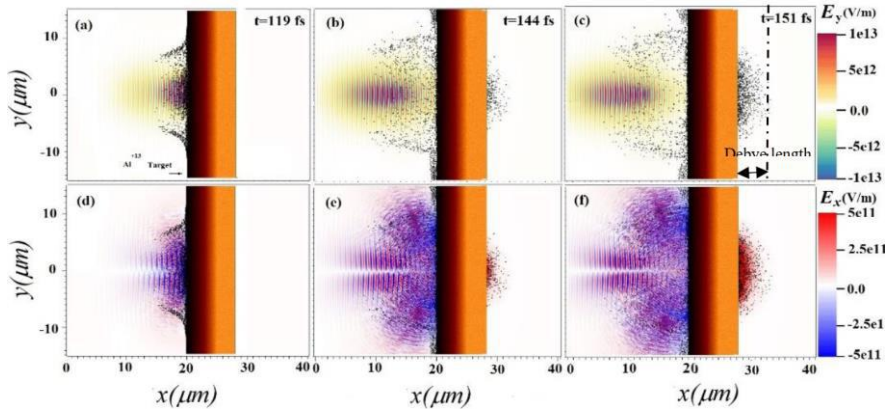

Fig. 2. Interaction of laser pulse with the Aluminum target:(a-c) the transverse electric field of laser pulse (Ey) interacting with the target, (d-f) the longitudinal electric field of laser and the induced normal field (Ex) at the rear side of the target.

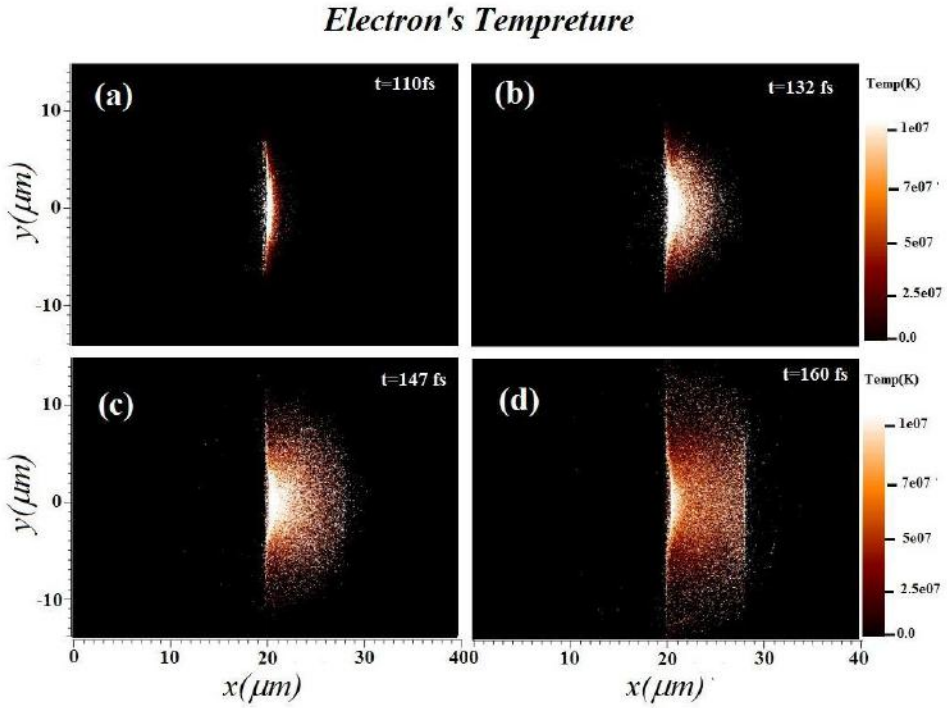

Fig. 3. The hot electron's temperature distribution. Hot electrons are generated in front of the target (a) by the $J \times B$ mechanism, penetrate through the target (b) expand in a cone shape (c), and escape in the vacuum region(d).

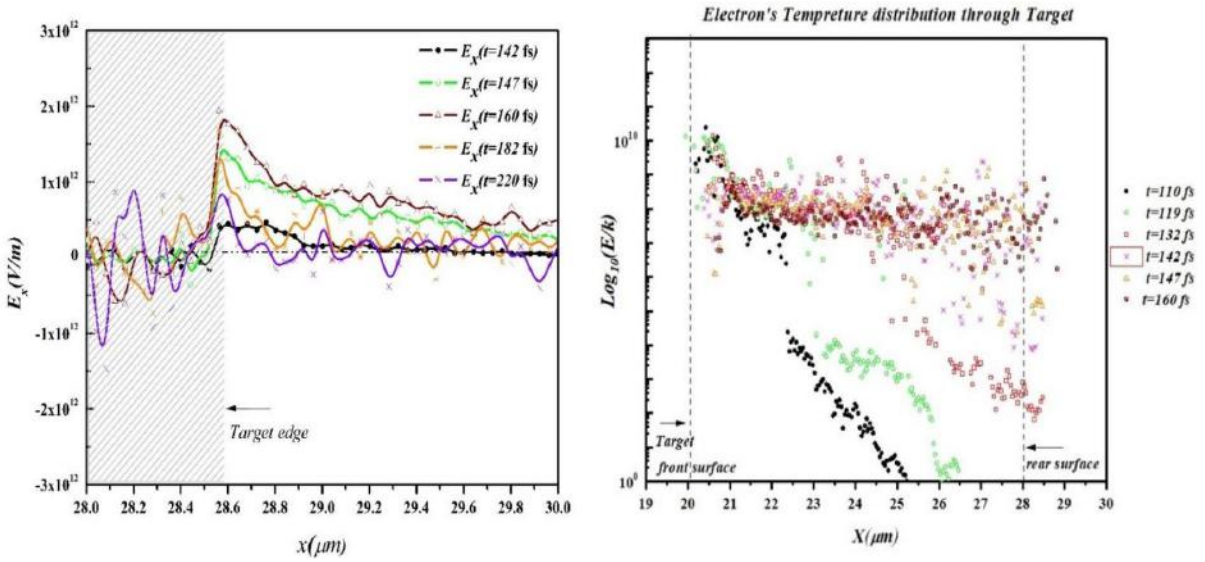

Fig. 4. Evolution of the induced longitudinal field (E_x) at the rear surface of the target (a), the distribution of hot electrons through the target when escaping to the vacuum (b).

according to the field ionization by barrier suppression (FIBS) model [21], an intense external electric field could overlap the Coulomb potential of the atom and deform it. As soon as the deformation is below the binding energy of the electron, the electron is instantly freed, hence the atom is ionized. The threshold electric field strength E_{ion} can be obtained with the binding energy U_{bind} as $E_{ion} = \frac{\pi \varepsilon_0 U_{bin}^2}{e^3}$ Taking the ionization energy of a hydrogen atom with U_{bind} = 13.6 eV, the field strength necessary for FIBS is $E_{ion} = 10_{10}$ V/m. This is two orders of magnitude less than the field strength developed by the electron sheath in vacuum calculated in our simulation (refer Fig.4(a) time 160 fs). Hence, nearly all atoms (protons, carbon, heavier particles) at the rear side of the target are instantly ionized and, since they are no longer neutral particles, they are then subject to the electric field and are accelerated. To prove this estimate, a proton-rich layer with a thickness of 200 nm is inserted at the rear surface of the target subject to the induced electric field as Figure 5. (a). It is clear that the proton layer takes a part from the target surface under the influence of the sheath's field. The proton energy is also shown in figure (7) by blue curve. A wide energy spectrum is produced within 420fs that shows a clear high-energy cut-off around 2.5 MeV.

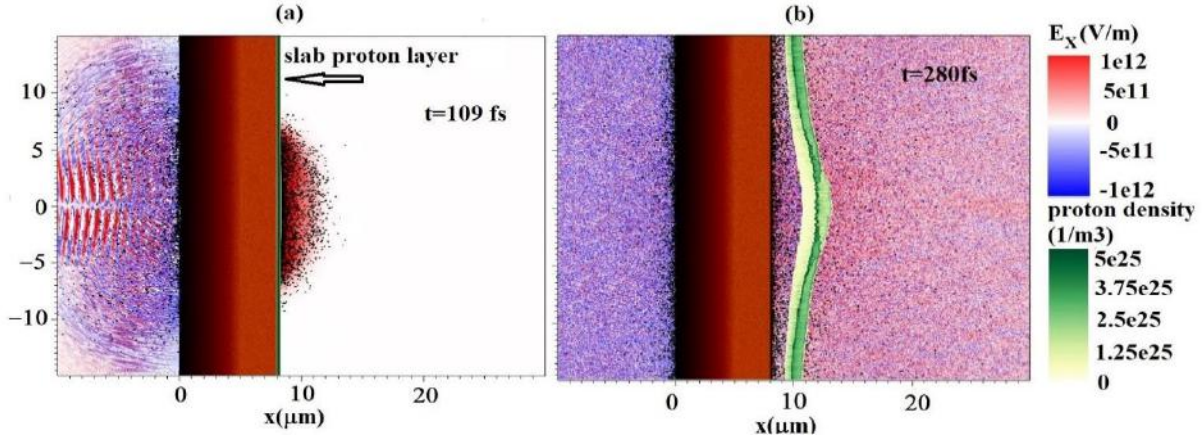

Fig. 5. Acceleration of slab target when subject to the induced field at the rear side of the target. (a) formation of sheath field, (b) separation of slab proton target and take energy.

However, since the relativistic electron sheath has a nearly Gaussian-radial distribution in its density profile and shows a transversally bell-shaped distribution, the highest energy protons are accelerated in the central, high-density portion of the sheath, whereas lower energies come from the wings of the sheath distribution and thus are emitted at a larger angle. This comes from the accelerating field $E = -\nabla\Phi = -(kT_{hot}/e)(\nabla n_{shaeth}/n_{shaeth})$ that causes to the broadening of the proton energy spectrum. To overcome this problem and shape the proton energy spectrum, as a quasi-monoenergetic bunch, it should be better to confine the proton layer at the central region of the sheath's field to subject with the uniform field distribution. For this reason, we simulate a rich dot target at the center of the electron sheath to generate a monoenergetic bunch. The results are shown in figs.6(a) and 6(b). As seen clearly, the whole of Rich.Dot.Proton target accelerates to the MeV range energy and offers the narrow energy spectrum with a peak energy of about 1.25 MeV depicted by the red line curve in Figure 7.

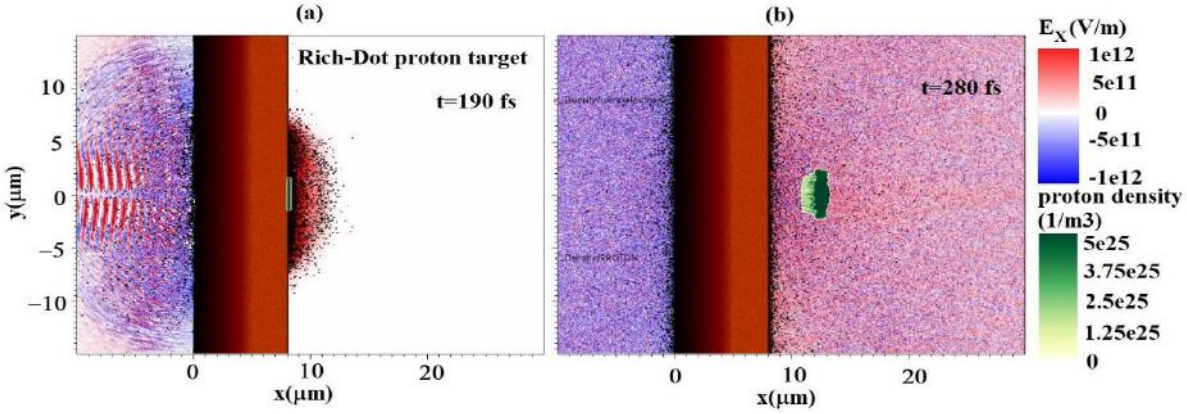

Fig. 6. Acceleration of Rich-Dot-Proton target when subject to the induced field at the rear side of the target. (a) formation of sheath field, (b) separation of slab proton target and take energy

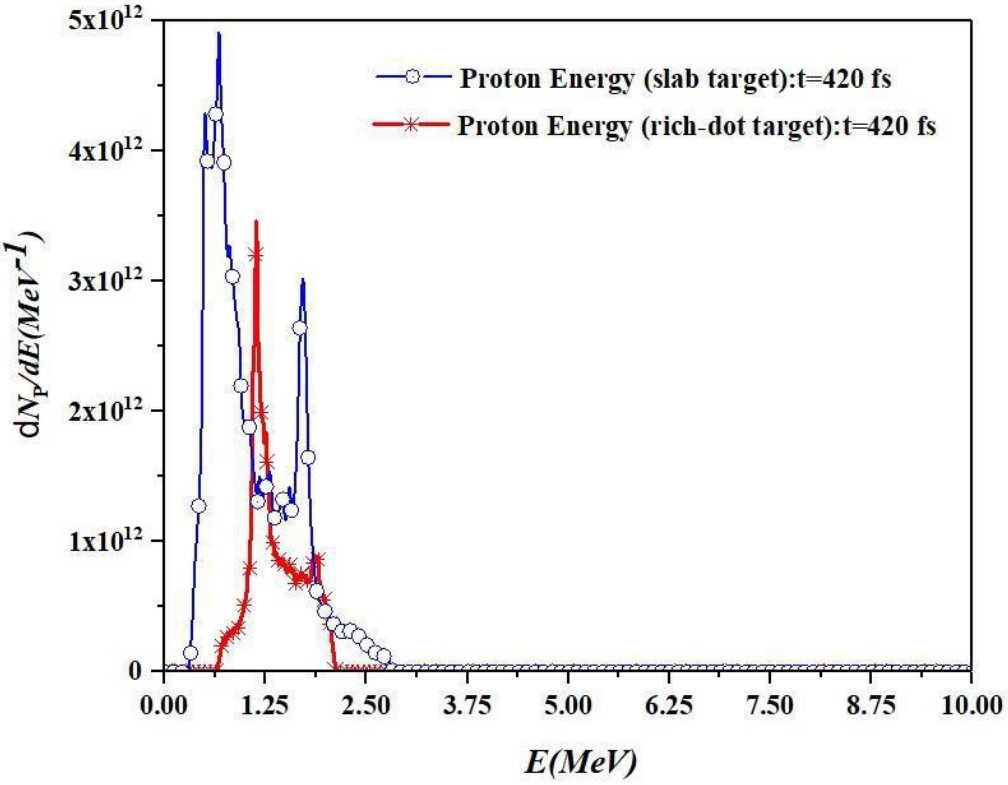

Fig. 7. Comparison of the Proton energy spectrum when the slab target is inserted at the rear side of the target (blue line) with the Rich-Dot-Proton target (red line).

Conclusions

In summary, we find that the energy spectral shape of the accelerated particle from the rear side of the target in the TNSA mechanism is strongly dependent on the initial position of the particle source at the rear surface. the induced field generated at the rear surface of the target that is responsible for accelerating the contamination particle from the rear surface has a bell-shaped distribution that leads to the nonuniform electric field in the transverse direction. Thus the particle that is located away from the sheath center, is subject to the weaker field strength and thus can not contribute to the accelerating process effectively. As a result, the lower section of the energy spectrum is produced. This fact could allow control of the energy spectrum of the accelerated particle in Target Normal Sheath Acceleration Mechainsmm as a mono-energetic bunch

References

[1] C. G. R. Geddes, Cs .Toth, J. Van. Tilborg, E. Esarey, C. B. Schroeder, D. Bruhwiler, C. Nieter, J. Cary and W. P. Leemans, *Nature* 431 538 (2004)

[2] J. Faure, C. Rechatin, A. Norlin, A. Lifschitz, Y. Glinec and V. Malka, *Nature* 444 737(2006)

[3] W. Lu, M. Tzoufras, C. Joshi, F. S. Tsung, W. B. Mori, J. Vieira, R A. Fonseca and L. O. Silva, *PhysRevSTAB* 10 061301(2007)

[4] J W Wang, W Yu, M Y Yu, H Xu, J J Ju, S X Luan, M Murakami, M Zepf and S Rykovanov, *Phys. Rev. Accel. Beams*,19 021301(2016)

[5] E. Esarey, C. B. Schroeder and W P. .Leemans , *Rev. Mod. Phys*. 81 1229 (2009)

[6] E. Esarey, P. Sprangle, J Krall, A Ting and G Joyce, *Phys. Fluids B* 5 2690 (1993)

[7] L. M. Gorbunov and V. I. Kirsanov, Sov. Phys. JETP 66 290 (1987)

[8] E. Esarey, P Sprangle, J. Krall and A. Ting, IEEE Trans. Plasma Sci. 24 252 (1996) [9] M. Borghesi et al., Fusion Sci. Technol. 49 (2006) 412.

[10] H. Schwoerer, S. Pfotenhauer, O. Ja¨ckel, K.-U. Amthor, B. Liesfeld, W. Ziegler, R. Sauerbrey, K. W. D. Ledingham, T. Esirkepov Nature volume 439, pages 445–448 (2006), doi:10.1038/nature04492

[11] M. Roth et al., Phys. Rev. ST-AB 5 (2002) 061301.

[12] T D Arber, K Bennett, C S Brady, A Lawrence-Douglas, M G Ramsay, N J Sircombe, P Gillies, R G Evans, H Schmitz, A R Bell, C P Ridgers, Plasma Phys Control Fusion 57(11) 113001(2015).

[13] M. Roth and M. Schollmeier, http://dx.doi.org/10.5170/CERN-2016-001.231

[14] J.J. Santos et al., Phys. Plasmas 14(10) (2007) 103107. http://dx.doi.org/10.1063/1.2790893

[15] J. Fuchs et al., Nature Phys. 2 (2006) 48. http://dx.doi.org/10.1038/nphys199

[16] R.B. Stephens et al., Phys. Rev. E 69(6) (2004) 066414.

[17] J.E. Crow et al., J. Plasma Phys. 14(1) (1975) 65. http://dx.doi.org/10.1017/S0022377800025538

[18] N.A. Krall and A.W. Trivelpiece, Principles of Plasma Physics (San Francisco Press, San Francisco, 1986).

[19] Y. Sentoku et al., Phys. Plasma 14(12) (2007) 122701. http://dx.doi.org/10.1063/1.2816439

[20] Y. Ping et al., Phys. Rev. Lett. 100(8) (2008) 085004. http://dx.doi.org/10.1103/PhysRevLett.100.085004

[21] S. Augst et al., Phys. Rev. Lett. 63(20) (1989) 2212. http://dx.doi.org/10.1103/PhysRevLett.63.2212

ICNST 2024 International Conference on Nuclear Science and Technology
6- 8 MAY 2024 | Isfahan, Iran

Calculation of the Incorporation Energy of Xenon in UO2 Crystal (Paper ID : 1540)

Sheykhi Samira *, **Payami Shabestar Mahmoud, Basaadat Mohammad Reza**

Physics and Accelerators Research School, Nuclear Science and Technology Research Institute, Atomic Energy Organization of Iran, Northen Kargar St., Tehran

ABSTRACT

In uranium dioxide nuclear fuel, xenon atoms are produced in the process of uranium fission. They form bubbles in combination with each other, cause the fuel to swell and eventually cause malfunction of the fuel. To fully understand how xenon bubbles are formed, it is very important to study the scattering of a single xenon atom. There are many places for the xenon atom in uranium dioxide. One possibility is the placement of the xenon atom in the octahedral site, which is not a suitable option due to its high incorporation energy. Another possibility is to be in a Schottky defect (SD). Schottky defect has more free space than interstitial and is more favorable in terms of energy. Another possibility is to examine xenon in tetravacancy defects and then xenon incorporation energy in double-Schottky defects. In this research, we investigated and calculated the xenon incorporation energy in all possibilities that mentioned above with different orientations and compare the results using interatomic potentials. The calculation results showed that the xenon atom incorporation energy in double Schottky defects was significantly lower than in a tetravacancy, a Schottky and interstitial defects. In our calculations, the xenon incorporation energy in a double-Schottky state composed of type 3(SD3-SD3) had the lowest energy, which was equal to 0.26 electron volts.

Keywords: Uranium dioxide, Interstitial, Xenon, Vacancy, Schottky defect, Tetravacancy, Incorporation energy.

INTRODUCTION

In uranium dioxide nuclear fuel, xenon atoms are produced in the process of uranium fission. Xenon fission fragments do not dissolve in uranium dioxide and they form bubbles in combination with each other, cause the fuel to swell and eventually cause malfunction of the fuel. To fully understand how xenon bubbles are formed, it is very important to study the scattering of a single xenon atom. There are many places for the xenon atom in uranium dioxide. One possibility is the placement of the xenon atom in the octahedral, which is not a suitable option due to its high incorporation energy. Another possibility is to be in a Schottky defect (SD). Schottky defect is the smallest uncharged vacancy group in uranium dioxide. Schottky defect has

more free space than interstitial and is more favorable in terms of energy. The volume of a Schottky defect cluster (is about 42 Angstroms) is very close to the van der Waals volume of a xenon atom, meaning that there is not enough space for movement of the xenon atom in SD. Other possibilities are to examine xenon in tetravacancy and double-Schottky defects. Several theoretical investigation of xenon in UO_2 have done using both density functional theory (DFT) as well as emperical potentials [i,ii,iii,iv,v]. Thompson *et al*. proposed a new interatomic potential for UO_2 and test it for different defects and interatomic potentials and compared their results[vi]. In this research, we investigated and calculated the xenon incorporation energy in tetravacancy and double-Schottky defects with different orientations using interatomic potentials.

Uranium dioxide is strongly correlated due to the presence of half-filled orbital f, and due to the presence of semi-stable states, finding the correct electronic ground state is difficult. According to the experiments, the uranium dioxide crystal is a mott insulator that has non-linear antiferromagnetic properties at temperatures below 30 K and is a paramagnet at higher temperatures. The crystal structure of this pure crystal belongs to space group 225 and fluorite with lattice constant a=b=c=5.47 angstroms [vii,viii]. Uranium atoms occupy the sites of an FCC structure, while oxygen atoms occupy sites with symmetry $Pa\bar{3}$ [ix](figure 1).

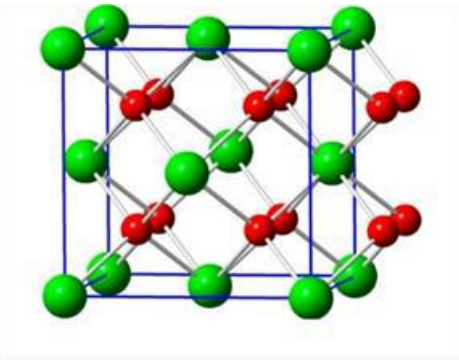

Fig. 1. Structure of UO2 fluorite. Green and red spheres represent oxygen and uranium atoms, respectively.

RESEARCH THEORIES

For Schottky clusters, we remove one uranium atom and two neighboring oxygen atoms from the lattice. In the structure of perfect fluorite, assuming that each oxygen element is the closest neighbor of uranium, there are only three structures for the elements of this defect. These three Schottky defect clusters differ in the distance between the two oxygen vacancies and are called SD1, SD2 and SD3 according to the distance between the two oxygens. As shown in Figure 2, in principle, none of the SD configurations are

symmetrically equivalent, which is caused by the disorder of the oxygen sub-lattice and the irregularities in the unit cell.

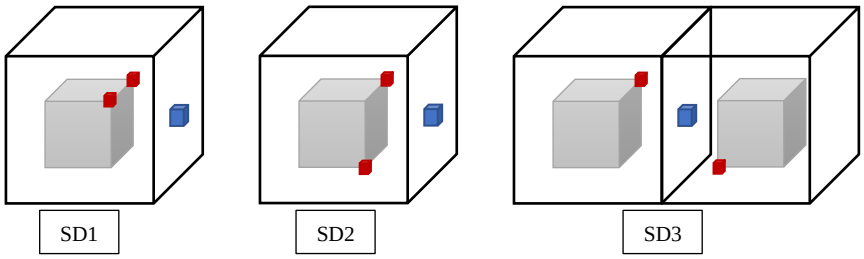

Fig. 2. Structures SD1, SD2, SD3. The red cubes show the oxygen vacancies and the gray cubes show the uranium vacancies.

The xenon incorporation energy, which is the energy required for xenon to sit in the octahedral interstitial site, is defined as follows [6] (1)

$$\Delta E_{Xe}^{f} = E_{Xe_i}^{N} - NE^{UO2} - E^{Xe}$$

The Schottky defect formation energy is calculated from the following equation (2)

$$\Delta E_{SD}^{f} = E^{N-1} - (N-1)E^{UO2}$$

Where E^{N-1} is the energy of a supercell with N formula units of UO_2 minus one formula unit (Schottky defect). The energy required to add a xenon to a Schottky defect in the crystal is defined as follows: (3)

$$\Delta E_{Xe-SD}^{f} = E_{Xe}^{N-1} - E^{N-1} - E^{Xe}$$

where the first term on the right side is the energy of a supercell with N formula units of UO_2 minus one formula unit (Schottky defect) and a xenon atom.

Also, the incorporation energy of a xenon atom in tetravacancy(TV) (4)

$$\Delta E_{Xe-TV}^{f} = E_{Xe}^{TV} - E^{TV} - E^{Xe}$$

And in double-Schottky defects is obtained from the following equation (5)

$$\Delta E_{Xe-2SD}^{f} = E_{Xe}^{N-2} - E^{N-2} - E^{Xe}$$

COMPUTATIONAL METHOD

GULP [x] software package was used for calculations in this research, which performs calculations based on force field methods. The force field used in this article is of the core-shell type, whose parameters are obtained by fitting the calculation results to the DFT constant using the genetic algorithm [xi]. In this research, Morlon's interatomic potentials [xii] for U and O forces and Cartier's interatomic potential [xiii] are used for Xe-U and Xe-O forces. In this work, we used a 96-atom supercell. We optimized the atoms of the system at zero pressure and temperature and obtained the equilibrium lattice constant. The equilibrium lattice constant was equal to 5.45 Angstroms. We placed xenon in different positions in the uranium dioxide crystal and calculated the incorporation energy in each case: 1. Xenon in an intermediate position, 2. Xenon in one Schottky defect 3. Xenon in TV and 4. Xenon in double-Schottky defects.

To calculate the incorporation energy of xenon in the interstitial site, we first placed xenon in the octahedral interstitial site and calculated the incorporation energy using equation number 1 (Table 1). In the following, we created different Schottky defects according to Figure 2 and placed the xenon atom in the uranium vacancy and obtained the incorporation energy in each case using equation 3 (Table 1). In the case of calculations 1 and 2, as shown in Table 1, there is a good agreement with the reference article. As can be seen from the results, the incorporation energy of interstitial xenon is much higher than the energy of xenon incorporation in Schottky defects, and therefore interstitial is not a suitable option for xenon.

Continuing the calculations, we considered the possible tetravacancy defects and calculated the incorporation energy of the xenon atom in each state. In this way, we considered all three types of Schottky defect 1, 2, and 3, and removed the closest uranium to the uranium vacancy in Schottky (SD1-U, SD2-U, SD3-U), replaced it with a xenon atom and finally calculated its incorporation energy using equation 4. For each Schottky defects, there were different combinations of Schottky and U vacancies, which differ in the distance between the U vacancy and two oxygen vacancies of the Schottky. We checked all possible permutations (15 different combinations), results show that the SD3-U has the lowest incorporation energy and its value is equal to 1.21 electron volts. This energy is significantly smaller than the xenon incorporation energy in a Schottky defect, and therefore the probability of xenon being placed in this defect is higher. According to the calculations, the more free space available to xenon, the lower its incorporation energy is and that state is more favorable for xenon atom placement. Considering the clustering and diffusion of xenon atoms in the uranium dioxide crystal, the more increasing the vacancies in the lattice, more favorable

conditions will be provided for the movement of xenon and their clustering in the lattice. To investigate this issue, we also investigated the different combinations of double-Schottky defects.

To calculate the xenon incorporation energy in double-Schottky defects, there were different combinations of 3 types of Schottky defects (SD1-SD1, SD1-SD2, SD1-SD3, SD2-SD2, SD2-SD3, SD3-SD3) and each including different placement states, for example SD1-SD1 state included 33 different states that we calculated all available states for all permutations to find the most probable state for xenon placement, the state that has the lowest incorporation energy in terms of energy and be the most desirable state.

Table 1. Xe incorporation energy calculated in terms of ev in this work and compared with existing data

	Xeinterstitial	Xe in SD1	Xe in SD2	Xe in SD3
Ref. [6]	11.76	4.10	4.43	4.61
This work	11.70	4.10	4.42	4.61

In our calculations, the xenon incorporation energy in a state composed of SD3-SD3 had the lowest energy, which was equal to 0.26 electron volts. Figure 3 shows an example of SD3-SD3 configurations. In each structure, a xenon atom takes the place of one of the uranium Schottky defects.

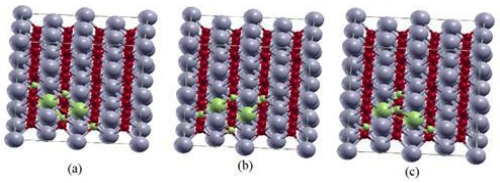

Fig. 3. Structures a, b, c shows an example of the investigated SD3-SD3 structures. Each structure shows a 96-atom supercell, the gray spheres represent uranium atoms and the red spheres represent oxygen atoms. Green spheres show the location of Schottky defects.

The xenon incorporation energy in each of the three structures a, b, c is calculated using equation 5 and is given in Table 2.

As it can be seen from the results of Table 2 (as an example of about 100 calculations), the xenon incorporation energy in double-Schottky defects is significantly lower than the xenon incorporation energy in a Schottky defect and intermediate xenon.

Table 2. Xe incorporation energy calculated in ev

	a	b	c
Formation Energy	3.076	4.15	0.26

CONCLUSIONS

Xenon atoms, which are produced during the fission of uranium in nuclear fuel, because they do not dissolve in the fuel, form bubbles and cause the fuel to swell and change the properties of the fuel. In this work, we calculated the lowest incorporation energy for the xenon atom. We investigated three interstitial xenon states in the octahedral site, one Schottky defect and double-Schottky defects. Among all investigated states, the xenon incorporation energy in double-Schottky defects is significantly lower than the xenon incorporation energy in a Schottky defect and interstitial xenon. In our calculations, the xenon incorporation energy in a state composed of SD3-SD3 had the lowest energy, which was equal to 0.26 electron volts.

References

[1] Y. Yun, H. Kim and K. Park, J. Nucl. Mater. 378 (2008) 40.

[1] Y. Yun, O. Eriksson and P. M. Oppeneer, J. Nucl. Mater. 385 (2009) 510.

[1] Y. Yun, O. Eriksson and P. M. Oppeneer, J. Nucl. Mater. 385 (2009) 364.

[1] K. Govers, S. E. Lemeov, and M. Verwerft, J. Nucl. Mater. 405 (2010)252.

[1] R. W. Grimes, in Fundamental Aspects of Inert Gases in Solids, edited by S. E. Donelly and J. H. Evans (Springer, New York, 1990), p.415.

[1] A. E. Thompson, B. Meredig and C. Wolverton, J. Phys.: Condens. Matter 26 105501 (2014)

[1] G. Amoretti, A. Blaise, R. Caciu_o, J. M. Fournier, M. T. Hutchings,R. Osborn, A. D. Taylor, Phys. Rev. B 40 (1989) 1856-1870.

[1] J. Faber, G. H. Lander, B. R. Cooper, Phys. Rev. Lett. 35 (1975) 1770-1773

[1]M. Idiri, T. Le Bihan, S. Heathman, J. Rebizant, Phys. Rev. B 70 (1) (2004) 014113.

[1] J. D. Gale, A. L. Rohl, Mol. Simul. 29 (2003) 291.

[1] A. E. Thompson, B. Meredig, M. Stan, C. Wolverton, J. Nucl. Mater. 446 (2014) 155–162.

[1] N.-D. Morelon, D. Ghaleb, J.-M. Delaye, and L. Van Brutzel, Philos. Mag. 83, 1533 (2003).

[1] A. Chartier, L. Van Brutzel and M. Freyss , Phys. Rev. B 81 174111 (2010).

ICNST 2024 International Conference on Nuclear Science and Technology
6- 8 MAY 2024 | Isfahan, Iran

Calculating the nuclear mass of some nuclei in the A~160 mass region at high angular momentum (Paper ID : 1554)

Mohadese Shayestefar*

[1] *School of Physics, Damghan University, Damghan, 36716-41167, Iran*

Abstract

As a fundamental property of nuclei, nuclear mass or their binding energy has a great importance to extract a lot of information about shell effects, magic number and many various aspects of nuclei. Nuclear experimentalists are always interested in creating of heavy and super-heavy nuclei and investigating of their properties, including mass. The increasing development of accelerators causes to become possible to study of nuclei up to high angular momenta. Nuclear ground-state masses have mainly obtained by using Yukawa potential. In the present work, we will calculate nuclear mass at high-spin applying the cranked Nilsson-Strutinsky (CNS) framework that is a powerful model to study of nuclei in different mass region at high spin. CNS model is based on the rotating oscillator potential. In the macroscopic- microscopic approach of CNS, the total nuclear energy for high spin states is calculated as the sum of the liquid drop energy (E_{ld}) and the shell correction energy (E_{shell}). We choose some nuclei in the A~160 mass region to study their masses. At three highest spins established in experiment, mass calculations will be performed. Then, these theoretical results will be compared to the experimental data.

Keywords: nuclear mass, cranked Nilsson-Strutinsky (CNS) model, high spin

INTRODUCTION

As a fundamental property of nuclei, nuclear mass or their binding energy has a great importance to extract a lot of information about shell effects, magic numbers, and many various aspects of nuclei [1]. It has a long history going back to George Gamow's idea of nuclei [2] (about 1928) in which was assumed the nucleus is similar to a drop of water and the particles are kept together by surface tension and then, formulated it as liquid drop model (LD model). This simple model was further developed by Heisenberg, von Weizsäcker, and Bohr after the discovery of neutrons in 1932, treats the collection of protons and neutrons inside an atomic nucleus as an incompressible, uniformly charged fluid [3,4]. To study basic properties of nuclei and determine the nuclear ground-state masses, considerable efforts have been carried out. It may use either a macroscopic or a microscopic approach [5].

One of the oldest problems in nuclear theory is the dependence of nuclear masses on deformation. Myers and Swiatecki [6] presented a semi-empirical theory of nuclear masses and deformations as a development in Thomas-Fermi (TF) model. The potential energy of a nucleus was given by the liquid- drop model which modified by a shell correction as a function of N, Z and the nuclear shape. The mass formula was contained seven adjustable parameters, four in the liquid drop part but there were some problems on determining these parameters in a reasonably perspicuous way. The results of this theory were compared to 1200 experimental nuclear masses.

Strutinsky proposed the method to calculate the shell corrections in models of the macroscopic- microscopic type. With this method, the potential energy of a nucleus can be obtained as a function of deformation and the occupation number. Therefore, the total nuclear energy is calculated by the sum of the liquid drop energy E_{ld}, the shell correction energy $E_{shell,}$ and then, to obtain the ground-state energy, this sum must be minimized over deformation parameters. It has been extensively applied to the study of nuclear ground-state and fission properties [7].

Moller and his coworkers calculated the ground-state masses of the 4678 nuclei from ^{16}O to $^{318}122$ by using a macroscopic-microscopic model. They used the finite-range droplet model (FRDM model) as the macroscopic model and the microscopic contribution was based on a folded-Yukawa single-particle potential. They improved the results by adding the exponential term (following Strutinsky's shell correction) in the macroscopic model [8]. After that, they tabulated nuclear ground-state masses and deformations within a new form of the average paring energy as finite-range liquid drop model (FRLDM) model and then, the results were compared with the FRDM model results. The rms deviation of the TF model for 2766 masses calculated by the FRLDM model was estimated at 0.758 MeV. It displayed a high precision as well as a good accuracy of the model [9].

In 2003, Promorski investigated the influence of the surface-curvature term which is proportional to $A^{1/3}$ as the Lublin-Strasbourg version of the nuclear drop energy formula (LSD). The results turned out a remarkable improvement in the performance of the liquid-drop model formula [10].

Since in recent years accelerators are developing more and more, it is possible to study the properties of nuclei, especially nuclear masses, up to high angular momentum. Cranking model is a strong way to investigate the nuclei at high-spin region [11,12]. The use of the CNS method in calculating the mass of nuclei at high energy was first performed by Carlsson and Ragnarsson in 2006 [1].

The objective of the present paper is to study the mass, or equivalently, the absolute energy of some nuclei with A~160 at highest established spins within cranking model as cranked Nilsson-Strutinsky (CNS) approach.

RESEARCH THEORIES

Cranked Nilsson-Strutinsky (CNS) [1,12,13] approach based on the modified oscillator potential is a good theoretical method to study of the nuclei in high-spin region. In this macroscopic-microscopic approach, the total nuclear energy is obtained as a function of deformation parameters and angular momentum. It is calculated at spin I by the sum of the rotating liquid drop energy E_{rld} and the shell correction energy E_{shell} as

Where E_{ld} and $\mathcal{J}_{rig}$ are the static liquid drop energy and the rigid-body moment of inertia, respectively.

The shell energy is obtained by the energy eigenvalues of the cranked single-particle Hamiltonian, h_i, taken as

h_{MO} denotes the modified oscillator potential and ωj_x is cranking term caused the deformed potential rotate around the principal x-axis. In the CNS model, pairing correlation effects are neglected. Most of the time, it is used only for high-spin states where pairing is not important.

We will apply CNS model to calculate the total energy for some nuclei in the A~160 mass region at high angular momentum. For the static liquid drop energy (E_{ld}), we will use two different macroscopic models that have recently been applied to mass calculations, namely the finite range liquid drop model (FRLDM)

[9] and the Lublin-Strasbourg drop (LSD) model [10] and a rigid-body moment of inertia with the radius parameter r_0 = 1.16 fm and the surface diffuseness parameter a = 0.6 fm [14]. The shell correction energy is calculated with the Strutinsky procedure [7].

Results and discussion

The aim of this work is the study of the nuclei masses in the A~160 mass region at the high-spin region. The nuclei are: ^{153}Tb, $^{154-156}Dy$, $^{155-157}Ho$, $^{156-160}Er$, ^{157}Tm. First, we studied experimental level

65 66 67 68 69

sheme (excitation states) of each nucleus and choose three of the latest established states in the rotational band which was identified up to higher energies (spins). These rotational bands are shown in Fig. 1

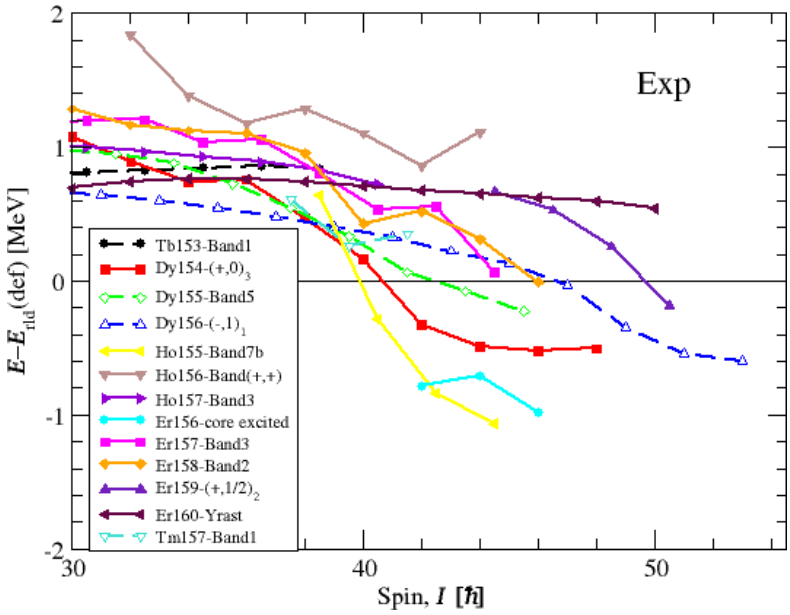

Fig. 1. The rotational bands of some nuclei in A~160 mass region which were established to higher spin [15-26].

Plots of the energy E vs. spin *I* are frequently used in the description of rotating nuclei. But where multiple rotational bands exist in the vicinity of the yrast line[1], such plots do not practically exhibit any information in detail. To solve this problem, an average rigid rotor reference approximately corresponding to the envelope of the observed rotational bands is to subtract the energy E. As illustrated in Fig. 1, the vertical axis was referred $E - E_{rld}$. As total angular momentum, spin, (I) increases, all of these rotational bands show a tendency to go down in energy. Most of them are yrast of the nucleus or very close to the Yrast band of it. Transitional rare earth nuclei in the A~160 mass region have a small number of nucleons outside the Z=64 and N=82 closed shells and they are investigated relative to the $^{146}_{64}Gd$ closed core. These nuclei are deformed in the ground state and mostly, have prolate shape and collective behavior. As the total angular momentum increases, alignments of their collective behavior gradually change and in the I=30-50, they experience a transition from a collective prolate to a noncollective oblate shape. Coming down in energy is related to this transition.

Secondly, it was calculated the total energy of these nuclei versus spin in the different configurations (The arrangement of nucleons) within CNS formalism, see the details of this approach in the manual of CNS code [27]. Among all of the calculated rotational bands for a nucleus, we choose the band that has the lowest

energies and most similarity to the selected experimental band (in Fig. 1). Indeed, it is the theoretical counterpart of the experimental band.

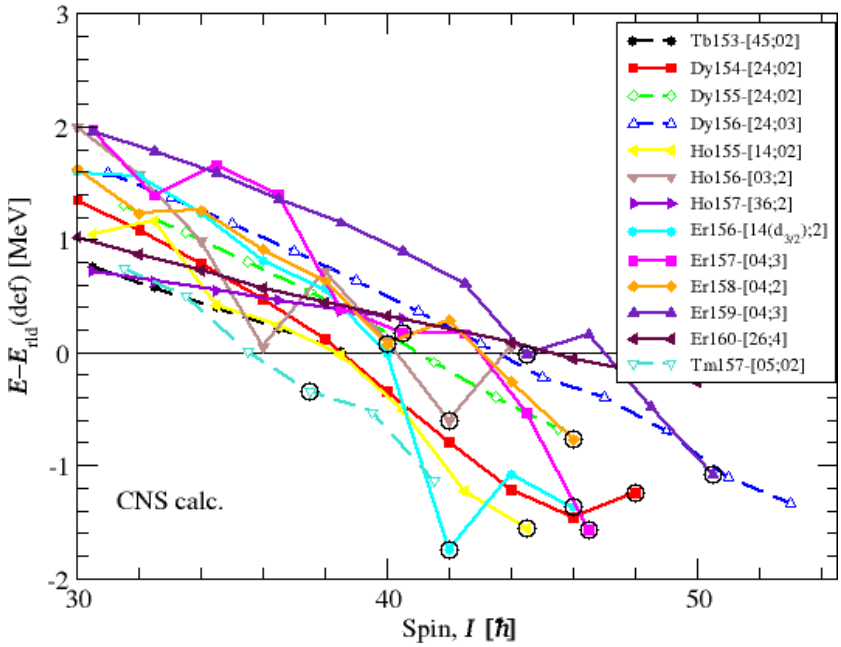

6

Fig. 2. The rotational bands of some nuclei in A~160 mass region which are the couterparts of the experimental bands shown in Fig. 1. Numbers written in the brackets show a short notation to simplify the CNS theoretical configurations labeling. Relative to the ^{146}Gd doubly magic core, it is shown as $[p_1 p_2; n_1]$ in which p_1, p_2 and n_1 present the number of proton holes in $(d_{5/2}\, g_{7/2})$ subshells, $h_{11/2}$ protons and $i_{13/2}$ neutrons, respectively.

To obtain $E_{ld}(Z\ N\ I\ \varepsilon_i)$ CNS calculations were using LSD model and also, FRLDM model. The results given in Fig. 2 related to the LSD model. Generally, FRLDM results are very similar LSD model (just a little higher or higher in energy). So, we just plotted the LSD results.

Finally, it was compared the total energy obtained CNS approach to the experimental ones and then, the difference between them was obtained. The differences are shown in Figs. 3 and 4 for the calculations based on LSD and FRLDM models, respectively. In Both of Figs. 3 and 4, the differences are negative. It means the total calculated energy of the nucleus underestimates than the experimental results. These differences for each nuclei at the three highest spins mostly have a smooth way or a little downward. However, some sudden slope changes are seen that they correspond to some changes in nuclear structure at that spin, for example change configuration of nucleons to acheive more stability. It seems that the nuclei with similar configuration show similar behavior. The uncertainties of calculating energies using the CNS code is considered as if the total energy difference between the experimental values and the calculations of this

method (CNS) is about ±1, the errors are normal and acceptable [28]. The obtained differences of our present work are in this range when the macroscopic energies were calculated by LSD model (see Fig. 3). But about the FRLDM results, some of the differences are bigger than -1MeV. One reason is the two model have different shell correction and also, they have different depencies to the deformation parameters.

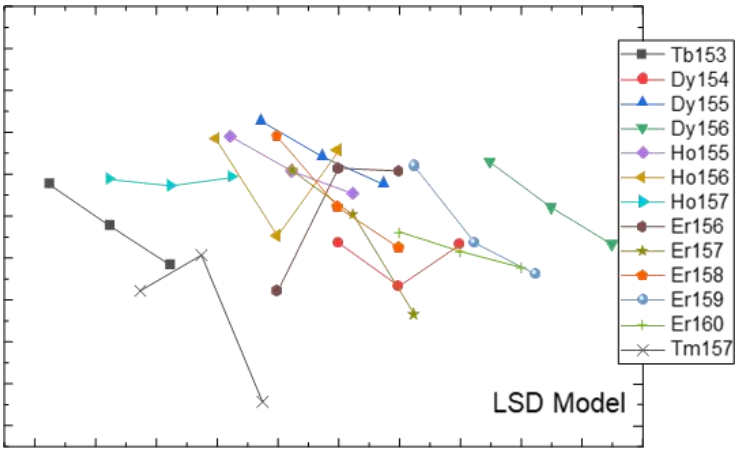

Fig. 3. The difference of the total energies between CNS calculations and experimental results. The macroscopic energies were obtained by LSD model.

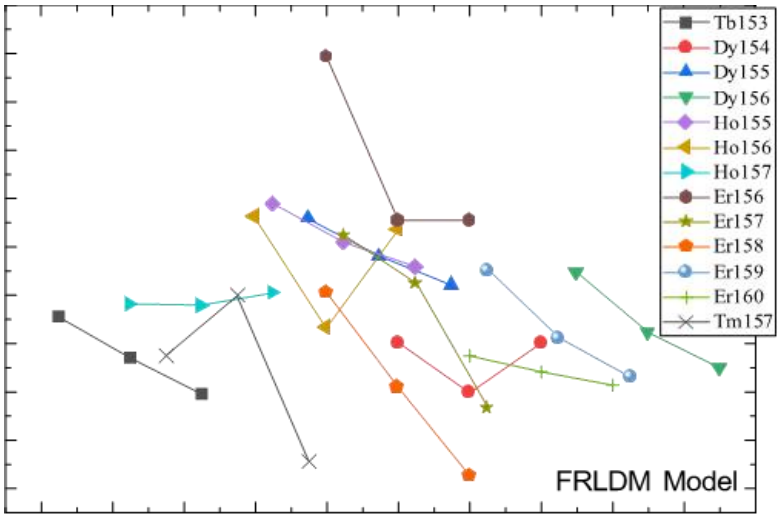

Fig. 4. The difference of the total energies between CNS calculations and experimental results. The macroscopic energies were obtained by FRLDM model.

For 39 high-spin states included of 13 nuclei, when using LSD model the rms value of the difference between CNS calculated and experimenatl masses is 0.6590 MeV while using FRLDM leds to the rms value is 0.9192. So, calculation of masses of nuclei using LSD model has more accurate. The results of Ref. [1]

confirm that. Rms value of the same difference in Carlsson and Ragnarsson study using LSD model became 0.856 MeV.

Conclusions

To sum up, the absolute energy (or equivalently their masses) of some nuclei in A~160 mass region at high spin were calculated by CNS model. The results of calculations were compared with the experimental data and it shows good agreement. CNS calculations were performed and the macroscopic energies were achieved using both LSD and FRLDM model. The total energies obtained by LSD model agree better with the experimental results than those obtained. So, mass calcualtion in the high-spin region within CNS framework using LSD model is a reliable way to obtain nuclear mass at high-spin.

References

[1] Carlsson, B. G., & Ragnarsson, I. (2006). Calculating the nuclear mass in the very high angular momentum regime. Physical Review C, 74(1), 011302.

[2] Gamow, G. (1930). Mass defect curve and nuclear constitution. Proceedings of the Royal Society of London. Series A, Containing Papers of a Mathematical and Physical Character, 126(803), 632-644.

[3] Weizsäcker, C. V. (1935). Zur theorie der kernmassen. Zeitschrift für Physik, 96(7-8), 431-458.

[4] Bethe, H. A., & Bacher, R. F. (1936). Nuclear physics A. Stationary states of nuclei. Reviews of Modern Physics, 8(2), 82.

[5] Nix, J. R. (1972). Calculation of fission barriers for heavy and superheavy nuclei. Annual Review of Nuclear Science, 22(1), 65-120.

[6] Myers, W. D., & Swiatecki, W. J. (1966). Nuclear masses and deformations. Nuclear Physics, 81(1), 1-60.

[7] Strutinsky, V. M. (1967). Shell effects in nuclear masses and deformation energies. Nuclear Physics A, 95(2), 420-442.

[8] Möller, P., Myers, W. D., Swiatecki, W. J., & Treiner, J. (1988). Nuclear mass formula with a finite-range droplet model and a folded-Yukawa single-particle potential. Atomic Data and Nuclear Data Tables, 39(2), 225-233.

[9] Möller, P., Nix, J. R., Myers, W. D., & Swiatecki, W. J. (1995). At. Data Nucl. Data Tables. At. Data Nucl. Data Tables, 59, 185.

[10] Pomorski, K., & Dudek, J. (2003). Nuclear liquid-drop model and surface-curvature effects.

Physical Review C, 67(4), 044316.

Bengtsson, T., & Ragnarsson, I. (1985). Rotational bands and particle-hole excitations at very high spin. Nuclear Physics A, 436(1), 14-82.

[11] Nilsson, S. G. and Ragnarsson, I. (1995). Shapes and Shells in Nuclear Structure.Cambridge University Press, Cambridge, England.

[12] Afanasjev, A. V., Fossan, D. B., Lane, D. B. and Ragnarsson, I. (1999). ”Termination of rotational bands: disappearance of quantum many-body collectivity.” Phys. Rep. 322, 1-124.

[13] Bengtsson, T., & Ragnarsson, I. (1985). Rotational bands and particle-hole excitations at very high spin. Nuclear Physics A, 436(1), 14-82.

[14] Davies, K. T., & Nix, J. R. (1976). Calculation of moments, potentials, and energies for an arbitrarily shaped diffuse-surface nuclear density distribution. Physical Review C, 14(5), 1977.

[15] Hartley, D. J., Riley, M. A., Wang, X., Miller, S., Janssens, R. V. F., Paul, E. S., ... & Ragnarsson, I. (2015). Persistence of collective behavior at high spin in the N= 88 nucleus Tb 153. Physical Review C, 91(5), 057301.

[16] Ma, W. C., Janssens, R. V. F., Khoo, T. L., Ragnarsson, I., Riley, M. A., Carpenter, M. P., ... & Zhu, S. J. (2002). Competition between terminating and collective structures above spin 40 ħ in 154 Dy. Physical Review C, 65(3), 034312.

[17] Vlastou, R., Papadopoulos, C. T., Serris, M., Kalfas, C. A., Fotiades, N., Harissopulos, S., ... & Rekstad, J. (1994). High-spin structure of 155Dy. Nuclear Physics A, 580(1), 133-155.

[18] Kondev, F. G., Riley, M. A., Janssens, R. V. F., Simpson, J., Afanasjev, A. V., Ragnarsson, I., ... & Varmette, P. G. (1998). Spin∼ 60 $\hbar$ in 156Dy: competition between collective and terminating structures at very high-spin. Physics Letters B, 437(1-2), 35-43.

[19] Rees, J. M., Paul, E. S., Simpson, J., Riley, M. A., Ayangeakaa, A. D., Carpenter, M. P., ... & Ragnarsson, I. (2015). High-spin terminating states in the N= 88 Ho 155 and Er 156 isotones. Physical Review C, 91(5), 054301.

[20] Cullen, D. M., Yu, C. H., Cline, D., Simon, M., Radford, D. C., Riley, M. A., & Simpson, J. (1998). High-spin states and the first signs of band termination in 156 Ho. Physical Review C, 57(5), 2170.

[21] Radford, D. C., Andrews, H. R., Ball, G. C., Horn, D., Ward, D., Banville, F., ... & Hamamoto, I. (1992). Multiple band structure and band termination in 157Ho towards complete high-spin spectroscopy. Nuclear Physics A, 545(3), 665-719.

[22] Evans, A. O., Paul, E. S., Simpson, J., Riley, M. A., Appelbe, D. E., Campbell, D. B., ... & Ragnarsson, I. (2006). High-spin structure in Er 157 up to and above band termination. Physical Review C, 73(6), 064303.

[23] Simpson, J., Riley, M. A., Gale, S. J., Sharpey-Schafer, J. F., Bentley, M. A., Bruce, A. M., ... & Ragnarsson, I. (1994). Single particle excitations and properties of multiple band terminations near spin

50ħ in 158Er. Physics Letters B, 327(3-4), 187-194.

[24] Mustafa, M., Ollier, J., Simpson, J., Riley, M. A., Paul, E. S., Wang, X., ... & Ragnarsson, I. (2011). Diverse collective excitations in 159 Er up to high spin. Physical Review C, 84(5), 054320.

[25] Ollier, J., Simpson, J., Riley, M. A., Paul, E. S., Wang, X., Aguilar, A., ... & Ragnarsson, I. (2011). Structure changes in Er 160 from low to ultrahigh spin. Physical Review C, 83(4), 044309.

[26] Riley, M. A., Brown, T. B., Johnson, N. R., Akovali, Y. A., Baktash, C., Halbert, M. L., ... & Bengtsson, T. (1995). Alignments, shape changes, and band terminations in Tm 157. Physical Review C, 51(3), 1234.

[27] Ragnarsson, I., & Carlsson, G. (2012). Calculating high-spin states using the configuration-dependent cranked Nilsson-Strutinsky (CNS) formalism. Division of Mathematical Physics, Lund Institute of Technology, Lund, Sweden, 1-47.

[28] Afanasjev, A. V., & Ragnarsson, I. (1995). Gradual loss of collectivity in rotational bands in the A∼ 110 (Z⩾ 50, N∼ 60) mass region. Nuclear Physics A, 591(3), 387-420.

Investigation of wake field effects in high power electron linear accelerator (Paper ID : 1560)

Kavusiomid, Reza [1*] ;Kalantari, S.Zafarollah[1] Sanayehajari, Shahin[2]; Ghasemi, Farshad [2]

[1] Department of Physics, Isfahan University of Technology, 841568311, Isfahan , Iran.
[2]Physics and Accelerators School, Nuclear Science and Technology Research Institute, AEOI, Tehran, Iran

Abstract

Radio frequency (RF) electron linear accelerators (LINACS) are known as the most versatile and the most numerous accelerators in the world. The application range of the RF electron LINACS increases with the beam current. From the RF cavity design point of view, with increasing the current, one should take care of the effects of the wake fields that in turn will cause various instabilities. The instabilities caused by wake fields are divided into short-range and long-range categories. The most concerning consequence is the beam breakup (BBU) effect. This instability imposes an upper limit on the beam current. This can limit the output power of the beam. The determining parameter of beam break up instability is called transverse shunt impedance. The transverse shunt impedance determines the transverse interaction of the beam and the cavity. In this article, the effects of wake fields have been investigated theoretically and by simulation as well. This allows the calculation of the threshold beam current.

Keywords: LINACS, wake fields, instability, beam breakup, transverse shunt impedance, threshold beam current

INTRODUCTION

During the development of LINACS in order to produce a high-power beam, the range of currents increases. By increasing the acceleration current, phenomena are observed in the LINACS that cause instability. By increasing the current, the beam itself appears as a generator and can excite multipole modes in the accelerator structure. Beam effects in exciting non-accelerating modes are called wake fields [1]. The excited fields of these modes are called wake fields because they follow the path of the electron beam. Examining the wake fields is important because the excited waves remain in the acceleration tube and can affect the movement of other electron bunch. Multipole fields can deflect the beam towards the walls and aperture and finally cause BBU phenomenon or Beam blow up or Pulse shortening. Beam

breakup is one of the most important and common transverse beam instabilities in RF electron LINACS. The BBU phenomenon was first observed in the late 1950s at the British Atomic Energy Institute in a 25 MeV electron constant impedance waveguide accelerator tube with a rated current of 1 A [2]. Shortly after that, in the United States, non-constant impedance was observed in accelerating tubes [3]. Studies on the BBU effect have been carried out in many high-energy structures, such as dielectric Wakefield accelerators, linear colliders, and recovery lines [4–8]. In this article, the purpose is to investigate the effect of BBU in high-power accelerators with lower energies, which has rarely been addressed in the world. The characteristics of the output beam of the intended accelerator are 30 MeV and 30 kW. This accelerator consists of 7 acceleration tubes according to the radio frequency design. The task of each tube is to increase the energy by 4.5 MeV. In this article, the effect of BBU in one of these tubes is investigated and the threshold current is calculated by performing CST software simulations.

Theory and models of BBU

Wake fields can appear as either longitudinal or transverse modes, giving rise to longitudinal or transverse instabilities. On the other hand, the fields excited by the beam are classified into two categories of short-range or long-range wake fields. For ultra relativistics bunches, the short-range fields produced by particles at the bunch head affect the trailing particles of the same bunch and cause energy loss, and for off-axis bunches, it causes a transverse deflection of the particles at the tail of the bunch. Long-range wake fields are generated by high-Q transverse deflection modes that induce transverse deflections in the trailing bunches. If the deflection modes are strongly excited by the beam, they may cause beam breaking instability (BBU), leading to effective emittance growth. Finally, the beam is lost on the walls. Examination of the disc-loaded accelerator structures shows that above the main acceleration mode TM_{010}, there are many other emission modes, some of which exhibit transverse deflection properties. Figure 1 shows the distribution of the field of different modes in a pillbox cavity. The deflection modes of real accelerator structures (with a beam aperture) as shown in Fig. 1 are generally neither pure TE nor pure TM, but linear combinations, called HEM, because the combined electromagnetic modes are "E" and "H". The ratio of the frequency of the higher order mode to the fundamental frequency of the accelerator is on the order of $\frac{3}{2}$, although there is no harmonic relationship [1, 9 ,10].

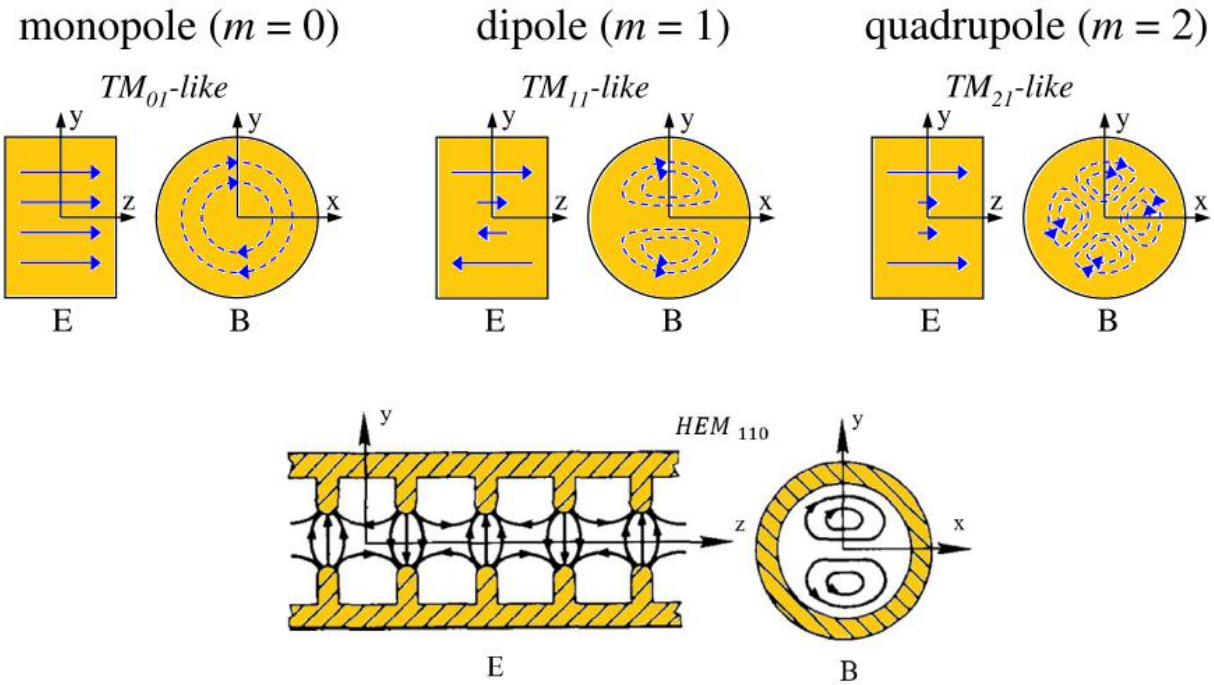

Fig. 1. Field distribution of deflection modes

The mechanism and model of beam break varies from one linear accelerator to another. Different beam break models are reconstructive and cumulative. Both regenerative and cumulative types of beam breakage are caused by the interaction with the HEM mode. Both instabilities start from noise, which consists of a small transverse modulation of the electron bunches at the breakdown frequency. The break of the beam in the regenerative model occurs in one section, and as we move along the structure, at the end of the structure due to the phase slippage, the beam has the ability to excite more deflection mode. On the contrary, in the cumulative and multi-section model, the break is due to the same initial small transverse modulation of the electron bunches, and this causes the subsequent electron bunches that see this field to receive a greater amount of transverse momentum and the amplitude of the resonant fields increase in the next sections. The mechanism of both models is shown in Fig.2. In a short, single-section linear accelerator, typically, for a tube several feet long and pulse lengths in the microsecond range, the beam break phenomenon appears for current amplitudes in the range of 500 mA. For a multi-section accelerator, typical thresholds of the beam break phenomenon are in the range of 10 mA [10].

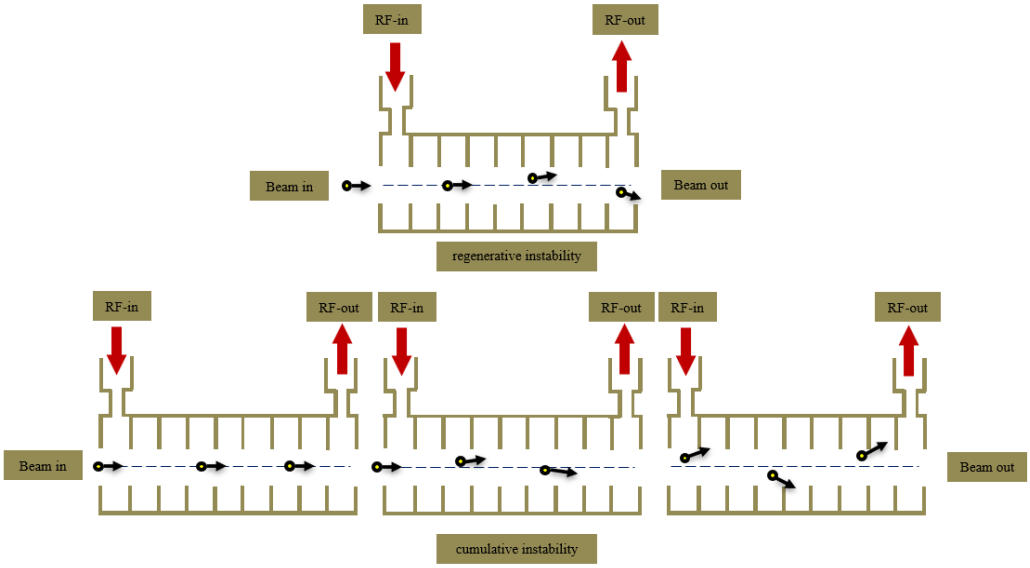

Fig. 2. Types of different mechanisms of beam break phenomenon

An important parameter that describes the transverse interaction of the beam and the accelerating structure is the transverse shunt impedance. From the Panofsky-Wenzel theorem, the change in transverse momentum of a particle passing through an excited accelerating structure in a single mode is proportional to the parameter $\frac{R_\perp}{Q}$. The ratio of transversal shunt impedance to quality factor is defined as the relation (1) [1].

$$\frac{R_\perp}{Q} = Z_0 \frac{C^3}{\omega_D^3} \frac{\left|\int \frac{\partial E_z}{\partial x} e^{j\omega_D z/c} dz\right|^2}{\int E^2 dV} \tag{1}$$

where $Z_0 = \sqrt{\frac{\mu_0}{\varepsilon_0}}$ is the impedance of the free space and ω_D is the frequency of the deflection mode. Also, a transverse shunt impedance per unit length often appears in the accelerator literature, which is used to express the BBU phenomenon, defined as $r_\perp = \frac{R_\perp}{l}$, where l is the effective length per tube for deflection mode. Threshold current for regenerative BBU has been investigated and shown to be dependent on various factors including wavelength (λ), group velocity (v_g) and HEM mode phase slip (α), length (L), transverse shunt impedance ($r_\perp$) and Q are dependent on the structure and longitudinal momentum of the input (p) and the output beam (p_0). For a constant impedance structure, the threshold current of the BBU phenomenon in the absence of a focusing field is shown in form [11]

$$I_s = \left(\frac{\pi}{g_2}\right)\left(\frac{|v_g|}{c}\right)\left(\frac{Q}{r_\perp \lambda}\right)\frac{pc}{e}\left(\frac{\lambda}{2L}\right)^3 F_a(p\ p_0) \quad (2)$$

where the coupling factor $\boldsymbol{g_2 = \frac{1}{2}(1 - cos\alpha - \frac{1}{2}\alpha\, sin\alpha)/\left(\frac{\alpha}{\pi}\right)^3}$ and F is a correction factor to calculate the longitudinal momentum change of the beam while passing through the acceleration structure. Among the techniques that can be used to increase the cumulative threshold current of BBU, we can mention the fine adjustment of the beam, strong focus, detuning of deviating modes from each cell to another, and adding wake-field damping.

Calculation of the threshold current for the beam breaking phenomenon

The radio frequency simulation of one of the linear electron accelerator tubes of 30 MeV and 30 kW was performed using CST software. The desired accelerator is a fixed impedance traveling wave loaded disk structure. The structural mode of the accelerator is $\frac{\pi}{2}$ and each accelerating tube contains 39 accelerating cells and two coupler cells. The basic parameters for the desired tube acceleration are shown in table (1).

Table 1. basic parameters of tube acceleration

Parameter	Value
Frequency [MHz]	2997.8
Input power[MW]	5
Output beam energy [MeV]	4.5
Beam current at Gun[A]	1
Beam aperture (radius) [mm]	11.59
Length[mm]	1000

Excitable structural modes in the TM_{110}waveguide mode have been extracted using the CST eigen mode solver, and its dispersion diagram in figure (3) has been calculated using Mathematica software. Also, the desired mode parameters are reported in the table (2).

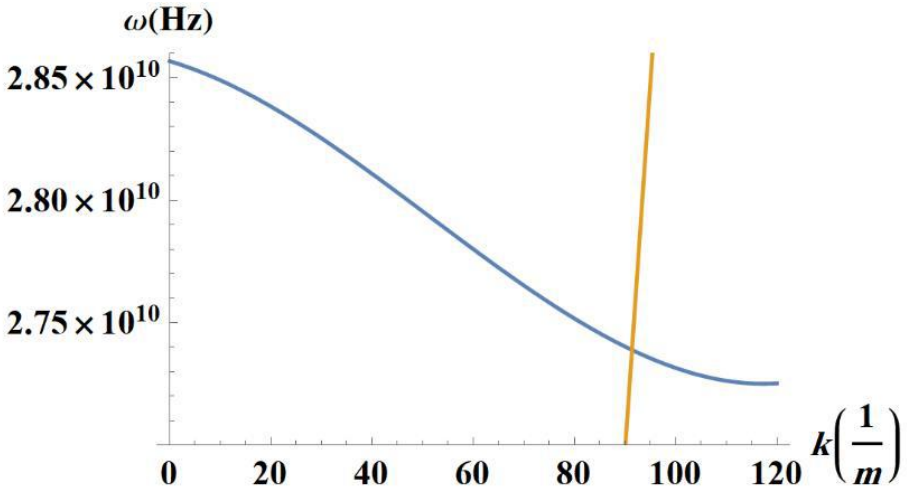

Fig. 3. dispersion diagram

Table 2. Deflection mode parameters TM_{110}

Parameter	TM_{110}
Frequency [MHz]	4358.96
Phase [degree]	130.91
Group velocity[/c]	0.032
k [/m]	91.3571
Q	11022
$\frac{r_\perp}{Q}$ [Ω]	3421.35
Threshold current[mA]	29

Figure 4 shows the general scheme of this acceleration tube in two states without couplers and with couplers. The material of the acceleration tube is copper with a conductivity of 58 MS/m. Also, from the CST frequency domain solver, the diagram S_{11} and the distribution of the electric field in the desired mode are extracted and shown in the figure 5.

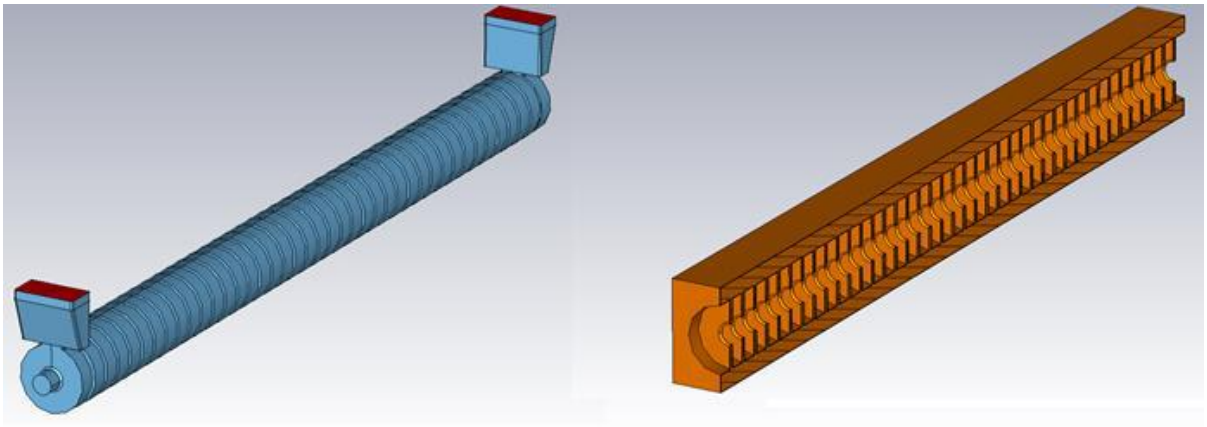

Fig. 4. General scheme of acceleration tube

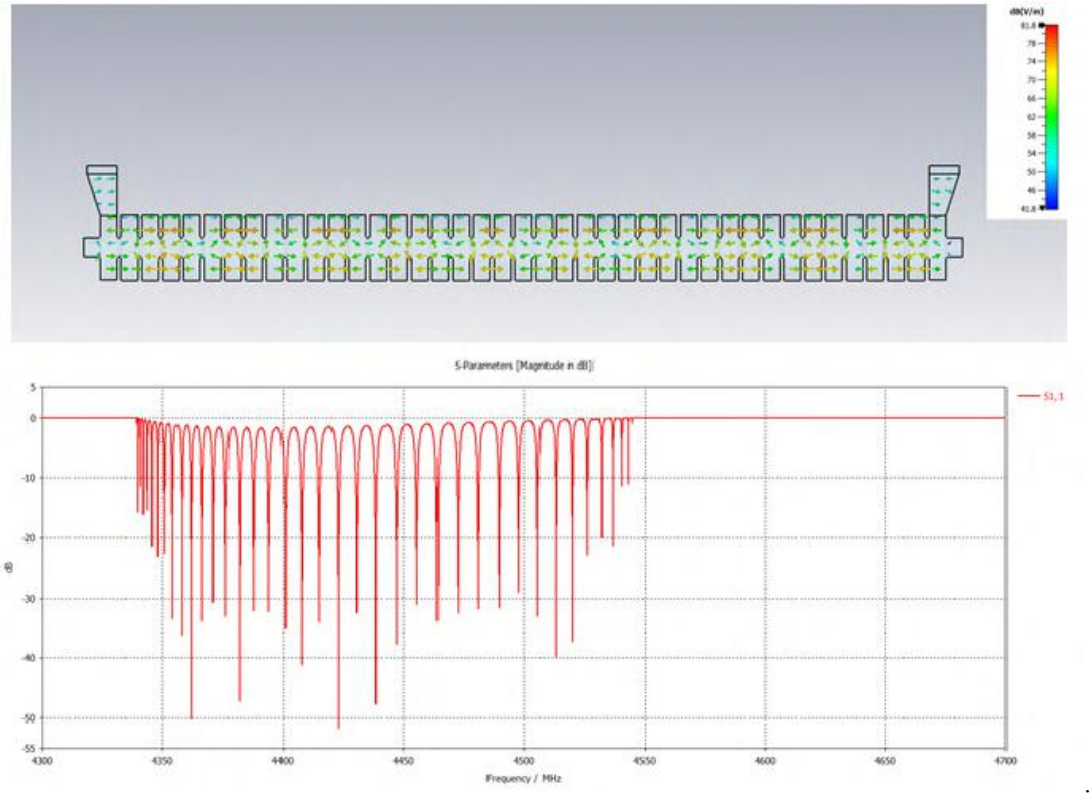

Fig. 5. diagram S_{11} and the distribution of the electric field

Conclusions

Investigating Wakefield effects on the growth of beam transverse emittance in high-power accelerators, which leads to the phenomenon of beam break up, is of great importance. In this article, the radio frequency design of the acceleration tube is done and the effects of Wakefield on the threshold current value for the beam breaking phenomenon are investigated. It should be noted that the amount of the threshold current in the absence of the magnetic field is concentrated, naturally the threshold current will increase in the presence of the magnetic field.

References

[1] T.P. Wangler et al., RF Linear Accelerator, 2nd edition, John Wile & Sons, 2008.

[2] R.B. Neal, D.W. Dupen, H.A. Hogg, G.A. Loew, The Stanford Two-Mile Accelerator, W.A. Benjamin, Inc., New York, 1968.

[3] W.K.H. Panofsky, "Transient Behavior of Beam Breakup," TN-66-27, Stanford Linear Accelerator Center, Stanford,California, 1966.

[4] W. Gai, A.D. Kanareykin, A.L. Kustov, et al., Numerical simulations of intense charged-particle beam propagation in a dielectric wake-field accelerator, Phys. Rev. E 55 (3) (1997) 3481.

[5] R. Brinkmann, O. Napoly, D. Schulte, Beam-beam instability driven by wakefield effects in linear colliders, in: PACS2001. Proceedings of the 2001 Particle Accelerator Conference (Cat. No. 01CH37268), Vol. 3, IEEE, 2001, pp. 2020–2022.

[6] D. Alesini, C. Biscari, A. Ghigo, et al., Beam instability induced by RF deflectors in the combiner ring of the CLIC test facility and mitigation by damped deflecting structures, Phys. Rev. Spec. Top.-Accel. Beams 14 (2) (2011) 022001.

[7] G.H. Hoffstaetter, I.V. Bazarov, Beam-breakup instability theory for energy recovery linacs, Phys. Rev. Spec. Top.-Accel. Beams 7 (5) (2004) 054401.

[8] W. Lou, G.H. Hoffstaetter, Beam breakup current limit in multiturn energy recovery linear accelerators, Phys. Rev. Accel. Beams 22 (11) (2019) 112801.

[9]Chao, A. W., Physics of Collective Beam Instabilities in High Energy Accelerators, John Wiley & Sons, 1993; and Coherent instabilities of a relativistic bunched beam, SLAC Summer School, AIP Conf. Proc. 105, 353 (1982).

[10]P.M. Lapostolle and A.L. Septier, "Linear Accelerators", North-Holland Publishing Company, 1970, pp. 190–192.

[11]Haimson, J., & Mecklenburg, B. (1992, April). Suppression of beam-induced pulse-shortening modes in high-power rf generator TW output structures. In Intense Microwave and Particle Beams III (Vol. 1629, pp. 209-219). SPIE.

ICNST 2024
International Conference on Nuclear Science and Technology
6- 8 MAY 2024 | Isfahan, Iran

Predictions of U(5) and O(6) dynamical symmetries for normal and intruder energy levels of 116Te nucleus (Paper ID : 1579)

Akbari S[1*], Poursharif F [1], Fouladi N [1] , Sabri H [1]

[1]*Department of Physics, University of Tabriz, P.O. Box 51664-16471, Tabriz, Iran*

Abstract

This paper presents a theoretical investigation on the energy levels of ground and excited bands of ^{116}Te nucleus in the framework of two different dynamical symmetry limits of interacting boson model. To this aim and due to the number of protons of this nucleus in the vicinity of Z=50 closed shell, the U(5) dynamical limit is choice and all the levels up to 10_1^+ are labeled by using the quantum numbers of this symmetry chain. Then, the parameters of energy formula in this limit are extracted by using least square fitting procedure in The MATLAB software in the comparison with the latest available experimental data.Theoretical predictions of U(5) formalism show great deviation in comparison with their experimental counterparts and only, describes $4_3^+ \& 8_1^+$ levels with high accuracy. On the other hand, selected levels are labeled by using the quantum numbers of O(6) dynamical limit chain and the parameters of energy formula of this limit have extracted by same process. The results of this dynamical limit for different energy levels are in satisfactory agreement with empirical data. The results suggest the ^{116}Te nucleus as a candidate for O(6) dynamical limit which $4_3^+ \& 8_1^+$ levels are the U(5) intruder levels.

Keywords: Intruder levels_ O(6) dynamical symmetry_ U(5) dynamical symmetry_ Interacting Boson Model (IBM).

INTRODUCTION

Investigation on the nuclear structure and levels can be considered as the main interesting topic in nuclear physics[1]. Tellurium isotopic chain due to their location in the vicinity of z=50 closed proton shell are regarded as a candidate for spherical nuclei which correspond to the U(5) dynamical symmetry of the Interacting Boson Model[4][2,3]. The existence of some levels that cannot described exactly by the predictions of the U(5) dynamical symmetry, forced us to consider another dynamical symmetry such as O(6) to suggest better predictions for these

[4] IBM

intruder levels[4]. This choice is equal to the combination of the mix of N and an N+2 bosons space which are usually used in the shell model for similar situations. In this manner the N boson space corresponds to the U(5) dynamical symmetry and N+2 corresponds to the O(6) dynamical symmetry[5]. Sometimes using the electromagnetic transitions increases our ability for a more exact description of intruder states, but due to the lack of enough experimental data on the transition rate of ^{116}Te, we only concentrate on the energy levels [6-8]. Mixing different symmetries and using predictions of different theoretical frameworks increase our insight into the nuclear structure and therefore in this paper we consider the energy levels of ^{116}Te in the framework of two isolated U(5) and O(6) dynamical symmetries.

RESEARCH THEORIES

In 1974, Arima and Iachello have been proposed a nuclear model called the interacting boson model [9]. This model is a combination of the shell model and collective model, in such a way that it describes the spin of levels from the structure of the shell model and the shape from the structure of the collective model. In its simplest form, this model is a two-level interacting boson model that examines the behavior of the nucleus based on the interaction of s and d bosons [10,11]. The s-d boson system is described as a 6-dimensional space with the structure of the algebraic group U(6) [12]. Nuclear systems have symmetrical and rotational characteristics. The rotation symmetry group is equivalent to SO(3). There are several modes to get from U(6) to SO(3) each mode has several subgroups. We have three suitable chains which are called symmetric limits:

$$\begin{cases} U(6)\supset U(5)\supset \mathrm{SO}(5)\supset \mathrm{SO}(3) & \text{(I)} \\ \quad N \quad n_d \quad \tau \quad n_\Delta \quad L \\ U(6)\supset \mathrm{SU}(3)\supset \mathrm{SO}(3) & \text{(II)} \\ \quad N \quad (\lambda\ \mu) \quad K' \quad L \\ U(6)\supset \mathrm{O}(6)\supset \mathrm{O}(5)\supset \mathrm{SO}(3) & \text{(III)} \\ \quad N \quad \sigma \quad \tau \quad \upsilon_\Delta \quad L \end{cases}$$

U(5) dynamical symmetry:

The first chain of symmetry is called U(5) dynamical symmetry and corresponds to the spherical or vibrational state of the nucleus [13,14]. In the U(5) dynamical symmetry we label

different levels by using the $|N, n_d, \tau, L\rangle$ quantum numbers which N is the total boson numbers, n_d is the number of d bosons that $n_d = N, N - n_s$. τ is the seniority quantum number that $\tau = n_d, n_d - 2, \dots, 1\ or\ 0$. L is the amount of angular momentum that $L = 2\lambda, 2\lambda - 2, \dots \lambda + 1, \lambda$.

If we have the same L for n_d, N, and τ, it will cause the degeneracy states, which we use n_Δ and n_β to break degeneracy:

$$n_d = 2n_\beta + 3n_\Delta + \lambda \quad Or \quad n_d = (n_d - \tau) + 3n_\Delta + \lambda \tag{1},$$

that n_Δ is the number of triplet d bosons pairing together and creating zero angular momentum; $n_\Delta = 0,1, \dots$ and n_β is the number of d bosons that are coupled together and creating zero angular momentum

that $n_\beta = \frac{(n_d - \tau)}{2}$.

The Casimir operator is used to write the Hamiltonian of the chain:

$$H = AC_{1U5} + BC_{2U5} + CC_{2O5} + DC_{2O3} \tag{2}$$

and the energy values corresponding to the Hamiltonian are obtained as follows:

$$E = E_0 + An_d + Bn_d(n_d + 4) + C\tau(\tau + 3) + DL(L + 1). \tag{3}$$

SU(3) dynamical symmetry:

The second chain, SU(3) dynamical symmetry, is used to describe the rotational states of the deformed nuclei [15,16].

O(6) dynamical symmetry:

This chain describes the axially deformed nuclei [17,18]. In the O(6) dynamical symmetry we label different levels by using the $|N, \sigma, \tau, L\rangle$ quantum numbers which σ is the quantum number that is the eigenstate of the Casimir operator in the O(6) subgroup and is defined as follows according to the quantum number N; $\sigma = N, N - 2, N - 4, \dots, 1\ or\ 0$. τ is the seniority quantum number corresponding to subgroup O(5) and is defined as $\tau = \sigma, \sigma - 1, \dots 0$, $\tau = 3\upsilon_\Delta + \lambda$, that υ_Δ is a quantum number using to break the degeneracy states; $\upsilon_\Delta = 0,1, \dots$.

The Casimir operator is used to write the Hamiltonian of chain:

$$H = AC_{2O6} + BC_{2O5} + CC_{2O5} \quad (4)\,,$$

The energy values corresponding to the Hamiltonian are obtained as follows:

$$E = E_0 + A\sigma(\sigma+4) + B\tau(\tau+3) + CL(L+1). \quad (5).$$

Results and discussion

In this article, we consider the low-lying states of the ^{116}Te nucleus and label them with quantum numbers of the U(5) and O(6) dynamical symmetry limits of IBM. The quantum numbers of U(5) dynamical symmetry for our considered nucleus are presented in Table 1.

Table 1. Quantum numbers of U(5) dynamical symmetry for low-lying states of ^{116}Te nucleus with total boson number N=8.

Levels	n_d	n_s	τ	n_Δ	n_β	L
0_1^+	8	0	0	0	4	0
2_1^+	7	1	1	0	3	2
2_2^+	8	0	4	1	2	2
4_1^+	8	0	2	0	3	4
4_2^+	7	1	5	1	1	4
4_3^+	8	0	8	2	0	4
6_1^+	7	1	3	0	2	6
6_2^+	8	0	6	1	1	6
8_1^+	8	0	4	0	2	8
10_1^+	7	1	5	0	1	10

Similarly the quantum numbers of O(6) dynamical symmetry for low-lying states of ^{116}Te nucleus are presented in Table 2.

Table 2. Quantum numbers of O(6) dynamical symmetry for low-lying states of ^{116}Te nucleus with total boson number N=8.

Levels	σ	τ	v_Δ	L
0_1^+	0	0	0	0
2_1^+	2	1	0	2
2_2^+	4	1	0	2
4_1^+	2	2	0	4
4_2^+	4	2	0	4
4_3^+	6	2	0	4
6_1^+	4	3	0	6
6_2^+	6	3	0	6
8_1^+	4	4	0	8
10_1^+	6	5	0	10

By using the quantum numbers of U(5) dynamical symmetry and Eq. (3) in MATLAB software, we have extracted the constants of this equation. In the next step, by using the parameters of Eq. (3), and appropriate labels for low-lying states of ^{116}Te nucleus, the energy levels are determined. The theoretical energy that we obtained from the U(5) dynamical symmetry limit, compared to the experimental energy values that are taken from Ref. [19], are presented in Table. 3. For the studied levels, the theoretical energy values obtained from the U(5) dynamical symmetry in comparison with the experimental energy, which are taken from Ref. [19], are shown in Figure.1.

Table 3. The theoretical predictions of U(5) dynamical symmetry in comparison with experimental energy for levels of ^{116}Te nucleus. Coefficients of energy values in Eq. (3), which are extracted by the least-square fitting procedure in MATLAB, are A=214.4607, B=−14.1754, C=10.4440 and D=37.5072.

Levels	$E_{exp}(KeV)$	$E_{U(5)}$
0_1^+	0.00	0.00
2_1^+	678.92	321.69
2_2^+	1719.10	517.47
4_1^+	1359.39	854.58
4_2^+	1746.00	1222.77
4_3^+	1811.77	1669.21
6_1^+	2002.24	1818.16
6_2^+	2564.05	2139.27
8_1^+	2773.10	2992.95
10_1^+	3574.80	4598.42

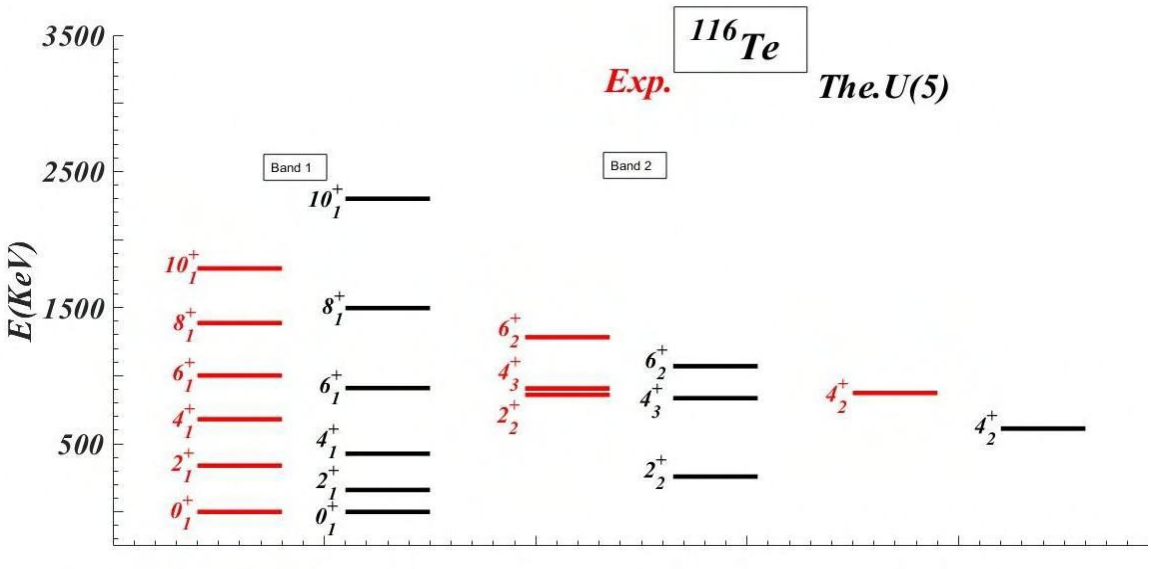

Fig. 1. Comparison between the predictions of U(5) dynamical symmetry for energy spectra of ^{116}Te nucleus and experimental counterparts which were taken from Ref.[19].

On the other hand, we perform similar operations as the same as the U(5) dynamical symmetry for the O(6) dynamical symmetry. The value of energy and its figure to comparison with experimental data, are presented respectively in Table. 4. and Figure. 2.

Table 4. The theoretical predictions of O(6) dynamical symmetry in comparison with experimental energy for levels of ^{116}Te nucleus. Coefficients of energy values in Eq. (5), which are extracted by the least-square fitting procedure in MATLAB, are A=13.5615, B=270.8841 and C= −76.9959.

Levels	$E_{exp}(KeV)$	$E_{O(6)}$
0_1^+	0.00	0.00
2_1^+	678.92	784.29
2_2^+	1719.10	1055.52
4_1^+	1359.39	1331.66
4_2^+	1746.00	1602.89
4_3^+	1811.77	1982.61
6_1^+	2002.24	2076.05
6_2^+	2564.05	2455.77
8_1^+	2773.10	2475.01
10_1^+	3574.80	3179.50

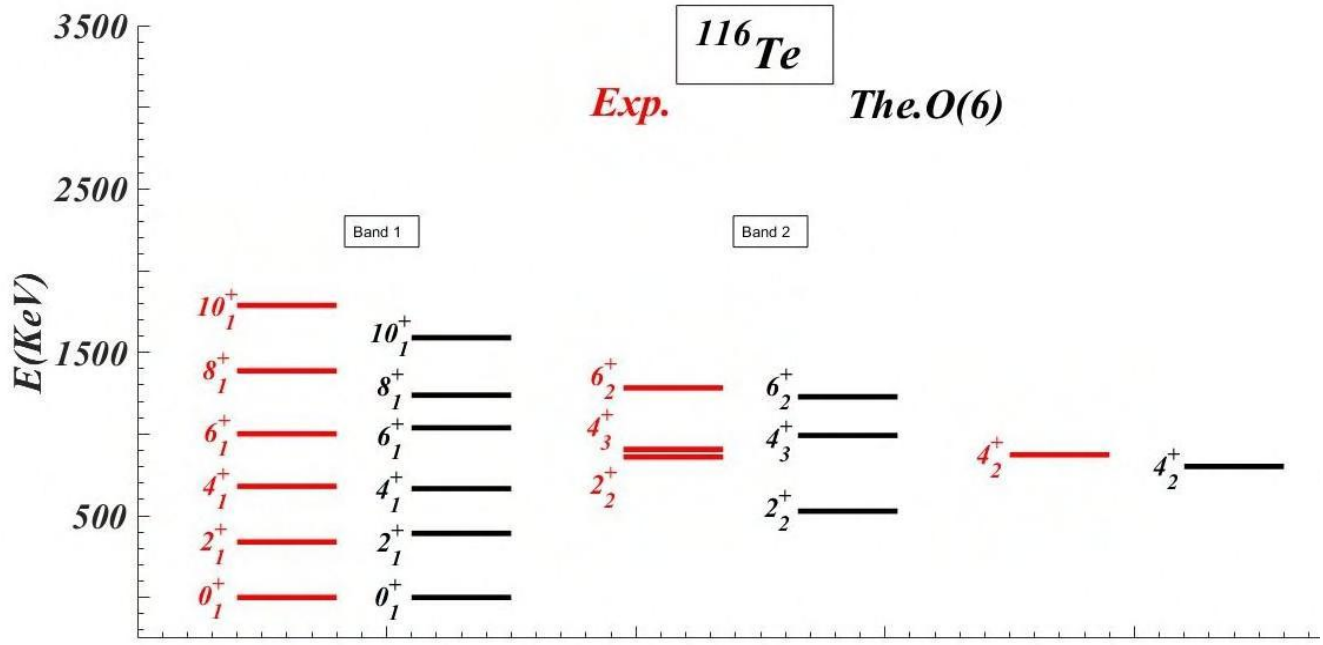

Fig. 2. Comparison between the predictions of O(6) dynamical symmetry for energy spectra of ^{116}Te nucleus and experimental counterparts which were taken from Ref.[19].

In this section the energy levels of low-lying states of the 116Te nucleus, that result from the U(5) and O(6) dynamical symmetry, are investigated in full detail.

The predictions of U(5) dynamical symmetry in the ground state band for $\mathbf{0_1^+, 2_1^+, 4_1^+, 6_1^+}$ and $\mathbf{8_1^+}$ levels are almost in good agreement with experimental counterparts. But by predictions of the U(5) dynamical symmetry, the $\mathbf{10_1^+}$ level, obviously is an intruder level that cannot be well justified. The O(6) dynamical limit is a suitable framework for justifying this level, which gives it appropriately. On the other hand, by examining all levels of the ground state band, for the desired nucleus, it can be seen that the O(6) dynamical symmetry for all of them provides a better justification than the U(5) dynamical symmetry.

For the first excited band, in both dynamical symmetries, the $\mathbf{2_2^+}$ and $\mathbf{4_3^+}$ levels, are well justified. But $\mathbf{6_2^+}$ level, by predictions of O(6) dynamical symmetry is in better agreement with the experimental counterpart. Also, the $\mathbf{4_2^+}$ level in the same conditions as the $\mathbf{6_2^+}$ level, is better described by the O(6) dynamical symmetry. According to the studies for $\mathbf{J \leq 10_1^+}$ levels of the 116Te nucleus, it can be seen that the energy values obtained from the O(6) dynamical symmetry, for most of the levels are in good agreement with the experimental values. But the two 4_3^+ & 8_1^+ levels are considered as intruder levels, which are justified by studies in the U(5) dynamical symmetry limit.

Conclusions

In this article, we studied the low-lying states of the ^{116}Te nucleus in the framework of the U(5) and O(6) dynamical symmetries of IBM. By using the quantum numbers of these symmetry

chains, we labeled the desired levels of this nucleus. With these quantum numbers and energy eigenstate of dynamical symmetry limits, via the least square fitting tool in MATLAB software, the coefficients of Eq. 3 and 5 and the energy levels of ^{116}Te nucleus were obtained. Contrary to the appearance that shows that ^{116}Te is a candidate for U(5) dynamical symmetry, according to the results and observations of this study, we concluded that the ^{116}Te nucleus is an appropriate candidate for O(6) dynamical symmetry. All low-lying states of this nucleus were justified in good agreement with experimental counterparts. Only the $4_3^+ \& 8_1^+$ levels are intruder levels that, predictions of U(5) dynamical symmetry, describe these levels with high accuracy.

Acknowledgements

This work is supported by the affairs research office of the University of Tabriz.

References

[1] Greiner, W. and Maruhn, A. J. (1996). NUCLEAR MODEL, Springer.

[2] Seidi, M and Sabri, H. (2020). The ^{116}Te nucleus as a candidate for U(5) dynamical symmetry. Acta Physica Polonica B. 51.

[3] Von Spee, F. Beckers. M. Jolie, J and etc. (2024). Structure of low-lying states in ^{116}Te . Phys. Rev. C, 109.

[4] Jahangiri, Z and Sabri, H. (2024). Description of intruder levels in the $^{162\,164\,166}$Dy nuclei by two different algebraic approaches. Nuclear Physics A. 1042.

[5] Lisetskiy, A. F. Pietralla, N. Fransen, C. and etc. (2000). Shell model description of "mixed-symmetry" states in ^{94}Mo. Nucl. Phys. A, 100-114.

[6] Cejnar, P and Jolie,J. (2009). Quantum phase transition in interacting boson model. Prog. Part. Nucl. Phys, 62-210.

[7] Cejnar, P and Jolie, J. (1998). Dynamical symmetry content of transitional IBM-1 hamiltonians. Phys Lett B, 241-247.

[8] Sabri, H and Seidi, M. (2016). Energy spectra and E2 transition rates of $^{124-130}$Ba. International Journal of Modern Physics E. 25-10. 17P.

[9] Iachello, F and Arima, A. (1974). Boson symmetries in vibrational nuclei. Phys.Lett.B, 53-309.

[10] Pfeifer, W. (1998). An Introduction to the Interacting Boson Model of Atomic Nucleus, ETH

Zurich.

[11] Feshbach, H and Iachello, F. (1974). The interacting boson model. Annal of physics, 211-231.

[12] Iachello, F. (2006). "Lie Algebras and Applications". Springer-Verlag.

[13] Garrett, P. E . Green, K. L and Wood, j. L. (2008). Breakdown of vibrational motion in the isotopes

$^{110\text{-}116}$Cd. Phys. Rev. C. 78.

[14] Kern, J. Garret, P.E. Jolie, J and Lehmann, H. (1995). Search for nuclei exhibiting the U(5) dynamical symmetry. Nuclear Physics A, 593, 21-47.

[15] Sabri, H. Seidi, M and Poursharif, F. (2021). Investigation of High-Spin states of $^{176-180}Hf$ nuclei by the extended interacting boson model. Eur. Phys. J. Plus. 136: 1149.

[16] Fouladi, N. Fouladi, J and Sabri, H. (2015). Investigation of low-lying energy spectra for deformed prolate nuclei via partial dynamical SU(3) symmetry. Eur. Phys. J. Plus,130-112.

[17] Iachello, F and Arima, A. (1979). Interacting Boson Model of collective nuclear states. The O(6) limit. Annal of physics 123, 468_492.

[18] Mizusaki, T. Otsuka, T. (1996). Microscpic calculation for O(6) nuclei by the interacting boson model.Progress of theoretical. Phys, 97-150.

[19] National Nuclear Data Center (NNDC), Brookhaven National Laboratory,

http://www.nndc.bnl.gov/.

ICNST 2024
International Conference on Nuclear Science and Technology
6- 8 MAY 2024 | Isfahan, Iran

Investigation of the physical parameters of the production of (_^103)Pd radioisotope by the Monte Carlo method (Paper ID : 1638)

Hoseain Hashemi [1], Mojtabi Tajik[1*], Mohammad Mirzaei [2], Hasan Yusefnia [3]

[1] Damghan University, Faculty of Physics and Engineering, Damghan,Iran
[2]Nuclear Science and Technology Research Institute, Agricultural, Medical and Industrial Research Institute, Karaj, Iran
[3] Atomic Energy Organization of Iran, Radiation Application Research Institute, Tehran

Abstract

The production of the ^{103}Pd radioisotope by ^{103}Rh(p,n)^{103}Pd reaction was determined using Monte Carlo simulations and nuclear codes. To verify the accuracy of the results, a comparison was made between the MCNPX2.6 code and the 2013 SRIM, TALYS, PSTAR (NIST) codes and experimental data. The results show that the data obtained with the MCNPX code agrees well with the other codes and experimental data. In the following, the excitation functions and the cross section of ^{103}Pd radioisotope production were calculated using the TALYS codes. The radiation yield was then evaluated using the RYC program based on the mass stopping power data and the excitation functions from the SRIM and TALYS codes. The results and data obtained confirmed the accuracy of the process in evaluating the production of the ^{103}Pd radioisotope. Overall, the use of Monte Carlo simulation and nuclear codes provided valuable insights into the production process of the ^{103}Pd radioisotope. The agreement between the MCNPX code, other codes and experimental data further strengthens the reliability of the findings. By employing TALYS codes and the RYC program, the excitation functions, cross section, and radiation yield were successfully determined, ensuring the accuracy of the evaluation process.

Keywords: Proton range, ^{103}Pd radioisotope, MCNPX2.6 code, reactions cross section, stack foil technique.

INTRODUCTION

Nuclear radiation and its study are important in all areas of life. In this field we can refer to radiotherapy, brachytherapy, medical imaging, quality control and sterilization. One example of these applications is therapeutic radioisotopes, which have long been of interest to researchers and cancer treatment centers. One of these useful radionuclides, ^{103}Pd with a half-life of 16.96 days, is produced by the decay of ^{103}Rh ($T_{\frac{1}{2}}$ =56.1min as EC by an experimental method in a proton accelerator. This radionuclide is used as a suitable alternative to

radionuclide ^{125}I for the treatment of melanoma eye cancer. Sudar et al. have investigated the production of the radioisotope ^{103}Pd in two proton and deuteron accelerators in the energy range from 0 to 40 MeV [1]. Herman et al. theoretically investigated the production method of ^{103}Pd using a proton beam with models of ^{103}Pd grains with an energy of 0 to 30 MeV [2].

Sadeghi et al. have investigated the dose in the eye phantom using the experimental method and the Monte Carlo method [4]. Other researchers have dealt with the optimization of the cooling system during proton bombardment, which increases the temperature of the target material, and the target system for the production of the radioisotope ^{103}Pd [5, 6]. To evaluate the production of ^{103}Pd in a system with targeting, we consider a proton beam with energies from 0 to 30 MeV. Using the MCNPX multipurpose code, the stopping power and range of protons in the target material and other materials were calculated [7]. In this article, the proton stopping power was calculated in materials such as rhodium, aluminum, copper, titanium and water in the energy range from zero to 30 MeV. At the end of, by determining the energy of incident protons on the cross-sectional area of the reaction in terms of functions on the excitation of protons with the said materials and thickness of ^{103}Rh with the stopping power and specific area, and the production yield of ^{103}Pd radioisotope was calculated.

RESEARCH THEORIES

For the simulation with the MCNPX code in this study, the geometry of the fountain was defined as one-sided isotropic. The collimator section with a length of 40 cm, the entrance side of the particles with a diameter of 3 cm and the other side with a diameter of 1 cm, i.e. where the protons exit, was considered according to Figure 1. In this design, the arrangement of the target materials under proton bombardment is shown in the form of stacked foils with an angle of 90 degrees to the proton exit beam. (According to the real target model with a thickness of 550 μm, it was.) as compressed and placed between aluminum and copper sheets, and water was placed behind the copper. as a coolant Oxygen and vacuum were considered.

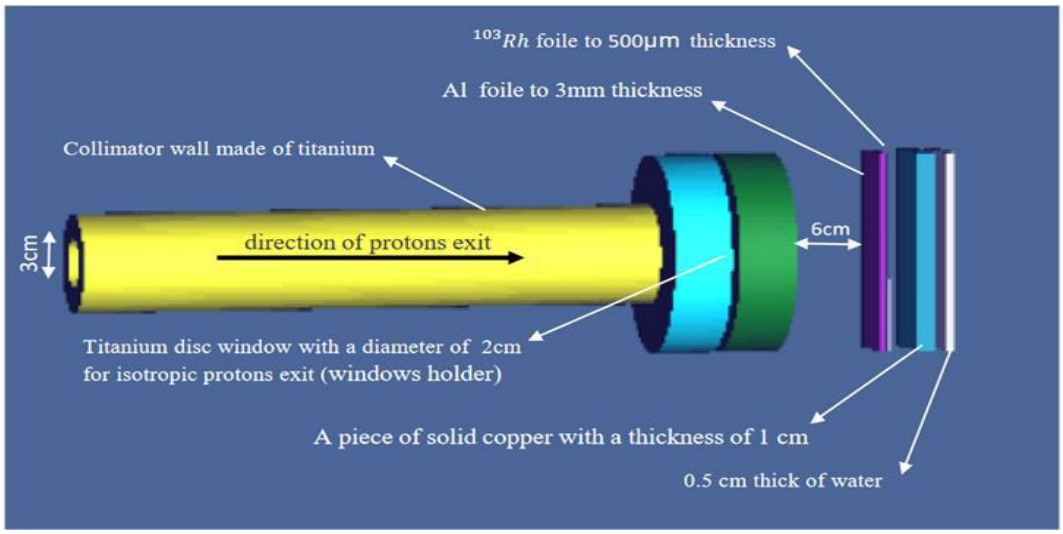

Figure .1. 3D view of the dimensions and simulated geometry of the proton accelerator collimator using the MCNPX code.

In fig. 2 (a) and (b) you can see the track of the ions when you remove the Holder window from this simulation and insert it into the acceleration system. Fig. 2 (b) A titanium foil window with a thickness of 50μm is located on the side of the proton exit, so that the proton beam is converted into a concentrated and isotropic form while maintaining the vacuum in the system, and the target material can be irradiated in an optimal and focused manner.

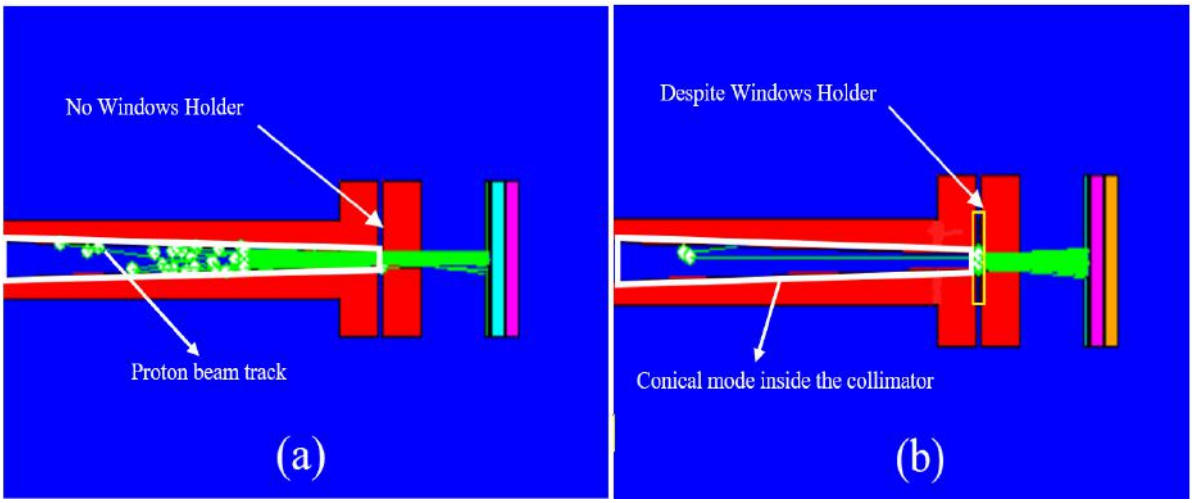

Figure .2. 2D view in the xz plane of Holder Window simulation in proton accelerator using MCNPX code

In order to produce targets with optimized thickness, it is necessary to investigate the range of the proton particles in the target. For this purpose, the proton stopping power in this design was calculated for different thicknesses of the target material. The relationship S=-dE/dx is used, which gives the energy loss per unit length of the path, or in other words, the average energy

lost by the charged particle per unit length of the path [9]. The mass stopping power is is equal to:

$$\frac{1}{\rho}.\mathbf{S_{Proton}} = -\left(\frac{dE}{dX}\right)_{Proton} = N_a Z \int_{w_{min}}^{W_{max}} m\left(-\frac{dE}{dX}\right) dW = -\frac{1}{\rho}.\frac{dE}{dX} = \frac{S}{\rho} \ (MeV/g) \quad (3)$$

In these calculations with the code MCNPX2.6, the flux distribution per unit volume of material from tally F4 (PARTICLE/CM^2) and the absorbed energy per unit volume of material from tally F6 (MeV/g) are determined and related to the relationship for the mass stopping power And we have the proton range:

$$\textbf{Stopping Power} = \frac{\text{Taly F6}}{\text{Taly F4}} = \frac{S}{\rho}\left(MeV.g^{-1}.cm^2\right) \quad (4)$$

$$\text{Range}=\int_0^E \frac{1}{-\frac{dE}{dX}}.dE\,(g/cm^2) = \int_0^E \frac{1}{\frac{\text{Taly F6}}{\text{Taly F4}}}.dE\,(g/cm^2) \quad (5)$$

In order to fitting the data obtained from the MCNPX 2.6 code with the data of SRIM and etc derived from the mathematical equation of fitting a square line for the stopping power and range of protons respectively:

$$(\text{Stoping power})_{\text{fitting}} = 206{,}7\left(\frac{\text{Taly F6}}{\text{Taly F4}}\right)^{-0{,}78} \quad (6)$$

$$(\text{Range})_{\text{fitting}} = 0{,}0023\left(\int_0^E \frac{1}{\frac{\text{Taly F6}}{\text{Taly F4}}}, dE\right)^{-1{,}75} \quad (7)$$

In this study, excitation distribution functions and cross sections for proton interactions and ^{103}Pd radioisotope production yield were investigated using the code TALYS, whose calculations are based on nuclear models (optical model). Using the Yield Radiation Calculation (YRC) program, which uses the experimental library data of the tendl 2015 proton file, the calculations are performed with the mass stopping power values and the results of the TALYS code. At the end, the experimental calculation results of other works were compared for the yield radiation and YRC [13].

Results and discussion

The codes TALYS, ALICE and YRC are used to calculate physical data such as the cross section, the excitation function and the production yield [11-13]. In this work, the reaction cross section of $^{103}\text{Rh}(p,n)^{103}\text{Pd}$ was calculated using the core codes Alice and Talys in the form of excitation functions.They take into account the results obtained with the theoretical, experimental and other

researchers data for the radioisotope ^{103}Pd and maximise the value of the cross section area of 729.87 mbarn with Gaussian fitting in Figure 3. The optimal energy range for the production of this radionuclide is in the range between 5 and 18 MeV (i.e. if the target consists of ^{103}Rh with an approximate thickness of 550 μm and a proton beam is bombarded with an energy of 18 MeV, the output energy is about 5 MeV). Considering that the optimum beam energy was determined during the reaction of $^{103}Rh(p,n)^{103}Pd$ on the rhodium target. According to Figs. 3 and 8 and by studying and checking the results of the stopping power, the area of the protons and the surface of the reaction cross-section should be selected to choose the optimal thickness of the 550 μm rhodium target for irradiation and production of the radioisotope ^{103}Pd. In these calculations, by comparing the reaction cross sections of $^{103}Rh(p,n)^{103}Pd$ in Figure.3 from both experimental methods and the results of this work with the research of Herman, Sudar, Harper et al have a relatively good agreement and to study the production of ^{103}Pd radioisotope in the energy range of 0 to 40 MeV [1-3].

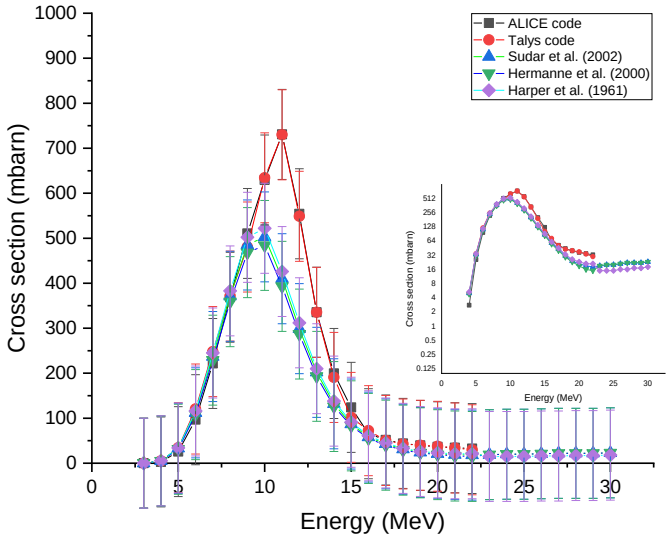

Figure. 3. The results of Talys and Alice codes and experimental and other theoretical data of reaction cross section $^{103}Rh(p,n)^{103}Pd$

The Calculation of the mass stopping power and projectile range for proton interaction with ^{103}Rh in $^{103}\mathrm{Rh}(\mathrm{p},\mathrm{n})^{103}\mathrm{Pd}$ reaction was performed with the codes SRIM and MCNPX2.6. The energy range of accelerator is between zero and the maximum energy of 30 MeV. The proton stopping force was determined from the above calculation relations for this reaction. In Figure 1, the stopping power increases with decreasing energy, indicating the interaction of protons with matter and the accuracy of the data according to Bethe-Bloch theory. For the range of protons in ^{103}Rh from zero to 1.3 mm (1300 μm) in the same energy range according to Fig. 4, as the energy increases, the penetration depth of the protons also increases, and as the proton energy increases, the stopping power also decreases. Based on the values obtained from the range of protons in the above materials, the results show that as the thickness of the target increases, more energy is required for the proton to have the optimum landing energy and exit energy from the target. It is clarified that the calculated values for mass stopping power and range of protons in the reaction with ^{103}Rh are not reported in publications as well as international databases such as PSTAR(NIST) and other researchers, and in this work the results were validated with the MCNPX code and the SRIM code 2013[17, 18].

Mass stopping power and range of protons were studied in ^{27}Al and water, in Figures 5 and 6 the

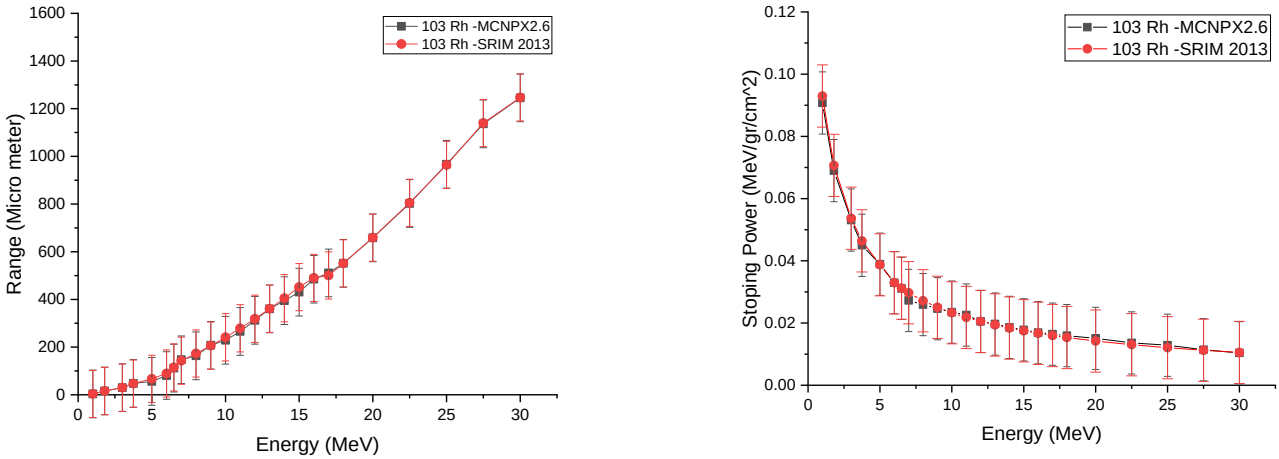

Figure. 4. Proton beam stopping power and range in^{103}Rh using MCNPX code and SRIM 2013 code

results of numerical calculations fitted with the MCNPX code and values obtained from SRIM and NIST are in good agreement. error resulting from the calculations of this code is estimated to be less than 0.01 for 10^8 particles. Findings for stopping power and range obtained from SRIM are in relatively good agreement compared to the present simulation results. In order to briefly compare the stopping power and range of protons in the materials and the results using the MCNPX code are summarized in Figure.7, which decreases with increasing energy. results

at energies below 10 MeV show the highest mass stopping power for water 0.24 $^{\mathrm{MeV}}/_{\mathrm{g}}.\mathrm{cm}^2$ and for ^{103}Rh 0.09 $^{\mathrm{MeV}}/_{\mathrm{g}}.cm^2$ and show The reason for the dependence of the mass stopping power for projectile on the atomic properties of the material is that stopping power decreases with increasing energy. These results are valid and true according to Bethe-Bloch theory [8]. For the range of protons in materials, in the article by Bose Court, using the GATE 4 code, a similar result has been obtained for the interaction of protons with water [10].

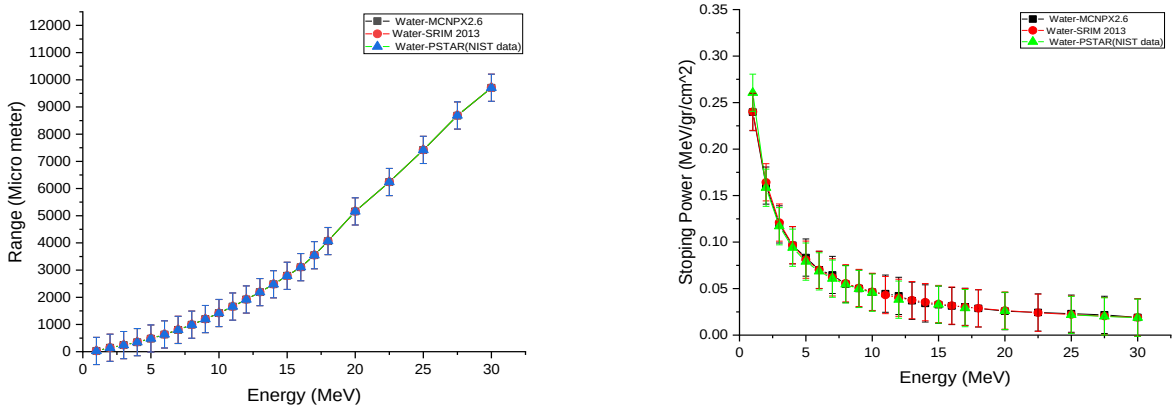

Figure .5. The stopping power and beam range of protons in water using MCNPX, SRIM 2013 and PSTAR codes

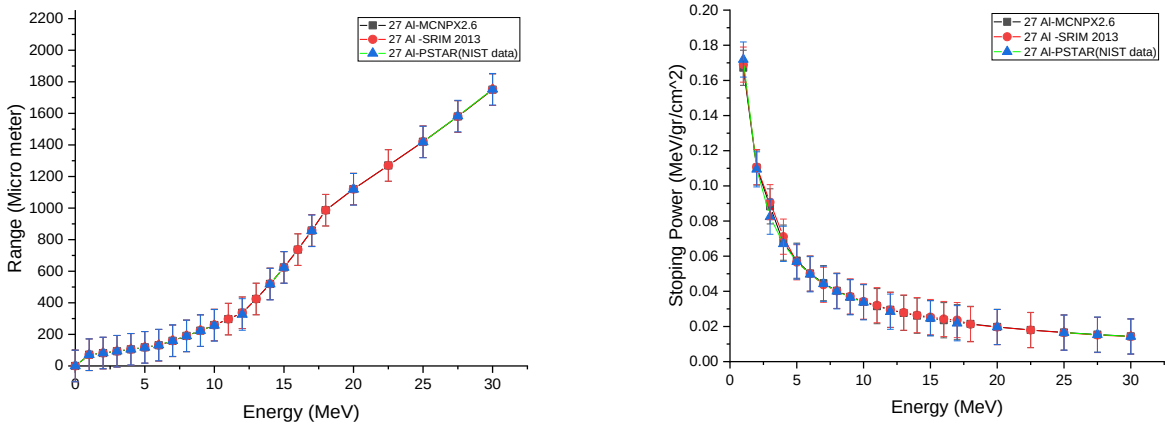

Figure .6. The stopping power and beam range of protons in ^{27}Al using MCNPX, SRIM 2013 and PSTAR codes

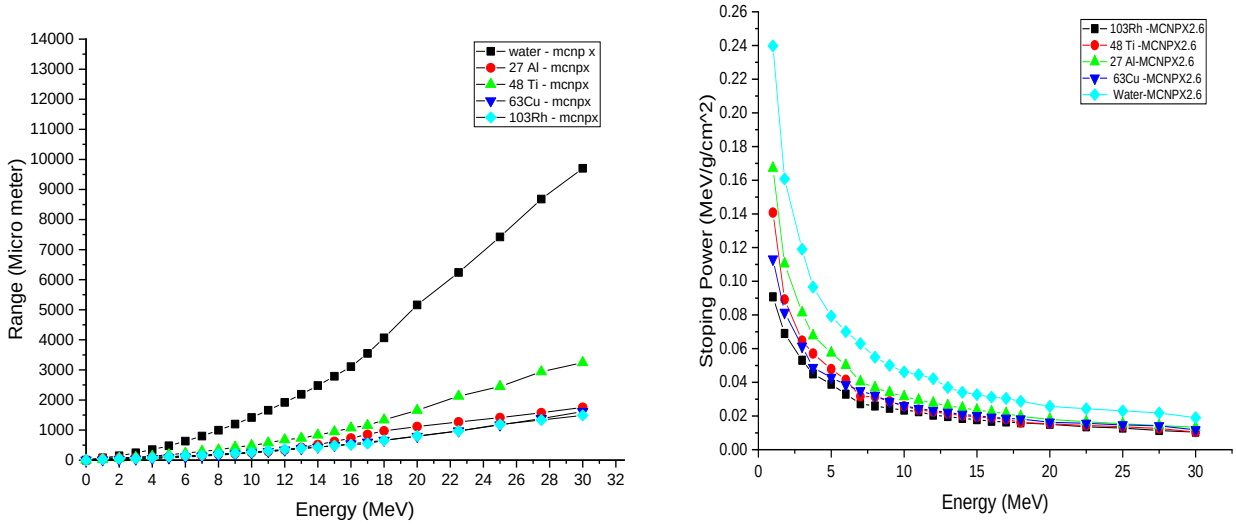

Figure. 7. stopping power and beam range of protons in water, ^{103}Rh, ^{63}Cu, ^{27}Al and ^{48}Ti using MCNPX code

In order to determine the energy of protons and ideal production threshold energy in the stack foil method, energy correction should be done in order to avoid the production of isotopic pollution in the collision of proton beams passing through the main target and other materials while determining the exact energy applied to the accelerator. This issue was investigated using the MCNPX code(*F1 Taly results) for the incident and output energies of the stacked foil layers according to Figure.1 and the results are collected in Table. 1 According to the data protons obtained by irradiating with an energy of 30 MeV and passing through a layer of aluminum foil with a thickness of 3 mm, the energy of the protons hitting the rhodium surface with a thickness of 550 μm is about 23.1 MeV, and the energy of the beam coming out of 5.7 MeV it is, which is at the level of contact with copper, and when it passes through a copper foil with a thickness of 5 mm, its output energy becomes almost zero, which does not produce isotopic impurity for energies less than 5 MeV according to figures 8 to 11 to be. Because it is below the threshold energy of their production, and by correcting this energy, we do not witness the production of pollution of other isotopes of copper, etc. In this simulation for all of calculation s relative error is less than 0.01 %.

Table. 1. Evaluation of the energy of incoming and outgoing protons between different layers of stacked foils *F1 Taly results using MCNP code

Target material	*Thickness*	*Angle of protons beam*	*Incident proton energy energy*	*Output proton*
Titanium(WINDOWS HOLDER)	50 µm	90°	28 MeV	26.3 MeV
Aluminium	3 mm	90°	26.3 MeV	23.1 MeV
Rhodium 103	550 µm	90°	23.1 MeV	5.7 MeV
Copper	1 cm	90°	5.7 MeV	0
Water	5 mm	90°	0	0

To describe the process of nuclear reactions and what is the reaction mode and which isotopes are produced during and after proton bombardment (EOB). The interaction of proton with other materials of the environment around the targeting system was investigated. Reactions of $^{63}\mathrm{Cu(p,xn)}^{62}\mathrm{Cu}$, $^{27}\mathrm{Al(p,xn)}^{28}\mathrm{Si}$ and $^{48}\mathrm{Ti(p,np)}^{47}\mathrm{V}$, $^{48}Ti(p,n)^{48}V$ was checked using the TALYS code and the data of the isotope abundance tables in order to determine the amount of impurities and isotopic contaminations, if any, in addition to the analysis of the reaction cross-section [14]. According to the results obtained from the reaction of $^{103}\mathrm{Rh(p,n)}^{103}\mathrm{Pd}$, the possibility of impurity production is the isotope $^{101}\mathrm{Rh}$ with a half-life of 207 days and the emission of β^+ and β^-, isotope $^{102\mathrm{m}}\mathrm{Rh}$ with a half-life of 4.34 days emits gamma rays with an energy of 157.32 KeV and internal conversion, and since this isotope can be produced in deuteron accelerator bombardment, Therefore, in the energy range of zero to 25 MeV, the results of the Thales code cannot be seen. Isotope $^{103}\mathrm{Rh}$ in the ground state and without excited state, isotope $^{101}\mathrm{Pd}$ with a half-life of 8.47 hours and emission of β^+ radiation and electron, $^{102}\mathrm{Pd}$ is also in the ground state. Figure.8 shows the results of impurity production after 10 MeV energy range. Similar results have been obtained in theoretical and experimental research by Webster et al [15].

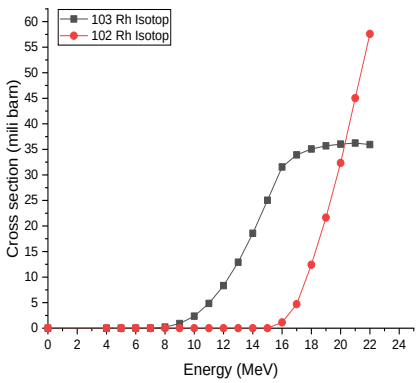

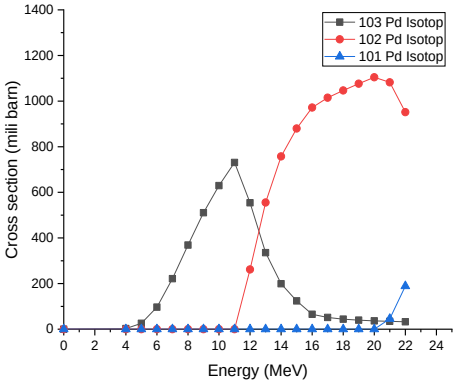

Figure.8. The results of the Talys code for the reaction cross section $^{103}\mathrm{Rh(p,n)}^{103}\mathrm{Pd}$, $^{103}\mathrm{Rh(p,3n)}^{101}\mathrm{Pd}$, $^{103}\mathrm{Rh(p,2n)}^{102}\mathrm{Pd}$, $^{103}\mathrm{Rh(p,d)}^{102\mathrm{m}}\mathrm{Rh}$

The probability of the reaction of $^{48}\mathrm{Ti(p,np)}^{47}\mathrm{V}$, $^{48}Ti(p,n)^{48}V$ proton and ^{48}Tito produce vanadium radioisotopes is shown in Figure.9 and according to The cross-sectional results of these reactions are in the ground state, but in the excited state, they will only have decay of β^+ particle. Figure.10 of $^{27}\mathrm{Al(p,xn)}^{27}\mathrm{Si}$ reaction shows the possibility of production of ^{26}Si and ^{27}Si isotopes, which in the excited state only by decay β^+ is associated and does not create isotopic impurity. In the cyclotron system, protons interaction with titanium due to the absence of an excited state and the absence of X-ray or gamma radiation spectrum, therefore, titanium is used in the construction of accelerators.

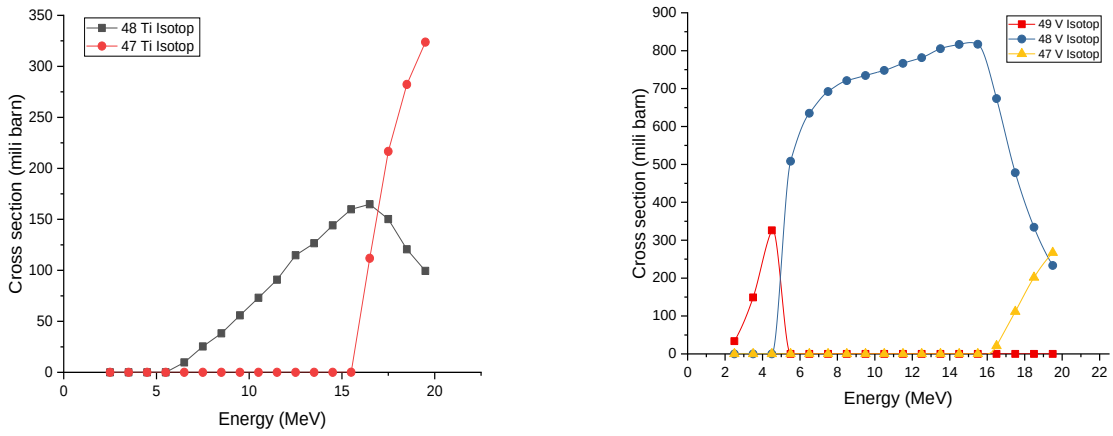

Figure.9. The results of Talys code for the $^{48}\mathrm{Ti(p,np)}^{47}\mathrm{V}$, $^{48}Ti(p,n)^{48}V$ reactions cross section

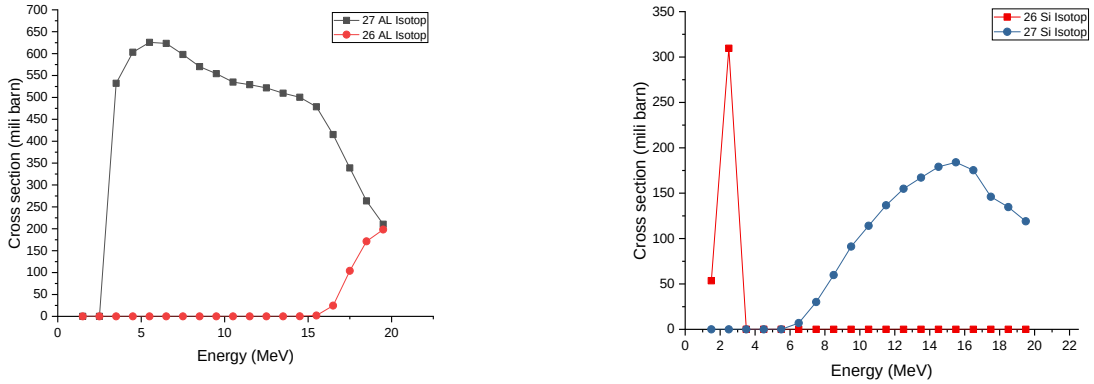

Figure.10. The results of the Talys code for the $^{27}\mathrm{Al(p,d)}^{26}\mathrm{Si}$, $^{27}\mathrm{Al(p,n)}^{27}\mathrm{Si}$ reactions cross section

According to Figure.11, the interaction of proton with ^{63}Cu at an energy higher than 16 MeV leads to the production of ^{62}Cu isotope, which has an excited state and emits beta and gamma particles. Another isotope resulting from this interaction is ^{64}Zn which has a stable state and ^{63}Zn which has decay β^+ but to . As a result, copper should not be placed as the first layer on ^{103}Rh to design the target in the targeting system of the accumulated foil method for proton bombardment. Because it causes radioisotope pollution in the production process of ^{103}Pd and the purification and separation process will be complicated and costly.

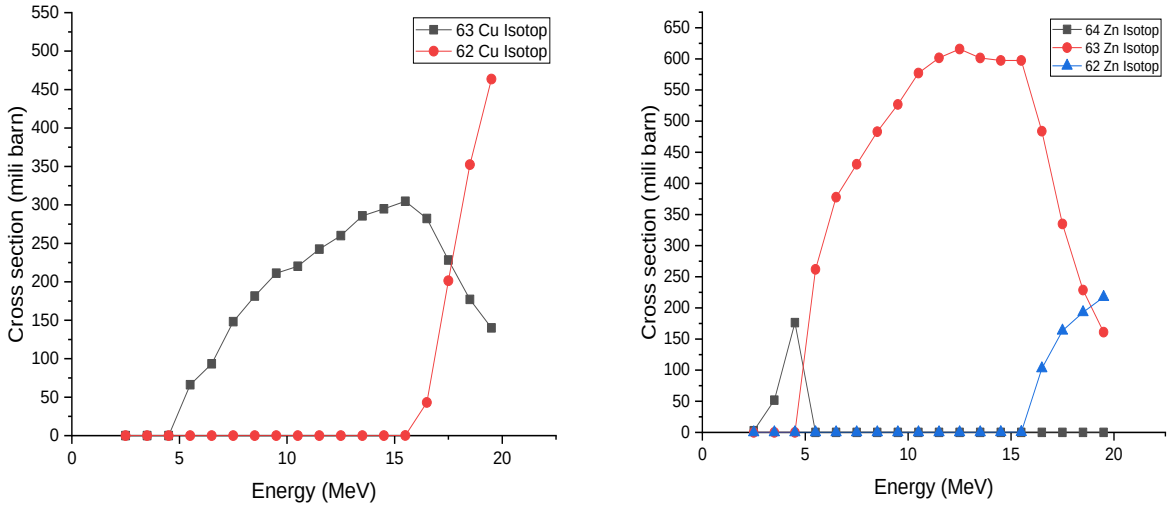

Figure. 11. The results of the Talys code for the reaction cross-section of $^{63}Cu(p,xn)^{62}Cu$ and $^{63}CU(p,x)^{62}Zn$

In this work, in order to evaluate the yield of ^{103}Pd isotope production derived from the Talys code and its calculations based on nuclear models (optical model) with the help of the YRC program, which is based on experimental data from the tendl 2015 proton file library, the calculations are made using the mass stopping power values. And results from the TALYS code do it. Calculations were made to calculate the yield of $^{103}Rh(p,n)^{103}Pd$ reaction. The numerical values of the production yield obtained from this work are similar to the production yield of the thick target obtained by the work of Sudar et al and compared to the values obtained from the results of the study by Herman and his colleagues for the production yield of ^{103}Pd and the investigation of the reaction of $^{103}Rh(p,2n)^{103}Pd$ using a deuteron accelerator and a thick target ^{103}Rh in the same energy range from zero to 30 MeV, the amount of

production gain in the proton accelerator is lower than in the deuteron accelerator [1, 16]. At 20 MeV energy, the present work (7.45 MBq/eμAh) yield is slightly lower than the value of 1.8 MBq/eμAh calculated by Sudar et al. As a result, the production gain obtained from this study is in good agreement with the research of Sudar et al. These results can be seen in Fig.12. [1, 2].

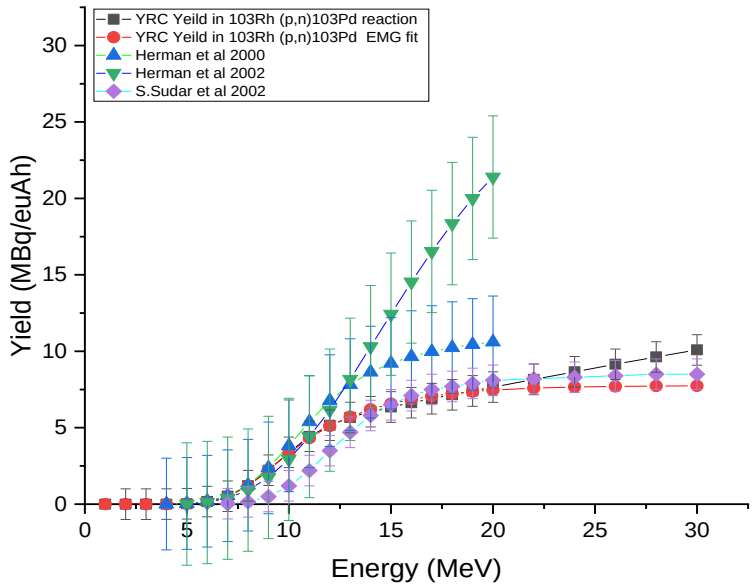

Figure.12. Comparison of the results of ^{103}Pd isotope production using YRC and the results of other researchers

Conclusions

To investigate the production probability of ^{103}Pd , the possible reaction cross section was determined using the Talys and Alice codes for protons, and the probability of contamination of other isotopes was also analyzed using the Talys code. According to the interaction cross section for impure isotopes, ^{102m}Rh is formed and can be isolated by chemical experimental methods, the ^{102}Cu isotope in the design of the target as a thick solid and the ^{103}Rh layer on it causes isotopic impurities, which will make the process It will make the separation time-consuming and complicated, it is proposed to make corrections in the design of the target and irradiated materials instead of this irradiation method, this problem still has a place for work and study in the production of the isotope ^{103}Pd . Finally, the yield of ^{103}Pd production was validated using international data and the available Talys and YRC codes. The calculations

show the agreement and concordance of the data obtained in this work with the research results of others and also the validity of the method used to study the production of ^{103}Pd .

References

[1] S.Sudar, F.Cserpak, S.M. Qaim "Measurements and nuclear model calculations on proton induced reactions on 103Rh up to 40 MeV: evaluation of the excitation function of the 103Rh(p,n)103Pd reaction relevant to the production of the therapeutic radionuclide 103Pd " Applied Radiation and Isotopes 56 821–831(2002).

[2]A.Hermanne, M.Sonck, A.Fenyvesi "Study on production of 103Pd and characterisation of possible contaminants in the proton irradiation of 103Rh up to 28 MeV" Nuclear Instruments and Methods in Physics Research B 170 281-292(2000).

[3] Harper, P.V, Lathrop,K.Need,"The thick target yield and excitation function for the reaction 103Rh(p,n)103Pd, ORNL-LR-DWG"51564 124 (1961).

[4] Pooneh Saidi, Mahdi Sadeghi, Claudio Tenreiro "Experimental measurements and Monte Carlo calculations for 103Pd dosimetry of the 12 mm COMS eye plaque " Physica Medica 29, 286e294 (2013).

[5] I. Silverman, E. Lavie, A. Arenshtam, D. Kijel “Study on production of 103Pd and characterisation of possible contaminants in the proton irradiation of 103Rh up to 28 Me" Nuclear Instruments and Methods in Physics Research B 261 747–750 (2007).

[6] J. Y. Kim, J. H. Kim, H. Park, J. S. Lee, K. S. Chun " Production of 103Pd Radioisotope by Using Cyclotron "Transactions of the Korean Nuclear Society Spring Meeting Jeju, Korea, May 10-11 (2007)

[7] Denise.B.Pelowitz,editor."MCNPXTM USER MANUALVersion2.6.0" LA-CP-07-1473 (2008).

[8] N J Carron "An Introduction to the Passage of Energetic Particles through Matter "ATK Mission Research Corporation Santa Barbara, California, USA 220-245 (2007).

[9] Olaseni M. Bello “ The Lung and Soft Tissue Stopping Power Estimates for a Modified Phantom Using MCNPX "International Journal of Innovative Science and Research Technology (2020) .

[10] Ahmet Bozkurt "Monte Carlo calculation of proton stopping power and ranges in water for therapeutic energies "EPJ Web of Conferences 154, 01007 (2017).

[11] A. Koning, S. Hilaire " Nuclear reaction calculations with the TALYS code" XII International Symposium on Nuclei in the Cosmos 5-10 Cairns, Australia August (2012).

[12] Herbert Blann, A. A. Konobeev " Manual for Code Alice" version July 7, (2008).

[13] Mateusz Sitarz, "Radionuclide Yield Calculator (version 2.0) MANUAL" (2018).

[14] http://nucleardata.nuclear.lu.se/toi/listnuc.asp.(2022)

[15] William.D. Webster , GeoffreyT. Parks , Dmitry Titov b, Paul Beasly "The production of radionuclides for nuclear medicine from a compact, low-energy accelerator system "Nuclear Medicine and Biology Volume 41, Supplement, , Pages e7-e15 May (2014).

[16] A. Hermanne, M. Sonck ,S. Takacs ,F. Tarkanyi &Y. Shubin "Deuteron Bombardment Of ^{103}Rh A New Promising Pathway For The Production Of ^{103}Pd" Medical, Environmental, Industrial , Pages 1286-1289 | Published online: 27 Aug (2014).

[17] physics.nist.gov/PhysRefData/Star/Text/PSTAR.html.

[18] J. F. Ziegler, M. D. Ziegler and J. P. Biersack, “SRIM— The Stopping and Range of Ions in Matter,” Nu clear Instruments and Methods in Physics Research Section (2013).

ICNST 2024
International Conference on Nuclear Science and Technology
6- 8 MAY 2024 | Isfahan, Iran

The role of optical potential energy dependent factor in the analyses of 12C+12C and 16O+16O elastic scattering using the LOCV-DDAEI (Paper ID : 1644)

Rahmat M. Correspondent[1*]

[1] *Department of Physics, Faculty of Science, University of Zanjan, Zanjan, Iran*
[*] *E-mail: m.rahmat@znu.ac.ir*

Abstract

The elastic scattering of $^{12}C + ^{12}C$ and $^{16}O + ^{16}O$ systems at several incident energies are analyzed, in the framework of double folding model, using the density-dependent averaged effective two-body interaction (DDAEI). The DDAEI is generated via the lowest order constrained variational (LOCV), method for the symmetric nuclear matter (SNM), using the input bare Reid68 nucleon-nucleon (NN) potential. A new energy dependent factor, g(E), is introduced to the LOCV-DDAEI to get a more realistic description of heavy ion (HI) scattering, at the different incident energies. It is shown that a linear energy dependent function, provides a good agreement with the energy dependence of the nuclear optical potential, and causes to increase the convergence speed of iteration method in evaluating the exchange part of folded potential, such that the computing time is considerably decreased. The calculated cross sections of the $^{12}C + ^{12}C$ and $^{16}O + ^{16}O$ systems in the above framework, are compared with the available experimental data, and the corresponding results of DDM3Y1-Reid. It is demonstrated that a quite good description of HI scattering can be obtained, using the above LOCV-DDAEI, by adjusting the parameters of the linear energy dependent factor, g(E). Finally in contrast to DDM3Y1-Reid method, there is no need for defining a parametrized density dependent function in the effective NN potential.

Keywords: LOCV, folding model, elastic scattering, energy dependent factor, Reid potential

INTRODUCTION

For many years, the elastic scattering of heavy-ion (HI) has been the main source of information on nuclear properties. So the HI scattering processes are investigated extensively both experimentally and theoretically. In this direction, there is a remarkable progress in the measurement of accurate and extensive elastic scattering differential cross section (DCS), that cover large range of scattering angles [1], and also many theoretical attempts are made to understand the HI scattering. The phenomenological study of this phenomena through the empirical parametrization of nuclear potential was very common

in the past, but the derivation of the nucleus-nucleus ($\mathcal{NN}$) interactions from the nucleon-nucleon (NN) potential via a reliable microscopic many-body technique is more desirable [2].

Recently, the double-folding (DF) model is widely applied to describe the HI scattering, due to a simple possibility of numerical handling in the colliding nuclei calculations [3]. In this approach, the $\mathcal{NN}$ potential is obtained by folding an effective NN interaction, over the ground-state density distribution of two colliding nuclei [1, 4]. In this direction, the determination of a well-defined effective NN interaction as one of the key inputs in the DF model, is a challenge in the nuclear many-body theory. Among different kinds of the effective potentials, the M3Y interaction [5] and its density dependent versions [6–16], are widely and successfully used in the DF model to describe light heavy ion collisions. But this model is achieved only by some parametrization and the potential itself does not come out of a realistic many-body nuclear matter theory. However, in the references [17, 18], the DF potentials are determined based on chiral effective field theory nucleon-nucleon interactions at leading, next-to-leading, and next-to-next-to-leading order for $^{16}O + {}^{16}O$ and $^{12}C + {}^{12}C$ and $^{12}C + {}^{16}O$ systems. In the reference [19], the experimental cross sections of the $^{16}O + {}^{16}O$ elastic scattering which over the wide range of incident energies have been analyzed in the optical model using the nonmonotonic nucleus-nucleus potentials from the energy-density functional (EDF) theory including the Pauli principle.

In our previous report [20], the lowest order constrained variational (LOCV) method for the symmetric nuclear matter with the input bare Reid68 potential [21], was applied to generate the direct and exchange parts of the NN density-dependent averaged effective two-body interaction (LOCV-DDAEI). Then in the references [22, 23], hereafter denoted by RM1 and RM2, respectively, we used the LOCV-DDAEI as the effective NN interaction in the folding model, in order to calculate the elastic scattering DCS of the $^{12}C + {}^{12}C$ and $^{16}O + {}^{16}O$ systems, using the FRESCO (finite-range with exact strong coupling) code [24]. In RM1, the calculated folded potentials, with the input LOCV-DDAEI, were entered directly in the F RESCO code, while in RM2, at first, the calculated folded potential was fitted to a Woods-Saxon (WS) potential, and then the obtained equivalent parameters were entered into the FRESCO code for calculating the elastic scattering DCS.

It should be noted that, the iterative method, which is used for evaluating the exchange part of folded potential, based on LOCV-DDAEI does not converge reasonably at small internuclear distances ($R \leq 1$

fm), and this leads to increase the computing time. So in RM1 and RM2, this region was extrapolated. The results of RM1 and RM2 were encouraging both with respect to the available experimental data [25–33] and the theoretical calculations in which the fitted parametrized density dependent NN potentials (M3Y) are used (DDM3Y1- Reid68) [3].

In the reference [34], by defining a new energy dependent factor, g(E), in the effective interaction of LOCV method (LOCV-DDAEI) for describing the $^{16}O + {}^{16}O$ elastic scatterin at various incident energies, ranging from 75 to 480 MeV, the problem of the slow convergence speed of iterative procedure for evaluating the exchange part of optical potential and long computing time have been solved and the results have been improved. In the present work, I intend to investigate the effect of using the new energy dependent function in the folding analysis of $^{12}C + {}^{12}C$ elastic scattering, so, I only concentrate on the elastic scattering of spherical colliding nuclei, e.g., the $^{12}C + {}^{12}C$ and $^{16}O + {}^{16}O$ systems. These nuclear systems are known as the key reactions in the formation of heavier elements in nuclear burning process [35, 36]. On the other hand, for these systems, abundant experimental scattering data covering a wide angular range is available at low and medium energies.

The LOCV formalism [37–40], which is based on the cluster expansion [41], is capable to produce the optimized state and the density-dependent effective NN interactions. The LOCV effective two-body interactions were tested, by calculating the properties of the light and the heavy closed shell nuclei [42–44], and recently it was used to calculate the in-medium nn cross section, the transport properties of neutron matter [45, 46] and the normal liquid helium-3 [47]. In the reference [20], the LOCV-DDAEI were derived through the LOCV calculation for SNM, with the Reid68 [21], the △-Reid68 [48] (which takes into account the effect of three-body force (TBF)) and the $A\upsilon_{18}$ [49] interactions as input phenomenological NN potentials, and reformulated in the radial and density-dependent parts, as well as, its direct and exchange components. In the present work, I will only consider the LOCV-DDAEI coming from the Reid68 potential, since I intend to compare our results with those coming from the Reid-M3Y interaction [5]. I hope to consider the other interactions, as well as, the effects of the TBF on the nucleus-nucleus DCS in future.

So, this paper is organized as follows: In the section 2, the theoretical formalism of the double folding model, as well as, the computational procedure are summarized. The results of the calculations are discussed in the section 3, and the section 4 is devoted to summary and conclusion.

THE THEORETICAL FORMALISM AND COMPUTATIONAL PROCEDURES

A detailed description of calculation and derivation of the DF model can be found in the references [1, 3, 4, 22, 50–53]. In order to make this paper self-contained, I give here only a brief description of DF

model. The real part of HI potential at a separation distance R between the center of mass of two colliding nuclei, consists of two parts:

$$U(E,\boldsymbol{R}) = U_D(E,\boldsymbol{R}) + U_{Ex}(E,\boldsymbol{R}) \tag{1}$$

where the direct term, U_D, and the exchange term, U_{Ex}, are generally energy-dependent. In the usual DF model, the direct part of HI potential is written as

$$U_D(E,\boldsymbol{R}) = \int d\boldsymbol{r}_p d\boldsymbol{r}_t\, \rho_p(\boldsymbol{r}_p)\rho_t(\boldsymbol{r}_t) v_D(\rho,E,s) \quad , \quad \boldsymbol{s} = \boldsymbol{r}_p - \boldsymbol{r}_t + R \tag{2}$$

while, the exchange part, within a generalized version of DF model [3], has the following form:

$$U_{EX}(E,\boldsymbol{R}) = \int d\boldsymbol{r}_p\, d\boldsymbol{r}_t \rho_p(\boldsymbol{r}_p;\boldsymbol{r}_p+\boldsymbol{s})\rho_t(\boldsymbol{r}_t;\boldsymbol{r}_t-\boldsymbol{s}) v_{EX}(\rho,E,s) e^{(i\boldsymbol{k}_{rel},\boldsymbol{s}/A_{red})} \tag{3}$$

In the above equations, v_D and v_{EX} are the direct and exchange parts of the effective NN interaction, ρ_p and ρ_t are the densities of two colliding nuclei and $\boldsymbol{k}_{rel}$ is associated with the relative momentum, which is given by:

$$k_{rel}{}^2(\boldsymbol{R}) = 2m_n A_{red}[E_{cm} - U(E,\boldsymbol{R}) - V_C(\boldsymbol{R})]/\hbar^2 \tag{4}$$

where $A_{red} = A_P A_t/(A_P + A_t)$, m_n, $E_{cm}$and E are the reduced mass number, the bare nucleon mass, the center-of-mass (c.m.) energy and the incident laboratory energy per nucleon, respectively. Here $U(E,\boldsymbol{R}) = U_D(E,\boldsymbol{R}) + U_{Ex}(E,\boldsymbol{R})$ is the total nuclear potential and $V_C(\boldsymbol{R})$ is the Coulomb potential.

The density matrix is usually approximated, using the density matrix expansion (DME) method of the references [54, 55], to avoid the non-locality through the exchange term, for simplicity of the numeric calculations, as,

$$\rho(\boldsymbol{R},\boldsymbol{R}+\boldsymbol{s}) \cong \rho\left(\boldsymbol{R}+\frac{\boldsymbol{s}}{2}\right)\hat{\jmath}_1\left(k_F\left(\boldsymbol{R}+\frac{\boldsymbol{s}}{2}\right)s\right) \tag{5}$$

where $\hat{\jmath}_1(x) = 3(\sin x - x\cos x)/x^3$ and $k_F(r)$ is the average local Fermi momentum, which in present work, is calculated using the extended Thomas-Fermi approximation [56], i.e.,:

$$k_F(r) = \left\{\left[\frac{3}{2}\pi^2\rho(\boldsymbol{r})\right]^{2/3} + \frac{5C_s|\nabla\rho(\boldsymbol{r})|^2}{3\rho^2(\boldsymbol{r})} + \frac{5\nabla^2\rho(\boldsymbol{r})}{36\rho(\boldsymbol{r})}\right\}^{1/2} \tag{6}$$

The second term is the Weizsäcker correction term with strength C_s, which represent the surface contribution to the kinetic energy density. Normally one takes $C_s \cong \frac{1}{36}$, for a finite fermionic system [3]. However, a detailed study by Baltin [57], shows that in a region of small density or high $\nabla\rho$, the

value of C_s should be $\frac{1}{4}$. In the previous works [22, 23], it was used the $C_s = \frac{1}{36}$, whereas in the present paper, the latter for C_s is considered, which gives a more realistic shape to our microscopic HI potential.

To specify the overlap density, ρ, which enters into the v_D and v_{EX}, see the equations (2) and (3), respectively, the local density approximation is usually used. In this procedure, ρ is taken to be the sum of the target and projectile densities at the midpoint of the inter-nucleon separation, i.e.,

$$\rho = \rho_p\left(\boldsymbol{r}_p + \frac{\boldsymbol{s}}{2}\right) + \rho_t\left(\boldsymbol{r}_t - \frac{\boldsymbol{s}}{2}\right) \tag{7}$$

To evaluate the exchange integral, the equation (3), an iterative method is used, since ${k_{rel}}^2(\boldsymbol{R})$ depends on the $U_{EX}(\boldsymbol{R})$. Therefore, we are faced with a self-consistency problem [58]. Similar to the previous works [22, 23], $U_D(E, \boldsymbol{R})$ is taken as the starting potential and the convergence obtained by the iterative process, to assure the final result.

In the calculation of the exchange potential, we also need the Coulomb potential, $V_C(\boldsymbol{R})$. According to the reference [59], the different models for the Coulomb potential do not have serious effect on the theoretical predictions. Here, the Coulomb potential is considered to be a simple interaction between a point charge, and a uniform one, with the radius R_C [2],

$$V_C(R) = Z_p Z_t e^2 \begin{cases} \frac{1}{R} & R > R_C \\ \frac{1}{2R_C}\left[3 - \left(\frac{R}{R_C}\right)^2\right] & R < R_C \end{cases} \tag{8}$$

with $e^2 = 1{,}44\ MeVfm$ and $R_C = R_p + R_t$, $R_i = 1{,}76Z_i^{1/3} - 0{,}96\ fm$, here i = p, t [31].

Since, the effective NN interactions applied into the folding model are real, the calculated HI potentials are also real, therefore the imaginary part of HI potential, is usually treated phenomenologically, and its parameters are adjusted to optimize the fit to the observed scattering. In the most cases, the Woods-Saxon (WS) shape (with the volume or surface type) is used, for the imaginary potential. Finally the general form of the HI potential can be written as [3],

$$U(E\ R) = N_R[U_D(E\ R) + U_{EX}(E\ R)] - iW_V\left(1 + \exp\left(\frac{r-R_V}{a_V}\right)\right)^{-1} + 4iW_D a_D \frac{d}{dR}\Big(1 + \exp\left(\frac{r-R_D}{a_D}\right)\Big)^{-1} \tag{9}$$

where N_R is the renormalization coefficient, which is needed to account roughly for many-nucleon exchange effects, and the dynamical polarization potential (ΔU) [50]. Any large deviation from unity of renormalization coefficient, may indicate the deficiency of the model [50, 51]. The N_R together with the parameters of the imaginary potential are adjusted such that, they give the best fit to the scattering data. In our previous works [22, 23], we only use the volume term for the imaginary part of potential, but in the current report, to improve the agreement of the calculated cross section with the experimental data, the volume and the surface (WSD) terms are applied in the calculations.

As it can be seen from the equations (2) and (3), there are two important inputs into folding model: (i) the nuclear densities of the colliding nuclei in their ground state, and (ii) the effective NN interaction. The density distributions are normalized as:

$$\int \rho_i(\boldsymbol{r}_i) d\boldsymbol{r}_i = A_i \tag{10}$$

where A_i , is the mass number of the projectile or target nucleus. In this paper, the nuclear densities are approximated as two-parameter Fermi distribution: $\rho(r) = \rho_0 \left[1 + exp\left(\frac{r-c}{a}\right)\right]^{-1}$, with the parameters taken from the table I of reference [60], which reproduce the shell-model densities for the considered nuclei.

After specifying the nuclear densities, it is still necessary to have an appropriate NN interaction to get a reasonable description of the $\mathcal{NN}$ potential. The most common choice of NN interactions, which are used as the density-dependent NN interactions, are the M3Y ones [5, 7–12]. They are based on the G-matrix elements of the Reid68 [5] and Paris [61] potentials. It is worth to mention that, the density-dependent factor, $F(\rho)$, is multiplied later to the original M3Y interaction to improve the description of nuclear matter properties and the HI scattering data, i.e., $v_{D(Ex)}(r, \rho) = F(\rho) v_{D(Ex)}(r)$.

According to the different choices for $F(\rho)$, there are various versions of the density-dependent NN interactions, the DDM3Y1 and BDM3Yn (n =0−3) and CDM3Yn (n =1−6) potentials. Usually $F(\rho)$ is parametrized as follows:

$$F(\rho) = C[1 + \alpha \exp(-\beta\rho) - \gamma\rho] \tag{11}$$

for the DDM3Y1 and CDM3Yn (n =1−6) potentials and

$$F(\rho) = C\left(1 - \alpha\rho^{\beta}\right) \tag{12}$$

for BDM3Yn (n =0−3) interactions [1, 4, 6, 59–62]. The parameters C, α, β and γ, are fitted to the cold symmetric nuclear matter saturation properties [1, 4, 6, 59–62]. Similar to RM1 and RM2, I focus on the finite range DDM3Y1 interaction [3] for the comparison of DCS to the results.

As it can be seen from the equation (4) that, the energy dependence of the optical potential, comes from the exchange term only. However, it is found that the intrinsic energy dependence of the optical potential arising from the exchange part, is not enough to reproduce the observed scattering data, and one should take into account an appropriate energy dependent factor into the original effective NN interaction. In the case of the M3Y interactions, the energy-dependent factor is a linear multiplier, g(E), [6]:

$$v_{D(Ex)}(r,\rho) = \mathrm{g}(E)F(\rho)v_{D(Ex)}(r) \tag{13}$$

where $\mathrm{g}(E) = [1 - k(E/A)]$ with $k = 0{,}002\ MeV^{-1}$, for the Reid interaction, or $k = 0{,}003\ MeV^{-1}$for the Paris potential [2]. However, none of the above potentials come from a Hamiltonian based many-body microscopic calculation.

In the present work, similar to RM1 and RM2, I use the direct and the exchange parts of the LOCV density dependent averaged effective two-body interaction (LOCV-DDAEI), which comes from the Hamiltonian based many-body calculation, see the reference [20] and the appendix of RM1 [22] for more details, as follows:

$$\bar{v}^{D}_{eff}(r,\rho) = \frac{\sum_{\alpha\, i\, j}\,(2T+1)(2J+1)\frac{1}{2}V_{\alpha}^{i\,j}(r\,\rho)a_{\alpha}^{(i)^2}(r,\rho)}{\sum_{\alpha\, k}(2T+1)(2J+1)\frac{1}{2}a_{\alpha}^{(k)^2}(r,\rho)} \tag{14}$$

$$\bar{v}^{EX}_{eff}(r,\rho) = \frac{\sum_{\alpha\, i\, j}(2T+1)(2J+1)\frac{\left[(-1)^{L+S+T}\right]}{2}V_{\alpha}^{i\,j}(r\,\rho)a_{\alpha}^{(1)^2}(r\,\rho)}{\sum_{\alpha\, k}(2T+1)(2J+1)\frac{\left[(-1)^{L+S+T}\right]}{2}a_{\alpha}^{(k)^2}(r\,\rho)} \tag{15}$$

where J , L, S and T are the familiar two nucleons quantum numbers. Then the pure density-dependent parts of the LOCV-DDAEI are extracted as [20, 22]:

$$\bar{v}^{D(EX)}_{eff}(r,\rho) = \bar{v}^{D(EX)}(r)F^{D(EX)}(\rho) = \bar{v}^{D(EX)}(r)\left[C^{D(Ex)}\left(1+\alpha^{D(Ex)}\exp\left(-\beta^{D(Ex)}\rho\right)\right)\right] \tag{16}$$

Similar to the DDM3Y1 interaction, the exponential dependent form for ρ, is assumed [20, 22], and its parameters are given in the table I. It is worth to mention that, the density dependent factor in the LOCV-DDAEI is not an external factor, and it comes from the LOCV calculation, which are just parametrized

it in a suitable form. The exponential parametrization of $F(\rho)$ allows us to easily calculate the double folding integrals in the momentum space [1].

Table I. The parameters of the density-dependent part of the direct and exchange components, ($F^{D(EX)}(\rho)$), of the LOCV-DDAEI, using the Reid68 interaction as the input potentials

	$\mathcal{C}$	α	β
direct component	0.38	5.03	**3.22**
exchange component	13.57	-0.9	**0.12**

Similar to the M3Y interactions, in order to apply LOCV-DDAEI to the $\mathcal{NN}$ scattering data, one needs to add an explicit energy-dependent factor to our LOCV-DDAEI, to obtain the best description of HI scattering at various incident energies, i.e.,

$$\bar{v}_{eff}^{D(EX)}(r,\rho) = \bar{v}^{D(EX)}(r)F^{D(EX)}(\rho)\mathrm{g}(E) \tag{17}$$

Different forms of $\mathrm{g}(E)$ are tested to fit the scattering data, in the simplest way, and it is found that a linear dependence to the incident energy per nucleon is the appropriate one, i.e.,

$$\mathrm{g}(E) = \zeta - k(E/A) \tag{18}$$

In our previous reports [22, 23], we took $\zeta = 1$ and $= 0{,}03\ MeV^{-1}$, but in the present work, I find that by choosing $\zeta = 0{,}4$ and $k = 0{,}003\ MeV^{-1}$, a more realistic description of HI scattering at different energies can be obtained. More details will be discussed in the section 3.

The computational procedure is carried out in the several steps. The real part of the optical potential for $^{12}\mathrm{C} + {}^{12}\mathrm{C}$ and $^{16}\mathrm{O} + {}^{16}\mathrm{O}$ systems, is calculated using the double folding formula, the equations (2) and (3), by inserting the LOCV-DDAEI as the effective NN interactions, and the two-parameter Fermi distribution for the nuclear densities of colliding nuclei. The imaginary part of optical potential is evaluated in the volume and surface WS form, i.e., the second and the third terms at of the equation (9), with the optimal parameters obtained through minimization of χ^2 , as defined below [11]:

$$\chi^2 = \frac{1}{N_\sigma}\sum_{i=1}^{N}\left(\frac{\sigma_{th}-\sigma_{ex}}{\Delta\sigma_{ex}}\right)^2 \quad (19)$$

where σ_{th} and σ_{ex} are the theoretical and the experimental cross sections, and $\Delta\sigma_{ex}$ is defined, as the uncertainties in the experimental cross sections, respectively. N_σ is the total number of angles at which measurements are made. Indeed, the goodness of the resulting cross sections is qualified via χ^2 , a lower value of χ^2 means a better description of the experimental scattering data in terms of the selected theoretical representation [35].

Here, in order to compute the differential scattering cross section, I use the FRESCO code [24], developed by Ian Thompson for the calculation of different types of the nucleon-nucleus, and nucleus-nucleus scattering cross sections. Then, the resulted folded potential are entered directly into the FRESCO code, to calculate the elastic scattering of cross section for $^{12}C + {}^{12}C$ and $^{16}O + {}^{16}O$ systems.

Results and discussion

According to the steps described in the computational procedure, the section 2, at first, by entering the direct and the exchange parts of the LOCV-DDAEI as an effective NN interaction in the double folding formula, the equations (2) and (3), the direct and the exchange components of the real part of the HI optical potential are calculated. As, it was pointed out before, due to the dependence of ${k_{rel}}^2(\boldsymbol{R})$ on $U_{EX}(\boldsymbol{R})$, the iterative method is used to evaluate the exchange potential.

The main difference between the current calculations and the previous calculations in RM1 and RM2, is in the definition of the energy-dependent factor, g(E), in the LOCV-DDAEI, when applying in the study of the HI scattering. A linear dependence to energy is assumed in the calculations: $g(E) = [\zeta - k(E/A)]$, but as it can be seen in RM1 and RM2, by taking $\zeta = 1$ and $k = 0{,}03\ MeV^{-1}$, the obtained folded potentials are not as good as they are expected. At small internuclear distances (R ≤ 1fm), the iterative method for calculating the exchange potential does not converge reasonably, so we need too much iterations and CPU computer time [22]. For this reason in RM1 and RM2, we extrapolated the folded potential for some points (R ≤ 1fm), that the iterative procedure did not converge rapidly. In the present work, after testing different forms of g(E) in the iterative calculations for $U_{EX}(\boldsymbol{R})$, it is found by choosing the new parameters, $\zeta = 0{,}4$ and $k = 0{,}003\ MeV^{-1}$, for the g(E) function, it is

possible to overcome the problem of low convergence speed of iteration method, and long computing time in evaluating the exchange part of HI potential at small distances. For example, as it was reported in RM1, the number of iterations required at the small radii was around 150 to 200, while by using the new g(E) function in the current calculations, it becomes around 80 to 90, which in turns decreases the computing time. Since by using the new g(E) function, the iterative method for calculating the $U_{EX}(\boldsymbol{R})$ based on LOCV-DDAEI converges reasonably at all internuclear distances, there is no need to extrapolate the folded potential at small radii (unlike our previous calculations in the RM1 and RM2).

In the left and right panels of the figure 1, the direct, exchange and total components of folded potentials, by using the LOCV-DDAEI, with the new g(E) function for the $^{12}\mathrm{C} + {}^{12}\mathrm{C}$ and $^{16}\mathrm{O} + {}^{16}\mathrm{O}$systems at the several incident energies, i.e., $E_{lab} = 112,\ 126{,}7\ ,\ 240,\ 300,\ 360\ \mathrm{MeV}$ and $E_{lab} = 124, 145,\ 250,\ 350,\ 480\ \mathrm{MeV}$, are plotted, respectively. Similar to the results of RM1, i.e., the figures 1 and 2 of the reference [22], one can conclude that the most of the energy dependence of the HI potential is coming from the exchange part, since as it can be seen from the middle parts of the different panels of the figure 1, the exchange potentials vary strongly with respect to the incident energy at small internuclear distances, while the direct parts have the quite same strength and slop at the different energies in this region. The figure 1 also shows that, increasing the incident energy of the projectile, leads to the decrease in the depth of the HI potential at the small radii systematically. Comparing of the exchange parts with the direct parts at each incident energy, shows that the density-dependent contribution of the HI potential strongly arises from the exchange part, since at small radii, which correspond to the large overlap densities ($\rho > \rho_0$), the exchange part of potential is deeper than the direct one, especially at lower energies. While in the surface region, which corresponds to the small overlap densities, the contribution of U_D becomes comparable, and even more than U_{EX}. Similar results were reported in the folded potential calculations, using the M3Y interactions [3, 63].

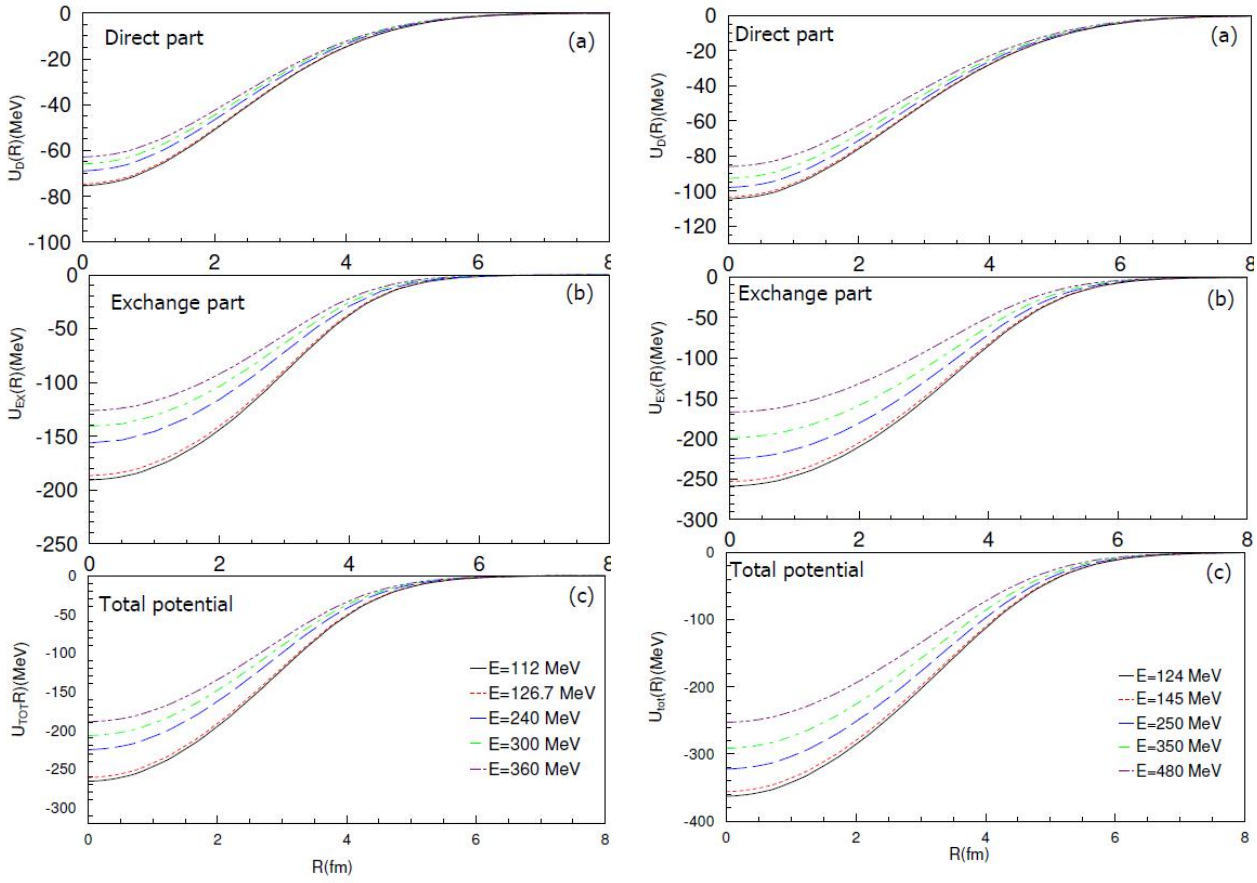

Fig. 1. The direct, exchange and total components of folded potential for the $^{12}C + {}^{12}C$ system at the several incident energies (the left panels). The right panels are as the left panels, but for the $^{16}O + {}^{16}O$ system.

A comparison between the calculated folded potential, using the LOCV-DDAEI with the new energy-dependent factor, g(E), and the corresponding results of the DDM3Y1 [3] and RM1, for the cases of $^{12}C + {}^{12}C$ at $E_{lab} = 300$ MeV and $^{16}O + {}^{16}O$ at $E_{lab} = 350$ MeV are presented in the left and right panels of the figure 2, respectively. As it was stated in RM1, by using the LOCV-DDAEI, the folded potentials are more deeper than the DDM3Y1 ones, at small distances. But, by defining the new g(E) function in the LOCV-DDAEI, the obtained folded potential, are shallower than the previous folded potential in RM1, while the new results become comparable with the DDM3Y1 ones, both at strength and slop, over the entire radial range. For the other energies, the similar results are obtained.

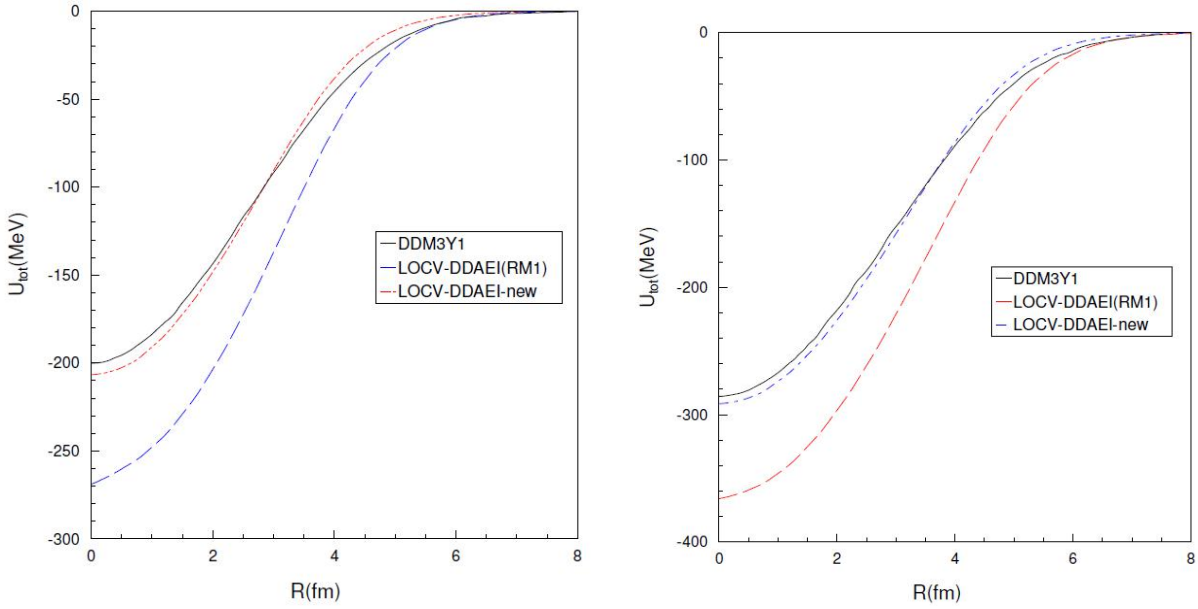

Fig. 2. The comparison of the calculated real folded potential, using the LOCV-DDAEI, DDM3Y 1 potentials and the corresponding result of RM1 for the $^{12}C + {}^{12}C$ ($^{16}O + {}^{16}O$) scattering at $E_{lab} = 300(350)$ MeV , in the left (right) panel. The LOCV-DDAEI-new is the results of present report

In order to study the energy dependence systematically, it is also necessary to consider the complex volume integral of the optical potential, per interacting nucleon pair, $J_U(E)$ [1, 64],

$$J_U(E) = \frac{-4\pi}{A_p A_t} \int U_E(r)\, r^2 dr = J_V(E) + iJ_W(E) \qquad (20)$$

The minus sign is used in this formula, such that *J* becomes positive for the attractive potentials. It is known that the volume integrals of the nuclear potential, can be better determined by the data than the individual potential itself [1]. Therefore, the realistic J_V values is often a criterion to get a real optical potential [64]. By using the above definition, for the real and imaginary parts of volume integral in the above equation, J_V and J_W respectively, I calculate these quantities for $^{12}C + {}^{12}C$ and $^{16}O + {}^{16}O$ systems at each incident energies, see the tables II and III, and the obtained volume integral J_V and J_W versus the incident energy is plotted in the left and right panels of the figure 3, respectively.

It is worth to note that, in the present paper the imaginary part of the HI potential is taken as the conventional WS volume and surface forms, with the parameters adjusted to achieve the best fit to the experimental scattering data. The obtained values of J_V for elastic $^{12}C + {}^{12}C$ and $^{16}O + {}^{16}O$ scattering, in the current calculations using the new g(E) function, are quite close to the J_V values which are coming from optical model analyses using the M3Y interactions [1,

65]. Our previous calculations in RM1, predicted the behaviour of J_V versus the incident energy qualitatively, but it overestimates the J_V values at each energy around one and a half times larger.

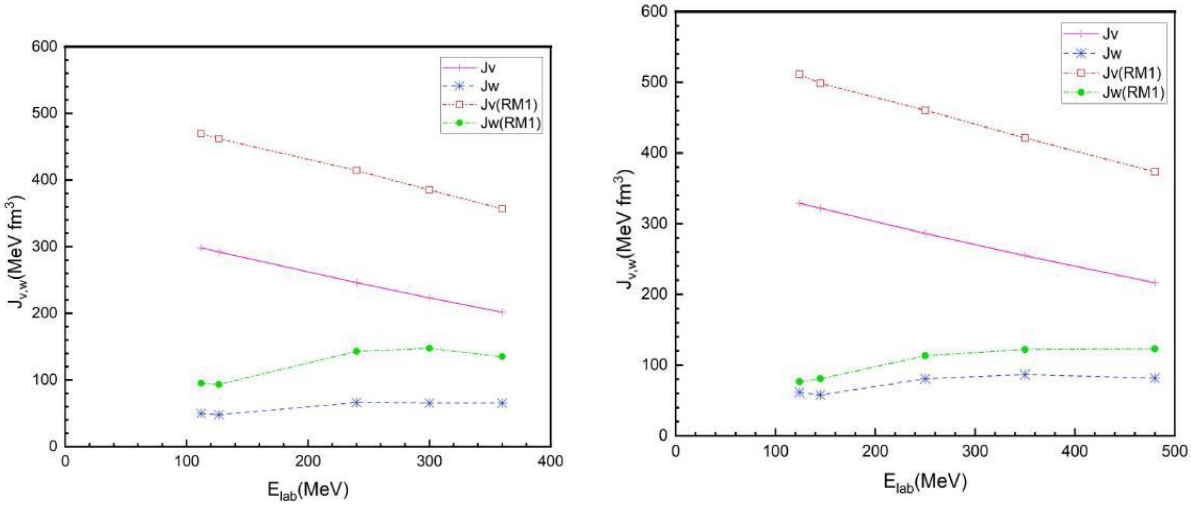

Fig. 3. The real and imaginary parts of the volume integral of the optical potential per interacting nucleon pair (J_V and J_W), versus the incident energies for the $^{12}C + {}^{12}C$ ($^{16}O + {}^{16}O$) systems, in the left (right) panel. The results of RM1 are also plotted. The lines are only the interpolation between the marked points.

As it can be observed from the figures 3, by increasing the incident energy, the real volume integral, J_V , decreases linearly for both $^{12}C + {}^{12}C$ and $^{16}O + {}^{16}O$ systems. These results are in good agreement with those reported for the same systems, using the M3Y interactions [1, 65]. Since for a given system and energy, all of the different real potentials, should have similar volume integrals per nucleon [1], one can conclude that the energy dependence of the real HI optical potential for the LOCV-DDAEI takes into account quite well, by the new definition of the g(E) function. The energy dependence of J_W which observes in the figure 3, are similar to the figure 6.7 in the reference [1] and the figure 17 in the reference [65]. All of them also agree well with the prediction of dispersion relation.

The calculated cross sections for $^{12}C + {}^{12}C$ elastic scattering at various incident energies, ranging from 112 to 360 MeV, and for $^{16}O + {}^{16}O$ system, at incident energies ranging from 124 to 480 MeV, using the LOCV-DDAEI folded potential in the framework of FRESCO code, are plotted in the different panels of the figures 4 and 5, respectively. The experimental scattering data [25–33] and the resulting cross section of the DDM3Y1 [3], as well as the previous results from RM1 [22] are also presented. In this work, the volume and surface WS

shapes are assumed for the imaginary part of HI potential of $^{12}C + ^{12}C$ and $^{16}O + ^{16}O$ systems. The WS parameters and the renormalization coefficient, N_R, are adjusted to obtain the best description of the experimental data scattering in the whole angular range at each incident energy. The tables II and III, show the corresponding imaginary WS parameters for $^{12}C + ^{12}C$ and $^{16}O + ^{16}O$ systems at several energies, as well as, χ^2 and N_R, respectively. The parameters in the tables II and III, favour a rather weak imaginary potential and show that they are close to those found in the earlier analysis for DDM3Y1-Reid, see the table II of reference [3], and our previous calculation [22, 23]. As can be observed from the tables II and III, the obtained renormalization coefficients, N_R, at the defined energies, do not deviate strongly from unity, which means that the high-order effects are negligible in the present calculations, and we are using a realistic model for the nucleus-nucleus potential.

Table II. The WS parameters of the imaginary part of HI potential, used in our folding analyses of the $^{12}C + ^{12}C$ elastic scattering at $E_{lab} = 112,\ 126{,}7\ ,\ 240,\ 300,\ 360$ MeV . The χ^2 value and the J_V and J_W values are also presented.

E_{lab} (MeV)	N_R	W_V (MeV)	R_V (fm)	a_V (fm)	W_D (MeV)	R_D (fm)	a_D (fm)	J_V $(MeV\ fm^3)$	J_W $(MeV\ fm^3)$	χ^2
112	0.933	12.67	5.35	0.65	1.85	2.79	0.62	298.22	49.69	46.64
126.7	0.927	11.23	5.40	0.66	3.24	2.88	0.67	291.91	47.93	45.89
240	0.962	19.83	4.97	0.70	3.42	2.74	0.68	245.87	66.07	49.13
300	0.884	22.92	4.74	0.65	3.40	2.70	0.60	223.17	65.19	34.75
360	0.945	23.24	4.76	0.58	2.72	2.75	0.67	201.69	65.07	37.29

Table III. The same as table II but for the $^{16}O + ^{16}O$ elastic scattering at $E_{lab} = 124, 145, 250, 350, 480$ MeV

E_{lab} (MeV)	N_R	W_V (MeV)	R_V (fm)	a_V (fm)	W_D (MeV)	R_D (fm)	a_D (fm)	J_V $(MeV\ fm^3)$	J_W $(MeV\ fm^3)$	χ^2
124	1.035	14.50	6.05	0.80	2.12	2.62	0.45	329.15	61.50	53.62
145	0.940	14.10	5.95	0.80	2.32	2.52	0.52	321.76	57.74	52.83
250	0.988	22.70	5.69	0.75	2.82	2.52	0.38	286.18	80.17	37.31
350	0.957	32.5	5.19	0.60	3.90	2.62	0.43	254.51	86.49	38.21
480	0.966	36.80	4.61	0.82	4.70	3.02	0.50	216.43	81.39	32.64

As it was pointed out before, from the figures 4 and 5, one can find out that, in general, a reasonable description of scattering data can be obtained by using the LOCV-DDAEI and

adjusting the imaginary potential parameters and renormalization coefficient. However, it seems that these results are not as good as the corresponding results of the DDM3Y1, but one should notice that DDM3Y1 potential is generated from the selected channels of the Reid68 potential, i.e., the singlet and triplet even and odd components and its density dependent factor is added later to original M3Y interaction to provide a reasonable description of HI data scattering and equation of state (EOS) of nuclear matter. So, it is natural that, by adjusting the parameters of density dependent factor, the desirable description of data scattering to be achieved. While the LOCV-DDAEI are based on the many-body calculations without any free parameters in our calculations and its density dependent part comes directly from the LOCV calculations (obviously the LOCV formalism has its own EOS, i.e., LOCV EOS), in which, the only adjustable parameters in the effective interaction is the energy dependent factor, g(E), that is taken in the simplest form, i.e., a linear function.

As it was mentioned before, the TBF has not been taken into account in this report, since it is intended to compare the new results with those of DDM3Y1-Reid and RM1, as well as the goal of this paper is that investigate the effect of insertion of the new g(E) in the resulted folding analysis. However, comparing the new calculated cross sections of this work with the results of the RM1[22], one can observe new results have limited improvements in reproducing the cross sections of the experimental data due to using new g(E) function. It is hoped that by including the TBF in the density-dependent effective interaction derived from the LOCV method, the results will be improved considerably, as in the case of the EOS of nuclear matter, the inclusion of TBF improved the results. It is well known, using the two-body interactions, one should not expect to get the justified EOS for the nuclear matter. Indeed, by including two-body interactions, the empirical saturation properties of the SNM, such as saturation density and the binding energy as well as incompressibility of SNM cannot be achieved, by taking into account of TBF, the resulted saturation properties will be close to the exact SNM empirical values (for more discussions about the effect of TBFs on the SNM EOS see the appendix of reference [22] and references therein). So, I hope to consider the effect of TBF on the nucleus-nucleus differential cross sections in near future.

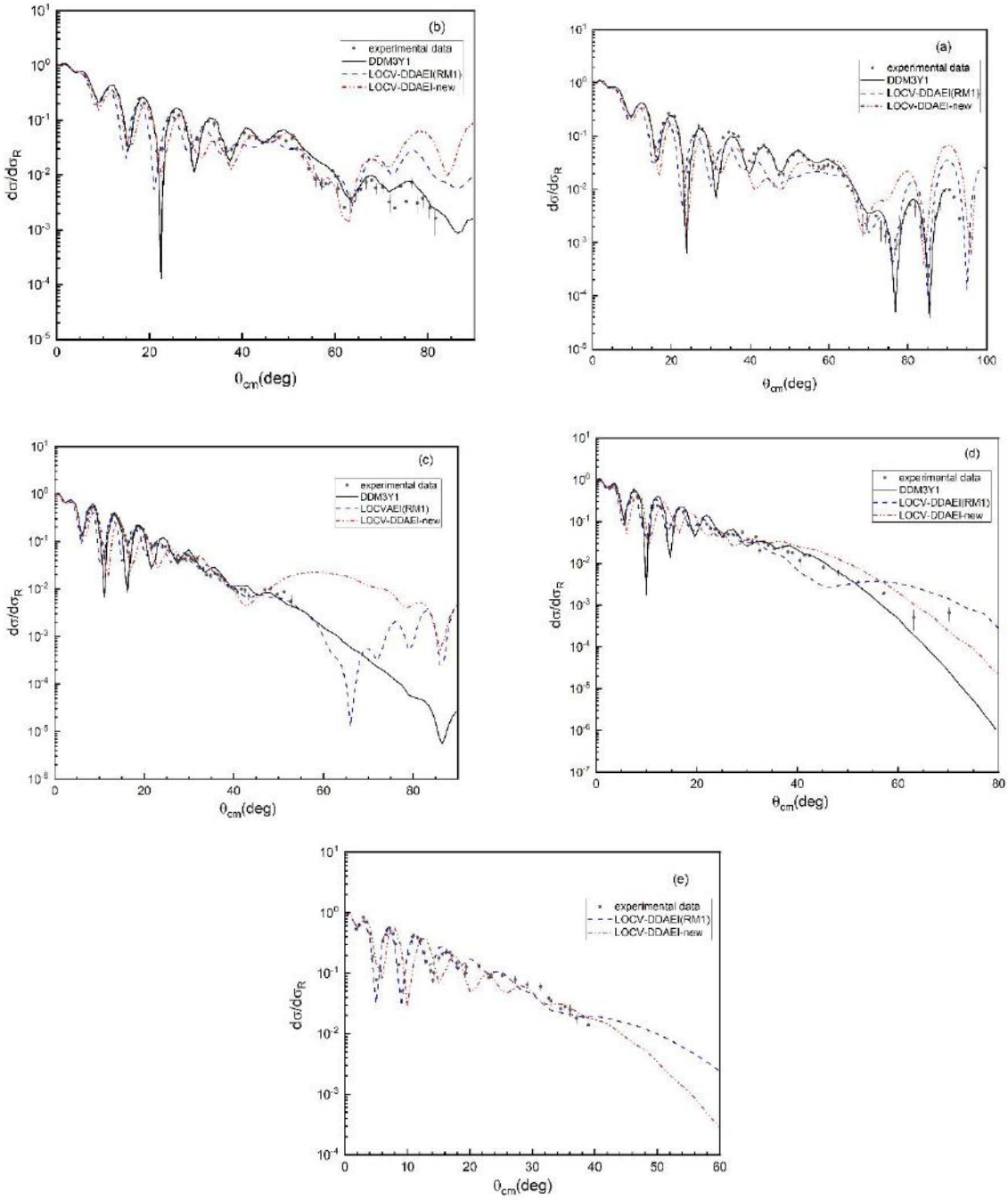

Fig. 4. The calculated cross sections of the $^{12}C + {}^{12}C$ elastic scattering at $E_{lab} = 112, 126{,}7\,, 240,\ 300, 360$ MeV by using the LOCV-DDAEI, the panels (a) to (e), respectively. The experimental scattering data [18–26] and the resulting cross section of the DDM3Y1 and RM1 are also presented. The LOCV-DDAEI-new is the results of present report.

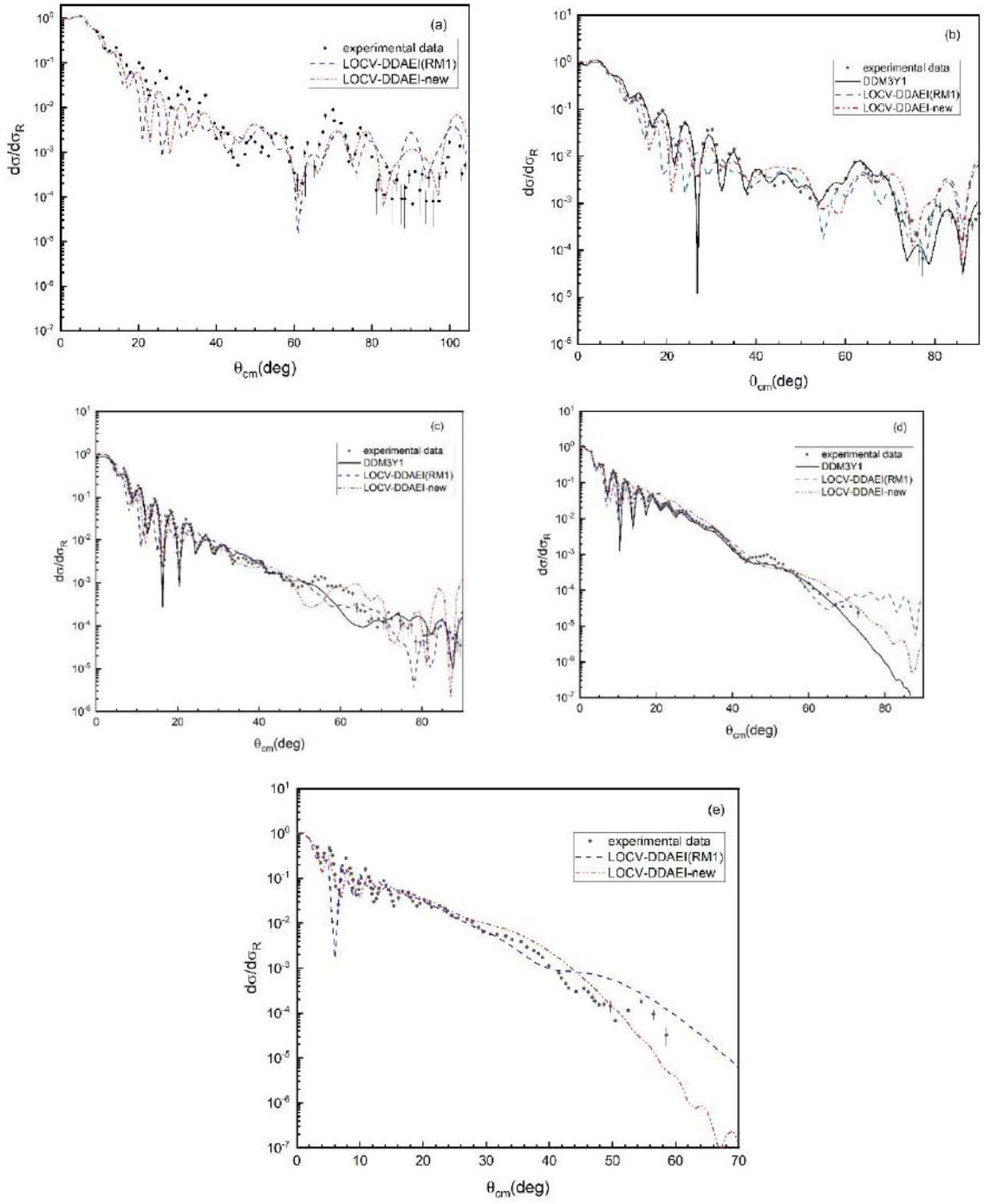

Fig. 5. . As the figure 4, but for the $1^{16}O + {}^{16}O$ scattering at $E_{lab} = 124,\ 145,\ 250,\ 350,\ 480$ MeV

Conclusions

In conclusion, I updated and reanalyzed the available experimental data of the $^{12}C + {}^{12}C$ and $^{16}O + {}^{16}O$ elastic scattering at various incident energies, within standard optical model (OM), using the density-dependent LOCV-DDAEI with a new energy dependent function. The direct and the exchange parts of LOCV-DDAEI were extracted via the LOCV method for the

symmetric nuclear matter with the Reid68 interaction as input phenomenological potential. Then, the radial and the density-dependent parts of the LOCV-DDAEI were separated to use into the folding model. In order to apply the LOCV-DDAEI to the scattering data, an energy dependent factor, g(E), was needed to add to the LOCV-DDAEI. It is found that a linear energy dependent multiplier, the equation (18), provide a good agreement with the energy dependence of the nuclear optical potential. The advantage of using the new energy dependent factor, g(E), is that the number of iterations required for evaluating the exchange potential will be reduced considerably, so the problem of the slow convergence speed of iterative procedure and long computing time can be solved. However, the new calculated cross sections do not show dramatic changes in comparison with the results of RM1 and limited improvements are achieved, it is worth mentioning that by increasing the incident energies, a better fit to the experimental data is observed. Due to the new g(E) predicts the behavior of the volume integral of the optical potential versus the incident energies correctly, one can conclude that by introducing new energy dependent factor for the LOCV-DDAEI, the energy dependence of the real HI optical potential has been taken into account quite well and the potential is more reasonable in theory.

The calculated cross sections for the $^{12}C + ^{12}C$ and $^{16}O + ^{16}O$ systems, show a quite reasonable description of scattering data and could be obtained, using the LOCV-DDAEI by adjusting the imaginary potential parameters and the renormalization coefficient. Despite of considerable differences between our resulting cross section and those of the DDM3Y1, since the LOCV-DDAEI are based on the many-body calculation with the phenomenological NN nucleon potential without any approximation, and its density dependent part comes directly from the LOCV self consistent calculation, so they are more trustable to use in the $\mathcal{NN}$ collision calculations and it is hoped that the present study may provide a good reference for the analysis of the HI scattering.

Finally, with respect the above arguments, because of the LOCV-DDAEI provides a reasonable description of the normal nuclear matter [20], as well, as the HI elastic scattering simultaneously, It can be claimed that the LOCV AEI, is a good candidate to approximate the NN interaction in the nuclear matter and finite nuclei and it is meaningful to apply the LOCV-DDAEI interaction to study of HI scattering as the first attempt, but I hope improvement of the present model could be obtained in the near future.

Acknowledgements

I would like to thank University of Zanjan for their support.

References

[1] M.E. Brandan, G.R. Satchler, Phys. Rep. 285, 143 (1997).

[2] G.L. Zhang, H. Liu, X.Y. Le, Chin. Phys. B 18, 136 (2009).

[3] D.T. Khoa, W. von Oertzen, H.G. Bohlen, Phys. Rev. C 49, 1652 (1994).

[4] K.Amos, P.J.Dortmans, H.V.von Geramb, S.Karataglidis, Avd. Nucl. Phys. 25, 275 (2000)

[5] G. Bertsch, J. Borysowicz, H. McManus, W.G. Love, Nucl. Phys. A 284, 399 (1977) .

[6] D.T. Khoa, W. von Oertzen, Phys. Lett. B 304, 8 (1993).

[7] D.T. Khoa, W. von Oertzen, Phys. Lett. B 324, 6 (1995).

[8] D.T. Khoa, W. von Oertzen, A.A. Ogloblin, Nucl. Phys. A 602, 98 (1996).

[9] D.T. Khoa, G.R. Satchler, W. von Oertzen, Phys. Rev. C 56, 954 (1997).

[10] D.T. Khoa, H.S. Than, D.C. Cuong, Phys. Rev. C 76, 014603 (2007).

[11] D.N. Basu, P. Roy Chowdhury, C. Samanta, Nucl. Phys. A 811, 140 (2008).

[12] P. Roy Chowdhury, C. Samanta, D.N. Basu, Phys. Rev. C 80, 011305 (2009).

[13] M. A. Hassanain, et al., Phys. Rev. C 87, 064606 (2013).

[14] Y. Kucuk, et al., Nucl. Phys. A 994, 121665 (2020).

[15] I. I. Gontchar , M. V. Chushnyakova , O. M. Sukhareva, Phys. Rev. C 105, 014612 (2022).

[16] S. B. Masadeh , D. A. Abdallah, and M. I. Jaghoub, Phys. Rev. C 107, 024616 (2023).

[17] V. Durant, P. Capel, L. Huth, A. B. Balantekin, and A. Schwenk, Phys. Lett. B 782, 668 (2018).

[18] V. Durant , P. Capel , A. Schwenk, Phys. Rev. C 102, 014622 (2022).

[19] S. Hossain, et al., Phys. Rev. C 91, 064613 (2015).

[20] M. Modarres, M. Rahmat, Nucl. Phys. A 934, 148 (2015).

[21] R.V. Reid, Ann. Phys. 50, 411 (1968).

[22] M. Rahmat, M. Modarres, Phys. Rev. C 97, 034611 (2018).

[23] M. Rahmat, M. Modarres, Nucl. Phys. A 997, 121715 (2020).

[24] I. Thompson, www.fresco.org.uk.

[25] R.G. Stokstad, R.M. Wieland, G.R. Satchler, C.B. Fulmer, D.C. Hensley, S. Raman, L.D. Rickertsen, A.H. Snell, P.H. Stelson, Phys. Rev. C 20, 655 (1979).

[26] H.G. Bohlen, X.S. Chen, J.G. Cramer, P. Frobrich, B. Gebauer, H. Lettau, A. Miczaika, W. von Oertzen, R. Ulrich, T. Wilpert, Z. Phys. A 322, 241 (1985).

[27] H.G. Bohlen, M.R. Clover, G. Ingold, H. Lettau, W. vonOertzen, Z. Phys. A 308, 121 (1982).

[28] M. Buenerd, A. Lounis, J. Chauvin, D. Lebrun, P. Martin, G. Duhamel, J.C. Gondrand, P. DeSaintignon, Nucl. Phys. A 424, 313 (1984).

[29] M.P. Nicoli, F. Haas, R.M. Freeman, N. Aissaoui, C. Beck, A. Elanique, R. Nouicer, A. Morsad, S. Szilner, Z. Basrak, M.E. Brandan, G.R. Satchler, Phys. Rev. C 60, 064608 (1999).

[30] Y. Sugiyama, et al., Phys. Lett. B 312, 35 (1993).

[31] E. Stiliaris, et al., Phys. Lett. B 223, 291 (1989).

[32] H.G. Bohlen, E. Stiliaris, B. Gebauer, W. yon Oertzen, M. Wilpert, Th. Wilpert, A. Ostrowski, Dao T. Khoa, A.S. Demyanova, A.A. Ogloblin, Z. Phys. A 346, 189 (1993).

[33] G. Bartnitzky, et al., Phys. Lett. B 365, 23 (1996).

[34] M.Rahmat, Iran.J.Phys.Res 23(3) (2023).

[35] Sh.Hamada, A A.Ibaheem, Indian. J. Phys 94 (2020).

[36] Sh.Hamada, N.Burtebayev, J. Mod. Phys 4 (2013).

[37] J. C. Owen, R. F. Bishop, and J.M. Irvine, Ann. Phys. (NY) 102, 170 (1976).

[38] M. Modarres, J. M. Irvine, J. Phys. G 5, 511 (1979).

[39] M. Modarres, G. H. Bordbar, Phys. Rev. C 58, 2781 (1998).

[40] M. Modarres, A.Tafrihi, Prog. Part. Nucl. Phys 131, 104047 (2023).

[41] J. W. Clark, Prog. Part. Nucl. Phys. 2, 89 (1979).

[42] M. Modarres, N. Rasekhinejad, Phys. Rev. C 72, 014301 (2005).

[43] M. Modarres, N. Rasekhinejad, Phys. Rev. C 72, 064306 (2005).

[44] M. Modarres, H. Mariji, Nucl. Phys. A 859, 16 (2011).

[45] M. Modarres, M. Rahmat, Nucl. Phys. A 903, 40 (2013).

[46] M. Modarres, M. Rahmat, Nucl. Phys. A 921, 19 (2014).

[47] M. Modarres, M. Rahmat,Physica A 466, 396 (2017).

[48] A.M. Green, J.A. Niskanen, M.E. Sainio, J. Phys. G, Nucl. Part. Phys. 4, 1055 (1978).

[49] R.B. Wiringa, V. Stoks, R. Schiavilla, Phys. Rev. C 51, 38 (1995).

[50] G.R. Satchler, W.G. Love, Phys. Rep. 55, 183 (1979).

[51] D.T. Khoa, A.Faessler, N.Ohtsuka, J. Phys. G: Nucl. Part. Phys. 16, 1253 (1990).

[52] D.T. Khoa, Nucl. Phys. A 484, 376 (1988).

[53] D.T. Khoa, O.M. Knyazkov, Z. Phys. A : Atomic Nuclei 328, 67 (1987).

[54] J.W.Negele, D.Vautherin, Phys. Rev. C 5,1472 (1972).

[55] X. Campi and A. Bouyssy, Phys. Lett. B 73, 263 (1978).

[56] P.Ring, P.Schuch, The Nuclear Many-Body Problem (Springer-Verlag, New York, 1980), p.542. [57] R.Baltin, Z.Naturforch. 27A, 1176 (1972).

[58] A.K. Chaudhuri, D.N. Basu, snd B. Sinha, Nucl. Phys. A 439, 415 (1985).

[59] R.M. DeVries and M.R. Clover, Nucl. Phys. A 243, 529 (1975).

[60] M. El-Azab Farid and G.R. Satchler, Nucl. Phys. A 438, 525 (1985).

[61] N. Anantaraman N, H. Toki,G.F. Bertsch, Nucl. Phys.A 398, 269 (1983).

[62] I.I. Gontchar, D.J. Hinde, M. Dasgupta, J.O. Newton, Phys. Rev. C 69, 024610 (2004).

[63] D. T. Khoa, W. von Oertzen, H.G. Bohlen, G. Bartnitzky, H. Clement, Y. Sugiyama, B. Gebauer, A. N. Ostrowski, T.Wilpert, M. Wilpert, and C. Langner, Phys. Rev. Lett. 74, 34 (1995).

[64] W. von Oertzen, H.G. Bohlen, D.T. Khoa, Nucl. Phys. A 722 (2003).

[65] D.T. Khoa, W. von Oertzen, H.G. Bohlen, F.Nuoffer, Nucl. Phys. A 672 (2000).

DFT study of lithium adsorption on α-CsPbBr3 2D perovskite (Paper ID : 1645)

Nazari, Safieh*, Babaei Bidmeshki, Nadia

Physics and Accelerators School, Nuclear Science and Technology Research Institute, Atomic Energy Organization of Iran, Tehran, Iran

Abstract

Inorganic hybrid perovskites have demonstrated versatile functionalities for optoelectronic, spintronic, scintillators for X- and gamma-ray detection and other applications. In this study using the density functional theory (DFT) and first principle calculation the effect of lithium adsorption on the band structure of α-CsPbBr3 2D perovskite has been investigated. Our results show that the presence of lithium leads to breaking the inversion symmetry. Lack of inversion symmetry gives rise to band splitting, in other words, degeneracy removal of spin bands. Removing degenerate energy bands leads to converting a direct-to-indirect band gap transition, and consequently reducing the rate of recombination of the charge carriers. According to the results, the band splitting parameters and the effective mass of the charge carriers in the valence band maximum are almost equal. While in the conduction band minimum, values of the band splitting and the effective mass of the charge carriers depend completely on the termination type and adsorption site.

Keywords: DFT, two-dimensional perovskite, lithium adsorption, band splitting, the effective mass.

INTRODUCTION

The last decade has witnessed a rapid surge of interest in developing hybrid organic/inorganic perovskites

(HOPs). Tremendous research efforts on the compositional design and mechanisms behind the efficient operation of these materials extended new horizons in photovoltaics, optoelectronics, field-effect transistors, memristors, and other potential applications[1-2]. In terms of crystal structure, perovskites can be categorized as three-dimensional (3D) and two-dimensional (2D). The first category has a higher light yield and faster decay than the second category, due to its higher exciton binding energy (hundreds of meV compared to tens of meV). According to the reported experimental results, doping could be a useful approach to modify or boost some scintillator performance [3]. Li dopant has been reported for modification of optical properties [4] and reduction of nonradiative loss in perovskite exciton recombination [5]. It will be of interest to combine the merits of 2D perovskite and Li dopant to develop low-cost X-/gamma-

ray scintillators with extra thermal neutron detection capability, and investigate the properties changes or develop new scintillator behaviors [6-7].

Despite great experimental successes on Li doping in 2D crystals, however, computation of Li interaction energetics with 2D materials and predicting other properties require ab initio methods such as density functional theory (DFT).

From a theoretical point of view, structural asymmetry plays a central role in the appearance of spin polarization. This asymmetry can be rooted in the external field, interfacial built-in field, and geometrical distortion [8].

Li adsorption significantly affects the electronic structure of the systems, in particular SOC-induced band splitting. In this regard, in the current study, the effect of Li adsorption on some of the electronic properties in the presence of spin-orbit coupling (SOC) is explored.

COMPUTATIONAL METHODS

All calculations were carried out using the Quantum-ESPRESSO DFT package with the Perdew-Burke-Ernzerhof (PBE) version of Generalized Gradient Approximation (GGA). The electronic wave functions are expanded onto a plane-wave basis set with the kinetic energy cut-off of 35 Ry. Fully relativistic pseudopotentials are used for Pb 5d6s6p, I 5s5p, and Cs 6s. The CsBr-terminated and $PbBr_2$-terminated slabs are considered in (001) about 18 (Å) vacuum between consecutive images to model perovskite surfaces. The 6 × 6 × 1 Monkhorst-Pack grids are used for Brillouin-zone (BZ) sampling. The atomic positions are relaxed until the residual forces on each atom become less than 0.001 Ry/Bohr.

RESULTS AND DISCUSSION

In the presence of spin-orbit coupling (SOC), the system Hamiltonian at the first approximation can be written as [9]:

$$H = \frac{P^2}{2m} + V + H_{SOC}$$
$$H_{SOC} = 4) \quad \frac{\hbar^2}{4m^2c^2}(\nabla V \times \mathbf{p}).\boldsymbol{\sigma} \qquad (1)$$

where V and p, **σ** stand for the lattice periodic crystal potential, the momentum operator, and Pauli matrix vectors respectively. In nonmagnetic systems lacking inversion symmetry can cause the band splitting of the degenerate bands in such a way that the degenerate spin band splits into two spin-up and spin-down and shifts toward opposite directions in k space. In this case, at the close vicinity of the valence band maximum (VBM) and conduction band minimum (CBM), the eigenvalues of H can be expressed by:

$$E = \frac{\hbar^2 k^2}{2m} \pm \alpha |\vec{k}_m| \qquad (2)$$

As shown in Fig. 1, $\vec{k}_m$ is the displacement of high-symmetry k-point, and α is the band-splitting coefficient directly related to the lattice potential gradient. These coefficients can be calculated by the below relation:

$$\alpha = \frac{E_0}{2|\vec{k}_m|} \qquad (3)$$

where E_0 is the energy splitting.

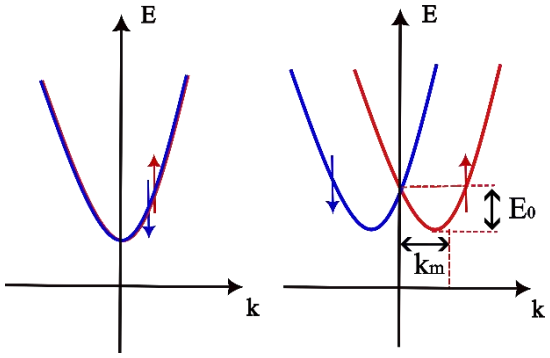

Fig 12: Spin-up (red) and spin-down (blue) branches are depicted after band splitting.

The α-$CsPbBr_3$ phase of perovskite has Pm-3m (No.221) space group with five atoms in the primitive unit cell. Cs, Pb, and Br atoms are set up in Wyckoff positions, a, b, c, and m-3 m, m-3m, and 4/mm,m site symmetries, respectively. Truncation of the bulk structure perpendicular to the c-axis with two possible CsBr-and $PbBr_2$ terminations yields two 2D slabs with a P4mm (No.99) space group. If we look at the (100) surface, several sites with special symmetry are intuitively appealing as potential binding sites for Li. These are illustrated in Fig. 2.

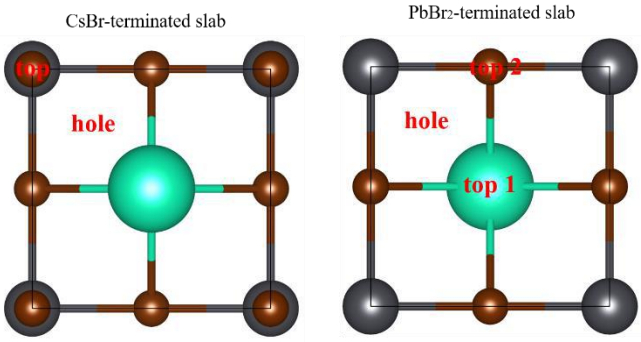

Figure 13: Illustration of potential high symmetry binding sites of Li on the CsBr-and PbBr2 terminated slabs.

To investigate the best site for lithium adsorption, Li adsorption energies at different sites are calculated by the below equation[10]:

$$E_{ad} = \frac{1}{N_{Li}}(E_{slab-Li} - E_{slab} - E_{Li}) \quad (4)$$

Here, the three terms on the right are the total energy of the surface with Li adsorbed on it, the total energy of a single Li atom by itself in the gas phase, and the total energy of the bare surface.

Table 1: adsorption energies of Li on the CsBr-and PbBr2 terminated slabs

case	CsBr-hole	CsBr-top	$PbBr_2$-hole	$PbBr_2$-top1	$PbBr_2$-top2
E_{ad} (eV)	-1.42	-1.41	-2.78	-1.83	-2.71

As indicated in Table 1, the adsorption of Li atoms at the hole and top2 sites on the $PbBr_2$ terminated slab is found to be more energetically favorable than other sites. When the Li atom is put on the hole site of the $PbBr_2$-terminated slab, during relaxation Li approaches the top2 site, for this reason, the binding energy in the two sites is almost the same. A similar situation occurs when the Li atom is put on the hole site of the CsBr-terminated slab also in this case Li atom approaches the top site. Although each of these pairs of sites has the same behavior in terms of absorption energy, the influence of Li adsorption on other electronic properties such as the band structure is not similar. In this regard, in the next step, the effect of Li adsorption in different sites on the band structure was explored.

In absent Li, both of the two terminations have the direct band gap. However, after Li adsorption due to breaking inversion symmetry, the degenerate spin bands of the spin-up and

spin-down in VBM and CBM shift toward the opposite direction. In other words, one can find that the direct-to-indirect band gap transition has occurred, which can be an important factor in the reduced rate of charge-carriers recombination.

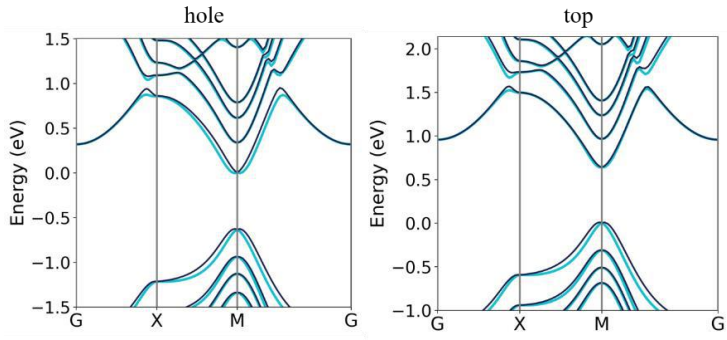

Figure 14: Band structure of the CsBr-terminated slab after Li adsorption on hole-site (left) and top-site (right).

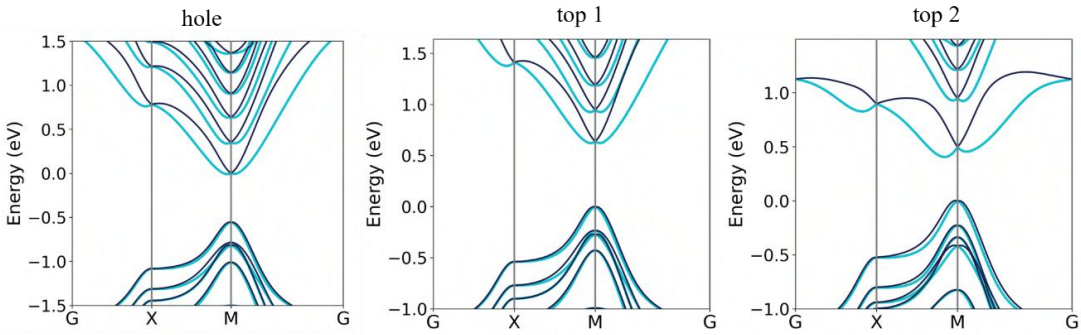

Figure 15: Band structure of the $PbBr_2$-terminated slab after Li adsorption on hole-site (left) , top1-site (middle), and top2-site (right).

On this point to characterize the extent of the splitting, the band-splitting coefficients were calculated, and the band structures of the two terminations are shown in Fig. 3 and 4. As depicted in these figures, the band spitting coefficient depends on the type of termination and adsorption sites.

The main other factor that can extracted from the band structure is the effective mass of the charge carriers (electrons and holes) that depend on the curvature of the energy band in VBM and CBM. This quantity indicates the difference in the electron-hole mobility and thus their recombination rate. The effective mass of the charge carriers is obtained by fitting the actual E-k diagram around VBM or CBM by a parabola. The splitting coefficients and effective masses for Li adsorption sites are given in Table 2.

Table 2: the band-splitting coefficient for VBM (α_v) and CBM (α_c) and the effective mass of the charge carriers for the CsBr- and $PbBr_2$ terminated slabs.

case	CsBr-hole	CsBr-top	$PbBr_2$-hole	$PbBr_2$-top1	$PbBr_2$-top2
α_v	0.11	0.21	0.11	0.11	0.11
α_c	0.21	0.11	0.28	0.28	0.74
m_v	0.53	0.53	0.52	0.52	0.56
m_c	0.52	0.52	0.57	0.79	1.25

The results indicate that the band-splitting does not follow an identical behavior, and rather it depends on the site symmetry of Li adsorption and the type of termination. The behavior of the energy band for the CsBr-terminated slab is almost similar, while the argument about the $PbBr_2$-terminated slab is completely different. As shown in Fig. 4, in VBM all of the sites have a similar band dispersion, however, the band splitting of CBM depends on the adsorption site. The most splitting relates to the top2 site, and the least spitting comes from the hole site. These results can be attributed to the different reductions of the system symmetries in various adsorption sites.

Conclusions

The last decade has seen explosive growth in developing halide perovskites (HPs). Substantial research efforts on the compositional design and mechanisms behind the efficient operation of these materials extended new horizons in photovoltaics, optoelectronics, field-effect transistors, memristors, and X-/gamma-ray scintillators. According to the reported experimental results, doping could be a useful approach to modify or boost some scintillator performance. Li dopant has been reported for modification of optical properties and reduction of nonradiative loss in perovskite exciton recombination. This study was designed to characterize the electronic structure and spin properties of two terminations of the $CsPbBr_3$ perovskite slabs in the (001) direction after Li atom adsorption. Our results show that the presence of lithium leads to breaking the inversion symmetry. Lack of inversion symmetry gives rise to band splitting, and thus degeneracy removal of spin bands. The results show that depending on the absorption site the extent of the energy band is different and therefore it is expected that the recombination rate of charge carriers can be different. Also, these results show that the effective mass of the charge carriers (electrons and holes) depends on the type of termination and adsorption site.

References

[1] C. R. Kagan, D. B. Mitzi and C. D. Dimitrakopoulos, Science, 1999, 286, 945–947.

[2] G. Lin, Y. Lin, R. Cui, H. Huang, X. Guo, C. Li, J. Dong, X. Guo and B. Sun, Journal of Materials Chemistry C, 2015, 3, 10793–10798.

[3] Wei, H. et al. Dopant compensation in alloyed CH3NH3PbBr3-xClx perovskite single crystals for gamma-ray spectroscopy. Nat. Mater. 16, 826–833 (2017).

[4] Shakti, N., Devi, C., Patra, A. K., Gupta, P. S. & Kumar, S. Lithium doping and photoluminescence properties of ZnO nanorods. AIP Adv. 8, 015306 (2018).

[5] Fang, Z., He, H., Gan, L., Li, J. & Ye, Z. Understanding the role of lithium doping in reducing nonradiative loss in lead halide perovskites. Adv. Sci. 5, 1800736 (2018).

[6] Chica, Daniel G., et al. "Direct thermal neutron detection by the 2D semiconductor $^{6}LiInP_2Se_6$." Nature 577.7790 (2020): 346-349.

[7] Xie, Aozhen, et al. "Lithium-doped two-dimensional perovskite scintillator for wide-range radiation detection." Communications Materials 1.1 (2020): 37.

[8] Zhang, Xiuwen, et al. "Hidden spin polarization in inversion-symmetric bulk crystals." *Nature Physics* 10.5 (2014): 387-393.

[9] Kepenekian, Mikaël, et al. "Rashba and Dresselhaus effects in hybrid organic–inorganic perovskites: from basics to devices." ACS nano 9.12 (2015): 11557-11567.

[10] Dehnavi, N. Zare, and M. Payami. "First-principles study of the effects of gold adsorption on the Al (001) surface properties." International Journal of Modern Physics C 19.10 (2008): 1563-1579.

ICNST 2024
International Conference on Nuclear Science and Technology
6- 8 MAY 2024 | Isfahan, Iran

Systematic study of heavy ion fusion cross sections for colliding systems with the coupled channel formula for $800 \leq Z1Z2 \leq 1500$ (Paper ID : 1653)

R. Gharaei [1,2,5], E. Sarvari[3]

[1] *Department of Physics, Sciences Faculty, Hakim Sabzevari University, Sabzevar, Khorasan Razavi, Iran*
[2] *Department of Physics, Faculty of Science, Ferdowsi University of Mashhad, Mashhad, Iran*
[3] *Department of Physics, Science Faculty, Tarbiat Modares University, Tehran, Iran*

Abstract

Within the coupled channels (CC) model approach, we have conducted a comprehensive theoretical study to find the best proximity potentials for reproducing the fusion excitation functions in 20 asymmetric colliding systems with a compound mass between 800 and 1500, concentrating on sub-barrier energies. The study is particularly relevant for systems with a heavy mass. We choose four versions of the phenomenological proximity potentials - Prox. 77, Prox. 2010, Bass 80 and Zhang 2013 - to calculate the nucleus-nucleus potential. Under these circumstances, we compare fusion cross-sections derived from theoretical results with the corresponding experimental data for our chosen mass range. Comparing fusion cross sections by theoretical results and corresponding experimental data suggests the coupled-channel calculations with Bass 80 provide a more accurate description of fusion data at above- and below-barrier energies. Furthermore, this study includes an in-depth analysis of Zhang 2013 and Bass 80. When comparing the present data with considering CC effects, we observed that the behavior of these two models aligns well with the experimental data in the heavy mass range under study. Therefore, it can be anticipated that Zhang 2013 and Bass 80 will also exhibit a good agreement in the super-heavy mass ranges.

Keywords: Heavy-ion fusion reactions; Fusion excitation functions; Proximity-type potentials; Coupled-channel calculations

INTRODUCTION

Heavy-ion fusion, a highly intricate process involving the interaction of two atomic nuclei, has been the subject of rigorous research for over seven decades. Investigations into fusion processes, particularly at energies near and below the barrier [1-6], have enhanced our understanding of nuclear structure effects and facilitated the synthesis of super-heavy nuclei.

[5] e-mail; r.gharaei@hsu.ac.ir

From a theoretical perspective, the exploration of heavy-ion fusion has consistently presented many challenges. As proposed by [1], the one-dimensional barrier penetration model (1D-BPM) provides a comprehensive explanation for fusion reactions of heavy ions above the barrier. However, the most striking challenge is seen in low-energy heavy-ion fusion [7].

The excitation functions associated with heavy-ion fusion near and below the Coulomb barrier are significantly impacted by many factors. These encompass couplings to nuclear surface vibrations [8-9], static deformations [10-11], and nucleon transfer channels between the colliding nuclei [12-13].

Another factor to consider is the calculation of nucleus-nucleus interaction potential. The significance of this interaction potential in establishing the theoretical estimates of the cross-sections in heavy-ion fusion is universally recognized. Various microscopic and macroscopic approaches have been developed to ascertain this potential. These include the improved quantum molecular dynamic model [14-16], the double folding model [17], the time-dependent Hartree-Fock theory [18-19], and the Skyrme energy-density functional [20]. One popular form of nuclear potential is proximity formalism. This phenomenological potential is based on the proximity force theorem [21], characterized as the product of a geometrical factor and a universal function.

Over recent years, the original proximity potential (Prox. 77) [21] has undergone numerous modifications. But, even with the presence of different modified versions of Prox. 77, the crucial impacts of the nuclear structure have not been incorporated into their formulation. Given the coupled-channel calculations [22] and the efficacy of the proximity formalism, we introduce a comparative systematic analysis carried out on different versions of proximity potentials such as Prox. 77, Prox. 2010 [23], Bass 1980 (Bass 80) [24] and Zhang 2013 model [25]. Fusion reactions at energies near and below the Coulomb barrier are greatly influenced by the coupling of the relative motion of the colliding nuclei to several nuclear intrinsic motions. The standard theoretical approach to studying these effects involves numerically solving the coupled channel equations, incorporating all relevant channels. Previously, coupled channel calculations were often performed using the linear coupling approximation, expanding the coupling potential in terms of the deformation parameter and keeping only the linear term. However, it has been demonstrated that non-linear couplings have a significant influence on fusion barrier distributions, therefore the linear approximation is inadequate for comparison

with recent high-quality fusion cross-section data. Based on this the CCFULL program solves fusion cross sections and mean angular momenta of a compound nucleus by solving coupled-channels equations. It considers all-order couplings without just expanding the coupling potential. The program is accurate, accounts for finite intrinsic motion excitation energies, includes Coulomb excitations, and applies the incoming wave boundary condition inside the Coulomb barrier. So, in this study, the models included couplings to the low-lying 2^+ and 3^- states in targets and projectiles, executed using the CCFULL code [26] applied to various proximity potentials. We utilized these states that derived nuclear structure input for various nuclei and compared the cross sections achieved by implementing the fusion excitation functions with corresponding chosen proximity potentials. Furthermore, we focused on 20 symmetric colliding systems with a mass of 800 and 1500 as a heavy mass range.

The structure of this paper is arranged in the following manner. Sec. 2 provides an overview of the versions of proximity potentials considered in this study. In Sec. 3, we display the calculation results and discussion. Finally, the results are provided in Sec. 4.

RESEARCH THEORIES

The interaction potential between target and projectile nuclei is one of the most important factors in describing the fusion reactions. This potential generally consists of short-range nuclear attraction $V_N(r)$ and large-range coulomb repulsion $V_C(r)$. The proximity model is one of the practical types in the calculation of nuclear potential. So, in this section, we first illustrate our different proximity formalisms in 4 subsections and then follow our approach based on these potential models.

Proximity 1977 (Prox. 77)

According to the original version of proximity, when the surface of two interacting nuclei reaches a distance of 2-3 fm from each other, a force will appear between them, called the "proximity force" [21]. In 1977, a group of scientists used this theory to propose a model for calculating the potential of a nucleus; based on this theory, the interaction potential $V_N(r)$ between two surfaces can be written as

$$V_N(r) = 4\pi\bar{R}b\gamma\phi(\xi = r - C_1 - C_2) \quad \text{MeV} \tag{1}$$

Where, $\bar{R}$ and b are the reduced radius of the target and projectile system and the surface thickness, respectively. In addition, γ is the surface energy coefficient taken from the Lysekil mass formula (in $\frac{\text{MeV}}{\text{fm}^2}$) [27], which depends on the symmetry or asymmetry of the nuclei in terms of the number of protons and neutrons.

$$\gamma = \gamma_0 \left[1 - ks\left(\frac{N-Z}{N+Z}\right)^2\right] \tag{2}$$

In this formula, $A_s = \left(\frac{N-Z}{N+Z}\right)$ is called the asymmetry parameter, and the coefficients γ_0 and K_s are called surface energy constant and surface-asymmetry constant, which have the values of 0.9517 MeV/fm^2 and 1.7826, respectively.

Proximity 2010 (Prox. 2010)

By using a suitable set of γ_0 and K_s, Prox. 77 is modified. In this approach, the surface energy coefficient γ fitted with the value $\gamma_0 = 1{,}460734$ MeV/fm^{2}and $K_s = 4{,}0$ in nuclear macroscopic energy calculations. This model is referred to as Prox 2010, and the corresponding potential as $V_N^{Prox2010}(r)$.

Bass 1980 (Bass 80)

Bass 1980, introduced a nucleus-nucleus potential based on potential derived from the liquid-drop model and the geometric interpretation of the fusion data. The nuclear part of the interaction potential can be written as

$$V_N(r) = \frac{R_1 R_2}{R_1 + R_2}\Phi\,(s_0) \tag{3}$$

where $s = r - R_1 - R_2$. Here, the universal function $\Phi(s_0)$ has the following form

$$\Phi\,(s_0) = \left[0{,}033\,exp\left(\frac{S}{3{,}5}\right) + 0{,}007exp\left(\frac{S}{0{,}65}\right)\right]^{-1} \quad (4)$$

with central radius, R_i, as

$$\boldsymbol{R_i = R_S(1 - \left(\frac{0,98}{R_S^2}\right))} \qquad \boldsymbol{(i = 1\ 2)} \quad (5)$$

Zhang 2013

With the same V_N (r) introduced in Prox. 77, universal function for Zhang 2013 was parameterized with the following form

$$\Phi\,(\boldsymbol{s_0}) = \frac{\boldsymbol{P_1}}{\boldsymbol{1 + e^{\frac{s_0+P_2}{P_3}}}} \quad (6)$$

The parameters P_1, P_2, P_3 are -7.65, 1.02, and 0.89, respectively.

Results and discussion

A systematic comparative study was carried out on different versions of proximity formalism. This study involved 20 fusion reactions, with conditions $800 \leq Z_1Z_2 \leq 1500$. The $^{48}Ca+^{96}Zr$ is the lightest collision system, and the $^{30}Si+^{238}U$ is the heaviest. We employ the different versions of phenomenological proximity potentials to compute the interaction potentials. In addition, the effects of nuclear structure on the heavy-ion fusion process are applied. These include the coupling to the low-lying inelastic excitation 2^+ and 3^- for the target nuclei and 2^+ for the projectile nuclei. The program used for this aim is CCFULL, which considers the impact of a finite number of rotational and vibrational states in both interacting nuclei during the fusion process. The parameters used in the calculations of the fusion cross-sections are presented in Table 9.

Table 9. Coupled-channel (CC) computations for each chosen nucleus are carried out with the excitation energy values (E*(MeV)) and the appropriate deformation parameters (β^{λ}) for the low-lying 2^+ and 3^- states. These values have been derived from [28].

Nucleus	λ^{π}	E*(MeV)	β^{λ}	Nucleus	λ^{π}	E*(MeV)	β^{λ}
^{28}Si	2^+	1.779	0.4082	^{90}Zr	2^+	2.1863	0.211
	3^-	6.879	0.401		3^-	2.748	0.1569
^{30}Si	2^+	2.2353	0.3107	^{92}Mo	2^+	1.5095	0.1061
	3^-	5.488	0.277		3^-	2.85	0.166
^{36}S	2^+	3.2909	0.1569	^{100}Mo	2^+	0.5356	0.234
	3^-	4.193	0.376		3^-	1.908	0.218
^{40}Ca	2^+	3.9044	0.1069	^{124}Sn	2^+	1.1405	0.1027
	3^-	3.737	0.411		3^-	2.493	0.121
^{48}Ca	2^+	3.8317	0.1054	^{122}Sn	2^+	1.1405	0.1027
	3^-	4.507	0.23		3^-	2.493	0.121
^{58}Ni	2^+	1.4542	0.1768	^{204}Pb	2^+	0.8992	0.04078
	3^-	4.475	0.198		3^-	2.621	0.118
^{60}Ni	2^+	1.3325	0.2018	^{206}Pb	2^+	0.8031	0.03198
	3^-	4.04	0.209		3^-	2.648	0.116
^{64}Ni	2^+	1.3458	0.1702	^{208}Pb	2^+	4.0855	0.0541
	3^-	3.56	0.201		3^-	2.615	0.111
^{70}Ge	2^+	1.0395	0.2264	^{238}U	2^+	0.0449	0.2741
	3^-	2.561	0.274		3^-	0.732	0.084
^{74}Ge	2^+	0.5959	0.285				
	3^-	2.536	0.145				
^{76}Ge	2^+	0.5629	0.265				
	3^-	2.692	0.144				
^{86}Kr	2^+	1.5648	0.1347				
	3^-	3.099	0.149				

In Fig. 16, we present a comparison of the theoretical (solid-line) and experimental (solid circles) values of the fusion cross-sections. This comparison is made to enhance our understanding of how σ_{fus} behaves in relation to energy, based on the Coupled Channels (CC) model. Specifically, we examine this behavior as a function of the center-of-mass energy $E_{c,m,}$.

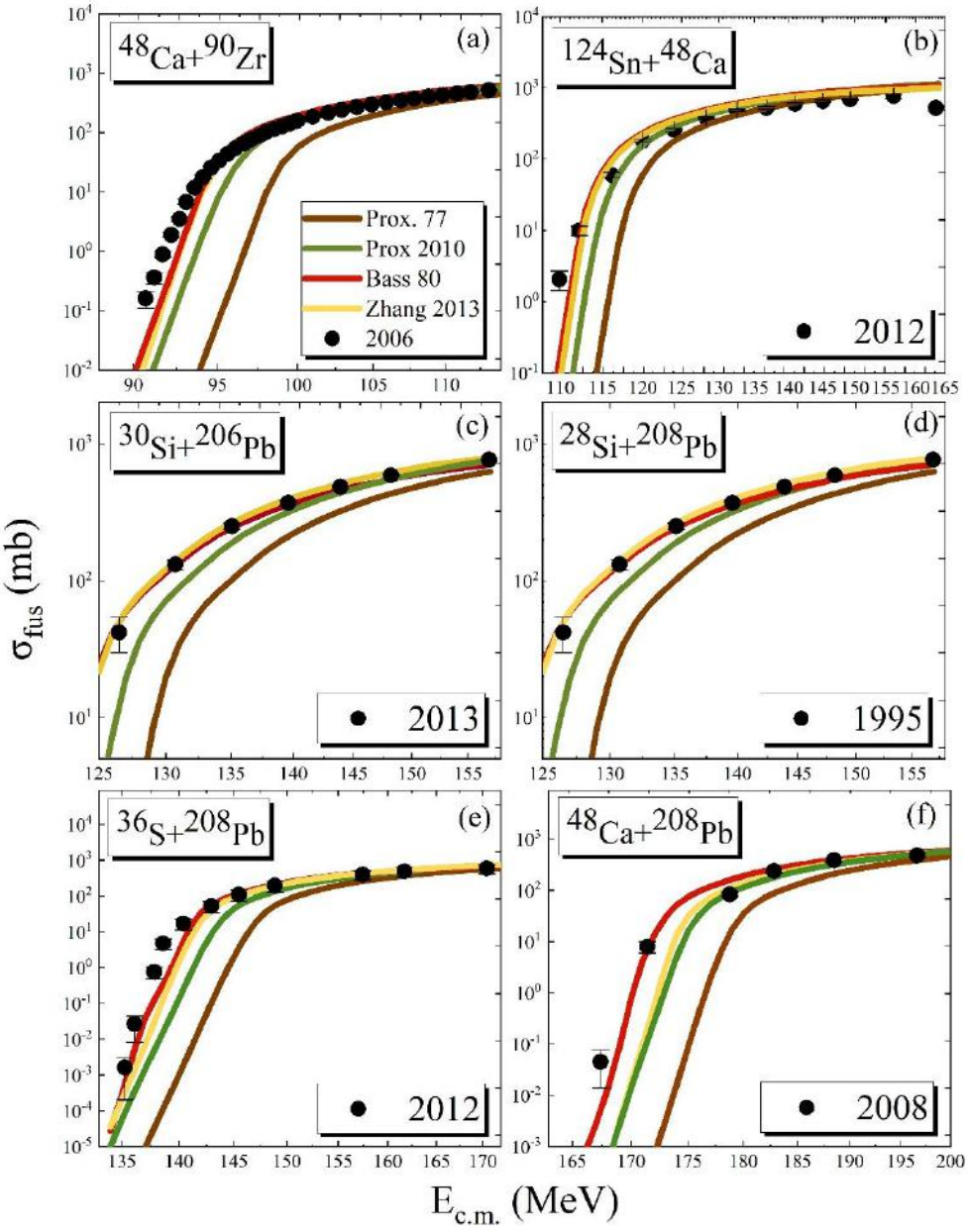

Fig. 16. Comparison between the calculated and experimental values of the fusion reactions (a) ^{48}Ca+ ^{90}Zr, (b) ^{124}Sn + ^{48}Ca, (c) ^{30}Si + ^{206}Pb, (d) ^{28}Si+^{208}Pb, (e) ^{36}S + ^{208}Pb, (f) ^{48}Ca + ^{208}Pb. The calculations are based on the Prox. 77, Prox 2010, Bass 80, and Zhang 2013 accompanied by the CC approach.

It is shown that Bass 80 and Zhang 2013 reproduce the experimental data well at energies below and above the Coulomb barrier for different heavy colliding systems. However, even when taking into account the fusion excitation functions, the original versions of Proximity Potential 1977 and Prox 2010 significantly underestimate the fusion cross section, particularly at sub-barrier energies.

While Zhang 2013 performs well, this study clearly shows that Bass 80 provides a more accurate representation of the theoretical fusion data within our selected heavy mass range. To gain a deeper understanding of these results, examining the deviation between the calculated fusion cross sections and their respective experimental data is beneficial. Its corresponding relation is

$$\chi^2 = \frac{1}{n}\sum_{i=1}^{n}\left(\frac{\sigma_i^{exp}(E_{c,m,}) - \sigma_i^{th}(E_{c,m,})}{\sigma_i^{exp}(E_{c,m,}) + \sigma_i^{th}(E_{c,m,})}\right)^2 \quad (7)$$

where n refers to the number of experimental data for each of the considered reactions. Notably, the calculations of this quantity were performed in the entire range of bombarding energies.

The relative errors, represented as $\boldsymbol{\chi^2}$ are calculated for each reaction and displayed in Fig. 17.

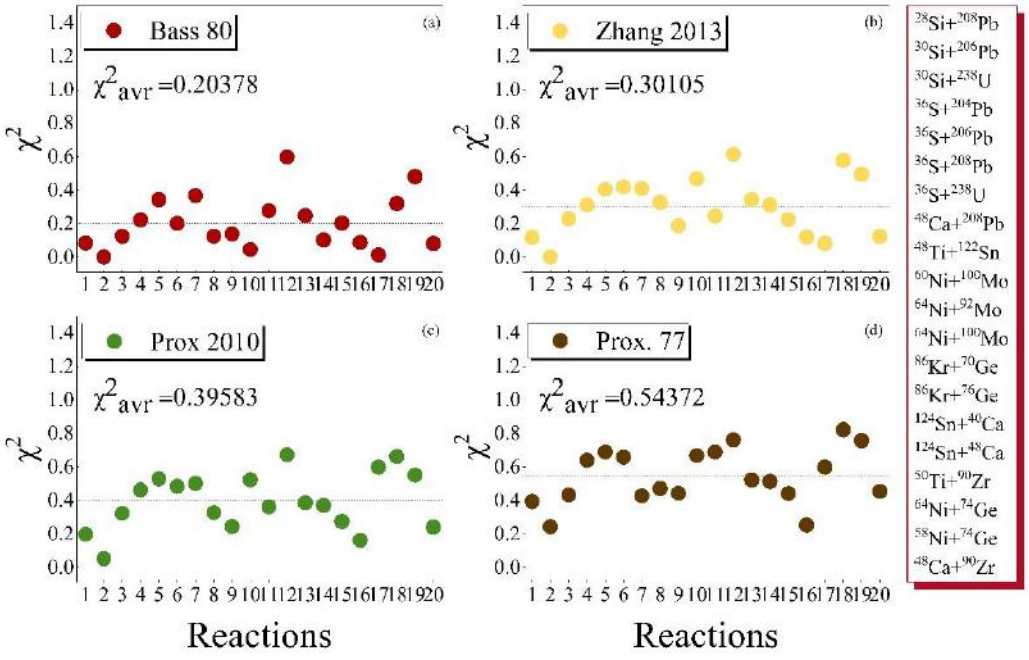

Fig. 17. Distributions of the relative error χ^2 values computed for each reaction using the proximity potentials including (a) Bass 80, (b) Zhang 2013, (c) Prox. 2010 and (d) Prox. 77 models. Average χ^2 are listed for each panel.

Our analysis reveals that, based on the Bass 80 potential model, the $\boldsymbol{\chi^2}$ values are less than 0.2 for ٦٠% of the fusion reactions in the heavy mass range. It is important to note that studies conducted on the analysis of nuclear radial behavior and total potentials using various proximity potential versions highlight that the universal function is a key factor influencing the

differing behaviors of proximity models [29]. Also, the choice of parameters, such as the nuclear density, charge, and deformation parameters, can affect the cross-section results. Different models might use various sets of parameters, leading to differences in the calculated cross-sections

Results

This study carries out a systematic comparative analysis utilizing 4 versions of proximity potentials and all nuclei considered here are assumed to be spherical. The current analysis clearly shows which of the proximity versions is better able to accurately represent the fusion data in our chosen heavy mass range. Our comparison analysis indicates that the Bass 80 and Zhang 2013 models exhibit a better agreement with experimental data than others in the heavy and super-heavy mass ranges. These two proximity potentials are capable of explaining the fusion cross-section calculations with an average deviation error, χ^2, of less than 0.300. The least deviation is provided using the Bass 80 nuclear potential model. Bass 80 offers a comprehensive explanation of the fusion cross sections at below and above barrier energies, with an average deviation error of 0.203.

References

[1] Wong, C., (1973). Interaction barrier in charged-particle nuclear reactions. Physical Review Letters, 31(12), p.766.

[2] Rowley, N., Satchler, G.R. and Stelson, P.H., (1991). On the “distribution of barriers” interpretation of heavy-ion fusion. Physics Letters B, 254(1-2), pp.25-29.

[3] Puri, R.K. and Gupta, R.K., (1992). Fusion barriers using the energy-density formalism: Simple analytical formula and the calculation of fusion cross sections. *Physical Review C*, *45*(4), p.1837.

[4] Santhosh, K.P., Jose, V.B., Joseph, A. and Varier, K.M., (2009). Heavy-ion fusion cross sections and barrier distributions for 12C, 16O, 28Si and 35Cl on 92Zr. *Nuclear Physics A*, *817*(1-4), pp.35-44.

[5] Wang, N., Li, Z. and Scheid, W., (2007). Systematic study of fusion barriers. *Journal of Physics G: Nuclear and Particle Physics*, *34*(9), p.1935.

[6] Gharaei, R. and Farkhonde, M.S., (2023). Systematic study of the isotopic dependence of heavy-ion fusion cross sections at below-and above-barrier energies. *Physica Scripta*, *98*(8), p.085307.

[7] Beckerman, M., (1988). Sub-barrier fusion of two nuclei. *Reports on Progress in Physics*, *51*(8), p.1047.

[8] Stefanini, A.M., Fortuna, G., Tivelli, A., Meczynski, W., Beghini, S., Signorini, C., Lunardi, S. and Morando, M., (1984). Sub-barrier fusion of Si 2 8, 3 0 with Ni 5 8, 6 2, 6 4. *Physical Review C*, *30*(6), p.2088.

[9] Newton, J.O., Morton, C.R., Dasgupta, M., Leigh, J.R., Mein, J.C., Hinde, D.J., Timmers, H. and Hagino, K., (2001). Experimental barrier distributions for the fusion of 12 C, 16 O, 28 Si, and 35 Cl with 92 Zr and coupled-channels analyses. Physical Review C, 64(6), p.064608.

[10] Leigh, J.R., Dasgupta, M., Hinde, D.J., Mein, J.C., Morton, C.R., Lemmon, R.C., Lestone, J.P., Newton, J.O., Timmers, H., Wei, J.X. and Rowley, N., (1995). Barrier distributions from the fusion of oxygen ions with Sm 1 4 4, 1 4 8, 1 5 4 and W 186. Physical Review C, 52(6), p.3151.

[11] Bierman, J.D., Chan, P., Liang, J.F., Kelly, M.P., Sonzogni, A.A. and Vandenbosch, R., (1996). Experimental fusion barrier distributions reflecting projectile octupole state coupling to prolate and oblate target nuclei. Physical Review Letters, 76(10), p.1587.

[12] Baby, L.T., Tripathi, V., Kataria, D.O., Das, J.J., Sugathan, P., Madhavan, N., Sinha, A.K., Radhakrishna, M.C., Badiger, N.M., Puttaswamy, N.G. and Vinodkumar, A.M., (1997). Transfer and higher-order phonon coupling effects in the sub-barrier fusion of 28 Si and 93 Nb. Physical Review C, 56(4), p.1936.

[13] Zagrebaev, V.I., (2003). Sub-barrier fusion enhancement due to neutron transfer. Physical Review C, 67(6), p.061601.

[14] Aguiar, C.E., Barbosa, V.C., Canto, L.F. and Donangelo, R., (1987). Liquid-drop model description of heavy ion fusion at sub-barrier energies. Nuclear Physics A, 472(3), pp.571-590.

[15] Wang, N., Li, Z. and Wu, X., 2002. Improved quantum molecular dynamics model and its applications to fusion reaction near barrier. Physical Review C, 65(6), p.064608.

[16] Wang, N., Li, Z., Wu, X., Tian, J., Zhang, Y. and Liu, M., (2004). Further development of the improved quantum molecular dynamics model and its application to fusion reactions near the barrier. *Physical Review C*, *69*(3), p.034608.

[17] Satchler, G.R. and Love, W.G., (1972). Folding model potentials from realistic interactions for heavy-ion scattering. *Physics Reports*, *55*(3), pp.183-254.

[18] Negele, J.W., (1982). The mean-field theory of nuclear structure and dynamics. Reviews of Modern Physics, 54(4), p.913.

[19] Umar, A.S. and Oberacker, V.E., (2006). Heavy-ion interaction potential deduced from density-constrained time-dependent Hartree-Fock calculation. Physical Review C, 74(2), p.021601.

[20] Vautherin, D. and Brink, D.T., (1972). Hartree-Fock calculations with Skyrme's interaction. I. Spherical nuclei. *Physical Review C*, *5*(3), p.626.

[21] Błocki, J., Randrup, J., Światecki, W.J. and Tsang, C.F., (1977). Proximity forces. Annals of Physics, 105(2), pp.427-462.

[22] Dasso, C.H., Landowne, S. and Winther, A., (1983). Channel-coupling effects in heavy-ion fusion reactions. *Nuclear Physics A*, *405*(2), pp.381-396.

[23] Dutt, I. and Bansal, R., (2010). A modified proximity approach in the fusion of heavy ions. Chinese Physics Letters, 27(11), p.112402.

[24] Reisdorf, W., (1994). Heavy-ion reactions close to the Coulomb barrier. *Journal of Physics G: Nuclear and Particle Physics*, *20*(9), p.1297.

[25] Zhang, G.L., Zheng, H.B. and Qu, W.W., (2013). Study of the universal function of nuclear proximity potential between α and nuclei from density-dependent nucleon-nucleon interaction. *The European Physical Journal A*, *49*, pp.1-6.

[26] Hagino, K., Rowley, N. and Kruppa, A.T., (1999). A program for coupled-channel calculations with all order couplings for heavy-ion fusion reactions. Computer Physics Communications, 123(1-3), pp.143-152.

[27] Dutt, I. and Puri, R.K., (2010). Analytical parametrization of fusion barriers using proximity potentials. Physical Review C, 81(6), p.064608.

[28] Karpov, A.V., Denikin, A.S., Samarin, V.V., Naumenko, M.A., Alekseev, A.P., Rachkov, V.A., Saiko, V.V., Lekala, L.M. and Mukeru, B., (2018). NRV web knowledge base: Scientific and educational applications. In *CEUR Workshop Proceedings* (pp. 195-199).

[29] Gharaei, R., & Sarvari, E. (2024). Investigating the impact of the universal function of nuclear proximity potential in the heavy-ion fusion cross sections. Communications in Theoretical Physics.

.

[ii] Y. Yun, O. Eriksson and P. M. Oppeneer, J. Nucl. Mater. 385 (2009) 510.

[iii] Y. Yun, O. Eriksson and P. M. Oppeneer, J. Nucl. Mater. 385 (2009) 364.

[iv] K. Govers, S. E. Lemeov, and M. Verwerft, J. Nucl. Mater. 405 (2010)252.

[v] R. W. Grimes, in Fundamental Aspects of Inert Gases in Solids, edited by S. E. Donelly and J. H. Evans (Springer, New York, 1990), p.415.

[vi] A. E. Thompson, B. Meredig and C. Wolverton, J. Phys.: Condens. Matter 26 105501 (2014)

[vii] G. Amoretti, A. Blaise, R. Caciu_o, J. M. Fournier, M. T. Hutchings,R. Osborn, A. D. Taylor, Phys. Rev. B 40 (1989) 1856-1870.

[viii] J. Faber, G. H. Lander, B. R. Cooper, Phys. Rev. Lett. 35 (1975) 1770-1773

[ix]M. Idiri, T. Le Bihan, S. Heathman, J. Rebizant, Phys. Rev. B 70 (1) (2004) 014113.

[x] J. D. Gale, A. L. Rohl, Mol. Simul. 29 (2003) 291.

[xi] A. E. Thompson, B. Meredig, M. Stan, C. Wolverton, J. Nucl. Mater. 446 (2014) 155–162.

[xii] N.-D. Morelon, D. Ghaleb, J.-M. Delaye, and L. Van Brutzel, Philos. Mag. 83, 1533 (2003).

[xiii] A. Chartier, L. Van Brutzel and M. Freyss , Phys. Rev. B 81 174111 (2010).